JANUARY 2021

AJNR

VOLUME 42 • PP 1–211

AJNR
AMERICAN JOURNAL OF NEURORADIOLOGY

JANUARY 2021
VOLUME 42
NUMBER 1
WWW.AJNR.ORG

THE JOURNAL OF DIAGNOSTIC AND INTERVENTIONAL NEURORADIOLOGY

Artificial intelligence and acute stroke imaging
Acute ischemic stroke or epileptic seizure
Decubitus CT myelography for CSF-venous fistulas
Idiopathic neonatal subpial hemorrhage with infarct

Official Journal ASNR • ASFNR • ASHNR • ASPNR • ASSR

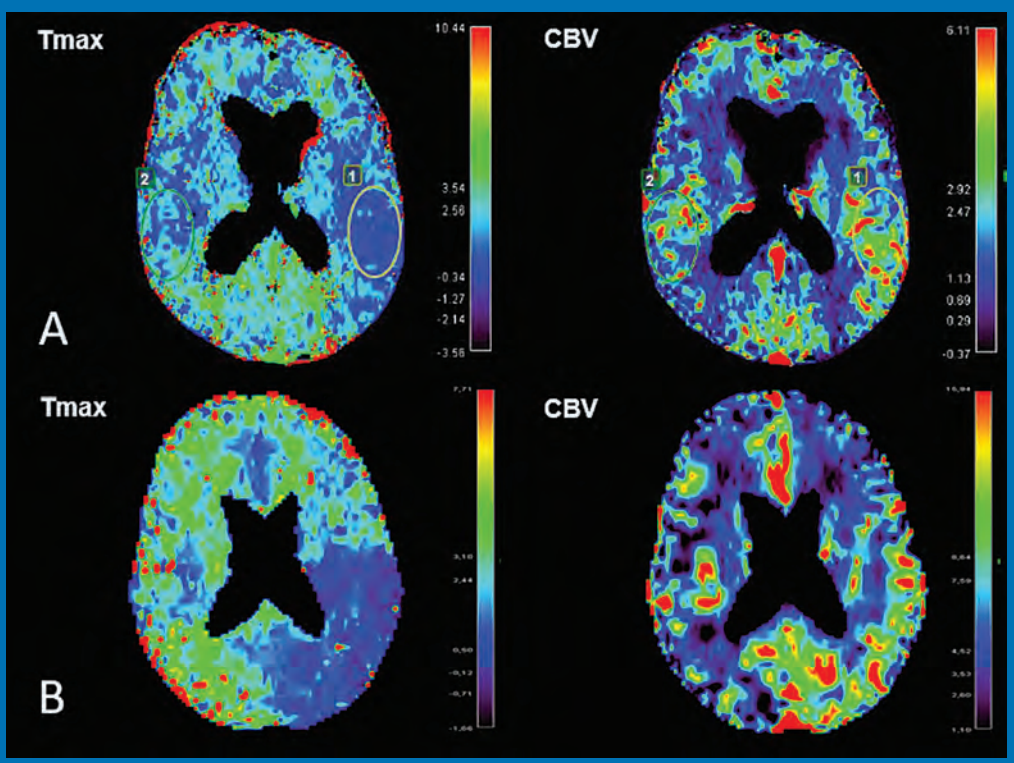

FRED™

Flow **R**e-**D**irection
Endoluminal **D**evice

FLOW DIVERSION.

SIMPLIFIED.

MicroVention™
TERUMO

MicroVention Worldwide Innovation Center
35 Enterprise
Aliso Viejo, CA 92656 USA
PH +1 714.247.8000

MicroVention UK Limted
PH +1 44 (0) 191 258 6777

MicroVention Europe S.A.R.L.
PH +33 (1) 39 21 77 46

MicroVention Deutschland GmbH
PH +49 211 210 798-0

Web
microvention.com

The New Standard of **Ease and Simplicity** in Flow Diversion Treatment.

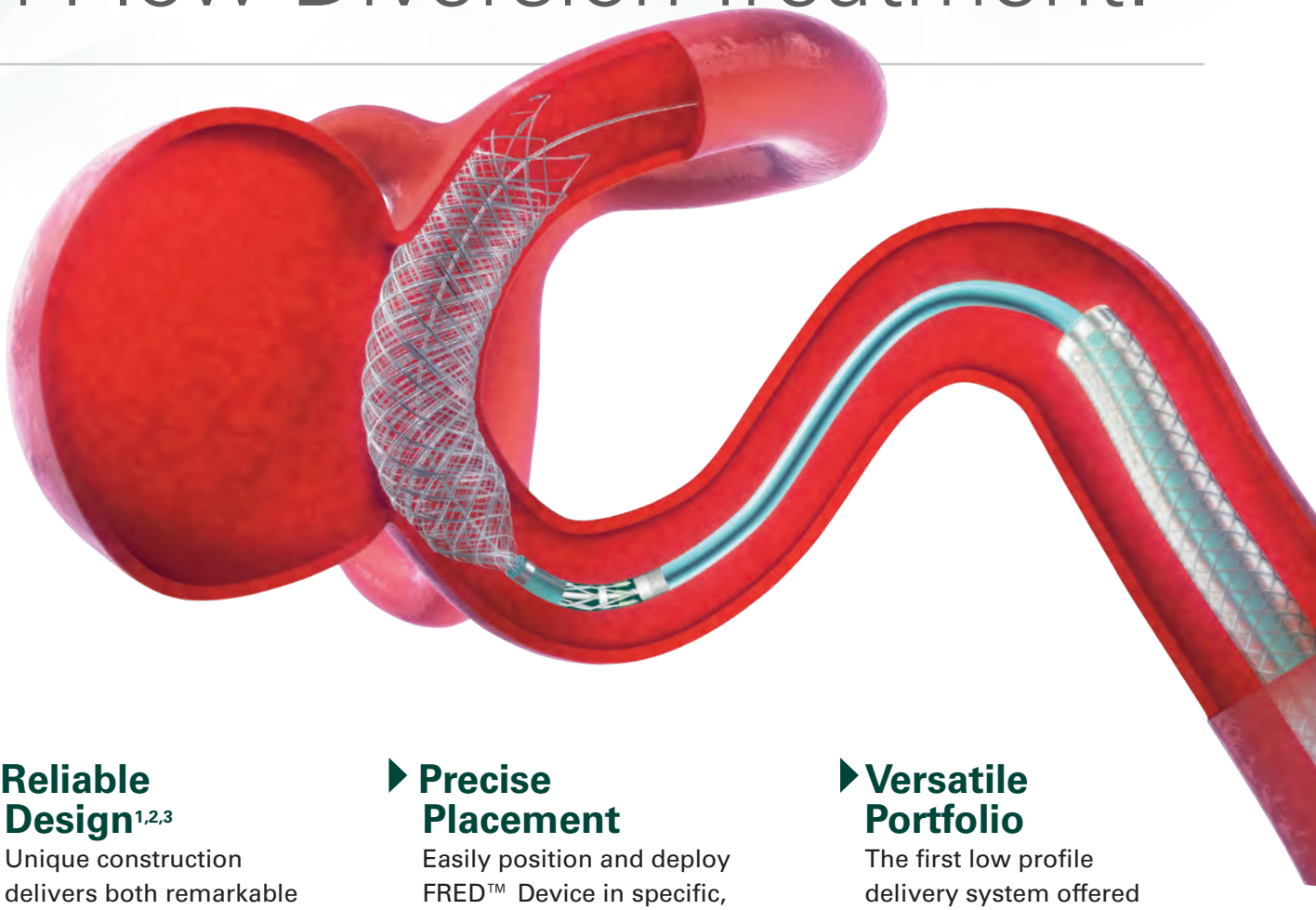

Reliable Design[1,2,3]

Unique construction delivers both remarkable ease of use and excellent flow diversion[1,2,3]

Precise Placement

Easily position and deploy FRED™ Device in specific, targeted locations[4,5,6]

Versatile Portfolio

The first low profile delivery system offered in combination with large diameter and long length options

References:
1. TR11-211 2. TR13-171 3. TR15-055 4. TR13-192 5. TR15-072 6. TR19-145

The Flow Re-Direction Endoluminal Device (FRED™) System is indicated for use in the internal carotid artery from the petrous segment to the terminus for the endovascular treatment of adult patients (22 years of age or older) with wide-necked (neck width ≥ 4 mm or dome-to-neck ratio < 2) saccular or fusiform intracranial aneurysms arising from a parent vessel with a diameter ≥ 2.0 mm and ≤ 5.0 mm.

Use of the FRED™ System is contraindicated under these circumstances: Patients in whom anticoagulant, anti-platelet therapy, or thrombolytic drugs are contraindicated. Patients with known hypersensitivity to metal such as nickel-titanium and metal jewelry. Patients with anatomy that does not permit passage or deployment of the FRED™ System. Patients with an active bacterial infection. Patients with a pre-existing stent in place at the target aneurysm. Patients in whom the parent vessel size does not fall within the indicated range. Patients who have not received dual anti-platelet agents prior to the procedure. For complete indications, contraindications, potential complications, warnings, precautions, and instructions, see instructions for use (IFU provided in the device).

RX Only: Federal (United States) law restricts this device to sale by or on the order of a physician.

Simplify
the MOC Process

Manage
your CME Credits Online

CMEgateway.org

Available to Members of Participating Societies

- American Board of Radiology (ABR)
- American College of Radiology (ACR)
- American Roentgen Ray Society (ARRS)
- American Society of Neuroradiology (ASNR)
- Commnission on Accreditation of Medical Physics Educational Programs, Inc. (CAMPEP)
- Radiological Society of North America (RSNA)
- Society of Interventional Radiology (SIR)
- SNM
- The Society for Pediatric Radiology (SPR)

It's Easy and Free!

Log on to CME Gateway to:

- View or print reports of your CME credits from multiple societies from a single access point.
- Print an aggregated report or certificate from each participating organization.
- Link to SAMs and other tools to help with maintenance of certification.

American Board of Radiology (ABR) participation!

By activating ABR in your organizational profile, your MOC–fulfilling CME and SAM credits can be transferred to your own personalized database on the ABR Web site.

Sign Up Today!

go to CMEgateway.org

AJNR

AMERICAN JOURNAL OF NEURORADIOLOGY

JANUARY 2021
VOLUME 42
NUMBER 1
WWW.AJNR.ORG

Publication Preview at www.ajnr.org features articles released in advance of print. Visit www.ajnrblog.org to comment on AJNR content and chat with colleagues and AJNR's News Digest at http://ajnrdigest.org to read the stories behind the latest research in neuroimaging.

AJNR (Am J Neuroradiol ISSN 0195–6108) is a journal published monthly, owned and published by the American Society of Neuroradiology (ASNR), 800 Enterprise Drive, Suite 205, Oak Brook, IL 60523. Annual dues for the ASNR include approximately 21% for a journal subscription. The journal is printed by Intellicor Communications, 330 Eden Road, Lancaster, PA 17601; Periodicals postage paid at Oak Brook, IL and additional mailing offices. Printed in the U.S.A. POSTMASTER: Please send address changes to American Journal of Neuroradiology, P.O. Box 3000, Denville, NJ 07834, U.S.A. Subscription rates: nonmember $410 ($480 foreign) print and online, $320 online only; institutions $470 ($540 foreign) print and basic online, $935 ($1000 foreign) print and extended online, $380 online only (basic), $825 online only (extended); single copies are $35 each ($40 foreign). Indexed by PubMed/MEDLINE, BIOSIS Previews, Current Contents (Clinical Medicine and Life Sciences), EMBASE, Google Scholar, HighWire Press, Q-Sensei, RefSeek, Science Citation Index, SCI Expanded, Meta/CZI, ReadCube, and Semantic Scholar.

BOOK REVIEWS *R.M. Quencer, Section Editor*

Please visit www.ajnrblog.org to read and comment on Book Reviews.

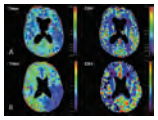

From Lucas, et al.: CTP images showing examples of hyperperfusion respecting (*A*) or not (*B*) a vascular territory (the left posterior cerebral artery was exclusively from the basilar artery) in the seizure group.

AJNR

AMERICAN JOURNAL OF NEURORADIOLOGY

Publication Preview at www.ajnr.org features articles released in advance of print. Visit www.ajnrblog.org to comment on AJNR content and chat with colleagues and AJNR's News Digest at http://ajnrdigest.org to read the stories behind the latest research in neuroimaging.

JANUARY 2021 • VOLUME 42 • NUMBER 1 • WWW.AJNR.ORG

We're Inside Every Great Neuroradiologist!

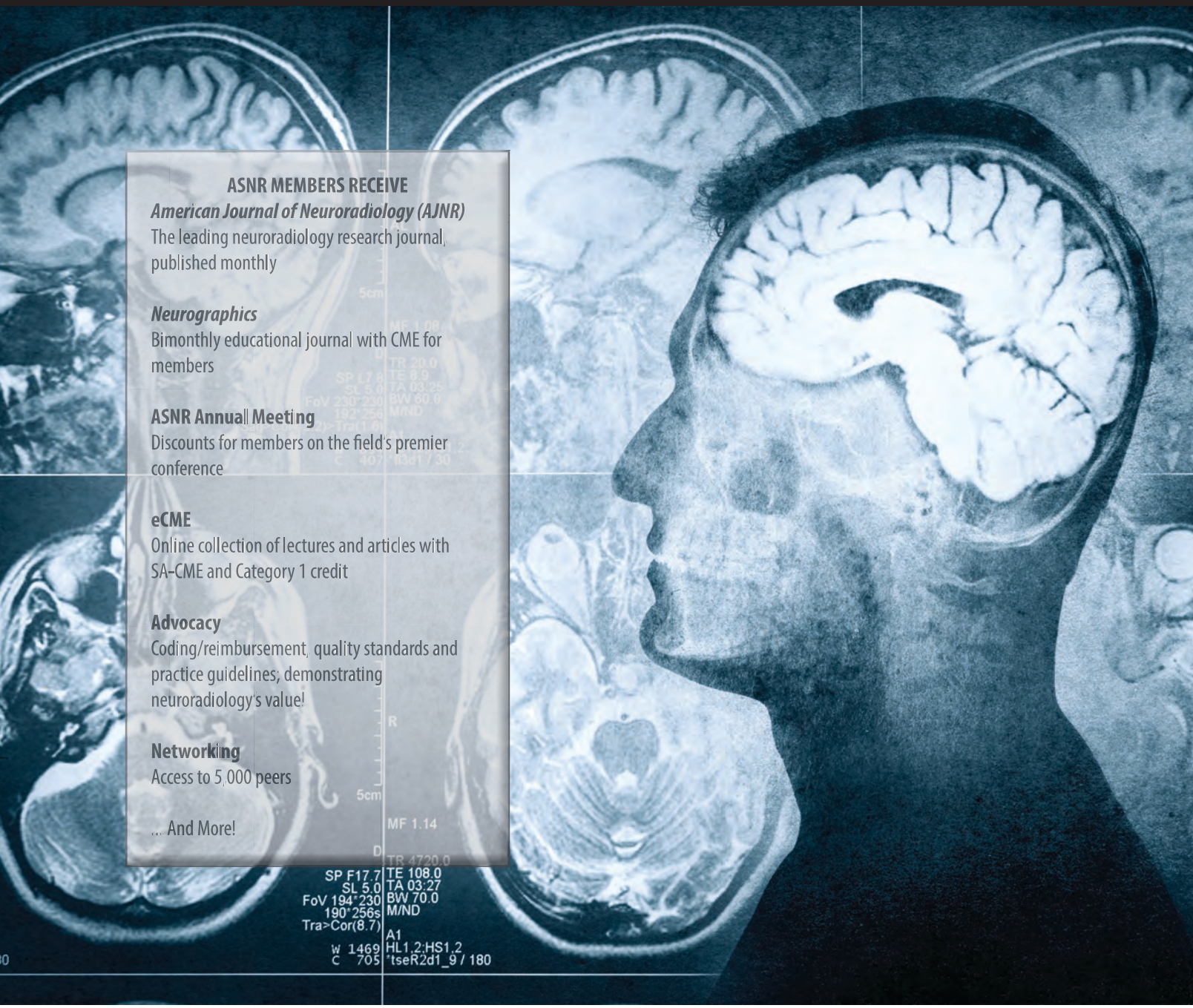

Join the leaders in neuroradiology today!
Learn more at www.asnr.org/join

ASNR
American Society of Neuroradiology

800 Enterprise Dr., Suite 205, Oak Brook, IL 60523 • (630)574-0220 • membership@asnr.org • www.asnr.org

AJNR go green

AJNR urges American Society of Neuroradiology members to reduce their environmental footprint by voluntarily suspending their print subscription.

The savings in paper, printing, transportation, and postage directly fund new electronic enhancements and expanded content.

The digital edition of *AJNR* presents the print version in its entirety, along with extra features including:

- **Publication Preview**
- **Case Collection**
- **Podcasts**
- **The *AJNR* News Digest**
- **The *AJNR* Blog**

It also reaches subscribers much faster than print. An electronic table of contents will be sent directly to your mailbox to notify you as soon as it publishes.

Readers can search, reference, and bookmark current and archived content 24 hours a day on www.ajnr.org.

ASNR members who wish to opt out of print can do so by using the AJNR Go Green link on the *AJNR* Website (http://www.ajnr.org/content/subscriber-help-and-services). Just type your name in the email form to stop print and spare our ecosystem.

AJNR
AMERICAN JOURNAL OF NEURORADIOLOGY

CALL FOR AJNR EDITORIAL FELLOWSHIP CANDIDATES

2021 Candidate Information and Requirements

ASNR and AJNR are pleased once again to join efforts with other imaging-related journals that have training programs on editorial aspects of publishing for trainees or junior staff (<5 years on staff), including Radiology (Olmsted fellowship), AJR (Figley and Rogers fellowships), JACR (Bruce J. Hillman fellowship), and Radiologia.

GOALS

- Increase interest in editorial and publication-related activities in younger individuals.
- Increase understanding and participation in the AJNR review process.
- Incorporate into AJNR's Editorial Board younger individuals who have previous experience in the review and publication process.
- Fill a specific need in neuroradiology not offered by other similar fellowships.
- Increase the relationship between "new" generation of neuroradiologists and more established individuals.
- Increase visibility of AJNR among younger neuroradiologists.

ACTIVITIES OF THE FELLOWSHIP

- Serve as Editorial Fellow for one year. This individual will be listed on the masthead as such.
- Review at least one manuscript per month for 12 months. Evaluate all review articles submitted to AJNR.
- Learn how electronic manuscript review systems work.
- Be involved in the final decision of selected manuscripts together with the Editor-in-Chief.
- Participate in all monthly Senior Editor telephone conference calls.
- Participate in all meetings of the Editors during the annual meetings of ASNR and RSNA and the Radiology Editors Forum as per candidate's availability. The Foundation of the ASNR will provide $2000 funding for this activity.
- Evaluate progress and adjust program to specific needs in annual meeting or telephone conference with the Editor-in-Chief.
- Embark on an editorial scientific or bibliometric project that will lead to the submission of an article to AJNR or another appropriate journal as determined by the Editor-in-Chief. This project will be presented by the Editorial Fellow at the ASNR annual meeting.
- Recruit trainees as reviewers as determined by the Editor-in-Chief.
- Organize and host a Fellows' Journal Club podcast.
- Serve as Guest Editor for an issue of AJNR's News Digest with a timely topic.

QUALIFICATIONS

- Be a fellow in neuroradiology from North America, including Canada (this may be extended to include other countries).
- Be a junior faculty neuroradiology member (< 5 years) in either an academic or private environment.
- Be an "in-training" or member of ASNR in any other category.

APPLICATION

- Include a short letter of intent with statement of goals and desired research project. CV must be included.
- Include a letter of recommendation from the Division Chief or fellowship program director. A statement of protected time to perform the functions outlined is desirable.
- Applications will be evaluated by AJNR's Senior Editors prior to the ASNR annual meeting. The name of the selected individual will be announced at the meeting.
- Applications should be received by March 1, 2021 and sent to Ms. Karen Halm, AJNR Managing Editor, electronically at khalm@asnr.org.

Title: Solomon R. Guggenheim Museum. The Guggenheim, originally commissioned in 1943, took Frank Lloyd Wright 16 years to complete. Just like the Eiffel Tower in its day, it was initially subject to vitriolic criticism, being seen, even by some avant-garde artists, as a traumatic, even barbaric, disruption to the morphology and mood of the neighborhood. It was derisively referred to as a washing machine, an inverted oatmeal bowl, and a hot cross bun, comments that are more understandable from an exterior perspective. In addition to jolting the neighborhood, it jolted traditions of art museum interiors and corresponding viewer experiences by replacing typical box-like rooms with linear and orthogonal doorways and passages, with a single continuous spiral ramp curving upwards to a glass dome. Some find the layout promotes a dream-like state, while others feel a sense of disequilibrium. It certainly provides a novel experience of seeing where you were, where you are, and where you are going all at once. Wright advised students to "study nature, love nature, stay close to nature. It will never fail you." It is claimed that the spiral shell of the nautilus was one of his inspirations for the Guggenheim.

Manfred Hauben, MD, MPH, Pfizer Inc and NYU Langone Health, New York City

Artificial Intelligence and Acute Stroke Imaging

J.E. Soun, D.S. Chow, M. Nagamine, R.S. Takhtawala, C.G. Filippi, W. Yu, and P.D. Chang

ABSTRACT

SUMMARY: Artificial intelligence technology is a rapidly expanding field with many applications in acute stroke imaging, including ischemic and hemorrhage subtypes. Early identification of acute stroke is critical for initiating prompt intervention to reduce morbidity and mortality. Artificial intelligence can help with various aspects of the stroke treatment paradigm, including infarct or hemorrhage detection, segmentation, classification, large vessel occlusion detection, Alberta Stroke Program Early CT Score grading, and prognostication. In particular, emerging artificial intelligence techniques such as convolutional neural networks show promise in performing these imaging-based tasks efficiently and accurately. The purpose of this review is twofold: first, to describe AI methods and available public and commercial platforms in stroke imaging, and second, to summarize the literature of current artificial intelligence–driven applications for acute stroke triage, surveillance, and prediction.

ABBREVIATIONS: AI = artificial intelligence; ANN = artificial neural network; AUC = area under the curve; CNN = convolutional neural network; DL = deep learning; ICC = intraclass correlation coefficient; ICH = intracranial hemorrhage; LVO = large vessel occlusion; ML = machine learning; MRP = MR perfusion; RF = random forest; SVM = support vector machine

Stroke is the second leading cause of death worldwide with an annual mortality of about 5.5 million.[1,2] In the United States, nearly 800,000 people have a stroke annually, and the economic burden of stroke is estimated at $34 billion per year.[3] Morbidity is high, with more than half of patients with stroke left chronically disabled.[2] Neuroimaging is an important tool for the detection, characterization, and prognostication of acute strokes, including ischemic and hemorrhagic subtypes. Artificial intelligence (AI) technology is a rapidly burgeoning field, providing a promising avenue for fast and efficient imaging analysis.[4] AI applications for imaging of acute cerebrovascular disease have been implemented, including tools for triage, quantification, surveillance, and prediction. This review aims to summarize the current landscape of AI-driven applications for acute cerebrovascular disease assessment focusing primarily on deep learning (DL) methods.

Received April 30, 2020; accepted after revision July 22.

From the Departments of Radiological Sciences (J.E.S., D.S.C., P.D.C.) and Neurology (M.N., W.Y.), Center for Artificial Intelligence in Diagnostic Medicine (D.S.C., R.S.T., P.D.C.), University of California, Irvine, Orange, California, and the Department of Radiology (C.G.F.), Northwell Health, Lenox Hill Hospital, New York, New York.

Please address correspondence to Daniel S. Chow, MD, Department of Radiological Sciences, UC Irvine Health, Douglas Hospital, Route 140, Rm 0115, Orange, CA 92868; e-mail: chowd3@hs.uci.edu; @TheCAIDM

Indicates open access to non-subscribers at www.ajnr.org

Indicates article with supplemental on-line tables.

http://dx.doi.org/10.3174/ajnr.A6883

OVERVIEW OF AI

Although AI, machine learning (ML), and DL are used interchangeably, these in fact represent subdisciplines. Specifically, DL is a subset of ML, and ML is a subset of AI (Fig 1). Broadly, AI uses computers to perform tasks that typically require human knowledge. ML, a subset of AI, uses statistical approaches to enable machines to optimize outcome prediction as they are exposed to data and train computers for pattern recognition, a task generally requiring human intelligence.[5] ML offers several potential advantages over visual inspection by human experts, including objective and quantitative evaluation, the ability to detect subtle voxel-level patterns, speed, and large-scale implementation. Feature selection, classifier type, and DL are key considerations for the application of ML techniques to imaging.

Feature Selection

Just as a radiologist summarizes an image with a few key descriptors (eg, hemorrhage volume), ML algorithms attempt to do the same with a matrix of voxels. Different feature selection methods can identify a subset of variables to develop a predictive model. Selecting relevant features is important for the explainability, speed, and cost efficiency of a model and to avoid overfitting.[6]

Classifier Type

After each image is converted into numeric descriptors, a method is chosen to leverage this information to predict 1 of multiple potential classes. For certain cases, even very simple models such

as basic logistic or linear regression could be effective.[7] However, if nonindependent, nonlinear relationships are expected between the various chosen features, a more complex model is required. Many such ML classifiers exist, and the most popular include random forest (RF), support vector machine (SVM), k-nearest neighbor clustering, and neural networks.[8] In general, these techniques are modeled by an underlying finite number of adjustable parameters. As a given set of features is passed through the model, these adjustable parameters act to convert the input descriptors into a predicted output class. Starting with randomly initialized parameters, a series of iterative updates is performed until an accurate mapping between numeric features and correct class is achieved, thus "training" the ML model.[9]

Deep Learning

DL through neural networks is distinguished by the ability to independently learn abstract, high-order features from data without requiring feature selection. Artificial neural networks (ANNs) are a subtype of DL that mimic biologic neurons and are composed of an input, 1 or more hidden layers, and an output. Generally, in computer vision, convolutional neural networks (CNNs) are most successful and popular for image classification in medical imaging. CNNs represent all recent winning entries within the annual ImageNet Classification challenge, consisting of more than 1 million photographs in 1000 object categories, with a 3.6% classification error rate.[10,11] CNNs are distinguished from traditional ML approaches by automatically identifying patterns in complex imaging datasets, thus combining both feature selection and classification into 1 algorithm and removing the need for direct human interaction during the training process. Recent advances in CNNs have achieved human accuracy in identification of everyday objects such as cats and dogs, which had previously been impossible to model using rigid mathematical formulas.[12] CNNs have already shown promise in the detection of pulmonary nodules,[13] colon cancer,[14] and cerebral microbleeds.[15]

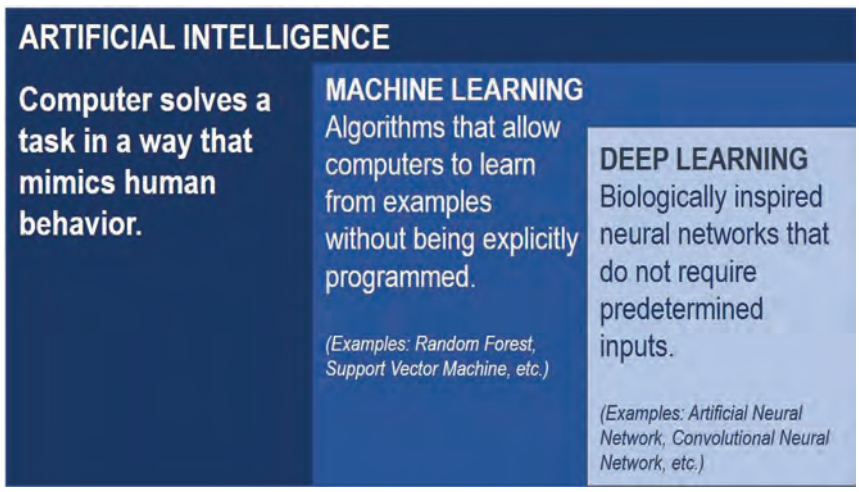

FIG 1. AI uses computers to mimic human intelligence. ML is a subset of AI, and DL is a subset of ML.

EVALUATION OF AI PERFORMANCE

Table 1 details performance metrics and limitations of AI methods.

Accuracy

It is imperative that evaluation of ML models assess the accuracy of algorithms. Often, when testing large numbers of potential features, a few numeric descriptors meet the threshold for statistical significance between 2 target classes. However, *P* values are more often a reflection of the underlying power (sample size) of an experiment and may or may not relate to the clinical significance of the identified difference in features. As a result, it is critical not only to prove that a difference in features exists but also to assess the sensitivity, specificity, and accuracy of the feature(s) to predict a given end point. For classification, receiver operating characteristic curves can evaluate a model's performance, with the area under the curve (AUC) representing an aggregate measure for performance across all possible classification thresholds of a receiver operating characteristic curve. For segmentation analysis, Dice similarity coefficients and Pearson correlation coefficients are typically used. The Dice score measures the spatial overlap between the manually segmented and neural network-derived segmentations. Dice scores range from 0 (no overlap) to 1 (perfect overlap) and are commonly used to evaluate segmentation performance.[16]

Limitations

ML and DL approaches have limitations that should be considered. First, the development of algorithms requires data sets that are large, organized, well-classified, and accurate. Interpretability is challenging, especially for DL algorithms. To mitigate this "black box"

Table 1: Machine learning performance metrics and limitations

Performance metrics	Classification	Sensitivity (recall): TP/(TP + FN)
		Specificity (true-negative rate): TN/(TN + FP)
		Accuracy: number of correct predictions/total predictions
		AUC: plot of true positive rate (sensitivity) against false positive rate (1 – specificity)
	Segmentation	Dice similarity coefficient: overlap of 2 samples
		Pearson correlation coefficient: strength of linear relationship between 2 variables
Limitations and ways to address them	Requires large datasets: multisite collaboration, open-source datasets	
	Interpretability: saliency maps	
	Overfitting: more training data, regularization, and batch normalization	

Note:—FP indicates false positive; FN, false-negative; ROC, receiver operating characteristic; TN, true-negative; TP, true positive.

Table 2: Open-source datasets for stroke and hemorrhage

Dataset	Cerebrovascular Disease	Annotated Data	Number of Scans	Imaging Technique
Anatomical Tracings of Lesions After Stroke (ATLAS)[19]	Subacute or chronic ischemic strokes	Manually segmented stroke lesions	304	T1-weighted MR imaging
CQ500[20]	Hemorrhage	Hemorrhage, subtype, location, and associated hemorrhage findings	491	CT
RSNA Brain Hemorrhage CT Dataset[21]	Hemorrhage	Hemorrhage, subtypes	874,035	CT
Ischemic Stroke Lesion Segmentation (ISLES) 2016–2017[22]	Ischemic stroke	Perfusion and diffusion MR imaging of patients with stroke and clinical outcomes	35 training and 19 testing (2016); 43 training and 32 testing (2017)	MR imaging, MRP
ISLES 2018[23]	Ischemic stroke	CT and perfusion of patients with stroke	94 labeled training images and 62 unlabeled testing images	CT, CTP

Note:—MRP indicates MR perfusion.

Table 3: Commercially available software platforms and their applications[a]

Software	Applications	Machine Learning Algorithm	Imaging Technique
Aidoc	ICH: identifies ICH, triage, and notification	DL	CT
	LVO: identifies LVO, triage, and notification	DL	CTA
	CTP: orchestration of third-party perfusion results	Other	CTP
Avicenna.AI	CINA ICH: identifies ICH, triage, and notification	DL	CT
	CINA LVO: identifies LVO, triage, and notification	DL	CTA
	CINA ASPECTS: ASPECTS scoring; provides heat map	DL	CT
Brainomix	e-Blood: identifies and quantifies ICH volume with mask overlay	DL	CT
	e-ASPECTS: identifies ASPECTS, voxelwise map of early ischemic change, and core infarct volume	Predominantly ML	CT
	e-CTA: identifies and notifies LVO, collateral score, and collateral vessel attenuation; voxelwise map of collateral deficit	Combination of DL and traditional ML	CTA
	e-ASPECTS HDVS: identifies and measures hyperattenuated vessel	DL	CT
	e-Mismatch: identifies mismatch on CTP and MR imaging	Deconvolution	CTP, MR imaging, MRP
RapidAI	Rapid ICH: identifies and classifies ICH	DL	CT
	Rapid ASPECTS: identifies ASPECTS, measurement, and scoring	RF	CT
	Rapid CTA: identifies and notifies LVO and collateral vessel attenuation	Other	CTA
	Rapid CTP: identifies mismatch on CTP, collateral maps, and scoring	Other	CTP
	Rapid MR: identifies mismatch on MR, collateral maps, and scoring	Other	MR imaging, MRP
Viz.ai	Viz ICH: identifies and triages ICH	DL	CT
	Viz LVO: identifies and triages LVO	DL	CTA
	Viz CTP: automated perfusion color maps and calculations	DL	CTP

Note:—HDVS indicates hyperattenuated vessel sign.

[a] Some, but not all, of these products have FDA, European, and/or worldwide regulatory clearance at the time of publication.

effect, explainable AI models incorporate tools such as saliency maps. Overfitting is a limitation for ML, when a model mistakenly learns the "noise" instead of the "signal" in a training dataset and thus does poorly with unseen data and is limited in generalizability.[17] More training data, regularization, and batch normalization are ways to mitigate overfitting. Differences in image acquisition and data storage among institutions and difficulties in sharing data are obstacles to collecting enough data to obtain useful models. Standardization of imaging methods and open-source data collection can address this issue. Additionally, several proprietary ML software platforms have recently been introduced in the market that incorporate various aspects of the stroke pathway into their algorithms; however, comparison and validation of their performance are still necessary to ensure their robustness in routine use.[18] Despite limitations, ML remains a powerful tool for detection and management of stroke and hemorrhage.

AI PLATFORMS IN STROKE AND HEMORRHAGE

Open-Source Datasets

Large datasets are required for ML algorithms to perform optimally. However, the availability of high-quality large-scale data remains a challenge given barriers in data sharing across institutions, the complexity of building imaging processing pipelines, and the time and cost of data annotation. To address these challenges, many publicly available imaging datasets are now available for ML in stroke (Table 2).[19-24] These datasets are valuable because they are already anonymized, postprocessed, and annotated, and they can be used for testing and comparing algorithms in diagnosing ischemic stroke and hemorrhage. Many of these datasets are initiated as AI challenges such as the RSNA (Radiology Society of North America) Head CT Challenge for Hemorrhage, ASFNR (American Society of Functional Neuroradiology) Head CT Challenge for Ischemic and Hemorrhagic Stroke, and ISLES

FIG 2. Aidoc stroke triage mobile interface. From *left* to *right*, a notification alert, a study list of cases, NCCT of an acute stroke, CTA of an LVO of the right MCA, CTP mean transit time in the right MCA territory, and a text messaging system. *Images courtesy of Aidoc*.

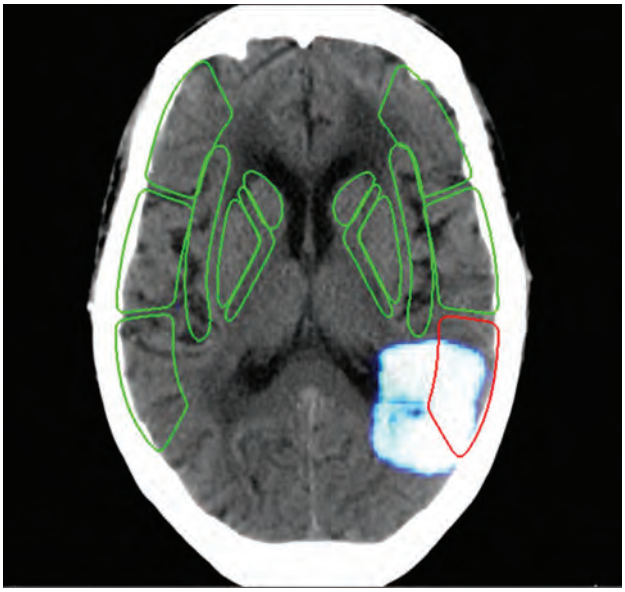

FIG 3. Avicenna.AI DL-based ASPECTS tool demonstrating identification of ASPECTS and a heat map overlay (white). *Image courtesy of Avicenna.AI*.

(Ischemic Stroke Lesion Segmentation) Challenge for Ischemic Stroke, supporting worldwide collaboration and new algorithm development.

Commercially Available Software Platforms

Increasingly, commercially available platforms providing automated information about various components of the acute stroke triage pathway are being integrated into routine clinical practice and clinical trials.[25-28] These tools offer fast and efficient analyses that seek to optimize the delivery of stroke care at spoke and hub hospitals and reduce turnaround times in the clinical workflow.[29] Table 3 lists some of the most popular commercially available stroke platforms and highlights their capabilities and AI-based algorithms. Figs 2–6 show the various web and mobile interfaces of these software platforms.

AI EVALUATION OF ISCHEMIC STROKE

Online Tables 1–4 provide an overview of the AI-based models of evaluating ischemic stroke discussed in this section, including detection and core infarct segmentation, identification of large-vessel occlusion (LVO), Alberta Stroke Program Early CT Score (ASPECTS) grading and additional factors in treatment selection, and prognostication.

Detection Methods

Rapid detection of ischemic infarction is important for triaging patients as potential candidates for thrombolysis because of the narrow window of therapeutic efficacy. Several studies have used ML algorithms for identification of ischemic infarction on CT or MR imaging.

Tang et al[30] developed a computer-automated detection (CAD) scheme using a circular adaptive region of interest (CAROI) method on noncontrast head CT to detect subtle changes in attenuation in patients with ischemic stroke. They found that CAD improved detection of stroke for emergency physicians and radiology residents (AUC of 0.879 improved to 0.942 for emergency physicians and AUC of 0.965 improved to 0.990 for radiology residents) but did not improve significantly detection for experienced radiologists who already had high stroke detection rates.[30] Another study showed that an ANN was able to distinguish acute stroke from stroke mimics within 4.5 hours of onset (which was verified by clinical and CT and MR imaging data), with a mean sensitivity of 80.0% and specificity of 86.2%.[31]

Core Infarct Volume Segmentation

Establishing infarct volumes is important to triage patients for appropriate therapy. AI has been able to establish core infarct volumes on DWI through automatic lesion segmentation. For example, 1 study used an ensemble of 2 CNNs to segment DWI lesions of any size and remove false positives.[32] This combined CNN approach had a Dice score of 0.61 for small lesions (<37 pixel size) and 0.83 for large lesions and outperformed other CNNs.[32] Guerrero et al[33] developed a CNN (uResNet) that segmented and differentiated white matter hyperintensities (WMHs) caused by chronic small-vessel disease from cortically or subcortically based strokes. The uResNet CNN mean Dice scores were 0.7 for white matter hyperintensities and 0.4 for strokes.[33] The uResNet slightly outperformed the DeepMedic CNN in distinguishing white matter hyperintensities and strokes compared with expert analysis (R^2 values 0.951 and 0.791 for white matter hyperintensities and strokes, respectively, using uResNet and 0.942 and 0.688 using DeepMedic).[33] One limitation of the study was the reliance on FLAIR and T1 images that do not fully account for

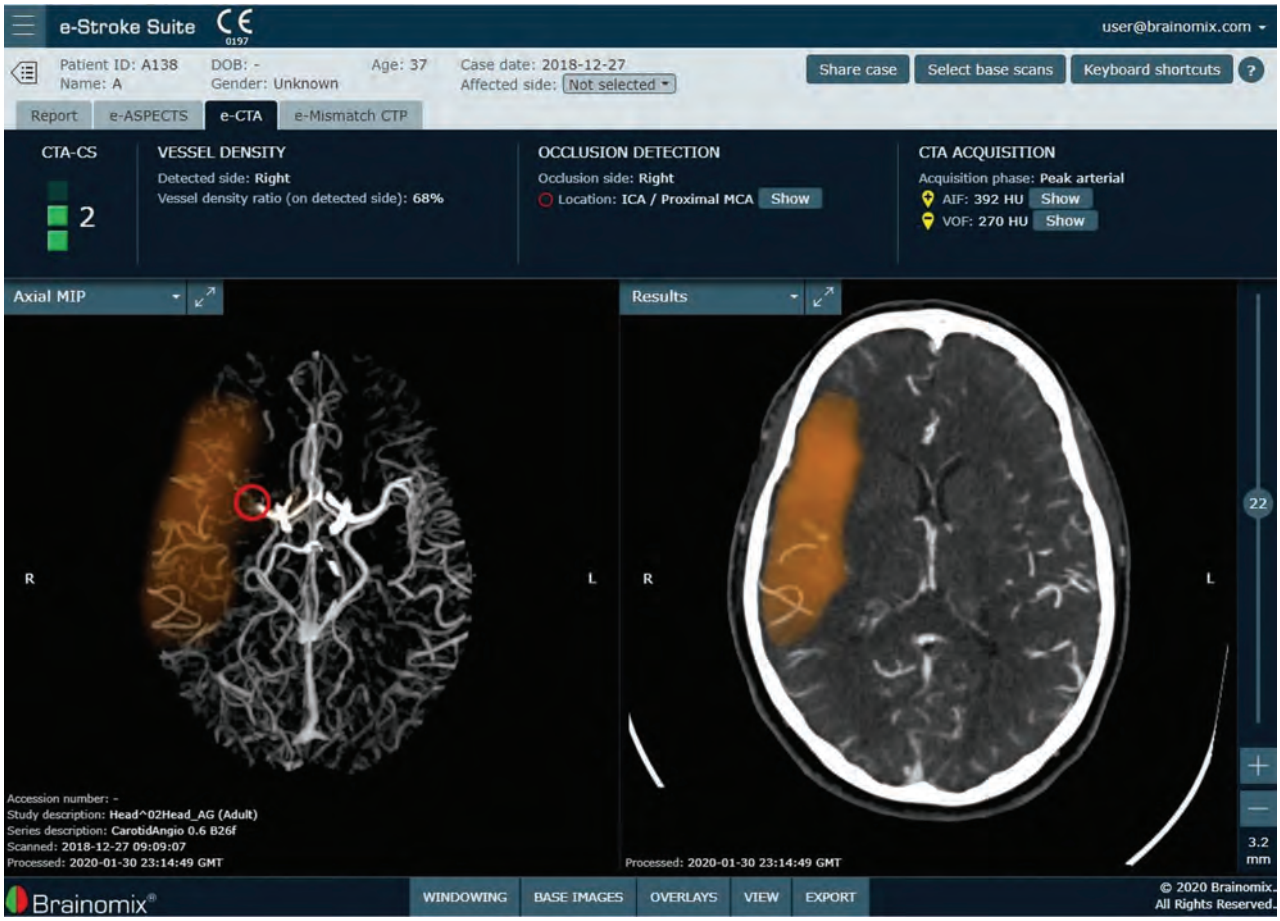

FIG 4. Brainomix e-CTA tool demonstrating identification and localization of an LVO of the right MCA, collateral score and collateral vessel attenuation, and a heat map of the collateral deficit (*orange*). *Images courtesy of Brainomix*.

FIG 5. The RapidAI stroke triage or transfer mobile interface, which integrates the hub and spoke model. From *left* to *right*, ICH and ASPECTS scoring and alerts on NCCT, LVO detection on CTA, perfusion mismatch on MR imaging or CTP with FDA mechanical thrombectomy indication, and a mobile communication platform with "GO" notification system for rapid treatment decision making. *Images courtesy of RapidAI*.

timing of stroke occurrence, and the value of uResNet in detection of acute strokes needs evaluation. The first study to use a DL approach on CTA source images to detect acute middle cerebral artery ischemic stroke, a 3D CNN (DeepMedic), performed with a sensitivity of 0.93, specificity of 0.82, AUC of 0.93, and Dice score of 0.61.[34] Specificity was maximized when the contralateral cerebral hemisphere on CTA was included, and a marginal reduction in false positives was seen when NCCT was included in the algorithm.[34] Limitations of this CNN were its tendency to overestimate the volume of small infarcts and underestimate large infarcts compared with manual segmentation by expert radiologists and difficulty in distinguishing old versus new strokes.[34]

FIG 6. Viz.ai mobile interface showing a left MCA territory infarction with mismatch on CTP. *Image courtesy of* Viz.*ai*.

The largest cohort using CTP for core infarct determination based on an ANN was able to accurately identify core infarct volume (AUC = 0.85; sensitivity = 0.9; specificity = 0.62) and was not significantly different from a model incorporating clinical data (AUC = 0.87; sensitivity = 0.91; specificity = 0.65).[35] Although the study minimized the time between CTP and MR imaging DWI reference standard acquisition, any time delay between the CTP and MR imaging may have limited accurate core infarct determination because of core expansion or reversal. A model incorporating a U-net architecture CNN and RF classifier segmented acute ischemic stroke on NCCT with high concordance with manually segmented DWI core volumes ($r = 0.76$, $P < .001$) and manually segmented DWI ASPECTS scores ($r = -0.65$, $P < .001$). Furthermore, the agreement approached significance when dichotomizing infarcts using a volume threshold of 70 mL (McNemar test, $P = .11$). Discrepancies in volumes were attributed to nondetectable early ischemic findings, partial volume averaging, and stroke mimics on CT.[36]

Large Vessel Occlusion

Diagnosing LVO is essential for identifying candidates who could potentially benefit from mechanical thrombectomy. On NCCT, an SVM algorithm detected the MCA dot sign in patients with acute stroke with high sensitivity (97.5%).[37] A neural network that incorporated various demographic, imaging, and clinical variables in predicting LVO outperformed or equaled most other prehospital prediction scales with an accuracy of 0.820.[38] A CNN-based commercial software, Viz-AI-Algorithm v3.04, detected proximal LVO with an accuracy of 86%, sensitivity of 90.1%, specificity of 82.5, AUC of 86.3% (95% CI, 0.83–0.90; $P \leq .001$), and intraclass correlation coefficient (ICC) of 84.1% (95% CI, 0.81–0.86; $P \leq .001$), and Viz-AI-Algorithm v4.1.2 was able to detect LVO with high sensitivity and specificity (82% and 94%, respectively).[39,40] No study has yet shown whether AI methods can accurately identify other potentially treatable lesions such as M2, intracranial ICA, and posterior circulation occlusions.

ASPECTS Grading

ASPECTS is a widely used clinical grading system for assessing extent of early ischemic stroke on NCCT and has been used in randomized clinical trials to select thrombectomy candidates.[26,41,42] However, grading can be challenging, and interobserver agreement is variable. One commercial software platform with automated ASPECTS scoring (e-ASPECTS, Brainomix) performed as well as neuroradiologists when scoring ASPECTS on NCCT in patients with acute stroke ($P < .003$).[43] However, e-ASPECTS did not perform as well as neuroradiologists when scoring ASPECTS in patients with acute stroke with baseline non–normal-appearing CT (eg, leukoencephalopathy, old infarcts, or other parenchymal defects), demonstrating a correlation coefficient of 0.59 versus 0.71–0.80 for experts.[44] One study found that an automated ASPECTS detection algorithm on NCCT using texture feature extraction to train a RF classifier generated ASPECTS values that had high agreement with expert-generated DWI ASPECTS scores (ICC = 0.76 and $\kappa = 0.6$ when used for all 10 ASPECTS regions).[45]

Another commercial software platform with automated ASPECTS scoring (Rapid ASPECTS, version 4.9; iSchemaView) showed higher agreement with a consensus ASPECTS grade that takes into account follow-up DWI ($\kappa = 0.9$) compared with neuroradiologists' moderate agreement ($\kappa = 0.56$–0.57), and the software performed well in the immediate time interval 1 hour after stroke onset ($\kappa = 0.78$) and even better 4 hours after stroke onset ($\kappa = 0.92$).[46] This platform had better agreement of ASPECTS grading with DWI infarct volume in patients with large hemispheric infarct compared with experienced readers (median DWI ASPECTS, 3 [IQR, 2–4]; Rapid ASPECTS, 3 [1–6]; and CT ASPECTS for the clinicians, 5 [4–7].[47]

Additional Factors in Treatment Selection

Various factors, including collaterals, penumbra, and stroke onset time, are important for evaluating potentially salvageable tissue

and determining treatment eligibility. An automated commercial software program (e-CTA; Brainomix) combining deep and traditional ML techniques for CTA collateral status determination improved consensus scoring among expert neuroradiologists compared with visual inspection alone, with an ICC of 0.58 (0.46–0.67) improving to 0.77 (0.66–0.85; $P = .003$).[48] Penumbra prediction on a noncontrast MR imaging pseudocontinuous arterial spin labeling technique using a DL model performed well (AUC = 0.958).[49] This algorithm outperformed traditional ML algorithms and was able to predict endovascular treatment eligibility based on DEFUSE 3 (Endovascular Therapy Following Imaging Evaluation for Ischemic Stroke) trial criteria. Another study evaluating various traditional ML models in predicting stroke onset time demonstrated that incorporation of DL features to the models improved AUC compared with the ground truth (ie, a DWI–FLAIR mismatch), with the optimal AUC of 0.765 incorporating logistic regression and DL features of MR imaging and MR perfusion (MRP) images.[50] Lee et al[51] used DWI–FLAIR mismatch to predict stroke onset time <4.5 hours and found that traditional ML models were more sensitive than stroke neurologists (sensitivity = 48.5% for stroke neurologists vs 75.8% for logistic regression; $P = .020$; 72.7% for SVM, $P = .033$; 75.8% for RF, $P = .013$).

Prognostication

Various ML algorithms have been used to predict imaging and clinical outcomes after ischemic stroke. An early classical ML study found that a generalized linear model combining DWI and perfusion-weighted imaging MR images was better than DWI ($P = .02$) or PWI ($P = .04$) alone at predicting voxelwise tissue outcomes.[52] A CNN-based patch sampling of the Tmax feature on MRP outperformed a single voxel-based regression model in predicting final infarct volume, with a mean accuracy of 85.3 ± 9.1% compared with 78.3 ± 5.5%, respectively.[53] Another CNN performed better than other ML methods in predicting final infarct volume by incorporating MR imaging DWI, MRP, and FLAIR data, with an AUC of 0.88 ± 0.12.[54] This CNN could predict tissue fate based on whether intravenous tissue plasminogen activator was administered, showing significantly different final infarct volumes ($P = .048$).[54] A CNN based on MRP source images was able to predict final infarct volume with an AUC of 0.871 ± 0.024.[55] A multicenter study showed that an attention-gated U-Net DL algorithm with DWI and MRP as inputs could predict final infarct volume regardless of reperfusion status, with a median AUC of 0.92 (IQR, 0.87–0.96) and significant overlap with the ground truth of a FLAIR sequence obtained 3–7 days after baseline presentation (Dice score, 0.53; IQR, 0.31–0.68).[56]

The e-ASPECTS software was able to predict poor clinical outcomes after thrombectomy (Spearman correlation = −0.15; $P = .027$) and was an independent predictor of poor outcome in a multivariate analysis (OR, 0.79; 95% CI, 0.63–0.99) while also demonstrating high consensus with 3 expert ASPECTS readers (ICC = 0.72, 0.74, and 0.76).[57] Traditional ML techniques combining clinical data and core-penumbra mismatch ratio derived from MR imaging and MRP to determine postthrombolysis clinical outcomes performed with an AUC of 0.863 (95% CI, 0.774–0.951) for short-term (day 7) outcomes and 0.778 (95% CI, 0.668–0.888) for long-term (day 90) outcomes.[58] Decision tree–based algorithms including extreme gradient boosting and gradient boosting machine were able to predict 90-day modified Rankin scale (mRS) >2 using imaging and clinical data with AUC of 0.746 (extreme gradient boosting) and 0.748 (gradient boosting machine), and performance improved when incorporating NIHSS at 24 hours and recanalization outcomes.[59] ML techniques, including regularized logistic regression, linear SVM, and RF, outperformed existing pretreatment scoring methods in predicting good clinical outcomes (mRS ≤2 at 90 days) of patients with LVO who will undergo thrombectomy, with AUC 0.85–0.86 for ML models compared with 0.71–0.77 for pretreatment scores.[60] A combination CNN and ANN approach incorporating clinical and NCCT data predicted functional thrombolysis outcomes with accuracy 0.71 for 24-hour NIHSS improvement of ≥4 and accuracy 0.74 for 90-day mRS of 0–1.[61] Finally, traditional ML techniques and neural networks were used to predict hemorrhagic transformation of acute ischemic stroke before treatment from MRP source images and DWI, with the highest AUC of 0.837 ± 2.6% using a kernel spectral regression ML technique.[62] One limitation of this study was the variable recanalization of the participants, which may have confounded results.

AI EVALUATION OF HEMORRHAGE

This section focuses primarily on DL methods that have been used for intracranial hemorrhage (ICH) detection and classification, quantification, and prognostication (Online Table 5).

Detection and Classification

A study using two 2D convolutional neural networks, GoogLeNet and AlexNet, to detect basal ganglia hemorrhages on NCCT found that GoogLeNet with augmented data in a pretrained network was the most accurate (AUC = 1.0; sensitivity and specificity = 100%) compared with the highest performing augmented, untrained AlexNet (AUC = 0.95; sensitivity = 100%; and specificity = 80%).[63] False positive results from basal ganglia calcification were seen in some of the methods, and sensitivity of detection of small basal ganglia hemorrhages remains to be investigated.

One of the largest cohorts for detection and classification of ICH examined more than 30,0000 NCCTs from different hospitals in India using DL algorithms.[64] The algorithm performed well on 2 different validation datasets, Qure25k and CQ500, achieving AUCs of 0.92 (95% CI, 0.91–0.93) and 0.94 (CI, 0.92–0.97), respectively, for detecting ICH. The algorithm was also able to classify subtypes of hemorrhage (parenchymal, intraventricular, subdural, extradural/epidural, and subarachnoid) with AUCs ranging from 0.90 to 0.96 for the Qure25K dataset and 0.93 to 0.97 for the CQ500 dataset. An additional feature of the algorithm was its ability to recognize associated pertinent CT findings, such as calvarial fracture, midline shift, and mass effect.

Another study using a fully 3D CNN with a large patient cohort was able to detect ICH and reprioritize studies as "stat" (defined as a positive ICH study) versus "routine."[65] The AUC

was 0.846 (95% CI, 0.837–0.856), specificity was 0.80 (0.790–0.809), and sensitivity was 0.73 (0.713–0.748). The algorithm was integrated into the radiologist's workflow, and time to detection was reduced from 512 to 19 minutes.

An explainable pretrained 2D convolutional neural networks system performed at a similar level to expert neuroradiologists on a relatively small cohort of cases when detecting acute ICH and classifying the 5 ICH subtypes on NCCT.[66] The algorithm incorporated techniques such as attention maps and prediction based modules to help mitigate the "black box" of the DL system. The system displayed a robust performance when detecting ICH on a retrospective dataset of 200 cases (AUC = 0.99; sensitivity = 98%; and specificity = 95%) and prospective dataset of 196 cases (AUC = 0.96; sensitivity = 92%; and specificity = 95%). Furthermore, the overall localization accuracy of the attention maps was 78.1% compared with bleeding points annotated by expert neuroradiologists.

Quantification

A custom DL-trained hybrid 3D–2D CNN was able to detect and quantify ICHs on NCCT in a retrospective training cohort and a prospective testing cohort from the emergency department.[67] Accuracy, AUC, sensitivity, specificity, positive predictive value, and negative predictive value for ICH detection for the training cohort were 0.975, 0.983, 0.971, 0.975, 0.793, and 0.997, respectively, and for the prospective cohort were 0.970, 0.981, 0.951, 0.973, 0.829, and 0.993. For ICH quantification, Dice scores were 0.931, 0.863, and 0.772, and Pearson correlation coefficients were 0.999, 0.987, and 0.953 for intraparenchymal hemorrhage, epidural or subdural hemorrhage, and SAH, respectively, compared with semiautomated segmentation by a radiologist. This study used real-life prospective testing of the algorithm and quantified hemorrhage volume during segmentation. The study also addresses the black box critique with the use of a custom mask ROI-based CNN architecture.

A patch-based fully DL CNN simultaneously classified and quantified hemorrhages at a level equal to or above that of expert radiologists (AUC = 0.991 ± 0.006).[68] The algorithm was able to identify some small hemorrhages that were missed by radiologists and performed well on a relatively small dataset. The strongly supervised approach took into account the heterogeneous morphology of hemorrhages and showed perfect sensitivity (1.00) while maintaining high specificity (0.87).

Prognostication

Identifying patients at risk for ICH expansion is important for prognostication. One study showed good performance when applying a SVM that incorporated various clinical and imaging variables to predict hematoma expansion on NCCT (AUC = 0.89; mean sensitivity = 81.3%; and mean specificity = 84.8%).[69] Rapid and accurate identification of ICH by AI methods could aid with triaging of positive studies.

CONCLUSIONS

Prompt detection and treatment of acute cerebrovascular disease is critical to reduce morbidity and mortality. The current application of AI in this field has allowed for vast opportunities to improve treatment selection and clinical outcomes by aiding in all parts of the diagnostic and treatment pathway, including detection, triage, and outcome prediction. Future studies validating AI techniques are needed to allow for more widespread use in various practice environments.

ACKNOWLEDGMENTS

The authors thank Aidoc, Avicenna, Brainomix, RapidAI, and Viz.ai for providing information regarding commercially available products and sample images of their applications for publication.

Disclosures: Daniel Chow—*RELATED: Grant:* Avicenna.ai*; *UNRELATED: Consultancy:* Canon Medical; *Expert Testimony:* Cullins & Grandy; *Grants/Grants Pending:* Canon Medical, Novocure; *Stock/Stock Options:* Avicenna.ai. Christopher Filippi—*UNRELATED: Consultancy:* Guerbet, Syntactx, *Comments*: Advisor on AI (Guerbet) and interpret brain MR for clinical trials (Syntactx); *Grants/Grants Pending:* FASNR grant and National MS Society grant; *Stock/Stock Options:* Minority stakeholder in start-up Avicenna. Wengui Yu—*UNRELATED: Employment:* University of California Irvine. Peter Chang—*UNRELATED: Consultancy:* Canon Medical, *Comments*: Consulting, travel expenses, honorarium for invited keynote speaker (RSNA); *Stock/Stock Options:* Avicenna.ai, *Comments*: Co-founder, board member. *Money paid to institution.

REFERENCES

1. Ovbiagele B, Nguyen-Huynh MN. **Stroke epidemiology: advancing our understanding of disease mechanism and therapy.** *Neurotherapeutics* 2011;8:319–29 CrossRef Medline
2. Donkor ES. **Stroke in the 21(st) century: a snapshot of the burden, epidemiology, and quality of life.** *Stroke Res Treat* 2018;2018:3238165 CrossRef Medline
3. Boehme AK, Esenwa C, Elkind MSV. **Stroke risk factors, genetics, and prevention.** *Circ Res* 2017;120:472–95 CrossRef Medline
4. Lee EJ, Kim YH, Kim N, et al. **Deep into the brain: artificial intelligence in stroke imaging.** *J Stroke* 2017;19:277–85 CrossRef Medline
5. Goodfellow I, Bengio Y, Courville A. *Deep Learning*. The MIT Press 2016
6. Saeys Y, Inza I, Larrañaga P. **A review of feature selection techniques in bioinformatics.** *Bioinformatics* 2007;23:2507–17 CrossRef Medline
7. Dreiseitl S, Ohno-Machado L. **Logistic regression and artificial neural network classification models: a methodology review.** *J Biomed Inform* 2002;35:352–59 CrossRef Medline
8. Wang S, Summers RM. **Machine learning and radiology.** *Med Image Anal* 2012;16:933–51 CrossRef Medline
9. Jordan MI, Mitchell TM. **Machine learning: trends, perspectives, and prospects.** *Science* 2015;349:255–60 CrossRef Medline
10. He K, Zhang X, Ren S, et al. **Deep residual learning for image recognition.** *arXiv*:1512:03385;10 Dec 2015;1–12
11. Krizhevsky A, Sutskever I, Hinton G. **Imagenet classification with deep convolutional neural networks.** *Proc Advances in Neural Information Processing Systems* 2012;1090–98
12. Krizhevsky A, Sutskever I, Hinton GE. **Imagenet classification with deep convolutional neural networks. Neural information processing systems.** *Stateline* 2012;1097–1105
13. Setio AA, Ciompi F, Litjens G, et al. **Pulmonary nodule detection in CT images: false positive reduction using multi-view convolutional networks.** *IEEE Trans Med Imaging* 2016;35:1160–69 CrossRef Medline
14. Roth HR, Lu L, Liu J, et al. **Improving computer-aided detection using convolutional neural networks and random view aggregation.** *IEEE Trans Med Imaging* 2016;35:1170–81 CrossRef Medline
15. Qi D, Hao C, Lequan Y, et al. **Automatic detection of cerebral microbleeds from MR images via 3D convolutional neural networks.** *IEEE Trans Med Imaging* 2016;35:1182–95 CrossRef Medline

16. Zou KH, Warfield SK, Bharatha A, et al. **Statistical validation of image segmentation quality based on a spatial overlap index1: scientific reports.** *Acad Radiol* 2004;11:178–89 CrossRef
17. Yamashita R, Nishio M, Do RKG, et al. **Convolutional neural networks: an overview and application in radiology.** *Insights Imaging* 2018;9:611–29 CrossRef Medline
18. Murray NM, Unberath M, Hager GD, et al. **Artificial intelligence to diagnose ischemic stroke and identify large vessel occlusions: a systematic review.** *J Neurointerv Surg* 2020;12:156–64 CrossRef
19. Liew S-L, Anglin JM, Banks NW, et al. **A large, open source dataset of stroke anatomical brain images and manual lesion segmentations.** *Sci Data* 2018;5:180011 CrossRef Medline
20. Chilamkurthy S, Ghosh R, Tanamala S, et al. **Development and validation of deep learning algorithms for detection of critical findings in head CT scans.** *arXiv* :1803:05854;30 March 2018; 1–18
21. Flanders AE, Prevedello LM, Shih G, et al. **Construction of a machine learning dataset through collaboration: the RSNA 2019 brain CT hemorrhage challenge.** *Radiol Art Int* 2020;2:e190211 CrossRef
22. Winzeck S, Hakim A, McKinley R, et al. **ISLES 2016 and 2017—benchmarking ischemic stroke lesion outcome prediction based on multispectral MRI.** *Front Neurol* 2018;9:679 CrossRef Medline
23. Clèrigues A, Valverde S, Bernal J, et al. **Acute ischemic stroke lesion core segmentation in CT perfusion images using fully convolutional neural networks.** *Comput Biol Med* 2019;115:103487 CrossRef Medline
24. American Society of Functional Neuroradiology. **ASFNR Ai challenge.** https://aichallenge.asfnr.org. Accessed July 5, 2020
25. Nogueira RG, Jadhav AP, Haussen DC, et al. **Thrombectomy 6 to 24 hours after stroke with a mismatch between deficit and infarct.** *N Engl J Med* 2018;378:11–21 CrossRef Medline
26. Saver JL, Goyal M, Bonafe A, et al. **Stent-retriever thrombectomy after intravenous t-PA vs. t-PA alone in stroke.** *N Engl J Med* 2015; 372:2285–95 CrossRef Medline
27. Albers GW, Marks MP, Kemp S, et al. **Thrombectomy for stroke at 6 to 16 hours with selection by perfusion imaging.** *N Engl J Med* 2018;378:708–18 CrossRef Medline
28. Campbell BCV, Mitchell PJ, Kleinig TJ, et al. **Endovascular therapy for ischemic stroke with perfusion-imaging selection.** *N Engl J Med* 2015;372:1009–18 CrossRef Medline
29. Wismüller A, Stockmaster L. **A prospective randomized clinical trial for measuring radiology study reporting time on artificial Intelligence-based detection of intracranial hemorrhage in emergent care head CT.** *arXiv* :2002:12515; 28 Feb 2020; 1–7
30. Tang FH, Ng DK, Chow DH. **An image feature approach for computer-aided detection of ischemic stroke.** *Comput Biol Med* 2011; 41:529–36 CrossRef Medline
31. Abedi V, Goyal N, Tsivgoulis G, et al. **Novel screening tool for stroke using artificial neural network.** *Stroke* 2017;48:1678–81 CrossRef Medline
32. Chen L, Bentley P, Rueckert D. **Fully automatic acute ischemic lesion segmentation in DWI using convolutional neural networks.** *NeuroImage Clin* 2017;15:633–43 CrossRef Medline
33. Guerrero R, Qin C, Oktay O, et al. **White matter hyperintensity and stroke lesion segmentation and differentiation using convolutional neural networks.** *NeuroImage Clin* 2018;17:918–34 CrossRef Medline
34. Oman O, Makela T, Salli E, et al. **3D convolutional neural networks applied to CT angiography in the detection of acute ischemic stroke.** *Eur Radiol Exp* 2019;3:8 CrossRef Medline
35. Kasasbeh AS, Christensen S, Parsons MW, et al. **Artificial neural network computer tomography perfusion prediction of ischemic core.** *Stroke* 2019;50:1578–81 CrossRef Medline
36. Qiu W, Kuang H, Teleg E, et al. **Machine learning for detecting early infarction in acute stroke with non–contrast-enhanced CT.** *Radiology* 2020;294:638–44 CrossRef Medline
37. Takahashi N, Lee Y, Tsai D-Y, et al. **An automated detection method for the MCA dot sign of acute stroke in unenhanced CT.** *Radiol Phys Technol* 2014;7:79–88 CrossRef Medline
38. Chen Z, Zhang R, Xu F, et al. **Novel prehospital prediction model of large vessel occlusion using artificial neural network.** *Front Aging Neurosci* 2018;10:181 CrossRef Medline
39. Chatterjee A, Somayaji NR, Kabakis IM. **Abstract WMP16: artificial intelligence detection of cerebrovascular large vessel occlusion—nine month, 650 patient evaluation of the diagnostic accuracy and performance of the Viz.ai LVO algorithm.** *Stroke* 2019;50: AWMP16 CrossRef
40. Barreira C, Bouslama M, Lim J, et al. **E-108 Aladin study: automated large artery occlusion detection in stroke imaging study—a multicenter analysis.** *J Neurointerv Surg* 2018;10:A101–02 CrossRef
41. Goyal M, Demchuk AM, Menon BK, et al. **Randomized assessment of rapid endovascular treatment of ischemic stroke.** *N Engl J Med* 2015;372:1019–30 CrossRef Medline
42. Jovin TG, Chamorro A, Cobo E, et al. **Thrombectomy within 8 hours after symptom onset in ischemic stroke.** *N Engl J Med* 2015;372:2296–2306 CrossRef Medline
43. Nagel S, Sinha D, Day D, et al. **e-ASPECTS software is non-inferior to neuroradiologists in applying the ASPECT score to computed tomography scans of acute ischemic stroke patients.** *Int J Stroke* 2017;12:615–22 CrossRef Medline
44. Guberina N, Dietrich U, Radbruch A, et al. **Detection of early infarction signs with machine learning-based diagnosis by means of the Alberta Stroke Program Early CT score (ASPECTS) in the clinical routine.** *Neuroradiology* 2018;60:889–901 CrossRef Medline
45. Kuang H, Najm M, Chakraborty D, et al. **Automated ASPECTS on noncontrast CT scans in patients with acute ischemic stroke using machine learning**. *AJNR Am J Neuroradiol* 2019;40:33–38 CrossRef Medline
46. Maegerlein C, Fischer J, Monch S, et al. **Automated calculation of the Alberta Stroke Program Early CT score: feasibility and reliability.** *Radiology* 2019;291:141–48 CrossRef Medline
47. Albers GW, Wald MJ, Mlynash M, et al. **Automated calculation of Alberta Stroke Program Early CT score: validation in patients with large hemispheric infarct.** *Stroke* 2019;50:3277–79 CrossRef Medline
48. Grunwald IQ, Kulikovski J, Reith W, et al. **Collateral automation for triage in stroke: evaluating automated scoring of collaterals in acute stroke on computed tomography scans.** *Cerebrovasc Dis* 2019;47:217–22 CrossRef Medline
49. Wang K, Shou Q, Ma SJ, et al. **Deep learning detection of penumbral tissue on arterial spin labeling in stroke.** *Stroke* 2020;51:489–97 CrossRef Medline
50. Ho KC, Speier W, Zhang H, et al. **A machine learning approach for classifying ischemic stroke onset time from imaging.** *IEEE Trans Med Imaging* 2019;38:1666–76 CrossRef Medline
51. Lee H, Lee E-J, Ham S, et al. **Machine learning approach to identify stroke within 4.5 hours.** *Stroke* 2020;51:860–66 CrossRef Medline
52. Wu O, Koroshetz WJ, Østergaard L, et al. **Predicting tissue outcome in acute human cerebral ischemia using combined diffusion- and perfusion-weighted MR imaging.** *Stroke* 2001;32:933–42 CrossRef Medline
53. Stier N, Vincent N, Liebeskind D, et al. **Deep learning of tissue fate features in acute ischemic stroke.** *Proceedings (IEEE Int Conf Bioinformatics Biomed)* 2015;2015:1316–21 CrossRef Medline
54. Nielsen A, Hansen MB, Tietze A, et al. **Prediction of tissue outcome and assessment of treatment effect in acute ischemic stroke using deep learning.** *Stroke* 2018;49:1394–1401 CrossRef Medline
55. Ho KC, Scalzo F, Sarma K, et al. **Predicting ischemic stroke tissue fate using a deep convolutional neural network on source magnetic resonance perfusion images.** *J Med Imag* 2019;6:1 CrossRef Medline
56. Yu Y, Xie Y, Thamm T, et al. **Use of deep learning to predict final ischemic stroke lesions from initial magnetic resonance imaging.** *JAMA Netw Open* 2020;3:e200772 CrossRef Medline

57. Pfaff J, Herweh C, Schieber S, et al. **e-ASPECTS correlates with and is predictive of outcome after mechanical thrombectomy.** *AJNR Am J Neuroradiol* 2017;38:1594–99 CrossRef Medline
58. Tang T-Y, Jiao Y, Cui Y, et al. **Development and validation of a penumbra-based predictive model for thrombolysis outcome in acute ischemic stroke patients.** *EBioMedicine* 2018;35:251–59 CrossRef Medline
59. Xie Y, Jiang B, Gong E, et al. **Use of gradient boosting machine learning to predict patient outcome in acute ischemic stroke on the basis of imaging, demographic, and clinical information.** *AJR Am J Roentgenol* 2019;212:44–51 CrossRef Medline
60. Nishi H, Oishi N, Ishii A, et al. **Predicting clinical outcomes of large vessel occlusion before mechanical thrombectomy using machine learning.** *Stroke* 2019;50:2379–88 CrossRef Medline
61. Bacchi S, Zerner T, Oakden-Rayner L, et al. **Deep learning in the prediction of ischaemic stroke thrombolysis functional outcomes: a pilot study.** *Acad Radiol* 2020;27:e19–23 CrossRef Medline
62. Yu Y, Guo D, Lou M, et al. **Prediction of hemorrhagic transformation severity in acute stroke from source perfusion MRI.** *IEEE Trans Biomed Eng* 2018;65:2058–65 CrossRef Medline
63. Desai V, Flanders A, Lakhani P. **Application of deep learning in neuroradiology: automated detection of basal ganglia hemorrhage using 2D-convolutional neural networks.** *arXiv* :1710:03823;10 Oct 2017;1–7
64. Chilamkurthy S, Ghosh R, Tanamala S, et al. **Deep learning algorithms for detection of critical findings in head CT scans: a retrospective study.** *Lancet* 2018;392:2388–96 CrossRef Medline
65. Arbabshirani MR, Fornwalt BK, Mongelluzzo GJ, et al. **Advanced machine learning in action: identification of intracranial hemorrhage on computed tomography scans of the head with clinical workflow integration.** *NPJ Digital Med* 2018;1:9 CrossRef Medline
66. Lee H, Yune S, Mansouri M, et al. **An explainable deep-learning algorithm for the detection of acute intracranial haemorrhage from small datasets.** *Nat Biomed Eng* 2019;3:173–82 CrossRef Medline
67. Chang PD, Kuoy E, Grinband J, et al. **Hybrid 3D/2D convolutional neural network for hemorrhage evaluation on head CT.** *AJNR Am J Neuroradiol* 2018;39:1609–16 CrossRef Medline
68. Kuo W, Häne C, Mukherjee P, et al. **Expert-level detection of acute intracranial hemorrhage on head computed tomography using deep learning.** *Proc Natl Acad Sci USA* 2019;116:22737–45 CrossRef Medline
69. Liu J, Xu H, Chen Q, et al. **Prediction of hematoma expansion in spontaneous intracerebral hemorrhage using support vector machine.** *EBioMedicine* 2019;43:454–59 CrossRef Medline

Beyond Tympanomastoidectomy: A Review of Less Common Postoperative Temporal Bone CT Findings

A. Panda, M.L. Carlson, F.E. Diehn, and J.I. Lane

ABSTRACT

SUMMARY: Postoperative temporal bone imaging after surgical procedures such as ossiculoplasty, tympanomastoidectomy, cochlear implantation, and vestibular schwannoma resection is often encountered in clinical neuroradiology practice. Less common otologic procedures can present diagnostic dilemmas, particularly if access to prior operative reports is not possible. Lack of familiarity with the less common surgical procedures and expected postoperative changes may render radiologic interpretation challenging. This review illustrates key imaging findings after surgery for Ménière disease, superior semicircular canal dehiscence, temporal encephalocele repairs, internal auditory canal decompression, active middle ear implants, jugular bulb and sigmoid sinus dehiscence repair, and petrous apicectomy.

ABBREVIATIONS: AMEI = active middle ear acoustic implants; ELS = endolymphatic sac; LSC = lateral semicircular canal; MCF = middle cranial fossa; PSC = posterior semicircular canal; SSC = superior semicircular canal; SSCD = superior semicircular canal dehiscence

Many neuroradiologists may be familiar with the imaging appearance of the middle and inner ear, internal auditory canal, and lateral skull base after common surgical procedures such as ossiculoplasty, tympanomastoidectomy, cochlear implantation, and vestibular schwannoma resection.[1-3] Less common otologic procedures can present diagnostic dilemmas, particularly if access to prior operative reports is lacking. Neuroradiologists may not be aware of these surgical procedures either due to the decreasing numbers of these surgeries performed today or some of the newer surgeries confined to specialized academic centers and thus less commonly encountered in routine practice. These postoperative temporal bone findings can have unique imaging features based on the type of surgical procedure and indication. Lack of familiarity with these surgical procedures and expected postoperative changes may render radiologic interpretation challenging. The purpose of this image-rich review is to illustrate less common postoperative temporal bone CT findings that neuroradiologists may encounter and would ideally be able to recognize and to differentiate from disease mimics. This review illustrates imaging findings after surgery for Ménière disease, superior semicircular canal dehiscence, temporal encephalocele repairs, internal auditory canal decompression, active middle ear implants, jugular bulb and sigmoid sinus dehiscence repair, and petrous apicectomy.

Received May 4, 2020; accepted after revision July 18.

From the Departments of Radiology (A.P., J.I.L., F.E.D.) and Otolaryngology–Head and Neck Surgery (M.L.C.), Mayo Clinic, Rochester, Minnesota.

Paper previously presented as an Educational Exhibit at: Annual Meeting of the Radiological Society of North America, December 1–6, 2019; Chicago, Illinois, and was awarded a Certificate of Merit.

Please address correspondence to John I. Lane, MD, Department of Radiology, Mayo Clinic, 200 1st St SW, Rochester, MN 55905; e-mail: lane.john@mayo.edu; @AnanyaPanda15; @MatthewLCarlso1; @MayoRadiology

http://dx.doi.org/10.3174/ajnr.A6802

Ménière Disease

Ménière disease is characterized by recurrent attacks of episodic vertigo, fluctuating low-frequency sensorineural hearing loss, tinnitus, and aural fullness. The pathophysiology is attributed to endolymphatic hydrops, a histologic finding in which the endolymphatic compartment including the scala media is dilated.[4] Endolymph is the fluid within the membranous labyrinth, including the vestibule, semicircular canals, and scala media of the cochlea. Although the physiology is debated, the endolymphatic sac (ELS) is thought to maintain hydrostatic pressure and endolymph homeostasis for the inner ear, and its dysfunction may contribute to the pathophysiology of this disease.[5] While many patients respond well to lifestyle changes such as low-salt diet and medical management with diuretics and betahistine, >20% of patients develop intractable Ménière disease. Treatment options for these patients with medically refractory symptoms include intratympanic corticosteroid injection, gentamicin injection, and surgery. Surgical treatment may be classified as "nonablative" (in which inner ear function is preserved), including endolymphatic sac decompression, or "ablative" (in which inner ear function is lost), including labryinthectomy and vestibular neurectomy.[6]

ELS surgery, ie, either ELS decompression or ELS shunting, is a nonablative surgical option with moderate efficacy and little

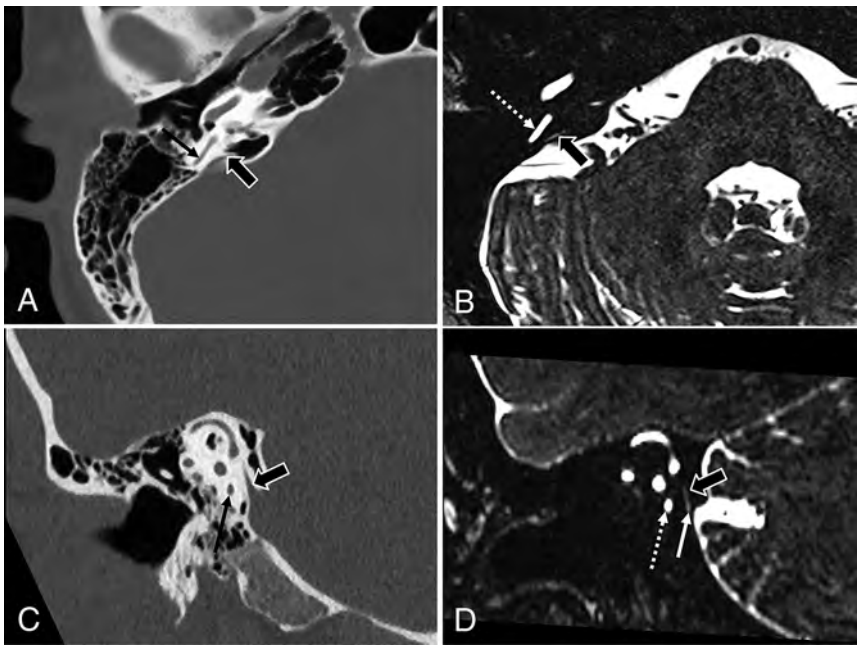

FIG 1. Anatomy of the endolymphatic duct and sac on axial (*A* and *B*) and Pöschl view (*C* and *D*) CT and 3D fast spin-echo T2-weighted MR images. The endolymphatic duct connects with the endolymphatic sac. Both structures are not directly seen on CT, but CT shows the osseous vestibular aqueduct that houses the endolymphatic duct (*block arrows*, *A* and *C*). Note the location of vestibular aqueduct extending to the cortex of the posterior temporal bone (*block arrow*, *A*). On MR imaging, the endolymphatic duct can be seen directly as a T2WI hyperintense tubular structure (*block arrows*, *B* and *D*), extending inferiorly beneath the dura of the posterior cranial fossa at the expected location of endolymphatic sac (*white arrow*, *D*). Note the close proximity of the posterior semicircular canal (*black arrows* on CT and *dotted white arrow* on MR imaging), an important anatomic landmark to identify the endolymphatic sac intraoperatively.

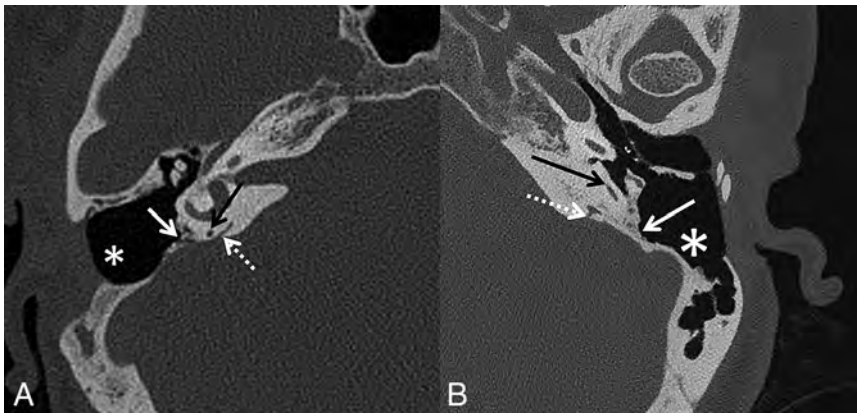

FIG 2. Endolymphatic sac decompression (*A*) versus mastoidectomy (*B*). *A*, Transmastoid endolymphatic sac shunt surgery: Postoperative changes of right canal wall-up mastoidectomy (*asterisk*). The posterior margins of the mastoidectomy defect extend up to the presigmoid osseous plate at the expected location of the endolymphatic sac (*solid white arrow* shows the location of transmastoid endolymphatic sac shunting). Removal of the bone overlying the posterior semicircular canal (*black arrow*) and vestibular aqueduct (*dotted white arrow*) indicates good surgical exposure of the endolymphatic sac. The silastic shunt is not directly visualized on CT. *B*, For comparison, an image from another patient with a simple canal wall-up mastoidectomy and ossiculoplasty for chronic otitis media. Note the mastoidectomy defect (*asterisk*) and the intact posterior cortex (*solid white arrow*) overlying the posterior semicircular canal (*black arrow*) and vestibular aqueduct (*dotted white arrow*).

risk to hearing.[5,6] The ELS is not directly visualized on CT imaging; one can, however, see the osseous margins of the vestibular aqueduct, which encase the membranous endolymphatic duct. On MR imaging, the endolymphatic duct that opens into the ELS at the operculum can be readily identified as a T2WI hyperintense structure. The location of the ELS is inferred at the terminal end of the endolymphatic duct at the dura of the posterior cranial fossa and just behind the posterior semicircular canal (PSC) (Fig 1).[7] The Donaldson line is a useful surgical landmark to identify the ELS during ELS decompression. This line is drawn along the long axis of the lateral semicircular canal (LSC) bisecting the PSC. The estimated location of the ELS is just anterior and inferior to the junction of this line and the sigmoid sinus. The surgical steps of ELS decompression comprise a wide canal wall-up mastoidectomy with decompression of the sigmoid sinus and the presigmoid dura, often referred to as the Trautman triangle. The ELS is identified as a thickening of dura mater posterior to the PSC and is sub sequently widely decompressed without inadvertent durotomy. Additional shunt placement is optional and has largely fallen by the wayside.[8,9] On postoperative imaging, surgical changes of ELS decompression comprise of canal wall-up mastoidectomy, which further extends up to the posterior osseous cortex with presigmoid dura decompression. Removal of the bone immediately posterior and inferior to the PSC and vestibular aqueduct indicates good surgical exposure of the ELS. Identifying the posterior extent of the mastoidectomy margin and exposure of the presigmoid dura differentiates this procedure from a simple cortical mastoidectomy (Fig 2).

While no longer performed today, sacculotomy via the Cody tack procedure is a surgery for Ménière disease that was initially popularized in the early 1970s. The premise behind the procedure was that an internal shunt

between the endolymphatic and perilymphatic compartments may alleviate excess pressure within the membranous labyrinth. Surgically, a prosthetic tack is introduced through the footplate of the stapes that will puncture the saccule whenever saccular dilation occurs, thereby providing "automatic repetitive sacculotomy" (Fig 3).[10] On CT, this should not be mistaken for vestibular migration of an ossicular prosthesis, most commonly a stapes prosthesis. The stapes is normal and intact in patients with sacculotomy hardware, in contradistinction to those with migrated stapes prostheses after stapedectomy procedures for otosclerosis (Fig 3).

Surgical labyrinthectomy is performed for intractable Ménière disease after exhaustion of more conservative nonablative procedures and in patients with poor residual hearing. The goal of labyrinthectomy is to destroy the labyrinthine neuroepithelium and thereby eliminate faulty vestibular stimuli from the diseased ear.[11] Several surgical approaches can be used to perform labyrinthectomy. Some authors advocate a transcanal approach through the external auditory canal, whereby the incus and stapes are removed to access the vestibule. More commonly, the transmastoid approach is used, in which a canal wall-up mastoidectomy is performed, the 3 semicircular canals are exenterated, and the vestibule is cleaned of neuroepithelium.[12,13] Surgical labyrinthectomy for any indication may lead to labyrinthitis ossificans and, much less commonly, CSF leak or facial nerve injury. In patients with surgical labyrinthectomy, air in the labyrinth is considered an expected finding; therefore, these cases should not be mistaken for traumatic or other acquired causes of perilymph fistula or pneumolabyrinth (Fig 4).

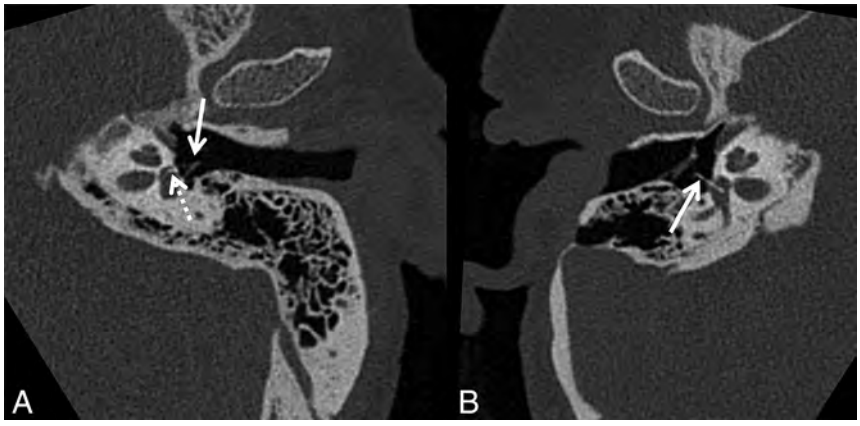

FIG 3. Sacculotomy (*A*) versus stapes prosthesis migration (*B*). *A*, Sacculotomy with insertion of a Cody tack prosthesis. Oblique CT image reformatted along the long axis of the stapes (*A*) shows a linear metallic device in the saccule (*dotted white arrow*). This was a Cody tack device for a sacculotomy. Note the intact stapes (*solid white arrow*). *B*, Vestibular migration of stapes prosthesis. Oblique CT image reformatted along the long axis of the stapes (*D*) shows that the stapes suprastructure is replaced by a prosthesis *(solid white arrow*), with intrusion of the prosthesis into the vestibule.

Semicircular Canal Dehiscence

Superior semicircular canal dehiscence (SSCD) is characterized by thinning of the osseous covering overlying the superior semicircular canal. Due to the dehiscence, there is a direct communication between membranous labyrinth and the overlying dura or superior petrosal sinus, leading to a "third window phenomenon," ie, abnormal dissipation of sound/pressure waves through the dehiscence. Clinically, a third window phenomenon is characterized by various signs such autophony (ie, prominently hearing one's own voice in the affected ear), sound- or pressure-induced vertigo and/or nystagmus (Tullio phenomenon and the Hennerbert sign, respectively), pulsatile tinnitus, and low-frequency conductive hearing loss with negative bone-conduction thresholds.[13,14] The

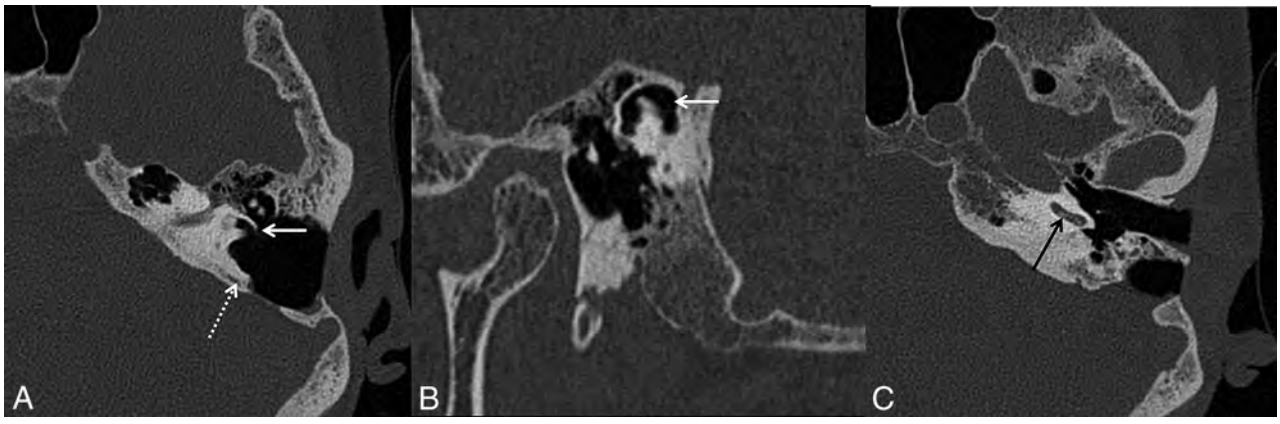

FIG 4. Surgical labyrinthectomy with cochlear labyrinthitis ossificans. Axial CT image (*A*) of the left temporal bone shows changes of prior transmastoid endolymphatic sac surgery (*dotted white arrow*), with a mastoidectomy defect extending posteriorly to the expected location of the endolymphatic sac. Postoperative changes of the subsequently performed hearing-ablative surgical labyrinthectomy are seen as surgical removal of bone overlying the lateral semicircular canal with a fistulous connection between the lateral semicircular canal and the mastoid defect (*solid white arrow*, *A*). Air also extends to the superior semicircular canal (*solid white arrow*, *B*). A more caudal image (*C*) shows mineralization within the basal turn of the cochlea (*black arrow*, *C*), consistent with labyrinthitis ossificans, an expected postoperative finding following labyrinthectomy.

Surgical approaches for superior semicircular canal dehiscence repair[a]

Approaches	Advantages	Disadvantages	Surgery Technique Approach Most Suitable for
Middle Cranial Fossa	Direct visualization of dehiscence	More invasive requiring craniotomy and limited temporal lobe retraction	All kinds of SSC repair: canal resurfacing, plugging, capping
Transmastoid	Less invasive, standard mastoidectomy approach	No direct visualization of dehiscence	Canal plugging and modified resurfacing (of SSC sidewalls and not directly over dehiscence)
Transcanal	Outpatient setting	Less efficacious in long-term	Reinforcement or occlusion of round window

[a] Modified with permission from Mau et al,[16] Ward et al,[17] and Succar et al.[19]

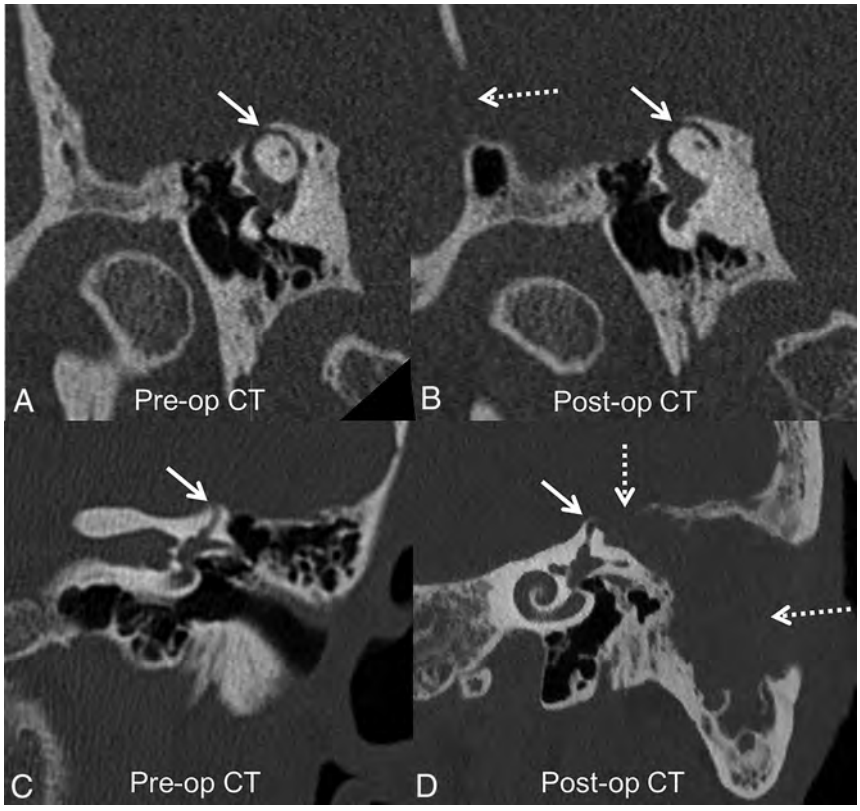

FIG 5. Superior semicircular canal dehiscence repair through a middle cranial fossa approach (*A* and *B*) and transmastoid approach (*C* and *D*). Preoperative Pöschl view (*A*) shows dehiscence of the mid-third of the left superior semicircular canal (*solid white arrow*). A middle cranial fossa approach *(dotted white arrow*, *B*) was used to plug the superior semicircular canal with bone wax and temporalis fascia. Postoperative CT (*B*) shows further loss of bone overlying the superior semicircular canal due to drilling of bone overlying the superior semicircular canal to plug it (*solid white arrow*). Bone wax and temporalis fascia are radiolucent and not directly seen on CT. Postoperative changes of middle cranial fossa repair can be missed on temporal bone CT if not specifically sought and in the absence of clinical details. Preoperative CT (*C*) shows a large left superior semicircular canal dehiscence (*solid white arrow*). A transmastoid approach (*dotted white arrows*, *D*) was used to access the roof of the superior semicircular canal and plug it with bone wax and temporalis fascia. There is expected soft tissue in the mastoidectomy defect without evidence of otitis media (not shown). Pre-op indicates preoperative; Post-op, postoperative.

diagnosis of SSCD can be suggested on heavily T2-weighted MR images but is best made on high-resolution axial and oblique reformatted CT views. On the Pöschl view (ie, images reformatted perpendicular to the long axis of petrous bone), SSCD is characterized by an absent or thinned-out osseous covering overlying the superior semicircular canal (SSC). On the Stenvers view (ie, images reformatted parallel to the long axis of petrous bone), SSCD is characterized by parallel or diverging walls of the SSC as they approach the floor of the middle cranial fossa (MCF).[15]

Surgeries for SSCD are directed toward repair of the dehiscence by canal plugging, resurfacing, or combinations thereof.[16] Both transmastoid and MCF approaches have been described with a >90% success rate (Table).[17,18] Examples of materials used include bone wax, bone chips, and temporalis fascia for canal plugging and cartilage, bone, temporalis fascia, and hydroxyapatite bone cement for resurfacing.[17] Most patients do not need imaging after SSCD repair. CT or MR imaging is typically performed in those patients with persistent vertigo or suspected contralateral dehiscence.[15] Postoperative imaging findings differ on the basis of the material used and the procedure performed. If the SSC has been plugged with bone cement or if there is secondary labyrinthitis ossificans, the occluded semicircular canal segment may appear hyperattenuating on CT. However, both bone wax and fascia are radiolucent materials and not directly visualized on CT. Thus, on postoperative CT, there may be persistent or greater thinning of bone overlying the SSC. This should not be mistaken for persistent SSCD or surgical failure if the patient is asymptomatic (Fig 5). Compared with CT, MR imaging can better depict SSC plugging by loss of T2WI hyperintensity within the semicircular canal. Other postoperative findings may include temporal lobe encephalomalacia due to retraction of the temporal lobe during the MCF approach.[15]

Round window occlusion is another minimally invasive approach for semicircular canal dehiscence treatment. This is performed through a transcanal approach and can be done as an outpatient surgery. Occluding or reinforcing the round window

with autologous material can lead to symptom improvement by eliminating the third window effect, but it may also contribute to a conductive hearing loss. Although this surgery is a less-invasive treatment option for these patients, it has less efficacy compared with direct dehiscence repair.[19] Postoperative imaging shows soft tissue obliterating the normal air-filled round window niche (Fig 6). This should not be mistaken for middle ear disease such as glomus tympanicum or cholesteatoma on imaging. Occlusion of the round window is also offered to patients with a localized perilymph fistula (spontaneous, traumatic, or secondary to erosive middle ear disease).[20] This can look similar to round window occlusion for semicircular canal dehiscence and again should not be mistaken for middle ear disease.

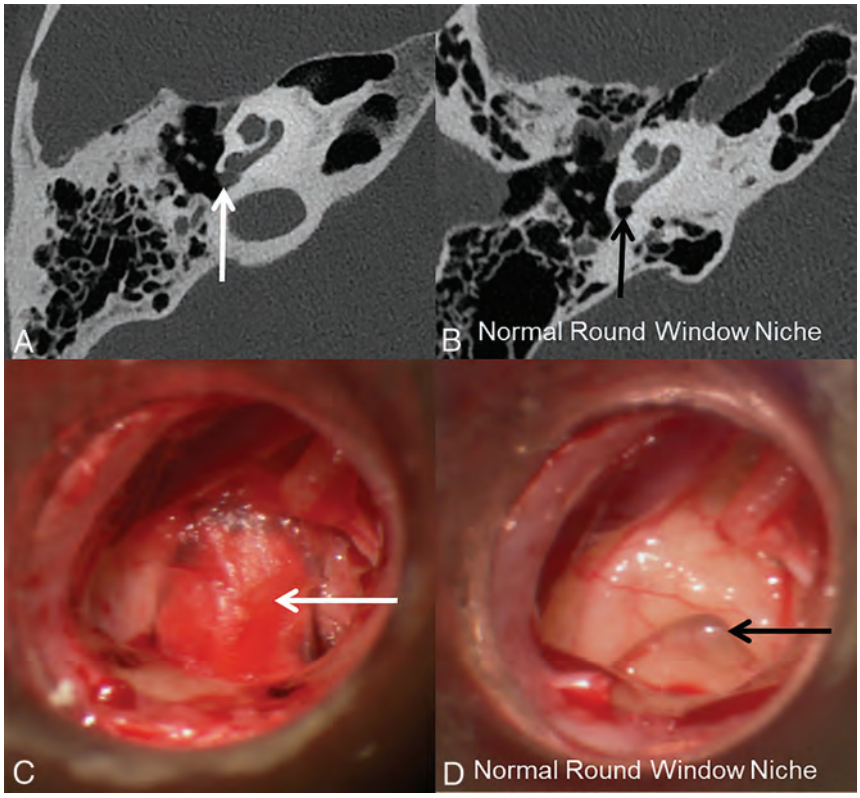

FIG 6. Transcanal occlusion of the round window for superior semicircular canal dehiscence. A patient with bilateral superior semicircular canal dehiscence underwent bilateral transcanal occlusion of the round windows with cartilage graft and fascia. Postoperative axial CT image of the right temporal bone (*A*) shows nodular soft tissue in the round window niche (*white arrow*). A normal round window niche is air-filled compared with that of a healthy patient (*black arrow*, *B*). Intraoperative image (C) shows a round window after occlusion with fascia/cartilage graft (*white arrow*), compared with that of a healthy patient (*black arrow*, *D*).

Isolated lateral semicircular canal dehiscence is rare. Defects in the LSC are more likely due to erosion secondary to infectious, inflammatory, or neoplastic conditions.[13] Very rarely, a radiologist may encounter a patient who underwent a remote LSC fenestration for otosclerosis. In LSC fenestration, an opening is made in the lateral semicircular canal through the mastoid; imaging findings can be mistaken for lateral semicircular canal dehiscence or LSC fistula if one is not aware of this procedure (Fig 7). Because this procedure is now replaced by more effective stapedotomy/stapedectomy procedures, these imaging findings are expected to be found only in patients with remote surgeries.

Temporal Encephaloceles and CSF Leak

Temporal meningoceles or encephaloceles secondary to skull base dehiscence may be congenital, posttraumatic, iatrogenic, or secondary to idiopathic intracranial hypertension (pseudotumor cerebri).[21] Studies have shown an association between SSCD and temporal meningoencephaloceles in patients with idiopathic intracranial hypertension.[22] The pathophysiology of both

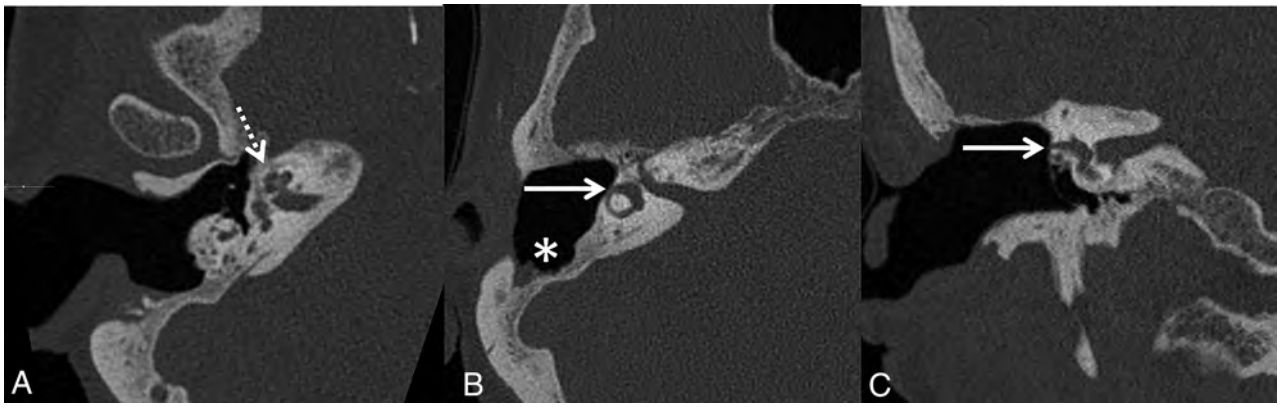

FIG 7. Postoperative changes of lateral semicircular canal fenestration performed for otosclerosis. Axial CT image shows lucency around the cochlea (the "double ring" sign) (*dotted white arrow, A*) consistent with retrofenestral otosclerosis. Postoperative axial (*B*) and coronal (*C*) CT images show an osseous defect over the lateral margin of lateral semicircular canal (*solid white arrows*) due to surgical fenestration of the lateral semicircular canal. This should not be mistaken for a lateral semicircular canal fistula. Note the associated mastoidectomy defect (*asterisk*).

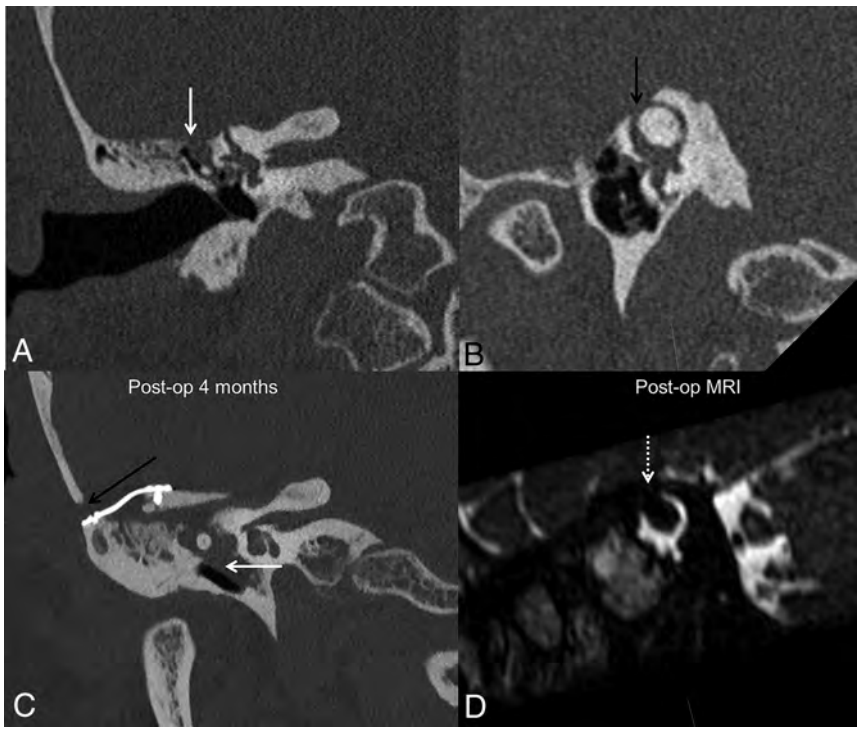

FIG 8. Temporal meningoencephalocele repair and superior semicircular canal dehiscence plugging complicated by CSF leak in a patient with idiopathic intracranial hypertension. Preoperative coronal CT of right temporal bone (*A*) shows a defect in the tegmen tympani. Soft tissue extends through the defect into the right middle ear (*solid white arrow*, *A*). Pöschl view (*B*) shows dehiscence of the mid-portion of the right superior semicircular canal (*black arrow*, *B*). Postoperative images show changes of right middle canal fossa repair with the bone and fascia graft held down with plate screws (*black arrow*, *C*). The right SSC was plugged with bone wax in the same setting, and the roof was resurfaced with fascia graft, better appreciated on the heavily T2-weighted MR imaging (*D*), which shows the expected focal loss of fluid signal in the right SSC at the site of plugging (*dotted white arrow*, *D*). Postoperatively, the patient developed a CSF leak requiring additional surgical repair (*solid white arrow*, *C*). The patient also had a small encephalocele on the left side (not shown) consistent with intracranial hypertension. Post-op indicates postoperative.

meningoencephaloceles and SSCD is attributed to the thinning of the skull base and the roof of the SSC due to raised intracranial pressure. Raised intracranial pressure can also lead to CSF leaks.[13] Surgical approaches for skull base dehiscence repairs include transmastoid and MCF approaches. The transmastoid approach is preferred for smaller defects and defects within the tegmen mastoideum, while the MCF approach is used for defects that are larger, multiple, or in the tegmen epitympanum or petrous apex.[23] Repair materials most commonly include fascia and bone grafts and, less commonly, bone cement. In those patients with concomitant SSCD, dehiscence repair can be performed at the time of meningoencephalocele repair (Fig 8). It is also recommended to look for meningoencephaloceles and SSCD on the contralateral side because bilateral involvement is relatively common in patients with idiopathic intracranial hypertension.[21]

Internal Auditory Canal Decompression

Internal auditory canal decompression is commonly performed for vestibular schwannoma to access the tumor but may also be used to treat osseous dysplasias of the temporal bone that are associated with progressive narrowing of the internal auditory canals leading to auditory, vestibular, or facial nerve dysfunction. Craniometaphyseal dysplasia and Camurati-Engelmann disease (progressive diaphyseal dysplasia) are two such examples that may necessitate internal auditory canal decompression due to seventh and eighth cranial nerve deficits.[24,25] Compressive effects may also be noted on other skull base foramina, cranial nerves, vessels, and brain stem. In these patients, internal auditory canal decompression is performed through the MCF approach to remove the superior and the anterior portions of the petrous bone. On postoperative imaging, one should evaluate the adequacy of internal auditory canal decompression, which should ideally include the labyrinthine segment of the facial nerve, and ensure that the arcuate eminence (the bone overlying the SSC) is intact (Fig 9). Unfortunately, long-term follow-up may show heterotopic or dystrophic ossification, necessitating revision decompression surgeries.

Implantable Active Middle Ear Acoustic Implants

Implantable active middle ear acoustic implants (AMEI) are alternatives to hearing aids in appropriately selected patients. These may be offered to patients with variable severity of conductive, sensorineural, or mixed hearing loss who cannot wear hearing aids due to infection or defects or atresia of the external auditory canal or who do not wish to wear hearing aids for cosmesis.[26,27] These implants transduce acoustic sound energy to the cochlear perilymph either through skull vibration via the temporal bone cortex or via the ossicular chain. These differ from passive middle ear implants such as an ossicular reconstruction prosthesis. They also differ from cochlear implants or auditory brain stem implants that directly simulate the cochlear nerve or brain stem nuclei, respectively.[28] There are a variety of AMEIs available, some of which are FDA approved in the United States while others are available in Europe.[26] From an imaging perspective, it is important for radiologists not to mistake AMEIs for cochlear implants on postoperative CT. A primary distinguishing feature is that a cochlear implant will have an electrode within the cochlear lumen that typically extends to a minimum angular depth of 270° to 360°, whereas AMEIs will not have an intracochlear component. Similar to earlier cochlear implant designs, many AMEIs are not MR imaging conditional.

AMEIs can either be partially implantable or fully implantable.[28] Partially implantable AMEIs have an external sound processor and an internal floating mass transducer. Partially implantable AMEIs can either have a fully external sound processor held by a magnet

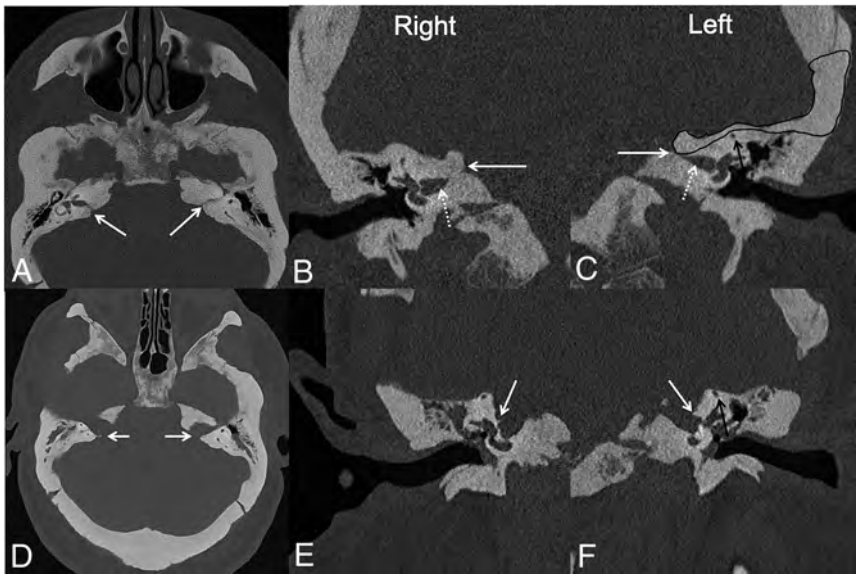

FIG 9. Internal auditory canal decompression for Camurati-Engelmann disease. *Upper row*: Preoperative CT images (*A–C*) in a patient with Camurati-Engelmann disease show extensive osseous skull base thickening and near-complete obliteration of both internal auditory canals (left > right) (*solid white arrows*, *A*). Coronal images (*B* and *C*) show marked narrowing of both internal auditory canals (*dotted white arrows*), more so medially where the porus acousticus is nearly obliterated due to hypertrophic osseous overgrowth of the walls of internal auditory canals (*solid white arrows*). *Lower row*: Postoperative CT images (*D–F*) show widely patent internal auditory canals bilaterally (*solid white arrows*, *D*). Coronal images (*E* and *F*) show decompression of the internal auditory canals by removal of the superior and anterior portions of the petrous bones (*solid white arrows*). The black polygon in *C* depicts the portion of the bone removed through the middle cranial fossa approach to decompress the internal auditory canal. Care is taken to preserve the arcuate eminence over the superior semicircular canal (*black arrows*, *C* and *F*).

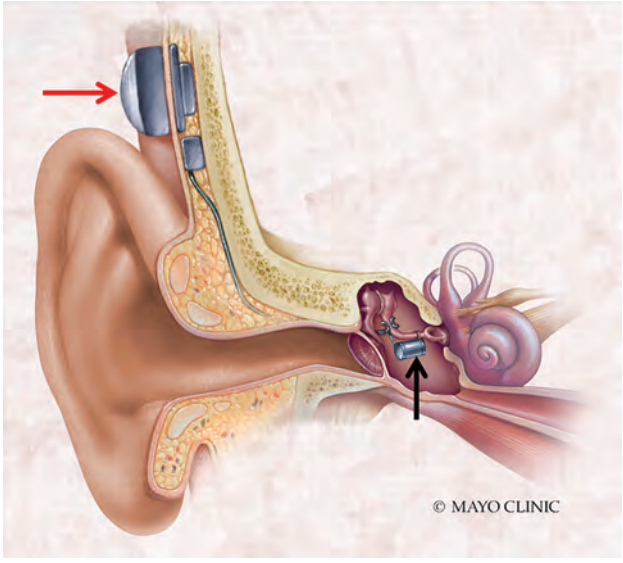

FIG 10. Normal active middle ear implant. Illustration of a partially implantable external audioprocessor (*red arrow*) attached to the mastoid bone that transmits vibrations to an internal floating mass transducer (*black arrow*) coupled with the intact ossicular chain. Images used with permission of the Mayo Foundation for Medical Education and Research. All rights reserved.

(eg, Vibrant Soundbridge; Med-EL) or an in-the-canal processor (eg, Maxum; Ototronix) (Fig 10).[28] The floating mass transducer can be crimped to the long process of the incus or the stapes footplate or suprastructure or coupled to the round window. The floating mass transducer is stimulated by the processor, which, in turn, creates a mechanical vibration that results in perilymph fluid movement within the cochlea.[29] Thus, for proper functioning, the implant must be correctly coupled to the ossicular system or round window. Any break in the coupling of the floating mass transducer leads to device malfunction. The goal of postoperative imaging in these patients is to identify the device components and the integrity of the coupling system (Fig 11).

In fully-implantable AMEIs (eg, Esteem; Envoy), the processor is internal and secured to the mastoid bone. It has a sensor coupled to the body of the incus and a driver coupled to the stapes.[30] The incudostapedial joint is disarticulated at the time of device implantation to separate the sensor and the driver functions. Thus, incudostapedial disarticulation on postoperative CT is expected and should not be interpreted as pathologic decoupling or discontinuity (Fig 12).[28]

Jugular Bulb and Sigmoid Sinus Dehiscence Repairs

Pulsatile tinnitus of venous origin may be caused by abnormalities in the jugular bulb or sigmoid sinus walls leading to jugular bulb or sigmoid sinus dehiscence.[31] Jugular bulb dehiscence may be seen in patients with a high-riding jugular bulb. Dehiscence can lead to an outpouching of the jugular vein forming a jugular diverticulum into the posterior hypotympanum. A large dehiscent jugular bulb is more common on the right side, where the jugular system is more commonly dominant. Although often asymptomatic, on the basis of the location of jugular diverticulum or dehiscence, symptoms may include conductive hearing loss, pulsatile tinnitus, or brisk venous bleeding after myringotomy.[32] Reconstruction of jugular bulb dehiscence with hydroxyapatite bone cement or bone pate is an emerging surgical option.[33] Sigmoid sinus dehiscence may also be seen in patients with idiopathic intracranial hypertension with or without concomitant stenosis at the transverse-sigmoid sinus junction and the more laterally placed sigmoid sinus.[34] Recently, transmastoid repair for sigmoid sinus dehiscence has been described. This comprises a cortical mastoidectomy, which is further extended to the lateral wall of the sigmoid sinus. The dehiscent sigmoid sinus wall is then reconstructed with bone

pate or bone cement. Other less preferred reconstruction materials include autologous bone graft or temporalis fascia.[31] On imaging, it is important to recognize both pre- and postoperative findings to avoid misdiagnosis (Fig 13). Postoperative imaging should also be scrutinized for potential complications such as deep cerebral venous thrombosis and mass effect on the sigmoid sinus or jugular bulb.[31]

Petrous Apicectomy

The petrous apex is anatomically complex and one of the least accessible areas of the skull base. It is prone to a variety of pathologies such as petrous apicitis, cholesterol granuloma, epidermoid, mucocele, and tumors.[35] Surgical drainage of the petrous apex is considered in the setting of locally compressive symptoms or in petrous apicitis with Gradenigo syndrome (triad of retro-orbital pain, otorrhea, and abducens nerve palsy).[35,36] Multiple surgical approaches have been described reflecting the anatomic complexity and the intent of the operation (ie, biopsy, drainage, or removal) and to safeguard the various vascular and neural structures in this region. The 3 most commonly used approaches are transmastoid retrolabyrinthine, transcanal infracochlear, and extended middle cranial fossa.[12] In the transmastoid infralabyrinthine approach, the surgical path extends below and posterior to the PSC, above the jugular bulb, and behind the facial nerve. In the infracochlear approach, the path extends through the external auditory canal, below the cochlea, and between the petrous carotid canal and jugular bulb.[12] The role of postoperative imaging is based on the goals of the original option: identification of recurrence if performed for tumor resection or epidermoid, resolution of infection if performed for apicitis, or adequate drainage if performed for cholesterol granuloma (Fig 14).

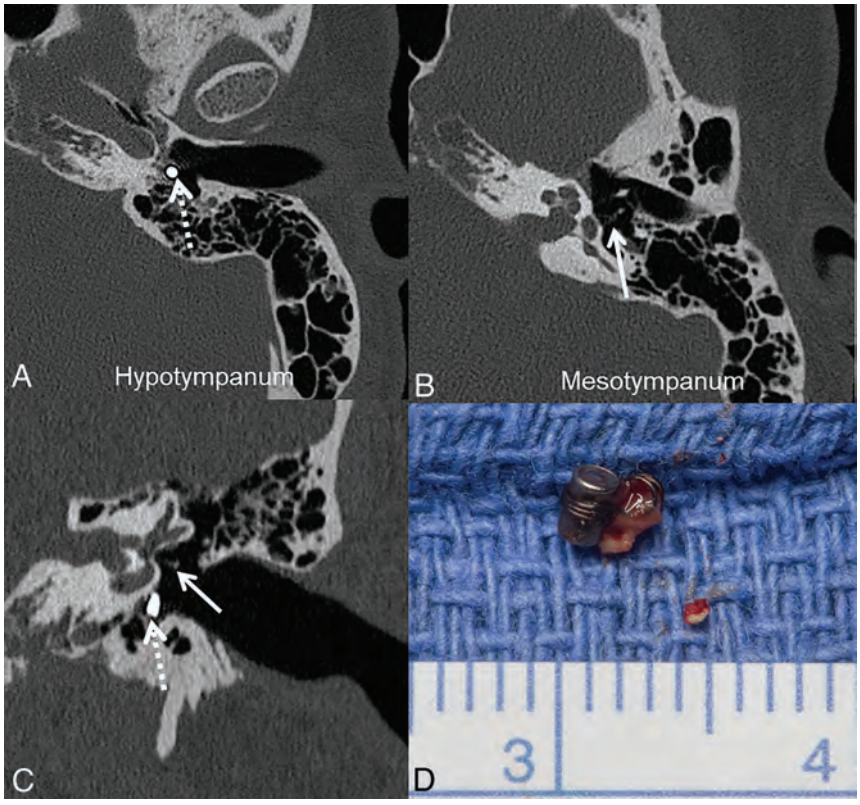

FIG 11. Dislodged floating mass transducer in a partially implantable active middle ear implant. Axial (*A*) and coronal (*C*) CT images show a dislodged floating mass transducer lying in the hypotympanum (*dotted white arrows*) instead of being attached to the stapes in the mesotympanum (*solid white arrows, B, C*). Postoperative photograph (*D*) shows the surgically retrieved floating mass transducer.

CONCLUSIONS

A wide spectrum of postoperative temporal bone findings may be encountered in practice. It is important not to misinterpret several expected postoperative findings for complications, surgical failure, or residual disease. Neuroradiologists' knowledge of the surgical approaches, in addition to associated expected and unexpected postoperative findings, can reduce the risk of misdiagnosis and unnecessary diagnostic testing.

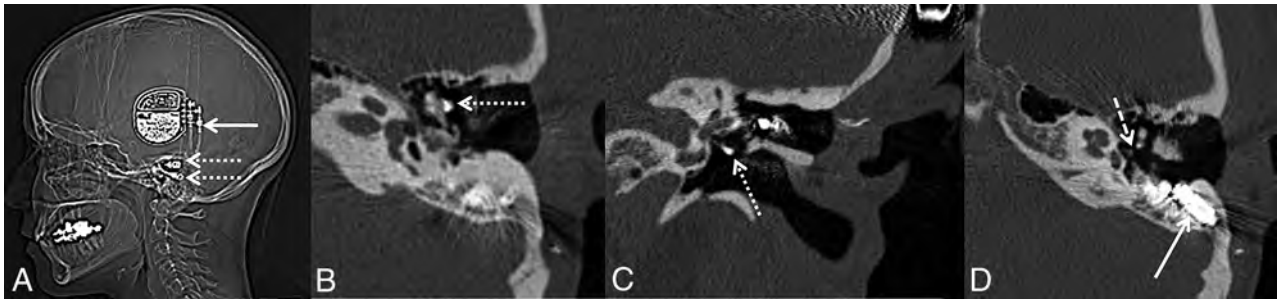

FIG 12. Expected CT findings in totally implantable AMEIs. Images show the different components of the totally implantable Esteem AMEI. The CT scout image shows the processor (*solid white arrow*) and separate internal sensor and driver leads (*dotted white arrows*). Axial (*B* and *D*) and coronal (*C*) CT images show the sensor on the incudomalleolar articulation (*dotted white arrow*, *B*), driver on the stapes (*dotted white arrow*, *C*), and audioprocessor in the mastoid (*solid white arrow*, *D*). The incudostapedial joint is disarticulated as part of the surgery (*dashed white arrow*, *D*) and should not be misdiagnosed as fracture/failure.

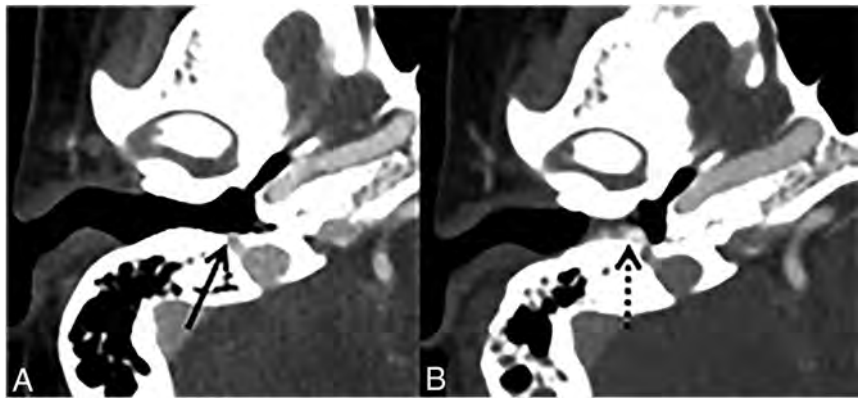

FIG 13. Jugular bulb dehiscence repair. Preoperative (*A*) and postoperative (*B*) axial CT images in a patient with pulsatile tinnitus show osseous dehiscence at the lateral margin of the high-riding right jugular bulb, with a diverticulum extending anteriorly to the tympanic annulus (*solid black arrow*, *A*). Intraoperatively, a bone pate was harvested from the mastoid cortex and used to cover the high-riding jugular bulb and jugular diverticulum. This is seen as hyperattenuating material at the tympanic annulus and external auditory canal on the postoperative CT (*dotted black arrow*, *B*).

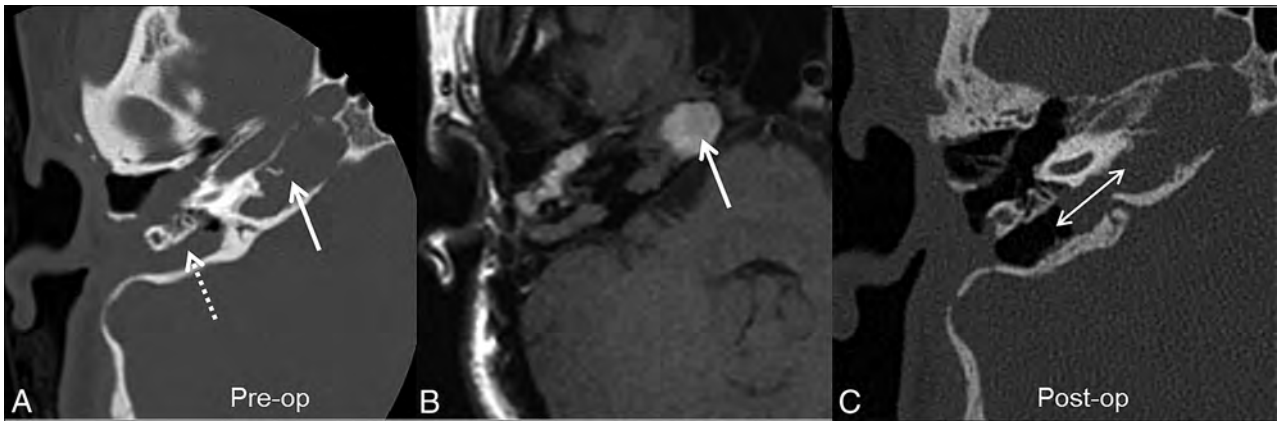

FIG 14. Petrous apex drainage surgery in a patient with recurrent right cholesterol granuloma. Predrainage CT image (*A*) shows a lesion expanding the petrous apex (*solid white arrow*) and extending to a prior postoperative mastoid defect (*dotted white arrow*). On T1-weighted MR imaging (*B*), the lesion is hyperintense (*solid white arrow*); it was also T2WI hyperintense and nonenhancing (not shown), consistent with a cholesterol granuloma. *C*, Postoperative CT image after drainage through a transmastoid infralabyrinthine approach shows the surgically created tract between the petrous and mastoid, allowing drainage of the petrous apex into the mastoid (*double-headed white arrow*). Pre-op indicates preoperative; Post-op, postoperative.

REFERENCES

1. Juliano AF, Ginat DT, Moonis G. **Imaging review of the temporal bone, Part II: traumatic, postoperative, and noninflammatory non-neoplastic conditions.** *Radiology* 2015;276:655–72 CrossRef Medline
2. Witte RJ, Lane JI, Driscoll CLW, et al. **Pediatric and adult cochlear implantation.** *Radiographics* 2003;23:1185–1200 CrossRef Medline
3. Mukherji SK, Mancuso AA, Kotzur IM, et al. **CT of the temporal bone: findings after mastoidectomy, ossicular reconstruction, and cochlear implantation.** *AJR Am J Roentgenol* 1994;163:1467–71 CrossRef Medline
4. Semaan MT, Megerian CA. **Meniere's disease: a challenging and relentless disorder.** *Otolaryngol Clin North Am* 2011;44:383–403, ix CrossRef Medline
5. Flores Garcia ML, Llata Segura C, Cisneros Lesser JC, et al. **Endolymphatic sac surgery for Meniere's disease: current opinion and literature review.** *Int Arch Otorhinolaryngol* 2017;21:179–83 CrossRef Medline
6. Nevoux J, Barbara M, Dornhoffer J, et al. **International consensus (ICON) on treatment of Meniere's disease.** *Eur Ann Otorhinolaryngol Head Neck Dis* 2018;135:S29–32 CrossRef Medline
7. Lo WW, Daniels DL, Chakeres DW, et al. **The endolymphatic duct and sac.** *AJNR Am J Neuroradiol* 1997;18:881–87 Medline
8. Kitahara M, Kitano H. **Surgical treatment of Meniere's disease.** *Am J Otol* 1985;6:108–09
9. Kitahara T. **Evidence of surgical treatments for intractable Meniere's disease.** *Auris Nasus Larynx* 2018;45:393–98 CrossRef Medline
10. Cody DT. **Automatic repetitive sacculotomy in endolymphatic hydrops.** *Otolaryng Clin N Am* 1968;1:637–42 CrossRef
11. Roberts DS, Slattery WH. **Labyrinthectomy for Meniere's disease.** *Operative Techniques in Otolaryngology-Head and Neck Surgery* 2016;27:188–93 CrossRef
12. Brackmann DE, Shelton C, Arriaga MA. *Otologic Surgery*. Elsevier; 2016
13. Ho ML. **Third window lesions.** *Neuroimaging Clin N Am* 2019;29:57–92 CrossRef Medline
14. Moonis G. **Imaging of third window lesions of the temporal bone.** *Semin Roentgenol* 2019;54:276–81 CrossRef Medline
15. Weindling SM, Broderick DF. **Semicircular canal dehiscence: imaging, diagnosis, classification, surgical options, and postoperative imaging.** *Neurographics* 2016;6:127–37 CrossRef

16. Mau C, Kamal N, Badeti S, et al. **Superior semicircular canal dehiscence: diagnosis and management.** *J Clin Neurosci* 2018;48:58–65 CrossRef Medline
17. Ward BK, Carey JP, Minor LB. **Superior canal dehiscence syndrome: lessons from the first 20 years.** *Front Neurol* 2017;8:177 CrossRef Medline
18. Rodgers B, Lin J, Staecker H. **Transmastoid resurfacing versus middle fossa plugging for repair of superior canal dehiscence: comparison of techniques from a retrospective cohort.** *World J Otorhinolaryngol Head Neck Surg* 2016;2:161–67 CrossRef Medline
19. Succar EF, Manickam PV, Wing S, et al. **Round window plugging in the treatment of superior semicircular canal dehiscence.** *Laryngoscope* 2018;128:1445–52 CrossRef Medline
20. Deveze A, Matsuda H, Elziere M, et al. **Diagnosis and treatment of perilymphatic fistula.** *Adv Otorhinolaryngol* 2018;81:133–45 CrossRef Medline
21. Larson TL, Wong ML. **Imaging of the mastoid, middle ear, and internal auditory canal after surgery: what every radiologist should know.** *Neuroimaging Clin N Am* 2009;19:307–20 CrossRef Medline
22. Oh MS, Vivas EX, Hudgins PA, et al. **The prevalence of superior semicircular canal dehiscence in patients with mastoid encephalocele or cerebrospinal fluid otorrhea.** *Otol Neurotol* 2019;40:485–90 CrossRef Medline
23. Peng T, Ramaswamy AT, Kim AH. **Common otologic surgical procedures: clinical decision-making pearls and the role of imaging.** *Neuroimaging Clin N Am* 2019;29:183–96 CrossRef Medline
24. Uezato S, Dias G, Inada J, et al. **Imaging aspects of Camurati-Engelmann disease.** *Rev Assoc Med Bras (1992)* 2016;62:825–27 CrossRef Medline
25. Andreu-Arasa VC, Sung EK, Fujita A, et al. **Otosclerosis and dysplasias of the temporal bone.** *Neuroimaging Clin N Am* 2019;29:29–47 CrossRef Medline
26. Svrakic M, Vambutas A. **Medical and audiological indications for implantable auditory devices.** *Otolaryngol Clin North Am* 2019;52:195–210 CrossRef Medline
27. Pok SM, Schlogel M, Boheim K. **Clinical experience with the active middle ear implant Vibrant Soundbridge in sensorineural hearing loss.** *Adv Otorhinolaryngol* 2010;69:51–58 CrossRef Medline
28. Loney EL. **The role of radiology in active middle ear implantation.** *Clin Radiol* 2014;69:e323–30 CrossRef Medline
29. Labassi S, Beliaeff M, Pean V, et al. **The Vibrant Soundbridge middle ear implant: a historical overview.** *Cochlear Implants Int* 2017;18:314–23 CrossRef Medline
30. Seidman MD, Janz TA, Shohet JA. **Totally implantable active middle ear implants.** *Otolaryngol Clin North Am* 2019;52:297–309 CrossRef Medline
31. Raghavan P, Serulle Y, Gandhi D, et al. **Postoperative imaging findings following sigmoid sinus wall reconstruction for pulse synchronous tinnitus.** *AJNR Am J Neuroradiol* 2016;37:136–42 CrossRef Medline
32. Manjila S, Bazil T, Kay M, et al. **Jugular bulb and skull base pathologies: proposal for a novel classification system for jugular bulb positions and microsurgical implications.** *Neurosurg Focus* 2018;45:E5 CrossRef Medline
33. DeHart AN, Shaia WT, Coelho DH. **Hydroxyapatite cement resurfacing the dehiscent jugular bulb: novel treatment for pulsatile tinnitus.** *Laryngoscope* 2018;128:1186–90 CrossRef Medline
34. Lansley JA, Tucker W, Eriksen MR, et al. **Sigmoid sinus diverticulum, dehiscence, and venous sinus stenosis: potential causes of pulsatile tinnitus in patients with idiopathic intracranial hypertension?** *AJNR Am J Neuroradiol* 2017;38:1783–88 CrossRef Medline
35. Razek AA, Huang BY. **Lesions of the petrous apex: classification and findings at CT and MR imaging.** *Radiographics* 2012;32:151–73 CrossRef Medline
36. Chapman PR, Shah R, Curé JK, et al. **Petrous apex lesions: pictorial review.** *AJR Am J Roentgenol* 2011;196:WS26–37 CrossRef Medline

Integrating New Staff into Endovascular Stroke-Treatment Workflows in the COVID-19 Pandemic

M. Goyal, J. Kromm, A. Ganesh, C. Wira, A. Southerland, K.N. Sheth, H. Khosravani, P. Panagos, N. McNair, and J.M. Ospel; On behalf of the AHA/ASA Stroke Council Science Subcommittees: Emergency Neurovascular Care (ENCC), the Cardiovascular and Stroke Nursing Council, the Telestroke and the Neurovascular Intervention Committees

ABSTRACT

SUMMARY: A health care crisis such as the coronavirus disease 2019 (COVID-19) pandemic requires allocation of hospital staff and resources on short notice. Thus, new and sometimes less experienced team members might join the team to fill in the gaps. This scenario can be particularly challenging in endovascular stroke treatment, which is a highly specialized task that requires seamless cooperation of numerous health care workers across various specialties and professions. This document is intended for stroke teams who face the challenge of integrating new team members into endovascular stroke-treatment workflows during the COVID-19 pandemic or any other global health care emergency. It discusses the key strategies for smooth integration of new stroke-team members in a crisis situation: 1) transfer of key knowledge (simple take-home messages), 2) open communication and a nonjudgmental atmosphere, 3) strategic task assignment, and 4) graded learning and responsibility. While these 4 key principles should generally be followed in endovascular stroke treatment, they become even more important during health care emergencies such as the COVID-19 pandemic, when health care professionals have to take on new and additional roles and responsibilities in challenging working environments for which they were not specifically trained.

ABBREVIATIONS: COVID-19 = coronavirus disease 2019; EVT = endovascular treatment; ICU = intensive care unit

The coronavirus disease 2019 (COVID-19) pandemic requires allocation of hospital staff and resources on short notice. As a consequence, new and sometimes less experienced team members might join the team to fill in the gaps. This scenario also applies to endovascular stroke treatment (EVT) workflows in the neuroangiography suite and post-EVT stroke care in the neuro-intensive care unit (Neuro-ICU) and stroke unit. There are several reasons why new members might join EVT teams. For example, stroke team members with ICU experience might be redeployed to an ICU and have to be replaced, or team members might be quarantined because they had close contact with a patient with COVID-19. Integrating new staff into EVT workflows is particularly challenging, given the time-critical nature of the disease, the need for seamless interdisciplinary and interprofessional cooperation, and the highly specialized skill sets of different team members.

This document is intended for stroke teams who face the challenge of integrating new staff into their EVT workflows during the COVID-19 pandemic or any other global health care emergency. It discusses strategies for smooth integration of new stroke-team members into EVT workflows in a crisis situation in 3 different settings: 1) the neuroangiography suite, 2) the Neuro-ICU ward, and 3) the stroke unit. The 4 overarching principles are the following: 1) transfer of key knowledge (simple take-home messages), 2) open communication and a nonjudgmental atmosphere, 3) strategic task assignment, and 4) graded learning and responsibility (Table 1). These 4 principles were developed during discussions among the members of the Emergency Neurovascular Care Committee, Cardiovascular and Stroke Nursing Council, and Telestroke and Neurovascular Intervention Committees and are mainly based on the joint experience of these committees. While it seems intuitively logical that those principles should generally be followed in clinical routine, and

Received August 7, 2020; accepted after revision August 21.

From the Departments of Clinical Neurosciences (M.G., J.K., A.G., J.M.O.), Critical Care Medicine (J.K.), and Diagnostic Imaging (M.G.), University of Calgary, Calgary, Alberta Canada; Department of Emergency Medicine and Stroke Program (C.W.) and Division of Neurocritical Care and Emergency Neurology (K.N.S.), Yale School of Medicine and Yale New Haven Hospital, New Haven, Connecticut; Departments of Neurology and Public Health Sciences (A.S.), University of Virginia, Charlottesville, Virginia; Neurology Quality and Innovation Laboratory (H.K.), Division of Neurology, Department of Medicine, Sunnybrook Health Sciences Centre, University of Toronto, Toronto, Ontario, Canada; Division of Emergency Medicine (P.P.), Washington University School of Medicine, St. Louis, Missouri; University of California (N.M.), Los Angeles, Los Angeles, California; and Department of Radiology (J.M.O.), University Hospital of Basel, Basel, Switzerland, On behalf of the AHA/ASA Stroke Council Science Subcommittees: Emergency Neurovascular Care (ENCC), the Cardiovascular and Stroke Nursing Council, the Telestroke and the Neurovascular Intervention Committees.

Please address correspondence to Mayank Goyal, MD, Departments of Radiology and Clinical Neurosciences, Foothills Medical Centre, 1403 29th S. NW, Calgary, AB, T2N2T9, University of Calgary, Calgary, AB, Canada; e-mail: mgoyal@ucalgary.ca; @mayank_G; @johanna_ospel

Indicates open access to non-subscribers at www.ajnr.org

Indicates article with supplemental on-line table.

http://dx.doi.org/10.3174/ajnr.A6854

Table 1: Four key principles for integration of new staff in the stroke team during a health care crisis

Key Principle	Explanation/Implementation Strategy	Example
Transfer of key knowledge	New staff members should be primarily taught the key principles of their new working environment; these should be kept as brief and concise as possible in order not to overwhelm new staff	Neuroangiography suite: never walk in the room without a lead apron if a patient is on the table Neuro-ICU: never use a nasogastric tube until proper placement has been confirmed by a clinician (most commonly by a portable chest x-ray) Stroke unit: never feed a patient with stroke with dysphagia solid food until a swallow screen has been performed
Open communication and nonjudgmental atmosphere	New staff members have to feel comfortable telling core members if they do not feel comfortable doing a certain task and should not hesitate to ask for help or advice	A new staff member is told to monitor a patient on an alteplase infusion but does not know what symptoms or signs to look for; he or she explains this to the supervisor who reassigns the patient to a more experienced member and helps train the new member in this important task
Strategic task assignment	To avoid mistakes and treatment delays, new team members should execute tasks that are as closely related as possible to their core field of expertise	A nurse from the nephrology ward joins the stroke team; he or she is familiar with management of patient vitals but not with neuroangiography-specific terminology, eg, guidewire, balloon-guide catheter; thus, the task should be focused on management of patient vitals rather than procedure-specific peculiarities
Graded responsibility and learning	New staff members should gradually take on new tasks and responsibilities; they should feel comfortable performing a certain task and be capable of executing it safely before they are assigned additional, more complicated tasks	A schedule that pairs shifts of new team members with core team members; new team members are intermixed in new roles, as they have to learn new and complex tasks

particularly when caring for patients with acute stroke, doing so becomes even more critical during health care emergencies such as the COVID-19 pandemic because in such a situation, health care professionals have to take on new and additional roles and responsibilities in challenging working environments for which they were not specifically trained.

This document is also intended to encourage and empower working groups and institutions to create a framework for fast decision-making in crisis situations. In the following, we summarize key knowledge, unique characteristics (ie, tasks that are not ideal for new team members), and generic aspects (ie, tasks that lend themselves to new team members because they can extrapolate their experience from their previous working environment) for acute stroke care in 3 different settings: the neuroangiography suite (Table 2), Neuro-ICU (Table 3), and stroke unit (Table 4). We believe that in a crisis such as the COVID-19 pandemic, the focus should be on the generic aspects of stroke care: New team members can build on their pre-existing knowledge and skills and therefore contribute best to guideline-based stroke care.[1] Given their greater experience, it might be reasonable to primarily assign stroke and particularly EVT-specific tasks to the "core members" of the stroke team.

Neuroangiography Suite

The neuroangiography environment differs from the Neuro-ICU and stroke unit in that the patient with stroke remains there for only a short time. The risk of radiation exposure and handling of thrombectomy equipment is unique to the neuroangiography suite and yields additional challenges for new staff members. Furthermore, the neuroangiography staff has to execute several highly specialized technical tasks, such as positioning of the neuroangiography table and preparing the appropriate catheters and thrombectomy devices. Because chances of good outcome rapidly decrease with increasing time to reperfusion, workflows in the neuroangiography suite need to be maximally time-efficient. Examples of more generic tasks in the neuroangiography suite that would be suitable for new stroke-team members would be managing IV lines and blood pressure monitoring, while management of access-site complications, handling of endovascular devices, and reconstruction and labeling of angiography images should preferably be performed by key staff members (Table 2).

Neuro-ICU and Stroke Unit

Acute ischemic stroke treatment does not stop once the occluded vessel has been opened. Post-EVT care on the Neuro-ICU and stroke unit is critical to support patient recovery and prevent poststroke complications, which may erase the benefits of EVT.[2] Typical Neuro-ICU and stroke units share many similarities, whereas stroke units often represent a "step-down" environment in which patients may be at risk of requiring escalation to critical care. A collaborative multidisciplinary team environment with effective role

Table 2: Take-home points for new staff and unique-versus-generic aspects of stroke care in the neuroangiography suite

Most Important Teaching Points (Take-Home Points) for New Team Members	Unique Characteristics of the Neuroangiography Suite Environment (Not Ideal Tasks for New Team Members)	Generic Aspects of the Neuroangiography Suite Environment That Are Similar to Those in Other Medical Areas (Appropriate Initial Tasks for New Team Members)
Radiation awareness	Handling the groin puncture/access site	Blood pressure control,[1] hemodynamic monitoring
Boundaries between sterile vs nonsterile environment	Handling of catheters and devices	Management of IV lines
Location of key emergency drugs and equipment (epinephrine, oxygen, intubation kit), key/safe combinations in case some drugs (eg, opiates) are stored in a safe	Navigating the angiography machine	Clinical monitoring of the patient during the procedure
Phone numbers and schedule of neurointerventionalists, anesthesiologists, techs, and nurses on call	Image reconstruction and labeling	Documentation of patient status

Table 3: Take-home points for new staff and unique-versus-generic aspects of stroke care in the Neuro-ICU[a]

Most Important Teaching Points (Take-Home Points) for New Team Members	Unique Characteristics of the Neuro-ICU Environment (Not Ideal Tasks for New Team Members)	Generic Aspects of the Neuro-ICU Environment That Are Similar to Those in Other Medical Areas (Appropriate Initial Tasks for New Team Members)
Key components of neuromonitoring (vital signs, neurologic vital signs: pupils, Glasgow Coma Scale, intracranial pressure, NIHSS score, and so forth)	Resuscitation of unstable patient on initial presentation or with complications (eg, procedures surrounding airway management, status epilepticus treatment, intracranial pressure/herniation treatment, shock management, and so forth)	Monitoring vital parameters, level of consciousness, and respiratory parameters of nonintubated patients
Recognizing potential life-threatening complications	Monitoring patients on invasive or noninvasive positive pressure ventilation	Management of enteral feeds and IV fluids
Location of key equipment (code cart, difficult airway cart) and medications	Care and use of arterial and central lines, administration of vasopressors	Basic medication administration (may include managing alteplase/tenecteplase infusions, depending on background)
Team members and roles Chain of help, contact information (pager/phone)Examples: ICU buddy team member (RN, RT, pharmacist, and so forth), charge nurse, NCC/stroke fellow, NCC/stroke attending physician on call	Use and interpretation of multimodal neuromonitoring: Intracranial pressure monitors (external ventricular drain) Cerebral oxygenation monitors: continuous brain tissue oxygenation, near-infrared spectroscopy, jugular venous catheter Cerebral blood flow monitors Cerebral microdialysis Continuous electroencephalography	Placement and care of nasogastric/orogastric tube, IV line, Foley catheter, and so forth
Key elements of AIS/ICH/SAH management (see also Table 4), basic and advanced life support	Brain death assessments and management	Bathing, turning, mobilizing patients
	Organ donation: donation after circulatory death or donation after neurologic death	Charting/documentation of patient course
	Palliation, depending on circumstances; for patients with COVID-19, institutions may have unique policies for automatic do-not-resuscitate orders or care limitations that incorporate neurologic prognosis formation	

Note:—RN indicates registered nurse; RT, respiratory therapist; NCC, neurocritical care; AIS, acute ischemic stroke; ICH, intracerebral hemorrhage.

[a] For specific Neuro-ICU take-home points for the management of patients with acute ischemic stroke, intracranial hemorrhage, and subarachnoid hemorrhage, see Online Table.

delegation is the cornerstone of both the Neuro-ICU and stroke unit, with most roles being quite similar (Figure), with the notable absence of respiratory therapists in most stroke units. Neuro-ICU tasks that lend themselves to new team members are, for example, placement of nasogastric and orogastric tubes and Foley catheters, while more ICU-specific aspects such as vasopressor therapy and optimization of positive pressure ventilation parameters should ideally remain with the core team members

Table 4: Take-home points for new staff and unique-versus-generic aspects of stroke care on the stroke unit

Most Important Teaching Points (Take-Home Points) for New Team Members	Unique Characteristics of the Stroke Unit Environment (Not Ideal Tasks for New Team Members)	Generic Aspects of the Stroke Unit Environment Similar to Other Medical Areas (Appropriate Initial Tasks for New Team Members)
Recognizing an acute stroke, recurrent stroke, and abrupt neurologic deterioration of recent ischemic or hemorrhagic stroke	Monitoring a patient in the unit after receiving IV alteplase (involves watching for angioedema, bleeding, frequent neurologic vital sign monitoring, close blood pressure control, and so forth)	Obtaining/interpreting scheduled vital signs (temperature, blood pressure, heart rate, respiratory rate, oxygen saturation) and point-of-care blood glucose in patients
Managing infusions of alteplase for stroke or of heparin (eg, for intraluminal thrombosis, venous sinus thrombosis)	Being part of the acute stroke thrombolysis team (being comfortable with the "code stroke" and mixing alteplase)	Foley catheter insertion, urinary dipstick testing, and identification of potential urinary tract infection
Grossly identifying patients who are potentially aspirating versus those safe to swallow	Managing a patient at risk of malignant middle cerebral artery or cerebellar stroke (involves closely watching for neurologic deterioration and liaising with stroke/neurosurgery team for potential decompressive craniectomy)	Managing the patient's routine medications and reconciling them with those taken preadmission
NG insertion, feeding, and NG medication administration	Managing a patient with a major intracranial hemorrhage (involves watching for emerging symptoms of hydrocephalus or major hematoma expansion that may warrant neurosurgical intervention or ICU transfer)	Caring for a patient in the subacute-to-chronic poststroke period with/without medical issues like urinary tract infection, cellulitis, or pressure ulcers
Performing a NIHSS bedside examination	Receiving a patient after thrombectomy (involves monitoring the groin puncture site or managing hematoma)	Evaluation and initial management of a patient with chest pain or shortness of breath (eg, poststroke myocardial infarction, aspiration pneumonia)
Pager or phone numbers and schedule of stroke fellows and neurologists on call	Receiving a patient after carotid endarterectomy (involves watching for reperfusion complications, lower cranial neuropathies interfering with swallowing)	Evaluation and initial management of a patient with deep vein thrombosis
Understanding basic stroke mechanisms for early secondary prevention	Defining a stroke mechanism through a sophisticated understanding of neurovascular anatomy, localization, and cerebrovascular syndromes	Working with patient and pharmacy to ensure proper dosing and administration of early secondary stroke prevention (eg, antithrombotics, statin therapy, blood pressure regimen, smoking cessation)

Note:—NG indicates nasogastric tube.

(Table 3). In the stroke unit, new staff might want to start with managing patients' routine medication and Foley catheter and IV-lines, while obtaining a detailed neurologic status such as the NIHSS would be a more suitable task for experienced team members (Table 4). Nevertheless, it would certainly be desirable for the newer team members to initiate structured training regarding stroke-specific tasks (eg, NIHSS score) under the guidance of pre-existent staff members as would be the local standard at that institution.

Simulation training ("dry" practice runs with a nurse or mannequin acting as the patient) can help to practice specific workflow steps, identify latent safety threats, and familiarize new team members with their new tasks.[3] Simulation team training has also been shown to improve team functioning—communication and cooperation of different members among a medical team.[4,5] This is particularly important for workflow in the neuroangiography suite because treatment delays at this stage will lead to delayed reperfusion and thereby directly affect patient outcome. It is important to establish continuous monitoring of treatment quality (eg, reperfusion quality and access site complications such as groin hematomas and infections following endovascular treatment) and workflow times (door-to-needle times, door-to-groin puncture times), particularly in a health care crisis, to ensure that treatment quality is maintained to the best of the ability of the system and to detect problems in EVT workflows and treatment quality early on, which grants the medical team the opportunity to intervene in a timely manner. One might be tempted to think that continuous performance monitoring for complex, multidimensional tasks involving numerous specialties as is the case in endovascular stroke treatment is impractical, but studies have repeatedly shown that team performance in medicine can be validly measured across complex settings and that doing so helps to improve treatment workflow.[6]

CONCLUSIONS

Endovascular stroke treatment reaches well beyond the neuroangiography suite and encompasses a wide range of specialties (neurology, neuroradiology, neurosurgery, anesthesia, intensive care) and designations (physicians [among them attendings, fellows, and residents], nurses, technologists, pharmacists, therapists, nutritionists, medical students, nurse practitioners, physician assistants), just to name a few. During the COVID-19 pandemic and other major health care emergencies, augmentation of staff from other areas may be required due to staff redeployment, staff exposures/required quarantines, and increased patient demands.[7] This carries the risk of decreasing the quality of EVT and post-EVT care.[8]

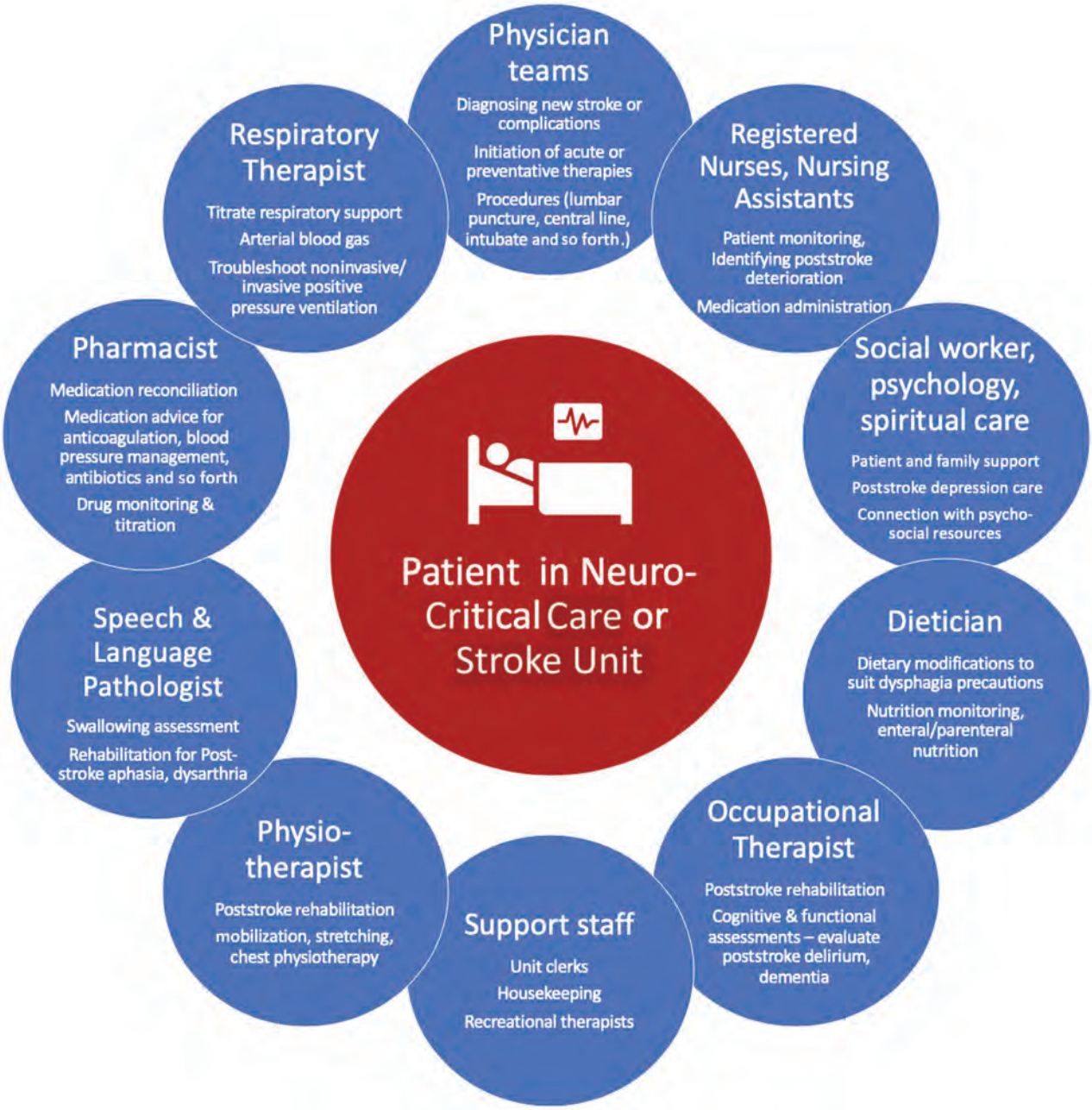

FIGURE. A model of patient-centered multidisciplinary care in the Neuro-ICU or stroke unit that is both helpful and reassuring for new staff members. The model is quite similar in both the neuro-critical care and stroke units with the notable exception of respiratory therapists who are often not part of medical stroke units. While this model is, of course, generalizable to nonstroke settings as well, some specific examples are illustrated to show how different members of the team may synergistically address a stroke-related problem. For example, in a patient with dysphagia, the nursing or physician team may be the first to notice a poststroke deterioration with the patient choking or coughing during a simple trial. This prompts the team to involve the speech and language pathologist who confirms poststroke dysphagia and recommends a temporary nasogastric tube, which is inserted by a nurse (perhaps with a new nursing team member observing this common task), with the dieticians then helping ensure that the nasogastric feed provided meets the patient's feeding requirements, potentially monitoring for a refeeding syndrome. These changes may be overwhelming for the patient and family, prompting the team to involve psychology to assess poststroke depression as well as social work and spiritual care to connect the patient and family to key resources.

Maintaining timely and comprehensive endovascular stroke care at a high quality during a health care crisis such as the COVID-19 pandemic is of utmost importance. Of note, the framework that was outlined in this article for integration of new members into existing stroke teams is based on personal experience of the American Heart Association/American Stroke Association Stroke Council Science Subcommittee members rather than objective data. Nevertheless, we would like to encourage individual stroke teams and their hospitals to collect data from their COVID-19 experience and publish them, because this would provide valuable information

to stroke teams and help them to further improve EVT workflows and post-EVT care in similarly challenging situations.

Disclosures: Aravind Ganesh—*UNRELATED*: *Consultancy*: MD Analytics, My Medical Panel, Adkins Research Group, and Genome BC; *Grants/Grants Pending*: Rhodes Trust, Wellcome Trust, the University of Calgary, Alberta Innovates, the Canadian Cardiovascular Society, and the Canadian Institutes of Health Information; *Payment for Lectures Including Service on Speakers Bureaus*: National Health Service Health Education England; *Patents (Planned, Pending Or Issued)*: a provisional patent application (US 63/024,239) for a system to deliver remote ischemic conditioning or other cuff-based therapies; *Stock/Stock Options*: SnapDx, TheRounds.ca, and Advanced Health Analytics; *Travel/Accommodations/Meeting Expenses Unrelated to Activities Listed*: University of Calgary; *OTHER RELATIONSHIPS*: unpaid membership in the editorial boards of *Neurology*, *Neurology: Clinical Practice,* and *Stroke*. Andrew Southerland—*RELATED*: *Consulting Fee or Honorarium:* Legal Expert Consultation, paid to the University of Virginia Physicians Group on his behalf. *UNRELATED*: *Board Membership*: *Neurology Podcast*, *Comments*: I served as past section editor of the journal *Neurology Podcast*; I completed the paid role in 2018; *Consultancy*: NeurovView Diagnostics, *Comments*: unpaid consultancy, work completed; *Employment*: University of Virginia Health System; *Expert Testimony*: legal expert consultation, *Comments*: I provide expert legal review for vascular neurology and stroke cases, both plaintiff and defense work*; *Grants/Grants Pending*: Diffusion Pharmaceuticals, *Comments*: Principal Investigator, PHAST-TSC Trial, https://clinicaltrials.gov/ct2/show/NCT03763929*; *Patents (Planned, Pending or Issued)*: US Patent Application No. 14/910,890 (iTREAT), US Provisional Patent Application No. 62/620,096 (BANDIT), *Comments*: patents pending. Peter Panagos—*RELATED*: *Grant*: National Institutes of Health/National Institute of Neurological Disorders and Stroke*; *UNRELATED*: *Employment*: Washington University. Norma McNair—*UNRELATED*: *Board Membership*: American Board of Neuroscience Nursing, *Comments*: reimbursement for travel expenses only, no payment. Kevin N. Sheth—*UNRELATED*: *Consultancy*: Ceribell, ZOLL; *Grants/Grants Pending*: National Institutes of Health, American Heart Association, Biogen, Bard, Novartis, Hyperfine; *Stock/Stock Options*: Alva. *Money paid to the institution.

REFERENCES

1. Powers WJ , Rabinstein AA, Ackerson T, et al. **Guidelines for the Early Management of Patients with Acute Ischemic Stroke: 2019 Update to the 2018 Guidelines for the Early Management of Acute Ischemic Stroke—A Guideline for Healthcare Professionals from the American Heart Association/American Stroke Association.** *Stroke* 2019;50:e344–418 CrossRef Medline
2. Ganesh A, Menon BK, Assis ZA, et al. **Discrepancy between post-treatment infarct volume and 90-day outcome in the ESCAPE randomized controlled trial.** *Int J Stroke* 2020 June 9. [Epub ahead of print] CrossRef Medline
3. Patterson MD, Geis GL, Falcone RA, et al. **In situ simulation: detection of safety threats and teamwork training in a high risk emergency department.** *BMJ Qual Saf* 2013;22:468–77 CrossRef Medline
4. Buljac-Samardzic M, Doekhie KD, van Wijngaarden JDH. **Interventions to improve team effectiveness within health care: a systematic review of the past decade.** *Hum Resour Health* 2020;18:2 CrossRef Medline
5. Kurz MW, Ospel JM, Advani R, et al. **Simulation methods in acute stroke treatment: current state of affairs and implications.** *Stroke* 2020;51:1978–82 CrossRef Medline
6. Rosen MA, DiazGranados D, Dietz AS, et al. **Teamwork in healthcare: key discoveries enabling safer, high-quality care.** *Am Psychol* 2018;73:433–50 CrossRef Medline
7. Qiu H, Tong Z, Ma P, et al; China Critical Care Clinical Trials Group (CCCCTG). **Intensive care during the coronavirus epidemic.** *Intensive Care Med* 2020;46:576–78 CrossRef Medline
8. Lee A, Cheung YSL, Joynt GM, et al. **Are high nurse workload/staffing ratios associated with decreased survival in critically ill patients? A cohort study.** *Ann Intensive Care* 2017;7:46 CrossRef Medline

Enhancing Education to Avoid Complications in Endovascular Treatment of Unruptured Intracranial Aneurysms: A Neurointerventionalist's Perspective

M. Goyal, J. Fiehler, W. van Zwam, J.H. Wong, and J.M. Ospel

ABSTRACT

SUMMARY: It is of utmost importance to avoid errors and subsequent complications when performing neurointerventional procedures, particularly when treating low-risk conditions such as unruptured intracranial aneurysms. We used endovascular treatment of unruptured intracranial aneurysms as an example and took a survey-based approach in which we reached out to 233 neurointerventionalists. They were asked what they think are the most important points staff should teach their trainees to avoid errors and subsequent complications in endovascular treatment of unruptured intracranial aneurysms. One hundred twenty-one respondents (51.9%) provided answers in the form of free text responses, which were thematically clustered in an affinity diagram and summarized in this Practice Perspectives. The article is primarily intended for neurointerventional radiology fellows and junior staff and will hopefully provide them the opportunity to learn from the mistakes of their more experienced colleagues.

A smart man makes a mistake, learns from it, and never makes that mistake again. But a wise man finds a smart man and learns from him how to avoid the mistake altogether.

Roy H. Williams

As neurointerventional fellows, we are bound to make mistakes. Human errors in neurointervention occur in up to 12% of cases,[1] and they are, to some degree, unavoidable, but mentorship can prevent some of them from happening. The weighing of treatment risks and benefits is of particular importance for low-risk conditions such as unruptured intracranial aneurysms, in which complications weigh heavily on the neurointerventionalist. Thoughtful mentors will share their experiences and, most important, their errors and failures with us so that we can learn from their mistakes. What do experienced neurointerventionalists wish they had been told as fellows? We used endovascular treatment of unruptured intracranial aneurysms as an example and took a survey-based approach in which we reached out to 233 neurointerventionalists to answer this question (mostly senior staff; for detailed demographics and countries of survey participants see Online Tables 1 and 2). Participants were asked the most important points staff should teach their trainees to avoid complications in endovascular treatment of unruptured intracranial aneurysms. One hundred twenty-one respondents (51.9%) provided answers in the form of free text responses, which were thematically clustered in an "Affinity Diagram" (Online Appendix). This format was deliberately chosen to avoid narrowing the responses down to certain topics by suggesting topics or providing examples. The free text answers were then screened, and it was determined whether they contained ≥1 thematically distinct message. If the latter was the case, the response was split accordingly. Responses were then manually clustered by identifying common themes. Thematically similar responses were clustered together. Those clusters with the largest number of responses were extracted and formed the basis for the article. They are shown in the Table and summarized below (for key recommendations, see also the Figure).

Asking for Help

Neurointerventional skills are learned progressively, and a realistic and honest appraisal of one's own skillset and limitations was considered crucial by most respondents. Fellows should know when to refer a case to a more experienced colleague and never be hesitant to reach out to colleagues for help and advice; not doing so means putting the patient at risk.

Received June 12, 2020; accepted after revision July 31.

From the Departments of Clinical Neurosciences (M.G., J.H.W., J.M.O.) and Radiology (M.G., J.H.W.), and Division of Neurosurgery (J.H.W.), University of Calgary, Calgary, Alberta, Canada; Department of Diagnostic and Interventional Neuroradiology (J.F.), University Medical Center Hamburg-Eppendorf, Hamburg, Germany; Department of Radiology and Nuclear Medicine (W.v.Z.), Cardiovascular Research Institute Maastricht, School for Mental Health and Sciences, Maastricht University Medical Center, Maastricht, the Netherlands; and Department of Radiology (J.M.O.), University Hospital of Basel, Basel, Switzerland.

Please address correspondence to Mayank Goyal, MD, PhD, Departments of Radiology and Clinical Neurosciences, Foothills Medical Centre, 1403 29th St NW, Calgary, AB, T2N2T9, University of Calgary, Calgary, AB, Canada; e-mail: mgoyal@ucalgary.ca; @johanna_ospel; @mayank_G0

Indicates article with supplemental on-line appendix and table.

http://dx.doi.org/10.3174/ajnr.A6830

Summary of the most common response clusters with exemplary responses

Response Cluster[a]	Explanation	Exemplary Responses[a]
General advice		
Humility and ethical standards	Realistic appraisal of one's skillset and its limitations	"We need calm and honest fellows, not cowboys" "Be aware of overestimating your own skills"
Interaction with colleagues and asking for advice	Reaching out for advice and help from more experienced colleagues when needed	"Don't be a hero—stop and ask!" "Be comfortable referring for a second opinion"
Critically revisiting complications and their management	Discussion of complications with colleagues in and outside M&M rounds and meetings, constructive feedback, root-cause analysis	"Show fellows their own complications and deaths, and how to deal with them if there was a second chance" "Honestly self-review all cases in which [a] complication has occurred and understand what went wrong. Never blame it on device quality or malfunction"
Preprocedural phase		
Indication and patient selection	Patient-centered treatment decision-making, knowing which patients one should not treat	"Learn when to say no" "What not to treat in the first 3–5 years of practice" "Knowing which patients can be safely followed"
Preoperative planning	Thorough review of prior imaging, a priori planning of specific procedure steps, anticipation of potential problems and alternative solutions	"Study the 3D angio, don't rush, plan your approach. What's the plan B, C?" "Work-up each case very carefully and try to predict complications" "Before doing a procedure, think of everything that can induce a procedural complication"
Keeping alternative treatment options in mind	Considering surgical options (clipping, sacrificing the parent vessel) and watch-and-wait strategies	"Less emphasis on endovascular being the be-all and end-all" "Never forget that competent and adequate surgical clipping is feasible and sometimes ideal!"
Theoretic knowledge	Solid knowledge about cerebrovascular anatomy	"Be properly trained, both technical and theoretical!, before you start." "More training in some programs on how to look at imaging"
Intraprocedural phase		
Technical skills	Acquiring technical skills in a simulation environment before performing real cases	"Always be careful with patients and train a lot in silicone models/computer simulators!!" "Simulators are how you need to learn and master the nuances of different cases, not trial and error on patients"
Standardization and simplification	Standardization of procedure steps, prespecified protocols for the management of complications	"Stick to the given protocols each and every time" "Meticulous planning of the procedure" "Show all types of possible complications and write protocols for how to deal with them"
Knowing when to stop	Recognizing the point at which continuing the procedure will likely cause more harm than benefit, avoiding the "perfection trap"	"If you think that you can put one more coil, that is [the] time to stop!" "Don't let the best be the enemy of the good" "How to reduce unnecessary and perfectionist steps"

Note:—M&M indicates morbidity and mortality.

[a] For a detailed overview of response clusters and individual responses, see the "Affinity Diagram" in the Online Appendix.

Many responses emphasized the importance of honestly discussing and revisiting complications and their management in an open and nonjudgmental environment,[2] be it in morbidity and mortality rounds,[3] interaction with colleagues,[4] or professional society meetings.

Treatment Indication

Ensuring successful treatment requires picking the right patients in the first place. Participants advised fellows to perform a thorough risk-benefit analysis before every treatment decision. Knowing which cases not to treat in the early years of practice was considered key knowledge for fellows.[5] Proper review of noninvasive imaging to anticipate and prevent potential complications and planning of alternative strategies, "having a plan A, B, and C" as one of the respondents stated, was thought to be essential to handle unexpected events.

The goal is to ensure that patients receive the best possible treatment, be it endovascular, surgical, or conservative ("watch

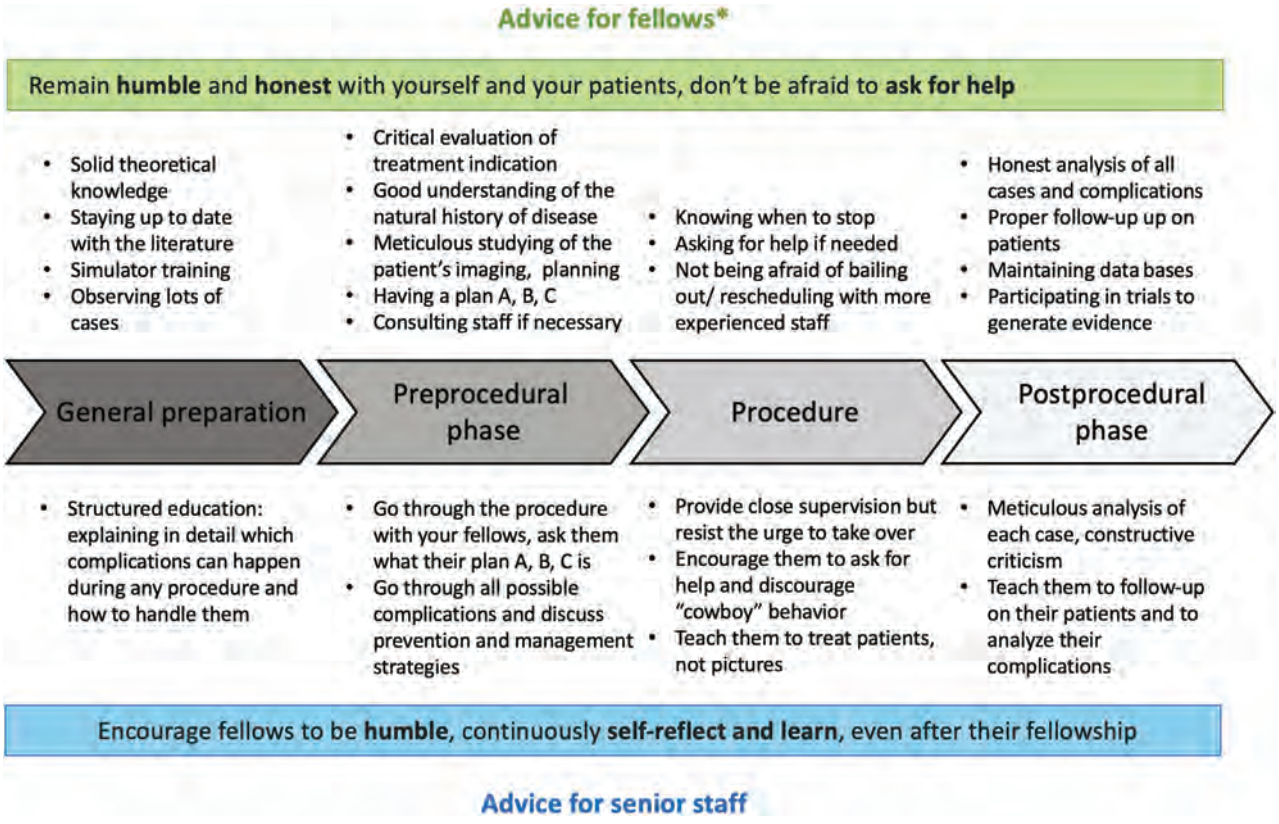

FIGURE. Key recommendations for fellows and senior staff on how to avoid complications in endovascular treatment of unruptured intracranial aneurysms regarding general preparation, preprocedural, intraprocedural, and postprocedural phases. The *asterisk* indicates that this advice also applies to junior staff.

and wait"), and this will require an open and unbiased discussion among physicians from different medical specialties, including diagnostic and interventional neuroradiology, neurosurgery, and neurology.

Simulation Training and Standardized Procedural Steps

Simulation training constitutes a safe environment to practice technical skills.[6-10] Physicians believed that fellows should train as much as possible in a simulation environment to learn basic catheter skills before performing real cases. Standard operating procedures for every procedure step, close adherence to protocols for the management of intraprocedural complications, and choosing the simplest treatment approach possible were additional points physicians considered of high importance.[11]

Safety

Using a few devices well was thought to be much wiser than the use of a wide variety of new devices, for which safety and efficacy data are often limited: "keeping it as simple and safe as possible," as many of them put it. Accepting imperfection and avoiding unnecessary and dangerous perfectionist steps toward the end of a procedure were perceived crucial for fellows: "If you think that you can put one more coil, this is [the] time to stop."

Humans make mistakes, and they make them frequently. Neurointervention is no exception to this rule, and the stakes are high. The advice summarized in this article (see the Figure for key recommendations for fellows and senior staff) is intended to help fellows and junior staff "to be wise" as Roy H. Williams put it—that is, to learn from the mistakes of their more experienced colleagues.

Disclosures: Mayank Goyal—*RELATED*: *Consulting Fee or Honorarium*: Mentice, *Comments*: advice on acute stroke intervention; *UNRELATED*: *Consultancy:* Stryker, Medtronic, MicroVention; *Patents (Planned, Pending or Issued)*: GE Healthcare, *Comments*: licensing agreement for systems of acute stroke diagnosis. Jens Fiehler—*UNRELATED*: *Consultancy:* Acandis, Cerenovus, Medtronic, MicroVention, Stryker, Penumbra; *Grants/Grants Pending*: Acandis, Cerenovus, Medtronic, MicroVention, Stryker, Route94*; *Stock/Stock Options*: Tegus; *OTHER RELATIONSHIPS*: CEO Eppdata. Wim van Zwam—*UNRELATED*: *Payment for Lectures Including Service on Speakers Bureaus*: Cerenovus, Stryker,* John H. Wong—*UNRELATED*: *Stock/Stock Options*: Fluid Biotech Inc, *Comments*: Cofounder and CEO of Fluid Biotech Inc. Johanna M. Ospel—*UNRELATED*: *Grants/Grants Pending*: Gottfried und Julia Bangerter Rhyner Stiftung, University of Basel Research Foundation, Freiwiliige Akademische Gesellschaft Basel, *Comments*: research scholarships. *Money paid to the institution.

REFERENCES

1. Gross BA, Jadhav AP, Jovin TG, et al. **Neurointerventional "near morbidity": a candid appraisal of an early case series.** *Interv Neurol* 2018;7:419–30 CrossRef Medline
2. Lyckholm L. **Medical errors and medical culture: there is no easy way around taking responsibility for mistakes.** *BMJ* 2001;323:570 CrossRef Medline
3. Mok PS, Tan EY, Baerlocher MO, et al. **The role of morbidity and mortality meetings in interventional radiology.** *Eur J Radiol* 2012;81:3344–47 CrossRef Medline
4. Fargen KM, Velat GJ, Lawson MF, et al. **Enhanced staff communication and reduced near-miss errors with a neurointerventional procedural checklist.** *J Neurointerv Surg* 2013;5:497–500 CrossRef Medline

5. Eskey CJ, Meyers PM, Nguyen TN, et al; American Heart Association Council on Cardiovascular Radiology and Intervention and Stroke Council. **Indications for the performance of intracranial endovascular neurointerventional procedures: a Scientific Statement from the American Heart Association.** *Circulation* 2018;137:e661–89 CrossRef Medline
6. Kreiser K, Gehling K, Zimmer C. **Simulation in angiography: experiences from 5 years teaching, training, and research** [In German]. *Rofo* 2019;191:547–52 CrossRef Medline
7. Kreiser K, Ströber L, Gehling KG, et al. **Simulation training in neuroangiography: validation and effectiveness.** *Clin Neuroradiol* 2020 April 27. [Epub ahead of print] CrossRef Medline
8. Spiotta AM, Rasmussen PA, Masaryk TJ, et al. **Simulated diagnostic cerebral angiography in neurosurgical training: a pilot program.** *J Neurointerv Surg* 2013;5:376–81 CrossRef Medline
9. Bechstein M, Buhk JH, Frolich AM, et al. **Training and supervision of thrombectomy by Remote Live Streaming Support (RESS): randomized comparison using simulated stroke interventions.** *Clin Neuroradiol* 2019 Dec 20. [Epub ahead of print] CrossRef Medline
10. Kreiser K, Gehling KG, Strober L, et al. **Simulation training in neuroangiography: transfer to reality.** *Cardiovasc Intervent Radiol* 2020;43:1184–91 CrossRef Medline
11. Frei D, McGraw C, McCarthy K, et al. **A standardized neurointerventional thrombectomy protocol leads to faster recanalization times.** *J Neurointerv Surg* 2017;9:1035–40 CrossRef Medline

Decubitus CT Myelography for CSF-Venous Fistulas: A Procedural Approach

M.D. Mamlouk, R.P. Ochi, P. Jun, and P.Y. Shen

ABSTRACT

SUMMARY: Decubitus CT myelography is a reported method to identify CSF-venous fistulas in patients with spontaneous intracranial hypotension. One of the main advantages of decubitus CT myelography in detecting CSF-venous fistulas is using gravity to dependently opacify the CSF-venous fistula, which can be missed on traditional myelographic techniques. Most of the CSF-venous fistulas in the literature have been identified in patients receiving general anesthesia and digital subtraction myelography, a technique that is not performed at all institutions. In this article, we discuss the decubitus CT myelography technique and how to implement it in daily practice.

ABBREVIATIONS: CTM = CT myelography; DSM = digital subtraction myelography; SIH = spontaneous intracranial hypotension

A spinal CSF-venous fistula is an abnormal connection that usually occurs between a meningeal diverticulum and a paraspinal vein that results in continuous shunting of CSF fluid and spontaneous intracranial hypotension (SIH).[1] CSF-venous fistulas are 1 of the 3 types of CSF leaks, while CSF leaks from dural tears and ruptured meningeal diverticula are the remaining types.[2] While the incidence of CSF-venous fistulas was originally thought to be rare, they may be present in a quarter of patients with SIH.[3] In our experience and in the published literature, CSF-venous fistulas are under-recognized and are mostly discussed at only a few quaternary SIH academic centers in the United States.

Various diagnostics techniques have been reported to identify CSF-venous fistulas, which include conventional fluoroscopy and CT myelography (CTM), digital subtraction myelography (DSM), MR imaging myelography, and decubitus myelography in the aforementioned modalities.[3-11] Of these techniques, decubitus CTM and DSM are the most frequently described in the literature to identify CSF-venous fistulas. The decubitus position permits contrast to flow into a CSF-venous fistula on the dependent side of the thecal sac via gravity. Because of this phenomenon, CSF-venous fistulas have been diagnosed on decubitus CTM and missed on prone or supine CTM.[11] DSM has also used a similar advantage with the decubitus technique. In 1 study, a CSF-venous fistula was detected in 17 of 23 patients on decubitus DSM compared with 4 of 26 patients who underwent prone DSM.[3] While both decubitus CTM and DSM can identify CSF-venous fistulas, there are no reported studies that have compared the sensitivities and specificities of detection.

There is a learning curve in some of these techniques, which may be challenging to perform and prevent radiologists from accurately diagnosing CSF-venous fistulas in daily practice. Kaiser Permanente Medical Center has explored many of the aforementioned myelographic techniques and found decubitus CTM to be a useful and relatively simple method to perform in most clinical practices and perhaps easier than DSM. There are many barriers to the DSM technique. First, familiarity with digital subtraction imaging is a requisite for DSM and may be challenging to implement if the operator does not have traditional interventional or neurointerventional training. Second, DSM is not performed at all institutions, and last, general anesthesia may be required.[8] The purpose of this article is to discuss the procedural technique of decubitus CTM and when to perform it in a patient with SIH so that radiologists of various backgrounds can implement it in their practices.

Patient Selection

In patients with clinical suspicion and intracranial imaging findings consistent with SIH seen on a contrast-enhanced brain MR imaging, the referring provider at our institution is instructed to obtain a noncontrast total spine MR imaging. Our spine MR imaging technique consists of sagittal and axial T2-weighted

Received June 3, 2020; accepted after revision August 12.

From the Department of Radiology (M.D.M., P.J., P.Y.S.), The Permanente Medical Group, Kaiser Permanente Medical Center, Santa Clara, Santa Clara, California; Department of Radiology and Biomedical Imaging (M.D.M.), University of California, San Francisco, San Francisco, California; and Department of Radiology (R.P.O.), The Permanente Medical Group, Kaiser Permanente Medical Center, Sacramento, Sacramento, California.

Please address correspondence to Mark D. Mamlouk, MD, Department of Radiology, The Permanente Medical Group, Kaiser Permanente Medical Center, Santa Clara, 700 Lawrence Expy, Santa Clara, CA 95051; e-mail: mark.d.mamlouk@kp.org; @MarkMamloukMD

http://dx.doi.org/10.3174/ajnr.A6844

imaging with a fat-suppression technique, which can detect extradural collections compatible with a CSF leak.[12] Because the main reason for scanning these patients is to detect a CSF leak, we do not perform T1-weighted imaging or administer contrast because these sequences do not provide much additional value and unnecessarily increase the examination time. Contrast-enhanced sequences can better identify distended dural veins compared with the T2 sequence, but the T2 technique can differentiate the veins from a CSF leak: the former will be hypointense, and the latter, hyperintense.[12] If MR imaging of the spine shows an extradural collection, the patient often has a fast CSF leak[7] and we perform dynamic CTM with the patient in the prone Trendelenburg position using 1–2 mL of contrast, followed by targeted epidural blood patches.[13] If MR imaging of the spine does not show an extradural collection, we perform decubitus CTM to exclude a CSF-venous fistula.

CSF-venous fistulas have been reported in a few patients with clinical symptoms of SIH but with normal brain MRI findings.[8] We have occasionally performed decubitus CTM in patients with suspected SIH with normal brain MRI findings but have not found a CSF-venous fistula. To our knowledge, there are no specific myelographic recommendations in this patient cohort, and further studies are needed for guidance because cost, radiation, and the intervention itself are additional factors to consider.

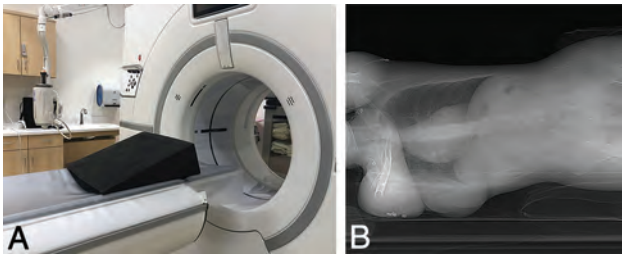

FIG 1. Patient positioning for decubitus CTM. *A*, A custom-made firm wedge with a 20° angle is placed on the CT gantry, and the hips are placed at the apex of the wedge with the feet closest to the scanner bore. If no wedge is available, 1–2 pillows can be placed instead. Pillows can also be used to support the legs. *B*, A lateral scout radiograph shows an adequate angle to facilitate contrast transit from the lumbar puncture to the remainder of the spine.

Procedural Technique

Decubitus Positioning. After review of the prior spine MR imaging and/or conventional myelograms if already performed, the operating physician decides whether to place the patient in the right or left decubitus position on the CT gantry table. This decision is usually predicated on which side has the greater number of enlarged or irregular-appearing meningeal diverticula on the prior imaging. While meningeal diverticula can occur normally in patients without SIH, their existence may harbor a CSF-venous fistula in patients with SIH.[5] If the meningeal diverticula are approximately equal between the 2 sides or they are few in number, the right side is usually chosen because we have witnessed the right being more commonly implicated in our experience (82%). Two additional studies[6,14] have noted predominance on the right, while 1 study[5] has reported CSF-venous fistulas more commonly occurring on the left.

We place the patient in the decubitus position with the use of a custom-made wedge, which is a firm sponge with a 20° angle (Fig 1*A*). This wedge is chosen to facilitate flow of contrast from the lumbar puncture to the thoracic and cervical spine. If no wedge is available, 1–2 pillows can be placed under the patient's hips to achieve the same result. Pillows can also be placed under the patient's legs for comfort. Before proceeding with the lumbar puncture, the operating physician should observe that an adequate Trendelenburg angle (10°–20°) is achieved. We also position the patient's hands above the head to prevent beam-hardening while scanning. If the patient is unable to raise his or her hands for a long duration, then the hands can be placed by the side or chest and simply raised at the time of the total spine myelogram scanning.

Lumbar Puncture and Image Planning. We perform the lumbar puncture directly on the CT table as opposed to puncturing under fluoroscopy and then scanning with CT. The main reason for this direct technique is because we have observed that when the contrast mixes throughout the spinal canal and becomes more dilute, the CSF-venous fistula is more difficult to see. We believe this practice is one of the keys to successful imaging of CSF-venous fistulas. We also typically administer moderate sedation to our patients to make them comfortable during the procedure.

Initial scout images of the total spine are obtained in the frontal and lateral planes. We scrutinize the lateral scout image to ensure that there is an adequate 10°–20° angle before proceeding

Table: Demographics and imaging characteristics of patients with CSF-venous fistulas

Patient	Age (yr)	Sex	MR Imaging Findings	Fistula Location
1	50	M	Sag, dural enhancement, subdural collection	R T9–T10
2	46	F	Sag	R T10–T11
3	90	M	Sag, dural enhancement	R L1–L2
4	61	F	Dural enhancement	R T6–T7
5	72	F	Sag, dural enhancement, subdural collection	R T10–T11
6	72	F	Sag, dural enhancement, subdural collection	L T11–T12
7	42	F	Sag	R T8–T9
8	39	M	Sag	R T1–T2
9	61	F	Sag, dural enhancement	R L1–L2
10	64	M	Sag, dural enhancement, subdural collection	R T9–T10
11	57	M	Sag, dural enhancement, subdural collection	L T4–L5

Note:—R indicates right; L, left.

with the lumbar puncture (Fig 1*B*). If the angle is suboptimal, then we reposition the patient. We subsequently obtain initial planning CT images of the lumbar spine and then typically puncture at the L2–L3 or L3–L4 levels with a 22-ga spinal needle.

Decubitus Myelographic Scanning. We administer 10 mL of preservative-free iohexol contrast (Omnipaque 300; GE Healthcare) for all decubitus CTMs. To ensure that the needle is in the subarachnoid space, we inject a test dose of approximately 0.5 mL. Subsequently, we communicate with our CT technologists to prepare the next CT acquisition to encompass the total spine, using a 0.625-mm section thickness and a diagnostic radiation dose with automatic exposure control. We have found that using a relatively larger section thicknesses can fail to capture subtle CSF-venous fistulas. We also typically acquire the CT images using standard or soft-tissue kernels, but a bone kernel can also be used, depending on user preference. After all the parameters are ready for scanning, we administer the remaining 9.5 mL of iohexol contrast, exit the CT scanning room, and scan immediately.

Most of our myelograms are obtained on either 16- or 64-section CT scanners, which contain an inherent adequate delay to ensure that the bolus has migrated throughout the spine. If one scans on faster CT machines, then one can consider a 15-second delay to prevent scanning before the contrast bolus migration. We also specify our scanning phase to image from inferior to superior to coincide with the direction of the contrast bolus transit. We scrutinize the images directly on the CT technologist's workstation to ensure the following: 1) that the bolus has flowed to at least the mid-cervical spine, and 2) that we identified a CSF-venous fistula. If contrast did not flow adequately, then we sometimes manually position the patient in a more Trendelenburg fashion and then rescan immediately. We also occasionally rescan confirmed CSF-venous fistulas about 1–2 minutes after the initial acquisition if confirmation is needed.

If no CSF-venous fistula is identified, then we typically bring the patient back on the subsequent day and perform decubitus CTM of the contralateral side. There are 2 reasons for this practice: 1) There are dose constraints of administering more intrathecal contrast,[15] and 2) when the patient is rotated to the contralateral side, the meningeal diverticula are less opacified because the contrast becomes more dilute after mixing throughout the spine. There are no published data comparing the practice of scanning the contralateral side in the same session versus in an additional session; however, at least 2 centers have reported the 2-day approach.[3,9] Nonetheless, we are investigating whether performing the contralateral side scanning in the same session without additional contrast can still be successful, because it would be a more convenient practice for the patient and department. Last, we do not typically instruct the patient to perform any specific breathing during the myelogram acquisition, but in the future, we may scan with the inspiratory technique because this has been recently shown to increase conspicuity of CSF-venous fistulas in some cases.[16]

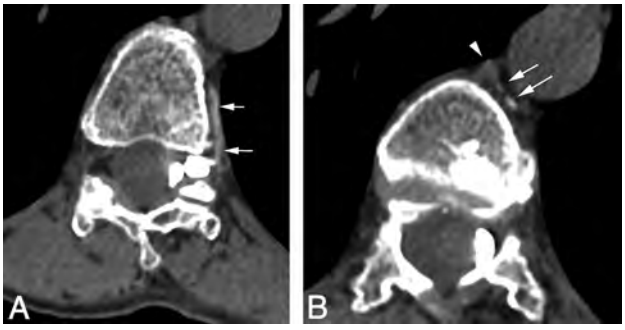

FIG 2. A CSF-venous fistula on decubitus CTM. *A*, Axial left-decubitus CTM shows a paravertebral vein (*arrows*) arising from a large left meningeal diverticulum at the T11–T12 level. *B*, On a more superior section, the vein (*arrows*) drains into the azygous vein (*arrowhead*).

RESULTS

During the past 16 months, we have performed decubitus CTMs on 22 patients and identified 11 patients with CSF-venous fistulas (Table). The mean age of patients with CSF-venous fistulas was 59 years (range, 39–90 years), and 6/11 were women. All patients with CSF-venous fistulas had at least 1 intracranial finding consistent with SIH, 10/11 had brain sag, 8/11 had dural enhancement, and 5/11 had subdural collections. Nine of 11 patients had right-sided CSF-venous fistulas, and 9/11 patients had thoracic CSF-venous fistulas, while the remaining 2 were at L1–L2. Of the 11/22 patients who did not have CSF-venous fistulas on decubitus CTM, 5 of those patients had normal contrast-enhanced brain MRI findings and may have had an alternative diagnosis.

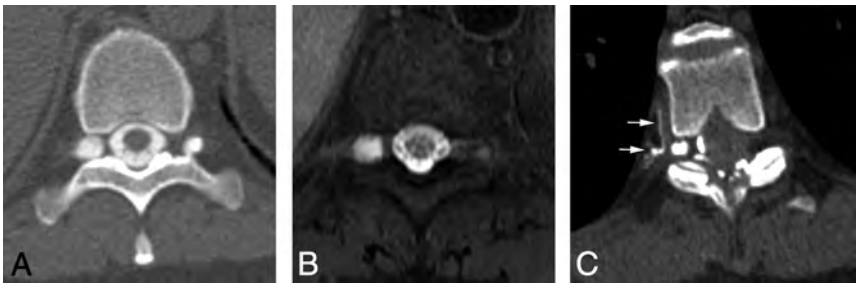

FIG 3. Value of decubitus CTM in diagnosing a CSF-venous fistula. *A*, An axial conventional CTM at the T10–T11 level shows bilateral meningeal diverticula without evidence of a CSF-venous fistula. *B*, An axial MR imaging myelogram with intrathecal gadolinium shows similar findings. *C*, A right-decubitus CTM in the axial oblique plane shows a right-sided CSF-venous fistula with a paravertebral course (*arrows*).

Image Review and Reporting

CSF-venous fistulas are nearly always seen in the thoracic spine, lower cervical spine, or high lumbar spine,[5,6,17] and attention should be paid to these regions for fistula identification. In most cases, a CSF-venous fistula arises from a meningeal diverticulum,[5] and the radiologist can identify a linear structure coursing from it that represents the abnormally connecting vein (Figs 2–6). CSF-venous fistula locations have been reported in 3 sites on CT:

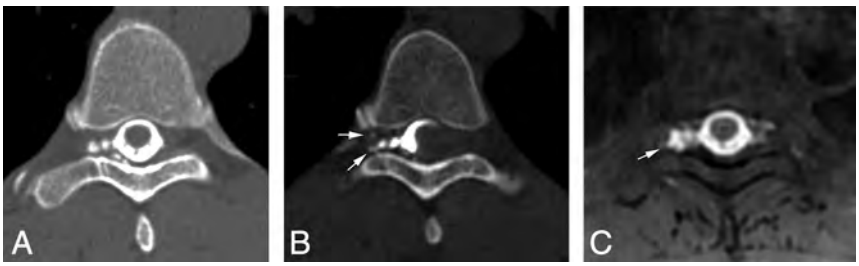

FIG 4. CSF-venous fistula on decubitus CT and intrathecal MR imaging myelograms. *A*, An axial conventional CTM shows a large, irregular right meningeal diverticulum at the T8–T9 level but no abnormal vein. *B*, An axial right-decubitus CTM shows a CSF-venous fistula (*arrows*). *C*, An axial MR imaging myelogram with intrathecal gadolinium faintly shows the CSF-venous fistula (*arrow*), but it is not as apparent as the decubitus CTM.

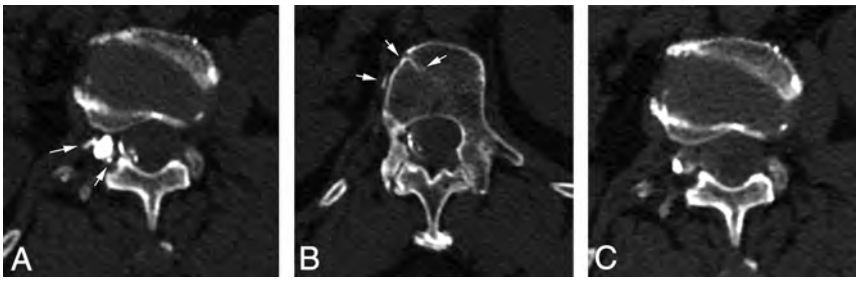

FIG 5. Importance of immediate scanning in decubitus CTM. *A*, An axial right-decubitus CTM scanned immediately after contrast injection shows abnormal veins (*arrows*) arising from a large right meningeal diverticulum at the L1–L2 level. *B*, On a more superior section, the vein (*arrows*) has a paravertebral course and terminates in the vertebral body. *C*, An axial right-decubitus CTM from a 3-minute delayed scan shows absence of the abnormal veins. If it were not for the initial scan, the CSF-venous fistula would have not been detected.

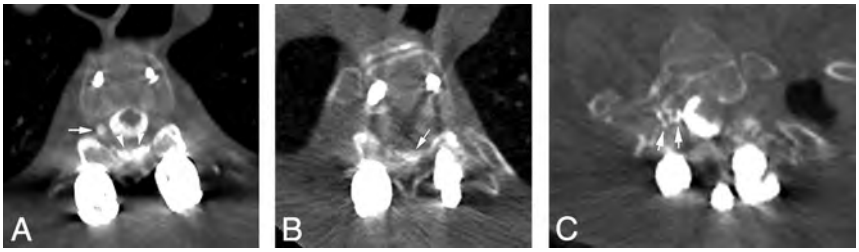

FIG 6. Value of precontrast imaging in a 39 year-old-man with a nearly 20-year history of SIH. Ten years previously, the patient underwent surgical removal of a spinal venous malformation in the T1 posterior elements and dorsal epidural space, which was causing cord compression (not shown). *A*, An axial conventional CTM shows a round hyperdense focus in the right, lateral epidural space (*arrow*) and a broad hyperdense structure in the dorsal epidural space (*arrowheads*) at the T2–T3 level. This was suspicious for a CSF-venous fistula, but in the context of the surgical fusion, it was unclear whether the dorsal epidural hyperdensity was postsurgical. In the same session as the decubitus CTM, noncontrast imaging of the upper thoracic spine (*B*) was performed, which confirmed that the dorsal epidural hyperdensity (*arrow*) was postsurgical. *C*, An axial oblique CT image from a right-decubitus CTM shows a large CSF-venous fistula (*arrows*) at the T1–T2 level, which is most likely associated with the prior venous malformation.

paravertebral, lateral (along the neural foramen and posterior elements), and central (within the internal vertebral epidural venous plexus).[5] The paravertebral location was most commonly reported in 1 study,[5] and this also coincides with our experience. The vein may be either single or cluster of veins and courses in multiple directions. Depending on the size of the vein and contrast timing, the abnormal vein can occasionally be seen draining into the azygous vein (Fig 2). We also scrutinize the myelogram for any additional fistulas or CSF leaks, though we have never seen either. Furthermore, if a CSF-venous fistula is identified, we do not image the contralateral side for additional fistulas because bilateral CSF-venous fistulas have not been reported, to our knowledge.

CSF-Venous Fistulas on Additional Modalities

In our experience, CSF-venous fistulas are more readily identifiable on decubitus CTM compared with conventional CTM. With the latter technique, the vein may often be absent (Figs 3, 4, and 6) or faintly shown. Furthermore, there may be false-positives with normal paravertebral veins, which can be a false-localizing sign.[18] Thus, we do not rely on conventional CTM for the assessment of CSF-venous fistulas. CSF-venous fistulas have been described in 3 patients with MR myelography after intrathecal gadolinium administration.[10] Our institution occasionally uses this MR imaging technique for presumed slow CSF leaks that are occult on other myelographic techniques, and we have witnessed CSF-venous fistulas that were concordant on decubitus CTM and MR imaging myelography with intrathecal gadolinium (Fig 4); however, in our experience, MR imaging either usually fails to show the fistula (Fig 3) or shows multiple paravertebral veins that can make assessment difficult if used in isolation. Thus, we do not typically perform MR imaging myelography to diagnose CSF-venous fistulas.

DSM is an excellent technique to identify CSF-venous fistulas and is useful in capable hands,[3,7,9,17] and we occasionally use this technique; however, in our experience, DSM requires a greater learning curve than decubitus CTM. In addition, if the radiologist is not well-versed in digital subtraction techniques or has training in traditional interventional or neurointerventional radiology, this may be more challenging to adopt in everyday practice. We believe that most radiologists of various academic and private practices can more readily perform decubitus CTM. DSM also sometimes necessitates the use of general anesthesia and may

require 2 sessions of general anesthesia if the CSF-venous fistula is not identified in the first session.[9] Thus, our institution relies on the decubitus CTM technique. To our knowledge, there are no reported studies that have compared the 2 techniques.

Pitfalls and Tricks

One of the major pitfalls of decubitus CTM is delayed imaging after intrathecal injection. We typically scan immediately after the injection of contrast to increase the likelihood of "catching" the CSF-venous fistula. The scanning parameters for the total spine CTM should be planned before the contrast injection so that the CSF-venous fistula is not missed. If more delayed scanning is performed, even a few minutes later, the fistula may be absent (Fig 5). This phenomenon suggests that performing decubitus CTM after fluoroscopy or DSM may have a lower yield, even if the patient's decubitus position is maintained between imaging modalities.

Calcification from the ligamentum flavum or high-density material from prior surgery can also mimic CSF-venous fistulas and leaks, and precontrast imaging in the area of interest may be performed for confirmation (Fig 6).

Insufficient contrast migration to the cervical spine can be a pitfall with decubitus CT myelography. We occasionally experience this if the Trendelenburg angle is not sufficient. In this event, we elevate the patient's trunk and legs to facilitate contrast to flow to the cervical spine and repeat scanning in the ROI immediately.

Early in our practice of decubitus CTM, we would occasionally inject intrathecal sterile saline if the spinal pressure was low to maximize visualization of the CSF-venous fistula before intrathecal contrast administration. Subsequently, we have realized that this practice did not improve identification of CSF-venous fistulas, and we have stopped it.

CONCLUSIONS

Decubitus CTM is a useful technique to identify CSF-venous fistulas in patients with SIH. The decubitus CTM technique has slight modifications compared with conventional myelography and can be used by radiologists of various practices to increase detection of CSF-venous fistulas.

REFERENCES

1. Schievink WI, Moser FG, Maya MM. **CSF-venous fistula in spontaneous intracranial hypotension.** *Neurology* 2014;83:472–73 CrossRef Medline
2. Schievink WI, Maya MM, Jean-Pierre S, et al. **A classification system of spontaneous spinal CSF leaks.** *Neurology* 2016;87:673–79 CrossRef Medline
3. Schievink WI, Maya MM, Moser FG, et al. **Lateral decubitus digital subtraction myelography to identify spinal CSF-venous fistulas in spontaneous intracranial hypotension.** *J Neurosurg Spine* 2019 Sept 13. [Epub ahead of print] CrossRef Medline
4. Kranz PG, Amrhein TJ, Schievink WI, et al. **The "hyperdense paraspinal vein" sign: a marker of CSF-venous fistula.** *AJNR Am J Neuroradiol* 2016;37:1379–81 CrossRef Medline
5. Kranz PG, Amrhein TJ, Gray L. **CSF venous fistulas in spontaneous intracranial hypotension: imaging characteristics on dynamic and CT myelography.** *AJR Am J Roentgenol* 2017;209:1360–66 CrossRef Medline
6. Clark MS, Diehn FE, Verdoorn JT, et al. **Prevalence of hyperdense paraspinal vein sign in patients with spontaneous intracranial hypotension without dural CSF leak on standard CT myelography.** *Diagn Interv Radiol* 2018;24:54–59 CrossRef Medline
7. Farb RI, Nicholson PJ, Peng PW, et al. **Spontaneous intracranial hypotension: a systematic imaging approach for CSF leak localization and management based on MRI and digital subtraction myelography.** *AJNR Am J Neuroradiol* 2019;40:745–53 CrossRef Medline
8. Schievink WI, Moser FG, Maya MM, et al. **Digital subtraction myelography for the identification of spontaneous spinal CSF-venous fistulas.** *J Neurosurg Spine* 2016;24:960–64 CrossRef Medline
9. Kim DK, Brinjikji W, Morris PP, et al. **Lateral decubitus digital subtraction myelography: tips, tricks, and pitfalls.** *AJNR Am J Neuroradiol* 2020;41:21–28 CrossRef Medline
10. Chazen JL, Robbins MS, Strauss SB, et al. **MR myelography for the detection of CSF-venous fistulas.** *AJNR Am J Neuroradiol* 2020;41:938–40 CrossRef Medline
11. Kranz PG, Gray L, Amrhein TJ. **Decubitus CT myelography for detecting subtle CSF leaks in spontaneous intracranial hypotension.** *AJNR Am J Neuroradiol* 2019;40:754–56 CrossRef Medline
12. Watanabe A, Horikoshi T, Uchida M, et al. **Diagnostic value of spinal MR imaging in spontaneous intracranial hypotension syndrome.** *AJNR Am J Neuroradiol* 2009;30:147–51 CrossRef Medline
13. Mamlouk MD, Shen PY, Jun P, et al. **Developing a spinal CSF leak program in a multihospital network.** *Curr Probl Diagn Radiol* 2020 April 9. [Epub ahead of print] CrossRef Medline
14. Duvall JR, Robertson CE, Cutsforth-Gregory JK, et al. **Headache due to spontaneous spinal cerebrospinal fluid leak secondary to cerebrospinal fluid-venous fistula: case series.** *Cephalalgia* 2019;39:1847–54 CrossRef Medline
15. **Omnipaque (iohexol).** https://www.gehealthcare.com/products/contrast-media/omnipaque. Accessed May 29, 2020
16. Amrhein TJ, Gray L, Malinzak MD, et al. **Respiratory phase affects the conspicuity of CSF-venous fistulas in spontaneous intracranial hypotension.** *AJNR Am J Neuroradiol* 2020;41:1754–56 CrossRef Medline
17. Schievink WI, Maya MM, Moser FG. **Digital subtraction myelography in the investigation of post-dural puncture headache in 27 patients: technical note.** *J Neurosurg Spine* 2017;26:760–64 CrossRef Medline
18. Schievink WI, Maya MM, Moser FG. **False localizing signs of spinal CSF-venous fistulas in spontaneous intracranial hypotension: report of 2 cases.** *J Neurosurg Spine* 2019 July 5. [Epub ahead of print] CrossRef Medline

Brain MR Spectroscopic Findings in 3 Consecutive Patients with COVID-19: Preliminary Observations

O. Rapalino, A. Weerasekera, S.J. Moum, K. Eikermann-Haerter, B.L. Edlow, D. Fischer, A. Torrado-Carvajal, M.L. Loggia, S.S. Mukerji, P.W. Schaefer, R.G. Gonzalez, M.H. Lev, and E.-M. Ratai

ABSTRACT

SUMMARY: Brain multivoxel MR spectroscopic imaging was performed in 3 consecutive patients with coronavirus disease 2019 (COVID-19). These included 1 patient with COVID-19-associated necrotizing leukoencephalopathy, another patient who had a recent pulseless electrical activity cardiac arrest with subtle white matter changes, and a patient without frank encephalopathy or a recent severe hypoxic episode. The MR spectroscopic imaging findings were compared with those of 2 patients with white matter pathology not related to Severe Acute Respiratory Syndrome coronavirus 2 infection and a healthy control subject. The NAA reduction, choline elevation, and glutamate/glutamine elevation found in the patient with COVID-19-associated necrotizing leukoencephalopathy and, to a lesser degree, the patient with COVID-19 postcardiac arrest, follow a similar pattern as seen with the patient with delayed posthypoxic leukoencephalopathy. Lactate elevation was most pronounced in the patient with COVID-19 necrotizing leukoencephalopathy.

ABBREVIATIONS: COVID-19 = coronavirus disease 2019; DPL = delayed posthypoxic leukoencephalopathy; Lac = lactate; PEA = pulseless electrical activity; SAE = sepsis-associated encephalopathy; SARS-CoV-2 = Severe Acute Respiratory Syndrome coronavirus 2

Coronavirus disease 2019 (COVID-19), caused by Severe Acute Respiratory Syndrome coronavirus 2 (SARS-CoV-2), was declared a pandemic by the World Health Organization on March 11, 2020.[1] COVID-19 primarily affects the lower respiratory tract, but many organs can be involved, including the central nervous system.[2,3] Neurologic manifestations of SARS-CoV-2 infection are increasingly reported and include cerebrovascular complications, leukoencephalopathy, and other CNS disorders.[4] Although COVID-19-associated white matter abnormalities resemble other forms of diffuse white matter injury (such as posthypoxic leukoencephalopathy or sepsis-associated leukoencephalopathy), there are also notable differences, such as the neuroanatomic distribution of white matter lesions. The pathogenesis of COVID-19 white matter abnormalities remains unknown, though "silent hypoxia" has been hypothesized to have a central role in their development.[5,6]

MR spectroscopy represents a noninvasive in vivo diagnostic tool for evaluating white matter injury and can provide valuable information regarding the underlying pathogenesis of white matter pathologies. In the setting of diffuse white matter injury, MR spectroscopy offers a complementary evaluation to structural MR brain imaging by providing a sensitive measurement of various in vivo metabolites. Most important, MR spectroscopy can identify neurochemical abnormalities even in the absence of corresponding findings on structural MR brain imaging.[7,8]

The metabolic profile of COVID-19-associated leukoencephalopathy using MRS has not been well established in the literature to date. We present examples of MR spectra in patients with COVID-19 and compare them with both other patients with leukoencephalopathy and a control.

Case Series

Six 3D multivoxel MRS datasets from 3 patients with COVID-19 (Fig 1 and Table 1), 2 control patients with leukoencephalopathy (posthypoxic and sepsis-related leukoencephalopathy), and 1 healthy age-matched control were acquired using 3T MR imaging scanners (Siemens, Erlangen, Germany). This 3D-MRS sequence was acquired using a Localization by Adiabatic SElective Refocusing (LASER) pulse sequence with a fast spiral *k*-space acquisition.[9] Acquisition parameters included the following: TE = 30 ms and 288 ms (except for the control and patient with delayed

Received June 14, 2020; accepted after revision August 13.

From the Departments of Radiology (O.R., A.W., K.E.-H., M.L.L., P.W.S., R.G.G., M.H.L., E.R.) and Neurology (B.L.E., D.F., S.S.M.), Massachusetts General Hospital and Harvard Medical School, Boston, Massachusetts; A.A. Martinos Center for Biomedical Imaging (A.W., A.T.-C., M.L.L., E.R.), Charlestown, Massachusetts; Ann & Robert H. Lurie Children's Hospital of Chicago and Northwestern University Feinberg School of Medicine (S.J.M.) and Medical Image Analysis and Biometry Laboratory (A.T.-C.), Universidad Rey Juan Carlos, Madrid, Spain.

O. Rapalino and A. Weerasekera contributed equally to this article.

M.L. Loggia was funded by the National Institutes of Health grant 1R01NS095937-01A1.

Please address correspondence to Otto Rapalino, MD, Neuroradiology Division, Department of Radiology, Massachusetts General Hospital, 55 Fruit Street, GRB 273A Boston, MA 02114; e-mail: orapalino@mgh.harvard.edu

http://dx.doi.org/10.3174/ajnr.A6877

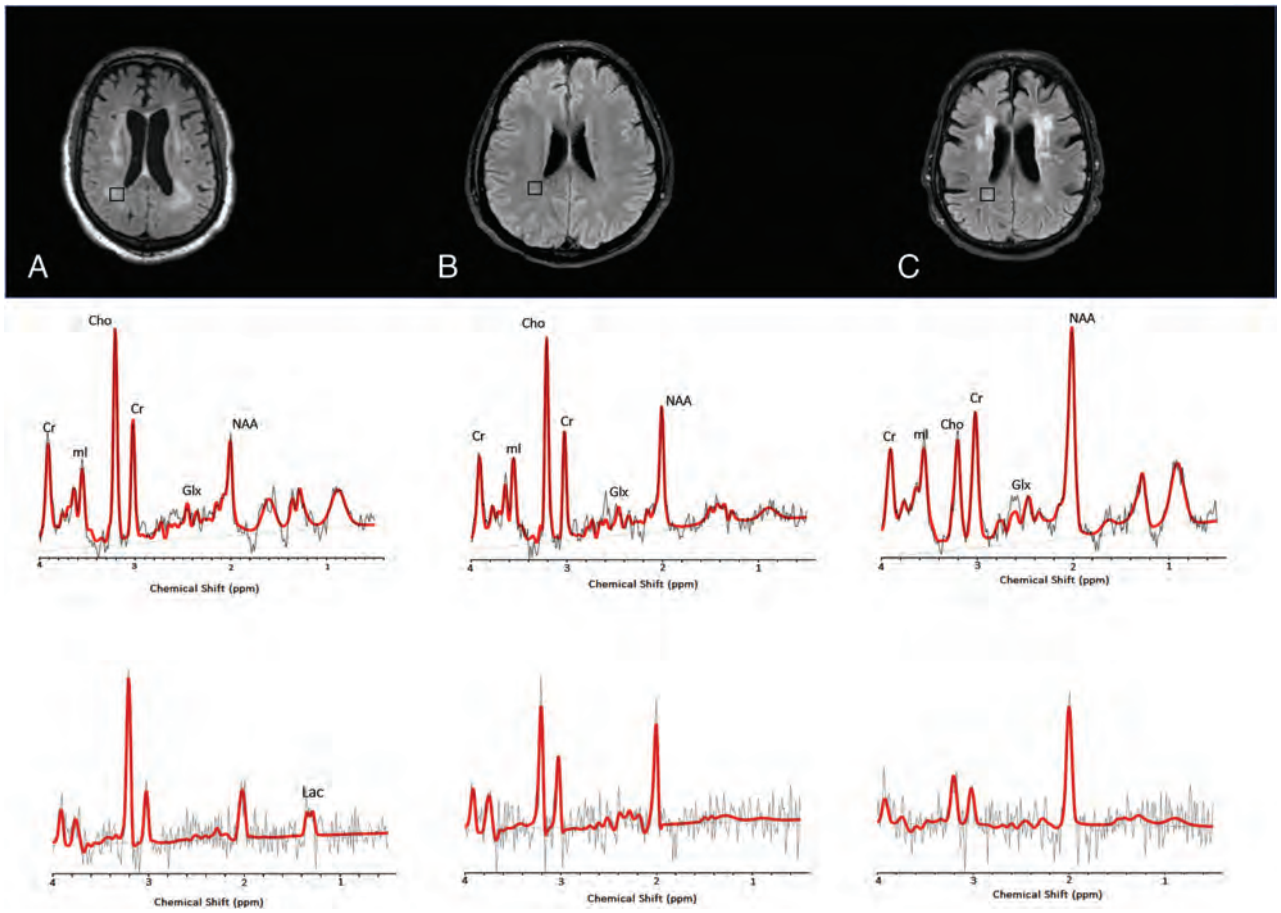

FIG 1. ^{1}H-MR spectra of 3 consecutive patients with COVID-19. *Upper row*: Axial FLAIR images at the corona radiata level show representative MRS voxels (*black squares*) from sampled periventricular regions. *Lower row*: Corresponding spectrum (black) and LCModel fit (red) from each patient acquired at TE = 30 ms (*upper row*) and TE = 288 ms (*lower row*). *A*, A patient with COVID-19-associated multifocal necrotizing leukoencephalopathy shows diffuse patchy WM lesions with markedly increased Cho and decreased NAA, as well as elevated Lac. *B*, A patient with COVID-19 after recent PEA cardiac arrest with subtle FLAIR hyperintense white matter changes also shows elevated Cho/Cr and decreased NAA/Cr ratios. However, these derangements are less severe than in the patient in *A*. There is no clear elevation of Lac. *C*, A patient with COVID-19 without encephalopathy or recent severe hypoxia has normal Cho/Cr, with mildly decreased NAA/Cr and no lactate elevation. Cho, Choline; NAA, N-Acetyl-Aspartate; mI, Myo-Inositol; Lac, Lactate; Glx, Glutamate + Glutamine.

Table 1: Demographics and clinical information

Subject	Diagnosis	Status	Age (yr)	Sex
COVID-A	COVID-19-related multifocal necrotizing leukoencephalopathy	ICU and intubated	63	M
COVID-B	COVID-19-related recent PEA cardiac arrest, without clear leukoencephalopathy	ICU and intubated	53	M
COVID-C	COVID-19 without clear leukoencephalopathy or recent severe hypoxia	Neurology ward and not intubated	72	M
DPL	Non-COVID-19 delayed posthypoxic/toxic leukoencephalopathy	Neurology ward and not intubated	44	F
SAE	Non-COVID-19 presumed sepsis-associated encephalopathy	ICU and mechanical ventilation via tracheostomy	55	F
Control	Healthy volunteer		65	M

Note:—ICU indicates intensive care unit.

posthypoxic leukoencephalopathy [DPL]), TR = 1500 ms, Number of Acquisitions = 5, isotropic resolution 1 cc. Excitation VOIs were placed using FLAIR or T2-weighted images to include the white matter abnormalities.

Raw data files were processed using the LCModel software package, Version 6.3 (http://www.lcmodel.com/) with the appropriate basis set.[10] For the data analysis, 6–8 white matter MR spectroscopy voxels of the section with the most prominent white matter abnormalities were chosen, and their metabolite ratios were averaged.

Of the patients with COVID-19, 1 patient had MR imaging findings compatible with a necrotizing leukoencephalopathy with abnormal reduced diffusivity and cavitation within the white matter

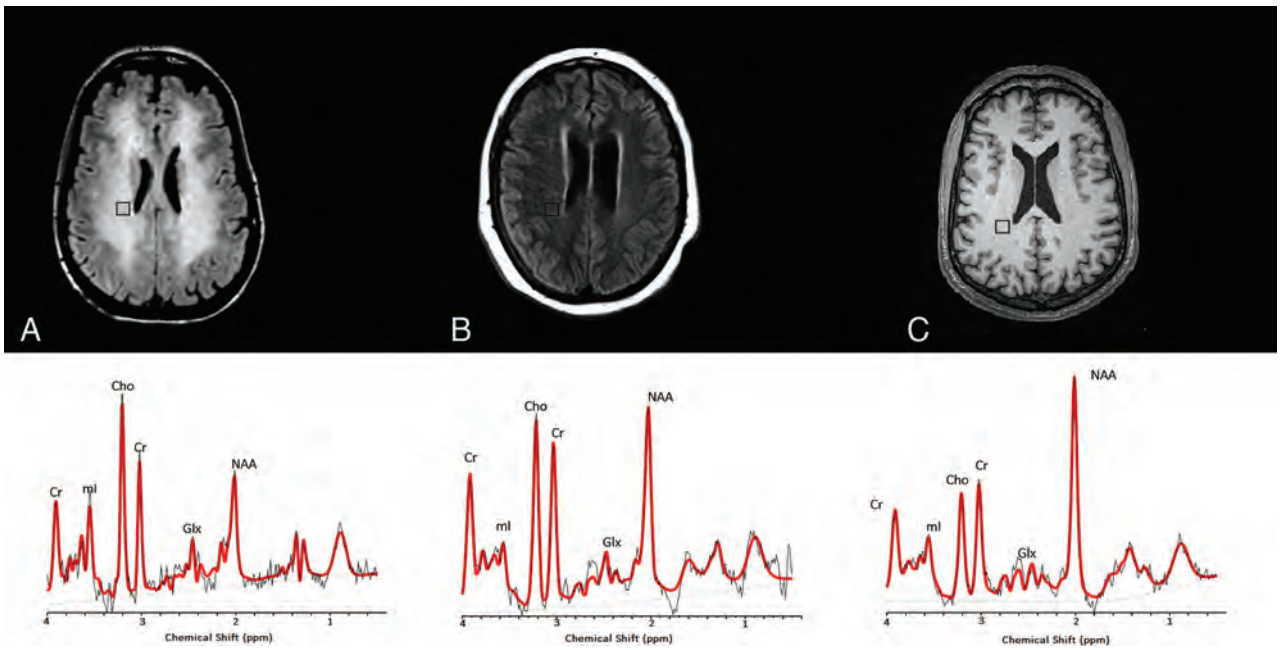

FIG 2. ^{1}H-MR spectra from 2 non-COVID leukoencephalopathy patients, compared with a spectrum from a healthy control patient. *Upper row*: Axial noncontrast FLAIR (*A* and *B*) and T1-weighted (*C*) images at the level of the corona radiata show representative MRS voxels (*black squares*) from sampled periventricular regions. *Lower row*: Corresponding spectrum (black) and LCModel fit (red) from each patient acquired at TE = 30 ms. *A*, A patient with delayed posthypoxic/toxic leukoencephalopathy shows an increase of Cho/Cr and decreased NAA/Cr ratios. *B*, A patient with sepsis-associated encephalopathy shows milder degrees of Cho/Cr elevation and NAA/Cr reduction. *C*, A healthy control subject with a normal MR spectrum. Cho, Choline; NAA, N-Acetyl-Aspartate; mI, Myo-Inositol; Lac, Lactate; Glx, Glutamate + Glutamine.

Table 2: Mean, SD, and percentage difference relative to controls of brain MRS metabolite ratios in 3 patients with and 3 patients without COVID-19[a]

Subject	No. Voxels	NAA/Cr[b]	Cho/Cr[b]	mI/Cr[b]	Glx/Cr[b]	Lac/Cr[c]
COVID-A	7	0.61 ± 0.13 (−85%)[d]	0.65 ± 0.05 (+80%)[d]	1.17 ± 0.07 (+39%)[d]	1.46 ± 0.20 (+51%)[d]	0.76 ± 0.1
COVID-B	8	1.10 ± 0.15 (−33%)[d]	0.54 ± 0.04 (+63%)[d]	1.16 ± 0.09 (+38%)[d]	1.40 ± 0.13 (+47%)[d]	0
COVID-C	6	1.47 ± 0.08 (−5%)	0.27 ± 0.03 (−4%)	1.23 ± 0.10 (+44%)[d]	1.04 ± 0.22 (+18%)	0
DPL	8	0.81 ± 0.11 (−62%)[d]	0.48 ± 0.02 (+53%)[d]	1.09 ± 0.05 (+32%)[d]	1.82 ± 0.14 (+71%)[d]	
SAE	7	0.95 ± 0.16 (−47%)[d]	0.32 ± 0.04 (+13%)	0.61 ± 0.06 (−26%)	1.10 ± 0.12 (+23%)	0
Control	6	1.54 ± 0.17	0.28 ± 0.04	0.79 ± 0.04	0.87 ± 0.07	

[a] Positive and negative percentages between parentheses indicate percentage difference compared to the control subject.
[b] Data measured on short-TE (TE = 30 ms) spectra.
[c] Data measured on long-TE (TE = 288 ms) spectra. No long-TE spectra were available for the DPL and control cases.
[d] Percentage differences of >30% in magnitude. The distribution of these metabolite ratio derangements in patients with COVID-A (leukoencephalopathy) and COVID-B (post-cardiac arrest) is similar to that of the patient with DPL.

lesions (COVID-A) (Fig 1*A*). The second patient had pulseless electrical activity (PEA) arrest while in the intensive care unit and subsequently developed altered mental status. His MR imaging showed cerebellar cortical and hippocampal signal abnormalities suggestive of prior hypoxic-ischemic injury and subtle bilateral cerebellar and supratentorial white matter T2/FLAIR hyperintensities (COVID-B) (Fig 1*B*). The third patient with COVID-19 without an encephalopathic syndrome had a history of parkinsonism and developed catatonia of unclear etiology (COVID-C) (Fig 1*C*). This patient's MR imaging showed mild nonspecific periventricular and deep white matter changes suggestive of small-vessel disease (considering their neuroanatomic distribution). None of these patients were found to have other neurologic comorbidities (eg, other metabolic encephalopathies, hydrocephalus, and so forth).

Data from these 3 patients were contrasted to multivoxel MRS data obtained before the COVID-19 pandemic from 2 patients with other leukoencephalopathies. One patient had DPL and developed severe encephalopathy, rigidity, and mutism, likely related to a prior toxic exposure (opiates) or a hypoxic episode (Fig 2*A*). The other patient without COVID-19 had sepsis-associated encephalopathy (SAE), with mild diffuse white matter abnormalities on brain MR imaging studies (Fig 2*B*).

Last, data of all 5 patients with leukoencephalopathy were compared with a dataset acquired using the same protocol from a healthy control subject, a 65-year-old man who volunteered for a research study (Fig 2*C*).

MRS datasets with short TEs (TE = 30 ms) were analyzed to quantify ratios of NAA, Cho, mI, and Glx relative to Cr. Lactate (Lac)/Cr levels were quantified using MRS datasets with long TEs (TE = 288 ms). Table 2 summarizes the means, SDs, and percentage differences of metabolite levels compared with the control.

Comparative analysis showed decreased NAA/Cr levels within the white matter in 2 of the patients positive for COVID-19 compared with the control. The patient with necrotizing leukoencephalopathy (COVID-A) had the most diminished NAA levels, which were completely absent in several MR spectroscopy voxels, followed by the patient with recent cardiac arrest and mild diffuse white matter changes without necrosis (COVID-B). The patient with COVID-C without recent cardiac arrest or overt leukoencephalopathy (Fig 1) had slightly decreased NAA/Cr levels compared with the age-matched control. The metabolic profiles of the 3 patients with COVID-19 were contrasted to those of 2 patients with other leukoencephalopathies without COVID-19 (described above) (Fig 2). The NAA/Cr levels of these patients without COVID leukoencephalopathy were also decreased but still higher than those in the patient with COVID-A (Table 2).

Compared with the control, 2 of the 3 patients with COVID-19 had elevated Cho/Cr levels (Table 2). The third patient with COVID-19 without leukoencephalopathy (COVID-C) showed Cho/Cr levels indistinguishable from those of the control. The patient without COVID-19 with DPL and extensive white matter abnormalities showed increased Cho/Cr ratios, while the patient with SAE had a relatively normal range of Cho/Cr ratios.

All 3 patients with COVID-19 and the patient without COVID-19 with DPL showed elevated mI/Cr levels (Table 2). Most interesting, our patient with sepsis-associated encephalopathy had decreased mI/Cr ratios. Glx/Cr was markedly increased in the 2 patients with COVID-19 with necrotizing leukoencephalopathy and after cardiac arrest as well as in the patient without COVID-19 with DPL. Lac/Cr ratios were increased in the patient with COVID-19 with necrotizing leukoencephalopathy on long-TE spectra. No elevation of Lac/Cr ratios was seen in the patient with SAE. The patient with DPL and control did not have long-TE spectra. Therefore, we cannot confirm or exclude the presence of lactate in these subjects (Fig 2*A*).

DISCUSSION

Multiple recent reports in the medical literature have confirmed the development of leukoencephalopathy as a potential CNS complication in SARS-CoV-2 infection,[11,12] though no study has reported the MR spectroscopic findings in these patients. We evaluated the metabolic differences among 3 patients with COVID-19 (1 with necrotizing leukoencephalopathy, another after cardiac arrest, and the third with mild nonspecific white matter changes without clinical encephalopathy) and other control groups with multivoxel MR spectroscopy to better understand the underlying pathophysiology of this disease. Markedly increased Cho/Cr, decreased NAA/Cr, and increased Lac/Cr ratios were observed in the patient with COVID-19 with multifocal necrotizing leukoencephalopathy. Less pronounced changes in Cho/Cr and NAA/Cr ratios were noted in the patient with COVID-19 with prior PEA arrest and subtle nonspecific white matter signal abnormalities. Notably, the magnitude of the Cho and NAA abnormalities in the patient with COVID-19 associated necrotizing leukoencephalopathy was more pronounced compared with the patients with delayed post-hypoxic leukoencephalopathy and SAE.

In our series, similar patterns of metabolic changes were observed in the setting of COVID-19-associated leukoencephalopathy and DPL, namely elevated Cho, elevated Lac, decreased NAA, increased mI, and increased Glx ratios in relation to Cr. This spectral pattern has been previously reported in the setting of DPL following carbon monoxide poisoning or medication overdose.[13-15] Prolonged impaired oxygenation to the subcortical white matter is thought to promote anaerobic metabolism and leads to elevated tissue Lactate.[14,15]

The observed increase of Cho/Cr ratios in the patients with leukoencephalopathy, particularly in the case of COVID-associated necrotizing leukoencephalopathy, likely reflects demyelination within these white matter lesions as recently described in an initial neuropathologic study of a patient with COVID-19.[16] Cho elevation could also be related to cell death and/or immune cellular infiltration within areas of demyelination.[17] Axonal damage was also reported on pathology[16] and likely contributes to the decreased NAA/Cr ratios we observed.

Increased levels of Myo-Inositol (mI) may reflect neuroinflammation, which when coupled with choline elevations in demyelinating pathologies may reflect glial proliferation.[18] The presence of elevated Glx levels has been reported in cases of acute excitotoxic leukoencephalopathy[19] and viral-associated acute leukoencephalopathy with restricted diffusion.[20] Both conditions are thought to be mediated by excitotoxic injury to the cerebral white matter and exhibit prominent reduced diffusivity within white matter lesions.

Notably, the metabolic derangements seen in the setting of COVID-19-associated multifocal necrotizing leukoencephalopathy are similar to those observed with DPL. However, more evidence is required to validate this conclusion. Some of the previously published MR spectroscopy studies of necrotizing encephalopathies from other etiologies[21] also showed increased Lac along with decreased NAA and increased Cho,[22] while others showed Glx and lipid elevations predominantly.[23] Certainly, additional research is warranted in this new field of COVID-19-related metabolic derangement.

The small patient cohort of our study limits our ability to generalize our observations. MRS was only performed in patients with SARS-CoV-2 infection when requested by referring providers for specific clinical indications. Furthermore, the controls without COVID-19 are slightly younger, especially the patient with DPL. Another limitation of our study is that only a single time point was assessed; thus, we cannot exclude other baseline conditions before the SARS-CoV-2 infection, such as chronic small-vessel disease, that may affect our results. Finally, some of these subjects (the patient with DPL and the healthy control) did not have a long-TE MRS acquisition, limiting our ability to unequivocally determine the presence or absence of Lac.

In conclusion, the reported spectroscopic abnormalities within the white matter lesions of COVID-19-associated leukoencephalopathy may reflect several pathophysiologic processes, including but not limited to the following: 1) an anaerobic metabolic environment produced by the well-described "silent hypoxia" seen in these patients, resulting in elevation of Lac levels; 2) neuronal dysfunction and axonal injury with decreased NAA/Cr ratios; and 3) increased membrane destruction or turnover with elevated Cho/Cr ratios. Continued data collection in a larger cohort is required to

validate these observations and better elucidate their significance in the pathophysiology of SARS-CoV-2 infection.

Disclosures: Otto Rapalino—*UNRELATED*: Travel and hotel expenses as a lecturer at an event were sponsored by GE Healthcare in August 2019. This lecture did not have any commercial content and did not have any relationship to the current work. Brian L. Edlow—*RELATED*: *Grant*: James S. McDonnell Foundation, *Comments*: McDonnell Foundation COVID-19 Recovery of Consciousness Consortium.* David Fischer—*RELATED*: *Grant*: R25NS06574309. Shibani Mukerji—*UNRELATED*: *Grants/Grants Pending*: National Institute of Mental Health, *Comments*: K23MH115812.* Michael H. Lev—*UNRELATED*: *Consultancy*: Takeda Pharmaceutical Company, GE Healthcare, *Comments*: Consultant; *Grants/Grants Pending*: National Institutes of Health, *Comments*: Coinvestigator on 2 technical development grants; *Patents (Planned, Pending or Issued)*: Electrical Impedance Spectroscopy, Artificial Intelligence-related. Eva-Maria Ratai—*UNRELATED*: *Employment*: Massachusetts General Hospital; *Grants/Grants Pending*: National Institutes of Health, National Science Foundation, *Comments*: R01NS080816, R01HD065762, R01HD085813, U01NS104326, R01DA047088, P01-AT009965, R01CA190901, R01NS112694.* Marco L. Loggia—*RELATED*: *Grant*: National Institute of Neurological Disorders and Stroke, *Comments*: 1R01NS095937-01A1*; *UNRELATED*: *Grants/Grants Pending*: National Institutes of Health. Angel Torrado-Carvajal—*UNRELATED*: *Employment*: Universidad Rey Juan Carlos, Assistant Professor (September 2019 until now); Massachusetts General Hospital, Research Fellow (August 2017 to August 2019); *Grants/Grants Pending*: Comunidad de Madrid, MIMC3 PET/MR Project.* *Money paid to the institution.

REFERENCES

1. Cucinotta D, Vanelli M. **WHO declares COVID-19 a pandemic.** *Acta Biomed* 2020;91:157–60 CrossRef Medline
2. Berlin DA, Gulick RM, Martinez FJ. **Severe Covid-19.** *N Engl J Med* 2020 May 15. [Epub ahead of print] CrossRef Medline
3. Romero-Sanchez CM, Diaz-Maroto I, Fernandez-Diaz E, et al. **Neurologic manifestations in hospitalized patients with COVID-19: the ALBACOVID registry.** *Neurology* 2020;95:e1060–70 CrossRef Medline
4. Helms J, Kremer S, Merdji H, et al. **Neurologic features in severe SARS-CoV-2 infection.** *N Engl J Med* 2020;382:2268–70 CrossRef Medline
5. Couzin-Frankel J. **The mystery of the pandemic's 'happy hypoxia.'** *Science* 2020;368:455–56 CrossRef Medline
6. Solomon IH, Normandin E, Bhattacharyya S, et al. **Neuropathological features of Covid-19.** *N Engl J Med* 2020;383:989–92 CrossRef Medline
7. Sun J, Song H, Yang Y, et al. **Metabolic changes in normal appearing white matter in multiple sclerosis patients using multivoxel magnetic resonance spectroscopy imaging.** *Medicine (Baltimore)* 2017;96:e6534 CrossRef Medline
8. Bizzi A, Castelli G, Bugiani M, et al. **Classification of childhood white matter disorders using proton MR spectroscopic imaging.** *AJNR Am J Neuroradiol* 2008;29:1270–75 CrossRef Medline
9. Andronesi OC, Gagoski BA, Sorensen AG. **Neurologic 3D MR spectroscopic imaging with low-power adiabatic pulses and fast spiral acquisition.** *Radiology* 2012;262:647–61 CrossRef Medline
10. Provencher SW. **Automatic quantitation of localized in vivo 1H spectra with LCModel.** *NMR Biomed* 2001;14:260–64 CrossRef Medline
11. Radmanesh A, Derman A, Lui YW, et al. **COVID-19-associated diffuse leukoencephalopathy and microhemorrhages.** *Radiology* 2020 May 21. [Epub ahead of print] CrossRef Medline
12. Sachs JR, Gibbs KW, Swor DE, et al. **COVID-19-associated leukoencephalopathy.** *Radiology* 2020;296:E184–85 CrossRef Medline
13. Beeskow AB, Oberstadt M, Saur D, et al. **Delayed post-hypoxic leukoencephalopathy (DPHL): an uncommon variant of hypoxic brain damage in adults.** *Front Neurol* 2018;9:708 CrossRef Medline
14. Shprecher DR, Flanigan KM, Smith AG, et al. **Clinical and diagnostic features of delayed hypoxic leukoencephalopathy.** *J Neuropsychiatry Clin Neurosci* 2008;20:473–77 CrossRef Medline
15. Terajima K, Igarashi H, Hirose M, et al. **Serial assessments of delayed encephalopathy after carbon monoxide poisoning using magnetic resonance spectroscopy and diffusion tensor imaging on 3.0T system.** *Eur Neurol* 2008;59:55–61 CrossRef Medline
16. Reichard RR, Kashani KB, Boire NA, et al. **Neuropathology of COVID-19: a spectrum of vascular and acute disseminated encephalomyelitis (ADEM)-like pathology.** *Acta Neuropathol* 2020;140:1–6 CrossRef Medline
17. Brenner RE, Munro PM, Williams SC, et al. **The proton NMR spectrum in acute EAE: the significance of the change in the Cho:Cr ratio.** *Magn Reson Med* 1993;29:737–45 CrossRef Medline
18. Bitsch A, Bruhn H, Vougioukas V, et al. **Inflammatory CNS demyelination: histopathologic correlation with in vivo quantitative proton MR spectroscopy.** *AJNR Am J Neuroradiol* 1999;20:1619–27 Medline
19. Takanashi JI, Murofushi Y, Hirai N, et al. **Prognostic value of MR spectroscopy in patients with acute excitotoxic encephalopathy.** *J Neurol Sci* 2020;408:116636 CrossRef Medline
20. Kamate M. **Acute leukoencephalopathy with restricted diffusion.** *Indian J Crit Care Med* 2018;22:519–23 CrossRef Medline
21. Premji S, Kang L, Rojiani MV, et al. **Multifocal necrotizing leukoencephalopathy: expanding the clinicopathologic spectrum.** *J Neuropathol Exp Neurol* 2019;78:340–47 CrossRef Medline
22. Raghavendra S, Nair MD, Chemmanam T, et al. **Disseminated necrotizing leukoencephalopathy following low-dose oral methotrexate.** *Eur J Neurol* 2007;14:309–14 CrossRef Medline
23. Aydin H, Ozgul E, Agildere AM. **Acute necrotizing encephalopathy secondary to diphtheria, tetanus toxoid and whole-cell pertussis vaccination: diffusion-weighted imaging and proton MR spectroscopy findings.** *Pediatr Radiol* 2010;40:1281–84 CrossRef Medline

Clot Burden Score and Collateral Status and Their Impact on Functional Outcome in Acute Ischemic Stroke

I. Derraz, M. Pou, J. Labreuche, L Legrand, S. Soize, M. Tisserand, C. Rosso, M. Piotin, G. Boulouis, C. Oppenheim, O. Naggara, S. Bracard, F. Clarençon, B. Lapergue, and R. Bourcier, on behalf of the ASTER and the THRACE Trials Investigators

ABSTRACT

BACKGROUND AND PURPOSE: Collateral status and thrombus length have been independently associated with functional outcome in patients with acute ischemic stroke. It has been suggested that thrombus length would influence functional outcome via interaction with the collateral circulation. We investigated the individual and combined effects of thrombus length assessed by the clot burden score and collateral status assessed by a FLAIR vascular hyperintensity–ASPECTS rating system on functional outcome (mRS).

MATERIALS AND METHODS: Patients with anterior circulation acute ischemic stroke due to large-vessel occlusion from the ASTER and THRACE trials treated with endovascular thrombectomy were pooled. The clot burden score and FLAIR vascular hyperintensity score were determined on MR imaging obtained before endovascular thrombectomy. Favorable outcome was defined as an mRS score of 0–2 at 90 days. Association of the clot burden score and the FLAIR vascular hyperintensity score with favorable outcome (individual effect and interaction) was examined using logistic regression models.

RESULTS: Of the 326 patients treated by endovascular thrombectomy with both the clot burden score and FLAIR vascular hyperintensity assessment, favorable outcome was observed in 165 (51%). The rate of favorable outcome increased with clot burden score (smaller clots) and FLAIR vascular hyperintensity (better collaterals) values. The association between clot burden score and functional outcome was significantly modified by the FLAIR vascular hyperintensity score, and this association was stronger in patients with good collaterals, with an adjusted OR = 6.15 (95% CI, 1.03–36.81).

CONCLUSIONS: The association between the clot burden score and functional outcome varied for different collateral scores. The FLAIR vascular hyperintensity score might be a valuable prognostic factor, especially when contrast-based vascular imaging is not available.

ABBREVIATIONS: AIS = acute ischemic stroke; CBS = clot burden score; EVT = endovascular thrombectomy; FVH = FLAIR vascular hyperintensity; IVT = intravenous thrombolysis; mTICI = modified TICI score

Therapeutic reperfusion with endovascular thrombectomy (EVT) is consistently associated with a better long-term functional outcome in anterior circulation acute ischemic stroke (AIS).[1] Early reperfusion is the mainstay of therapy because it strongly predicts functional outcome.[2] Many factors impact clinical outcomes, including the extent of clot and collateral supply.[3–7]

Received May 12, 2020; accepted after revision August 12.

From the Department of Neuroradiology (I.D.), Hôpital Gui de Chauliac, Montpellier University Medical Center, Montpellier, France; Department of Neuroradiology (M.P., F.C.) and Institut du Cerveau et de la Moelle épinière (C.R.), Sorbonne Université, Institut du Cerveau, National Institute for Health and Medical Research U 1127, Urgences Cérébro-Vasculaires, Pitié-Salpêtrière Hospital, Paris, France; Santé publique: épidémiologie et qualité des soins (J.L.), University of Lille, Centre Hospitalier Universitaire Lille, Lille, France; Department of Neuroradiology (L.L., G.B., C.O., O.N.), Groupe Hospitalier Universitaire site Sainte-Anne, Institut de Psychiatrie et Neurosciences de Paris, National Institute for Health and Medical Research, Université de Paris, Paris, France; Department of Neuroradiology (S.S.), Centre Hospitalier Universitaire Reims, Reims, France; Departments of Neuroradiology (M.T.) and Stroke Center (B.L.), Foch Hospital, Suresnes, France; Department of Interventional Neuroradiology (M.P.), Rothschild Fondation, Paris, France; Department of Neuroradiology (S.B.), Regional and University Hospital Centre Nancy, Nancy, France; and Department of Diagnostic and Interventional Neuroradiology (R.B.), Guillaume et René Laennec University Hospital, Nantes, France.

The ASTER trial was sponsored by the Fondation Ophtalmologique Adolphe de Rothschild. An unrestricted research grant was provided by Penumbra, Alameda, California. The THRACE trial was funded by the French Ministry for Health as part of its 2009 STIC (Soutien aux Techniques Innovantes Coûteuses) program for the support of costly innovations (grant No. 2009 A00753-54).

The funders of the study had no role in study design, data collection, data analysis, data interpretation, or writing of the report. The corresponding author had full access to all the data in the study and had final responsibility for the decision to submit for publication.

Clinical Trial Registration: ClinicalTrials.gov Identifier NCT02523261 and NCT01062698.

Please address correspondence to Imad Derraz, MD, MSc, Department of Neuroradiology, Hôpital Gui de Chauliac, Montpellier University Medical Center, 80, Ave Augustin Fliche, Montpellier, France; e-mail: i-derraz@chu-montpellier.fr

Indicates open access to non-subscribers at www.ajnr.org

Indicates article with supplemental online tables.

Indicates article with supplemental online photos.

http://dx.doi.org/10.3174/ajnr.A6865

The clot burden score (CBS) assessed by the T2* MR imaging sequence (T2*-CBS), which was adapted from the CTA-CBS,[8] has been used to assess the extent of the clot[9] and has been independently associated with functional outcome in patients undergoing EVT.[10]

Good collaterals have been related to better clinical outcome through 2 distinct mechanisms. First, collaterals are thought to contribute to prolonged penumbra sustenance.[11,12] Second, good retrograde collateral filling beyond the occlusion could promote successful reperfusion by providing more access to thrombolytics at the distal end of the clot and robust collaterals dissolving clot fragments in the distal vasculature.[13,14] The Highly Effective Reperfusion evaluated in Multiple Endovascular Stroke Trials (HERMES) collaboration analysis suggested a benefit with EVT across all strata of collateral circulation status;[15] however, patients with poor collaterals are less likely to benefit from EVT than those with better collaterals.

Most interesting, FLAIR vascular hyperintensity (FVH) on baseline MR imaging could indicate the formation of a leptomeningeal collateral circulation and serve as a prognostic marker for patients with AIS.[16-18] Both collaterals and the CBS were separately associated with functional outcome in patients undergoing EVT,[10,16] but their combined effect regarding clinical outcome is still poorly understood and has been assessed and quantified only with CTA or contrast-enhanced MRA in patients with AIS.[14,15] Furthermore, the lack of adjustment for possible confounders because of the small number of patients with very low collateral scores might also have influenced results in these studies.

The purpose of this study was to determine whether there is an association between the CBS and FVH score and whether the association between the CBS and functional outcome is modified by the FVH score for patients who were treated by EVT for large-vessel occlusion within the framework of the Contact Aspiration versus Stent Retriever for Successful Revascularization (ASTER) and the THRombectomie des Artères CErebrales (THRACE) randomized trials.[19,20]

MATERIALS AND METHODS

Ethics and Data Availability Statement

The ASTER (ClinicalTrials.gov No. NCT02523261) and THRACE (ClinicalTrials.gov No. NCT01062698) protocols were approved by an independent institutional review board (Comité de Protection des Personnes Ile de France VI and Comité de Protection des Personnes III Nord Est Ethics Committee, respectively) and the research boards of the participating centers. All patients or their legal representatives provided written informed consent. This article has been prepared according to the Consolidated Standards Of Reporting Trials (CONSORT statement; http://www.consort-statement.org/). The data that support the findings of this study are available from the corresponding author on reasonable request and after clearance by the local ethics committees.

Study Design and Patient Selection

The designs of the 2 trials from which our study population is derived have already been reported.[19,20] Briefly, the ASTER study was designed to compare the effect of 2 first-line strategies for EVT (contact aspiration versus stent retriever use) on reperfusion rates at the end of endovascular procedures. Use of intravenous thrombolysis (IVT) was permitted. The THRACE trial aimed to compare IVT alone with IVT plus EVT using a stent retriever to determine their effects on clinical independence at 3 months in patients with AIS caused by large-vessel occlusion.

We included patients screened by MR imaging as a first-line imaging triage from the ASTER trial (between October 2015 and October 2016) and from the THRACE trial (patients who received IVT plus EVT as a first-line strategy between June 2010 and February 2015). Patients with posterior circulation and tandem occlusion were excluded, as were patients for whom baseline FVH information was not available because of motion artifacts during imaging acquisition or because a 3D-FLAIR sequence was performed instead of axial 2D-FLAIR. The inclusion flow chart is presented in Online Fig 1. ASTER and THRACE did not use the CBS or collateral score as an imaging-selection criterion.[19,20]

Clinical and Imaging Assessment

Demographic and clinical data (including sex, age, history of hypertension, systolic and diastolic blood pressure, diabetes mellitus, dyslipidemia, glycemia, smoking habits, initial NIHSS score, IVT use, and time metrics) were extracted from the ASTER and THRACE data bases.

For both trials, all neuroimaging data were stored centrally and reanalyzed by a central imaging committee. All images and angiograms before and after EVT were reviewed by an independent committee of 2 experienced neuroradiologists who were blinded to the randomization group and patient clinical outcome. Discordance was resolved in consensus.

Baseline DWI-ASPECTS and occlusion site (either the M1 or M2 segment of the MCA or ICA) were also recorded. Reperfusion status was assessed on digital subtraction angiograms in the EVT arm using the modified TICI (mTICI) score, and successful reperfusion was defined as mTICI $\geq$ 2b.[21]

Clot Burden Score

Clot extent was determined according to the CBS, which is a 10-point scoring system in which a lower score reflects a more extensive thrombus, as described previously.[8,9] A score of 10 implies clot absence or a clot with no susceptibility vessel sign.[22] A score of 0 implies complete multisegment vessel occlusion. The CBS was subsequently dichotomized using a $\geq$6-point cutoff, according to and for comparison with previous studies.[6,10]

Collateral Score

Collaterals were assessed on baseline FLAIR sequence. FVHs were defined as focal, tubular, or serpentine hyperintensities in subarachnoid spaces with a typical arterial course.[23] Quantification of FVH was performed using an FVH–ASPECTS rating system as described previously.[16,23] An ASPECTS cortical area was considered positive when it coincided with an FVH. The FVH score ranged from 0 (no FVH) to 6 (FVHs abutting all ASPECTS cortical areas). For further analyses, the FVH score was considered in 4 categories (0 versus 1–2 versus 3–4 versus 5–6) to avoid small numbers in extreme FVH scores.

Table 1: Main patient characteristics according to favorable outcome[a]

Characteristics	Favorable Outcome (90-Day mRS 0–2) No ($n = 151$)	Yes ($n = 165$)	P
Demographics			
Age (mean) (SD) (yr)	72.8 ± 12.8	64.2 ± 14.1	<.001
Men	77 (51.0)	93 (56.4)	.34
Medical history			
Hypertension	97 (65.1)	77 (47.5)	.002
Diabetes	31 (21.1)	14 (8.5)	.002
Hypercholesterolemia	58 (40.8)	58 (36.0)	.39
Current smoking	16 (12.9)	42 (29.6)	.001
Coronary artery disease	26 (18.2)	18 (11.1)	.08
Current stroke event			
Systolic blood pressure (mean) (SD) (mm Hg)	148 ± 25	144 ± 23	.08
Diastolic blood pressure (mean) (SD) (mm Hg)	82 ± 18	81 ± 14	.50
Glycemia (median) (IQR)	6.8 (5.9–8.4)	6.3 (5.8–7.4)	.01
NIHSS score (median) (IQR)	19 (16–22)	15 (10–19)	<.001
ASPECTS (median) (IQR)	6 (4–8)	7 (6–9)	<.001
Site of occlusion			
M1 MCA	119 (78.8)	144 (87.3)	.10
ICA	28 (18.5)	17 (10.3)	
Tandem	4 (2.6)	4 (2.4)	
Intravenous tPA	72 (47.7)	92 (55.8)	.15
Cardioembolic	57 (38.5)	78 (47.6)	.11
Interval times (median) (IQR) (min)			
Onset-to-groin puncture time	219 (180–266)	216 (170–264)	.33
Onset to imaging	110 (85–145)	112 (85–143)	.89
Onset to clot	254 (200–297)	242 (189–285)	.14

Note:—IQR indicates interquartile range.

[a] Values are (No.) (%) unless otherwise indicated. Onset-to-groin puncture is defined as the interval between the onset of symptoms and the groin puncture; onset to imaging is defined as the interval between the onset of symptoms and the beginning of the first acquisition of MR imaging sequence; and onset to clot is defined as the interval between the onset of symptoms and the first contact of the mechanical thrombectomy device with the clot that occluded the vessel.

Outcome Assessment

Neurologic functional outcome was assessed by the mRS score at 90 days. The mRS ranges from 0 (no residual stroke symptoms) to 6 (death) and was evaluated across the entire score range as an ordinal variable.[24] Favorable outcome was clinical independence, defined as a 90-day mRS score of 0–2. In both trials, the 90-day mRS score was assessed by trained research nurses unaware of the group assignments during face-to-face interviews or via telephone conversations.

Statistical Analysis

Categoric variables were expressed as frequencies and percentages. Quantitative variables were expressed as means (SD) or medians (interquartile range) for non-normal distribution. Normality of distributions was assessed graphically using the Shapiro-Wilk test. Baseline characteristics and outcomes were described in patients included and not included in the primary analysis due to missing CBS values. Between-group imbalances were assessed by calculating absolute standardized differences (Cohen D effect size); an absolute standardized difference >20% was considered meaningful.[25] Comparisons in baseline characteristics according to favorable outcome status (mRS 0–2) were made using the Student t test for Gaussian continuous variables, the Mann-Whitney U test for non-Gaussian continuous variables, and the χ^2 test (or Fisher exact test when the expected cell frequency was <5) for categoric variables, as appropriate. The correlation between the CBS and FVH score was examined by calculating the Spearman rank correlation coefficient.

We assessed the association of favorable outcome with the CBS and FVH score using univariable and multivariable logistic regression models. The shape of relationships was examined by a graphic approach using nonparametric smoothing techniques. Because we observed a non-log-linear relationship between the CBS and favorable outcome, the CBS was also analyzed according to the previously published threshold (≥6).[6,10] The associations were adjusted on study and prespecified confounders (age, sex, admission NIHSS, use of intravenous tPA, and onset-to-groin puncture time). Finally, we explored the interaction between a high CBS (≥6) and the FVH score by including the corresponding multiplicative term in the logistic regression models. To illustrate the interaction, we calculated ORs with their 95% CIs of favorable outcome for a high CBS according to the FVH score (0 versus 1–2 versus 3–4 versus 5–6).

Primary analysis was conducted in patients with available CBS measures. Sensitivity analysis, including all eligible patients, was performed after handling missing values by a multiple-imputation procedure. Missing data were imputed under a missing at random assumption via a regression-switching approach (chained equation with Mean n = 10 imputations) using all baseline characteristics and the study outcome with a predictive mean-matching method for continuous variables and a multinomial or binary logistic regression model for categoric variables.[26] Estimates obtained in the different imputed datasets were combined using the Rubin rules.[27] Statistical testing was conducted at the 2-tailed α-level of .05. Data were analyzed using SAS software, Version 9.4 (SAS Institute).

RESULTS

Of the 793 patients randomized in the ASTER and THRACE trials, 416 patients received thrombectomy following MR imaging–based triage and were eligible for this study (Online Fig 1). Of them, 90 patients without CBS assessment (missing values) were excluded from primary analysis. Main baseline characteristics and outcomes of the study population according to the availability of the CBS are available in Online Table 1. Several meaningful differences were observed (standardized difference, >20%); favorable outcome was observed in 165 of 326 patients with a CBS by comparison with 27 of 90 patients without CBS assessment. Table 1 shows the characteristics of patients in the primary analysis sample, according to favorable outcome (see Online Table 2 for characteristics of all eligible

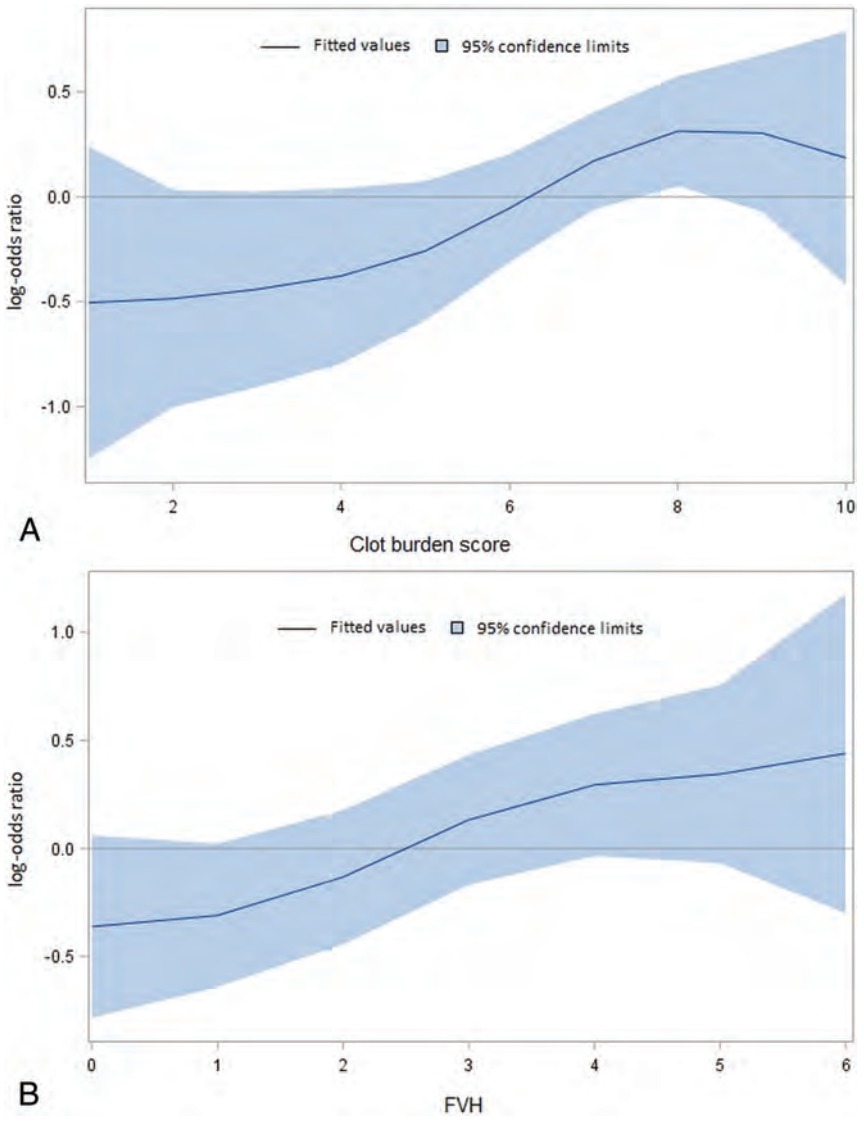

FIG 1. Shape of association of favorable outcome with the CBS (*A*) and FVH score (*B*). Curves were obtained by fitting a generalized additive model (binomial distribution with a logit link function) with a cubic smoothing spline term.

patients after treating missing values by multiple imputation). Patients with favorable outcome were younger and more often smokers, less often had hypertension and diabetes, and had a lower glycemia level at admission, a lower NIHSS score, and a higher ASPECTS than patients without favorable outcome.

Association of Favorable Outcome with the CBS and FVH Score

As shown in Fig 1, the rate of favorable outcome increased with higher CBS (smaller clots) and FVH (higher collaterals) values; for CBS, a non-log-linear relationship was observed. As shown in Table 2, a high CBS (≥6) was significantly associated with an increased likelihood of favorable outcome, with an unadjusted OR of 1.84 (95% CI, 1.13–3.00). Similarly, a significant association was found when the CBS was analyzed as a quantitative trait (unadjusted OR = 1.12; 95% CI, 1.01–1.23 per 1-point increase). After adjustment on prespecified confounders (study, age, sex, admission NIHSS, intravenous tPA, and onset-to-groin puncture time), the association of the CBS and favorable outcome was no longer significant (Table 2). After handling missing values by multiple imputations, every FVH grade increase was significantly associated with an increased likelihood of favorable outcome, with an unadjusted OR = 1.17 (95% CI, 1.03–1.32). In multivariate analysis,

Table 2: Association of favorable outcome with CBS and FVH score

	Favorable Outcome		Unadjusted		Adjusted[b]	
	No	Yes	OR (95% CI)	*P*	OR (95% CI)	*P*
Complete case analysis	(*n* = 151)	(*n* = 165)				
CBS (median) (IQR)	6 (5–8)	7 (6–8)	1.12 (1.01–1.23)[c]	.02	1.05 (0.93–1.19)[c]	.38
≥6 (No.) (%)	95 (62.9)	125 (75.8)	1.84 (1.13–3.00)	.01	1.35 (0.75–2.41)	.31
FVH (median) (IQR)	2 (1–4)	3 (1–4)	1.17 (1.03–1.32)[c]	.01	1.14 (0.98–1.33)[c]	.07
Sensitivity analysis[a]	(*n* = 218)	(*n* = 198)				
CBS (median) (IQR)	6 (4–8)	7 (5–8)	1.15 (1.04–1.26)[c]	.003	1.05 (0.94–1.18)[c]	.37
≥6 (No.) (%)	134 (61.6)	150 (75.6)	1.93 (1.24–3.00)	.003	1.33 (0.78–2.27)	.29
FVH (median) (IQR)	2 (0–3)	3 (1–4)	1.21 (1.08–1.35)[c]	<.001	1.17 (1.02–1.34)[c]	.02

[a] Sensitivity analysis was performed in all patients with MR imaging (*n* = 416) after handling missing values by multiple imputation.
[b] Prespecified adjustment on study (ASTER versus THRACE), age, sex, admission NIHSS, intravenous tPA, and onset-to-groin puncture time.
[c] OR per 1-point increase in CBS or FVH.

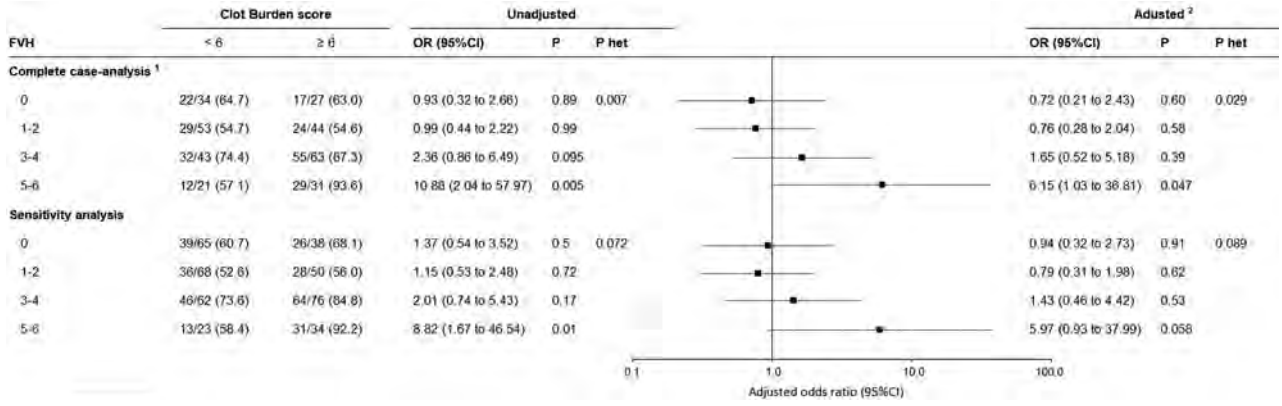

FIG 2. Association of favorable outcome and a high CBS according to the FVH Score. [1]Sensitivity analysis was performed in all patients with MR imaging ($n = 416$) after handling missing values by multiple imputation. [2]Prespecified adjustment on the study (ASTER versus THRACE), age, sex, admission NIHSS, intravenous tPA, and onset-to-groin puncture time. *P* het indicates an interaction test between the clot burden score and the FVH grade (treated as a 6-level ordinal variable).

FVH was of borderline significance in primary analysis (OR = 1.14; 95% CI, 0.98–1.33) and was significant in the sensitivity analysis (OR = 1.17; 95% CI, 1.02–1.34).

The association of successful reperfusion (mTICI ≥ 2b) with the CBS and FVH score is presented in Online Table 3.

Association between the CBS and FVH Score

A weak, positive correlation between the CBS and FVH score was found (Online Fig 2), with a Spearman rank correlation coefficient of 0.20 (95% CI, 0.09–0.31).

Association between a High CBS and Favorable Outcome Modified by the FVH Score

As shown in Fig 2, an interaction was found between a high CBS and FVH grade on favorable outcome, which reached the significance level in primary analysis. The positive association between a high CBS and favorable outcome was mainly observed for the highest FVH grades, with an adjusted OR for the CBS of ≥6 of 6.15 (95% CI, 1.03–36.81) in the primary analysis and 5.97 (95% CI, 0.93–37.99) in sensitivity analysis.

DISCUSSION

In this study, the 3-month functional outcome was better with a higher CBS and a higher FVH score in unadjusted analysis. However, only the FVH score was an independent factor related to outcome in the adjusted analysis. Because an interaction was observed between the CBS and FVH score, we showed an independent stronger association between clot extent (CBS) and functional outcome for patients with good collaterals (FVH ≥5).

A weak positive correlation between the CBS and FVH score was found with a Spearman rank correlation coefficient of 0.20 (95% CI, 0.09–0.31). This observation does not contradict our main results. Furthermore, this is not surprising because the FVH–ASPECTS rating system, unlike the CBS, does not provide a strict ordinal variable.

Thrombus and collaterals can be part of the imaging assessment in patients with AIS and may play a role in clinical practice to guide physicians to the best reperfusion strategy.[28] Recently, Seners et al[29] showed that better collaterals, smaller thrombus, and more distal occlusion sites were independently associated with early post-IVT recanalization in patients eligible for EVT. Thus, advanced imaging may play a key role in personalized medicine in identifying which patients with large-vessel occlusion are most likely to benefit from reperfusion therapies.

Associations of thrombus location and the length of the occlusion with functional outcome and recanalization are well-described in patients treated with IVT,[30] and recently in patients undergoing EVT.[6,10] Both parameters are included in the CBS, in which a lower score reflects a more extensive thrombus.[8,9] Patients with a lower CBS (longer thrombus) have lower odds of reperfusion, larger final infarct volumes at follow-up, and worse functional outcome.[7,10] Besides, longer thrombi may be more difficult to retrieve, requiring more attempts and prolonging the procedural time.[7,31]

Few studies have assessed the relation between collateral status and clot extent and the role of collateral status in the association of clot extent with functional outcome.[13,14] Our findings are in accordance with previous studies in which patients with poor baseline collaterals had longer clots.[13,32] Patients with proximal occlusion in the anterior circulation (ICA and proximal M1) are likely to have a greater amount of brain tissue at risk because of the involvement of the lenticulostriate vessels and poorer collateral status because of decreased collateral flow via the anterior cerebral artery pial vessels.[7] Conversely, patients with a smaller clot are more likely to have patent anterior cerebral arteries and posterior communicating arteries, leading to increased pial collateral flow.[14] Moreover, collateral status and arterial branching patterns may influence clot length and clot characteristics.[13] Qazi et al[13] suggested that patients with poor collaterals and/or inefficient angioarchitecture—defined as the absence of branching arteries around the original clot despite collaterals that lead to the secondary thrombus extension—will have longer clots extending into the pial arteries because of blood flow stagnation.

Our study, with a larger population sample size screened with first-line MR imaging and treated by EVT for AIS, confirms a previous one in which a significant effect of collateral status on the association of clot extent and clinical outcome was observed in patients with moderate and high collateral scores, supporting

the thesis that collateral circulation at least partially underlies the association between clot extent and functional outcome.[14]

Indeed, the optimal imaging technique for efficient patient triage in the acute setting remains a conundrum. CT offers the advantages of being fast, almost universally available, and conspicuous for hemorrhage. However, CTA may overestimate the extent of thrombus involvement. Indeed, if the collateral circulation is weak or with short delays between contrast injection and imaging acquisition,[33] an overestimation of clot length is possible. Furthermore, the current methods of collateral assessment with CTA require expert image evaluation and, though shown to be applicable in clinical trials, can be prone to measurement error in less expert hands.[34] Of note, CT perfusion, which also provides accurate collateral assessment, could overcome issues of CTA timing with the temporal maximum intensity projection of CT perfusion, which gives a relevant reflection of the CBS.[35,36]

Although less readily available, MR imaging is more sensitive for ischemic extent, the presence of hemorrhage, thrombus characterization, and stroke mimics and can be used as a prime and sole imaging technique without delaying treatment decisions.[37] FLAIR and T2* sequences have several advantages over traditional imaging techniques for detecting collaterals and thrombus; this technique is routinely used in all MR imaging units, requires a relatively short scan time, and requires no exogenous contrast agent or radiation exposure. Furthermore, T2*-CBS and the FVH score reproducibility have been demonstrated in multiple studies,[9,10,16,18] and images are assessable by the naked eye directly on any DICOM viewer without the need for postprocessing. Nevertheless, in our study, we did not use the thrombus size but rather the T2*-CBS, which is, by definition, an overestimation of the clot length through the extent of the blooming effect.

Strengths and Limitations

The strengths of this study include the analysis of the CBS and FVH score in 2 randomized, multicenter study designs that evaluated highly effective thrombectomy devices and that included patients irrespective of clot length and collateral status. To our knowledge, this is also the first study to assess the interaction effect of collateral status assessed by the FVH score on functional outcome based on clot extent in patients with AIS. Taken together, our data provide insight into the association between clot extent and functional outcome, which appears to be partially explained by a higher collateral score leading to a smaller clot.

However, our study also has limitations. First, patients were included on the basis of the criteria of the 2 randomized controlled trials, leading to a selection bias. Second, in the emergency setting for AIS, the acquisition of MR imaging may be impossible in patients who are claustrophobic or in patients who cannot be still, especially with dominant-hemisphere strokes. Third, FVH collateral grading can quantify the abundance of the vasculature, but not the flow velocity, and this feature may be relevant in acute stroke triage: Plentiful collaterals with fast delivery may designate a patient who will benefit more from EVT than a patient with plentiful-but-slow collaterals with late delivery.[38] Fourth, the CBS quantifies thrombi but omits information on characteristics that are relevant for outcome, (ie, perforators occlusion). Indeed, as emphasized by Qazi et al,[13] the thrombus extent can have different implications through the angioarchitecture patterns. However, we were unable to assess the anterior temporal artery and perforator artery patency in our study. Fifth, there was no imaging or histologic characterization of clot nature to further characterize the relationship of EVT results with clot types. Indeed, a CBS of 10 implies clot absence or a clot with no susceptibility vessel sign, the latter situation representing between 20% and 30% of occlusions.[39] Additionally, MR imaging acquisition parameters of the gradient recalled-echo sequence were left to the discretion of the recruitment centers; and the susceptibility vessel sign, used to quantify the CBS, is known to be a radiologic marker that varies among MR imaging scanners.[40] However, this lack of standardization, which, in fact, corresponds to the real-life daily use of MR imaging sequences, points out the generalizability of our findings. Indeed, previous similar pragmatic multicentric assessments of the CBS have already emphasized clinically relevant results.[10] Finally, we did not assess the predictive power of patient selection. Future studies should evaluate the clinical utility of such radiomarkers in the screening of candidates for endovascular treatment in case of large-vessel occlusion and to elucidate the pathways linking collateral status to clot extent and vice versa.

CONCLUSIONS

There is an influence of collateral status, quantified by the FVH scoring system, on the association of clot extent with functional outcome. The independent association of a high FVH score and good functional outcome at 3 months supports the idea that the FVH score might be a prognostic factor, especially when contrast-based vascular imaging is not available. Future work should assess the mechanism underlying the interaction between thrombus extent and collaterals.

ACKNOWLEDGMENTS

We thank Mary Osborne-Pellegrin for her help in editing the final draft of the article.

Disclosures: Frédéric Clarençon—*UNRELATED*: *Board Membership*: Artedrone; *Grants/Grants Pending*: EMPROTECT, DISCOUNT*; *Payment for Lectures Including Service on Speakers Bureaus*: Balt, Penumbra, Medtronic. Bertrand Lapergue—*UNRELATED*: *Grants/Grants Pending*: research grants from Stryker, Penumbra, and MicroVention.* *Money paid to the institution.

REFERENCES

1. Goyal M, Menon BK, Zwam WH, van, et al; HERMES collaborators. **Endovascular thrombectomy after large-vessel ischaemic stroke: a meta-analysis of individual patient data from five randomised trials.** *Lancet* 2016;387:1723–31 CrossRef Medline
2. Rha JH, Saver JL. **The impact of recanalization on ischemic stroke outcome: a meta-analysis.** *Stroke* 2007;38:967–73 CrossRef Medline
3. Berkhemer OA, Jansen IGH, Beumer D, et al; MR CLEAN Investigators. **Collateral status on baseline computed tomographic angiography and intra-arterial treatment effect in patients with proximal anterior circulation stroke.** *Stroke* 2016;47:768–76 CrossRef Medline
4. Singer OC, Berkefeld J, Nolte CH, et al. **Collateral vessels in proximal middle cerebral artery occlusion: the ENDOSTROKE study.** *Radiology* 2015;274:851–58 CrossRef Medline
5. Shuaib A, Butcher K, Mohammad AA, et al. **Collateral blood vessels in acute ischaemic stroke: a potential therapeutic target.** *Lancet Neurol* 2011;10:909–21 CrossRef Medline

6. Treurniet KM, Yoo AJ, Berkhemer OA, et al; MR CLEAN Investigators. **Clot burden score on baseline computerized tomographic angiography and intra-arterial treatment effect in acute ischemic stroke.** *Stroke* 2016;47:2972–78 CrossRef Medline
7. Dutra BG, Tolhuisen ML, Alves HC, et al; MR CLEAN Registry Investigators. **Thrombus imaging characteristics and outcomes in acute ischemic stroke patients undergoing endovascular treatment.** *Stroke* 2019;50:2057–64 CrossRef Medline
8. Puetz V, Dzialowski I, Hill MD, et al. **Intracranial thrombus extent predicts clinical outcome, final infarct size and hemorrhagic transformation in ischemic stroke: the clot burden score.** *Int J Stroke* 2008;3:230–36 CrossRef Medline
9. Legrand L, Naggara O, Turc G, et al. **Clot burden score on admission T2*-MRI predicts recanalization in acute stroke.** *Stroke* 2013;44:1878–84 CrossRef Medline
10. Derraz I, Bourcier R, Soudant M, et al; THRACE Investigators. **Does clot burden score on baseline T2*-MRI impact clinical outcome in acute ischemic stroke treated with mechanical thrombectomy?** *J Stroke* 2019;21:91–100 CrossRef Medline
11. McVerry F, Liebeskind DS, Muir KW. **Systematic review of methods for assessing leptomeningeal collateral flow.** *AJNR Am J Neuroradiol* 2012;33:576–82 CrossRef Medline
12. Rocha M, Jovin TG. **Fast versus slow progressors of infarct growth in large vessel occlusion stroke: clinical and research implications.** *Stroke* 2017;48:2621–27 CrossRef Medline
13. Qazi EM, Sohn SI, Mishra S, et al. **Thrombus characteristics are related to collaterals and angioarchitecture in acute stroke.** *Can J Neurol Sci* 2015;42:381–88 CrossRef Medline
14. Alves HC, Treurniet KM, Dutra BG, et al; MR CLEAN trial investigators. **Associations between collateral status and thrombus characteristics and their impact in anterior circulation stroke.** *Stroke* 2018;49:391–96 CrossRef Medline
15. Román LS, Menon BK, Blasco J, et al; HERMES collaborators. **Imaging features and safety and efficacy of endovascular stroke treatment: a meta-analysis of individual patient-level data.** *Lancet Neurol* 2018;17:895–904 CrossRef Medline
16. Nave AH, Kufner A, Bücke P, et al. **Hyperintense vessels, collateralization, and functional outcome in patients with stroke receiving endovascular treatment.** *Stroke* 2018;49:675–81 CrossRef Medline
17. Liu D, Scalzo F, Rao NM, et al. **Fluid-attenuated inversion recovery vascular hyperintensity topography, novel imaging marker for revascularization in middle cerebral artery occlusion.** *Stroke* 2016;47:2763–69 CrossRef Medline
18. Legrand L, Tisserand M, Turc G, et al. **Fluid-attenuated inversion recovery vascular hyperintensities–diffusion-weighted imaging mismatch identifies acute stroke patients most likely to benefit from recanalization.** *Stroke* 2016;47:424–27 CrossRef Medline
19. Lapergue B, Blanc R, Gory B, et al; ASTER Trial Investigators. **Effect of endovascular contact aspiration vs stent retriever on revascularization in patients with acute ischemic stroke and large vessel occlusion: the ASTER randomized clinical trial.** *JAMA* 2017;318:443–52 CrossRef Medline
20. Bracard S, Ducrocq X, Mas JL, et al; THRACE investigators. **Mechanical thrombectomy after intravenous alteplase versus alteplase alone after stroke (THRACE): a randomised controlled trial.** *Lancet Neurol* 2016;15:1138–47 CrossRef Medline
21. Zaidat OO, Yoo AJ, Khatri P, et al; STIR Thrombolysis in Cerebral Infarction (TICI) Task Force. **Recommendations on angiographic revascularization grading standards for acute ischemic stroke: a consensus statement.** *Stroke* 2013;44:2650–63 CrossRef Medline
22. Flacke S, Urbach H, Keller E, et al. **Middle cerebral artery (MCA) susceptibility sign at susceptibility-based perfusion MR imaging: clinical importance and comparison with hyperdense MCA sign at CT.** *Radiology* 2000;215:476–82 CrossRef Medline
23. Legrand L, Tisserand M, Turc G, et al. **Do FLAIR vascular hyperintensities beyond the DWI lesion represent the ischemic penumbra?** *AJNR Am J Neuroradiol* 2015;36:269–74 CrossRef Medline
24. Savitz SI, Lew R, Bluhmki E, et al. **Shift analysis versus dichotomization of the modified Rankin Scale outcome scores in the NINDS and ECASS-II trials.** *Stroke* 2007;38:3205–12 CrossRef Medline
25. Cohen J. **A power primer.** *Psychol Bull* 1992;112:155–59 CrossRef Medline
26. van Buuren S, Groothuis-Oudshoorn K. **MICE: multivariate imputation by chained equations in R.** *J Stat Softw* 2011;45:1–67 CrossRef
27. Rubin DB. *Multiple Imputation for Nonresponse in Surveys*. John Wiley & Sons; 1987
28. Menon BK, Campbell BCV, Levi C, et al. **Role of imaging in current acute ischemic stroke workflow for endovascular therapy.** *Stroke* 2015;46:1453–61 CrossRef Medline
29. Seners P, Roca P, Legrand L, et al. **Better collaterals are independently associated with post-thrombolysis recanalization before thrombectomy.** *Stroke* 2019;50:867–72 CrossRef Medline
30. Rohan V, Baxa J, Tupy R, et al. **Length of occlusion predicts recanalization and outcome after intravenous thrombolysis in middle cerebral artery stroke.** *Stroke* 2014;45:2010–17 CrossRef Medline
31. Yoo AJ, Khatri P, Mocco J, et al; THERAPY Trial Investigators. **Impact of thrombus length on outcomes after intra-arterial aspiration thrombectomy in the THERAPY trial.** *Stroke* 2017;48:1895–900 CrossRef Medline
32. Tan IYL, Demchuk AM, Hopyan J, et al. **CT angiography clot burden score and collateral score: correlation with clinical and radiologic outcomes in acute middle cerebral artery infarct.** *AJNR Am J Neuroradiol* 2009;30:525–31 CrossRef Medline
33. Frölich AM, Schrader D, Klotz E, et al. **4D CT angiography more closely defines intracranial thrombus burden than single-phase CT angiography.** *AJNR Am J Neuroradiol* 2013;34:1908–13 CrossRef Medline
34. Mair G, von Kummer R, Adami A, et al; IST-3 Collaborative Group. **Observer reliability of CT angiography in the assessment of acute ischaemic stroke: data from the Third International Stroke Trial.** *Neuroradiology* 2015;57:1–9 CrossRef Medline
35. Heo JH, Kim K, Yoo J, et al. **Computed tomography-based thrombus imaging for the prediction of recanalization after reperfusion therapy in stroke.** *J Stroke* 2017;19:40–49 CrossRef Medline
36. Puhr-Westerheide D, Tiedt S, Rotkopf LT, et al. **Clinical and imaging parameters associated with hyperacute infarction growth in large vessel occlusion stroke.** *Stroke* 2019;50:2799–804 CrossRef Medline
37. Provost C, Soudant M, Legrand L, et al. **Magnetic resonance imaging or computed tomography before treatment in acute ischemic stroke.** *Stroke* 2019;50:659–64 CrossRef Medline
38. Boers AM, Jansen IG, Berkhemer OA, et al; MR CLEAN trial investigators. **Collateral status and tissue outcome after intra-arterial therapy for patients with acute ischemic stroke.** *J Cereb Blood Flow Metab* 2017;37:3589–98 CrossRef Medline
39. Bourcier R, Mazighi M, Labreuche J, et al. **Susceptibility vessel sign in the ASTER trial: higher recanalization rate and more favourable clinical outcome after first line stent retriever compared to contact aspiration.** *J Stroke* 2018;20:416–16 CrossRef Medline
40. Bourcier R, Détraz L, Serfaty JM, et al. **MRI interscanner agreement of the association between the susceptibility vessel sign and histologic composition of thrombi.** *J Neuroimaging* 2017;27:577–82 CrossRef Medline

Acute Ischemic Stroke or Epileptic Seizure? Yield of CT Perfusion in a "Code Stroke" Situation

L. Lucas, F. Gariel, P. Menegon, J. Aupy, B. Thomas, T. Tourdias, I. Sibon, and P. Renou

ABSTRACT

BACKGROUND AND PURPOSE: The clinical differentiation between acute ischemic stroke and epileptic seizure may be challenging, and making the correct diagnosis could avoid unnecessary reperfusion therapy. We examined the accuracy of CTP in discriminating epileptic seizures from acute ischemic stroke without identified arterial occlusion.

MATERIALS AND METHODS: We retrospectively identified consecutive patients in our emergency department who underwent CTP in the 4.5 hours following the development of an acute focal neurologic deficit who were discharged with a final diagnosis of acute ischemic stroke or epileptic seizure.

RESULTS: Among 95 patients, the final diagnosis was epileptic seizure in 45 and acute ischemic stroke in 50. CTP findings were abnormal in 73% of the patients with epileptic seizure and 40% of those with acute ischemic stroke. Hyperperfusion was observed more frequently in the seizure group (36% versus 2% for acute ischemic stroke) with high specificity (98%) but low sensitivity (35%) for the diagnosis of epileptic seizure. Hypoperfusion was found in 38% of cases in each group and was not confined to a vascular territory in 24% of patients in the seizure group and 2% in the acute ischemic stroke group. The interobserver agreement was good (κ = 0.60) for hypo-, hyper-, and normoperfusion patterns and moderate (κ = 0.41) for the evaluation of vascular systematization.

CONCLUSIONS: CTP patterns helped to differentiate acute ischemic stroke from epileptic seizure in a "code stroke" situation. Our results indicate that a hyperperfusion pattern, especially if not restricted to a vascular territory, may suggest reconsideration of intravenous thrombolysis therapy.

ABBREVIATIONS: AIS = acute ischemic stroke; EEG = electroencephalography; NPV = negative predictive value; PPV = positive predictive value; Tmax = time-to-maximum

"Code stroke" status, a sudden-onset neurologic deficit, is a common cause of admission to emergency departments. Stroke is the first diagnosis to explore because it requires early reperfusion therapy such as thrombolysis and/or mechanical thrombectomy because as many as 30% of patients with code stroke involve conditions that mimic stroke,[1] with epileptic seizure being one of the most frequent (~10%).[2] Up to 15% of patients receiving rtPA after NCCT have a stroke mimic.[3] Although some studies have demonstrated that intravenous rtPA in stroke mimics is relatively safe,[3] complications such as such hemorrhage or angioedema can occur in 1% of cases each[4] and increase the cost and length of hospitalization.[5]

Imaging modalities that can differentiate an acute ischemic stroke from an epileptic seizure could facilitate the appropriate choice of urgent treatment. Intracranial arterial imaging is insufficient to diagnose ischemic stroke because up to 40% of patients with stroke have no identified occlusion.[6]

Although brain MR imaging with diffusion-weighted imaging is regarded as the criterion standard for detecting early ischemia, CTP is a more widely accessible imaging technique, with shorter acquisition times. In recent thrombectomy studies, CTP screening was performed 11 times more frequently than MR imaging screening.[7]

Cerebral perfusion imaging related to acute ischemic stroke has been widely investigated,[8] but few studies on the role of cerebral perfusion imaging in seizure diagnosis have been published.[9,10]

Received April 9, 2020; accepted after revision August 27.

From the Department of Neurology (L.L., I.S., P.R.), Stroke Unit, and Departments of Neuroradiology (F.G., B.T., T.T.), Neurology (??????), Epileptology, and Clinical Neuroscience (L.L., J.A., B.T., T.T., I.S.), Bordeaux University Hospital, Bordeaux, France; and Institut des Matériaux Jean Rouxel, (J.A.), Union Mutualiste Retraite, Centre national de la recherche scientifique, University of Bordeaux, Bordeaux, France.

Please address correspondence to Lucas Ludovic, MD, Unité Neuro-vasculaire, Hôpital Pellegrin, 33076 Bordeaux, France; e-mail: ludovic.lucas @ch-arcachon.fr

Indicates article with supplemental online tables.

Indicates article with supplemental online photo.

http://dx.doi.org/10.3174/ajnr.A6925

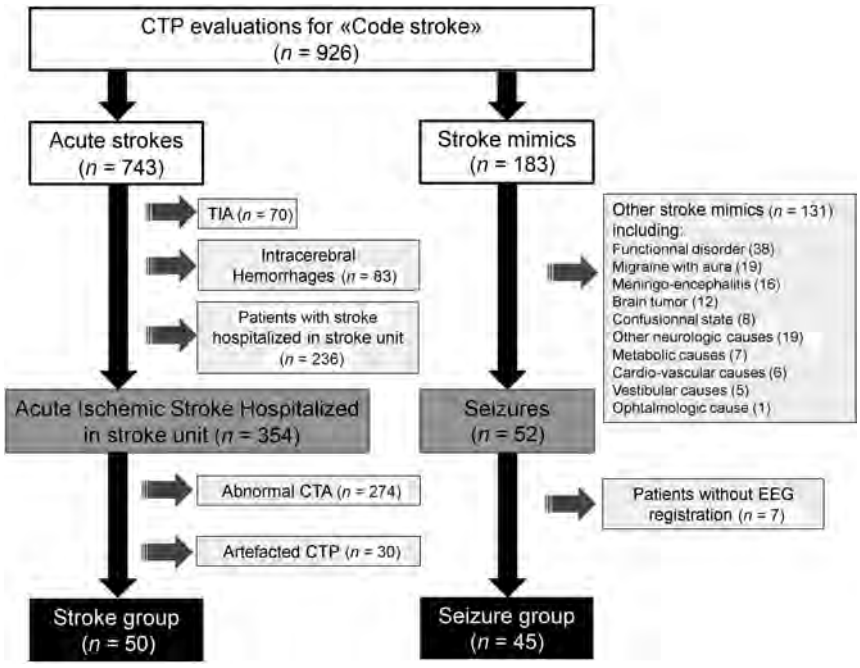

FIG 1. Flow chart.

During the ictal period, neuronal activation may be associated with an increase in regional brain perfusion, whereas the postictal period is characterized more frequently by hypoperfusion.[11,12]

The aim of our study was to identify cerebral perfusion imaging patterns that help differentiate an acute focal neurologic deficit related to an epileptic seizure from an acute ischemic stroke in code stroke alerts, in the absence of vessel occlusion or stenosis on CTA.

MATERIALS AND METHODS

Patients

This monocentric study was conducted on a retrospective and consecutive unselected cohort of patients admitted to our emergency department with an acute focal neurologic deficit on code stroke alert between January 2014 and October 2015.

We retrospectively obtained all CTP examinations performed in emergency settings by query of the PACS. We obtained clinical data from a review of systematic Electronic Medical Records, and an NIHSS was administered by a stroke neurologist (with NIHSS certification) immediately before the CTP (Online Appendix).

The inclusion criteria were as follows: 1) CTP was performed during the first 4.5 hours following the onset of symptoms in code stroke status; 2) the final diagnosis was either epileptic seizure (seizure group) or acute ischemic stroke (stroke group); 3) patients in the stroke group were hospitalized in our stroke unit and had normal CTA findings and evidence of ischemic stroke on follow-up MR imaging; and 4) patients in the seizure group had undergone electroencephalography (EEG) during hospitalization and had no evidence of an acute ischemic stroke on follow-up MR imaging or, in rare cases of incompatibility, on follow-up CT (Fig 1).

The diagnosis of seizure was based on converging clinical evaluation and electroencephalographic evidence and was classified according to the current International Classification of Epileptic Seizure by specialists in epilepsy (J.A., B.T.). A clinical suspicion of seizure was based on witness descriptions of typical manifestations of seizure, new occurrence of seizure during early follow-up, or suggestive evidence on EEG.

The main exclusion criterion was the presence of any vessel occlusion in the artery supplying the symptomatic brain region on initial CTA, the presence of which is strong evidence in favor of a stroke diagnosis. Patients with arterial stenosis on initial CTA were also excluded because of their risk of brain perfusion modification, which can bias the interpretation of CTP.

Our study complied with the protection of personal health data and the protection of privacy within the framework of the application provided by article 65-2 of the amended Data Protection Act and general regulations for the protection of personal data.

CTP Image Acquisition, Protocol, and Analysis

CTP Acquisition. CTP studies were obtained on a 64-section CT scanner (Optima 660; GE Healthcare). The acquisition parameters were as follows: 80 kV, 160 mAs, 250-mm FOV, 512 × 512 matrix, 16 slices covering 80 mm, 3 -second time resolution (time rotation, 0.4 seconds). Typical dosimetry delivery was CT dose index volume, 70 mGy (phantom head 16), and dose length product, 550 mGy × cm.

CTP Postprocessing and Analysis. Parametric maps from CTP were obtained from Olea Sphere 3.0. (Olea Medical). This software applies deconvolution according to the cSVD method, which allows the computation of CBF, CBV, MTT. and time-to-maximum (Tmax) maps (Online Appendix).

All CTP maps were interpreted by 2 independent readers blinded to the final diagnosis but aware of the clinical symptoms included in the NIHSS score. Reader 1 (F.G.) is a neuroradiologist with 4 years of experience, and reader 2 (P.R.) is a stroke neurologist with 10 years of experience.

For the qualitative analysis, the 2 readers identified the presence or absence of perfusion abnormalities on color-coded maps as defined by visible perfusion changes relative to the contralateral hemisphere. In the case of visible perfusion asymmetry, whether the pathologic side was contralateral to the side showing clinical symptoms was evaluated. The nature of any asymmetry (hypo- or hyperperfusion), its anatomic localization, and whether it was limited to the vascular territory were described. The absence of vascular anatomic variations, such as in the fetal posterior cerebral artery, was systematically confirmed on each CTA. Hyperperfusion was

Table 1: Baseline characteristics of the study patient[a]

	Stroke Group ($n = 50$)	Seizure Group ($n = 45$)	*P*
Age (yr)	63.68 [SD, 14.45]	73.81 [SD, 12.6	<.01
Female sex	20 (40)	22 (49)	<.68
Cardiovascular risk factors	37 (74)	35 (78)	<.66
Hypertension	22 (44)	33 (73)	.01
Current smoking	24 (48)	5 (11)	.01
Diabetes	5 (10)	9 (20)	<.17
Dyslipidemia	15 (30)	16 (36)	.57
History of epileptic seizures	2 (4)	11 (24)	.<01
History of stroke	6 (12)	16 (36)	<.01
Initial NIHSS score	4.54 [SD, 4.10]	7.44 [SD, 6.34]	.01
Symptoms			
Aphasia	13 (26)	37 (82)	<.01
Motor deficit	39 (78)	27 (60)	.06
Sensitive deficit	16 (32)	8 (18)	.12
Impaired consciousness	0 (0)	4 (9)	.025
Hemianopsia	4(8)	8 (18)	.15
Dysarthria	15 (30)	1 (2)	<.01
Ataxia	16 (32)	1 (2)	<.01
CTP delay from symptom onset (min)	153.08 [SD, 73.24]	154.98 [SD, 62.71]	.77
Received thrombolysis	26 (52)	8 (18)	<.01
Stroke mechanisms (according to ASCOD classification)			
Cardioembolism	20 (40)	–	
Small-vessel disease	15 (30)	–	
Atherothrombosis	5 (10)	–	
Other causes	4 (8)	–	
Dissection	0 (0)	–	
Undetermined	6 (12)	–	

Note:—ASCOD indicates ?????; –, ???????.
[a] Values are mean [SD] or No. (%).

defined as visibly reduced MTT and Tmax. Hypoperfusion was defined as visibly prolonged MTT and Tmax. CBV and CBF were also calculated for each pattern. An additional third reader (P.M.) with 20 years of experience in neuroradiology participated in a consensus meeting to analyze any discrepancies. The 3 readers reached agreement by consensus for each case.

To investigate the presence of more subtle perfusion abnormalities, including asymptomatic areas, we performed an additional quantitative analysis. Reader 1 selected an ROI in the visibly abnormal perfusion region or, in the absence of a visible abnormality, in the suspected symptomatic region, based on the clinical presentation. A symmetric ROI on the contralateral hemisphere was automatically generated. Additional ROIs, outside the abnormal perfusion region, were also selected with an automatic mirror ROI. These ROIs were placed in other cortical regions, such as the ipsilateral frontal and temporal lobes, as well as in subcortical regions, such as the ipsilateral thalamus and contralateral cerebellar hemisphere. Although focal epilepsy is considered a cortical disease, particularly in the temporal and frontal lobes, the subcortical regions are associated with important pathways involved in seizure propagation and regulation,[13] and crossed cerebellar diaschisis has been previously described.[14] For each ROI, ratios for Tmax, MTT, CBF, and CBV were calculated as ROI symptomatic/ROI symmetric.

MR Imaging Evaluation

All MR imaging–compatible patients underwent a brain MR imaging evaluation using at least diffusion-weighted imaging, FLAIR, and T2*-weighted gradient recalled echo sequences within 2 days after admission.

EEG Acquisition and Analysis

In the seizure group, at least one 20-minute EEG was recorded within 72 hours of hospital admission, using surface electrodes and conforming to the international 10–20 system. EEG recordings were retrospectively interpreted by an EEG specialist (J.A.) aware of the clinical presentation. These recordings were classified into 3 subtypes: normal, epileptiform activity (seizure or epileptiform discharges during EEG, spike and slow wave complex), and nonspecific activity (focal or diffuse slowing, isolated spikes, or slow waves).

Statistical Analysis

Continuous variables are presented as mean [SD], and categoric variables, as number (percentage). Wilcoxon or Mann-Whitney *U* tests were used to compare continuous variables. χ^2 tests, with or without the Yates correction, and Fisher exact tests were used to compare categoric variables.

Interobserver agreement between the 2 readers in the qualitative analysis was calculated using the Cohen κ statistic. The agreement results were defined as follows: poor, ≤ 0.2; mild, 0.2–0.4; moderate, 0.4–0.6; good, 0.6–0.8; and excellent, 0.8–1. Sensitivity, specificity, negative predictive values (NPV), and positive predictive values (PPV) for each CTP pattern according to each disease point of view were analyzed. We used receiver operating characteristic curve analysis to estimate optimal perfusion values in discriminating stroke and seizure. All statistical analyses were performed using R Studio software (http://rstudio.org/download/desktop) (R version 4.0.0; http://www.r-project.org).

RESULTS

Study Population Characteristics

Among the 926 patients who underwent CTP evaluation for code stroke status during the study period, 45 had a final diagnosis of seizure, and 50, a final diagnosis of ischemic stroke, fulfilling the inclusion criteria (Fig 1 and Online Tables 1 and 2). Among the 50 patients with stroke, 46 (92%) had supratentorial stroke. Patients in the seizure group were older (73.81 [SD,12.67] versus 63.68 [SD, 14.45] years, $P < .01$) and had higher NIHSS scores (7.44 [SD, 6.34] versus 4.54 [SD, 4.10], $P < .01$, Table 1). Four patients in the seizure group did not have an MR imaging due to the presence of a pacemaker. Eight patients (18%) in the seizure group and 26 (52%) in the stroke group received thrombolysis (Table 1).

Table 2: Qualitative analyses of CTP[a]

	Stroke Group ($n = 50$)	Seizure Group ($n = 45$)	*P*
Perfusion abnormality	20 (40)	33 (73)	.01
Perfusion abnormality not restricted to the vascular territory	1 (2)	20 (44)	<.01
Hypoperfusion	19 (38)	17 (38)	.1
Restricted to vascular territory	18 (36)	6 (13)	.01
Not restricted to vascular territory	1 (2)	11 (24)	<.01
Hyperperfusion	1 (2)	16 (36)	<.01
Restricted to vascular territory	1 (2)	7 (16)	.02
Not restricted to vascular territory	0 (0)	9 (20)	<.01

[a] Values are numbers (%).

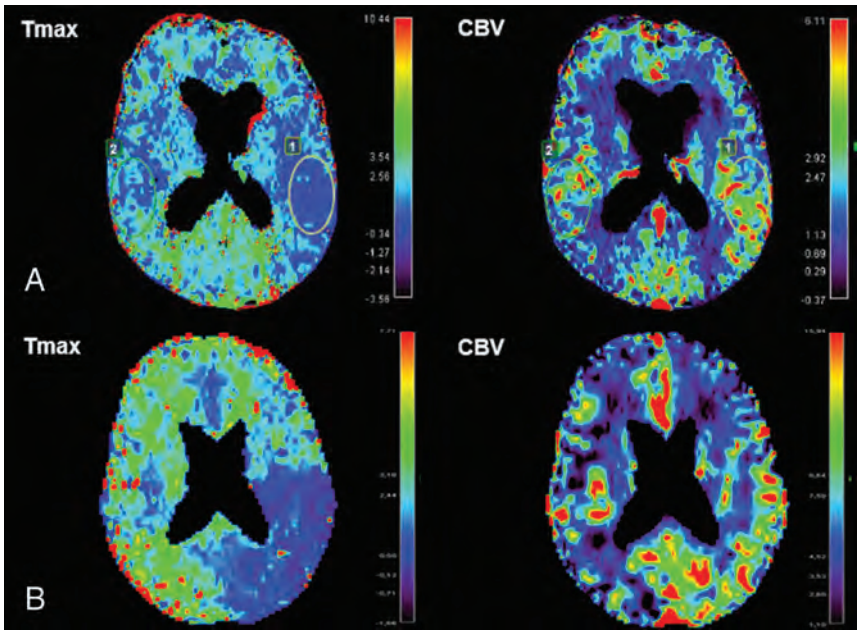

FIG 2. CTP images showing examples of hyperperfusion respecting (*A*) or not (*B*) a vascular territory in the seizure group. *A*, An 84-year-old woman presenting with Wernicke aphasia and complete right hemianopsia: left fronto-parieto-occipital hyperperfusion, which may correspond with the posterior cortical branch of left middle cerebral artery. *B*, An 80-year-old woman presenting with mutism, right hemiplegia, and left forced gaze deviation: left parieto-occipital hyperperfusion not respecting a vascular territory (the left posterior cerebral artery was exclusively from the basilar artery).

CTP Analysis

Good interobserver agreement between the 2 readers in terms of the type of perfusion abnormality (hypo-, hyper- and normal perfusion) was found (Cohen $\kappa = 0.67$; 95% CI, 0.54–0.80).

Hyperperfusion Pattern. In the qualitative analysis, hyperperfusion patterns were significantly more frequent in the seizure group than in the stroke group (36% versus 2%, $P < .01$, Table 2 and Fig 2). Only 1 patient with stroke had a hyperperfusion pattern (Fig 3). A hyperperfusion pattern has a high specificity of 98% and a PPV of 94% for diagnosing seizure, despite a weak sensitivity of 35% and a moderate NPV of 63%. When the characteristic "not restricted to the vascular territory" was added, the specificity and PPV of the hyperperfusion pattern for diagnosing seizure improved to 100%, though the sensitivity remained low (20%), and the NPV, moderate (58%) (Online Table 3).

Hypoperfusion Pattern. A hypoperfusion pattern was found in approximately one-third of the cases in each group (38% in both, Table 2 and Fig 4). Hypoperfusion had a weak predictive value for discriminating stroke and seizure: For diagnosing stroke, the sensitivity was 38%; specificity, 62%; PPV, 53%; and NPV, 47%; and for diagnosing seizure, the sensitivity was 38%; specificity, 62%; PPV, 47%; and NPV, 53%. Hypoperfusion was more frequently restricted to the vascular territory in the stroke group than in the seizure group (95% versus 35%). When the characteristic "restricted to a vascular territory" was added, the hypoperfusion pattern improved its predictive value for diagnosing stroke with a specificity of 87% and a PPV of 75%, and the sensitivity and NPV remained low (25% and 55%, respectively) (Online Table 4). When the characteristic "not restricted to a vascular territory" was added, the hypoperfusion pattern improved its predictive value for diagnosing seizure with a specificity of 98% and a PPV of 92%, though the sensitivity and NPV remained low (24% and 59%).

The Tmax and MTT ratios in the hypoperfused region were significantly higher in the stroke group than in the seizure group (mean, 1.98 [SD, 0.62] versus 1.50 [SD, 0.36], $P = .01$ for Tmax, and 1.15 [SD, 0.14] versus 0.99 [SD, 0.16], $P = .002$ for MTT, Table 3). The CBV ratio was not different between the stroke and seizure groups (0.88 [SD, 0.19] versus 0.86 [SD, 0.31], $P = .41$, Table 3). In comparisons between the stroke and seizure groups, the CBV ratio was decreased ($n = 22$ versus $n = 14$), normal ($n = 13$ versus $n = 10$), or increased ($n = 15$ versus $n = 21$) (data not shown). With the receiver operating characteristic curve, there was a moderate prediction of Tmax ratio (area under the curve = 0.7; 95% CI, 0,51–0.88; $P = .05$) (Online Appendix). A threshold Tmax ratio of >2 allowed a specificity of 89%, despite a low sensitivity (44%) for the diagnosis of acute ischemic stroke (Online Figure)

Among the patients with a hypoperfusion pattern, we observed an increased Tmax ratio in the seizure group within additional frontal and temporal ROIs (Table 3).

Normal Perfusion Pattern. A normal perfusion pattern in the clinically suspected ROI was more frequent in the stroke group than in the seizure group (60% versus 37%). This pattern has a moderate predictive value for the diagnosis of stroke with a sensitivity of

60%, a specificity of 73%, a PPV of 71%, and an NPV of 62%. In this pattern, we found no significance in the perfusion ratios on other ROIs in the temporal or frontal lobe, thalamus, or cerebellum between the 2 groups (Table 3).

Perfusion Abnormality Restricted to the Vascular Territory. Among patients with abnormal perfusion (hyper- or hypoperfusion), the pattern of perfusion abnormality restricted to the vascular territory differed between the stroke and seizure groups. Perfusion abnormality was not restricted to the vascular territory in 44% of patients with seizure compared with only 2% of patients with stroke (Table 2). Although the pattern not restricted to vascular territory appears to have a high specificity (98%) and PPV (95%, for seizure), interobserver agreement was only moderate (Cohen κ = 0.41; 95% CI, 0.12–0.71).

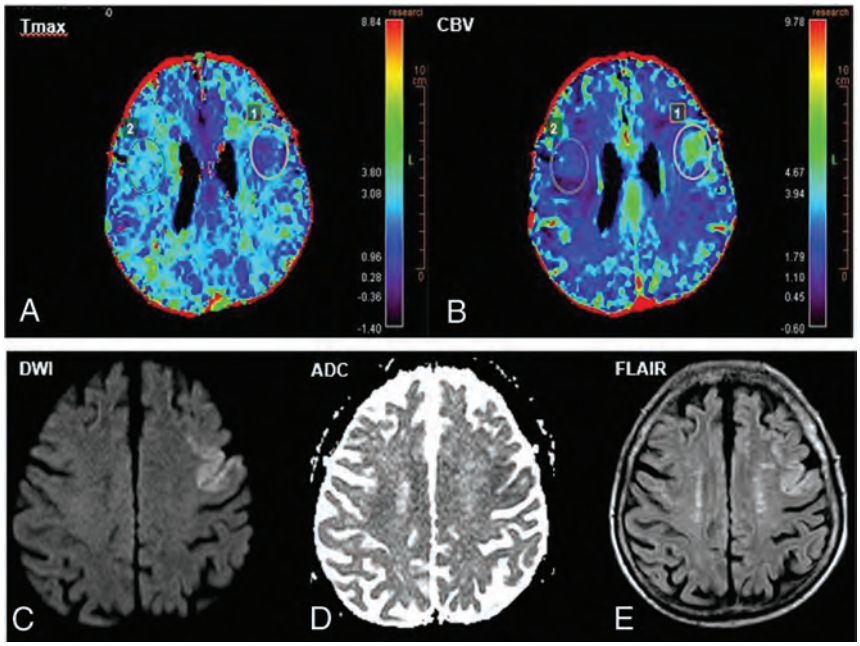

FIG 3. A 92-year-old patient presenting with aphasia and right central facial palsy: focal hyperperfusion on CTP in favor of immediate poststroke "luxury perfusion." *A*, Focal decrease of the Tmax parameter in the left prefrontal area in favor of relative hyperperfusion. *B*, Focal increase of the CBV parameter in the same area. *C*, Correlation with follow-up MR imaging performed 26 hours after clinical presentation identifying a bifocal acute ischemic stroke.

DISCUSSION

Our study suggests that CTP patterns may help differentiate neurologic deficits related to acute ischemic stroke from those related to epileptic seizure in the absence of visible occlusion or stenosis of a supplying vessel on CTA. A hyperperfusion pattern on CTP was significantly more frequent in the seizure group, with a high specificity for the diagnosis of seizure, especially when the hyperperfusion was not restricted to the vascular territory. This hyperperfusion pattern had good interobserver reproducibility. In the stroke

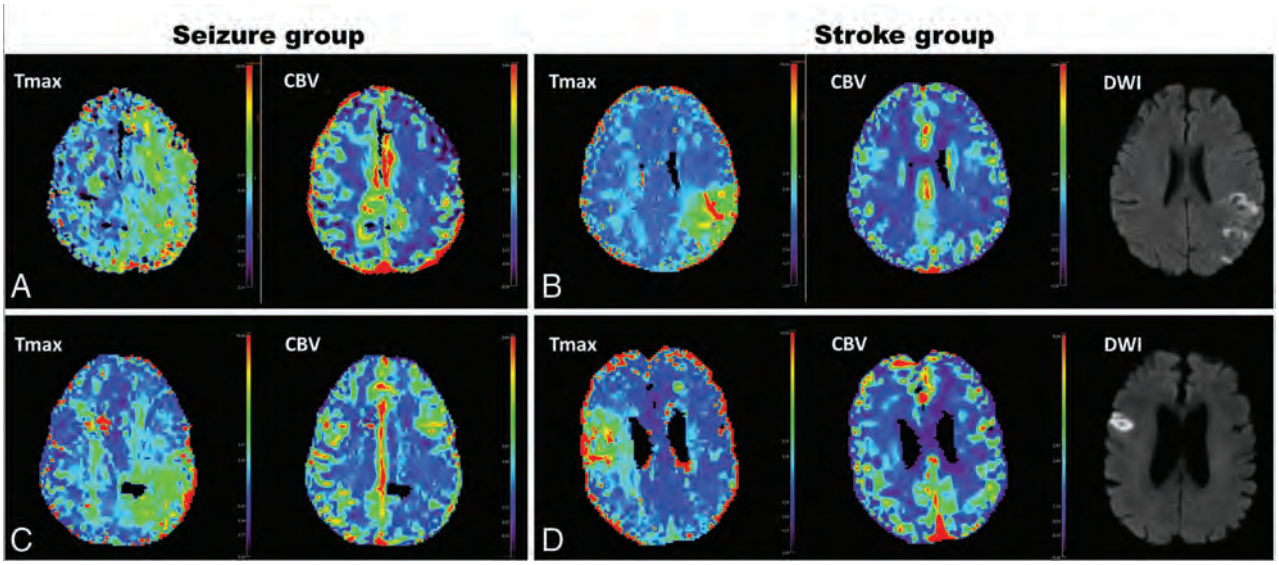

FIG 4. Comparison of CTP hypoperfusion patterns between seizure and stroke groups. *A*, A 61-year-old man presenting with seizure-related aphasia and right face and arm palsy: left holohemispheric hypoperfusion, absence of modification of the CBV parameter. *B*, A 47-year-old woman presenting with seizure-related aphasia and right-arm palsy: hypoperfusion, which may correspond with a vascular territory, and a relative decrease (33%) of the CBV parameter in the same area. *C*, A 60-year-old man with stroke-related aphasia and right-arm and facial palsy: hypoperfusion corresponding with posterior territory of the left middle cerebral artery, absence of modification of the CBV parameter, and MCA acute ischemic stroke within the hypoperfusion region on follow-up MR imaging. *D*, A 77-year-old man with stroke-related dysarthria and left facial palsy: hypoperfusion corresponding to a part of the cortical ribbon of the right medium cerebral artery, no modification of the CBV parameter, and MCA acute ischemic stroke within the hypoperfusion territory on follow-up MR imaging.

Table 3: Quantitative analysis of perfusion CTP

	Stroke Group ($n = 19$)	Seizure Group ($n = 17$)	*P*
Hypoperfusion pattern			
Symptomatic ROI			
Tmax ratio	1.98 [SD, 0.62]	1.50 [SD, 0.36]	.01
MTT ratio	1.15 [SD, 0.14]	0.99 [SD, 0.16]	.002
CBV ratio	0.88 [SD, 0.19]	0.86 [SD, 0.31]	.42
CBF ratio	0.97 [SD, 0.39]	0.84 [SD, 0.19]	.38
Frontal ROI			
Tmax ratio	1.01 [SD, 0.24]	1.18 [SD, 0.27]	.05
MTT ratio	1.02 [SD, 0.09]	0.95 [SD, 0.19]	.12
CBV ratio	1.03 [SD, 0.18]	0.90 [SD, 0.26]	.23
CBF ratio	1.01 [SD, 0.13]	0.93 [SD, 0.15]	.36
Temporal ROI			
Tmax ratio	0.99 [SD, 0.24]	1.35 [SD, 0.45]	<.01
MTT ratio	0.92 [SD, 0.21]	0.95 [SD, 0.24]	1
CBV ratio	0.90 [SD, 0.27]	0.92 [SD, 0.32]	.67
CBF ratio	0.98 [SD, 0.14]	0.93 [SD, 0.24]	.12
Thalamic ROI			
Tmax ratio	1.05 [SD, 0.41]	1.32 [SD, 0.70]	.20
MTT ratio	0.99 [SD, 0.23]	1.03 [SD, 0.21]	.53
CBV ratio	0.94 [SD, 0.26]	0.97 [SD, 0.22]	.66
CBF ratio	0.99 [SD, 0.21]	0.97 [SD, 0.24]	.57
Cerebellar ROI	$n = 10$[b]	$n = 8$[b]	
Tmax ratio	0.95 [SD, 0.32]	0.98 [SD, 0.21]	1
MTT ratio	1.02 [SD, 0.14]	1.09 [SD, 0.3]	.69
CBV ratio	0.99 [SD, 0.21]]	1.14 [SD, 0.45]	.62
CBF ratio	0.97 [SD, 0.13]	1.03 [SD, 0.21]	.46
Normoperfusion pattern	$n = 30$	$n = 12$	
Symptomatic ROI			
Tmax ratio	1.15 [SD, 0.51]	1.00 [SD, 0.45]	.55
MTT ratio	0.99 [SD, 0.12]	1.04 [SD, 0.24]	.85
CBV ratio	1.08 [SD, 0.53]	1.18 [SD, 0.41]	.67
CBF ratio	1.06 [SD, 0.39]	1.14 [SD, 0.34]	.45
Frontal ROI			
Tmax ratio	1.01 [SD, 0.12]	1.02 [SD, 0.14]	.72
MTT ratio	1 [SD, 0.05]	1.01 [SD, 0.06]	.46
CBV ratio	1.01 [SD, 0.08]	0.99 [SD, 0.13]	.61
CBF ratio	1 [SD, 0.06]	0.98 [SD, 0.08]	.60
Temporal ROI			
Tmax ratio	1.15 [SD, 0.3]	0.96 [SD, 0.20	.07
MTT ratio	1 [SD, 0.19]	1.02 [SD, 0.19]	.99
CBV ratio	0.97 [SD, 0.23]	0.99 [SD, 0.19]	.38
CBF ratio	0.96 [SD, 0.13]	0.99 [SD, 0.14]	.30
Thalamic ROI			
Tmax ratio	1.11 [SD, 0.36]	1.04 [SD, 0.34]	.94
MTT ratio	0.95 [SD, 0.17]	0.95 [SD, 0.23]	.99
CBV ratio	0.97 [SD, 0.25]	1.09 [SD, 0.40]	.52
CBF ratio	0.98 [SD, 0.14]	1.08 [SD, 0.18]	.1
Cerebellar ROI	$n = 10$[b]	$n = 8$[b]	
Tmax ratio	1.01 [SD, 0.16]	0.94 [SD, 0.08]	.14
MTT ratio	1.02 [SD, 0.15]	1.10 [SD, 0.30]	.93
CBV ratio	1.04 [SD, 0.17]	1.13 [SD, 0.33]	.87
CBF ratio	1.02 [SD, 0.09]	1.07 [SD, 0.10]	.21

[a] Values are mean [SD].
[b] For 9 patients in each group, perfusion analysis of the cerebellar ROI could not be performed because of the poor quality of perfusion maps.

group, the only case with a hyperperfusion pattern involved early postischemic hyperperfusion, also called "luxury perfusion." Postischemic hyperperfusion occurs after recanalization of the occluded artery and is observed in approximately 50% of patients after 7 days.[15] Its frequency in a code stroke situation is unknown.

A hypoperfusion pattern on CTP was encountered at the same rate in the seizure and stroke groups. The specificity of this pattern for diagnosing seizure was improved when hypoperfusion was not restricted to the vascular territory, despite a low sensitivity. In cases of hypoperfusion, quantitative analysis of perfusion parameters revealed an increased Tmax ratio in the stroke group compared with the seizure group. However, given the moderate accuracy of the Tmax ratio to separate the 2 groups (area under the curve = 0.7), we could not identify a relevant Tmax ratio

cutoff to discriminate stroke from seizure. Although this is the first time that a direct comparison of quantitative perfusion parameters between patients with stroke and seizures has been performed, this result seems relevant because deep hypoperfusion is observed downstream of the occluded artery in patients with stroke, which is responsible for the constitution of the infarct core. This is in contrast to the moderate hypoperfusion expected in the postictal phase, related to neuronal inhibition[16] or hypoactivity of the involved region. Moreover, additional ipsilateral frontal and temporal lobe hypoperfusion was found more frequently in the seizure group. This result is suggestive of the spreading physiopathology of seizures, the so-called "surrounding inhibition," which seems to be in opposition to the epileptic wave front as it propagates.

Only 1 previously published study by Kubiak-Balcerewicz et al[17] made direct comparisons of CTP parameters between the seizure and stroke groups. That study failed to identify perfusion patterns differentiating strokes from seizures, probably due to the small number of patients and methodologic limitations. The authors chose to measure perfusion parameters in only 1 section at the level of the basal ganglia. Moreover, angiography was not used to confirm the absence of occlusion, stenosis, or vascular anatomic variations. In another study, Van Cauwenberge et al[9] found that CTP accurately differentiated seizure-related deficits from strokes but only in the suspected ictal period with hyperperfusion. In that study, patients with ictal ????? displayed more hyperperfusion than did patients with postictal ??????, with a specificity of 86% and a low sensitivity of 38%. However, this study compared patients with peri-ictal and postictal ?????? instead of matched strokes. These results are in agreement with previous CTP and PET studies performed in epilepsy units, which demonstrated a typical postictal switch from ictal hyperperfusion to postictal hypoperfusion.[18] Hypoperfusion was also the most frequent pattern observed in a previous case series of postictal neurologic deficits.[11] The results of our study support these previous data, and our quantitative analyses provide additional information that, in the context of hypoperfusion, may help discriminate patients with seizure from those with stroke, who potentially have deeper hypoperfusion.

Our study has some limitations. First, the data collection was retrospective. A relevant number of patients with stroke were excluded because they were not hospitalized in the stroke unit. This exclusion concerns minor strokes discharged to home, very severe strokes with patients hospitalized in the intensive care unit, and very old patients hospitalized in the geriatric unit. This could represent a selection bias. Second, there was a high rate of normal perfusion in the stroke group (60%), probably explained by our selection of patients with acute ischemic stroke without CTA abnormalities (vessel occlusion or stenosis). This may have led to an over-representation of cardioembolic, small cortical infarcts and lacunar strokes.[19] However, particularly in this population, the diagnosis of stroke versus postictal deficits is challenging. Third, there was an absence of certainty regarding the seizure-related deficits, despite the performance of anamnesis, clinical evaluation, and EEG. The accuracy was also reduced by the substantial delay between clinical manifestations and EEG recordings. The absence of simultaneous EEG prevented specifying peri- or postictal status and focal or generalized seizure. Fourth, the quality of the CTP maps might appear suboptimal; this is mainly due first to a radiation dose that was intentionally limited (dose length product, $<$550 mGy $\times$ cm) to fit with FDA recommendations and, second, to limit smoothing to avoid an averaging effect, and, finally, to frequent motion artifacts due to the emergency context (confused or agitated patients). The good interobserver agreement between the 2 readers showed that this did not affect the results of our study. Further studies could aim to determine whether hyperperfusion is predominantly present in the cortex in case of seizure as previously demonstrated[12] and to analyze whether this pattern could increase the discrimination between seizure and stroke.

CONCLUSIONS

CTP patterns might help differentiate focal neurologic deficits related to seizure from those related to acute stroke in patients with a code stroke status when CTA findings are normal, facilitating the appropriate choice of emergency treatment. Our results suggest that CTP hyperperfusion patterns, especially those not restricted to the vascular territory, are highly specific for the diagnosis of epileptic seizure and could lead to reconsidering the decision to administer intravenous thrombolytic therapy. These results should be confirmed by further prospective studies with larger patient groups.

Disclosures: Thomas Tourdias—*RELATED*: *Grant*: ANR-10-LABX-57 trial; *UNRELATED*: *Grants/Grants Pending*: national grant from the French Ministry (Programme Hospitalier de Recherche Clinique). Igor Sibon—*UNRELATED*: *Board Membership*: Editorial Board of *Revue Neurologique*; *Consultancy*: Medtronic, Servier Pharmaceuticals, Boehringer Ingelheim; *Grants/Grants Pending*: French National Institute of Health*; *Payment for Lectures Including Service on Speakers Bureaus*: Bayer, Servier Pharmaceuticals. *Money paid to the institution.

REFERENCES

1. Merino JG, Luby M, Benson RT, et al. **Predictors of acute stroke mimics in 8187 patients referred to a stroke service.** *J Stroke Cerebrovasc Dis* 2013;22:e397–403 CrossRef Medline
2. Quenardelle V, Lauer-Ober V, Zinchenko I, et al. **Stroke mimics in a stroke care pathway based on MRI screening.** *Cerebrovasc Dis* 2016;42:205–12 CrossRef Medline
3. Tsivgoulis G, Zand R, Katsanos AH, et al. **Safety of intravenous thrombolysis in stroke mimics: prospective 5-year study and comprehensive meta-analysis.** *Stroke* 2015;46:1281–87 CrossRef Medline
4. Zinkstok SM, Engelter ST, Gensicke H, et al. **Safety of thrombolysis in stroke mimics: results from a multicenter cohort study.** *Stroke* 2013;44:1080–84 CrossRef Medline
5. Liberman AL, Choi HJ, French DD, et al. **Is the cost-effectiveness of stroke thrombolysis affected by proportion of stroke mimics?** *Stroke* 2019;50:463–68 CrossRef Medline
6. Rennert RC, Wali AR, Steinberg JA, et al. **Epidemiology, natural history, and clinical presentation of large vessel ischemic stroke.** *Neurosurgery* 2019;85:S4–8 CrossRef Medline
7. Warach SJ, Luby M, Albers GW, et al; Stroke Imaging Research (STIR) and VISTA-Imaging Investigators. **Acute Stroke Imaging Research Roadmap III Imaging Selection and Outcomes in Acute Stroke Reperfusion Clinical Trials: Consensus Recommendations and Further Research Priorities.** *Stroke* 2016;47:1389–98 CrossRef Medline
8. Bivard A, Levi C, Krishnamurthy V, et al. **Perfusion computed tomography to assist decision making for stroke thrombolysis.** *Brain* 2015;138(Pt 7):1919–31 CrossRef Medline
9. Van Cauwenberge MG, Dekeyzer S, Nikoubashman O, et al. **Can perfusion CT unmask postictal stroke mimics? A case-control study of 133 patients.** *Neurology* 2018;91:e1918–27 CrossRef Medline

10. Gugger JJ, Llinas RH, Kaplan PW. **The role of CT perfusion in the evaluation of seizures, the post-ictal state, and status epilepticus.** *Epilepsy Res* 2020;159:106256 CrossRef Medline
11. Gelfand JM, Wintermark M, Josephson SA. **Cerebral perfusion-CT patterns following seizure.** *Eur J Neurol* 2010;17:594–601 CrossRef Medline
12. Hauf M, Slotboom J, Nirkko A, et al. **Cortical regional hyperperfusion in nonconvulsive status epilepticus measured by dynamic brain perfusion CT.** *AJNR Am J Neuroradiol* 2009;30:693–98 CrossRef Medline
13. Aupy J, Wongwiangjunt S, Wang ZI, et al. **Subcortical SISCOM hyperperfusion: should we pay more attention to it?** *Seizure* 2018;62:43–48 CrossRef Medline
14. Lin DD, Kleinman JT, Wityk RJ, et al. **Crossed cerebellar diaschisis in acute stroke detected by dynamic susceptibility contrast mr perfusion imaging.** *AJNR Am J Neuroradiol* 2009;30:710–15 CrossRef Medline
15. Kidwell CS, Saver JL, Mattiello J, et al. **Diffusion-perfusion MRI characterization of post-recanalization hyperperfusion in humans.** *Neurology* 2001;57:2015–21 CrossRef Medline
16. Nelissen N, Van Paesschen W, Baete K, et al. **Correlations of interictal FDG-PET metabolism and ictal SPECT perfusion changes in human temporal lobe epilepsy with hippocampal sclerosis.** *Neuroimage* 2006;32:684–95 CrossRef Medline
17. Kubiak-Balcerewicz K, Fiszer U, Nagańska E, et al. **Differentiating stroke and seizure in acute setting-perfusion computed tomography?** *J Stroke Cerebrovasc Dis* 2017;26:1321–27 CrossRef Medline
18. Engel J, Kuhl DE, Phelps ME. **Patterns of human local cerebral glucose metabolism during epileptic seizures.** *Science* 1982;218:64–66 CrossRef Medline
19. Benson JC, Payabvash S, Mortazavi S, et al. **CT perfusion in acute Lacunar stroke: detection capabilities based on infarct location.** *AJNR Am J Neuroradiol* 2016;37:2239–34 CrossRef Medline

Increased Perviousness on CT for Acute Ischemic Stroke is Associated with Fibrin/Platelet-Rich Clots

T.R. Patel, S. Fricano, M. Waqas, M. Tso, A.A. Dmytriw, M. Mokin, J. Kolega, J. Tomaszewski, E.I. Levy, J.M. Davies, K.V. Snyder, A.H. Siddiqui, and V.M. Tutino

ABSTRACT

BACKGROUND AND PURPOSE: Clot perviousness in acute ischemic stroke is a potential CT imaging biomarker for mechanical thrombectomy efficacy. We investigated the association among perviousness, clot cellular composition, and first-pass effect.

MATERIALS AND METHODS: In 40 mechanical thrombectomy–treated cases of acute ischemic stroke, we calculated perviousness as the difference in clot density on CT angiography and noncontrast CT. We assessed the proportion of fibrin/platelet aggregates, red blood cells, and white blood cells on clot histopathology. We tested for linear correlation between histologic components and perviousness, differences in components between "high" and "low" pervious clots defined by median perviousness, and differences in perviousness/composition between cases that did and did not achieve a first-pass effect.

RESULTS: Perviousness significantly positively and negatively correlated with the percentage of fibrin/platelet aggregates ($P = .001$) and the percentage of red blood cells ($P = .001$), respectively. Higher pervious clots had significantly greater fibrin/platelet aggregate content ($P = .042$). Cases that achieved a first-pass effect ($n = 14$) had lower perviousness, though not significantly ($P = .055$). The percentage of red blood cells was significantly higher ($P = .028$) and the percentage of fibrin/platelet aggregates was significantly lower ($P = .016$) in cases with a first-pass effect. There was no association between clot density on NCCT and clot composition or first-pass effect. Receiver operating characteristic analysis indicated that clot composition was the best predictor of first-pass effect (area under receiver operating characteristic curve: percentage of fibrin/platelet aggregates = 0.731, percentage of red blood cells = 0.706, perviousness = 0.668).

CONCLUSIONS: Clot perviousness on CT is associated with a higher percentage of fibrin/platelet aggregate content. Histologic data and, to a lesser degree, perviousness may have value in predicting first-pass outcome. Imaging metrics that more strongly reflect clot biology than perviousness may be needed to predict a first-pass effect with high accuracy.

ABBREVIATIONS: AIS = acute ischemic stroke; AUC = area under the curve; CV = coefficient of variation; FP = fibrin/platelet aggregates; FPE = first-pass effect; MMI = Mattes mutual information; MT = mechanical thrombectomy; mTICI = modified TICI; RBC = red blood cells; ROC = receiver operating characteristic; WBC = white blood cells

CT is the most common imaging technique used to evaluate patients with acute ischemic stroke (AIS). Together, NCCT and CTA can provide valuable information about the occlusive clot, such as its location, length, and density.[1-3] One parameter derived from these images is clot permeability, or perviousness, which indicates the amount of contrast that diffuses through the clot tissue.[1,4] Several clinical studies have claimed that perviousness may be an important indicator of how easily occlusive clots can be treated by tPA or mechanical thrombectomy (MT).[1,5] However, the underlying biology behind why some clots are more pervious than others remains largely unknown.

Received June 2, 2020; accepted after revision August 21.

From the Canon Stroke and Vascular Research Center (T.R.P., S.F., M.W., M.T., J.K., J.T., E.I.L., J.M.D., K.V.S., A.H.S., V.M.T.) and Departments of Mechanical and Aerospace Engineering (T.R.P., V.M.T.), Pathology and Anatomical Sciences (S.F., J.K., J.T., V.M.T.), Neurosurgery (M.W., M.T., E.I.L., J.M.D., K.V.S., A.H.S., V.M.T.), Biomedical Engineering (V.M.T.), and Biomedical Informatics (J.M.D.), University at Buffalo, Buffalo, New York; Department of Medical Imaging (A.A.D.), University of Toronto, Toronto, Ontario, Canada; and Department of Neurosurgery (M.M.), University of South Florida, Tampa, Florida.

Research reported in this publication was supported by the National Center for Advancing Translational Sciences of the National Institutes of Health under award number UL1TR001412 to the University at Buffalo (A.H.S., V.M.T.). The content is solely the responsibility of the authors and does not necessarily represent the official views of the NIH. This work was also funded by the Cummings Foundation (V.M.T.).

Data are available on reasonable request. The data are composed of deidentified participant data and can be obtained upon request from Dr Vincent Tutino at vincentt@buffalo.edu.

Please address correspondence to Vincent M. Tutino, PhD, 875 Ellicott St, Canon Stroke and Vascular Research Center, University at Buffalo, Buffalo, NY 14203; e-mail: vincentt@buffalo.edu

Indicates open access to non-subscribers at www.ajnr.org

Indicates article with supplemental online photos.

http://dx.doi.org/10.3174/ajnr.A6866

The advent of MT for the treatment of AIS has enabled the biologic investigation of retrieved clots by histopathology.[6] Recent studies have shown large-scale heterogeneity in the composition of retrieved clots, in terms of the percentage of fibrin/platelet aggregates (FP), red blood cell (RBC), and white blood cells (WBC).[7] Differences in clot composition have been associated with stroke etiology and MT treatment outcomes. In several studies, FP-rich clots have been found to be cardioembolic in origin[8-10] and less responsive to revascularization attempts.[6,10,11] Intrinsically, perviousness is likely to be related to the cellular composition of a clot because different biologic components have different densities and thus alter how soluble molecules diffuse through them.[4,5] Experimental studies have shown that thrombi composed of higher fibrin fractions allowed greater contrast agent permeation than those packed with RBC.[12] Nevertheless, this association has not been established in clinical studies.

To this end, the goal of this study was to investigate the relationship between clot perviousness calculated at the time of admission CT and its histopathologic composition after retrieval by MT. Furthermore, to explore whether perviousness could be used to indicate MT effectiveness, we also explored the relationships among perviousness, composition, and MT outcome, measured by the first-pass effect (FPE).[13] Characterization of the occlusive clot based on pretreatment NCCT/CTA could impact the clinical management of patients with AIS.

MATERIALS AND METHODS

Clinical Study Parameters

This study was approved by the institutional review board at the University at Buffalo (study 00002092). All methods were performed in accordance with the approved protocol, and written informed consent was obtained for all subjects. Clot samples and imaging were collected from patients receiving MT by either stent retriever, aspiration, or a combined therapy between November 2018 and November 2019 at the Gates Vascular Institute in Buffalo, New York. Patients considered for this study had the following criteria: 1) They had undergone MT for AIS due to an occlusive clot in the intracranial vasculature, 2) had pretreatment CT available with sufficient image quality and an identifiable clot, and 3) had a clot of sufficient size and quality for histopathologic analysis that was retrieved during MT. Cases were excluded for the following reasons: 1) They were lacking pretreatment CT, 2) had CT with insufficient quality (ie, unidentifiable clot), or 3) received intra-arterial tPA. Treatment success was assessed on DSA using the modified TICI (mTICI) score,[14] which is based on the degree of reperfusion in the downstream territory of the original occlusion: mTICI 2b (50%–89% reperfusion), mTICI 2c (90%–99% reperfusion), or mTICI 3 (100% reperfusion). First-pass effect was defined as having achieved mTICI scores of 2c or 3 at the end of the first use of MT.[13] Modified FPE was further defined as an mTICI score of 2b, 2c, or 3 after the first MT pass.[13]

CT

For all patients, CT was performed on an Aquilion ONE scanner (Canon Medical Systems). The tube voltage and tube current were set to 135 kV(peak) and 370–600 mA, respectively, for NCCT, and 120 kVp and 150–205 mA, respectively, for CTA. The reconstructed voxel sizes for NCCT and CTA were set to $0.4 \times 0.4 \times 0.5$ mm^3 and $0.5 \times 0.5 \times 0.5$ mm^3, respectively. For CTA, Omnipaque 350 contrast agent (iohexol; GE Healthcare) was given at a rate of ~5 mL/s in CT perfusion during image acquisition. The CTA image with the lowest thickness (0.5 mm) and highest resolution was selected for analysis of the clot region.

Analysis of CT

Analysis of CT was blinded to clinical outcomes and clot composition. For clots that were hyperdense on NCCT images, no image registration techniques were used, and the CTA and NCCT images were placed side-by-side and Hounsfield units were calculated in the clot region on each image. For clots that were not hyperdense on NCCT, the CTA and the corresponding NCCT images were coregistered using the open source software, 3D Slicer (https://www.slicer.org/), which implemented the BRAINSFit algorithm (https://www.slicer.org/wiki/Modules:BRAINSFit) for mutual-information rigid registrations of whole-brain 3D images.[15] During coregistration, we used the following input parameters: rigid ($df = 6$), 0.2% of samples (percentage of sampled pixels, high) and linear interpolation (to scale image size). After each coregistration, the Mattes mutual information (MMI), a quantitative measure of how similar the coregistered images are (higher MMI implies greater entropy reduction and better image alignment), was recorded and the coregistered images were inspected to ensure proper overlay. See Online Fig 1 for an example of coregistration. The average MMI across all 11 coregistered nondense cases was 92.2% ± 1.1%, with a range of 85.2%–98.7%, showing highly accurate coregistration across all cases. After coregistration, the occlusion on the CTA image was used to identify the clot in the corresponding location on the NCCT image, and the Hounsfield units (averaged from 2–3 regions) were obtained from both NCCT and CTA images.

As shown in Fig 1*A*, perviousness was calculated as the difference in Hounsfield units,[16] in which larger differences indicate higher permeability. Cases were categorized as "high" or "low" perviousness based on a cutoff of the median perviousness across all cases in the dataset. Because clot density on NCCT may be independently associated with clot biology and FPE, we also recorded density on NCCT and categorized cases as high or low density based on a cutoff of the median density across all cases in the dataset.

We assessed the inter- and intrauser error in calculating clot perviousness and density in a subset of 10 representative cases (3 dense and 7 nondense; numbers chosen to maintain proportionality to entire dataset). The perviousness and density calculations were performed by the same trained operator in triplicate to calculate intrauser error in the measurement and were performed once by 2 additional trained operators to calculate interuser error among the 3 operators. The average intrauser error (with coefficient of variation [CV]) in perviousness and density on NCCT for dense ($error_{perviousness}$: ± 1.6HU [10.40%], CV = 0.18; $error_{density}$: ± 1.6 HU [2.79%], CV = 0.048) and nondense ($error_{perviousness}$: ± 1.8 HU [17.52%], CV = 0.30; $error_{density}$: ± 1.0 HU [1.66%], CV = 0.029) clots was low. The average interuser error in perviousness and density for the dense ($error_{perviousness}$: ± 1.8 HU [10.75%], CV = 0.19; $error_{density}$: ± 4.0 HU [7.06%], CV = 0.122) and nondense ($error_{perviousness}$: ± 1.6 [12.10%], CV = 0.21; $error_{density}$: ± 2.0 HU [3.38%], CV =

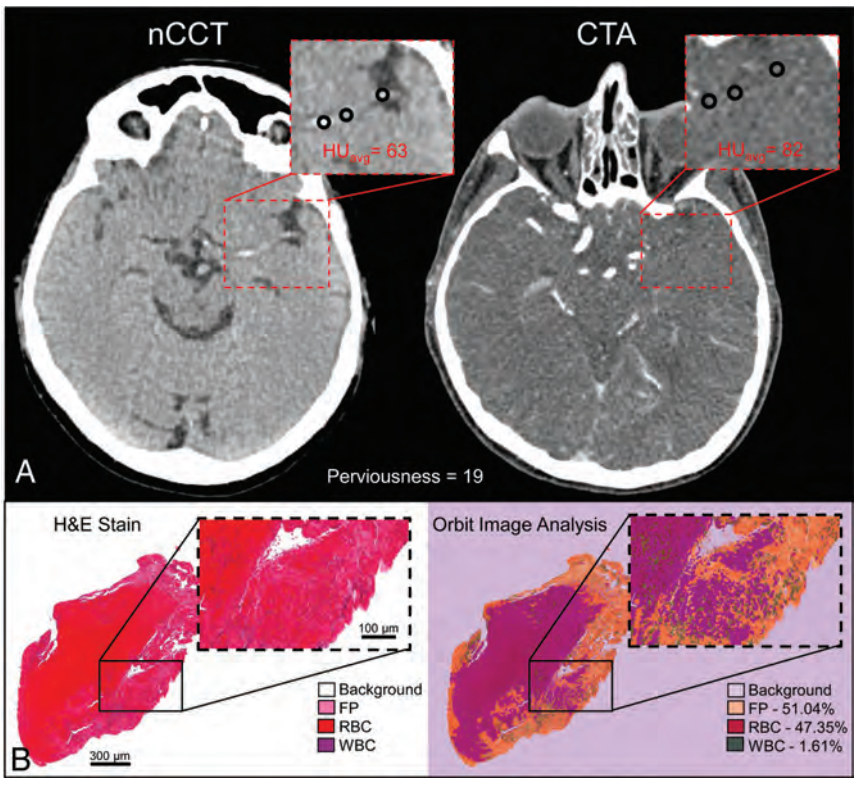

FIG 1. Data acquisition: calculation of perviousness and clot composition. *A*, Perviousness was calculated from the difference in Hounsfield units in the clot region between CTA and NCCT. *B*, To identify the percentage composition of major clot components, we analyzed H&E-stained slides (*left*) with Orbit Image Analysis (*right*, colorized output) to automatically identity %FP, %RBC, and %WBC.

Quantification of Clot Composition

Quantification of clot composition was performed on digital histology images using the open source software, Orbit Image Analysis (www.orbit.bio) (Fig 1*B*).[17] Before quantification, all slide images were adjusted to be of the same resolution, and errors in slide preparation (ie, small folds or debris) were manually removed from the image. Next, the Orbit Image Analysis software trained machine learning algorithms for image segmentation, classification, and quantification using a support vector machine based on a sliding window feature-extraction approach.[17] The models for classification and quantification of histology were adjusted for inter- and intraslide variability in H&E staining by manually marking regions of RBC, WBC, and FP aggregates as representative regions for the model to be retrained/adjusted. Once trained, these models were applied to the entire slide, classifying each pixel. This pipeline was used to identify regions of FP, RBC, and WBC and to calculate their percentage across each slide.

0.059) clots was also low. There was no significant difference in error or CV between dense and nondense measurements and between intra- and interuser measurements (all $P < .05$, Student t test), showing good user agreement and reproducibility.

Clot Histology

For histologic analysis, clots were collected immediately after MT and stored in 10% phosphate buffered formalin for 24–28 hours, after which they were transferred to 70% ethanol. In the Histology Core Lab at the University at Buffalo's Jacobs School of Medicine and Biomedical Sciences, tissue was automatically prepared in a tissue processor, where it was serially infused with 70% ethanol, 90% ethanol, 100% ethanol, xylenes, and paraffin. All steps were performed under pressure to ensure proper infusion. Samples were then embedded in paraffin and sectioned at 4 μm. Sections were collected on SuperFrost Plus (Fisher) slides to ensure tissue adhesion. For H&E staining, samples were deparaffinized in xylene, incubated in serial solutions of ethanol (100%–50%), and hydrated in water. Next, they were incubated in hematoxylin for 7–8 minutes and washed and incubated in eosin for 1–2 minutes. Stained sections were then dehydrated in graded ethanol, cleared in xylenes, and mounted on a glass microscope slide with a xylene-based mounting medium. Stained slides were imaged by whole-slide scanning at 40× on the ImageScope digital histology platform (Leica Biosystems).

Statistical Analyses

All analysis was performed in Matlab (Version 2020a; MathWorks). Pearson correlation tests were performed to assess the correlation between 2 continuous variables. We used univariate tests to assess significant differences among groups. Sharpiro-Wilk tests were performed to test parameters for normality. To test parameters for significance, we performed a Student t test (for normally distributed parameters) or a Mann-Whitney U test (for non-normally distributed parameters). Data values were reported as mean ± standard error. To test significant differences between 2 categoric variables, we performed a χ^2 test. A parameter was deemed significant at $P < .05$.

RESULTS

Patient Characteristics

A total of 40 patients with AIS were included in this study. Clinical parameters, treatment methods, mTICI scores, and pre- and post-treatment NIHSS score are summarized in the Table. Occlusions were primarily located at the MCA (67.5%), supraclinoid ICA (20%), and basilar artery (12.5%) and were treated with stent retrievers (2.5%), direct aspiration alone (12.5%), or a combination therapy (85%). A total of 14 of the 40 (35%) cases achieved FPE (21/40 [(52.5%] cases achieved a modified FPE). The average density on NCCT and CTA images for clot regions was 59.42 ± 0.88 HU and 85.40 ± 2.31 HU, respectively. The corresponding perviousness values ranged from 5 to 62, with an average perviousness

Baseline clinical parameters with clot locations, treatment information, and treatment outcomes

Sample Characteristics (n = 40)	
Age (mean ± SE) (yr)	71 ± 2.37
(median) (Q1/Q3)	74 (64/81)
Sex, female/male (No.) (%)	22 (55%):18 (45%)
Clot location (No.) (%)	
Middle cerebral artery	27 (67.5%)
Internal carotid artery	8 (20%)
Basilar artery	5 (12.5%)
Treatment method (No.) (%)	
Stent retriever alone	1 (2.5%)
Aspiration alone	5 (12.5%)
Combination therapy	34 (85%)
IV-tPA administration (No.) (%)	12 (30%)
Cases with FPE achieved (No.) (%)	14 (35%)
Cases with modified FPE achieved (No.) (%)	21 (52.5%)
Mean No. of passes (mean ± SE)	2 ± 0.22
Range (minimum–maximum)	1–6
mTICI score postrecanalization (No.) (%)	
0	0 (0%)
1	0 (0%)
2a	1 (2.5%)
2b	18 (45%)
2c	6 (15%)
3	15 (37.5%)
NIHSS (mean ± SE)	
Pretreatment	15 ± 1.42
Posttreatment	8 ± 1.27

Note:—Q indicates quartile; SE, standard error.

of 26.38 ± 2.26 HU. On the basis of the median perviousness (23.5 HU), we delineated "lower" perviousness clots as those with <23.5 HU, and "higher" perviousness clots as those with >23.5 HU. This cutoff system was markedly similar to others reported in the literature; eg, Santos et al[18] found an optimal perviousness cutoff of ≥23 HU to define high-pervious clots in a dataset of 308 patients with AIS treated with tPA. For analysis of clot density on NCCT, we also used the median clot density from NCCT (60 HU) to independently define low-density clots as those with <60 HU and high-density clots as those with >60 HU.

Clot Composition Was Correlated with Clot Perviousness but Not Density

We first explored the relationship between clot presentation on CT and composition. For all clots, the average percentage composition of FP, RBC, and WBC was 50.62% ± 3.83%, 43.43% ± 3.81%, and 5.95% ± 0.50%, respectively. As shown in Fig 2*A*–*C*, Pearson correlation analysis revealed a significant positive linear correlation between the %FP and perviousness ($r = 0.496$, $P = 0.001$) and a significant negative linear correlation between %RBC and perviousness ($r = -0.491$, $P = 0.001$). No significant relationship between %WBC and perviousness was observed ($r = -0.057$, $P = 0.726$). Conversely, there was no significant correlation between clot density on NCCT and clot composition (%FP, $r = -0.004$, $P = 0.978$; %RBC: $r = 0.009$, $P = 0.955$; %WBC: $r = -0.036$, $P = 0.825$) (Fig 2*D*–*F*).

Comparing composition between clots with higher and lower perviousness in Fig 3*A*, we found that the %FP in higher perviousness clots (54.63% ± 5.76%) was statistically significantly greater than that in lower perviousness clots (39.87% ± 4.00%) ($P = .042$). On the other hand, the %RBC in clots with higher perviousness (38.40% ± 5.72%) was statistically significantly lower than in those with lower perviousness (53.23% ± 3.99%) ($P = .040$). The difference in %WBC between the high (6.97% ± 0.55%) and low (6.90% ± 0.62%) perviousness groups was not statistically significant ($P = .936$). When density on NCCT alone was considered, differences in biologic composition between higher and lower density clots were less pronounced. Higher density clots had greater %RBC (50.67% ± 4.55% versus 45.26% ± 5.58%, $P = .493$) and %WBC (7.63% ± 0.62% versus 6.27% ± 0.57%, $P = .147$) and lower %FP (41.70% ± 4.34% versus 48.47% ± 5.65%, $P = .388$), but the differences were not statistically significant (Fig 3*B*).

Because some patients in the preceding analysis had received IV-tPA during the first 4.5 hours after symptom onset, but before imaging, we tested whether the administration of IV-tPA affected our observations. We again compared %FP, %RBC, and %WBC in high-versus-low perviousness and density clots, this time separating cases that were given IV-tPA from those that were not. These data showed that the trend of greater %FP and lesser %RBC in higher perviousness clots was still evident regardless of IV-tPA administration. However, some differences did not reach statistical significance, likely due to the decreased sample size in these small subcohorts (Online Fig 2).

First-Pass Effect is Correlated with Clot Composition, but Not Perviousness

We also explored the relationship between clot presentation on CT and FPE and observed lower perviousness in cases that achieved FPE (20.50 ± 2.82 HU versus 29.58 ± 2.98 HU in cases that did not achieve FPE, Fig 4*A*). However, this difference was not statistically significant ($P = .055$). There was no significant difference in clot density on NCCT between cases that did (59.64 ± 1.74 HU) and did not achieve FPE (59.31 ± 1.09 HU, $P = .859$). On the other hand, we did observe that the %FP on histology was statistically significantly lower in cases that achieved FPE (38.25% ± 4.45%) compared with those that did not (57.29% ± 4.95%) ($P = .016$) (Fig 4*B*). Furthermore, %RBC on histology was statistically significantly higher in cases that achieved FPE (54.69% ± 4.41%) compared with cases that did not (37.36% ± 5.01%) ($P = .028$). The difference in %WBC between cases that did (7.06% ± 0.71%) and did not achieve FPE (5.35% ± 0.64%) was not statistically significant ($P = .103$). On the basis of these data, post hoc power analysis demonstrated an average power of 0.78 in detecting differences in these significant parameters (%FP, power = 0.82; %RBC, power = 0.74) given our sample size, and an $\alpha = .05$. Analogous results were also observed when modified FPE was considered (Online Fig 3).

To explore whether IV-tPA administration affected these observations, we performed our analysis on the subcohorts that either were and were not given IV-tPA. Yet again, similar trends were observed regardless of IV-tPA administration. The most significant differences were seen in the subcohort with IV-tPA administration (cases without IV-tPA administration showed similar trends but no statistically significant differences in these parameters between cases with and without FPE) (Online Fig 4).

To determine predictive ability of perviousness and histologic parameters in assessing FPE, we performed receiver operating characteristic (ROC) analysis on our data. The ROC curves in Fig 4 show that %FP and %RBC were the best predictors of FPE

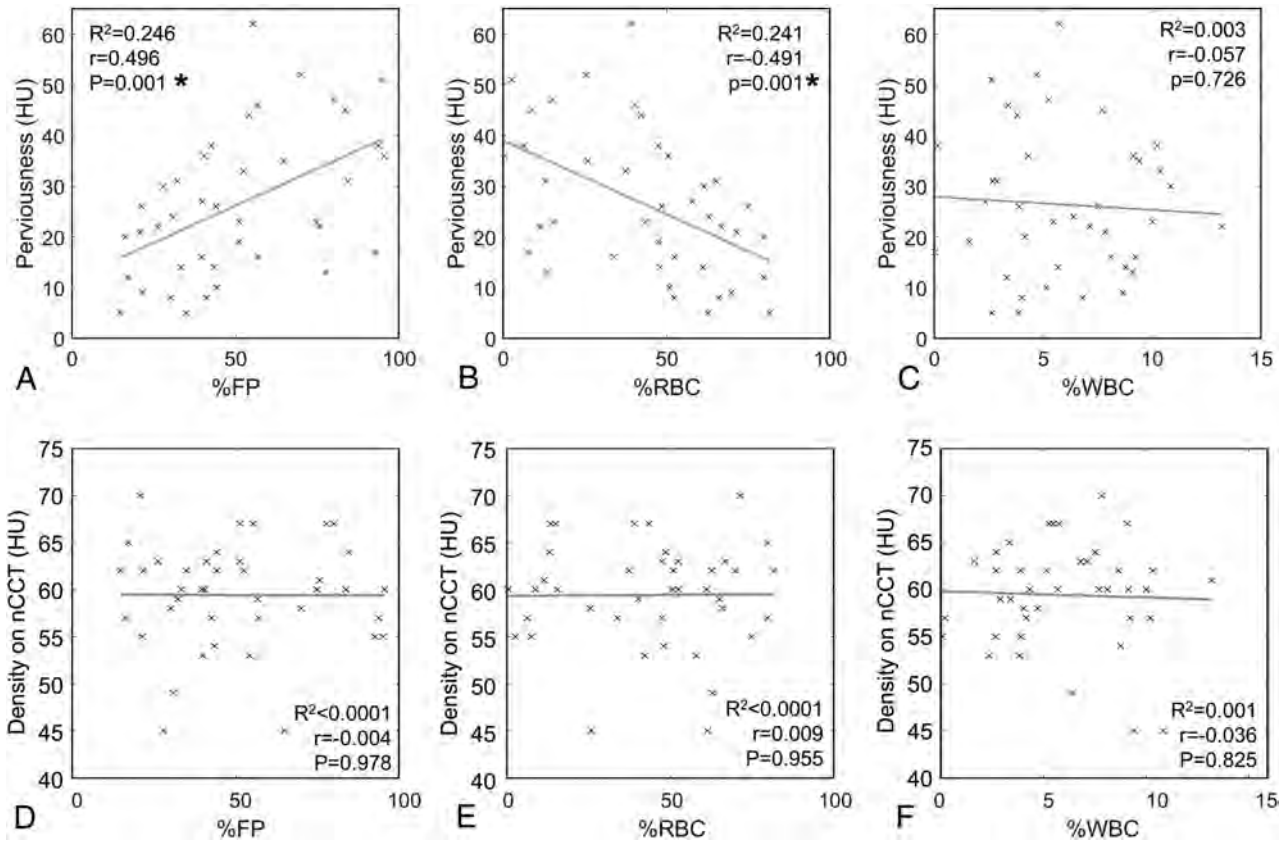

FIG 2. Correlation of perviousness and density with clot biology. *A*, Pearson correlation of perviousness and %FP shows a statistically significantly positive association. *B*, Pearson correlation of perviousness and %RBC shows a statistically significantly negative association. *C*, Pearson correlation of perviousness and %WBC shows no significant relationship. *D*, Pearson correlation of density on NCCT and %FP shows no association. *E*, Pearson correlation of density on NCCT and %RBC shows no association. *F*, Pearson correlation of density on NCCT and %WBC shows no association. The *asterisk* indicates statistical significance ($P < 0.05$).

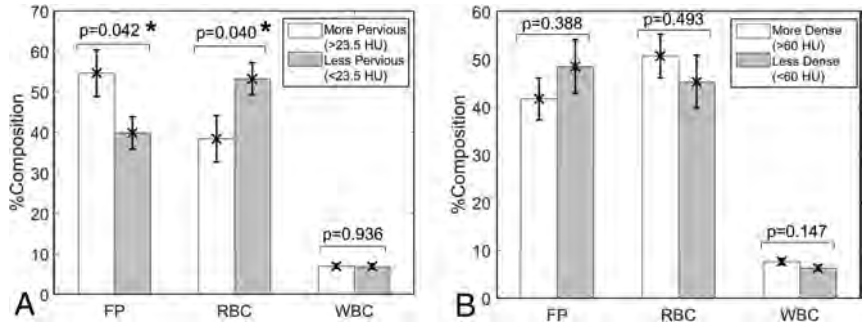

FIG 3. Difference in clot biology in high-versus-low perviousness and density clots. *A*, Significantly greater %FP and lower %RBC were evident in higher pervious clots (>23.5 HU, $n = 20$) compared with lower pervious clots (<23.5 HU, $n = 20$). *B*, There was no significant difference in %FP, %RBC, or %WBC in higher density clots (>60 HU) compared with lower density clots (<60 HU). The *asterisk* indicates statistical significance ($P < 0.05$).

(%FP: area under the curve [AUC] = 0.731, %RBC: AUC = 0.706), while perviousness on NCCT/CTA had moderate predictive ability (AUC = 0.668). Clot density on NCCT performed inferior to all other metrics with an AUC = 0.571. Similar results were observed when modified FPE was used as the predictive end point (Online Fig 3).

DISCUSSION

In this preliminary study, we explored the utility of perviousness as a pre-MT imaging parameter by investigating the relationship among perviousness, clot composition, and MT treatment effectiveness (ie, FPE). Our results demonstrated a statistically significant correlation between perviousness and clot composition, with higher perviousness associated with greater %FP. There was no significant correlation between clot composition and density measured on NCCT. Furthermore, we found that clots from cases that achieved FPE had statistically significantly higher %RBC and lower %FP. From ROC analysis, %FP and %RBC on histology and (to a lesser extent) perviousness on imaging potentially had value in predicting FPE by MT.

In exploring the relationship between clot composition and perviousness, we found that the %FP was significantly positively correlated with perviousness. On the basis of a 23.5-HU (median

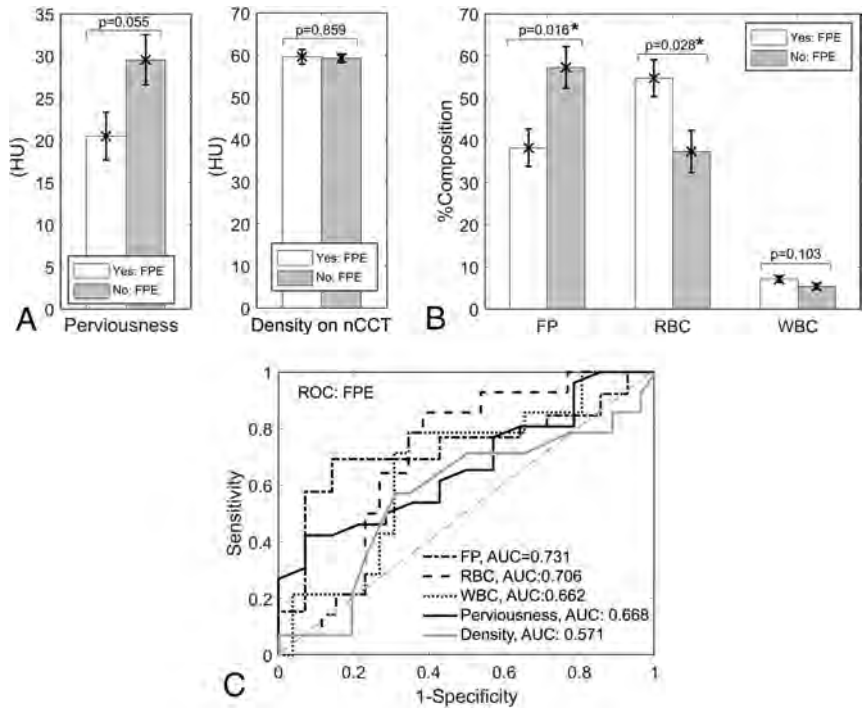

FIG 4. Association of perviousness and clot biology with first-pass success. *A*, Cases that achieved a first-pass effect had lower perviousness compared with cases that did not achieve a first-pass effect, albeit the difference was not statistically significant. There was little difference between cases that achieved first-pass effect when considering clot density on NCCT alone. *B*, Clots from cases with a first-pass effect had statistically significantly lower %FP and higher %RBC. *C*, ROC analysis demonstrated that clot composition (and, to a lesser extent, perviousness) has the ability to predict first-pass effect. The asterisk indicates statistical significance ($P < 0.05$).

perviousness) cutoff, we also found statistically significantly higher %FP and lower %RBC in those with higher perviousness compared with clots with lower perviousness. This trend seemed to exist independent of whether the patient had previously received IV-tPA. These results are similar to those published by Berndt et al,[19] who also investigated the relationship between MT-retrieved clots and perviousness on NCCT/CTA. On the basis of Pearson correlation analysis, they also found that the %FP and the %RBC were positively and negatively related to perviousness, respectively. Remarkably, their correlation coefficients (FP $\propto$ perviousness = 0.45; RBC $\propto$ perviousness = −0.49) were patently similar to ours (FP $\propto$ perviousness = 0.50; RBC $\propto$ perviousness = −0.49).

Only 1 other study has explored the relationship between clot composition and perviousness in MT-treated patients with AIS. In a study of $n = 57$ patients, Benson et al[20] dichotomized both perviousness and clot composition (RBC-rich versus FP-rich) and found that the pervious group consisted of a higher fraction of clots in the RBC-rich group. This contradictory result is likely because unlike in our study and that of Berndt et al,[19] Benson et al[20] did not directly investigate the association between clot composition and perviousness (both of which are continuous variables). Due to their statistical methods, it is difficult to reliably interpret these findings. One must be careful when dichotomizing variables, especially with both independent and dependent variables as in Benson et al,[20] because dichotomization is known to reduce statistical power and increase the risk of false-positive results.[21] Thus, we chose to first perform Pearson correlation analysis to assess the relationship between perviousness and clot composition in our study in an unbiased manner.

The relationship between increased perviousness and increased %FP has also been shown in in vitro reports. Borggrefe et al[12] explored thrombus composition of histologically-defined ovine blood clots with NCCT and CTA using spectral-detector CT and found that higher FP content was an independent predictor of the increase in thrombus density (ie, perviousness).[12] They speculated that this phenomenon occurred because fibrin proteins can have an intrinsic affinity to iodine, as shown in several benchtop studies.[22,23] Their affinity to iodine could cause them to retain contrast media and therefore exhibit higher perviousness. Alternatively, the observed relationship may exist because tightly-packed RBC (that have impenetrable cell walls and may exist in dense rouleaux) can be trapped in fibrin filaments and inhibit blood flow,[24,25] while porous fibrin meshes can allow contrast agent to penetrate into the clot more easily.[8,26] Indeed, this difference could be a reason why higher perviousness has been related to treatment success by tPA in several studies, because increased fluid penetration into the clot may bolster the effectiveness of tPA.[1,18]

Another goal of our study was to determine the relationship between FPE and clot composition and perviousness. Our data show that cases of FPE had significantly more %RBC than those that did not achieve FPE, which, in turn, had significantly greater %FP. This trend was also evident in both subcohorts of patients who did and did not receive IV-tPA. In the clinical literature, it has been widely demonstrated that fibrin-rich clots are more difficult to retrieve (ie, take multiple passes) than RBC-rich clots.[11,27] Poorer MT device integration in FP-rich thrombi may be due to the high static coefficient of friction, as demonstrated by Gunning et al.[28] This can result in increased adherence to the vessel wall and decreased compressibility of fibrin-rich clots.[20] Conversely, high RBC density has been associated with successful recanalization after thrombectomy and reduced thrombectomy procedure time.[27]

While clot biology was significantly related to FPE, we did not find a statistically significant association between perviousness and FPE, even though perviousness and clot composition were correlated with each other. This result may be because of their weak relationship seen on Pearson correlation analysis, which could lead to information loss when inferring clot composition from perviousness.[12] It is possible that a larger sample size would find a more robust correlation. Studies on the relation between clot perviousness and FPE remain scant; only 1 report, Byun et al,[29] compared FPE with CT parameters across 58 cases of AIS treated by stent retrievers. They also

demonstrated that perviousness did not predict FPE or overall successful recanalization. However, even though it was not significant on univariate examination, our ROC analysis demonstrated that perviousness had moderate ability in predicting FPE (AUC = 0.668). Thus, we postulate that other, more informative parameters or combinations of parameters (ie, clot length,[2] device angulation,[30] or higher-level radiomics features[31]) that more closely reflect the biology or morphology of the occlusive clot could provide better prediction of FPE from pretreatment imaging.

In addition to perviousness, we also investigated the relationship between clot density on NCCT and clot composition and FPE in this study. Unlike perviousness, Pearson correlation analysis did not show any linear relationship between density and biologic composition. We did, however, observe that higher density clots tended to have greater %RBC, albeit the difference was not statistically significant. This trend echoes other findings in the literature, which have demonstrated that increased %RBC is associated with hyperdensity on CT imaging.[12,25,32] Similar to perviousness, clot density on NCCT showed no statistically significant difference between cases that did and did not achieve FPE. Yet on ROC analysis, density had a much lower AUC than perviousness, suggesting that density has little predictive ability for FPE. These results are similar to the report by Jagani et al,[33] who studied $n = 80$ cases of MT treated with aspiration, a stent retriever, or a combination therapy and found no association between clot density and successful recanalization. Another study from the Multicenter Randomized Clinical Trial of Endovascular Treatment for Acute Ischemic Stroke in the Netherlands (MR CLEAN) Registry Investigators[34] investigated a total of 408 patients with AIS, calculating a gamut of imaging parameters such as location, clot burden score, thrombus length, and clot density and found that clot density was not significantly associated with functional outcome measured using the mRS, degree of reperfusion (TICI), or duration of endovascular treatment. However, at least 1 other study has demonstrated a significant association between density and first-pass outcome.[35] Thus, further research in larger datasets is likely required to elucidate the relationship between perviousness and density and MT effectiveness measured by FPE.

Our study has limitations. First, to increase our sample size, we did not control for some variables that may affect our results. Specifically, we included cases of MT that used all endovascular approaches and cases that both did and did not receive IV-tPA before MT. To explore whether IV-tPA affected our results, we performed subcohort analyses and observed little influence of IV-tPA (Online Figs 2 and 4). Larger sample sizes will be required to further establish relationships among perviousness, clot biology, and MT outcomes in more controlled populations (ie, cases using only 1 type of MT therapy). We also note that the calculation of perviousness is highly dependent on both image coregistration and the neuroradiologist's ability to identify the clot region. We investigated these factors by calculating the MMI for each coregistered case and by calculating inter- and intrauser error for image-derived parameters (perviousness and density from NCCT) in a subset of our data. Our results showed that there was high coregistration accuracy (MMI = 92.2%) and low inter- and intrauser calculation error (>15% across dense and nondense clots), though measurement of density on NCCT alone had a much lower error. In the future, automated software platforms for segmenting the clot region in the NCCT and CTA image pairs could make the calculation of perviousness more accurate and reproducible.

CONCLUSIONS

The goal of this preliminary study was to investigate the relationship between clot perviousness and the biology of the retrieved clot and to test whether perviousness could directly predict FPE. We found that greater perviousness was related to higher %FP composition. The biologic composition of the clot was significantly related to FPE, with higher %FP clots being more difficult to retrieve in the first pass. From ROC analysis, there was only a moderate ability of perviousness to predict FPE. Imaging metrics that more strongly reflect clot biology or multivariate predictive models may be needed to more accurately predict FPE on pretreatment imaging.

ACKNOWLEDGMENTS

We thank the patients who participated in this study. The authors acknowledge Mohammed Imtiaz, PhD, and Amber Worral, PhD, for histology assistance; Christopher Bigley, MS, and Arvind Ramaswamy for biobanking assistance; and Jennifer L. Gay, CCRP, and Elizabeth Shisler for study protocol management.

Disclosures: Maxim Mokin—*UNRELATED*: *Consultancy*: Medtronic, Cerenovus, Canon Medical Systems; *Grants/Grants Pending*: National Institutes of Health R21NS109575*; *Stock/Stock Options*: Serenity Medical, Synchron, EndoStream, Vicis. John Kolega—*RELATED*: *Grant*: National Science Foundation, National Institutes of Health, Cummings Foundation, *Comments*: National Science Foundation award #1746694, National Institutes of Health National–National Institute of Neurological Disorders and Stroke award #NS115314-0, and Cummings Foundation grant (all with Vincent M. Tutino as Principal Investigator).* John Tomaszewski—*OTHER RELATIONSHIPS*: I am an investor and consultant for Neurovascular Diagnostics, which is a startup company seeking to model vascular aneurysm progression from neutrophil-expressed gene data. Dr Tutino is a principal in the company. Elad I. Levy—*UNRELATED*: *Board Membership*: Stryker, NeXtGen Biologics, MedX Health, Cognition Medical, EndoStream; *Consultancy*: Claret Medical, GLG Consulting, Guidepoint, Imperative Care, Medtronic, Rebound Therapeutics, StimMed; *Employment*: University at Buffalo Neurosurgery Inc; *Expert Testimony*: renders medical/legal opinions as an expert witness; *Stock/Stock Options*: NeXtGen Biologics, Cognition Medical, Rapid Medical, Claret Medical, Imperative Care, Rebound Therapeutics, StimMed. Jason M. Davies—*UNRELATED*: *Consultancy*: Medtronic; *Grants/Grants Pending*: American Heart Association; *Stock/Stock Options*: Rist Neurovascular, Cerebrotech Medical Systems. Kenneth V. Snyder—*RELATED*: *Grant*: Canon Medical Systems, Medtronic, Abbott Vascular ev3; *Consulting Fee or Honorarium*: Toshiba, Canon Medical Systems, ev3, Medtronic*. Adnan H. Siddiqui—*UNRELATED*: *Consultancy*: Amnis Therapeutics, Boston Scientific, Canon Medical Systems, Cerebrotech Medical Systems, Cerenovus, Corindus, EndoStream, Imperative Care, Integra LifeSciences, Medtronic, MicroVention, Minnetronix Neuro, Northwest University, Data and Safety Monitoring Board Chair for the HEAT Trial, Penumbra, Q'Apel Medical, Rapid Medical, Rebound Therapeutics, Serenity Medical, Silk Road Medical, StimMed, Stryker, Three Rivers Medical, VasSol, W.L. Gore & Associates; *Grants/Grants Pending*: Coinvestigator: National Institutes of Health/National Institute of Neurological Disorders and Stroke 1R01NS091075, Virtual Intervention of Intracranial Aneurysms; role: Co-Principal Investigator of National Institutes of Health–National Institute of Neurological Disorders and Stroke R21 NS109575-01, Optimizing Approaches to Endovascular Therapy of Acute Ischemic Stroke; *Stock/Stock Options*: Adona Medical, Amnis Therapeutics, Blinktbi, Boston Scientific (for purchase of Claret Medical), Buffalo Technology Partners, Cardinal Consultants, Cerebrotech Medical Systems, Cognition Medical, EndoStream, Imperative Care, International Medical Distribution Partners, Neurovascular Diagnostics, Q'Apel Medical, Radical Catheter Technologies, Rebound Therapeutics (purchased in 2019 by Integra LifeSciences), Rist Neurovascular, Sense Diagnostics, Serenity Medical, Silk Road Medical, Spinnaker Medical Consultants, StimMed, Synchron, Three Rivers Medical, Vastrax, VICIS, Viseon; *Other:* National Principal Investigator/Steering Committees: Cerenovus NAPA Trial and ARISE II Trial; Medtronic SWIFT PRIME and SWIFT DIRECT Trials; MicroVention FRED Trial and CONFIDENCE study; MUSC

POSITIVE Trial; Penumbra 3D Separator Trial, COMPASS Trial, INVEST Trial. Vincent M. Tutino—*RELATED*: *Grant*: Clinical and Translational Science Awards Program, *Comments*: pilot study grant through the University at Buffalo Clinical and Translational Science Institute*; *UNRELATED*: *Employment*: Neurovascular Diagnostics, *Comments*: Cofounder. *Money paid to the institution.

REFERENCES

1. Santos EM, Marquering HA, Den Blanken MD, et al; MR CLEAN Investigators. **Thrombus permeability is associated with improved functional outcome and recanalization in patients with ischemic stroke.** *Stroke* 2016;47:732–41 CrossRef Medline
2. Riedel CH, Zimmermann P, Jensen-Kondering U, et al. **The importance of size: successful recanalization by intravenous thrombolysis in acute anterior stroke depends on thrombus length.** *Stroke* 2011;42:1775–77 CrossRef Medline
3. Moftakhar P, English JD, Cooke DL, et al. **Density of thrombus on admission CT predicts revascularization efficacy in large vessel occlusion acute ischemic stroke.** *Stroke* 2013;44:243–45 CrossRef Medline
4. Welsh JD, Stalker TJ, Voronov R, et al. **A systems approach to hemostasis, 1: the interdependence of thrombus architecture and agonist movements in the gaps between platelets.** *Blood* 2014;124:1808–15 CrossRef Medline
5. Voronov RS, Stalker TJ, Brass LF, et al. **Simulation of intrathrombus fluid and solute transport using in vivo clot structures with single platelet resolution.** *Ann Biomed Eng* 2013;41:1297–1307 CrossRef Medline
6. Hashimoto T, Hayakawa M, Funatsu N, et al. **Histopathologic analysis of retrieved thrombi associated with successful reperfusion after acute stroke thrombectomy.** *Stroke* 2016;47:3035–37 CrossRef Medline
7. Fitzgerald S, Wang S, Dai D, et al. **Orbit image analysis machine learning software can be used for the histological quantification of acute ischemic stroke blood clots.** *PLoS One* 2019;14:e0225841 CrossRef Medline
8. Boeckh-Behrens T, Kleine JF, Zimmer C, et al. **Thrombus histology suggests cardioembolic cause in cryptogenic stroke.** *Stroke* 2016;47:1864–71 CrossRef Medline
9. Marder VJ, Chute DJ, Starkman S, et al. **Analysis of thrombi retrieved from cerebral arteries of patients with acute ischemic stroke.** *Stroke* 2006;37:2086–93 CrossRef Medline
10. Sporns PB, Hanning U, Schwindt W, et al. **Ischemic stroke: histological thrombus composition and pre-interventional CT attenuation are associated with intervention time and rate of secondary embolism.** *Cerebrovasc Dis* 2017;44:344–50 CrossRef Medline
11. Shin JW, Jeong HS, Kwon HJ, et al. **High red blood cell composition in clots is associated with successful recanalization during intra-arterial thrombectomy.** *PLoS One* 2018;13:e0197492 CrossRef Medline
12. Borggrefe J, Kottlors J, Mirza M, et al. **Differentiation of clot composition using conventional and dual-energy computed tomography.** *Clin Neuroradiol* 2018;28:515–22 CrossRef Medline
13. Zaidat OO, Castonguay AC, Linfante I, et al. **First pass effect.** *Stroke* 2018;49:660–66 CrossRef Medline
14. Higashida RT, Furlan AJ; Technology Assessment Committee of the American Society of Interventional and Therapeutic Neuroradiology; Technology Assessment Committee of the Society of Interventional Radiology. **Trial design and reporting standards for intra-arterial cerebral thrombolysis for acute ischemic stroke.** *Stroke* 2003;34:e109–37 CrossRef Medline
15. Johnson H, Harris G, Williams K. **BRAINSFIT: Mutual Information Rigid Registrations of Whole-Brain 3D Images, Using the Insight Toolkit.** https://www.nitrc.org/docman/view.php/52/639/BRAINSFit.pdf. Accessed 08/15/2020
16. Santos EM, Yoo AJ, Beenen LF, et al; MR CLEAN investigators. **Observer variability of absolute and relative thrombus density measurements in patients with acute ischemic stroke.** *Neuroradiology* 2016;58:133–39 CrossRef Medline
17. Stritt M, Stalder AK, Vezzali E. **Orbit image analysis: an open-source whole slide image analysis tool.** *PLoS Comput Biol* 2020;16:e1007313 CrossRef Medline
18. Santos EM, Dankbaar JW, Treurniet KM, et al. **Permeable thrombi are associated with higher intravenous recombinant tissue-type plasminogen activator treatment success in patients with acute ischemic stroke.** *Stroke* 2016;47:2058–65 CrossRef Medline
19. Berndt M, Friedrich B, Maegerlein C, et al. **Thrombus permeability in admission computed tomographic imaging indicates stroke pathogenesis based on thrombus histology.** *Stroke* 2018;49:2674–82 CrossRef Medline
20. Benson JC, Fitzgerald ST, Kadirvel R, et al. **Clot permeability and histopathology: is a clot's perviousness on CT imaging correlated with its histologic composition?** *J NeuroIntervent Surg* 2020;12:38–42 CrossRef Medline
21. Altman DG, Royston P. **The cost of dichotomising continuous variables.** *BMJ* 2006;332:1080 CrossRef Medline
22. McDonald MM, Archeval-Lao JM, Cai C, et al. **Iodinated contrast does not alter clotting dynamics in acute ischemic stroke as measured by thromboelastography.** *Stroke* 2014;45:462–66 CrossRef Medline
23. Hertig G, Zehnder M, Woloszyk A, et al. **Iodixanol as a contrast agent in a fibrin hydrogel for endodontic applications.** *Front Physiol* 2017;8:152 CrossRef Medline
24. Niesten JM, van der Schaaf IC, van Dam L, et al. **Histopathologic composition of cerebral thrombi of acute stroke patients is correlated with stroke subtype and thrombus attenuation.** *PLoS One* 2014;9:e88882 CrossRef Medline
25. Kirchhof K, Welzel T, Mecke C, et al. **Differentiation of white, mixed, and red thrombi: value of CT in estimation of the prognosis of thrombolysis phantom study.** *Radiology* 2003;228:126–30 CrossRef Medline
26. Gersh KC, Nagaswami C, Weisel JW. **Fibrin network structure and clot mechanical properties are altered by incorporation of erythrocytes.** *Thromb Haemost* 2009;102:1169–75 CrossRef Medline
27. Maekawa K, Shibata M, Nakajima H, et al. **Erythrocyte-rich thrombus is associated with reduced number of maneuvers and procedure time in patients with acute ischemic stroke undergoing mechanical thrombectomy.** *Cerebrovasc Dis Extra* 2018;8:39–49 CrossRef Medline
28. Gunning GM, McArdle K, Mirza M, et al. **Clot friction variation with fibrin content; implications for resistance to thrombectomy.** *J NeuroIntervent Surg* 2018;10:34–38 CrossRef Medline
29. Byun JS, Nicholson P, Hilditch CA, et al. **Thrombus perviousness is not associated with first-pass revascularization using stent retrievers.** *Interv Neuroradiol* 2019;25:285–90 CrossRef Medline
30. Bernava G, Rosi A, Boto J, et al. **Direct thromboaspiration efficacy for mechanical thrombectomy is related to the angle of interaction between the aspiration catheter and the clot.** *J Neuronterv Surg* 2020;12:396–400 CrossRef Medline
31. Qiu W, Kuang H, Nair J, et al. **Radiomics-based intracranial thrombus features on CT and CTA predict recanalization with intravenous alteplase in patients with acute ischemic stroke**. *AJNR Am J Neuroradiol* 2019;40:39–44 CrossRef Medline
32. Boeckh-Behrens T, Schubert M, Förschler A, et al. **The impact of histological clot composition in embolic stroke.** *Clin Neuroradiol* 2016;26:189–97 CrossRef Medline
33. Jagani M, Kallmes DF, Brinjikji W. **Correlation between clot density and recanalization success or stroke etiology in acute ischemic stroke patients.** *Interv Neuroradiol* 2017;23:274–78 CrossRef Medline
34. Dutra BG, Tolhuisen ML, Alves H, et al; MR CLEAN Registry Investigators. **Thrombus imaging characteristics and outcomes in acute ischemic stroke patients undergoing endovascular treatment.** *Stroke* 2019;50:2057–64 CrossRef Medline
35. Mokin M, Morr S, Natarajan SK, et al. **Thrombus density predicts successful recanalization with Solitaire stent retriever thrombectomy in acute ischemic stroke.** *J Neurointerv Surg* 2015;7:104–07 CrossRef Medline

Time-to-Maximum of the Tissue Residue Function Improves Diagnostic Performance for Detecting Distal Vessel Occlusions on CT Angiography

S.A. Amukotuwa, A. Wu, K. Zhou, I. Page, P. Brotchie, and R. Bammer

ABSTRACT

BACKGROUND AND PURPOSE: Detecting intracranial distal arterial occlusions on CTA is challenging but increasingly relevant to clinical decision-making. Our purpose was to determine whether the use of CTP-derived time-to-maximum of the tissue residue function maps improves diagnostic performance for detecting these occlusions.

MATERIALS AND METHODS: Seventy consecutive patients with a distal arterial occlusion and 70 randomly selected controls who underwent multimodal CT with CTA and CTP for a suspected acute ischemic stroke were included in this retrospective study. Four readers with different levels of experience independently read the CTAs in 2 separate sessions, with and without time-to-maximum of the tissue residue function maps, recording the presence or absence of an occlusion, diagnostic confidence, and interpretation time. Accuracy for detecting distal occlusions was assessed using receiver operating characteristic analysis, and areas under curves were compared to assess whether accuracy improved with use of time-to-maximum of the tissue residue function. Changes in diagnostic confidence and interpretation time were assessed using the Wilcoxon signed rank test.

RESULTS: Mean sensitivity for detecting occlusions on CTA increased from 70.7% to 90.4% with use of time-to-maximum of the tissue residue function maps. Diagnostic accuracy improved significantly for the 4 readers ($P < .001$), with areas under the receiver operating characteristic curves increasing by 0.186, 0.136, 0.114, and 0.121, respectively. Diagnostic confidence and speed also significantly increased.

CONCLUSIONS: All assessed metrics of diagnostic performance for detecting distal arterial occlusions improved with the use of time-to-maximum of the tissue residue function maps, encouraging their use to aid in interpretation of CTA by both experienced and inexperienced readers. These findings show the added diagnostic value of including CTP in the acute stroke imaging protocol.

ABBREVIATIONS: ACA = anterior cerebral artery; AUC = area under the curve; DVO = distal vessel occlusion; EVT = endovascular thrombectomy; NECT = nonenhanced CT; PCA = posterior cerebral artery; ROC = receiver operating characteristic; Tmax = time to maximum of the tissue residue function; SCA = Superior Cerebellar Artery

Intravenous thrombolysis is the mainstay for treatment of arterial occlusions distal to the internal carotid artery, M1 segment of the MCA, and the vertebral and basilar arteries.[1] These occlusions are referred to as distal vessel occlusions (DVOs), to distinguish them from proximal large-vessel occlusions.[2] While demonstration of DVOs is not a requirement for thrombolysis,[1] their detection is becoming increasingly relevant to clinical decision-making. The main reason is that endovascular thrombectomy (EVT) can be used to treat occlusions involving large- and medium-sized distal arteries in carefully selected patients.[2] There is evidence of improved functional outcomes with EVT compared with standard medical management in patients with occlusion of the M2 segment of the MCA.[2-4] M2 occlusions are, therefore, increasingly considered for EVT, which is also safe and technically feasible for occlusions involving the M3 segment of the MCA, the anterior cerebral artery (ACA), or the posterior cerebral artery (PCA).[1,3,5,6]

Advances in endovascular device technology have led to the development of smaller and more navigable stent retrievers and thromboaspiration devices that can reach smaller distal arteries, including the M4 segment of the MCA and the A4 segment of the ACA.[2] Because these DVOs can cause severe neurologic deficits when eloquent brain regions are supplied, EVT may be justified to achieve rapid reperfusion.[4,7] It is also the only option for reperfusion in patients who are ineligible for thrombolysis. Thus, distal-vessel EVT is considered a "promising next potential

Received July 22, 2020; accepted after revision August 28.

From the Department of Diagnostic Imaging (S.A.A., A.W., K.Z.), Monash Health, Clayton, Australia; Department of Radiology (S.A.A., P.B.), Barwon Health, Geelong, Australia; and Department of Radiology (I.P., R.B.), The Royal Melbourne Hospital, Parkville, Australia.

Please address correspondence to Shalini A. Amukotuwa, MD, Diagnostic Imaging, Monash Health, Clayton, Australia 3168; e-mail: samukotuwa@gmail.com

Indicates article with supplemental online appendix and tables.

Indicates article with supplemental online photos.

http://dx.doi.org/10.3174/ajnr.A6891

frontier" for stroke therapy and is the subject of current research.[2] Because demonstration of a target arterial occlusion is required for triage to EVT, fast and accurate detection of DVOs is important to ensure timely treatment.

Detecting DVOs also allows the correct diagnosis to be made. This, in turn, is important for prognostication and ongoing management such as work-up for an embolic source and secondary prevention. It is also possible that detection of a target DVO may become a requirement for thrombolysis if the treatment window is extended beyond 4.5 hours, to avoid futile treatment and justify the increased risk of thrombolysis.[8]

CTA has become a routine part of the acute stroke imaging protocol.[9,10] Its main purpose is to identify patients with proximal large-vessel occlusions for triage to EVT. DVOs are more difficult to detect on CTA than these proximal occlusions, due to the smaller caliber, larger number, and poorer opacification of distal arteries. Reported sensitivity is as low as 33%, with 35% of M2-segment MCA occlusions missed at the time of initial CTA evaluation in 1 recent study.[11-13]

CTP is now widely included in acute stroke CT protocols.[14] The time-to-maximum of the tissue residue function (Tmax) is a parameter that is routinely obtained from CTP when deconvolution-based postprocessing is used.[15] Tmax is well-established for identifying salvageable ischemic penumbra in patients with proximal vessel occlusions.[16,17] We have observed, in our clinical practice, that Tmax delay within a vascular territory indicates severe stenosis or occlusion of the supplying artery. This information can, in turn, be used to detect and localize distal arterial occlusions on CTA. These occlusions may otherwise be missed or difficult to find. Despite its real-world value in routine clinical practice, no previous studies have assessed and quantified the diagnostic utility of Tmax for detecting intracranial arterial occlusions.

The purpose of this study was to assess the added value of Tmax maps and verify our clinical impression that they facilitate detection of distal occlusions on CTA. We hypothesized that diagnostic accuracy, speed, and confidence for detecting DVOs on CTA would increase with the use of Tmax for readers with different levels of experience.

MATERIALS AND METHODS

Patient Selection

Five hundred one consecutive patients who presented to our institution (Barwon Health), a primary stroke center, between January 1, 2017, and December 31, 2018, and underwent multimodal CT for a suspected stroke were screened using our PACS and electronic medical records. Raw and postprocessed images were assessed for technical adequacy by a neuroradiologist with 9 years' postfellowship experience. We retrospectively identified patients who met the following inclusion criteria: 1) 18 years of age or older, 2) having undergone multimodal CT with CTA and CTP, and 3) within 24 hours of symptom onset or last known well. Exclusion criteria were the following: 1) technically inadequate CTP or CTA (poor contrast bolus or substantial motion), 2) thin-section CTA images not available, and 3) occlusion of the internal carotid artery, M1 segment of the MCA, vertebral artery, or basilar artery (excluded to allow specific assessment of diagnostic performance for detection of more distal occlusions). We excluded 128 patients: 84 with a large-vessel occlusion and 44 with a technically inadequate CTA or CTP (the patient selection flow chart is shown in Online Fig 1).

The multimodal stroke CTs of all consecutive patients who met the inclusion criteria were reviewed by the neuroradiologist, who had access to all clinical records and imaging. All consecutive patients with a DVO were identified and included in the study. The same number of patients without any vessel occlusion was randomly selected from the remaining patients (see Online Appendix, Part 1) and included in the study. Data processing, scan anonymization, and randomization were performed by this neuroradiologist.

A DVO was defined as an arterial occlusion involving the following: A2 to A5 segments of the ACA; M2 to M4 segments of the MCA; P2 to P4 segments of the PCA; or the PICA, AICA, or SCA. Proximal M2 occlusions are challenging to classify due to large interpatient anatomic variability in size and dominance.[2] While some may be considered proximal or large-vessel occlusions, they are not recognized as such by the American Heart Association guidelines, are more difficult to detect than M1 occlusions on CTA, and have, therefore, been included as DVOs in the study.

The study was approved by the local institutional review board, which granted a waiver of written consent based on the retrospective study design and anonymization of all data. This investigator-initiated study received no financial support.

CT Image Acquisition, Reconstruction, and Postprocessing

All patients were scanned on a 256-section multidetector CT scanner (iCT 256; Philips Healthcare). Our routine multimodal stroke CT protocol consisted of nonenhanced CT (NECT) followed by CTP and then CTA. Scan techniques and parameters are detailed in the Online Appendix (Part 2).

For CTP, images were acquired axially, reconstructed at 10-mm section thickness, and processed using a commercially available software platform (RAPID 4.9; iSchemaView) that uses a delay-insensitive deconvolution algorithm with automated arterial input function selection.[18] The software calculates Tmax values for each image voxel, ranging from 0 to 12 seconds in 2-second increments, and displays them on a color-scale map.

Helically acquired CTA images were reconstructed axially at 0.8-mm sections. Three-plane (axial, coronal, and sagittal) 4-mm-thick MPRs and 10-mm-thick MIPs were also reconstructed.

Reference Standard

Two neuroradiologists (with 9 and 20 years' postfellowship experience, respectively) interpreted the CTAs in consensus using a systematic approach in conjunction with NECT and all available clinical and imaging data, including all CTP parametric maps (CBF, CBV, MTT, and Tmax) as well any available follow-up scans. These expert reads served as the reference standard.

Image Review

The CTAs were interpreted independently by 4 readers with different levels of experience: a second-year radiology resident, a neuroradiology fellow, an attending radiologist (2 years' post-cardiovascular fellowship), and an imaging scientist. These readers had 18 months, 6 years, 8 years, and 20 years of experience, respectively, in interpreting acute stroke imaging. All had pre-existing knowledge of the major cerebral arteries, their segments, and their supply

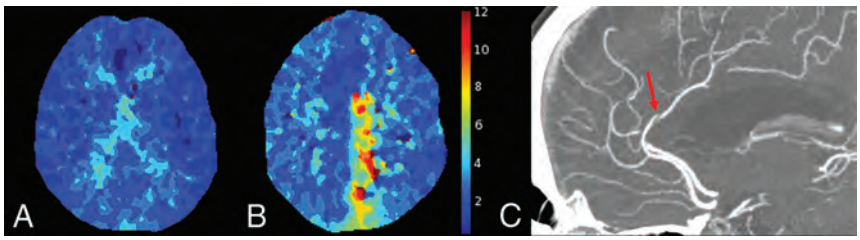

FIG 1. *A*, Selected section of a normal Tmax map, with no areas of delay, in a patient without a DVO. *B*, Tmax map (selected section) shows marked delay in the left distal ACA territory. *C*, Axial CTA MIP shows the culprit A-segment ACA occlusion (*red arrow*) in this 72-year-old woman who presented with right-leg weakness.

Table 1: Patient demographics and location of vessel occlusions

	No.	Age (Median) (Interquartile Range)	NIHSS[a] (Median) (Interquartile Range)	Male (%)
All patients	140	73 (64–83)	5 (1–7)	77 (55.0%)
Patients without a DVO	70	68 (55–82)	4 (1–7)	34 (48.6%)
Patients with a DVO	70	76 (69–84)	5 (1–8)	43 (61.1%)
Location of DVO				
MCA: M2 segment[b]	38			
Proximal	22			
Distal	16			
MCA: M3 segment	5			
MCA: M4 segment	8			
ACA: A3 or A4 segment	3			
PCA: P2 segment	5			
PCA: P3 or P4 segment	8			
PICA	2			
SCA	1			

[a] Fourteen patients had an occlusion at 2 sites (Online Table 1) and were categorized here according to the most proximal occlusion.
[b] The midpoint of the Sylvian fissure on coronal imaging was used to divide M2 occlusions into proximal (if inferior) and distal (if superior). Occlusions of the superior and inferior division trunks as well as their ascending branches were included under M2-segment occlusions.

territories, acquired through routine radiology training and clinical work. No additional training was provided for this study. Details of the patients' presenting neurologic deficits were provided (to reflect clinical practice); however, the readers were blinded to all other clinical and follow-up imaging data. There were no cases in which the CTP acquisition did not cover the territory supplied by an occlusion detected by the neuroradiologists.

Reads were performed in 2 separate sittings, 2 months apart, to negate the effects of memory and learning. CTA, and NECT raw data and reconstructions were made available at each sitting and were viewed using a public domain DICOM viewer (Horos, Version 3.3.5; www.horosproject.org). Scans were anonymized and presented in random order. Readers were permitted to manipulate the provided NECT and CTA data (eg, windowing and performing MIPS) as they would in routine clinical practice. In the first sitting, Tmax maps were provided for the first half of the patient cohort but not the second. This was reversed in the second sitting.

The readers were asked to perform the following:

1) Review Tmax maps, when available, prior to interpreting the CTA, to determine whether there was any territorial Tmax delay (Fig 1).
2) Assess the CTA, recording the presence and location of a DVO/DVOs, and marking the location on thin-slice CTA images. When Tmax maps were available, the following approach was suggested to localize an occlusion on CTA:
   a) If present, use the distribution Tmax delay conforming to an arterial territory to narrow down the side, major vascular territory, and likely occluded segment. Perform a focused search.
   b) If this fails, progressively broaden the search because there is considerable anatomic variability in the areas supplied by the major intracranial arteries and their segments.
3) Rate diagnostic confidence using a 5-point Likert scale: 1 (occlusion very unlikely), 2 (occlusion unlikely), 3 (uncertain), 4 (occlusion likely), and 5 (occlusion very likely).

Statistical Analysis

All statistical analyses were performed using MedCalc (MedCalc Software, Version 17.2, 64 bit).

Each reader's diagnostic performance for detecting a DVO on CTA was assessed against the reference standard (expert reads) using receiver operating characteristic (ROC) analysis. A true-positive required both the presence and site of a DVO to be correctly identified. Change in accuracy with the addition of Tmax was assessed by pair-wise comparison of the areas under the ROC curves (AUCs) using the DeLong algorithm.

The added value of Tmax on diagnostic confidence was assessed with shift analysis, using the Wilcoxon signed rank test to assess the significance of any change. Interreader agreement was assessed using the Fleiss κ statistic (κ_F). The Cohen κ statistics were used to determine agreement between each pair of readers.

The Wilcoxon signed rank test was used to determine whether there was a significant difference in the time taken to interpret CTA when Tmax was added.

Confidence intervals were calculated using a bootstrap procedure with 10,000 samples with replacement. An α level of .001 was taken to indicate significance for all tests except the shift analysis of confidence in which a level of .05 was applied.

RESULTS

CTAs were analyzed from 140 patients (median age, 73 years; interquartile range, 64–83 years), of which 77 were men and 70 had a DVO (including 22 with proximal M2 occlusions). Patients' baseline characteristics and the details of vessel occlusion are provided in Table 1.

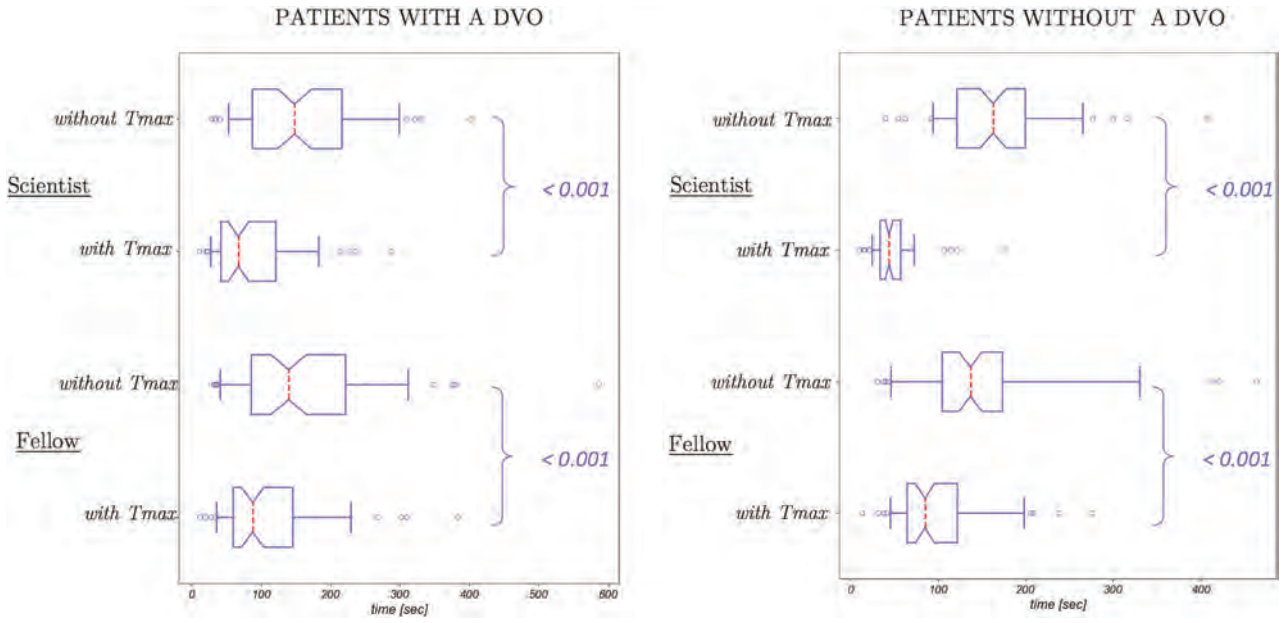

FIG 2. Box-and-whisker plots of time taken to interpret CTA in patients with and without a DVO on the reference standard. The *dashed red line* indicates median time; the *upper and lower edges of the boxes* indicate the first and third quartiles, respectively; the *notches* represent the 95% confidence intervals of the median; and the *whiskers* extend to the fifth and 95th centiles. Outliers are shown in the *circles*. For both readers, interpretation was significantly faster ($P < .001$) with Tmax than without it. The spread of times also decreased with Tmax.

Diagnostic Accuracy

The results of ROC analyses for detecting a DVO on CTA are given in Online Table 2. For all readers, sensitivity and specificity increased with the addition of Tmax, and accuracy (as measured by the AUC) increased significantly ($P < .001$). The mean sensitivity for detecting a DVO increased from 70.7% to 90.4% with the addition of Tmax, while mean specificity increased from 87.5% to 95.7%.

Analysis was repeated following exclusion of the 22 patients with proximal M2 MCA occlusions, including 10 with occlusion of the proximal trunk of a dominant or codominant M2 division, which may be considered proximal vessels (Online Tables 4 and 5). The mean sensitivity for detecting a DVO on CTA increased from 61.0% without Tmax to 86.5% when Tmax was used. The gain in sensitivity was, therefore, larger than when proximal M2 occlusions were included. Following exclusion of the 43 patients with either an M2 MCA or P2 PCA occlusion (Online Table 6), which allowed diagnostic sensitivity for detecting more distal occlusions to be isolated, mean sensitivity increased from 42.6% without Tmax to 81.5% with Tmax. The sensitivity for detecting DVOs on CTA alone was, therefore, much lower than when M2 and P2 occlusions were included. However, the gain in sensitivity with the addition of Tmax and, therefore, an increase in the AUC was larger. On all 3 analyses, the AUC increased significantly ($P < .001$) for all readers when Tmax was used, with the largest improvement occurring when only the most distal DVOs were considered (ie, following exclusion of M2 or P2 occlusions).

Interreader agreement on CTA improved with the addition of Tmax, from $\kappa_F = 0.61$ (95% CI, 0.54–0.68) to $\kappa_F = 0.79$ (95% CI = 0.72–0.86). There was also greater agreement between pairs of readers (Online Fig 2) when CTA was interpreted with Tmax than without it.

Diagnostic Confidence

The gain in confidence with the addition of Tmax is shown in Online Fig 3 and Online Table 7. In patients deemed to have a DVO on the reference standard, diagnostic confidence that an occlusion was present increased significantly ($P < .05$) for all 4 readers. Each reader had fewer false-negatives and more patients in whom an occlusion was deemed very likely.

All readers were more confident in dismissing a DVO on CTA when Tmax was used. The increase in confidence reached significance ($P < .05$) for all readers except the resident, who had a larger number of false-positives ($n = 8$). The number of patients in whom an occlusion was considered very unlikely increased for all readers.

Time to Interpret CTA

CTA was interpreted significantly faster ($P < .001$) with use of Tmax (Online Table 8): The median interpretation time was 1.6 times faster for the fellow and 3.3 times faster for the scientist with Tmax. Box-and-whisker plots of CTA interpretation time are shown for the 2 readers who were timed (Fig 2). Patients were dichotomized into those with a DVO and those without a DVO on the reference standard. Interpretation time was significantly ($P < .001$) shorter with Tmax than without it for both groups. This result indicates that DVOs were both detected and dismissed faster. The median time to detect M2 occlusions was less than that for M3 and M4 occlusions, but this did not reach significance (Online Table 9).

Post Hoc Analysis

False-negatives and false-positives are detailed in Online Tables 10 and 11, respectively.

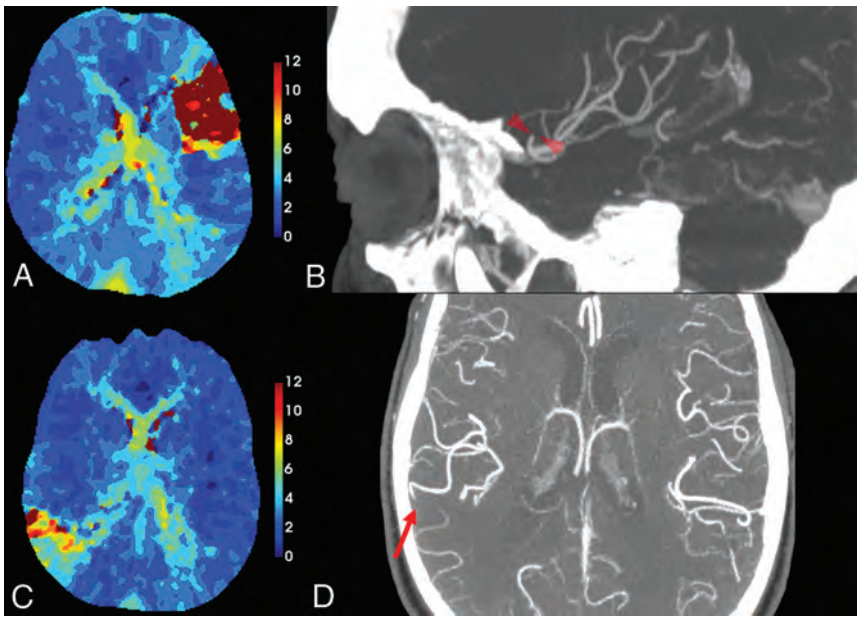

FIG 3. Examples in which Tmax aided detection of a DVO on CTA. *A*, A Tmax delay of >10 seconds is evident in the left MCA, superior M2-division territory in a 54-year-old woman who presented with sudden-onset aphasia. *B*, Sagittal CTA MIP (selected section) shows the occlusion (*red arrowheads*). This was detected by only 2 readers without Tmax, but by all 4 readers with Tmax. *C*, Wedge-shaped, territorial Tmax delay is seen in a right parietal lobe in an 83-year-old man. *D*, The right parietal M4 occlusion (*red arrow*), shown on an axial CTA MIP, was detected by only 2 readers without Tmax and all 4 readers with Tmax.

The number of false-negatives decreased for all readers with the addition of Tmax. Four proximal M2 occlusions were missed by ≥1 of the readers on CTA without Tmax (Fig 3*A*, -*B*). Only one was missed by 1 reader with Tmax. Fewer distal DVOs were missed on CTA when Tmax was used (Fig 3*C*, -*D*). M4-segment MCA occlusions remained a challenge, however, with the fellow and radiologist each missing 5 even with Tmax. There were too few distal ACA occlusions in the cohort for meaningful analysis. All 8 PCA occlusions distal to the P2 segment were detected on CTA with Tmax.

There were a number of false-positives for a DVO on CTA without Tmax. All were related to small-caliber distal vessels, especially branch and turning points. The few false-positives on CTA with Tmax were also related to small-caliber, poorly opacified distal vessels. Tmax delay was present in all except one of these cases, but it did not conform to the territory of an intracranial artery. A recurrent cause of false-positives for the 2 less experienced readers was Tmax delay in the deep white matter and external watershed (borderzone pattern) (Online Fig 4*E*).

Fourteen patients had 2 DVOs (Online Table 1). The benefit of Tmax was greater for the 2 experienced readers; both occlusions were detected and correctly identified in 3 additional patients by the radiologist and in 7 additional patients by the scientist.

DISCUSSION

The added value of Tmax maps on diagnostic performance for detecting DVOs on CTA was assessed in this study. Diagnostic accuracy, confidence, and speed were shown to improve significantly with addition of Tmax for readers with different levels of experience in interpreting stroke imaging. The beneficial effect of Tmax in aiding detection of DVOs on CTA was greater for more distal occlusions.

CTP is now widely included in the acute stroke CT protocol.[14] Its primary purpose is to identify patients with proximal arterial occlusions with salvageable brain tissue who may, therefore, benefit from EVT. It also provides information about the macrovasculature that can be leveraged to improve detection of vessel occlusions.[11,19] Perfusion maps were shown to improve detection of intracranial arterial occlusions in 1 previous study that was not specifically designed to evaluate DVOs and included only a small number of these distal occlusions.[11] Another important point of distinction between this previous study and ours is that Tmax was not used in theirs.

Tmax was used in some EVT trials to identify salvageable ischemic penumbra and is now routinely available on most CTP-postprocessing software platforms.[16,17] It can also be used to assess early reperfusion with treatment.[17] Tmax reflects the delay in contrast arrival in tissue relative to a proximal arterial reference point.[18,19] This arterial reference point is called the arterial input function and is an essential part of deconvolution-based perfusion analysis. An intracranial arterial occlusion prolongs arterial transit time and, therefore, Tmax within the territory that is supplied.[19] TTP, another time-based parameter that has been used to assess penumbra, is also prolonged when there is delayed arterial transit.[18] However, unlike Tmax, it is not obtained through deconvolution and is, therefore, not corrected for the shape of the contrast bolus. Thus, Tmax is less sensitive than TTP to bolus delay proximal to the arterial input function and is more specific for delays in arterial transit between the arterial input function and tissue caused by an occlusion.[18] The distribution of Tmax delay can be used to narrow down the laterality, major territory, probable segment (eg, M2 versus M3), and likely location of an arterial occlusion. A more focused search can then be performed. The alternative of systematically interrogating all cerebral arteries to the most distal discernible level is very time-consuming and therefore not feasible under clinical time pressures. Clinical information regarding neurologic deficits narrows the search field but is not always available or reliable. Tmax maps are objective and consistently available when CTP is performed. To our knowledge, this is the first study evaluating the utility of Tmax for detecting intracranial arterial occlusions.

As hypothesized, diagnostic performance for detecting DVOs on CTA improved significantly with the use of Tmax. The effect

size was sufficiently large to show significant improvement using a *P* value cutoff of .001, even with a sample size of 140, including 70 patients with a DVO. Because information on neurologic deficit was provided, the beneficial effect of Tmax was additive to any gain provided by clinical notes. Sensitivity for the detection of DVOs on CTA alone is likely lower, and improvement in performance with Tmax may, therefore, be even greater when reliable clinical information is unavailable.

Most important, fewer proximal M2 occlusions were missed. Patients with M2 occlusions are increasingly considered for EVT because it may improve their functional outcomes.[3,4] M2 occlusions are easily detected by experienced neuroradiologists but can be missed by trainees and general radiologists as shown in this study; 35% of M2 occlusions were missed on CTA evaluation in a previous study performed at a primary stroke center.[13] Trainees interpret the bulk of CTAs performed at stroke referral centers, while these scans are typically interpreted by general radiologists at primary stroke centers. Improving detection of M2 occlusions by these less experienced readers is, therefore, of high clinical relevance, to ensure that patients do not miss out on potentially beneficial treatment.

The gain in sensitivity with the addition of Tmax and, therefore, the benefit were greater for more distal occlusions. Poor sensitivity for detecting M4 and distal ACA occlusions on CTA alone can be explained by the small caliber and large number of these vessels, making detection akin to finding a needle in a haystack, even with accurate clinical notes. Tmax maps narrowed the search field, increasing the chances of finding the culprit occlusion on CTA. Despite improvement in sensitivity, some distal anterior circulation occlusions were still missed by the readers. An occlusion is sometimes not clearly visible on CTA (due to the small caliber and poor opacification of the occluded artery), despite unequivocal territorial Tmax delay suggestive of a DVO. If an alternative cause cannot be found, it may be reasonable to diagnose a likely distal occlusion in these cases. The readers fared better in detecting distal PCA than MCA occlusions. This result may be due to the smaller spatial extent and less arborization of the PCA, compared with the MCA. Because sensitivity on CTA with Tmax was imperfect, it cannot be used to definitively exclude a DVO. Of note, sensitivity was not related to reader experience level. The scientist and the resident had the highest sensitivity, both with and without Tmax. A possible explanation is that these readers had a more methodical approach to reading the CTAs.

Specificity for detecting a DVO on CTA exceeded 95% with the addition of Tmax for all readers except the resident, which is important if the findings are used to guide treatment, to ensure that futile and potentially harmful reperfusion is avoided in patients without a DVO. Specificity was related to the level of experience in interpreting CTA and CTP; greater experience enabled the senior readers to differentiate between occlusions and poorly opacified distal vessels and to recognize and dismiss Tmax delay that did not conform to a vascular territory.

Interpretation of CTAs was significantly faster with the addition of Tmax. As expected, DVOs were detected faster due to the search field being narrowed, but occlusions were also dismissed more quickly. Faster diagnosis not only expedites treatment, it also improves workflow efficiency. The latter is important in clinical practice, particularly in the setting of busy comprehensive stroke centers. An important caveat in using Tmax to expedite interpretation is that readers must continue to methodically scrutinize CTAs for other, incidental findings and avoid succumbing to "streetlight effect."

Diagnostic confidence in the presence or absence of a DVO on CTA increased for all readers with Tmax. One likely reason is that the Tmax maps provide additional evidence to corroborate or reject the findings on CTA alone; diagnostic confidence is greater when 2 separate tests indicate that an occlusion is either present or absent. Another factor that likely contributed to improvement in all metrics of diagnostic performance is that Tmax maps are easy to interpret. They have a high contrast-to-noise ratio. While CBF and CBV have substantial gray-white matter contrast, Tmax values do not vary with tissue type[20] and have rather flat contrast in the normal brain. Even small or subtle areas of Tmax delay, therefore, appear conspicuous and can be detected and characterized reliably and confidently. This feature, in turn, contributes to increased sensitivity when the findings on Tmax are used to guide the search for a DVO on CTA. Conversely, maps with no Tmax delay appear monochromatic, making it easy to interpret the absence of an abnormality and dismiss an occlusion with high certainty. While the findings of a DVO on CTA can be subtle due to the small caliber and poor opacification of distal vessels, the findings on Tmax are more apparent and therefore less prone to variable interpretation. Accordingly, the use of Tmax led to greater consistency of CTA interpretation, with higher interreader agreement.

An alternative method that has been reported to improve detection of DVOs is wavelet-transformed angiography (waveletCTA), which is also obtained by postprocessing of CTP data.[21] Its clinical uptake has been limited by the requirement for thin-section CTP and specialist postprocessing software that is not widely available. In contrast, most CTP-postprocessing software packages are able to produce Tmax maps and can do so from thick-section CTP, making the use of Tmax feasible in routine clinical practice at even small peripheral centers.

An important limitation is that CTP is only recommended by the AHA guidelines in the late (6- to 24-hour) time window. Not all stroke centers routinely perform CTP in the early window because it incurs an additional radiation dose and its role in patients within 6 hours of stroke onset has not been established. However, because CTP has diagnostic utility beyond tissue classification, aiding the diagnosis of stroke and some stroke mimics such as migraine, and is therefore performed even in the early window at some centers, including ours.

A limitation of using Tmax maps to aid detection of DVOs on CTA is that nonterritorial Tmax delay can lead to false-positives and lower specificity. The experienced readers dismissed DVOs in these cases, suggesting that such errors can be avoided with training in the interpretation of Tmax maps, specifically to differentiate Tmax delay in a vascular territory from delays that either cross territories (eg, due to migraine) or are artifactual or "borderzone" in distribution. Borderzone Tmax delay occurs with contrast bolus dispersion, for example, due to a poor injection, proximal arterial steno-occlusive disease, and impaired cardiac output. It is manifested as Tmax delay in arterial watershed areas.[18,19] CTP acquisition with limited brain coverage is a potential cause of false-negatives if the territory supplied by the

occluded vessel is not included. This situation is avoided with a whole-brain CTP acquisition on modern multidetector array CT scanners.[11] When only limited coverage is feasible, targeting the CTP acquisition to the clinical presentation (eg, posterior circulation) can avoid false-negatives.

A limitation of the study is that only 1 CT scanner and CTP postprocessing software package were used. This may limit the generalizability of the findings. The algorithms used by different postprocessing software packages are variable and most, but not all, use deconvolution-based postprocessing, a requirement for obtaining Tmax.[22] There are also substantial differences in the derived perfusion parameters, even between packages that use deconvolution-based postprocessing, resulting in variability in quantification of the infarct core and penumbra.[22,23] The variability is less likely to affect qualitative assessment; however, differences in the display of parametric maps (eg, color scale) may impact visual assessment. In turn, these may affect diagnostic performance for the detection of territorial Tmax delay, which warrants further evaluation in a future study.

A potential limitation of the study is that the prevalence of DVOs in the study cohort (50%) was higher than in the population of patients with stroke who undergo multimodal CT. The true prevalence of DVOs is much lower and likely closer to the 14% observed in the cohort screened for the study. Use of a balanced sample may bias the absolute sensitivity and specificity for detecting a DVOs on CTA, both with and without Tmax. These values should, therefore, be interpreted with caution. However, the primary purpose of this study was to assess the relative change in diagnostic performance for detecting DVOs on CTA when Tmax was added, rather than absolute diagnostic performance.

Another potential limitation of the study is the choice of the reference standard: an expert read of the CTAs instead of DSA, which is the reference standard for detecting intracranial vascular pathology. Using CTA was justified because DVOs can recanalize or migrate between angiographic modalities, especially when thrombolysis is administered, which would render DSA inaccurate as a reference standard. The authors recognize that some very distal DVOs may have been missed by all readers, including the expert reader. This possibility would affect the determination of absolute accuracy. It is, however, less relevant for comparative assessment of the diagnostic performance on CTA with and without Tmax, which was the purpose of this study.

CONCLUSIONS

DVOs were detected with greater accuracy, confidence, and speed on CTA when Tmax maps were used to focus the search for a vessel occlusion. While the beneficial effect was greater for more distal occlusions, Tmax also helped detect M2 occlusions, which is important clinically because they are considered a target for EVT. Our findings demonstrate significant added value of CTP beyond tissue classification, with the potential to benefit management of more patients than simply those with proximal arterial occlusions. By showing that Tmax can be leveraged to improve detection of vessel occlusions by trainees and a generalist, our findings encourage the inclusion of CTP in the acute stoke imaging protocol at both comprehensive and primary stroke centers.

Disclosures: Shalini A. Amukotuwa—*UNRELATED*: *Employment*: Monash Health. Angel Wu—*UNRELATED*: *Employment*: Monash Health. Roland Bammer—*UNRELATED*: *Board Membership*: iSchemaView Inc; *Payment for Lectures Including Service on Speakers Bureaus*: American Society of Neuroradiology; *Stock/Stock Options*: iSchemaView Inc.

REFERENCES

1. Powers WJ, Rabinstein AA, Ackerson T, et al; American Heart Association Stroke Council. **Guidelines for the Early Management of Patients with Acute Ischemic Stroke: A Guideline for Healthcare Professionals From the American Heart Association/American Stroke Association.** *Stroke* 2018;49:e46–110 CrossRef Medline
2. Saver JL, Chapot R, Agid R, et al; Distal Thrombectomy Summit Group. **Thrombectomy for distal, medium vessel occlusions: a consensus statement on present knowledge and promising directions.** *Stroke* 2020;51:2872–84 CrossRef Medline
3. Sarraj A, Sangha N, Hussain MS, et al. **Endovascular therapy for acute ischemic stroke with occlusion of the middle cerebral artery M2 segment.** *JAMA Neurol* 2016;73:1291–96 CrossRef Medline
4. Sheth SA, Yoo B, Saver JL, et al; UCLA Comprehensive Stroke Center. **M2 occlusions as targets for endovascular therapy: comprehensive analysis of diffusion/perfusion MRI, angiography, and clinical outcomes.** *J Neurointerv Surg* 2015;7:478–83 CrossRef Medline
5. Grossberg JA, Rebello LC, Haussen DC, et al. **Beyond large vessel occlusion strokes: distal occlusion thrombectomy.** *Stroke* 2018;49:1662–68 CrossRef Medline
6. Almekhlafi M, Ospel JM, Saposnik G, et al. **Endovascular treatment decisions in patients with M2 segment MCA occlusions.** *AJNR Am J Neuroradiol* 2020;41:280–85 CrossRef Medline
7. Kurre W, Vorlaender K, Aguilar-Perez M, et al. **Frequency and relevance of anterior cerebral artery embolism caused by mechanical thrombectomy of middle cerebral artery occlusion.** *AJNR Am J Neuroradiol* 2013;34:1606–11 CrossRef Medline
8. Clark WM, Albers GW, Madden KP, et al. **The rtPA (alteplase) 0- to 6-hour acute stroke trial, part A (A0276g): results of a double-blind, placebo-controlled, multicenter study: Thrombolytic Therapy in Acute Ischemic Stroke Study Investigators.** *Stroke* 2000;31:811–16 CrossRef Medline
9. Demchuk AM, Menon BK, Goyal M. **Comparing vessel imaging: noncontrast computed tomography/computed tomographic angiography should be the new minimum standard in acute disabling stroke.** *Stroke* 2016;47:273–81 CrossRef Medline
10. Wintermark M, Luby M, Bornstein NM, et al. **International survey of acute stroke imaging used to make revascularization treatment decisions.** *Int J Stroke* 2015;10:759–62 CrossRef Medline
11. Becks MJ, Manniesing R, Vister J, et al. **Brain CT perfusion improves intracranial vessel occlusion detection on CT angiography.** *J Neuroradiol* 2019;46:124–29 CrossRef Medline
12. Lev MH, Farkas J, Rodriguez VR, et al. **CT angiography in the rapid triage of patients with hyperacute stroke to intraarterial thrombolysis: accuracy in the detection of large vessel thrombus.** *J Comput Assist Tomogr* 2001;25:520–28 CrossRef Medline
13. Fasen B, Heijboer RJJ, Hulsmans FH, et al. **CT angiography in evaluating large-vessel occlusion in acute anterior circulation ischemic stroke: factors associated with diagnostic error in clinical practice.** *AJNR Am J Neuroradiol* 2020;41:607–11 CrossRef Medline
14. Kansagra AP, Goyal MS, Hamilton S, et al. **Collateral effect of Covid-19 on stroke evaluation in the United States.** *N Engl J Med* 2020;383:400–01 CrossRef Medline
15. Campbell BC, Christensen S, Levi CR, et al. **Comparison of computed tomography perfusion and magnetic resonance imaging perfusion-diffusion mismatch in ischemic stroke.** *Stroke* 2012;43:2648–53 CrossRef Medline

16. Campbell BC, Mitchell PJ, Kleinig TJ, et al; EXTEND-IA Investigators. **Endovascular therapy for ischemic stroke with perfusion-imaging selection.** *N Engl J Med* 2015;372:1009–18 CrossRef Medline
17. Lansberg MG, Straka M, Kemp S, et al; DEFUSE 2 Study Investigators. **MRI profile and response to endovascular reperfusion after stroke (DEFUSE 2): a prospective cohort study.** *Lancet Neurol* 2012;11:860–67 CrossRef Medline
18. Straka M, Albers GW, Bammer R. **Real-time diffusion-perfusion mismatch analysis in acute stroke.** *J Magn Reson Imaging* 2010;32:1024–37 CrossRef Medline
19. Calamante F, Christensen S, Desmond PM, et al. **The physiological significance of the time-to-maximum (Tmax) parameter in perfusion MRI.** *Stroke* 2010;41:1169–74 CrossRef Medline
20. Parkes LM, Rashid W, Chard DT, et al. **Normal cerebral perfusion measurements using arterial spin labeling: reproducibility, stability, and age and gender effects.** *Magn Reson Med* 2004;51:736–43 CrossRef Medline
21. Kunz WG, Sommer WH, Havla L, et al. **Detection of single-phase CTA occult vessel occlusions in acute ischemic stroke using CT perfusion-based wavelet-transformed angiography.** *Eur Radiol* 2017;27:2657–64 CrossRef Medline
22. Kudo K, Sasaki M, Yamada K, et al. **Differences in CT perfusion maps generated by different commercial software: quantitative analysis by using identical source data of acute stroke patients.** *Radiology* 2010;254:200–09 CrossRef Medline
23. Austein F, Riedel C, Kerby T, et al. **Comparison of perfusion CT software to predict the final infarct volume after thrombectomy.** *Stroke* 2016;47:2311–17 CrossRef Medline

CT Perfusion: More Than What You Thought

Acute stroke treatment has dramatically changed in the past decade. Boundaries are crossed, and previous axioms are no longer relevant. The results of the DWI or CTP Assessment with Clinical Mismatch in the Triage of Wake-Up and Late Presenting Strokes Undergoing Neurointervention with Trevo (DAWN) and Endovascular Therapy Following Imaging Evaluation for Ischemic Stroke 3 (DEFUSE-3) trials,[1,2] examining endovascular thrombectomy (EVT) in the late timeframe (6–24 hours from stroke onset), have thrust perfusion imaging into the evaluation of acute stroke protocol.[3] The primary purpose of CTP is to distinguish salvageable tissue from infarct core and thus improve patient selection for EVT.[3-5] It is now widely used as part of an acute stroke CT protocol. However, many stroke centers worldwide routinely perform CTP only for patients beyond the early timeframe. This is in accordance with the recent acute stroke guidelines, recommending CTP in the late (6–24 hour) timeframe.[6]

CTP offers other diagnostic utilities.[7] First, CTP may help differentiate ischemic stroke from stroke mimics, including seizure, migraine aura, and conversion disorder.[7-9] Although the suspicion for a stroke mimic should not be based solely on CTP, it may add supportive data and help clinicians better diagnose these elusive cases. Second, CTP may contribute valuable information for the selection of candidates for EVT and intravenous thrombolysis (IVT), despite a low NIHSS score.[3] The NIHSS gives much weight to motor function and dominant hemisphere. However, various infarcts may result in neurologic sequelae, not fully revealed by the NIHSS.[10] These patients may greatly benefit from IVT in case a penumbral lesion is identified. Third, CTP can demonstrate the severity of hypoperfusion in the presence of carotid occlusion or dissection and thus help determine the need for reperfusion therapy.[7,11]

In this issue of the *American Journal of Neuroradiology*, Amukotuwa et al[12] examined the use of CTP to aid in interpretation of CTA for distal vessel occlusion (DVO) identification. They demonstrated that the use of time-to-maximum (Tmax) maps significantly improved the diagnostic performance for detecting DVO.

Detection of DVO has great importance. The field of endovascular thrombectomy is rapidly emerging, and evidence is growing regarding the beneficial effect of EVT on distal M2 occlusions.[13] Furthermore, EVT targeting very distal occlusions including M3/M4, A3/A4, and P3 has become feasible, and although it still lacks evidence is probably the next frontier of EVT.[12,13] Such DVOs are likely to be considered for EVT, especially in patients with disabling neurological deficit ineligible for IVT. This emphasizes the importance of fast and accurate DVO detection.

The identification of DVOs may be challenging due to their small caliber, large number, and lower resolution compared with large vessels.[12] Systematic manual interrogation of these vessels is complex and time-consuming. The authors show that the use of Tmax increased the rate of DVO detection, the level of confidence, and the speed of interpretation. These beneficial effects were greater for more distal occlusions, though improved detection of M2 occlusions was also demonstrated, emphasizing the clinical relevance. The results were consistent across both experienced and inexperienced raters. The added benefit of CTP use may be especially valuable for inexperienced radiologists in remote hospitals or during night shifts. Furthermore, CTP may give the sole hint of a DVO with the increased use of automated interpretation software, which has yet to identify a DVO on CTA.

The limitations of the study arise mainly from the use of a single CTP feature and a single postprocessing software package. The authors discuss these limitations, including the possibility of false-positive results due to nonterritorial Tmax delay. Future studies are needed to compare various types of CTP software and different Tmax cutoff values and to examine the use of Tmax versus other parameters such as CBF, CBV, and MTT.

Currently, DWI is the most accurate technique for infarct detection.[14] Nevertheless, CT has some main advantages over MR imaging, including the wider availability, rapid imaging, superior vascular imaging of extracranial and distal intracranial vessels, and fewer absolute contraindications.[14]

CTP has several limitations.[4,5,7,15] There is still no standardization of CTP acquisition protocol or postprocessing techniques and thresholds.[5] These thresholds are usually defined on the basis of the normal values of CBF and CBV of the gray matter and may be inaccurate in examining white matter lesions.[4,15] Furthermore, in most cases, CTP has limited coverage and low sensitivity for the detection of lacunar infarcts.[4,7,15] It may also be susceptible to the influence of impaired cardiac output and carotid artery stenosis.[4,7] Therefore, obtaining accurate interpretation can be challenging, and CTP

should be interpreted with caution, acknowledging both its advantages and pitfalls.

In the near future, the use of whole-brain CTP acquisitions on modern multidetector array CT scanners and high-resolution and standardized algorithms will optimize the diagnostic accuracy of CTP, allowing the detection of small lacunar infarcts and lowering the probability of false-negative results.[7]

Current guidelines recommend the use of CTP for patient selection for EVT in the late timeframe (6–24 hours).[6] However, as CTP gains more diagnostic utilities, we should broaden the use of CTP and include it as a routine part of the CT stroke protocol. The results of the current study demonstrate one important advantage of CTP for patients in the early timeframe: The use of perfusion imaging adds valuable information and improves interpretation, resulting in better treatment of patients with stroke.

REFERENCES

1. Nogueira RG, Jadhav AP, Haussen DC, et al; DAWN Trial Investigators. **Thrombectomy 6 to 24 hours after stroke with a mismatch between deficit and infarct.** *N Engl J Med* 2018;378:11–21 CrossRef Medline
2. Albers GW, Marks MP, Kemp S, et al; DEFUSE 3 Investigators. **Thrombectomy for stroke at 6 to 16 hours with selection by perfusion imaging.** *N Engl J Med* 2018;378:708–18 CrossRef Medline
3. Campbell BC, Majoie CB, Albers GW, et al; HERMES Collaborators. **Penumbral imaging and functional outcome in patients with anterior circulation ischaemic stroke treated with endovascular thrombectomy versus medical therapy: a meta-analysis of individual patient-level data.** *Lancet Neurol* 2019;18:46–55 CrossRef Medline
4. Vagal A, Wintermark M, Nael K, et al. **Automated CT perfusion imaging for acute ischemic stroke: pearls and pitfalls for real-world use.** *Neurology* 2019;93:888–98 CrossRef Medline
5. Heit JJ, Wintermark M. **Perfusion computed tomography for the evaluation of acute ischemic stroke: strengths and pitfalls.** *Stroke* 2016;47:1153–58 CrossRef Medline
6. Powers WJ, Rabinstein AA, Ackerson T, et al; American Heart Association Stroke Council. **American Heart Association Stroke Council: 2018 Guidelines for the Early Management of Patients with Acute Ischemic Stroke—A Guideline for Healthcare Professionals From the American Heart Association/American Stroke Association.** *Stroke* 2018;49:e46–110 CrossRef Medline
7. Mangla R, Ekhom S, Jahromi BS, et al. **CT perfusion in acute stroke: know the mimics, potential pitfalls, artifacts, and technical errors.** *Emerg Radiol* 2014;21:49–65 CrossRef Medline
8. Gugger JJ, Llinas RH, Kaplan PW. **The role of CT perfusion in the evaluation of seizures, the post-ictal state, and status epilepticus.** *Epilepsy Res* 2020;159:106256 CrossRef Medline
9. Granato A, D'Acunto L, Ajčević M, et al. **A novel computed tomography perfusion-based quantitative tool for evaluation of perfusional abnormalities in migrainous aura stroke mimic.** *Neurol Sci* 2020;41:3321–28 CrossRef Medline
10. Wendt M, Tütüncü S, Fiebach JB, et al. **Preclusion of ischemic stroke patients from intravenous tissue plasminogen activator treatment for mild symptoms should not be based on low National Institutes of Health Stroke Scale scores.** *J Stroke Cerebrovasc Dis* 2013;22:550–53 CrossRef Medline
11. Brown SC, Falcone GJ, Hebert RM, et al. **Stenting for acute carotid artery dissection.** *Stroke* 2020;51:e3–e6 CrossRef Medline
12. Amukotuwa SA, Wu A, Zhou K, et al. **Tmax improves diagnostic performance for detecting distal vessel occlusions on CT angiography.** *AJNR Am J Neuroradiol* 2020;42:65–72 CrossRef
13. Saver JL, Chapot R, Agid R, et al; Distal Thrombectomy Summit Group. **Thrombectomy for distal, medium vessel occlusions: a consensus statement on present knowledge and promising directions.** *Stroke* 2020;51:2872–84 CrossRef Medline
14. Biesbroek JM, Niesten JM, Dankbaar JW, et al. **Diagnostic accuracy of CT perfusion imaging for detecting acute ischemic stroke: a systematic review and meta-analysis.** *Cerebrovasc Dis* 2013;35:493–501 CrossRef Medline
15. Sotoudeh H, Bag AK, Brooks MD. **"Code-Stroke" CT perfusion: challenges and pitfalls.** *Acad Radiol* 2019;26:1565–79 CrossRef Medline

J. Molad
Department of Stroke and Neurology
Tel-Aviv Sourasky Medical Center
Tel-Aviv, Israel

http://dx.doi.org/10.3174/ajnr.A6969

Impacts of Glycemic Control on Intracranial Plaque in Patients with Type 2 Diabetes Mellitus: A Vessel Wall MRI Study

S. Jiao, J. Huang, Y. Chen, Y. Song, T. Gong, J. Lu, T. Guo, J. Zhang, C. Zhang, and M. Chen

ABSTRACT

BACKGROUND AND PURPOSE: The relationship between glycemic control in patients with type 2 diabetes mellitus and intracranial atherosclerotic plaque features has remained understudied. This study aimed to investigate the association of type 2 diabetes mellitus and glycemic control with the characteristics of intracranial plaques using vessel wall MR imaging.

MATERIALS AND METHODS: In total, 311 patients (217 [69.8%] men; mean age, 63.24 ± 11.44 years) with intracranial atherosclerotic plaques detected on vessel wall MR imaging were enrolled and divided into 3 groups according to type 2 diabetes mellitus and glycemic control statuses: the non-type 2 diabetes mellitus group, the type 2 diabetes mellitus with good glycemic control group, and the type 2 diabetes mellitus with poor glycemic control group. The imaging features of intracranial plaque were analyzed and compared among the groups. The clinical risk factors for atherosclerosis were also analyzed using logistic regression analysis.

RESULTS: The plaque length and thickness were significantly higher in the type 2 diabetes mellitus with poor glycemic control group than in the non-type 2 diabetes mellitus group. The prevalence of strongly enhanced plaques was significantly higher in the type 2 diabetes mellitus with poor glycemic control group than in the non-type 2 diabetes mellitus and type 2 diabetes mellitus with good glycemic control groups (92.9%, 63.4%, and 72.7%, respectively; $P < .001$). Multivariate logistic regression analysis showed a significant association of poor glycemic control with the plaque length (OR = 1.966; 95% CI, 1.170–3.303; $P = .011$), plaque thickness (OR = 1.981; 95% CI, 1.174–3.340; $P = .010$), and strongly enhanced plaque (OR = 5.448; 95% CI, 2.385–12.444; $P < .001$).

CONCLUSIONS: Poor glycemic control, compared with the history of diabetes, might have a greater impact on the burden and vulnerability of intracranial atherosclerotic plaques.

ABBREVIATIONS: ICAS = intracranial atherosclerosis; HbA1c = hemoglobin A1c; NDM = non-T2DM; T2DM = type 2 diabetes mellitus; VW = vessel wall

Type 2 diabetes mellitus (T2DM) is a highly prevalent disease associated with an increased risk of coronary artery disease, peripheral artery disease, and cerebrovascular disease, which are major causes of mortality.[1] Diabetes alters the function of multiple cell types, including the endothelium, smooth muscle cells, and platelets, thus contributing to atherosclerosis and its complications.[2-4] Diabetes also increases the breakdown and decreases the synthesis of collagen, so that the stability of the plaque fibrous cap may decrease and the plaques may rupture more readily.[4]

The association between glycemic control and extracranial atherosclerosis in patients with T2DM has been extensively investigated.[5-7] Patients with T2DM or poor glycemic control have a predisposition to a higher burden and vulnerability of extracranial atherosclerotic disease. Compared with the extracranial arteries, intracranial arteries exhibit different histologic features, including denser internal elastic lamina, thinner media, less abundant adventitia, only a few elastic fibers, without an external elastic lamina.[8,9] These unique histologic structures of the intracranial arteries may lead to different characteristics of intracranial atherosclerosis (ICAS) compared with extracranial atherosclerosis. However, few studies have analyzed the association between glycemic control and the properties of intracranial atherosclerotic plaques in patients with T2DM.

In recent years, high-resolution vessel wall (VW) MR imaging has been used to demonstrate the characteristics of intracranial

Received June 16, 2020; accepted after revision August 27.

From the Departments of Radiology (S.J., J.H., Y.S., T. Guo, J.Z., C.Z., M.C.), Neurology (Y.C., T.Gong), and Neurosurgery (J.L.), Beijing Hospital, National Center of Gerontology, Institute of Geriatric Medicine, Chinese Academy of Medical Sciences, P.R. China, Beijing, China.

This study was supported by the Capital's Funds for Health Improvement and Research, grant No. CFH 2020-2-4052.

Please address correspondence to Yan Song, MD, Department of Radiology, Beijing Hospital, National Center of Gerontology, Institute of Geriatric Medicine, Chinese Academy of Medical Sciences, P.R. China. No. 1 Dahua Rd, Dong Dan, Beijing, 100730, P.R. China; e-mail: firesong@sina.com

http://dx.doi.org/10.3174/ajnr.A6878

plaques, including plaque morphology, plaque components, and inflammation.[10] In this study, the association between glycemic control and characteristics of intracranial atherosclerotic plaques in patients with T2DM was investigated by imaging plaques with VW MR imaging. The risk factors for the heavy burden and vulnerability of intracranial atherosclerotic plaques in patients with T2DM were also investigated. The findings of this study provided novel insights into the role of glycemic control status of patients with T2DM in the progression of ICAS, which, in turn, provided necessary information to educate patients about the importance of glycemic control.

MATERIALS AND METHODS

Patients

The records of patients with cerebrovascular symptoms who underwent VW MR imaging between December 2017 and July 2019 were retrospectively reviewed. The inclusion criteria were as follows: 1) VW MR imaging performed within 2 weeks of symptom onset; and 2) at least 1 intracranial atherosclerotic plaque identified on VW MR imaging. The exclusion criteria were as follows: 1) nonatherosclerotic intracranial artery stenosis diseases, such as Moyamoya disease, artery dissection, or vasculitis; 2) autoimmune diseases or systemic/local infectious diseases; 3) extracranial carotid artery stenosis ≥50%; 4) evidence of cardiac sources of emboli; 5) incomplete clinical record; and 6) poor image quality. This study was approved by the ethics committee of Beijing Hospital and was performed in accordance with the 1964 Declaration of Helsinki and its later amendments or comparable ethical standards. Informed consent of patients for this retrospective study was waived.

We obtained the following data on clinical characteristics from electronic medical records: age, sex, body mass index, smoking status (current smokers or time interval since abstinence being <5 years), hypertension (systolic blood pressure ≥ 140 mm Hg and/or diastolic blood pressure ≥ 90 mm Hg or current use of antihypertensive agents), grade of hypertension (grade 1, systolic blood pressure = 140–159 mm Hg and/or diastolic blood pressure = 90–99 mm Hg; and grade 2, systolic blood pressure ≥160 mm Hg and/or diastolic blood pressure ≥100 mm Hg), blood pressure uncontrolled (systolic blood pressure ≥ 140 mm Hg and/or diastolic blood pressure ≥ 90 mm Hg after treatment), T2DM (fasting glucose ≥ 7.0 mmol/L, random glucose ≥ 11.1 mmol/L, or hemoglobin A1c [HbA1c] ≥ 7%, or use of medication for glycemic control), HbA1c, hyperlipidemia (total cholesterol ≥ 5.18 mmol/L, triglycerides ≥ 1.7 mmol/L, low-density lipoprotein cholesterol ≥ 3.37 mmol/L, high-density lipoprotein cholesterol < 1.04 mmol/L, or use of lipid-lowering medication), total cholesterol, low-density lipoprotein cholesterol, high-density lipoprotein cholesterol, triglycerides, low-density lipoprotein cholesterol/high-density lipoprotein cholesterol ratio, history of coronary artery disease, and a family history of cardiovascular disease.

Good glycemic control was defined as an HbA1c level of <7.0%, and poor glycemic control was defined as an HbA1c level of ≥7.0%.[11] All enrolled patients were categorized into one of the following 3 groups according to the T2DM history and HbA1c level: 1) NDM group: patients without T2DM; 2) the T2DM with good glycemic control group; and 3) the T2DM with poor glycemic control group.

MR Imaging Protocol

All patients underwent MR imaging using an Achieva TX 3T MR imaging scanner (Philips Healthcare) with a 16-channel neurovascular coil. VW MR images were acquired using a T1-weighted sequence (volume isotropic turbo spin-echo acquisition) before and after contrast agent injection using the following parameters: TR = 800 ms, TE = 18 ms, FOV = $200 \times 180 \times 40\ mm^3$, voxel size = $0.6 \times 0.6 \times 0.6\ mm^3$, and acquisition time = 6 minutes 28 seconds. Postcontrast T1WI was performed 5 minutes after the injection of a single-dose (0.1 = mmol/kg of body weight) gadolinium-based contrast agent (gadopentetate dimeglumine, Magnevist; Bayer HealthCare Pharmaceuticals). Imaging parameters for TOF-MRA were as follows: TR = 25 ms, TE = 3.45 ms, FOV = $180 \times 180\ mm^2$, voxel size = $0.55 \times 0.55 \times 1.1\ mm^3$, and acquisition time = 3 minutes 34 seconds.

Image Analysis

All the VW MR images were transferred to a PACS workstation. The image quality was evaluated using a 3-point scale: grade 0, outer boundary of the artery and lumen not identifiable; grade I, outer boundary and/or lumen is partially obscured; and grade II, wall architecture depicted in detail and lumen and outer boundary clearly defined. A senior neuroradiologist with 12 years of experience (S.J.) assessed all the VW MR images. Only patients with grade II image quality were enrolled in this study. Because of the small size of the intracranial artery, the analysis of the plaque mainly focused on the proximal arteries, including cavernous (C4) to communicating (C7) segments of the internal carotid artery, A1 and A2 segments of the anterior cerebral artery, M1 and M2 segments of the middle cerebral artery, the basilar artery, V4 segment of the vertebral arteries, and P1 and P2 segments of the posterior cerebral artery.

The plaque length, plaque thickness, strength of plaque enhancement, and degree of luminal stenosis were analyzed with the following steps: With the multiplanar reformations tool in the PACS, the T1-weighted images were reconstructed in both long and short axes according to the orientation of the vessels at the site of the maximum stenosis. Intracranial atherosclerotic plaque was defined as eccentric wall thickening with or without luminal stenosis identified on both the reconstructed pre- and postcontrast T1-weighted images. The plaque length, plaque thickness, and luminal stenosis were measured 3 times by a senior neuroradiologist with 12 years of experience (S.J.) who was blinded to the clinical information at the site of the most stenotic lesion on reconstructed postcontrast T1-weighted images of each patient, and the values were then averaged. The degree of luminal stenosis was evaluated according to the Warfarin-Aspirin Symptomatic Intracranial Disease Study.[12] Severe stenosis was defined as the degree of luminal stenosis of ≥70%. The strength of plaque enhancement was compared with that of the pituitary parenchyma and was determined qualitatively on the postcontrast T1-weighted images as strong or not strong. If the plaque enhancement was equal to the pituitary enhancement, it was deemed strong; if the enhancement was less than the pituitary

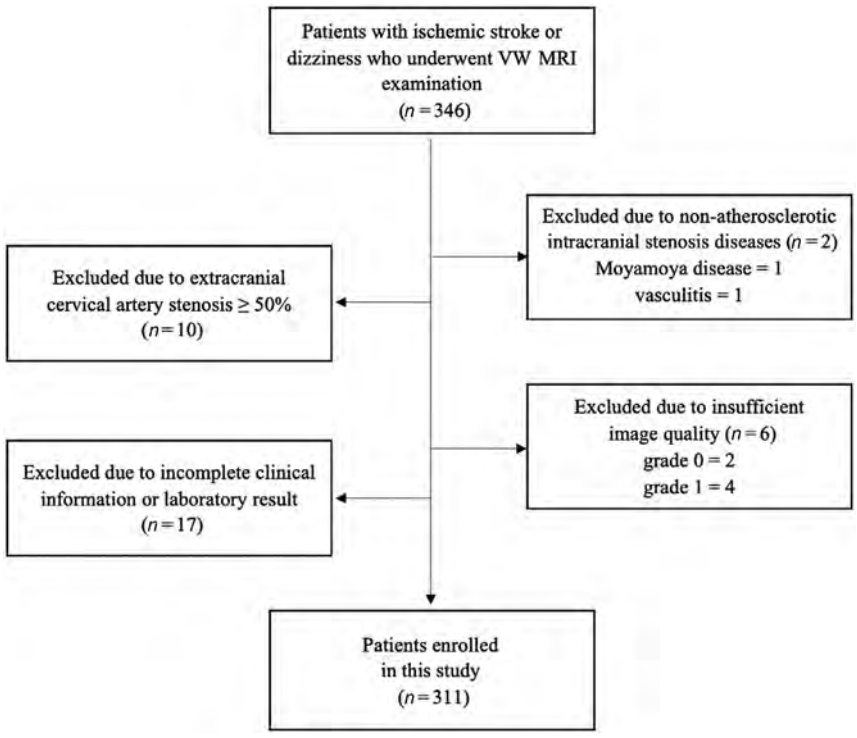

FIG 1. Flow diagram of study identification.

enhancement or showed no change compared with the precontrast images, it was deemed not strong.[13] The strength of plaque enhancement was independently determined by 2 experienced neuroradiologists (S.J. and J.H.) with >10 years of experience who were blinded to the clinical data, and all disagreements were resolved by consensus.

Statistical Analysis

All continuous variables conforming to normal distribution were expressed as means ± SD, the continuous variables with nonnormal distribution were described as median (25th–75th percentiles), and categoric variables were summarized as count and percentage. The characteristics of plaques were compared among the 3 groups using the 1-way ANOVA or Kruskal-Wallis test for continuous variables as appropriate and the χ^2 test for categoric variables. Univariate and multivariate logistic regression analyses were performed to determine the independent risk factors for the heavy burden and vulnerability of intracranial atherosclerotic plaques. The plaque length, thickness at the median value, and luminal stenosis degree at 70% were dichotomized to investigate the risk factors for the heavy burden (plaque length, plaque thickness, and luminal stenosis degree) and vulnerability (strong enhancement) of intracranial atherosclerotic plaques.

The clinical data were also dichotomized for statistical analysis, including age (65 years or older versus younger than 65 years), sex (male), hypertension (≥140/90 mm Hg versus <140/90 mm Hg), HbA1c (≥7% versus <7%), high total cholesterol level (≥5.18 mmol/L), high triglyceride level (≥1.7 mmol/L), high low-density lipoprotein cholesterol (≥3.37 mmol/L), and low high-density lipoprotein cholesterol level (<1.04 mmol/L). Intrareader agreement in the measurement of plaque burden was performed by intraclass correlation coefficient analysis, and interreader agreement in the identification of plaque enhancement was assessed by Cohen κ analysis. All statistical analyses were performed using SPSS 25.0 (IBM). A P value < .05 was considered statistically significant.

RESULTS

Clinical Characteristics

In total, 311 patients (217 [69.8%] men; mean age, 63.24 ± 11.44 years) were enrolled in this study. A flow diagram summarizing the exclusion information is shown in Fig 1. Among all 311 patients, 281 (90.4%) patients were diagnosed with ischemic stroke (162 patients positive for infarction on DWI, 119 patients with TIA), and the other 30 (9.6%) patients had dizziness. Of the 311 patients, 139 (44.69%) had T2DM and 172 (55.31%) did not have T2DM. Of the 139 patients with T2DM, 55 (39.57%) had good glycemic control and 84 (60.43%) had poor glycemic control. The duration of T2DM was from 2 months to 30 years, with an average duration of 8.5 years, 95 (68.35%) patients took oral medication, 32 (23.02%) patients were on insulin therapy, and 12 (8.63%) patients did not have any regular treatment. The clinical characteristics of the NDM, T2DM with good glycemic control, and T2DM with poor glycemic control groups are presented in Table 1. Compared with the NDM group, the T2DM with poor glycemic control group had a significantly lower high-density lipoprotein cholesterol level (0.92 mmol/L [interquartile range, 0.76–1.09 mmol/L] versus 1.00 mmol/L [interquartile range, 0.89–1.15 mmol/L], $P < .05$). No significant difference was found in the proportion of patients with hypertension, the grade of hypertension, or patients with uncontrolled blood pressure after treatment among the 3 groups. No significant differences were observed among the groups for other clinical parameters.

Plaque Characteristics among NDM, T2DM with Good Glycemic Control, and T2DM with Poor Glycemic Control Groups

The mean plaque length and thickness in all 311 patients were 6.72 and 1.80 mm, respectively. The plaques were significantly longer (6.45 mm [interquartile range, 4.63–10.95 mm] versus 4.90 mm [interquartile range, 3.43–7.58 mm], $P < .001$) and thicker (1.80 mm [interquartile range, 1.40–2.38 mm] versus 1.40 mm [interquartile range, 1.10–2.18 mm], $P = .005$), and the luminal stenosis was significantly greater (66.67% [interquartile range, 34.47%–80.15%] versus 38.52% [interquartile range, 16.67%–72.67%], $P < .001$) in the T2DM with poor glycemic control group than in the NDM group.

Of the 311 patients, plaques in 227 patients (72.99%) were strongly enhanced. The prevalence of strongly enhanced plaques

Table 1: Clinical characteristics among NDM, DMGGC, and DMPGC groups[a]

	NDM Group (n = 172)	DMGGC Group (n = 55)	DMPGC Group (n = 84)	χ^2/F	P Value
Male (No.) (%)	117 (68.02)	44 (80)	56 (66.67)	3.362	.186
Age (yr)	62.44 ± 11.87	63.71 ± 9.90	64.60 ± 11.47	1.061	.347
BMI (Kg/m^2)	25.66 ± 3.37	25.60 ± 3.00	25.50 ± 3.37	0.066	.936
Smoking (No.) (%)	73 (42.44)	19 (34.55)	36 (42.86)	1.210	.546
Hypertension (No.) (%)	129 (75)	48 (87.28)	69 (82.14)	4.441	.109
Grade 1 hypertension (No.) (%)	90 (69.77)	37 (77.08)	52 (75.36)	1.271	.530
Grade 2 hypertension (No.) (%)	39 (30.23)	11 (22.92)	17 (24.64)		
BP uncontrolled (No.) (%)	84 (65.12)	36 (75)	50 (72.5)	2.107	.349
History of CAD (No.) (%)	25 (14.53)	15 (27.27)	17 (20.24)	4.798	.091
Family history of CVD (No.) (%)	22 (12.79)	5 (9.09)	9 (10.71)	0.641	.726
Hyperlipemia (No.) (%)	111 (64.53)	37 (67.27)	47 (55.95)	2.375	.305
Total cholesterol (mmol/L)	3.81 (3.10–4.70)	3.24 (2.94–4.48)	3.35 (2.96–4.22)	5.946	.051
LDL (mmol/L)	2.22 (1.67–2.93)	1.81 (1.48–2.81)	2.07 (1.58–2.63)	4.918	.086
HDL (mmol/L)	1.00 (0.89–1.15)[b]	0.99 (0.87–1.19)	0.92 (0.76–1.09)[b]	9.796	.008
Triglycerides (mmol/L)	1.37 (0.97–1.93)	1.16 (0.90–1.82)	1.32 (0.96–1.82)	1.749	.417
LDL/HDL ratio	2.12 (1.64–2.93)	1.81 (1.53–2.40)	2.21 (1.77–2.87)	4.565	.102

Note:—DMGGC indicates T2DM with good glycemic control; DMPGC, T2DM with poor glycemic control; BMI, body mass index; LDL, low-density lipoprotein cholesterol; HDL, high-density lipoprotein cholesterol; CAD, coronary artery disease; CVD, cardiovascular disease; BP, blood pressure.

[a] Continuous variables with normal distribution are presented as means ± SD; continuous variables with non-normal distribution are presented as median (25th–75th percentiles); and categoric variables are presented as (No.) (%).

[b] P value < .05.

Table 2: The characteristics of intracranial plaque among NDM, DMGGC, and DMPGC groups[a]

	NDM Group (n = 172)	DMGGC Group (n = 55)	DMPGC Group (n = 84)	χ^2	P Value
Plaque length (mm)	4.90 (3.43–7.58)[b]	6.10 (3.70–8.00)	6.45 (4.63–10.95)[b]	19.086	<.001
Plaque thickness (mm)	1.40 (1.10–2.18)[b]	1.60 (1.20–2.20)	1.80 (1.40–2.38)[b]	10.043	.005
Lumen stenosis (%)	38.52 (16.67–72.67)[b]	54.83 (39.29–72.41)	66.67 (34.47–80.15)[b]	17.757	<.001
Strong enhancement (No.) (%)	109 (63.37)	40 (72.73)		1.617	.203
	109 (63.37)[b]		78 (92.86)[b]	24.921	<.001
		40 (72.73)[b]	78 (92.86)[b]	10.501	.001

Note:—DMGGC indicates T2DM with good glycemic control; DMPGC, T2DM with poor glycemic control.

[a] Continuous variables with non-normal distribution are presented as median (25th–75th percentiles); categoric variables are presented as (No.) (%).

[b] P value < .05.

was significantly higher in the T2DM with poor glycemic control group (92.9%) than in the NDM (63.4%) and T2DM with good glycemic control (72.7%) groups (P < .001). Although the prevalence of strongly enhanced plaques was higher in the T2DM with good glycemic control group than in the NDM group, no significant difference was observed.

The characteristics of intracranial plaques (plaque length, plaque thickness, luminal stenosis, and plaque enhancement) among the NDM, T2DM with good glycemic control, and T2DM with poor glycemic control groups are presented in Table 2. The representative cases with strongly enhanced plaque are presented in Fig 2.

Risk Factors for the Heavy Burden and Vulnerability of Intracranial Atherosclerotic Plaques

In univariate logistic regression analysis, male sex and poor glycemic control were significantly associated with plaque length (OR = 1.789; 95% CI, 1.095–2.924; P = .020; and OR= 1.888, 95% CI, 1.132–3.150; P = .015, respectively), low high-density lipoprotein cholesterol and poor glycemic control were significantly associated with plaque thickness (OR = 1.833; 95% CI, 1.168–2.876; P = .008; and OR = 2.091; 95% CI, 1.247–3.50; P = .005, respectively), poor glycemic control was significantly associated with severe luminal stenosis (OR = 1.962; 95% CI, 1.169–3.294; P = .011), and low high-density lipoprotein cholesterol and poor glycemic control were significantly associated with strong enhancement of intracranial plaques (OR = 2.213; 95% CI, 1.329–3.685; P = .002; and OR = 5.758; 95% CI, 2.534–13.085; P <.001, respectively).

The multivariate logistic regression analysis showed that poor glycemic control was an independent risk factor for plaque length, plaque thickness, severe luminal stenosis, and strong enhancement of intracranial plaque (OR = 1.966; 95% CI, 1.170–3.303; P = .011; OR = 1.981, 95% CI, 1.174–3.340; P = .010; OR = 1.962; 95% CI, 1.169–3.294; P = .011; and OR = 5.448; 95% CI, 2.385–12.444; P <.001 for plaque length, plaque thickness, severe luminal stenosis, and strong enhancement, respectively) after adjustment for age, hypertension, smoking, history of coronary heart disease, and family history of cardiovascular disease. In addition, male sex was significantly associated with plaque length (OR = 1.864; 95% CI, 1.132–3.068; P = .014), and low high-density lipoprotein cholesterol was significantly associated with plaque thickness (OR = 1.739, 95% CI, 1.102–2.745; P = .017) and strong enhancement of intracranial plaques (OR = 2.046; 95% CI, 1.208–3.465; P = .008). The results of univariate and multivariate logistic regression analyses are presented in Table 3.

Intraobserver and Interobserver Reliability for Measurement

The intraobserver reliability was good for the measurement of plaque length (intraclass correlation coefficient = 0.821; 95% CI, 0.645–0.931; P <.001; plaque thickness (intraclass correlation

coefficient = 0.846, 95% CI, 0.632–0.953; $P < .001$), and luminal stenosis (intraclass correlation coefficient = 0.973; 95% CI, 0.968–0.978; $P < .001$). The interobserver reliability was also high for the evaluation of the strength of plaque enhancement (κ value = 0.856; 95% CI, 0.791–0.921; $P < .001$).

DISCUSSION

The burden and vulnerability of intracranial atherosclerotic plaques are very important parameters when analyzing atherosclerosis due to their strong association with ischemic stroke.[14-16] In the present study, these intracranial plaque features were compared among patients with different diabetes and glycemic control statuses. The patients with T2DM having poor glycemic control tended to have a much heavier plaque burden and more vulnerable plaque. Poor glycemic control was an independent risk factor for intracranial plaque severity based on the multivariable logistic regression analysis. This finding suggested that the glycemic control status might have a greater impact than the history of diabetes on ICAS.

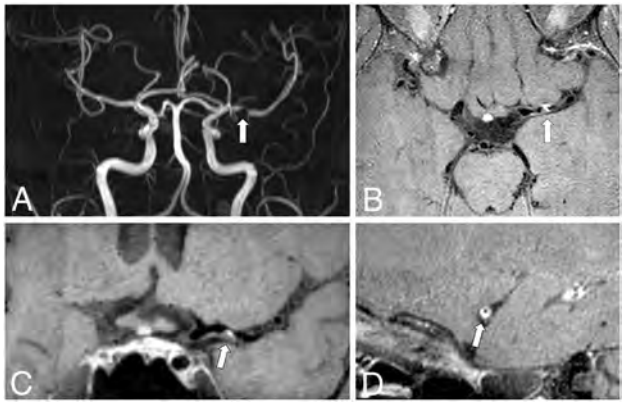

FIG 2. Strong enhancement of plaque in the MCA. *A*, TOF-MRA shows severe stenosis in the M1 segment of the left MCA (*arrow*). *B*, Postcontrast T1-weighted image (axial acquisition) shows wall thickening at the corresponding location (*arrow*). *C*, Reconstructed T1-weighted image shows the length of plaque (*arrow*) in the long axis of the MCA at the site of the most stenotic lesion. *D*, Reconstructed T1-weighted image shows the thickness of plaque (*arrow*) in the short axis of the MCA at the site of the most stenotic lesion.

Previous studies showed that the plaque burden of the extracranial vessels was significantly heavier in patients with T2DM or poor glycemic control than in those without T2DM or with good glycemic control. According to a meta-analysis of 23 studies, including 4019 patients with T2DM and 1110 patients with impaired glucose tolerance among 24,111 patients, the patients with T2DM and impaired glucose tolerance had greater carotid intima-media thickness than the control patients. The mean difference was 0.13 mm (95% CI, 0.12–0.14 mm) and 0.04 mm (95% CI, 0.014–0.071 mm), respectively.[17] The parameters of carotid plaque burden, such as percentage of luminal stenosis, maximum wall thickness, and percentage wall volume, were significantly greater in patients with hypertension with a high HbA1c than in those with a low HbA1c.[18]

The results of the present study were consistent with those of previous studies on extracranial atherosclerosis. The intracranial plaque burden was significantly heavier in patients with T2DM and poor glycemic control than in those without T2DM. Long-term hyperglycemia has been recognized as a major factor in the pathogenesis of atherosclerosis.[19] The results of the present study suggested that although the histologic structure of intracranial arteries was different from that of extracranial arteries, the progression of ICAS was affected by long-term hyperglycemia, consistent with the results on extracranial atherosclerosis. This finding might be because continuous exposure to hyperglycemia induced a series of alterations at the cellular level of vascular tissues, for example, overproduction of reactive oxygen species, increased formation of advanced glycation end-products, and activation of the advanced glycation end-product receptors for advanced glycation end-product axis, polyol and hexosamine flux, protein kinase C activation, and chronic vascular inflammation,[20] which potentially promote accelerated atherosclerosis. However, no significant difference in the intracranial plaque burden was found between patients with T2DM and good glycemic control and those without T2DM. These findings indicated that the long-term glycemic control status might have a greater impact than the history of diabetes on the intracranial plaque burden, and the risk of heavy plaque burden in patients with T2DM and good glycemic control might not be higher than that in those without T2DM.

The plaque enhancement is related to the neovascularity within plaques and the increased endothelial permeability, which

Table 3: Association between risk factors of cardiovascular disease and heavy burden and vulnerability of intracranial plaques

	Univariate Regression			Multivariate Regression[a]		
	OR	95% CI	*P* Value	OR	95% CI	*P* Value
Plaque length						
Male	1.789	1.095–2.924	.020	1.864	1.132–3.068	.014
Poor glycemic control	1.888	1.132–3.150	.015	1.966	1.170–3.303	.011
Plaque thickness						
Low HDL	1.833	1.168–2.876	.008	1.739	1.102–2.745	.017
Poor glycemic control	2.091	1.247–3.507	.005	1.981	1.174–3.340	.010
Severe lumen stenosis						
Poor glycemic control	1.962	1.169–3.294	.011	1.962	1.169–3.294	.011
Strong enhancement						
Low HDL	2.213	1.329–3.685	.002	2.046	1.208–3.465	.008
Poor glycemic control	5.758	2.534–13.085	<.001	5.448	2.385–12.444	<.001

Note:—LDL indicates low-density lipoprotein cholesterol; HDL, high-density lipoprotein cholesterol.
[a] Multivariate logistic regression adjusted for age, smoking, hypertension, history of coronary artery disease, and family history of cardiovascular disease.

facilitate the entry of contrast agents from the blood plasma.[21-24] The strong enhancement of intracranial plaques was reported as an imaging marker of plaque vulnerability, which correlated with recent ischemic stroke.[25-27] Moreno et al[28] demonstrated that coronary artery plaques from patients with diabetes exhibited a larger content of lipid-rich atheroma and macrophage infiltration, suggesting an increased vulnerability compared with those from patients without diabetes. Gao et al[29] reported that patients with diabetes had a significantly higher prevalence of high-risk carotid plaque (29.7% versus 19.9%, $P = .011$) than those without diabetes. In this study, the intracranial plaque vulnerability was compared between different diabetes and glycemic control statuses; a higher prevalence of strongly enhanced plaques was found more often in patients with T2DM and poor glycemic control than in patients with T2DM and good glycemic control and patients without T2DM. This result might be due to the diabetic arterial endothelial dysfunction expressed by increased vascular permeability and vasa vasorum neovascularization related to hyperglycemia.[2] Moreover, no significant difference in the prevalence of strongly enhanced plaques was found between patients without T2DM and those with T2DM and good glycemic control. These findings suggested that the poor glycemic control might have a greater impact than the history of T2DM on the plaque vulnerability, and the risk of plaque vulnerability in patients with T2DM and good glycemic control might not be higher than that in those without T2DM.

This study found an HbA1c value of >7% to be an independent risk factor for the heavy burden and vulnerability of intracranial atherosclerotic plaques based on the multivariate logistic regression analysis. HbA1c was used as a serum biochemical index to estimate the long-term glycemic control, which represented an average blood glucose during the preceding 2–3 months and tracked well in individuals across time.[30] Only a limited number of studies have reported the relationship between glycemic control status and MR imaging morphologic and enhancement parameters of plaques in atherosclerosis. Mukai et al[31] indicated that the multivariable-adjusted odds ratios of the presence of carotid wall thickening significantly increased with elevated HbA1c levels. Sun et al[18] reported a positive association between HbA1c and the presence of a lipid-rich necrotic core in carotid arterial plaques on MR imaging. However, few previous studies showed the impact of poor glycemic control in patients with T2DM on the heavy burden and vulnerability of intracranial atherosclerotic plaques. A recent study by Choi et al[32] showed that poor glycemic control was associated with multiple intracranial stenoses, reflecting the extent and severity of ICAS. The results of the present study were consistent with the findings of Choi et al from a totally new point of view.

The present study has several limitations. First, only the length and thickness of plaques and the prevalence of strongly enhanced plaques were measured. In a future study, the volume of plaque and the degree of plaque enhancement should be measured to quantitatively evaluate the burden and vulnerability of intracranial atherosclerotic plaques more precisely. Second, only the large-to-middle-sized intracranial arteries were assessed in this study due to the small size of the intracranial artery and the limit of the spatial resolution of VW MR imaging. Further investigation on small intracranial arteries should be performed with the improvement in MR imaging. Finally, this was a retrospective cross-sectional study. In the future, prospective longitudinal studies should be conducted to further estimate the changes of intracranial plaques after treating poor glucose control.

CONCLUSIONS

This study showed that the burden and vulnerability of intracranial atherosclerotic plaques were significantly greater in patients with T2DM and poor glycemic control than in those without T2DM, while no significant difference was found between patients without T2DM and those with T2DM and good glycemic control. Poor glycemic control might have a greater impact than the history of diabetes on the burden and vulnerability of intracranial plaques.

Disclosures: Yan Song—*RELATED*: *Grant*: Capital's Funds for Health Improvement and Research, *Comments*: We received this grant with the research topic: Constructing the risk model for predicting acute stroke recurrence: a study with intra- and extracranial artery one-stop vessel wall imaging and artificial intelligence image analysis.

REFERENCES

1. Christen AI, Armentano RL, Miranda A, et al. **Arterial wall structure and dynamics in type 2 diabetes mellitus methodological aspects and pathophysiological findings.** *Curr Diabetes Rev* 2010;6:367–77 CrossRef Medline
2. Moreno PR, Fuster V. **New aspects in the pathogenesis of diabetic atherothrombosis.** *J Am Coll Cardiol* 2004;44:2293–2300 CrossRef Medline
3. Creager MA, Lüscher TF, Cosentino F, et al. **Diabetes and vascular disease: pathophysiology, clinical consequences, and medical therapy, Part I.** *Circulation* 2003;108:1527–32 CrossRef Medline
4. Beckman JA, Creager MA, Libby P. **Diabetes and atherosclerosis: epidemiology, pathophysiology, and management.** *JAMA* 2002;287:2570–81 CrossRef Medline
5. Selvin E, Coresh J, Golden SH, et al; Atherosclerosis Risk in Communities Study. **Glycemic control, atherosclerosis, and risk factors for cardiovascular disease in individuals with diabetes: the Atherosclerosis Risk in Communities Study.** *Diabetes Care* 2005;28:1965–73 CrossRef Medline
6. Yang DJ, Lee MS, Kim WH, et al. **The impact of glucose control on coronary plaque composition in patients with diabetes mellitus.** *J Invasive Cardiol* 2013;25:137–41 Medline
7. Tavares CA, Rassi CH, Fahel MG, et al. **Relationship between glycemic control and coronary artery disease severity, prevalence and plaque characteristics by computed tomography coronary angiography in asymptomatic type 2 diabetic patients.** *Int J Cardiovasc Imaging* 2016;32:1577–85 CrossRef Medline
8. Moossy J. **Morphology, sites and epidemiology of cerebral atherosclerosis.** *Res Publ Assoc Res Nerv Ment Dis* 1966;41:1–22 Medline
9. Velican C. **Studies on the age-related changes occurring in human cerebral arteries.** *Atherosclerosis* 1970;11:509–29 CrossRef Medline
10. Ryu CW, Kwak HS, Jahng GH, et al. **High-resolution MRI of intracranial atherosclerotic disease.** *Neurointervention* 2014;9:9–20 CrossRef Medline
11. American Diabetes Association. **Standards of Medical Care in Diabetes-2019 Abridged for Primary Care Providers.** *Clin Diabetes* 2019;37:11–34 CrossRef Medline
12. Chimowitz MI, Kokkinos J, Strong J, et al. **The Warfarin-Aspirin Symptomatic Intracranial Disease Study.** *Neurology* 1995;45:1488–93 CrossRef Medline
13. Skarpathiotakis M, Mandell DM, Swartz RH, et al. **Intracranial atherosclerotic plaque enhancement in patients with ischemic stroke.** *AJNR Am J Neuroradiol* 2013;34:299–304 CrossRef Medline
14. Li F, Chen QX, Chen ZB, et al. **Magnetic resonance imaging of plaque burden in vascular walls of the middle cerebral artery correlates with cerebral infarction.** *CNR* 2016;13:263–70 CrossRef Medline

15. Ryu CW, Jahng GH, Kim EJ, et al. **High-resolution wall and lumen MRI of the middle cerebral arteries at 3 Tesla.** *Cerebrovasc Dis* 2009;27:433–42 CrossRef Medline
16. Huang J, Jiao S, Zhao X, et al. **Characteristics of patients with enhancing ICAS and association between plaque enhancement and recent cerebrovascular ischemic events: a high-resolution magnetic resonance imaging study.** *Acta Radiol* 2019;60:1301–07 CrossRef Medline
17. Brohall G, Odén A, Fagerberg B. **Carotid artery intima-media thickness in patients with type 2 diabetes mellitus and impaired glucose tolerance: a systematic review.** *Diabet Med* 2006;23:609–16 CrossRef Medline
18. Sun B, Zhao H, Liu X, et al. **Elevated hemoglobin A1c is associated with carotid plaque vulnerability: novel findings from magnetic resonance imaging study in hypertensive stroke patients.** *Sci Rep* 2016;6:33246 CrossRef Medline
19. Aronson D, Rayfield EJ. **How hyperglycemia promotes atherosclerosis: molecular mechanisms.** *Cardiovasc Diabetol* 2002;1:1 CrossRef Medline
20. Katakami N. **Mechanism of development of atherosclerosis and cardiovascular disease in diabetes mellitus.** *J Atheroscler Thromb* 2018;25:27–39 CrossRef Medline
21. O'Brien KD, Allen MD, McDonald TO, et al. **Vascular cell adhesion molecule-1 is expressed in human coronary atherosclerotic plaques. implications for the mode of progression of advanced coronary atherosclerosis.** *J Clin Invest* 1993;92:945–51 CrossRef Medline
22. O'Brien KD, McDonald TO, Chait A, et al. **Neovascular expression of E-selectin, intercellular adhesion molecule-1, and vascular cell adhesion molecule-1 in human atherosclerosis and their relation to intimal leukocyte content.** *Circulation* 1996;93:672–82 CrossRef Medline
23. Moulton KS, Vakili K, Zurakowski D, et al. **Inhibition of plaque neovascularization reduces macrophage accumulation and progression of advanced atherosclerosis.** *Proc Natl Acad Sci U S A* 2003;100:4736–41 CrossRef Medline
24. Celletti FL, Waugh JM, Amabile PG, et al. **Vascular endothelial growth factor enhances atherosclerotic plaque progression.** *Nat Med* 2001;7:425–29 CrossRef Medline
25. Lou X, Ma N, Ma L, et al. **Contrast-enhanced 3T high-resolution MR imaging in symptomatic atherosclerotic basilar artery stenosis.** *AJNR Am J Neuroradiol* 2013;34:513–17 CrossRef Medline
26. Ryu CW, Jahng GH, Shin HS. **Gadolinium enhancement of atherosclerotic plaque in the middle cerebral artery: relation to symptoms and degree of stenosis.** *AJNR Am J Neuroradiol* 2014;35:2306–10 CrossRef Medline
27. Qiao Y, Zeiler SR, Mirbagheri S, et al. **Intracranial plaque enhancement in patients with cerebrovascular events on high-spatial-resolution MR images.** *Radiology* 2014;271:534–42 CrossRef Medline
28. Moreno PR, Murcia AM, Palacios IF, et al. **Coronary composition and macrophage infiltration in atherectomy specimens from patients with diabetes mellitus.** *Circulation* 2000;102:2180–84 CrossRef Medline
29. Gao X, Song J, Watase H, et al; CARE-II Investigators. **Differences in carotid plaques between symptomatic patients with and without diabetes mellitus.** *Arterioscler Thromb Vasc Biol* 2019;39:1234–39 CrossRef Medline
30. Meigs JB, Nathan DM, Cupples LA, et al. **Tracking of glycated hemoglobin in the original cohort of the Framingham Heart Study.** *J Clin Epidemiol* 1996;49:411–17 CrossRef Medline
31. Mukai N, Ninomiya T, Hata J, et al. **Association of hemoglobin A1c and glycated albumin with carotid atherosclerosis in community-dwelling Japanese subjects: the Hisayama Study.** *Cardiovasc Diabetol* 2015;14:24 CrossRef Medline
32. Choi N, Lee JY, Sunwoo JS, et al. **Recently uncontrolled glycemia in diabetic patients is associated with the severity of intracranial atherosclerosis.** *J Stroke Cerebrovasc Dis* 2017;26:2615–21 CrossRef Medline

Radiation-Induced Imaging Changes and Cerebral Edema following Stereotactic Radiosurgery for Brain AVMs

B.J. Daou, G. Palmateer, D.A. Wilkinson, B.G. Thompson, C.O. Maher, N. Chaudhary, J.J. Gemmete, J.A. Hayman, K. Lam, D.R. Wahl, M. Kim, and A.S. Pandey

ABSTRACT

BACKGROUND AND PURPOSE: T2 signal and FLAIR changes in patients undergoing stereotactic radiosurgery for brain AVMs may occur posttreatment and could result in adverse radiation effects. We aimed to evaluate outcomes in patients with these imaging changes, the frequency and degree of this response, and factors associated with it.

MATERIALS AND METHODS: Through this retrospective cohort study, consecutive patients treated with stereotactic radiosurgery for brain AVMs who had at least 1 year of follow-up MR imaging were identified. Logistic regression analysis was used to evaluate predictors of outcomes.

RESULTS: One-hundred-sixty AVMs were treated in 148 patients (mean, 35.6 years of age), including 42 (26.2%) pediatric AVMs. The mean MR imaging follow-up was 56.5 months. The median Spetzler-Martin grade was III. The mean maximal AVM diameter was 2.8 cm, and the mean AVM target volume was 7.4 mL. The median radiation dose was 16.5 Gy. New T2 signal and FLAIR hyperintensity were noted in 40% of AVMs. T2 FLAIR volumes at 3, 6, 12, 18, and 24 months were, respectively, 4.04, 55.47, 56.42, 48.06, and 29.38 mL. Radiation-induced neurologic symptoms were encountered in 34.4%. In patients with radiation-induced imaging changes, 69.2% had new neurologic symptoms versus 9.5% of patients with no imaging changes ($P = .0001$). Imaging changes were significantly associated with new neurologic findings ($P < .001$). Larger AVM maximal diameter ($P = .04$) and the presence of multiple feeding arteries ($P = .01$) were associated with radiation-induced imaging changes.

CONCLUSIONS: Radiation-induced imaging changes are common following linear particle accelerator–based stereotactic radiosurgery for brain AVMs, appear to peak at 12 months, and are significantly associated with new neurologic findings.

ABBREVIATIONS: ARE = adverse radiation effects; LINAC = linear particle accelerator; SRS = stereotactic radiosurgery

Stereotactic radiosurgery (SRS) has become a standard tool for treating brain arteriovenous malformations (AVMs), especially for AVMs in deep or eloquent locations and those with complex angioarchitecture for which surgical treatment and endovascular embolization are more challenging and riskier. AVM obliteration rates of about 80% have been reported with long-term follow-up.[1-3] Radiosurgery, however, results in gradual obliteration of the AVM over several years following treatment. During this time period and until the AVM is obliterated, patients continue to be at risk of intracranial hemorrhage.[4] Patients are routinely followed with brain MRI/MRA during this latency period, with close monitoring for treatment-related adverse effects, including cerebral edema and radiation-induced necrosis. Following SRS, the hemodynamics of the treated AVM are progressively altered, and various degrees of T2 signal and Fluid-attenuated inversion recovery (FLAIR) hyperintensity, suggestive of cerebral edema, have been observed in these patients.[1,5,6] In addition, notable adverse radiation effects (ARE) with new neurologic signs and symptoms may arise, particularly during this time period and may affect patient outcomes.[6]

In this study, we aimed to investigate the characteristics of the T2 signal and FLAIR response on follow-up MRIs in patients undergoing SRS for brain AVMs, evaluate the frequency of these radiation-induced imaging changes, attempt to quantify the degree of T2 signal and FLAIR changes, identify factors associated with this response, and evaluate its impact on patient outcomes.

MATERIALS AND METHODS

Patient Selection

The study protocol was approved by the institutional review board. The informed consent of patients was not required for this

Received April 30, 2020; accepted after revision August 17.

From the Departments of Radiation Oncology (J.A.H., K.L., D.R.W., M.K.), Neurosurgery (B.J.D., G.P., D.A.W., B.G.T., C.O.M., N.C., J.J.G., A.S.P.), Radiology (N.C., J.J.G.), and Radiation Oncology (J.A.H., K.L., D.R.W., M.K.), University of Michigan, Ann Arbor, Michigan.

Please address correspondence to Aditya S. Pandey, MD, Department of Neurosurgery, University of Michigan, 1500 E Medical Center Dr, 3552 Taubman Center, Ann Arbor, MI 48109-5338; e-mail: adityap@med.umich.edu

http://dx.doi.org/10.3174/ajnr.A6880

retrospective review of medical records. A combination of International Classification of Diseases codes for brain AVMs in association with the Current Procedural Terminology code for SRS was used to identify our target population. Electronic medical records were retrospectively reviewed to identify patients with the diagnosis of cerebral AVM treated with SRS during a 28-year period. Our institutional Electronic Medical Record Search Engine data base was used for patient identification and data collection.[7]

All patients with brain AVMs confirmed with diagnostic cerebral angiography and treated with SRS between January 1990 and December 2018 were included in the initial analysis, resulting in 210 patients with 222 treated AVMs. Exclusion criteria were patients who lacked at least 1 year of clinical follow-up as well as MR imaging follow-up ($n = 62$ patients). Patients who were followed clinically but without available brain MRIs that included T2 and T2 FLAIR sequences for analysis were excluded. Post-SRS hemorrhage was encountered after treatment of 10 AVMs in the study population. The hemorrhage was not fatal in 8 patients who continued to get follow-up and was fatal in 1 patient and occurred at 18 months post-SRS. Therefore, these patients were included in the study population. One additional fatal post-SRS hemorrhage was excluded, given that the event occurred at 6 months (did not meet inclusion criteria).

Variables and Outcomes

We evaluated patient age, sex, clinical presentation, treatment time period, AVM maximal diameter, venous drainage, eloquence, previous embolization, the Spetzler-Martin grading scale, AVM location, angioarchitecture of the AVM (including the presence of multiple arterial feeders or multiple draining veins), presence of a venous varix, anatomy of the draining vein (large cortical vein or other), presence of an intranidal aneurysm, delivered radiation dose, nidus volume, and isodose volume, along with clinical, angiographic, and MR imaging follow-up periods.

The primary end points of this study were the following: 1) to evaluate the frequency of radiation-induced imaging changes, 2) quantify the degree of T2 signal and FLAIR changes, 3) identify factors associated with the development of prominent T2 signal and FLAIR changes, and 4) evaluate the impact of these radiologic changes on patient outcomes.

T2 signal and FLAIR hyperintensity were evaluated on brain MR imaging (patients who did not have a brain MR at least at 1 year posttreatment were not included in the analysis). Radiation-induced imaging changes were defined as new areas of increased T2 and FLAIR signal surrounding the treated AVM on follow-up MR imaging. Volumes were calculated using T2 FLAIR axial sequences, through a section-by-section analysis, and the ABC/2 technique to quantify the volume of perinidal T2 FLAIR changes.[8] For each patient, we evaluated all available posttreatment MRIs in a longitudinal fashion. AVM obliteration was determined on diagnostic cerebral angiography and MRI/MRA studies in patients with at least 2 years of imaging follow-up after treatment. All reported new symptoms determined to be related to SRS by the treating team were included under radiation-induced neurologic signs and symptoms.

Procedure Description

Informed consent was obtained for linear particle accelerator (LINAC)-based stereotactic radiosurgery, and options of conservative management and surgical resection were discussed with the patient. Patients were premedicated with an oral narcotic and anxiolytic before frame placement with administration of a local anesthetic at the pin sites. Patients then underwent placement of a Cosman-Roberts-Wells (CRW) frame. With the CRW frame in place, a CT of the head was performed. These images were fused to a previously obtained contrasted thin-section MR imaging of the brain, and the AVM volume was drawn around the nidus. Depending on the location of the AVM relative to radioeloquent structures (brain stem, optic apparatus, and so forth), the radiation oncology and neurosurgery teams developed a plan to allow maximal dose delivery to the nidus while minimizing the dose to radioeloquent regions. A single dose of dexamethasone, 10 mg, was given 1–2 hours before treatment without a taper. Our goal was to deliver 18–20 Gy to the nidus using a LINAC-based system; however, generally, this dose was reduced in cases in which the AVM was located near a radiosensitive structure. In addition, the dose was also commonly reduced for larger volume AVMs. Post-SRS, patients were discharged and were then imaged with brain MRIs with gadolinium at 6- to 12-month intervals.

Statistical Analysis

Data are presented as mean and range for continuous variables and as frequency for categoric variables. Analysis was performed using the unpaired t test and χ^2 and Fisher exact tests as appropriate. Statistical analysis was performed using STATA (StataCorp). Univariate analysis was used to test covariates predictive of the following dependent outcomes: radiation-induced imaging changes and new neurologic signs or symptoms post-SRS. Factors predictive in univariate analysis ($P < .10$) were entered into a backward multivariate logistic regression analysis. P values $\leq .05$ were considered statistically significant.

RESULTS

Baseline Patient Characteristics

One-hundred-sixty AVMs in 148 patients treated with SRS made up the study population. The mean patient age was 35.6 years (range, 3–75 years). Patients 18 years of age or younger had 42 treated AVMs (26.2%). There were 84 AVMs (52.5%) in males and 76 AVMs (47.5%) in females. Eighty-eight AVMs (55%) had ruptured and bled before SRS treatment. Twenty-two AVMs (13.7%) were previously embolized before SRS. The mean clinical follow-up was 61.2 months, the mean MR imaging follow-up was 56.5 months, and the mean angiographic follow-up was 54 months.

AVM and Treatment Characteristics

The locations of the AVMs were as follows: the frontal lobe in 47 patients (29.4%), parietal lobe in 24 patients (15%), temporal lobe in 24 patients (15%), occipital lobe in 21 patients (13.1%), cerebellar in 25 patients (15.6%), brain stem in 6 patients (3.8%), corpus callosum in 5 patients (3.1%), thalamic in 4 patients (2.5%), and basal ganglia in 4 patients (2.5%). The median Spetzler-Martin grade was 3. Thirteen AVMs (8.1%) were classified as

Spetzler-Martin grade I; 42 (26.3%), as grade II; 71 (44.4%), as grade III; 29 (18.1%), as grade IV; and 5 (3.1%), as grade V. The mean maximal AVM diameter was 2.8 cm (range, 0.5–6.3 cm). One hundred thirty-four AVMs (83.8%) were determined to be in an eloquent location. Seventy-one treated AVMs (44.4%) had deep venous drainage. Seventy AVMs (43.8%) had multiple draining veins, and 95 (59.4%) had multiple feeding arteries. A venous varix was present in 13 AVMs (8.1%), and an associated perinidal or intranidal aneurysm, in 23 AVMs (14.4%).

The mean AVM target volume was 7.4 mL, the mean isodose surface volume was 12.5 mL, and the median radiation dose was 16.5 Gy.

Radiation-Induced Imaging Changes

New T2 signal and FLAIR hyperintensity were noted following treatment of 64 AVMs (40%) (Fig 1). We divided the MR imaging observations into 6 time periods following SRS. At 3 months, 13 MRIs were available for analysis, and 7 (53.8%) were positive for imaging changes, with a mean T2 FLAIR volume of 4.04 mL. Thirty-nine patients had MRIs at 6 months, and 28 (71.8%) had imaging changes with a mean T2 FLAIR volume of 55.47 mL; 131 patients had MRIs at 1 year, with 52 patients (39.7%) having radiation changes with a mean T2 FLAIR volume of 56.42 mL; 54 patients had MRIs at 18 months with 25 patients (46.3%) having T2 FLAIR changes with a volume of 48.06 mL; and 93 patients had MRIs at 2 years, 34 of whom (36.6%) had radiation-induced changes with a mean T2 FLAIR volume of 29.38 mL. In addition, in 78 patients with MRIs at >2 years, 29 patients (37.2%) had radiation-induced imaging changes with a mean T2 FLAIR volume of 50.76 mL, reflecting some cases that developed delayed prominent T2 FLAIR signal change. Specifically, new T2 FLAIR signal changes were delayed or worsened >2 years after SRS in 8 cases (5% of the total cases and 12.5% of the cases developing prominent T2 FLAIR signal change posttreatment) (Fig 2).

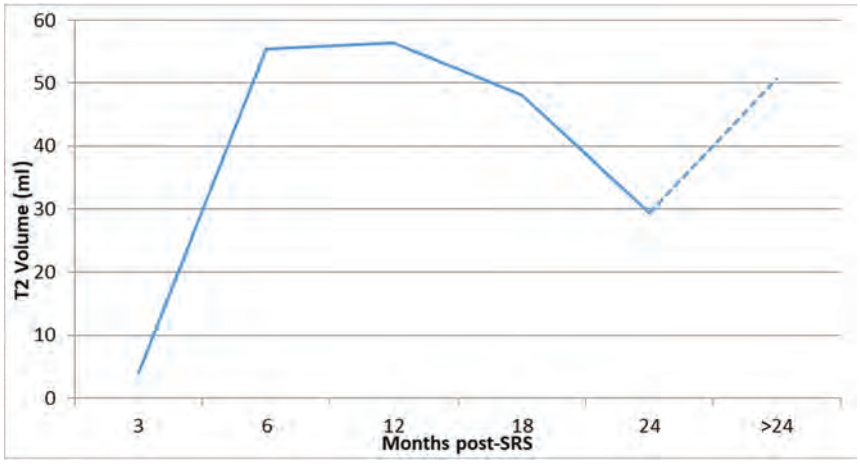

FIG 1. Evolution of radiation-induced imaging changes, with evaluation at 3, 6, 12, 18, 24, and >24 months.

Radiation-Induced Neurologic Signs and Symptoms

New radiation-induced neurologic signs and symptoms were encountered in 55 cases (34.4%). These included headaches following 30 treatments (18.7%), new seizures following 16 treatments (10%), new cognitive deficits in 6 cases (3.7%), a new focal deficit (including motor or cranial nerve deficit) in 10 cases (6.2%), severe nausea/vomiting after 8 treatments (5%), unsteadiness/imbalance in 7 cases (4.4%), transient sensory symptoms in 6 cases (3.7%), and word-finding difficulties in 2 patients (1.2%).

Three patients developed a cyst in the radiated region, and 2 patients developed a cavernoma in the SRS region on follow-up. Cysts were diagnosed at 29, 54, and 62 months post-SRS, and cavernomas, at 9 and 11 years post-SRS. All 5 patients underwent surgical treatment of these acquired lesions, which were symptomatic in all cases. Four of these 5 patients had

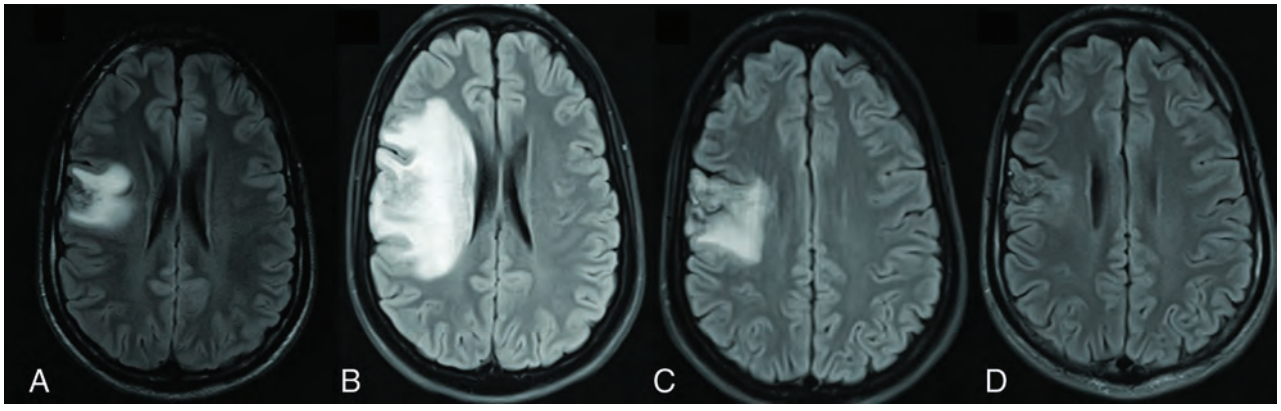

FIG 2. Case illustration of a 17-year-old adolescent boy with a frontal arteriovenous malformation. He developed new seizures 6 months following stereotactic radiosurgery. MR imaging (*A*) shows an area of increased FLAIR signal change. The FLAIR changes increased and peaked at 12 months (*B*). At 18 months (*C*), there were persistent but reduced FLAIR changes, and at 24 months (*D*), these imaging changes had resolved.

developed prominent T2 and FLAIR signal changes early after treatment.

Association of Radiation-Induced Imaging Changes with Outcomes

In patients who developed radiation-induced imaging changes, 45/65 patients (69.2%) had new neurologic signs or symptoms post-SRS. In patients who did not develop imaging changes, 9/95 patients (9.5%) had new neurologic signs or symptoms ($P = .0001$).

One hundred twenty-two patients had 2-year imaging follow-up to assess AVM obliteration. In patients who developed radiation-induced imaging changes, 39/46 patients (84.8%) had complete obliteration of their AVMs and 7/46 patients (15.2%) had incomplete AVM obliteration. In patients who did not develop imaging changes, 55/76 patients (72.4%) had complete AVM obliteration and 21/76 (27.6%) had incomplete AVM obliteration. This difference approached significance with $P = .1$.

Factors Associated with Radiation-Induced Imaging Changes

In univariate and multivariate analyses, Spetzler-Martin grade IV (OR = 7.03; 95% CI, 1.5–32; $P = .012$), larger maximal diameter (OR = 1.3; 95% CI, 1.01–1.67; $P = .04$), and the presence of multiple feeding arteries (OR = 2.4; 95% CI, 1.2–4.7; $P = .01$) were associated with radiation-induced imaging changes.

The occurrence of new neurologic signs and symptoms post-SRS was significantly associated with the presence of radiation-induced imaging changes in both univariate and multivariate analysis (OR = 20; 95% CI, 8.4–47.6; $P < .001$).

Factors Associated with New Neurologic Signs and Symptoms Post-SRS

In univariate analysis, AVMs with multiple feeding arteries (OR = 2.4; 95% CI, 1.2–4.9; $P = .01$ and the presence of radiation-induced imaging changes after SRS (OR = 20; 95% CI, 8.4–47.6; $P < .001$) were associated with new neurologic signs and symptoms post-SRS. In multivariate analysis, only the development of radiation-induced imaging changes was associated with ARE (OR = 19.3; 95% CI, 7.8–47.8; $P < .001$).

DISCUSSION

Rate of Radiation-Induced Imaging Changes

We reviewed our experience with LINAC-based SRS treatment of brain AVMs and report a high rate of radiation-induced imaging changes in the posttreatment period. Forty percent of patients had prominent T2 signal or FLAIR hyperintensity on follow-up MRIs. The reported frequency of these radiologic changes in the literature has been variable, ranging from 16% to 62%.[5] This result is likely related to differences in the interpretation and classification of these findings and variable follow-up times. Lunsford et al[1] reviewed follow-up MRIs for 227 patients and reported increased T2 signal in 24% of patients at a mean interval of 10 months after SRS. In a study that evaluated 107 patients with brain AVMs, in addition to some tumors, Ganz et al[9] reported a 60% incidence of radiation-induced imaging changes. Yen et al[5] evaluated 1426 gamma knife surgery procedures and noted radiation-induced imaging changes in 33.8% of treatments. New T2 signal and FLAIR hyperintensity following SRS are common and are suggestive of a high rate of cerebral edema or radiation necrosis following treatment. Our usual practice involves obtaining MR imaging at 6- to 12-month intervals to evaluate parenchymal and AVM changes posttreatment. The higher rate of radiation-induced imaging changes at 3 and 6 months posttreatment is likely related to patients presenting with symptoms that prompted additional early imaging, therefore resulting in this higher observed rate of imaging changes at 3 and 6 months.

Symptoms Related to Radiation-Induced Imaging Changes

Despite the high rate of imaging changes, the rate of symptomatic ARE is reported to be much lower, ranging from 3.7% to 10.8%, with only a very small number of patients having permanent deficits.[5] Radiation-induced imaging changes were commonly found with new neurologic signs or symptoms following SRS in the present study. This finding is in contrast to that of Lunsford et al,[1] reporting that 6% of patients who developed radiologic changes were symptomatic and only 1% had permanent treatment-related deficits.

In a meta-analysis by Ilyas et al[10] on radiation-induced changes following SRS for brain AVMs, the rates of radiologic, symptomatic, and permanent changes were noted to be 35.5% (1143/3222 patients), 9.2% (499/5447 patients), and 3.8% (202/5272 patients), respectively. They concluded that approximately 1 in 4 patients who develop radiologic changes will become symptomatic. Yen et al[5] reported that 8.6% of patients with imaging changes developed neurologic symptoms and 1.8% had permanent deficits. Our analysis shows that the presence of radiation-induced imaging changes is associated with a higher rate of neurologic symptoms than previously reported (69.2% versus 9.5% in patients without imaging changes, $P = .0001$). We agree that these changes result in temporary symptoms in most patients, and permanent symptoms are uncommon. Furthermore, the volume of the new T2 signal change posttreatment varied greatly, very likely affecting the development and severity of symptoms. The developing response on MR imaging reflects underlying edema or radiation necrosis that could result in a significant mass effect, midline shift, and sometimes hydrocephalus.

Proposed Mechanisms Leading to Radiation-Induced Imaging Changes

The mechanisms behind these T2 and FLAIR changes are not completely understood but are thought to be related to either the direct effects of the radiation treatment on the treated tissue or a vascular/hemodynamic phenomenon resulting in edema or potentially radiation necrosis.[5,11,12] Mechanisms in which radiation results in these findings through direct tissue damage include injury of glial cells, endothelial cell damage followed by breakdown of the blood-brain barrier, excessive generation of free radicals, and the induction of an autoimmune response.[5,13,14] Vascular mechanisms inducing imaging changes were first suggested by Pollock[15] and Chapman et al,[16] who proposed the concept of occlusive hyperemia, in which local hemodynamic changes can occur if venous outflow is obstructed, with resultant stasis of the blood flow and clot formation in the draining veins.

Factors Associated with Radiation-Induced Imaging Changes

Kano et al[11] analyzed 755 patients undergoing SRS therapy, examining risk factors for adverse events after radiosurgery, and found that the risk of symptomatic ARE increased with larger AVM volume, higher margin dose, a higher Spetzler-Martin grade, and a higher radiosurgery-based score. They also noted that patients with AVMs located in the brain stem (22%)/thalamus (16%) versus other locations (4%–8%) were more likely to develop symptomatic ARE.[11] Cohen-Inbar et al[6] examined radiographic changes following gamma knife surgery for AVMs and reported that the radiographic presence of ARE (specifically the ratio of T2 change to nidus volume, or the ARE index) was predicted by nidus volume, deep location, and multiple draining veins. Yen et al[5] reported a negative history of prior surgery or prior hemorrhage, large nidus, and a single draining vein to be associated with a higher risk of radiation-induced imaging changes. A study from van den Berg et al[17] also reported that nidi with single draining veins were more common in the group of patients with extensive imaging changes than in the those with mild or no imaging changes. Overall, several factors have been reported to be associated with radiation-induced imaging changes, including patient age, AVM size and volume, high-grade AVMs, SRS dose, prior embolization, prior hemorrhage, number of draining veins, and AVM location.[5,6,10,11]

In our analysis, patients with larger AVMs and AVMs with multiple feeding arteries had higher odds of radiation-induced imaging changes. Even though the edema response is thought to be primarily of venous origin, we argue that occlusion of several arterial branches could worsen this phenomenon by increasing the associated arterial injury/thrombosis and worsening the associated ischemic insult with resultant edema adjacent to the nidus.

Radiation-Induced Imaging Changes and AVM Obliteration

Not only do radiation-induced imaging changes predict ARE, but they are further thought to represent a precursor to AVM obliteration, given similar underlying pathophysiologic mechanisms dictating both processes. In our study, AVM obliteration was achieved in 84.8% of nidi with surrounding edema versus 72.4% in patients without this response, with the association approaching significance ($P = .1$). Yen et al[5] reported that 62.8% of AVMs that developed radiation-induced imaging changes were completely obliterated versus 52.1% of AVMs without imaging changes ($P < .001$). They also added that treatment that resulted in extensive imaging findings was more likely to result in AVM obliteration compared with treatment with mild changes. A similar observation was reported by van den Berg et al.[17] They reported an AVM obliteration rate of 88% in patients with extensive radiation-induced imaging changes compared with 50% in patients without extensive signal changes on MR imaging following SRS. The edema response could be related to the AVM obliteration process in which there is premature thrombosis of a draining vein or early occlusion of a feeding artery.

Timing of Radiation-Induced Imaging Changes

Radiation-induced imaging changes appear to peak at 12 months after treatment. This response continues to be present in most patients who develop these imaging changes at 18 months. However, the response is not uniform and could appear a few months after treatment or >1–2 years after SRS. Yen et al[5] reported a median duration of 13 months from SRS to the development of radiation-induced imaging changes, with a range of 2–124 months. The imaging changes disappeared completely within a median duration of 22 months from their identification. Another study reported that the development of radiation-induced imaging changes follows a temporal pattern, peaking at 7–12 months after SRS.[6] They also added that if these imaging findings peak at 7–12 months post-SRS, AVMs have higher odds of complete obliteration.

We did observe another late peak in T2 signal and FLAIR hyperintensity >2 years from treatment in some patients. Cohen-Inbar et al[6] also observed late ARE (appearing at >1 year of follow-up) and attributed those late changes to the direct tissue effects of radiation and to an inflammatory process as opposed to a vascular process that could be related to earlier imaging changes. In addition, radiation-induced imaging changes have also been associated with late complications after SRS, such as cyst formation and late-onset edema through a continued inflammatory process.[10,18] In our study, 3 patients developed a cyst and 2 patients developed a cavernoma, all requiring surgical treatment. Patients who develop radiation-induced imaging changes may require longer clinical and radiologic follow-up.

Management of Symptomatic Radiation-Induced Imaging Changes

Patients with radiation-induced imaging changes who were symptomatic were treated with an oral regimen of steroids, typically dexamethasone. Patients with severe radiation-induced imaging changes and acute neurologic decline were admitted to the hospital with initiation of intravenous steroids and close neurologic monitoring. Some patients who develop large volumes of T2 or FLAIR signal change could be dependent on steroids for several months, with the potential for worsening if steroids are weaned too quickly. Asymptomatic patients or patients with minimal symptoms should still be considered for medical management if they have extensive imaging changes. The course of steroids was variable and related to the symptoms and imaging findings. Other agents reported to attenuate the radiation-induced imaging changes include pentoxifylline and bevacizumab.[19,20] Furthermore, extensive imaging changes could result in hydrocephalus, elevated intracranial pressure, and mass effect, which could necessitate surgical measures related to CSF diversion (shunt versus ventriculostomy). None of the patients in our series required a direct surgical intervention to target the imaging changes or their acute consequences. Neurologic follow-up with frequent MR imaging should be pursued in patients with extensive imaging changes.

Limitations

This study is limited by its retrospective design, the chart-review process, and the inherent selection bias. This study is a single-institution series using LINAC SRS and is based on institutional practice, which could affect the generalizability of the study. Furthermore, follow-up brain MRIs were not available for all patients at all time periods, limiting the analysis and impeding us

from performing a full temporal analysis of the radiation-induced imaging findings. We did not routinely obtain MRIs to document resolution of the imaging changes, and MRIs were obtained as clinically indicated outside the 2-year follow-up MRIs. We documented resolution of the imaging changes in 13/64 patients (20.3%), though it is likely that more patients had resolution of these imaging findings but were not captured by our study.

CONCLUSIONS

Radiation-induced imaging changes are common in the post-treatment period following LINAC-based SRS for brain AVMs. These imaging changes are significantly associated with new neurologic signs or symptoms following treatment. Patients with larger AVMs and AVMs with multiple feeding arteries may have higher odds of developing radiation-induced imaging changes. These changes are variable in severity and timing but appear to peak at 12 months.

Disclosures: Daniel R. Wahl—*UNRELATED: Consultancy*: Agios Pharmaceuticals Inc, *Comments*: consulting fees for work related to radiation and brain tumors; *Grants/Grants Pending*: Agios Inc, Innocrin Inc, *Comments*: research funding for unrelated work regarding radiation resistance in brain tumors; *Patents (Planned, Pending or Issued)*: University of Michigan, *Comments*: patent pending related to methods to predict treatment responsiveness in brain tumors. Aditya S. Pandey—*UNRELATED*: *Grants/Grants Pending*: National Institutes of Health–based grants for ultrasound-based treatment of intracerebral hemorrhage*; *Patents (Planned, Pending Or Issued)*: ultrasound-based treatment of intracerebral hemorrhage, hypothermia tool, thrombectomy-based tools, Smart Drill, *Comments*: None of these have been issued, and none have been licensed or led to financial gain.* *Money paid to the institution.

REFERENCES

1. Lunsford LD, Kondziolka D, Flickinger JC, et al. **Stereotactic radiosurgery for arteriovenous malformations of the brain.** *J Neurosurg* 1991;75:512–24 CrossRef Medline
2. Steiner L, Lindquist C, Adler JR, et al. **Clinical outcome of radiosurgery for cerebral arteriovenous malformations.** *J Neurosurg* 1992;77:1–8 CrossRef Medline
3. Friedman WA, Bova FJ, Mendenhall WM. **Linear accelerator radiosurgery for arteriovenous malformations: the relationship of size to outcome.** *J Neurosurg* 1995;82:180–89 CrossRef Medline
4. Karlsson B, Lax I, Soderman M. **Risk for hemorrhage during the 2-year latency period following gamma knife radiosurgery for arteriovenous malformations.** *Int J Radiat Oncol Biol Phys* 2001;49:1045–51 CrossRef Medline
5. Yen CP, Matsumoto JA, Wintermark M, et al. **Radiation-induced imaging changes following gamma knife surgery for cerebral arteriovenous malformations.** *J Neurosurg* 2013;118:63–73 CrossRef Medline
6. Cohen-Inbar O, Lee CC, Xu Z, et al. **A quantitative analysis of adverse radiation effects following gamma knife radiosurgery for arteriovenous malformations.** *J Neurosurg* 2015;123:945–53 CrossRef Medline
7. Hanauer DA, Mei Q, Law J, et al. **Supporting information retrieval from electronic health records: a report of University of Michigan's nine-year experience in developing and using the Electronic Medical Record Search Engine (EMERSE).** *J Biomed Inform* 2015;55:290–300 CrossRef Medline
8. Kothari RU, Brott T, Broderick JP, et al. **The ABCs of measuring intracerebral hemorrhage volumes.** *Stroke* 1996;27:1304–15 CrossRef Medline
9. Ganz JC, Reda WA, Abdelkarim K. **Adverse radiation effects after gamma knife surgery in relation to dose and volume.** *Acta Neurochir (Wien)* 2009;151:9–19 CrossRef Medline
10. Ilyas A, Chen CJ, Ding D, et al. **Radiation-induced changes after stereotactic radiosurgery for brain arteriovenous malformations: a systematic review and meta-analysis.** *Neurosurgery* 2018;83:365–76 CrossRef Medline
11. Kano H, Flickinger JC, Tonetti D, et al. **Estimating the risks of adverse radiation effects after gamma knife radiosurgery for arteriovenous malformations.** *Stroke* 2017;48:84–90 CrossRef Medline
12. Blamek S, Boba M, Larysz D, et al. **The incidence of imaging abnormalities after stereotactic radiosurgery for cerebral arteriovenous and cavernous malformations.** *Acta Neurochir Suppl* 2010;106:187–90 CrossRef Medline
13. Vrdoljak E, Bill CA, Stephens LC, et al. **Radiation-induced apoptosis of oligodendrocytes in vitro.** *Int J Radiat Biol* 1992;62:475–80 CrossRef Medline
14. Hong JH, Chiang CS, Campbell IL, et al. **Induction of acute phase gene expression by brain irradiation.** *Int J Radiat Oncol Biol Phys* 1995;33:619–26 CrossRef Medline
15. Pollock BE. **Occlusive hyperemia: a radiosurgical phenomenon?** *Neurosurgery* 2000;47:1178–82; discussion 1182–74 CrossRef Medline
16. Chapman PH, Ogilvy CS, Loeffler JS. **The relationship between occlusive hyperemia and complications associated with the radiosurgical treatment of arteriovenous malformations: report of two cases.** *Neurosurgery* 2004;55:228–33; discussion 233–24 CrossRef Medline
17. van den Berg R, Buis DR, Lagerwaard FJ, et al. **Extensive white matter changes after stereotactic radiosurgery for brain arteriovenous malformations: a prognostic sign for obliteration?** *Neurosurgery* 2008;63:1064–69; discussion 1069–70 CrossRef Medline
18. Pollock BE, Link MJ, Branda ME, et al. **Incidence and management of late adverse radiation effects after arteriovenous malformation radiosurgery.** *Neurosurgery* 2017;81:928–34 CrossRef Medline
19. Williamson R, Kondziolka D, Kanaan H, et al. **Adverse radiation effects after radiosurgery may benefit from oral vitamin E and pentoxifylline therapy: a pilot study.** *Stereotact Funct Neurosurg* 2008;86:359–66 CrossRef Medline
20. Levin VA, Bidaut L, Hou P, et al. **Randomized double-blind placebo-controlled trial of bevacizumab therapy for radiation necrosis of the central nervous system.** *Int J Radiat Oncol Biol Phys* 2011;79:1487–95 CrossRef Medline

Preliminary Findings Associate Hippocampal ^{1}H-MR Spectroscopic Metabolite Concentrations with Psychotic and Manic Symptoms in Patients with Schizophrenia

D. Malaspina, E. Lotan, H. Rusinek, S.A. Perez, J. Walsh-Messinger, T.M. Kranz, and O. Gonen

ABSTRACT

BACKGROUND AND PURPOSE: Previous hippocampal proton MR spectroscopic imaging distinguished patients with schizophrenia from controls by elevated Cr levels and significantly more variable NAA and Cho concentrations. This goal of this study was to ascertain whether this metabolic variability is associated with clinical features of the syndrome, possibly reflecting heterogeneous hippocampal pathologies and perhaps variability in its "positive" (psychotic) and "negative" (social and emotional deficits) symptoms.

MATERIALS AND METHODS: In a sample of 15 patients with schizophrenia according to the *Diagnostic and Statistical Manual of Mental Disorders, Fourth Edition*, we examined the association of NAA and Cho levels with research diagnostic interviews and clinical symptom ratings of the patients. Metabolite concentrations were previously obtained with 3D proton MR spectroscopic imaging at 3T, a technique that facilitates complete coverage of this small, irregularly shaped, bilateral, temporal lobe structure.

RESULTS: The patient cohort comprised 8 men and 7 women (mean age, 39.1 [SD, 10.8] years, with a mean disease duration of 17.2 [SD, 10.8] years. Despite the relatively modest cohort size, we found the following: 1) Elevated Cho levels predict the positive (psychotic, $r = 0.590$, $P = .021$) and manic ($r = 0.686$, $P = .005$) symptom severity; and 2) lower NAA levels trend toward negative symptoms ($r = 0.484$, $P = .08$). No clinical symptoms were associated with Cr level or hippocampal volume (all, $P \geq .055$).

CONCLUSIONS: These preliminary findings suggest that NAA and Cho variations reflect different pathophysiologic processes, consistent with microgliosis/astrogliosis and/or lower vitality (reduced NAA) and demyelination (elevated Cho). In particular, the active state–related symptoms, including psychosis and mania, were associated with demyelination. Consequently, their deviations from the means of healthy controls may be a marker that may benefit precision medicine in selection and monitoring of schizophrenia treatment.

ABBREVIATIONS: AP = anterior-posterior; ^{1}H-MRSI = proton MR spectroscopic imaging; IS = inferior-superior; LR = left-right

Schizophrenia and related psychoses are debilitating disorders affecting >1% of the population. Its clinical features include psychosis (hallucinations, delusions, disorganization) and decreased emotional expression and avolition (negative symptoms), along with declining function and frequent mood symptoms.[1] While commonly approached and treated as 1 disorder, schizophrenia is a heterogeneous syndrome with mounting evidence that different genetic susceptibilities and exposures may produce different initiating pathophysiologies.[2,3]

Hippocampal disruption may be a central pathology for psychosis because many of its measures differ between patients with schizophrenia and healthy controls, eg, reduced volume, increased resting blood flow, impaired task-related activation, decreased neurogenesis, and reduced connectivity with other regions.[4-10] Because the disease entails cognitive and attention deficits, effort-independent methods, eg, 3D proton MR spectroscopic imaging (^{1}H-MRSI) of the hippocampal formation, are well-suited to both elucidating the etiology of schizophrenia and monitoring its treatments.[11] ^{1}H-MRSI yields metabolic markers of several cellular processes, most notably NAA for neuronal integrity, Cr (phosphocreatine and creatine) for energy metabolism, Cho (choline, phosphocholine, and glycerophosphocholine) for membrane turnover and astroglia proliferation, and mIns for inflammation and gliosis.[12,13]

Received April 1, 2020; accepted after revision August 17.

From the Departments of Psychiatry, Neuroscience, Genetics, and Genomics (D.M.), Icahn School of Medicine at Mount Sinai, New York, New York; Department of Radiology (E.L., H.R., S.A.P., O.G.), Center for Advanced Imaging Innovation and Research, New York University Grossman School of Medicine, New York, New York; Department of Psychology (J.W.-M.), University of Dayton, Dayton, Ohio; Department of Psychiatry (J.W.-M.), Wright State University Boonshoft School of Medicine, Dayton, Ohio; and Department of Psychiatry, Psychosomatics, and Psychotherapy (T.M.K.), Goethe University, Frankfurt, Germany.

This work was supported by National Institutes of Health grants MH59114, MH088843, MH001699, MH086651 and P41 EB017183.

Please address correspondence to Dolores Malaspina, MD, Department of Psychiatry, Icahn School of Medicine at Mt Sinai, One Gustave Levy Place, Box 1230, New York, NY, 10016; e-mail: Dolores.malaspina@mssm.edu

http://dx.doi.org/10.3174/ajnr.A6879

Table 1: Demographics, metabolic, and symptomatic characteristics of the 15 patients, arranged in ascending age

No.	Age[a]	Sex	Disease Duration[a]	NAA[b]	Cr[b]	Cho[b]	Volume[c]
1	23	M	3	10.57	10.91	2.76	8.56
2	23	M	4	8.42	10.8	2.5	7.99
3	29	F	8	10.6	10.51	2.37	8.42
4	34	M	5	11.31	10.77	2.03	7.71
5	41	M	22	8.91	7.2	2.35	5.71
6	42	M	18	4.95	4.44	1.84	8.84
7	42	F	20	9.62	10.6	3.31	7.16
8	42	F	23	9.81	7.72	1.46	7.18
9	44	M	26	9.04	4.46	3.85	8.78
10	48	M	23	9.36	9.44	2.9	7.41
11	49	F	31	-	12.01	1.75	6.83
12	51	F	10	7.74	10.07	3.28	6.65
13	52	M	32	8.43	8.68	1.88	7.11
14	52	M	30	15.69	7.15	4.56	7.16
15	52	F	15	8.38	8.7	2.15	5.9
Mean ± SD	41.60 [10.08]		18 [10.02]	9.49 [2.35]	8.90 [2.31]	2.60 [0.86]	7.43 [0.97]

Note:—-indicates missing value.
[a] Years.
[b] Millimolar.
[c] Bilateral hippocampus volume, cubic centimeters.

Most hippocampus ^{1}H-MR spectroscopy literature reports on schizophrenia consider group-level differences in metabolite concentrations between patients and matched healthy controls.[11,14,15] For example, a recent whole-hippocampus ^{1}H-MRSI study of patients with schizophrenia found only significant, 19%, elevated mean Cr concentrations and 10% lower structure volume compared with healthy controls.[16] Although the mean NAA and Cho levels in that study did not differ between the 2 cohorts, their within-group variability was significantly greater in the schizophrenia group than in the controls.[16] While this greater variance may have reduced statistical power to detect group differences, it may come as no surprise, considering the etiologic and clinical heterogeneity of the disease and myriad treatment paradigms and durations.

Because this heterogeneity impedes therapeutic success, there is an ongoing research to define biologic subtypes with clinical significance. Because ^{1}H-MR spectroscopy is often used to identify disease markers leading to personalized treatments,[17] we set out to investigate whether this variability of Cho and NAA levels in patients with schizophrenia could reflect clinical symptoms, even absent group differences from the controls. This report presents preliminary findings and analysis of NAA, Cr, Cho, and mIns variability with respect to the clinical symptoms of patients with schizophrenia to test the hypothesis that their variations reflect the patient's clinical presentation.

MATERIALS AND METHODS

Participants

Subjects were recruited from a pool of 19 patients with established schizophrenia according to the *Diagnostic and Statistical Manual of Mental Disorders, Fifth Edition*, who participated in a previous ^{1}H-MRSI and MR imaging study. Fifteen (9 men, 6 women, mean age 41.60 [SD, 10.8] years; mean disease duration 18 [SD, 10.02] years) consented to enroll (see Table 1 for demographic information). All were on stable medication regimens for at least a month before their recruitment. They were assessed with the Positive and Negative Syndrome Scale,[18] to generate ratings for positive (psychotic), negative (social and emotional deficits), and general psychopathology statuses. Depression and anxiety were assessed with the Hamilton Depression Rating Scale and the Hamilton Anxiety Rating Scale;[19] the Young Mania Rating Scale was used to assess manic symptoms,[20] all compiled in Table 2. All subjects provided New York University School of Medicine Institutional Review Board–approved written informed consent.

MR Imaging Acquisition and Postprocessing

MR imaging and ^{1}H-MRSI were performed on a 3T whole-body MR imaging scanner (Trio; Siemens) with an after-market, circularly-polarized transmit-receive head coil (TEM-3000 MRInstruments Inc. Minneapolis MN). For tissue segmentation and ^{1}H-MRSI VOI guidance, T1-weighted, 3D MPPAGE images were obtained from each subject: TE/TI/TR = 2.6/800/1360 ms, matrix = 256 × 256, FOV = 256 × 256 mm^2, 1-mm-thick slices = 160, reformatted into sagittal and coronal slices at 1-mm^3 isotropic resolution, tilted along the hippocampal axis, as shown in Fig 1*A*–*C*.

A 6-cm anterior-posterior (AP) × 9-cm left-right (LR) × 2-cm inferior-superior (IS) = 108 cm^3 VOI was then image-guided over the bilateral hippocampi (Fig 1 *A*–*C*), angled along its long axis, and excited into 4 Hadamard-encoded axial slices, with a point-resolved spectroscopy sequence (TE/TR = 35/1400 ms). It yielded 6 × 9 × 4 (AP × LR × IS) = 216 voxels in the VOI, 1.0 × 1.0 × 0.5 cm^3 each, as shown in Fig 1*A*–*C*.[21] The 3D ^{1}H-MRSI data were reconstructed off-line using in-house software, as shown in Fig 1*D*. The relative NAA, Cr, Cho, and mIns levels of each voxel were obtained with the spectral modeling package of Soher et al[22] as shown in Fig 1*E* and scaled into absolute millimolar concentrations with phantom replacement, according to Meyer et al.[16]

Bilateral (left + right) hippocampal masks were traced by a trained neuroradiologist on the original sagittal MPRAGE images. The tracing was based on the well-known, extensively validated Harmonized Protocol, developed by the European Alzheimer's Disease Consortium.[23,24] It prescribes guidelines for labeling the entire hippocampal formation from native-space high-resolution T1-weighted MR imaging. To edit and inspect the 3D hippocampal masks in axial, sagittal, and coronal views, we used the FireVoxel

Table 2: Corresponding psychiatric symptoms for each of the 15 patients in Table 1

No.	PANSS POS[a]	PANSS NEG[b]	PANSS GEN[c]	YMRS[d]	HAM-D[e]	HAM-A[f]
1	18.00	7.00	22.00	15.00	2.88	5.00
2	9.00	13.00	19.00	0.00	2.00	0.00
3	14.00	16.00	29.00	0.00	4.00	2.00
4	20.00	17.00	33.00	4.00	7.61	17.00
5	8.00	16.00	20.00	0.00		2.00
6	9.00	8.00	26.00	4.00	10.58	11.85
7	7.00	9.00	23.00	3.00	3.26	14.00
8	10.00	12.00	29.00	0.00	17.00	17.50
9	25.00	21.00	49.00	9.00	11.54	4.00
10	18.00	15.00	26.00	15.00	8.65	8.00
11	9.00	7.00	23.00	2.00	11.00	6.46
12	32.00	20.00	37.00	22.00	27.00	11.00
13	19.00	14.00	45.00	6.00	23.91	27.00
14	25.00	22.00	44.00	20.00	25.00	21.00
15	10.00	22.00	32.00	1.00	6.73	4.67
Mean ± SD	15.53 [7.63]	14.60 [5.28]	30.47 [9.48]	6.73 [7.64]	11.52 [8.52]	10.10 [7.88]

Note:—YMRS indicates the Young Mania Rating Scale; POS, positive; NEG, negative; HAM-D, Hamilton Depression Scale; HAM-A, Hamilton Anxiety Scale; GEN, general psychopathology symptoms; PANSS, Positive and Negative Syndrome Scale.

[a] Positive and Negative Syndrome Scale; positive (psychotic).

[b] Positive and Negative Syndrome Scale; negative.

[c] General psychopathology symptoms assessed with the PANSS.[18]

[d] Manic symptoms, measured with the Young Mania Rating Scale.[20]

[e] Hamilton Depression.

[f] Hamilton Anxiety Scales.

package (https://firevoxel.org). FireVoxel then resampled the left + right hippocampal masks along the long axis of each subject's hippocampus at the same inclination (ie, parallel and naturally coregistered) to the ^{1}H-MRSI VOI, as shown in Fig 1. The CSF and white matter partial volume–corrected ^{1}H-MRSI metabolite concentrations within each subject's hippocampus mask, as well as the volume of the masks themselves, were then estimated using the Matlab software package (MathWorks), described by Tal et al.[25]

Statistical Analyses

SPSS (Version 21.0; IBM) was used for analyses. The data were normally distributed (all Kolmogorov–Smirnov test P values were $\geq .20$ except the Young Mania Rating Scale, which was $P = .09$); thus, the association between clinical symptom ratings and the Cho, NAA, Cr levels and hippocampal volumes were examined using Pearson correlations. All tests were 2-tailed, and the α for significance was set at $P < .05$.

RESULTS

Individual scores and sample means ± SDs for the hippocampal metabolite concentrations and volumes are compiled in Table 1, and the psychiatric symptoms are presented in Table 2. There was a positive association between Cho levels and the Positive and Negative Syndrome Scale–positive symptoms ($r = 0.59$, $P = .021$) and manic symptoms ($r = 0.69$, $P = .005$), as shown in Fig 2. There was a trend association of the NAA with negative symptoms ($r = 0.48$, $P = .08$). No clinical symptoms were associated with Cr levels or the hippocampal volume (all, P values $\geq .055$).

DISCUSSION

Most of the ^{1}H-MR spectroscopy schizophrenia studies published to date focus on the search for group-concentration differences from matched healthy controls.[14] The usual rationale is the search for a singular underlying disease pathology, rather than a clinical phenotype within the syndrome. Moreover, the variability in metabolite concentrations that could be used to explore different subtypes of the disease with different molecular pathologies may, instead, reduce the power to find group differences. Thus, approaching schizophrenia as a singular condition (though acknowledged to be a heterogeneous syndrome) may lead to the findings of "no intercohort difference." This may explain the paucity of Cho, mIns, and Cr patient-versus-control intercohort difference reports in the literature and perhaps, consequently, the even greater rarity of these concentration relationships to the patient's clinical symptoms.

These preliminary findings support the hypothesis that some of the variability in the patent's clinical symptoms is related to the hippocampal metabolite concentrations and the different molecular pathologies they indicate. This is especially germane because biomarkers that follow clinical symptoms would be particularly helpful in early-psychosis groups, including first-episode, prodromal, and clinical high-risk subjects. For example, during early-psychosis presentation, psychiatric history is often limited, but successful long-term outcomes rely on accurate diagnosis and quick intervention.[26] Identifying molecular pathologies in the hippocampus is particularly poignant in this population. Indeed, studies of subjects at high risk for psychosis have identified changes in hippocampal volume and glutamate and glutamine concentrations.[27,28]

This study suggests that 2 different hippocampal inflammatory pathologies may occur in different cases of schizophrenia, identified by elevated Cho, a marker for demyelination, and reduced NAA, an indicator of neuronal integrity. In support of the proposition that these processes are independent, the cases with the highest Cho levels also had mild NAA elevation. Elevated Cho was specifically related to state-related active symptoms of psychosis and mania.

Reduced hippocampal NAA is consistent with astrocytosis and/or microgliosis, shown in a murine model of HIV-1 encephalitis[29]

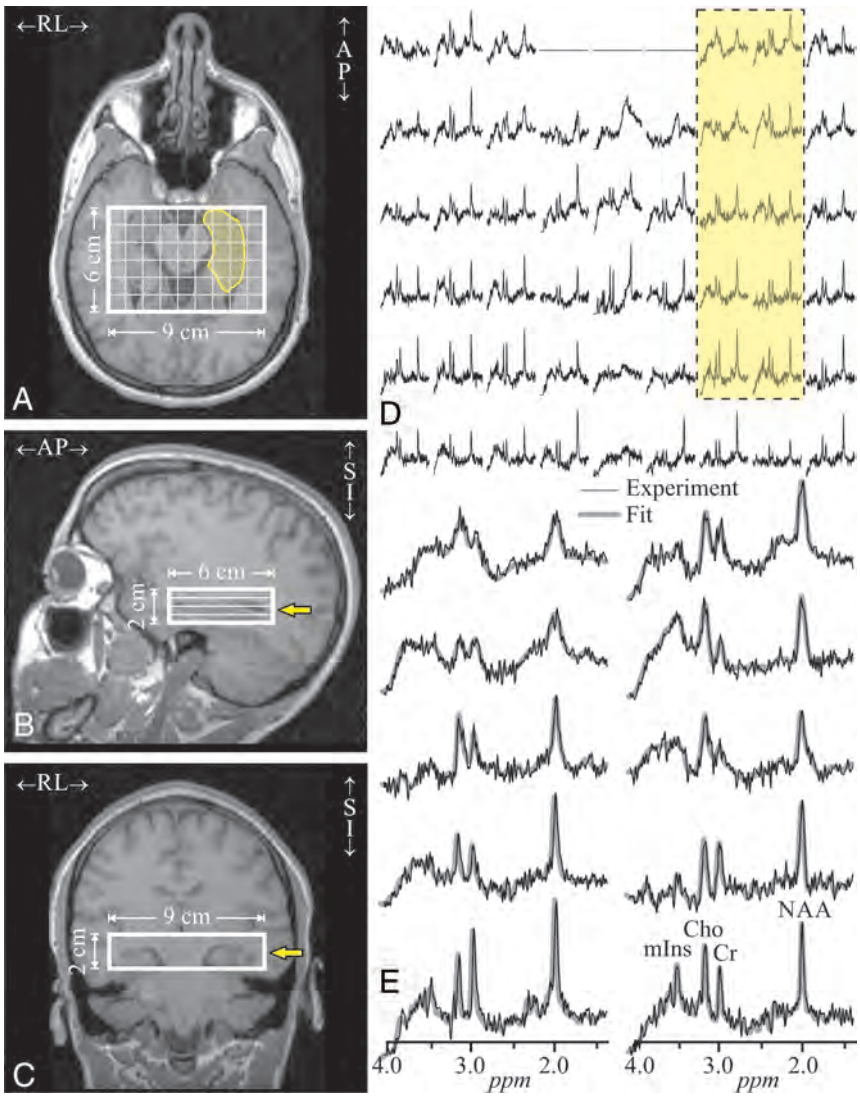

FIG 1. Imaging and ^{1}H-MRSI position, size, and analysis. *Left images*: Axial (*A*), coronal (*B*), and sagittal (*C*) TI-weighted MRIs from a 23-year-old male patient (No. 2 in Table 1), superimposed on the 9 × 6 × 2 cm^{3} LR × AP × IS VOI and the ^{1}H-MRSI grid (*thick and thin white frames*) and the left hippocampus outline (transparent yellow on *A*). *Yellow arrows* on *B* and *C* indicate the level of *A*. *Right upper image*: *D*, Real part of the 9 × 6 (LR × AP) axial ^{1}H spectra matrix from the VOI slice on *A* (level marked with *yellow arrows* on *B* and *C*). Spectra within the hippocampus on *A* are marked by the *dashed yellow-filled frame*. Spectra are on a common frequency and intensity scale. *Right lower image*: *E*, The 10 spectra in the frame (*D*) that mostly covers the left hippocampus, expanded for greater detail (*black lines*) and superimposed with the spectral fit (gray). Note the good signal-to-noise ratio and spectral resolution (mean, 8.1 [SD, 3.0] Hz line width) from the high-spatial-resolution (0.5 cm^{3}) voxels and the fidelity of the spectral fit. SI indicates superior-inferior.

and consistent with the elevated Cr levels, which correlated with mIns levels for the entire group of cases versus controls.[16] The relationship of Cho with the cases of more severe manic and psychotic symptoms suggests that the pathologic processes associated with their active positive symptoms may entail myelination disruption.

Note that the inhibitory parvalbumin-positive GABAergic hippocampal interneurons are myelinated in an experience-dependent manner.[30] With diminished hippocampal input, the number and function of the inhibitory GABAergic neurons would be reduced, shifting the balance to the more numerous *N*-methyl-D-aspartate receptor glutamatergic activity, thereby activating pathways that can deregulate dopamine homeostasis and produce psychosis.[31] Such a model would support our finding of Cho predicting psychotic and manic symptoms. Furthermore, the fact that Cho, a marker of membrane de- and remyelination, is linked to psychosis severity supports a mechanism of dysmyelination in schizophrenia that is also supported by a postmortem study showing that 35 of 89 cases examined expressed abnormal myelination in the prefrontal lobes.[32]

This study focused on the variability of metabolite concentrations as a probe of the underpinnings of hippocampal pathology in psychosis. The presence of separate hippocampus-related pathologies may help reconcile the diverse findings reported for schizophrenia better than single models that include effects of age or progression of a single pathophysiology.[33] These findings are also consistent with a model of increased hippocampal hyperactivation or perfusion[9] and pathology that reduces hippocampal volumes.[34]

This study is also subject to some limitations. First, it is a small ($n = 15$) sample comprising patients of varying disease durations. While all were on clinically determined medication doses, unchanged for at least a month, their treatments varied in both type and duration. Second, the quantitative metabolic results are subject to inherent limitations of ^{1}H-MR spectroscopy: relatively low spatial resolution compared with the hippocampus internal structure, precluding, for example, differentiation of its subfields. Yet, even despite these limitations, our results suggest that individual ^{1}H-MRSI metrics may be used to help characterize the clinical presentation of patients with schizophrenia with hippocampal metabolic deviations compared with healthy controls.

CONCLUSIONS

A combination of advanced multivoxel 3D ^{1}H-MRSI acquisition facilitating total spatial coverage of this bilateral structure and postprocessing methodology that corrects for partial volume effects allowed us to detect and distinguish separate hippocampal pathologies consistent with glial activation and demyelination that predict different psychiatric symptoms in patients with schizophrenia. These preliminary findings, if replicated in a larger study, also suggest that a patient's specific ^{1}H-MRSI metrics may

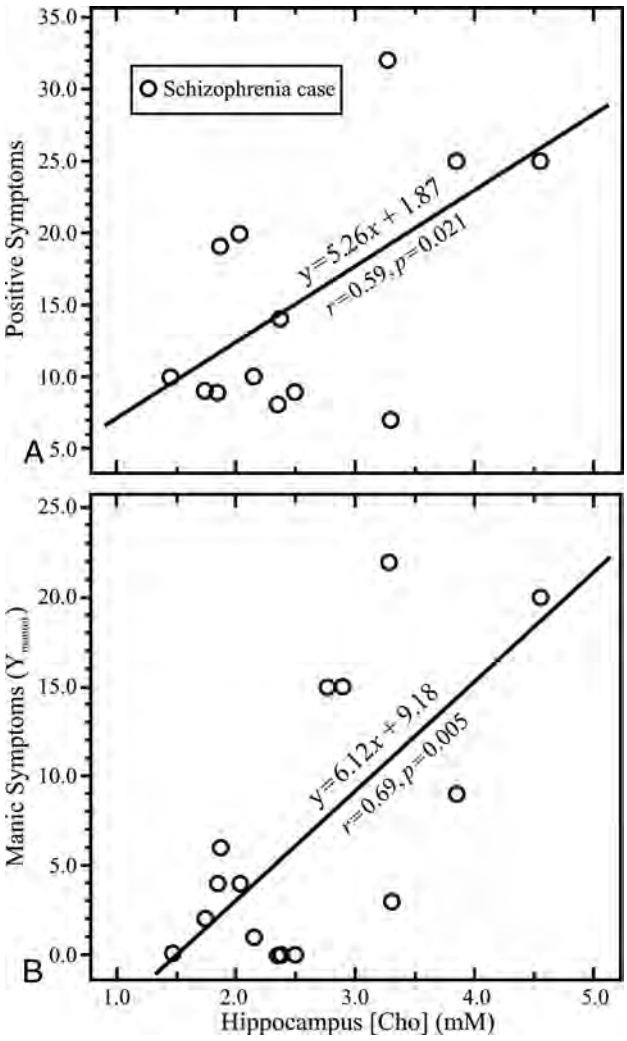

FIG 2. Symptoms and metabolite concentrations. *Upper graph*: *A*, Correlations between positive (psychotic) symptoms assessed with the Positive and Negative Syndrome Scale[18] and whole-hippocampus multivoxel average choline millimolar concentration of Cho. *Lower graph*: *B*, Same for manic symptoms measured with the Young Mania Rating Scale and whole-hippocampus average of Cho.

be used to select and monitor individually tailored treatments for psychosis and mania;[17] for example, they may benefit from anti-inflammatory treatments.

ACKNOWLEDGMENT

The authors wish to acknowledge the contributions of Emma J. Meyer, who died before the publication of this article.

Disclosures: Dolores Malaspina—*RELATED*; *Grant*; National Institute of Mental Health*; *UNRELATED*: *Employment*: Icahn School of Medicine at Mount Sinai, New York, New York, *Comments*: Professor. Julie Walsh-Messinger—*UNRELATED*: *Expert Testimony*: Strauss Troy LLC, *Comments*: I provided expert witness testimony on schizophrenia in November 2018. My purpose was to educate the court on the disease, and I did not conduct a forensic evaluation; *Stock/Stock Options*: I do not believe I have relevant stock. I have a retirement account that my financial advisor handles, but I do not know what he has invested it in. Oded Gonen—*RELATED*: *Grant*: National Institutes of Health, *Comments*: MH59114, MH088843, MH001699, MH086651, EB017183*; *UNRELATED*: *Employment*: New York University School of Medicine, *Comments*: salary. *Money paid to the institution.

REFERENCES

1. American Psychiatric Association. *Diagnostic and Statistical Manual of Mental Disorders*, 5th ed, *DSM-5*. American Psychiatric Association; 2013
2. Tamminga CA, Pearlson GD, Stan AD, et al. **Strategies for advancing disease definition using biomarkers and genetics: the bipolar and schizophrenia network for intermediate phenotypes.** *Biol Psychiatry Cogn Neurosci Neuroimaging* 2017;2:20–27 CrossRef Medline
3. Nenadic I, Gaser C, Sauer H. **Heterogeneity of brain structural variation and the structural imaging endophenotypes in schizophrenia.** *Neuropsychobiology* 2012;66:44–49 CrossRef Medline
4. Schobel SA, Chaudhury NH, Khan UA, et al. **Imaging patients with psychosis and a mouse model establishes a spreading pattern of hippocampal dysfunction and implicates glutamate as a driver.** *Neuron* 2013;78:81–93 CrossRef Medline
5. Talati P, Rane S, Skinner J, et al. **Increased hippocampal blood volume and normal blood flow in schizophrenia.** *Psychiatry Res* 2015;232:219–25 CrossRef Medline
6. Balu DT, Lucki I. **Adult hippocampal neurogenesis: regulation, functional implications, and contribution to disease pathology.** *Neurosci Biobehav Rev* 2009;33:232–52 CrossRef Medline
7. Rametti G, Junque C, Vendrell P, et al. **Hippocampal underactivation in an fMRI study of word and face memory recognition in schizophrenia.** *Eur Arch Psychiatry Clin Neurosci* 2009;259:203–11 CrossRef Medline
8. Watson DR, Bai F, Barrett SL, et al. **Structural changes in the hippocampus and amygdala at first episode of psychosis.** *Brain Imaging Behav* 2012;6:49–60 CrossRef Medline
9. Heckers S, Konradi C. **Hippocampal pathology in schizophrenia.** *Curr Top Behav Neurosci* 2010;4:529–53 CrossRef Medline
10. Haukvik UK, Hartberg CB, Agartz I. **Schizophrenia: what does structural MRI show** [in Norwegian]? *Tidsskr Nor Laegeforen* 2013;133:850–53 CrossRef Medline
11. Bustillo JR. **Use of proton magnetic resonance spectroscopy in the treatment of psychiatric disorders: a critical update.** *Dialogues Clin Neurosci* 2013;15:329–37 Medline
12. Mountford CE, Stanwell P, Lin A, et al. **Neurospectroscopy: the past, present and future.** *Chem Rev* 2010;110:3060–86 CrossRef Medline
13. Zhu H, Barker PB. **MR spectroscopy and spectroscopic imaging of the brain.** *Methods Mol Biol* 2011;711:203–26 CrossRef Medline
14. Iwata Y, Nakajima S, Plitman E, et al. **Neurometabolite levels in antipsychotic-naive/free patients with schizophrenia: a systematic review and meta-analysis of (1)H-MRS studies.** *Prog Neuropsychopharmacol Biol Psychiatry* 2018;86:340–52 CrossRef Medline
15. Port JD, Agarwal N. **MR spectroscopy in schizophrenia.** *J Magn Reson Imaging* 2011;34:1251–61 CrossRef Medline
16. Meyer EJ, Kirov II, Tal A, et al. **Metabolic abnormalities in the hippocampus of patients with schizophrenia: a 3D multivoxel MR spectroscopic imaging study at 3T.** *AJNR Am J Neuroradiol* 2016;37:2273–79 CrossRef Medline
17. Tognin S, van Hell HH, Merritt K, et al; PSYSCAN Consortium. **Towards precision medicine in psychosis: benefits and challenges of multimodal multicenter studies-PSYSCAN: translating neuroimaging findings from research into clinical practice.** *Schizophr Bull* 2020;26;46:432–41 CrossRef Medline
18. Kay SR, Fiszbein A, Opler LA. **The Positive and Negative Syndrome Scale (PANSS) for schizophrenia.** *Schizophr Bull* 1987;13:261–76 CrossRef Medline
19. Hamilton M. **Development of a rating scale for primary depressive illness.** *Br J Soc Clin Psychol* 1967;6:278–96 CrossRef Medline
20. Young RC, Biggs JT, Ziegler VE, et al. **A rating scale for mania: reliability, validity and sensitivity.** *Br J Psychiatry* 1978;133:429–35 CrossRef Medline
21. Goelman G, Liu S, Hess D, et al. **Optimizing the efficiency of high-field multivoxel spectroscopic imaging by multiplexing in space and time.** *Magn Reson Med* 2006;56:34–40 CrossRef Medline

22. Soher BJ, Young K, Govindaraju V, et al. **Automated spectral analysis III: application to in vivo proton MR spectroscopy and spectroscopic imaging.** *Magn Reson Med* 1998;40:822–31 CrossRef Medline
23. Boccardi M, Bocchetta M, Apostolova LG, et al; EADC-ADNI Working Group on the Harmonized Protocol for Manual Hippocampal Segmentation. **Delphi definition of the EADC-ADNI Harmonized Protocol for hippocampal segmentation on magnetic resonance.** *Alzheimers Dement* 2015;11:126–38 CrossRef Medline
24. Frisoni GB, Jack CR Jr, Bocchetta M, et al; EADC-ADNI Working Group on The Harmonized Protocol for Manual Hippocampal Volumetry and for the Alzheimer's Disease Neuroimaging Initiative. **The EADC-ADNI harmonized protocol for manual hippocampal segmentation on magnetic resonance: evidence of validity.** *Alzheimers Dement* 2015;11:111–25 CrossRef Medline
25. Tal A, Kirov I, Grossman RI, et al. **The role of gray and white matter segmentation in quantitative proton MR spectroscopic imaging.** *NMR Biomed* 2012;25:1392–1400 CrossRef Medline
26. Fusar-Poli P, McGorry PD, Kane JM. **Improving outcomes of first-episode psychosis: an overview.** *World Psychiatry* 2017;16:251–65 CrossRef Medline
27. Allen P, Moore H, Corcoran CM, et al. **Emerging temporal lobe dysfunction in people at clinical high risk for psychosis.** *Front Psychiatry* 2019;10:298 CrossRef Medline
28. Tibbo P, Hanstock C, Valiakalayil A, et al. **3-T proton MRS investigation of glutamate and glutamine in adolescents at high genetic risk for schizophrenia.** *Am J Psychiatry* 2004;161:1116–18 CrossRef Medline
29. Nelson JA, Dou H, Ellison B, et al. **Coregistration of quantitative proton magnetic resonance spectroscopic imaging with neuropathological and neurophysiological analyses defines the extent of neuronal impairments in murine human immunodeficiency virus type-1 encephalitis.** *J Neurosci Res* 2005;80:562–75 CrossRef Medline
30. Stedehouder J, Couey JJ, Brizee D, et al. **Fast-spiking parvalbumin interneurons are frequently myelinated in the cerebral cortex of mice and humans.** *Cereb Cortex* 2017;27:5001–13 CrossRef Medline
31. Lisman JE, Coyle JT, Green RW, et al. **Circuit-based framework for understanding neurotransmitter and risk gene interactions in schizophrenia.** *Trends Neurosci* 2008;31:234–42 CrossRef Medline
32. Hakak Y, Walker JR, Li C, et al. **Genome-wide expression analysis reveals dysregulation of myelination-related genes in chronic schizophrenia.** *Proc Natl Acad Sci U S A* 2001;98:4746–51 CrossRef Medline
33. Small SA, Schobel SA, Buxton RB, et al. **A pathophysiological framework of hippocampal dysfunction in ageing and disease.** *Nat Rev Neurosci* 2011;12:585–601 CrossRef Medline
34. Harrisberger F, Smieskova R, Vogler C, et al. **Impact of polygenic schizophrenia-related risk and hippocampal volumes on the onset of psychosis.** *Transl Psychiatry* 2016;6:e868 CrossRef Medline

Noninvasive Determination of *IDH* and 1p19q Status of Lower-grade Gliomas Using MRI Radiomics: A Systematic Review

A.P. Bhandari, R. Liong, J. Koppen, S.V. Murthy, and A. Lasocki

ABSTRACT

BACKGROUND: Determination of *isocitrate dehydrogenase* (*IDH*) status and, if *IDH*-mutant, assessing 1p19q codeletion are an important component of diagnosis of World Health Organization grades II/III or lower-grade gliomas. This has led to research into noninvasively correlating imaging features ("radiomics") with genetic status.

PURPOSE: Our aim was to perform a diagnostic test accuracy systematic review for classifying *IDH* and 1p19q status using MR imaging radiomics, to provide future directions for integration into clinical radiology.

DATA SOURCES: Ovid (MEDLINE), Scopus, and the Web of Science were searched in accordance with the Preferred Reporting Items for Systematic Reviews and Meta-Analyses for Diagnostic Test Accuracy guidelines.

STUDY SELECTION: Fourteen journal articles were selected that included 1655 lower-grade gliomas classified by their *IDH* and/or 1p19q status from MR imaging radiomic features.

DATA ANALYSIS: For each article, the classification of *IDH* and/or 1p19q status using MR imaging radiomics was evaluated using the area under curve or descriptive statistics. Quality assessment was performed with the Quality Assessment of Diagnostic Accuracy Studies 2 tool and the radiomics quality score.

DATA SYNTHESIS: The best classifier of *IDH* status was with conventional radiomics in combination with convolutional neural network–derived features (area under the curve = 0.95, 94.4% sensitivity, 86.7% specificity). Optimal classification of 1p19q status occurred with texture-based radiomics (area under the curve = 0.96, 90% sensitivity, 89% specificity).

LIMITATIONS: A meta-analysis showed high heterogeneity due to the uniqueness of radiomic pipelines.

CONCLUSIONS: Radiogenomics is a potential alternative to standard invasive biopsy techniques for determination of *IDH* and 1p19q status in lower-grade gliomas but requires translational research for clinical uptake.

ABBREVIATIONS: AI = artificial intelligence; AUC = area under the curve; CNN = convolutional neural network; *IDH* = *isocitrate dehydrogenase*; *IDH*-mut = *IDH*-mutant; LGG = lower-grade gliomas; ML = machine learning; PRISMA-DTA = Preferred Reporting Items for Systematic Reviews and Meta-Analyses for Diagnostic Test Accuracy; QUADAS-2 = Quality Assessment of Diagnostic Accuracy Studies 2; RQS = radiomics quality score; SVM = support vector machine; VASARI = Visually Accessible Rembrandt Images; WHO = World Health Organization

Lower-grade gliomas (LGG), World Health Organization (WHO) grades II/III, are diffusely infiltrative tumors of the CNS. With time, these tumors typically progress to glioblastoma (WHO grade IV), which has a median survival of only 12–18 months despite treatment.[1] A growing understanding of the prognostic and therapeutic importance of molecular markers has led to their incorporation into the 2016 WHO classification, and they now constitute a key component of the diagnosis of LGG.[2] The 2 key markers of LGG are *isocitrate dehydrogenase* (*IDH*), with tumors classified as either *IDH*-mutant (*IDH*-mut) or *IDH*-

Received May 2, 2020; accepted after revision August 17.

From the Department of Anatomy (A.P.B.) and College of Medicine and Dentistry (S.V.M.), James Cook University, Townsville, Queensland, Australia; Townsville University Hospital (A.P.B., J.K.), Douglas, Queensland, Australia; Department of Medical Imaging Research Office (R.L.), Royal Brisbane and Women's Hospital, Herston, Queensland, Australia; Department of Cancer Imaging (A.L.), Peter MacCallum Cancer Centre, Melbourne, Victoria, Australia; Griffith University School of Medicine (R.L.), Gold Coast, Queensland, Australia; and Sir Peter MacCallum Department of Oncology (A.L.), The University of Melbourne, Melbourne, Victoria, Australia.

Please address correspondence to Abhishta Bhandari, MBBS MMI, Department of Anatomy, 1 James Cook Dr, James Cook University, Douglas, Townsville, 4814, Queensland, Australia; e-mail: Abhishta.bhandari@my.jcu.edu.au

Indicates open access to non-subscribers at www.ajnr.org
Indicates article with supplemental on-line tables.
Indicates article with supplemental on-line photos.
http://dx.doi.org/10.3174/ajnr.A6875

wild-type, and 1p19q, with 1p19q-codeletion representing a combined loss of both the short arm of chromosome 1 and the long arm of chromosome 19.

Determining *IDH* and 1p19q status is invasive, requiring a tissue specimen via stereotactic biopsy or definitive resection, with the associated operative risks[3] and possibility of sampling error. While the possibility of sampling error is perhaps of greatest relevance to the determination of tumor grade,[4] it is also relevant to the determination of tumor genetic status.[5,6] For example, *IDH* sequencing may be falsely negative if there are few glioma cells within the sample,[5] and intratumoral genetic heterogeneity can occur.[6] These considerations have led to research into characterizing *IDH* and 1p19q status by imaging, known as "radiogenomics" or "imaging genomics." The most specific visual MR imaging feature is the "T2-FLAIR mismatch sign," which has been shown to predict an *IDH*-mut 1p19q-codeletion gliomas with 100% specificity and high interobserver correlation ($\kappa = 0.38–0.88$).[7-9] Other useful features include the presence of calcification (suggestive of a 1p19q-codeletion glioma)[8,9] and homogeneous signal (likely 1p19q-intact).[10] While some features such as >50% T2-FLAIR mismatch and the presence of calcification have high interobserver correlation, other features are limited by greater variability in interpretation. Furthermore, a substantial proportion (29%–37%) of gliomas do not exhibit these features, limiting sensitivity.[8]

Artificial intelligence (AI) is emerging as a solution to the limitations of conventional visual assessment. AI techniques may identify features hidden to the naked eye by extracting data from images and relating them to outcomes. Given the inherent signal and volume heterogeneity of gliomas, a perceived signature or pattern may be modelled to genetic, clinical, and biochemical outcomes.[11] Features can be learned from the image or predefined. The field of radiomics involves the extraction of predefined features such as shape, intensity, and texture from a segmented (tumor) volume of interest.[12] This is opposed to deep learning–derived features, which are identified without human predefinition. Radiomic features can be correlated with genetic status through a subset of AI known as machine learning (ML). The ML algorithm is trained to a clinical outcome via a training dataset and validated using a testing/validation dataset. Extracted radiomic features undergo selection and can then be related to molecular markers such as *IDH* and 1p19q, providing a more objective method of radiogenomic correlation.

Radiomic analysis has several advantages compared with human observers, including the ability to rapidly assess multiple imaging features, less interobserver variability,[13] and potentially higher sensitivity and specificity. The aim of this article was to perform a systemic review of the use of MR imaging radiomics for the classification of *IDH* and 1p19q status in LGG.

MATERIALS AND METHODS

Search methodology and study synthesis were performed in line with the Preferred Reporting Items for Systematic Reviews and Meta-Analyses for Diagnostic Test Accuracy (PRISMA-DTA) checklist.[14] The search was performed on the Web of Science, Ovid (MEDLINE), and Scopus on April 18, 2020. Online Table 1 summarizes the search strategy. Search terms were developed from the PICO framework and Medical Subject Headings, which included terms relating to radiomics or radiogenomics, gliomas, and *IDH*/1p19q status. The PRISMA flowchart is available in Online Fig 1.

Study Selection

Studies were included if they were original research articles relating radiomic features to *IDH* and/or 1p19q status in LGG (WHO grades II/III) with pathologic confirmation. Studies were excluded under the following circumstances: 1) They investigated the effects of radiogenomic pipelines on factors that affect imaging quality rather than assessing diagnostic potential or 2) they included imaging modalities other than MR imaging because recent literature has not shown superior outcomes.[15] There was no restriction on study date.

The references were imported from the Web of Science, Ovid (MEDLINE), and Scopus into EndNote (Version X9; https://www.endnote.com/product-details/). Duplicates were removed using the "Find Duplicates" function in EndNote and manual review of the reference list. Two independent authors (A.P.B. and J.K.) screened the titles and abstracts for eligibility. The full texts were then screened. When questions arose regarding inclusion of articles, these were resolved through discussion between both authors responsible for data extraction (experience: A.P.B., medical doctor with a master's degree in medical imaging analysis, and J.K., medical doctor with 4 years' clinical experience). Ties were to be reviewed together with the senior author, but none were encountered.

Data Collection and Analysis

The primary outcome was the classification of *IDH* and/or 1p19q status by MR imaging radiomics. This was based on the receiver operating or precision recall curve and associated sensitivity (%), specificity (%), and area under the curve (AUC) if available. The AUC is presented as a value between 0.5 and 1, with 1 representing perfect classification (and 100% sensitivity and specificity). For studies that did not include ML in the pipeline, descriptive statistics (for example, mean and SD with *t* testing) were also included. Only significant findings for descriptive statistics were reported or the highest AUC for ML classifiers, given that some studies related numerous radiomic features to genetic status (*IDH* and/or 1p19q) or reported a considerable number of ML classifiers. If training and validation set data were reported, only the validation set was used. Secondary outcome measures were related to pipeline features and included the number of lesions, imaging sequences and segmentation method, features and their selection method, ML classifier, genetic status, and WHO tumor grade. A meta-analysis using random effects[16] was performed on AUC values with 95% confidence intervals when available in MedCalc (MedCalc Software). A Higgins I^2 index of heterogeneity was reported, in which 0% represents no heterogeneity and 100% represents maximum heterogeneity.

Quality Assessment

Quality assessment was performed using the Quality Assessment of Diagnostic Accuracy Studies 2 (QUADAS-2) tool and the radiomics quality score (RQS).[12] The QUADAS-2 scoring system

Table 1: Derived aims and key findings of studies comparing *IDH*-mut and *IDH* wild-type LGG

First Author and Year	Derived Aim	Key Findings
Fukuma 2019[22]	To integrate CNN deep learning features with conventional radiomic features	Conventional radiomic features: accuracy (mean ± 95% CI) = 71.7% ± 8.3%; AUC (± 95% CI) = 0.718 ± 0.139 CNN features: accuracy = 69.6% ± 5.6%; AUC = 0.619 ± 0.132 CNN and conventional radiomic features: accuracy = 73.1% ± 9.4%; AUC = 0.699 ± 0.145
Gihr 2020[23]	To determine if intensity features relate to *IDH* status	Entropy, a second-order histogram parameter of the ADC volume was significant: *IDH*-mut versus *IDH* wild-type, mean ± SD = 5.5 ± 0.63 vs 4.75 ± 0.69; $P = .0144$
Jakola 2018[24]	To determine if texture features can predict *IDH* status on FLAIR	Homogeneity and volume could classify *IDH* status with an AUC = 0.940 (85% sensitivity, 100% specificity) using the generalized linear model
Kim 2020[25]	To determine if DWI- and DSC perfusion-based image integration with standard imaging (T1WI postcontrast and FLAIR) can improve classification	Integration increased the AUC (95% CI) = 0.747 (0.663–0.832); (53.6% sensitivity and 86.7% specificity) from 0.705 (0.613–0.796) (43.9% sensitivity and 88.8% specificity) compared with conventional MR imaging radiomics
Li 2017[27]	To determine if integration of deep learning features into the radiogenomic pipeline improves classification	Conventional radiomics produced an AUC = 0.85 (sensitivity of 82.9%, specificity of 73.5%) CNN deep learning–derived features plus conventional radiomic features with feature selection produced an AUC = 0.95 (sensitivity of 94.4%; specificity of 86.7%)
Lu 2018[28]	To determine the best ML classifier	Linear SVM classified *IDH* status with an AUC = 0.936 (sensitivity of 85.7%, specificity of 93.0%)
Park 2020[29]	To determine if DTI improves classification when added to conventional radiomics	Addition of DTI radiomic features to conventional imaging radiomics increased the AUC (95% CI) = 0.900 (0.855–0.945) from 0.835 (0.773–0.896)
Ren 2019[30]	To compare radiomic, VASARI, and radiomic plus VASARI features derived from FLAIR, ADC, eADC, and CBF	Radiomics: AUC (95% CI) = 0.931 (0.842–1); sensitivity of 100%, specificity of 85.71% VASARI: AUC = 0.843 (sensitivity of 91.67%; specificity of 61.90%) Radiomics plus VASARI: AUC = 0.888 (0.786–0.989); sensitivity of 94.44% and specificity of 71.43%
Yu 2017[32]	To classify using the improved genetic algorithm for feature selection and leave-one-out cross-validation method in WHO grade II LGG	Using the proposed method and the SVM ML classifier, an AUC = 0.71 (sensitivity = 56% and specificity = 74%) was achieved
Zhou 2017[34]	To determine if VASARI annotations were superior to standard radiomic classification analysis	*IDH* classification through texture features found an AUC (± 95% CI) = 0.79 ± 0.02; sensitivity 90%, specificity of 89% *IDH* classification through VASARI features, AUC = 0.73 ± 0.02; sensitivity of 69%, specificity of 69%
Zhang 2018[33]	To classify by conventional radiomics	AUC = 0.830 (sensitivity = 82%, specificity = 92%) using SVM

Note:—eADC indicates exponential ADC.

was developed to assess bias and the applicability of diagnostic-accuracy studies.[17] The RQS is specific to radiomics and is based on the Transparent Reporting of a multivariable prediction model for Individual Prognosis Or Diagnosis initiative, which examines domains of application for predictive models.[18] Application of RQS and QUADAS-2 was performed by discussion between A.P.B. and J.K. A κ statistic[19] was considered for the RQS, similar to that used in previous studies;[20] however, for quantitatively-defined criteria, it was determined that resolution by discussion would be superior.[21]

RESULTS

The initial search obtained 610 articles; 431 articles were from Ovid (MEDLINE); 111, from Scopus; and 68, from the Web of Science. After duplicates were removed, a total of 532 articles

Table 2: Derived aims and key findings of studies examining 1p19q status of *IDH*-mut LGG

First Author and Year	Derived Aim	Key Findings
Han 2020[35]	To determine if clinical and standard imaging factors improve classification	The AUC (95% CI) = 0.753 (0.654–0.852) for clinical plus radiomic features versus AUC = 0.760 (0.663-0.857) for just radiomic features; radiomic features were superior to clinical features alone, AUC = 0.627 (0.551–0.703)
Kocak 2020[26]	To determine the best ML classifier	The neural network produced the highest AUC (95% CI) = 0.869 (0.751–0.981); sensitivity of 87.5%, specificity of 75.8%
Lu 2018[28]	To determine the best ML classifier	Classification occurred with an AUC = 0.92 (sensitivity of 88.5%, specificity of 86.2%) using quadratic SVM
Shofty 2018[31]	To determine the best ML classifier	Classification occurred with an AUC = 0.87 (sensitivity of 92%, specificity of 83%) using ensemble bagged trees classifier
Zhou 2017[34]	To determine if VASARI annotations were superior to standard radiomic analysis for classification	Texture features classified with an AUC (± 95% CI) = 0.96 ± 0.01; sensitivity of 90% ± 2%, specificity of 89% ± 2% VASARI features classified with an AUC = 0.78 ± 0.02; sensitivity of 72% ± 3%, specificity of 67% ±3%
Fukuma 2019[22]	To determine if integration of CNN deep learning with radiomic features improved classification	Conventional radiomic features (± 95% CI): accuracy = 59.0 ± 9.0%; AUC = 0.656 ± 0.113 CNN features: accuracy = 84.0 ± 9.3%; AUC = 0.868 ± 0.099 CNN and conventional radiomic features: accuracy = 79.8 ± 11.0%; AUC = 0.861 ± 0.116

remained. The articles were screened by title and abstract, and 18 remained. Full texts were reviewed, and 14 articles[22-35] fit the review question and inclusion criteria. The publication dates of the 14 included studies[22-35] ranged from 2017 to 2020. A total of 1655 LGG were analyzed. Online Table 2 summarizes the pipeline features for each study.

All segmentations incorporated manual components except for 2 studies, both of which used convolutional neural network (CNN)-based segmentation.[28,32] Standard imaging sequences included pre- and postcontrast T1WI, T2WI, and FLAIR. ADC,[23,25,30] cerebral blood flow/volume,[28,30] DTI,[29] and exponential ADC[30] were used as adjuncts in some studies. Radiomic features were extracted most commonly by programs developed in-house on the Matlab software platform (MathWorks).[23,25,27] AlexNet (https://www.mygreatlearning.com/blog/alexnet-the-first-cnn-to-win-image-net/) was used in 1 study for deep learning–derived features in the highest discriminating pipeline.[27] The most common method of feature selection was support vector machine (SVM)–recursive feature elimination,[25,30,33,34] followed by a Student *t* test.[27-29] All categories of radiomic features were used. Two studies did not use ML.[23,24] Most studies assessed WHO grade II and III LGG,[22-30,32-34] apart from one that assessed only WHO grade II LGG.[31] Table 1 demonstrates the derived aims and key findings of studies that examined the *IDH* status of LGG, while Table 2 summarizes studies examining the 1p19q status of *IDH*-mut LGG. Figures 1 and 2 provide the associated forest plots for studies assessing *IDH* and 1p19q, respectively. Further details are provided in the online material. A meta-analysis on *IDH* status was performed on 5 studies[22,26,29,30,34] that had sufficient data with a pooled value of 0.827 (95% CI, 0.760–0.894; $I^2 = 88.55\%$). For 1p19q status, a meta-analysis was performed on 4 studies[22,26,34,35] that had sufficient data with a pooled value of 0.872 (95% CI, 0.789–0.954; $I^2 = 86.19\%$).

The QUADAS-2 score showed low bias and high applicability (see Online Fig 2 for individual studies). The radiomic-specific RQS average score was low, with a mean of 10 (range, 2–14). On average, the RQS was 29% (range, 6%–39%) of the highest possible score. There were no studies that reported on cost-effectiveness, imaging used on phantom models, a prospectively validated radiomic signature in an appropriate clinical trial or performed clinical utility statistics (beyond just discussion of uses).[21] Further details are provided in Online Table 3.

DISCUSSION

The systemic literature review found that the highest classifier for *IDH* status was conventional radiomics with CNN deep learning–derived features, which achieved an AUC = 0.95 (sensitivity of 94.4%, specificity of 86.7%).[27] For classification of 1p19q status, conventional texture-based radiomics was optimal, with an AUC = 0.96 (sensitivity of 90%, specificity of 89%).[34]

Segmentation had manual components in both studies[28,32] and was generally performed by trained personnel and approved by neuroradiologists or neurosurgeons. Manual segmentation is time-consuming, resource-intensive and introduces interobserver variability. Automation of segmentation is being actively progressed by the Brain Tumour Segmentation Challenge, and ongoing improvements have the potential to address the limitations of manual segmentation and thus improve the accuracy and efficiency of radiomic methods.[36-38] For the whole tumor, the 2018 winning team achieved a Sørensen–Dice coefficient of 0.88, in which a value of 1 represents perfect consistency between manual (ground truth) and automated segmentation.[39]

For *IDH* status, the literature indicates that a standard sequence image acquisition, use of texture-based features (most common being gray-level co-occurrence matrix,[23-25,27-29,34,40]

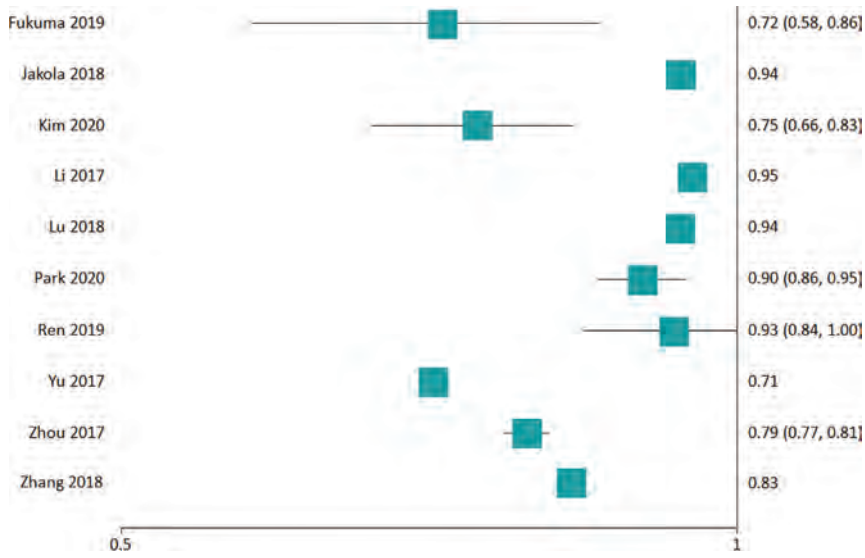

FIG 1. *IDH* status forest plot of included studies with an AUC.

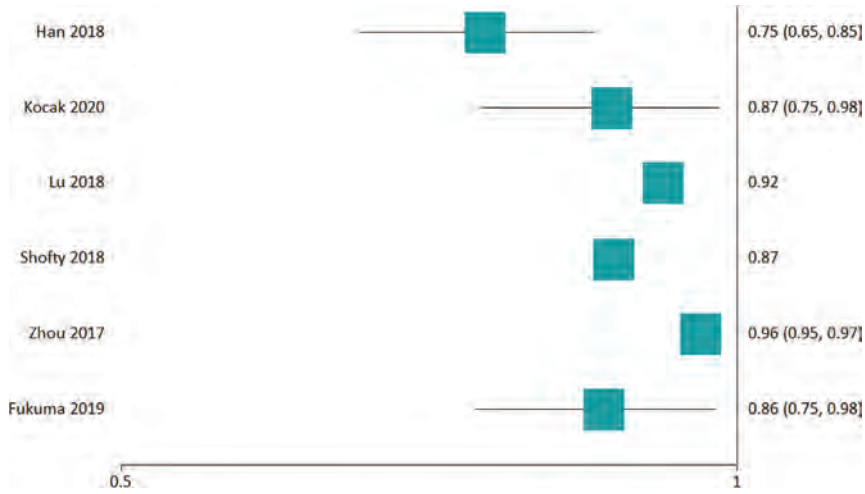

FIG 2. 1p19q status forest plot of included studies with an AUC.

followed by the gray-level run-length matrix[25,27-30,34,40]) with deep learning–derived features, and an SVM machine learning model may result in an optimal radiomic pipeline. One study classified solely using texture-based radiomic features and achieved an AUC = 0.79.[34] Integration of deep learning with radiomic features did not increase the AUC in 1 study[22] but produced the highest AUC = 0.95 in another study.[27] Features derived from qualitative visual inspection (Visually Accessible Rembrandt Images; VASARI) did not increase the AUC compared with just radiomic features.[34] Four studies examined multiparametric imaging.[23,25,29,30] The entropy (randomness of voxel intensities) feature derived from ADC images was significantly different between *IDH*-mut and *IDH* wild-type LGG,[23] suggesting that heterogeneity of ADC values may be helpful in predicting *IDH* status. Nevertheless, while integration of diffusion/perfusion imaging showed improved classification in 3 studies,[25,29,30] ultimately it was not superior to using standard sequences with a different radiogenomic pipeline.[28]

For 1p19q status, the literature indicates that standard image sequences, use of texture-based features (the most common being grey-level run length matrix[26,28,34,35] followed by gray-level co-occurrence matrix[26,28,34]), and a linear SVM machine learning model may result in an optimal radiomic pipeline. The highest AUC = 0.96 was achieved solely using texture-based radiomic features.[34] Clinical and imaging-feature (such as age, sex, and the presence of bleeding or enhancement) integration did not improve the classification performance,[38] nor did solely examining visually-created features.[34] Deep learning feature integration with radiomic features increased classification performance; however, solely examining deep features was superior.[22] The best-performing ML model classifier was achieved by a linear SVM.[28]

For studies included in the meta-analysis, there was high heterogeneity, given the variation in the unique elements of each radiomic pipeline. Heterogeneity is inevitable with any meta-analysis; however, acceptable levels may be a Higgins I^2 of 0%–40%.[41] The meta-analysis found 88.55% and 86.19% heterogeneity for *IDH* and 1p19q status, respectively. Although the QUADAS-2 showed low bias and high applicability, the radiomic-specific RQS assessment showed an overall inadequate clinical applicability of studies, identifying issues, including a lack of cost-effectiveness analysis, clinical utility statistics, or prospective validation. This is consistent with other neuro-oncologic radiomic studies in the literature.[21] The RQS has some limitations, however. For example, greater emphasis is placed on the image-acquisition parameters[12] than on the image-normalization process (making the voxel, section thickness, and matrix size similar among MR imaging scans), despite the latter being important for optimal translation into multi-institutional contexts. Of note, a perceived advantage of the AI algorithms is greater objectivity and thus a more consistent diagnosis, but this has yet to be convincingly proved in the literature.[42]

Classification of LGG for *IDH* status followed by further classification of 1p19q status (when *IDH*-mut) will have multiplicative

effects. There was a sensitivity of 94.4% and specificity of 86.7%[27] for *IDH* status, with a sensitivity of 90% and specificity of 89%[34] for 1p19q. Thus, by using multiplication, we can find the maximum literature prediction of 1p19q status in an *IDH*-mut LGG to have a sensitivity of 85.0% (94.4% × 90%) and a specificity of 77.2% (86.7% × 89%). The conventional radiogenomic pipelines assume that the features assessed are independent, though they are not. For example, to take an example from the visual-feature literature, ill-defined tumor margins have been correlated with *IDH* wild-type LGG,[43] but if the tumor is *IDH*-mut, it is more likely 1p19q-codeletion.[10] There is also uncertainty regarding the interaction between radiomic and conventional visual MR imaging features. For example, if the T2-FLAIR mismatch sign is present, the literature would suggest that this can predict an *IDH*-mut 1p19q-intact glioma with greater confidence than radiomics.[8,44] Yet, when these conventional features with the greatest predictive value are absent, one could expect that radiomics would predict the genotype better than other conventional MR imaging features. Thus, optimal classification may be achieved using a combination of conventional and radiomic features.

Acceptance of AI into clinical practice remains an issue. Much of the literature on integration is opinion-based,[45-48] and research related to understanding challenges is in its early stages.[49-51] Acceptance by patients also remains an issue; a recent study by Palmisciano et al[52] found that only 66.3% of patients found it acceptable for AI to be used during imaging interpration.[53] Issues raised by patients include distrust, lack of knowledge, a lack of personal interaction, questions about the efficacy of the AI algorithm, and the importance of being properly informed of its uses.[54] Similar relevant issues were identified by a computer science literature review[55] on human-AI interaction, such as task allocation, lack of knowledge and/or trust, incorrect use due to confusion, and integration issues due to a potentially radically different work practice.

Future directions for integration into the clinical sphere may come in the form of examining the nonmedical sphere,[55] given successful implementation in other fields such as failure detection in truck engines and welding robots.[56] One specific issue is that some AI programs used were developed in-house and may not be readily available to other institutions; important next steps include comparisons between programs and subsequent validation on larger external cohorts. There is also a lack of clinical trials assessing the integration of radiomic analysis into clinical practice,[44] which was confirmed on our RQS assessment. Guidelines have recently been developed to address these issues, which may provide a framework for integration. For example, Microsoft has recently released a set of 18 general principles for integration into systems, such as explaining to the user (clinician) what the AI algorithm can do, how well it can be done and making it clear how it is performed.[57] A thinking paradigm that may solve this is treating radiomic analysis as a new intervention or drug and applying ideas from existing protocols such as Phase I–IV clinical trials.[58] The Food and Drug Administration has also recently released guidelines for AI integration into health care systems.[59] Given that radiomic analysis is rapidly progressing and combining AI with standard radiologist assessment may show superior outcomes, there needs to be greater effort to translate findings into an interpretable format for clinical radiology.

CONCLUSIONS

The greatest classifier of *IDH* status in LGG was achieved with conventional radiomics in combination with convolutional neural network–derived features, providing a sensitivity of 94.4% and specificity of 86.7% (AUC = 0.95). Optimal classification of 1p19q status occurred using texture-based radiomics, with a sensitivity of 90% and a specificity of 89% (AUC = 0.96). The literature is limited by the use of manual segmentation, suboptimal study design, and the lack of translational work to integrate radiogenomic analysis into clinical practice.

Disclosures: Arian Lasocki—*RELATED*: *Grant*: Peter MacCallum Cancer Foundation, *Comments*: Arian Lasocki was supported by a Peter MacCallum Cancer Foundation Discovery Partner Fellowship, providing clinical backfill to allow dedicated research time.* *Money paid to the institution.

REFERENCES

1. Stark AM, van de Bergh J, Hedderich J, et al. **Glioblastoma: clinical characteristics, prognostic factors and survival in 492 patients.** *Clin Neurol Neurosurg* 2012;114:840–45 CrossRef Medline
2. Louis DN, Perry A, Reifenberger G, et al. **The 2016 World Health Organization Classification of Tumors of the Central Nervous System: a summary.** *Acta Neuropathol* 2016;131:803–20 CrossRef Medline
3. Akay A, Rüksen M, Islekel S. **Magnetic resonance imaging-guided stereotactic biopsy: a review of 83 cases with outcomes.** *Asian J Neurosurg* 2019;14:90–95 CrossRef Medline
4. Lasocki A, Tsui A, Tacey MA, et al. **MRI grading versus histology: predicting survival of World Health Organization grade II-IV astrocytomas.** *AJNR Am J Neuroradiol* 2015;36:77–83 CrossRef Medline
5. Horbinski C. **What do we know about IDH 1/2 mutations so far, and how do we use it?** *Acta Neuropathol* 2013;125:621–36 CrossRef Medline
6. Preusser M, Wöhrer A, Stary S, et al. **Value and limitations of immunohistochemistry and gene sequencing for detection of the IDH 1-R132H mutation in diffuse glioma biopsy specimens.** *J Neuropathol Exp Neurol* 2011;70:715–23 CrossRef Medline
7. Broen MPG, Smits M, Wijnenga MM, et al. **The T2-FLAIR mismatch sign as an imaging marker for non-enhancing IDH-mutant, 1p/19q-intact lower-grade glioma: a validation study.** *Neuro Oncol* 2018;20:1393–99 CrossRef Medline
8. Lasocki A, Gaillard F, Gorelik A, et al. **MRI features can predict 1p/19q status in intracranial gliomas.** *AJNR Am J Neuroradiol* 2018;39:687–92 CrossRef Medline
9. Patel SH, Poisson LM, Brat DJ, et al. **T2-FLAIR mismatch, an imaging biomarker for IDH and 1p/19q status in lower-grade gliomas: a TCGA/TCIA Project.** *Clin Cancer Res* 2017;23:6078–85 CrossRef Medline
10. Johnson DR, Diehn FE, Giannini C, et al. **Genetically defined oligodendroglioma is characterized by indistinct tumor borders at MRI.** *AJNR Am J Neuroradiol* 2017;38:678–84 CrossRef Medline
11. Gillies RJ, Kinahan PE, Hricak H. **Radiomics: images are more than pictures: they are data.** *Radiology* 2016;278:563–77 CrossRef Medline
12. Lambin P, Leijenaar RT, Deist TM, et al. **Radiomics: the bridge between medical imaging and personalized medicine.** *Nat Rev Clin Oncol* 2017;14:749–62 CrossRef Medline
13. van den Bent MJ. **Interobserver variation of the histopathological diagnosis in clinical trials on glioma: a clinician's perspective.** *Acta Neuropathol* 2010;120:297–304 CrossRef Medline

14. McInnes MD, Moher D, Thombs BD, et al; PRISMA-DTA Group. **Preferred Reporting Items for a Systematic Review and Meta-analysis of Diagnostic Test Accuracy Studies: the PRISMA-DTA Statement.** *JAMA* 2018;319:388–96 CrossRef Medline
15. Matsui Y, Maruyama T, Nitta M, et al. **Prediction of lower-grade glioma molecular subtypes using deep learning.** *J Neurooncol* 2020;146:321–27 CrossRef Medline
16. Zhou XH, McClish DK, Obuchowski NA, et al. *Statistical Methods in Diagnostic Medicine*. John Wiley & Sons; 2011
17. Whiting PF, Rutjes AW, Westwood ME, et al; QUADAS-2 Group. **QUADAS-2: a revised tool for the quality assessment of diagnostic accuracy studies.** *Ann Intern Med* 2011;155:529–36 CrossRef Medline
18. Collins GS, Reitsma JB, Altman DG, et al. **Transparent Reporting of a multivariable prediction model for Individual Prognosis Or Diagnosis (TRIPOD).** *Ann Intern Med* 2015;162:735–36 CrossRef Medline
19. McHugh ML. **Interrater reliability: the kappa statistic.** *Biochem Med (Zagreb)* 2012;22:276–82 CrossRef Medline
20. Ursprung S, Beer L, Bruining A, et al. **Radiomics of computed tomography and magnetic resonance imaging in renal cell carcinoma-a systematic review and meta-analysis.** *Eur Radiol* 2020;30:3558–66 CrossRef Medline
21. Park JE, Kim HS, Kim D, et al. **A systematic review reporting quality of radiomics research in neuro-oncology: toward clinical utility and quality improvement using high-dimensional imaging features.** *BMC Cancer* 2020;20:29 CrossRef Medline
22. Fukuma R, Yanagisawa T, Kinoshita M, et al. **Prediction of IDH and TERT promoter mutations in low-grade glioma from magnetic resonance images using a convolutional neural network.** *Sci Rep* 2019;9:20311 CrossRef Medline
23. Gihr GA, Horvath-Rizea D, Hekeler E, et al. **Histogram analysis of diffusion weighted imaging in low-grade gliomas: in vivo characterization of tumor architecture and corresponding neuropathology.** *Front Oncol* 2020;10:206 CrossRef Medline
24. Jakola AS, Zhang YH, Skjulsvik AJ, et al. **Quantitative texture analysis in the prediction of IDH status in low-grade gliomas.** *Clin Neurol Neurosurg* 2018;164:114–20 CrossRef Medline
25. Kim M, Jung SY, Park JE, et al. **Diffusion- and perfusion-weighted MRI radiomics model may predict isocitrate dehydrogenase (IDH) mutation and tumor aggressiveness in diffuse lower grade glioma.** *Eur Radiol* 2020;30:2142–51 CrossRef Medline
26. Kocak B, Durmaz ES, Ates E, et al. **Radiogenomics of lower-grade gliomas: machine learning-based MRI texture analysis for predicting 1p/19q codeletion status.** *Eur Radiol* 2020;30:877–86 CrossRef Medline
27. Li Z, Wang Y, Yu J, et al. **Deep Learning-Based Radiomics (DLR) and its usage in noninvasive IDH 1 prediction for low grade glioma.** *Sci Rep* 2017;7:5467 CrossRef Medline
28. Lu CF, Hsu FT, Hsieh KLC, et al. **Machine learning–based radiomics for molecular subtyping of gliomas.** *Clin Cancer Res* 2018;24:4429–36 CrossRef Medline
29. Park CJ, Choi YS, Park YW, et al. **Diffusion tensor imaging radiomics in lower-grade glioma: improving subtyping of isocitrate dehydrogenase mutation status.** *Neuroradiology* 2020;62:319–26 CrossRef Medline
30. Ren Y, Zhang X, Rui W, et al. **Noninvasive prediction of IDH 1 mutation and ATRX expression loss in low-grade gliomas using multiparametric MR radiomic features.** *J Magn Reson Imaging* 2019;49:808–17 CrossRef Medline
31. Shofty B, Artzi M, Ben Bashat D, et al. **MRI radiomics analysis of molecular alterations in low-grade gliomas.** *Int J Comput Assist Radiol Surg* 2018;13:563–71 CrossRef Medline
32. Yu J, Shi Z, Lian Y, et al. **Noninvasive IDH 1 mutation estimation based on a quantitative radiomics approach for grade II glioma.** *Eur Radiol* 2017;27:3509–22 CrossRef Medline
33. Zhang X, Tian Q, Wang L, et al. **Radiomics strategy for molecular subtype stratification of lower-grade glioma: detecting IDH and TP53 mutations based on multimodal MRI.** *J Magn Reson Imaging* 2018;48:916–26 CrossRef Medline
34. Zhou H, Vallieres M, Bai H, et al. **MRI features predict survival and molecular markers in diffuse lower-grade gliomas.** *Neuro Oncol* 2017;19:862–70 CrossRef Medline
35. Han Y, Wang W, Yang Y, et al. **Amide proton transfer imaging in predicting isocitrate dehydrogenase 1 mutation status of grade II/III gliomas based on support vector machine.** *Front Neurosci* 2020;14:144 CrossRef Medline
36. Bakas S, Akbari H, Sotiras A, et al. **Advancing The Cancer Genome Atlas glioma MRI collections with expert segmentation labels and radiomic features.** *Sci Data* 2017;4:170117 CrossRef Medline
37. Bakas S, Reyes M, Jakab A, et al. **Identifying the best machine learning algorithms for brain tumor segmentation, progression assessment, and overall survival prediction in the BRATS challenge.** 2018 https://arxiv.org/abs/1811.02629. Accessed April 18, 2020
38. Menze BH, Jakab A, Bauer S, et al. **The Multimodal Brain Tumor Image Segmentation Benchmark (BRATS).** *IEEE Trans Med Imaging* 2015;34:1993–2024 CrossRef Medline
39. Myronenko A. 3D MRI brain tumor segmentation using autoencoder regularization. *International MICCAI Brainlesion Workshop:* Springer; 2018:311–20
40. Zhang Z, Xiao J, Wu S, et al. **Deep convolutional radiomic features on diffusion tensor images for classification of glioma grades.** *J Digit Imaging*.2020;33:826–37 CrossRef Medline
41. Higgins JP, Thomas J, Chandler J, et al. *Cochrane Handbook for Systematic Reviews of Interventions*. John Wiley & Sons; 2019
42. van der Voort SR, Incekara F, Wijnenga MM, et al. **Predicting the 1p/19q codeletion status of presumed low-grade glioma with an externally validated machine learning algorithm.** *Clin Cancer Res* 2019;25:7455–62 CrossRef Medline
43. Delfanti RL, Piccioni DE, Handwerker J, et al. **Imaging correlates for the 2016 update on WHO classification of grade II/III gliomas: implications for IDH, 1p/19q and ATRX status.** *J Neurooncol* 2017;135:601–09 CrossRef Medline
44. Zhou Q, Cao YH, Chen ZH. **Lack of evidence and criteria to evaluate artificial intelligence and radiomics tools to be implemented in clinical settings.** *Eur J Nucl Med Mol Imaging* 2019;46:2812–13 CrossRef Medline
45. Lew C. **The promise of clinical AI: an adaptive future.** *Applied Radiol* 2018;47:3–6 https://www.appliedradiology.com/articles/the-promise-of-clinical-ai-an-adaptive-future#:~:text=The%20Promise%20of%20Clinical%20AI%3A%20An%20Adaptive%20Future.,predictive%20analytics%20for%20population%20health%20management%2C%20and%20beyond. Accessed April 18, 2020
46. Sana M. **Machine learning and artificial intelligence in radiology.** *J Am Coll Radiol* 2018;15:1139–42 CrossRef Medline
47. Shader RI. **Some thoughts about artificial intelligence.** *Clin Ther* 2019;41:1401–03 CrossRef Medline
48. Topol EJ. **High-performance medicine: the convergence of human and artificial intelligence.** *Nat Med* 2019;25:44–56 CrossRef Medline
49. European Society of Radiology. **Impact of artificial intelligence on radiology: a EuroAIM survey among members of the European Society of Radiology.** *Insights imaging* 2019;10:105 CrossRef Medline
50. van Hoek J, Huber A, Leichtle A, et al. **A survey on the future of radiology among radiologists, medical students and surgeons: students and surgeons tend to be more skeptical about artificial intelligence and radiologists may fear that other disciplines take over.** *Eur J Radiol* 2019;121:108742 CrossRef Medline
51. Waymel Q, Badr S, Demondion X, et al. **Impact of the rise of artificial intelligence in radiology: what do radiologists think?** *Diagn Interv Imaging* 2019;100:327–36 CrossRef Medline
52. Palmisciano P, Jamjoom AA, Taylor D, et al. **Attitudes of patients and their relatives toward artificial intelligence in neurosurgery.** *World Neurosurg* 2020;138:e627–33 CrossRef Medline

53. Likert R. **A technique for the measurement of attitudes.** *Archives of Psychology* 1932;22:55
54. Ongena YP, Haan M, Yakar D, et al. **Patients' views on the implementation of artificial intelligence in radiology: development and validation of a standardized questionnaire.** *Eur Radiol* 2020;30:1033–40 CrossRef Medline
55. Janssen CP, Donker SF, Brumby DP, et al. **History and future of human-automation interaction.** *International Journal of Human-Computer Studies* 2019;131:99–107 CrossRef
56. IBM Services. **Beyond the hype: a guide to understanding and successfully implementing artificial intelligence within your business.** https://www.ibm.com/downloads/cas/8ZDXNKQ4. 2018. Accessed April 18, 2020
57. Amershi S, Weld D, Vorvoreanu M, et al. **Guidelines for human-AI interaction.** In: *Proceedings of the Cultural Homestay International Conference on Human Factors in Computing System*, Glasgow, UK; May 4–9, 2019
58. Friedman LM. Furberg CD, DeMets Dl, et al. *Fundamentals of Clinical Trials*. Springer-Verlag; 2010
59. He J, Baxter SL, Xu J, et al. **The practical implementation of artificial intelligence technologies in medicine.** *Nat Med* 2019;25:30–36 CrossRef Medline

Estimating Local Cellular Density in Glioma Using MR Imaging Data

E.D.H. Gates, J.S. Weinberg, S.S. Prabhu, J.S. Lin, J. Hamilton, J.D. Hazle, G.N. Fuller, V. Baladandayuthapani, D.T. Fuentes, and D. Schellingerhout

ABSTRACT

BACKGROUND AND PURPOSE: Increased cellular density is a hallmark of gliomas, both in the bulk of the tumor and in areas of tumor infiltration into surrounding brain. Altered cellular density causes altered imaging findings, but the degree to which cellular density can be quantitatively estimated from imaging is unknown. The purpose of this study was to discover the best MR imaging and processing techniques to make quantitative and spatially specific estimates of cellular density.

MATERIALS AND METHODS: We collected stereotactic biopsies in a prospective imaging clinical trial targeting untreated patients with gliomas at our institution undergoing their first resection. The data included preoperative MR imaging with conventional anatomic, diffusion, perfusion, and permeability sequences and quantitative histopathology on biopsy samples. We then used multiple machine learning methodologies to estimate cellular density using local intensity information from the MR images and quantitative cellular density measurements at the biopsy coordinates as the criterion standard.

RESULTS: The random forest methodology estimated cellular density with $R^2 = 0.59$ between predicted and observed values using 4 input imaging sequences chosen from our full set of imaging data (T2, fractional anisotropy, CBF, and area under the curve from permeability imaging). Limiting input to conventional MR images (T1 pre- and postcontrast, T2, and FLAIR) yielded slightly degraded performance ($R^2 = 0.52$). Outputs were also reported as graphic maps.

CONCLUSIONS: Cellular density can be estimated with moderate-to-strong correlations using MR imaging inputs. The random forest machine learning model provided the best estimates. These spatially specific estimates of cellular density will likely be useful in guiding both diagnosis and treatment.

ABBREVIATIONS: AUC = area under the curve; CD = cellular density; DCE = dynamic contrast-enhanced; RF = random forest; T1C = T1 postcontrast

Increased cellular density (CD) is a hallmark of cancer and a key feature in histologic glioma analysis.[1] Mapping cellular density throughout a tumor would be a valuable tool to probe how tumors infiltrate and analyze the transition between diseased and healthy brain. However, measuring CD requires tissue, which entails additional risks and is expensive to obtain. There is no currently accepted clinical algorithm to translate imaging data into quantitative assessments of CD.

There is great need for a method to estimate CD noninvasively in human patients with gliomas. In this article, we describe the development of such a method using MR imaging data inputs by correlating with multiple biopsy specimens acquired during a prospective human clinical trial. We obtained comprehensive MR imaging, including conventional, diffusion, perfusion, and permeability imaging sequences. We used machine learning approaches to correlate imaging findings with CD measurements from pathology, devised an algorithm to estimate CD from MR imaging inputs, and

Received April 13, 2020; accepted after revision August 22.

From the Departments of Imaging Physics (E.D.H.G., J.S.L., J.D.H., D.T.F.), Neurosurgery (J.S.W., S.S.P.), Neuroradiology (J.H., D.S.), Pathology (G.N.F.), and Cancer Systems Imaging (D.S.), University of Texas MD Anderson Cancer Center, Houston, Texas; The University of Texas MD Anderson Cancer Center UTHealth Graduate School of Biomedical Sciences (E.D.H.G.), Houston, Texas; Baylor College of Medicine (J.S.L.), Houston, Texas; Department of Bioengineering (J.S.L.), Rice University, Houston, Texas; Radiology Partners (J.H.), Houston, Texas; and Department of Computational Medicine and Bioinformatics (V.B.), University of Michigan School of Public Health, Ann Arbor, Michigan.

E.D.H. Gates is supported by a training fellowship from the Gulf Coast Consortia and the National Library of Medicine Training Program in Biomedical Informatics & Data Science (T15LM007093) and acknowledges support from the American Legion Auxiliary. Partial support for this study is provided by the Dunn Chair funds (to Dr Bill Murphy), the MD Anderson Cancer Center Internal Research Grant and Clinical Research Support mechanisms for physician-sponsored clinical trials, and the Greenspun neurosurgical research fund. Funding was also provided by the National Cancer Institute (P30 CA016672).

Please address correspondence to Dawid Schellingerhout, MD, Neuroradiology and Cancer Systems Imaging, UT MD Anderson Cancer Center, 1400 Pressler St, Unit 1482, Houston, TX, 77030; e-mail: Dawid.Schellingerhout@mdanderson.org

Indicates open access to non-subscribers at www.ajnr.org
Indicates article with supplemental online appendix and tables.
http://dx.doi.org/10.3174/ajnr.A6884

generated CD maps for the visual display of the predictions. We identified the most informative imaging data subset. This work has multiple applications in the diagnosis and treatment of patients with gliomas: For example, the method can be used to guide biopsy, resection, and surgery and delineate tumor borderzones both pre- and postoperatively.[2]

MATERIALS AND METHODS

Data were collected as part of a Health Insurance Portability and Accountability Act–compliant institutional review board–approved imaging clinical trial protocol (NCT03458676) for adult, treatment-naïve patients with gliomas at MD Anderson Cancer Center. See Table 1 for demographics. We have previously reported results in the estimation of Ki-67 and tumor grade.[3,4] Up to 5 separate biopsies were collected per patient, which were targeted by 2 alternative methods:

- The conventional biopsy site was defined as enhancing tumor if present or T2 bright signal closest to an accessible brain surface
- The advanced biopsy site was defined, in order, by high relative CBV, high volume transfer constant, and/or restricted diffusion.

Additional biopsies could be obtained en route to the sites defined above, with preference given to sampling normal brain and the brain-tumor interface when possible. Biopsy locations were sampled under stereotactic guidance using iPlan cranial neuronavigation software (Brainlab), and the final sampling coordinate locations were recorded. Tissue samples were sectioned at 4-μm thickness and stained with H&E. Some slides were also immunohistochemically stained with proliferation and vascularity markers, but these data were not used in the cell density measurement. The H&E-stained tissue was analyzed by a board-certified neuropathologist, and the cell density was measured semiautomatically in nuclei/square millimeter using Aperio ImageScope software (Leica Biosystems).

Image Acquisition

Four clinical categories of imaging were obtained for every patient on a Signa HDxt 3T or Discovery MR750 3T clinical MR imaging scanner (GE Healthcare): anatomic/conventional, diffusion, perfusion, and permeability. Detailed acquisition parameters are given in the Online Appendix and Online Tables 1 and 2. A total of 23 imaging parameters were acquired or generated.

Anatomic images were T1-weighted, T1 postgadolinium, T2-weighted, T2*/susceptibility, FLAIR, and T2*-weighted angiography (SWAN).

DWI and DTI were both acquired for each patient. They were then processed to generate maps of ADC, exponential ADC (eADC), and fractional anisotropy.[5,6]

Finally, we acquired 2 image series using a dynamic acquisition after the injection of contrast. The dynamic contrast-enhanced (DCE) image series was acquired using a 0.1-mmol/kg contrast bolus, and this same bolus was used for the conventional T1 contrast-enhanced image. The raw data were processed using nordicICE (NordicNeuroLab) using the full extended Tofts model, including leakage correction[7-9] and arterial input deconvolution. This process yielded maps of forward and backwards transfer constants (K_{trans} and k_{ep} respectively), plasma and extravascular extracellular contrast fractions (v_p and v_e), time to peak enhancement (TTP), area under enhancement curve (AUC), and peak enhancement.[7-9] Later in the same study, a second bolus of contrast (again 0.1 mmol/kg) was injected to acquire dynamic susceptibility contrast image data. This time-series was similarly processed to yield maps of relative CBV, CBF, MTT, delay time, and leakage correction K2.[10-12]

Image Normalization and Measurement

Anatomic images were normalized on the basis of patient-specific average tissue intensities. The T1-weighted, FLAIR, and T2*-weighted angiography images were linearly scaled so that white matter (WM) and CSF had average intensities of 1 and 0, respectively. Similarly, T2-weighted and T2*-weighted images were scaled with WM and CSF having average intensities of 0 and 1. T1 postcontrast was scaled using CSF and gray matter. Parametric maps from DWI, DSC, and DCE are quantitative and were used as provided. Although all images were acquired in the same study, we mutually coregistered them using a 6-*df* and 12-*df* affine registration in ANTs[13] to correct for patient motion and geometric distortion.[14,15] For each biopsy, a 5-mm spheric VOI was placed at the sampling coordinates, and the average intensity in this VOI was recorded for each image parameter.

Cell Density in Control Regions

To record imaging characteristic in normal brain, a neuroradiologist placed an ROI in normal-appearing white matter contralateral to the location of each tissue biopsy, and the average image intensity was recorded. These "virtual biopsies" were assumed to have cell density equal to that of normal white matter. We used values provided by Roetzer et al[16] and corrected the CD estimates for histologic section thickness using the Abercrombie method (see On-line Appendix).[17,18] We obtained a best estimate for normal white matter cell density of 2912

Table 1: Patient demographics

Demographics	
No. (Sex)	23 Patients (14 women, 9 men)
Age (mean) (range) (yr)	43.9 [SD, 16.9] range, 21–80
WHO grade (I/II/III/IV)	0/7/9/7
Biopsy samples/patient (mean)	2.26 [SD, 0.54]
No. of biopsy samples in final analysis	52 real + 52 virtual

Note:—WHO indicates World Health Organization.

Table 2: Normal brain tissue cell density estimates (1/mm^2)

	Mean	SD	Mean, Corrected to 4-μm Thickness	SD, Corrected to 4-μm Thickness
Cortex	2473[a]	716[a]	2011	582
White matter	3581[a]	828[a]	2912	673
Tumor	5714[a]	1786[a]	4646	1452

[a] Data reproduced from Table 1 with permission from Roetzer et al.[16] Virtual biopsies used mean and SD for white matter.

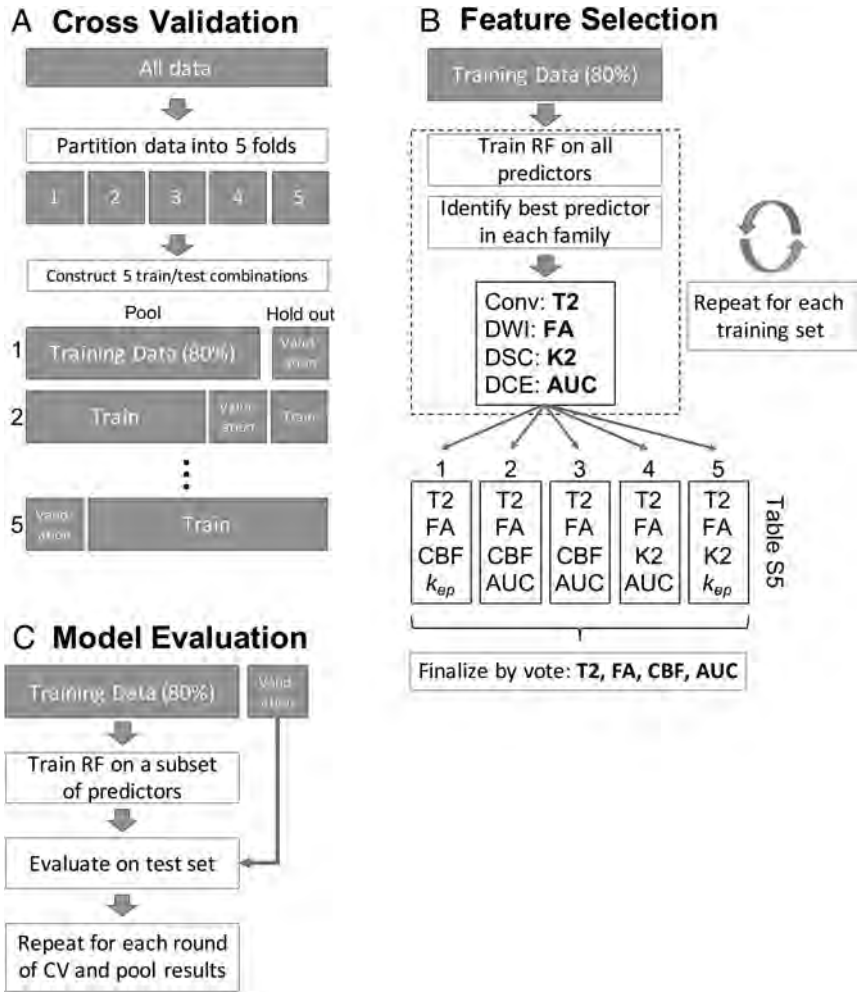

FIG 1. Schematic of each of the 3 main stages of the model-building procedure. *A*, The data are partitioned into 5 homogeneous folds, each comprising 80% of the data for training and 20% for validation, repeated 5 times. Within each round of cross-validation (CV) 1 fold is held out for validation while the other 4 (80%) are pooled to form a training set. *B*, A random forest (RF) model was fit to the training data, and the best predictor variable from each imaging family was selected. Because there are 5 rounds of CV, this procedure was repeated 5 times and the selections (listed in Online Tables 4 and 5) were combined by voting. *C*, Using the consensus subset of predictor variables after feature selection, we trained another random forest on each training set and made predictions on the corresponding holdout set. The average correlations between predicted and observed values across all rounds of CV are given in Table 4. K_{ep} indicates reverse transfer constant from DCE imaging.

[SD, 673] nuclei/mm^2. Table 2 lists values reproduced from Roetzer et al,[16] and the corrected values were used in our study.

Model-Building Procedure

To avoid overfitting, we performed 5-fold cross-validation using disjoint training and testing subsets of the biopsy data within each round (Fig 1*A*). We partitioned our data into 5 groups, each containing about 20% of our data. To further preserve independence, we placed each sample in the same fold as its paired virtual biopsy.

Variable selection was performed to reduce the number of model inputs from the 23 available parameters to something more parsimonious and to reduce information redundancy among related imaging variables. Within each round of cross-validation, we fit a random forest model to the training subset (4 of 5 groups) using all input variables and computed a variable importance ranking on the basis of the permuted out-of-bag data.[19] After the rankings were computed, the most important predictor from each imaging family was used to select 4 final predictors, 1 each from anatomic, diffusion, perfusion, and permeability.[3,20] Because this was repeated for each round of cross-validation, 5 variable selections resulted. When the 5 rankings gave different results regarding the most important imaging variable, simple voting was used to determine a consensus. This process is illustrated in Fig 1*B* and yielded a final set of imaging variables to include in the final model. To provide a fair comparison, we used the final 4-variable set in all model classes tested.

The cross-validation procedure was performed using both the selected variables within each round and the final 4 variables based on consensus among all rounds. The predicted estimates of CD were compared with the actual values known in the 20% validation set and assessed using the Pearson correlation (R^2) between predicted and observed CD. This process is explained in Fig 1*C*. Figure 1 illustrates the full process with the random forest model (our eventual winner), but several models were tested (single decision tree, single-layer neural network, and linear regression). Model descriptions are given in Online Table 3. The model building process was implemented in R, Version 3.4.2 (http://www.r-project.org/).

RESULTS

Patient Data

Thirty-one patients were enrolled in the trial between 2013 and 2016 (mean age, 46 ± [SD, 16] years). Patient demographics are summarized in Table 1. Tissue could not be harvested from 5 patients due to surgical complexity or technical difficulties. For another 3 patients, missing DCE imaging data (1 patient) or unanalyzable tissue samples (2 patients) excluded them from analysis. After exclusions, 23 evaluable patients with 52 image-guided biopsies remained in the final analysis. Of these patients, 7 had clinical grade II gliomas, 9 had grade III, and 7 had grade IV. Among the tissue samples themselves, 9 were collected from contrast-enhancing regions, 2 were collected from just outside the visible T2 hyperintensity, none were collected from necrotic regions, and the remainder were collected from the visible T2-hyperintense tumor. The cell density among all tissue samples increased with increasing sample grades as listed in Table 3.

Three samples were histologically graded as normal cortex and provide some comparison with the normal cell densities used for virtual biopsies. The recorded CD values were 2169, 1729, and 1432 nuclei/mm^2, comparing well with the CD values of Roetzer et al[16] for normal cortex at 2011 [SD, 582] nuclei/mm^2. See Table 2 for the original estimates and corrected values comparable with our measurements.

Table 3: Number of samples of each WHO grade[a]

Sample Grade	No. of Samples	Cell Density (Mean) (SD)
Normal[b]	3	1777 [SD, 371]
II	39	5790 [SD, 2667]
II/III	3	6085 [SD, 2022]
III[c]	2	2584, 14,634
IV	5	11,547 [SD, 4252]

[a] The grade of a sample is not necessarily the same as the patient's clinical grade. As expected, the cell density of the samples increases with increasing sample grade.
[b] These samples appeared histologically tumor-free but showed Ki-67-positive endothelial cells.
[c] Because only 2 samples were grade III, the values are listed.

Variable Selection and Predictive Modeling

The best predictor from each imaging sequence family for the random forest model was determined by the most votes from each fold of cross-validation and is summarized in Online Table 4. Combining the selections produced a 4-variable set: T2, fractional anisotropy, CBF, and AUC. Of these 4 predictors in the final model, the T2-weighted image intensity had the greatest importance as measured by the random forest with a 27% increase in mean-square error when variables are permuted. Fractional anisotropy and AUC have a smaller importance at 18.0% and 16.1%, respectively. Finally, CBF, despite being the best predictor from the DSC family in 3 of 5 folds of cross-validation, had only an importance of 11.3% increased mean-square error in the final model.

Similar magnitude variable importance was measured for the conventional-only model, ranging from 26.7% for the T2-weighted image down to 9.4% for the FLAIR image, shown in Online Table 5. While the importance measures provide some information about how each predictor relates to CD, they do not measure the combined nonlinear relationships modeled by the random forest.

We compared the reduced variable set selected with modeling done with no selection to show the effects of variable selection. We found comparable modeling performance using the random forest trained on all 23 variables and using the much smaller 4-variable set chosen by random forest importance (R^2 = 0.572 versus 0.586). The predicted-versus-observed R^2 values are given in Table 4 and Fig 2. Additionally, root-mean-square error values are listed in Online Table 6. Overall, the high average R^2 = 0.586 with 4 imaging variables and the random forest model suggest a strong ability to predict cell density with imaging data.

Using only conventional imaging variables yielded marginally lesser predictive performance. For conventional imaging only, the highest performance was also with all 6 conventional images as variables in a random forest model, and there was a small improvement made by reducing the number of input

Table 4: Average R^2 for predicted-versus-observed cell density for cross-validation[a]

	All Variables (23 Inputs)	Variables Selected by RF Importance (4 Inputs)	All Conventional Variables (6 Inputs)	Variables Selected by RF Importance: Conventional Only (4 Inputs)
Random forest	0.572	0.586	0.513	0.523
Linear	0.542	0.572	0.444	0.475
Neural network	0.265	0.460	0.382	0.379
Decision tree	0.301	0.325	0.376	0.376

[a] The columns list variables used to train the predictive model. "All Variables" is simply using all 23 imaging parameters of all 6 conventional sequences, whereas "RF Importance" and "RF Importance, Conventional" use the final 4 variable sets shown in Online Tables 4 and 5. A larger average R^2 indicated better performance.

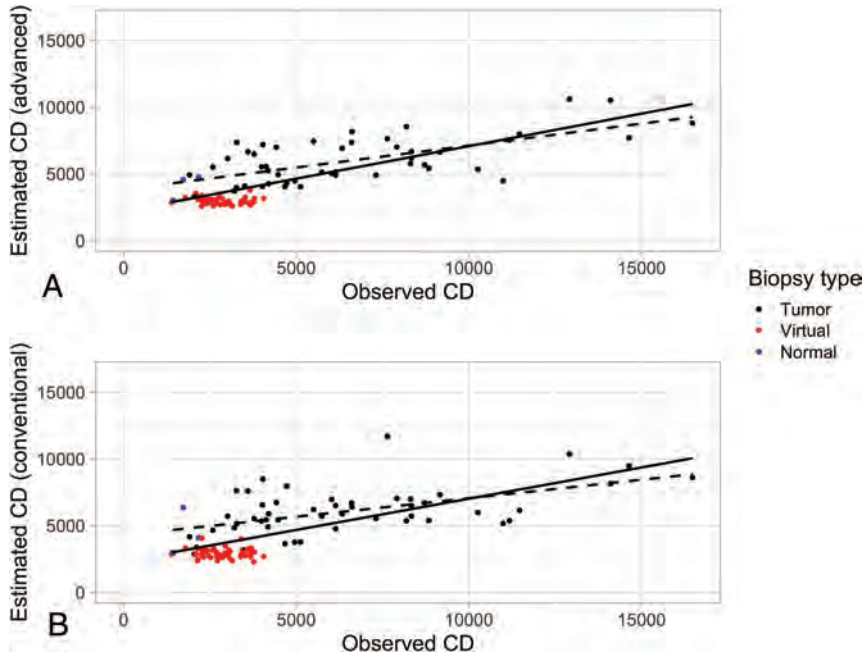

FIG 2. Predicted and observed cell density (nuclei/square millimeter) for the random forest model using 4 fixed inputs from conventional-plus-advanced imaging. *A*, The *solid line* is the best fit for all predictions (R^2 = 0.56), and the *dashed black line* is the best fit for real-sample predictions only (R^2 = 0.39), that is, excluding virtual samples (*red points*). *B*, The predictions using conventional imaging only. The model performance decreased slightly with R^2 = 0.50 for all observations and R^2 = 0.30 for real observations only. *Blue points* are real tissue biopsies that were graded as histologically normal-appearing. The cell density for these points is generally lower than the CD for tumor samples and falls within the range of the virtual biopsies.

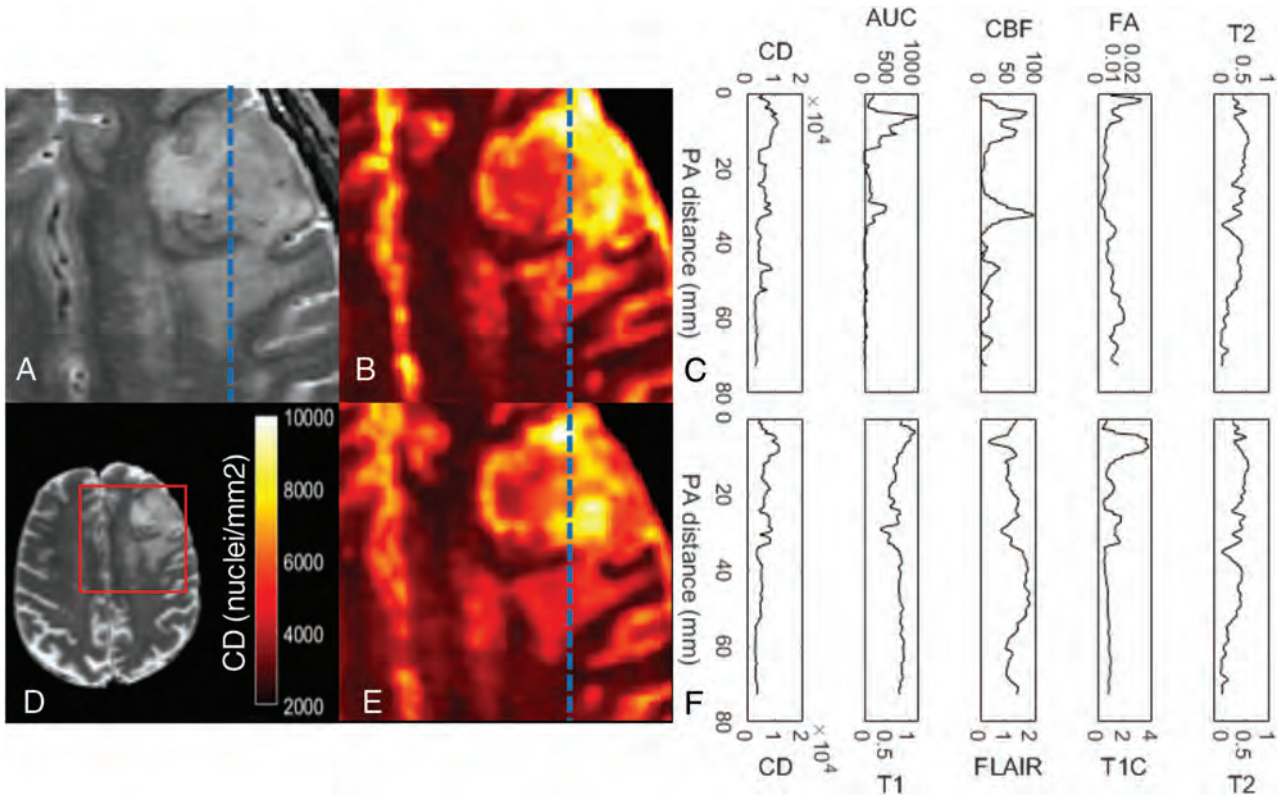

FIG 3. Estimated map of cell density using machine learning models. *A*, The T2-weighted image of a glioblastoma. *B*, The estimated cell density map using the 4 inputs to the final model (T2, fractional anisotropy, CBF, and AUC) selected from all the available imaging data (conventional and advanced) and smoothed by a 1-mm radius filter. The profiles shown in *C* correspond to the *dashed blue line* in *A, B, a*nd *E*. We can see in *C* that the predicted CD is strongly related to the AUC and CBF within the tumor volume. *E*, The estimated cell density map using conventional imaging only with the analogous profiles shown in *F*. The model predicts less extreme values than seen with the model using advanced imaging. *D*, The whole axial section of the T2-weighted image for reference with the cropped area for *A, B, a*nd *E* is *outlined in red*. PA indicates poster-oanterior distance.

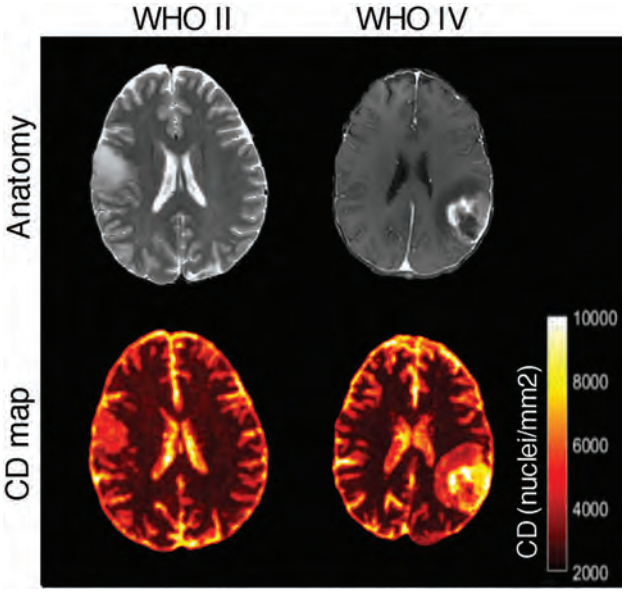

FIG 4. Sample cell density maps for a low-grade glioma (World Health Organization II, left images) and a high-grade glioblastoma (World Health Organization IV, images). The T2-weighted or TI-weighted post-contrast images are shown for reference. As expected, the low-grade tumor shows lower and more homogeneous cell density estimates.

variables from 6 to 4 ($R^2 = 0.513$ versus 0.523). The 4-variable set consisted of T2, T1 postcontrast (T1C), FLAIR, and T1 (Online Table 5). These predictions also are strong enough to still be clinically meaningful. No other model tested using only conventional imaging performed better than the random forest.

Maps of cell density generated using the random forest model and the selected conventional and advanced imaging variables are shown in Figs 3 and 4. As expected, the estimated cell density is heightened in regions of increased blood flow, permeability, and contrast enhancement. The estimated CD is also increased in regions of T2 hyperintensity relative to the normal white matter, which may represent infiltrative tumor growth. By looking at a line profile in Fig 3, we observe how the estimates based on the final predictive model change with the input images across the tumor. The importance of AUC and CBF in predicting CD within the visible tumor can be visually appreciated by studying these plotted transects. Additionally, these maps demonstrate the increased CD and heterogeneity of high-grade gliomas (Fig 4), showing the potential value of making local predictions of cell density because such a map may be useful for guiding therapeutic interventions for a range of glioma grades.

DISCUSSION

We have derived an algorithm for the point-wise local estimation of CD in gliomas using MR imaging data. Using only conventional anatomic imaging sequences, T1, FLAIR, T1C, and T2, CD can be estimated to a R^2 of 0.523. When advanced imaging from diffusion tensor imaging, perfusion, and permeability sequences is also used, CD can be estimated to an R^2 of 0.586. The final inputs to these predictions are areas under the curve from DCE, cerebral blood flow, fractional anisotropy, and T2. This algorithm allows the construction of CD maps of the brain, translating imaging information into quantitative pathologic estimates that may be useful to guide biopsy and treatment.

Our work has avoided global-level image analysis, including "radiomics,"[20-22] due to biologic limitations imposed by histologic heterogeneity exhibited by gliomas.[23] Instead, we performed point-wise spatially specific analysis using tissue samples as the criterion standard, which allows local correlation with MR image characteristics and, in turn, point-wise estimates of CD. CD is 1 characteristic that varies considerably between tumor and healthy brain tissue[16,24] and also correlates with tumor aggressiveness, making it a useful target for predictive modeling.

In previous work, similar methods have shown effective correlation of imaging with proliferation, grade, and genetic heterogeneity.[3,4,25] We used a similar and effective methodology here to develop predictive models for CD as reported in our previous work.[3,4] However, estimating cell density represents a very different biologic target with different applications and stands separately from estimating proliferation or tumor grade. Our final model also takes advantage of different derivates of advanced imaging sequences.

Other previous studies have also estimated glioma cell density with spatially specific tissue samples. These studies are characterized by similar imaging protocols, including DTI or DSC, and generally find correlations with CD.[24,26] However, the exact image features like CBV versus CBF, ADC versus fractional anisotropy, or mean intensity versus 90th percentile intensity vary. Possible explanations for these discrepancies are differences in sample grades, such as only including samples from glioblastoma,[27] or subtle differences in measurement methods for imaging or cell density, cellularity, or related quantities. Overall, our work finds similar results and includes the addition of imaging features from DCE, a greater number of samples, advanced machine learning modeling via random forest, and a smaller number of variables included in the final model.

Our study confirmed the relationship between nuclear density and fractional anisotropy,[24] which is a natural expectation, considering that increased nuclei mean increased cell packing. This reduces water movement and affects diffusion parameters. While not used in the final predictive model, we also observed the well-established correlation between ADC and cell density.[27] The selection of fractional anisotropy over ADC within the 5 folds of cross-validation does not exclude ADC as a strong predictor of CD; it means simply that FA was a stronger predictor and we chose a priori to include only 1 diffusion parameter in the final model to reduce redundancy. There are many strongly correlated quantities derived from similar source data that are equally useful for predictive modeling and could be substituted with similar performance.

These correlations among sequences may also explain our success in predicting CD (R^2 = 0.523) using only conventional imaging sequences: T1, T1 postcontrast, T2, and FLAIR. The DCE parameter AUC is a rough measure of total blood-brain-barrier disruption;[28] thus, we would expect similar information to be contained in the T1 postcontrast image data. Correlating imaging with pathology (like cell density) is a rich way to help understand the degree to which these advanced sequences and their similar conventional sequences may probe the same underlying biologic processes. Such sequences have evolved in clinical practice because they are informative of biology and highlight pathology (ie, heightened CD).

The technical demands of collecting spatially specific tissue samples and comprehensive preoperative imaging with diffusion-weighted, DSC, and DCE imaging mean that our study is somewhat limited by the small sample size. However, the 52 samples used in the final analysis and the additional 52 corresponding virtual controls were sufficient to make useful estimates of cell density. Increased sample size would help improve model confidence and would likely help stabilize some of the variable selections that changed between cross-validation folds. An additional limitation is the assumption of cell density for normal white matter. Ethical constraints prohibit sampling healthy brain, so we must impute values for normal tissue on the basis of literature values.[16,17] The values we used from Roetzer et al[16] do appear to agree with our values in both normal samples and tumor.

CONCLUSIONS

Our methodology allows noninvasive estimation of CD at points in the gliomatous brain with clinically useful accuracy using a combination of MR imaging sequences that are already in wide clinical use. CD estimates can be used to generate a map of estimated cell density for the whole brain. Our work is consistent with previous studies[3,24] and with clinical intuition. Maps of CD could be a useful clinical tool to guide biopsies and resections, measure the extent of resection, or plan radiation treatments. Additional trials to prospectively validate our estimating algorithms are justified.

Disclosures: Veera Baladandayuthapani—*UNRELATED*: *Employment*: University of Michigan.

REFERENCES

1. Louis DN, Perry A, Reifenberger G, et al. **The 2016 World Health Organization Classification of Tumors of the Central Nervous System: a summary.** *Acta Neuropathol* 2016;131:803–20 CrossRef Medline
2. Li YM, Suki D, Hess K, et al. **The influence of maximum safe resection of glioblastoma on survival in 1229 patients: can we do better than gross-total resection?** *J Neurosurg* 2016;124:977–88 CrossRef Medline
3. Gates EDH, Lin JS, Weinberg JS, et al. **Guiding the first biopsy in patients with gliomas using estimated Ki-67 maps derived from MRI: conventional versus advanced imaging.** *Neuro Oncol* 2019;21:527–36 CrossRef Medline
4. Gates ED, Lin JS, Weinberg JS, et al. **Imaging-based algorithm for the local grading of glioma.** *AJNR Am J Neuroradiol* 2020;41:400–07 CrossRef Medline

5. Arlinghaus L, Yankeelov TE. Diffusion-Weighted MRI. In: Yankeelov TE, Pickens DR, Price RR, eds. *Quantitative MRI in Cancer*. Taylor & Francis; 2011:81–98
6. Basser PJ, Pierpaoli C. **Microstructural and physiological features of tissues elucidated by quantitative-diffusion-tensor MRI.** *J Magn Reson B* 1996;111:209–19 CrossRef Medline
7. Tofts PS, Brix G, Buckley DL, et al. **Estimating kinetic parameters from dynamic contrast-enhanced T(1)-weighted MRI of a diffusable tracer: standardized quantities and symbols.** *J Magn Reson Imaging* 1999;10:223–32 CrossRef Medline
8. Sourbron SP, Buckley DL. **Classic models for dynamic contrast-enhanced MRI.** *NMR Biomed* 2013;26:1004–27 CrossRef Medline
9. Sung YS, Park B, Choi Y, et al. **Dynamic contrast-enhanced MRI for oncology drug development.** *J Magn Reson Imaging* 2016;44:251–64 CrossRef Medline
10. Ostergaard L, Sorensen AG, Kwong KK, et al. **High-resolution measurement of cerebral blood flow using intravascular tracer bolus passages, Part II: experimental comparison and preliminary results.** *Magn Reson Med* 1996;36:726–36 CrossRef Medline
11. Østergaard L, Weisskoff RM, Chesler DA, et al. **High-resolution measurement of cerebral blood flow using intravascular tracer bolus passages, Part I: mathematical approach and statistical analysis.** *Magn Reson Med* 1996;36:715–25 CrossRef Medline
12. Boxerman JL, Schmainda KM, Weiskoff RM. **Relative cerebral blood volume maps corrected for contrast agent extravasation significantly correlate with glioma tumor grade, whereas uncorrected maps do not.** *AJNR Am J Neuroradiol* 2006;27:859–67 Medline
13. Avants BB, Tustison NJ, Stauffer M, et al. **The Insight ToolKit image registration framework.** *Front Neuroinf* 2014;8:44 CrossRef Medline
14. Lin JS, Fuentes D, Chandler A, et al. **Performance assessment for brain MR imaging registration methods.** *AJNR Am J Neuroradiol* 2017;38:973–80 CrossRef Medline
15. Avants BB, Tustison NJ, Song G, et al. **A reproducible evaluation of ANTs similarity metric performance in brain image registration.** *Neuroimage* 2011;54:2033–44 CrossRef Medline
16. Roetzer T, Leskovar K, Peter N, et al. **Evaluating cellularity and structural connectivity on whole brain slides using a custom-made digital pathology pipeline.** *J Neurosci Methods* 2019;311:215–21 CrossRef Medline
17. Abercrombie M. **Estimation of nuclear population from microtome sections.** *Anat Rec* 1946;94:239–47 CrossRef Medline
18. Hedreen JC. **What was wrong with the Abercrombie and empirical cell counting methods? A review.** *Anat Rec* 1998;250:373–80 CrossRef Medline
19. Breiman L. **Random Forests.** *Mach Learn* 2001;45:5–32 CrossRef
20. Aerts HJ, Velazquez ER, Leijenaar RT, et al. **Decoding tumour phenotype by noninvasive imaging using a quantitative radiomics approach.** *Nat Commun* 2014;5:4006 CrossRef Medline
21. Parmar C, Grossmann P, Bussink J, et al. **Machine learning methods for quantitative radiomic biomarkers.** *Sci Rep* 2015;5:13087 CrossRef Medline
22. Kumar V, Gu Y, Basu S, et al. **Radiomics: the process and the challenges.** *Magn Reson Imaging* 2012;30:1234–48 CrossRef Medline
23. Autry A, Phillips JJ, Maleschlijski S, et al. **Characterization of metabolic, diffusion, and perfusion properties in GBM: contrast-enhancing versus non-enhancing tumor.** *Transl Oncol* 2017;10:895–903 CrossRef Medline
24. Durst CR, Raghavan P, Shaffrey ME, et al. **Multimodal MR imaging model to predict tumor infiltration in patients with gliomas.** *Neuroradiology* 2014;56:107–15 CrossRef Medline
25. Gates ED, Yang J, Fukumura K, et al. **Spatial distance correlates with genetic distance in diffuse glioma.** *Front Oncol* 2019;9:676 CrossRef Medline
26. Sadeghi N, D'Haene N, Decaestecker C, et al. **Apparent diffusion coefficient and cerebral blood volume in brain gliomas: relation to tumor cell density and tumor microvessel density based on stereotactic biopsies.** *AJNR Am J Neuroradiol* 2008;29:476–82 CrossRef Medline
27. Barajas RF Jr, Phillips JJ, Parvataneni R, et al. **Regional variation in histopathologic features of tumor specimens from treatment-naive glioblastoma correlates with anatomic and physiologic MR imaging.** *Neuro Oncol* 2012;14:942–54 CrossRef Medline
28. Heye AK, Culling RD, Valdés Hernández M del C, et al. **Assessment of blood–brain barrier disruption using dynamic contrast-enhanced MRI: a systematic review.** *Neuroimage Clin* 2014;6:262–74 CrossRef Medline

Effects of Acquisition Parameter Modifications and Field Strength on the Reproducibility of Brain Perfusion Measurements Using Arterial Spin-Labeling

K.P.A. Baas, J. Petr, J.P.A. Kuijer, A.J. Nederveen, H.J.M.M. Mutsaerts, and K.C.C. van de Ven

ABSTRACT

BACKGROUND AND PURPOSE: Although the added diagnostic value of arterial spin-labeling is shown in various cerebral pathologies, its use in clinical practice is limited. To encourage clinical adoption of ASL, we investigated the reproducibility of CBF measurements and the effects of variations in acquisition parameters compared to the recommended ASL implementation.

MATERIALS AND METHODS: Thirty-four volunteers (mean age, 57.8 ± 17.0 years; range, 22–80 years) underwent two separate sessions (1.5T and 3T scanners from a single vendor) using a 15-channel head coil. Both sessions contained repeated 3D and 2D pseudocontinuous arterial spin-labeling scans using vendor-recommended acquisition parameters (recommendation paper–based), followed by three 3D pseudocontinuous arterial spin-labeling scans, two with postlabeling delays of 1600 and 2000 ms and one with increased spatial resolution. All scans were single postlabeling delay. Intrasession (identical acquisitions, scanned five minutes apart) and intersession (first 2D and 3D acquisitions of two sessions) reproducibility was examined as well as the effect of parameter variations on CBF.

RESULTS: Intrasession CBF reproducibility was similar across image readouts and field strengths (within-subject coefficient of variation between 4.0% and 6.7%). Intersession within-subject coefficient of variation ranged from 6.6% to 14.8%. At 3T, the 3D acquisition with a higher spatial resolution resulted in less mixing of GM and WM signal, thus decreasing the bias in GM CBF between the 2D and 3D acquisitions (ΔCBF = 2.49 mL/100g/min [$P < .001$]). Postlabeling delay variations caused a modest bias (ΔCBF between −3.78 [$P < .001$] and 2.83 [$P < .001$] mL/100g/min).

CONCLUSIONS: Arterial spin-labeling imaging is reproducible at both field strengths, and the reproducibility is not significantly correlated with age. Furthermore, 3T tolerates more acquisition parameter variations and allows more extensive optimizations so that 3D and 2D acquisitions can be compared.

ABBREVIATIONS: ASL = arterial spin-labeling; CoV = coefficient of variation; GraSE = gradient spin-echo; pCASL = pseudocontinuous arterial spin-labeling; PLD = postlabeling delay; PVC = partial volume correction; WB = whole-brain; wsCV = within-subject coefficient of variation

Arterial spin-labeling (ASL) MR imaging has the potential to be a cost-effective and safe alternative to contrast agent–based perfusion imaging.[1] However, despite its proved clinical value,[2-4] technologic improvements,[5-7] and consensus recommendation on the implementation,[8] clinical use of ASL remains limited to date.[9] ASL is also regularly used in clinical and pharmaceutical trials because in these cases, the preference is to avoid the use of gadolinium-based contrast agents. In such trials, it remains a challenge to harmonize imaging protocols over different MR imaging systems, which use different readout types and ASL labeling and imaging parameters.[10-12] Overcoming these challenges is especially important in multicenter trials as well as in longitudinal studies, in which scanner hardware or software updates and subsequent sequence changes are common.

Several practical limitations hamper the adoption of ASL to image CBF in clinical practice. First, the recommended use of ASL is at a field strength of 3T.[8] However, if ASL is used as an alternative to contrast agent perfusion MR imaging to reduce the

Received April 23, 2020; accepted after revision August 17.

From the Department of Radiology and Nuclear Medicine (K.P.A.B., A.J.N.), Amsterdam University Medical Center, Academic Medical Center, University of Amsterdam, Amsterdam, the Netherlands; Institute of Radiopharmaceutical Cancer Research (J.P.), Helmholtz-Zentrum Dresden-Rossendorf, Dresden, Germany; Department of Biomedical Engineering (J.P., H.J.M.M.M.), Institute Hall, Rochester Institute of Technology, Rochester, New York; Department of Radiology and Nuclear Medicine (J.P.A.K., H.J.M.M.M.), Amsterdam University Medical Center, VU University Medical Center, Amsterdam, the Netherlands; Department of Radiology and Nuclear Medicine (H.J.M.M.M.), University Hospital Ghent, Ghent, Belgium; and BIU MR (K.C.C.v.d.V.), Philips Healthcare, Best, the Netherlands.

Please address correspondence to Koen P.A. Baas, MSc, Amsterdam University Medical Center, Location AMC, Department of Radiology and Nuclear Medicine, Room Z0-178, Meibergdreef 9, 1105 AZ, the Netherlands; e-mail: k.p.baas@amsterdamumc.nl

Indicates article with supplemental online tables.

Indicates article with supplemental online photo.

http://dx.doi.org/10.3174/ajnr.A6856

duration and cost of MR imaging examinations, it would also be preferably conducted at 1.5T, a field strength that is more widely available. Another limiting factor in clinical practice is that the sensitivity of CBF values to changes in the acquisition parameters is not well-understood.

Despite the relatively large body of literature on the precision of ASL, in which studies have shown that ASL has a similar reproducibility to PET[13] and that whole-brain (WB) reproducibility is comparable among various labeling and readout strategies,[10,14,15] investigators still question the effects of acquisition parameter changes on the precision of ASL with respect to the recommended implementation as described by the ASL consensus paper.[8] Other challenges for clinical adoption may be that most ASL reproducibility studies were conducted in young participants and may not be applicable to the elderly population.[16] Moreover, many studies apply partial volume correction (PVC) to mathematically correct for mixing of GM and WM perfusion, which is inherently present in ASL data due to the relatively large voxels and long readout durations in 3D acquisitions specifically.[17] Studies are often inconsistent on the corrections applied when reporting CBF values, complicating comparison among studies.

A final challenge for ASL-based perfusion imaging is that standard ASL acquisitions aim to quantify CBF from a single postlabeling delay (PLD) measurement without measuring whether the labeled blood arrived in the tissue. Therefore, it might be unclear whether a low ASL signal is due to decreased perfusion or a delay in arrival. Recently, a novel ASL parameter, which can be derived from single-PLD CBF maps, the spatial coefficient of variation (CoV), was introduced as a proxy of arterial transit time.[18] Correlation of spatial CoV with clinical parameters was shown in recent studies,[19-21] but the reproducibility of this parameter has not yet been reported.

To address the practical issues mentioned above and to encourage further adoption of ASL in clinical practice, this study aims to extend the knowledge on the precision of CBF and spatial CoV measurements. Specifically, this work focuses on studying ASL reproducibility with respect to three common sources of ASL signal variation: 1) age: studying healthy subjects over a large range of adult ages, focusing mostly on older adults because reproducibility studies in this age group are lacking in the literature; 2) field strength and scan parameter variations: assessing the influence of small acquisition parameter variations[8] at both 3T and 1.5T; and 3) partial volume correction: showing the effect of partial volume correction on deriving pure GM CBF with different scan parameter variations and imaging field strengths.

MATERIALS AND METHODS

Participants

In this study, 34 healthy participants (20 men, 14 women; mean age, 57.8 ± 17.0 years) were included. Detailed information about the distribution of participants over different field strengths is given in Online Table 1. This technical study with human participants has been performed under a waiver of institutional review board approval by the Medical Research Ethics Committees United (Nieuwegein, the Netherlands). All participants provided written informed consent and received remuneration for their participation. All experiments were performed in accordance with the Declaration of Helsinki guidelines. Volunteers included in this study participate regularly in MR imaging experiments and are, therefore, trained to lie still for longer periods of time.

On arrival, participants were instructed to refrain from intake of caffeine and smoking during the whole experiment. All participants underwent two scan sessions of 50 minutes with approximately 15 minutes of rest between, during which they were taken out of the scanner. Eight participants were scanned twice at 1.5T, 12 participants were scanned at 1.5T and 3T in a randomized order, and 14 participants were scanned twice at 3T. To describe the precision of the CBF and spatial CoV measurements, we define here intrasession repeatability, considering two within-session repeated measurements, and intersession reproducibility, considering two between-session repeated measurements. Experiments were performed on the following scanner types: 1.5T Ingenia and IngeniaCx and 3T Achieva, Ingenia, and IngeniaCx (Philips Healthcare, Best, the Netherlands). All acquisitions were performed using the standard 15-channel head coil on MR imaging scanner software, Version R5.3 and R5.4, with identical implementation of the ASL sequence. All scanners were in close proximity to one another.

Image Acquisition

All sessions started with a 3D-T1w scan followed by two identical pseudocontinuous ASL (pCASL) scans with a 3D gradient spin-echo (GraSE) readout and two identical pCASL scans with a 2D-EPI readout (in an interleaved fashion with an approximately 5-minute gap between identical scans) for intrasession repeatability assessment. Next, we acquired two 3D-GraSE pCASL scans with different PLDs: 1600 and 2000 ms. Last, a 3D-GraSE pCASL scan with a higher spatial resolution was acquired (in-plane resolution of 2.75 × 2.75 mm^2 instead of 3.75 × 3.75 mm^2). In all pCASL examinations, a labeling duration of 1800 ms was used, as well as a 4-pulse background-suppression scheme and an integrated M0 scan. Further acquisition parameters are listed in Online Table 2. The initial 3D and 2D ASL scans (sequence numbers 2–5) were obtained from the vendor's imaging data base and in agreement with the consensus recommendation on ASL implementation.[8]

The labeling plane was positioned 9 cm below the anterior/posterior commissure plane. A phase-contrast angiography survey scan was performed to check the position of the labeling plane, and if required, the distance was adapted to avoid the labeling plane overlapping the siphons. The full sequence protocol was repeated after a 15-minute break for intersession reproducibility assessment.

Postprocessing

During reconstruction on the scanner, all ASL scans were quantified according to the single-compartment model recommended in the ASL consensus review.[8] This includes generation of M0, label, and control images using standard image corrections, including coil sensitivity corrections. Subsequently, a voxel-based calculation was performed to derive the CBF values, as explained in the ASL recommendation paper, using the same assumptions for the T1 of blood (1650 ms at 3T, 1350 ms at 1.5T), labeling efficiency ($\alpha = 0.85$), and the blood-brain partition coefficient (λ = 0.9 mL/g).[8]

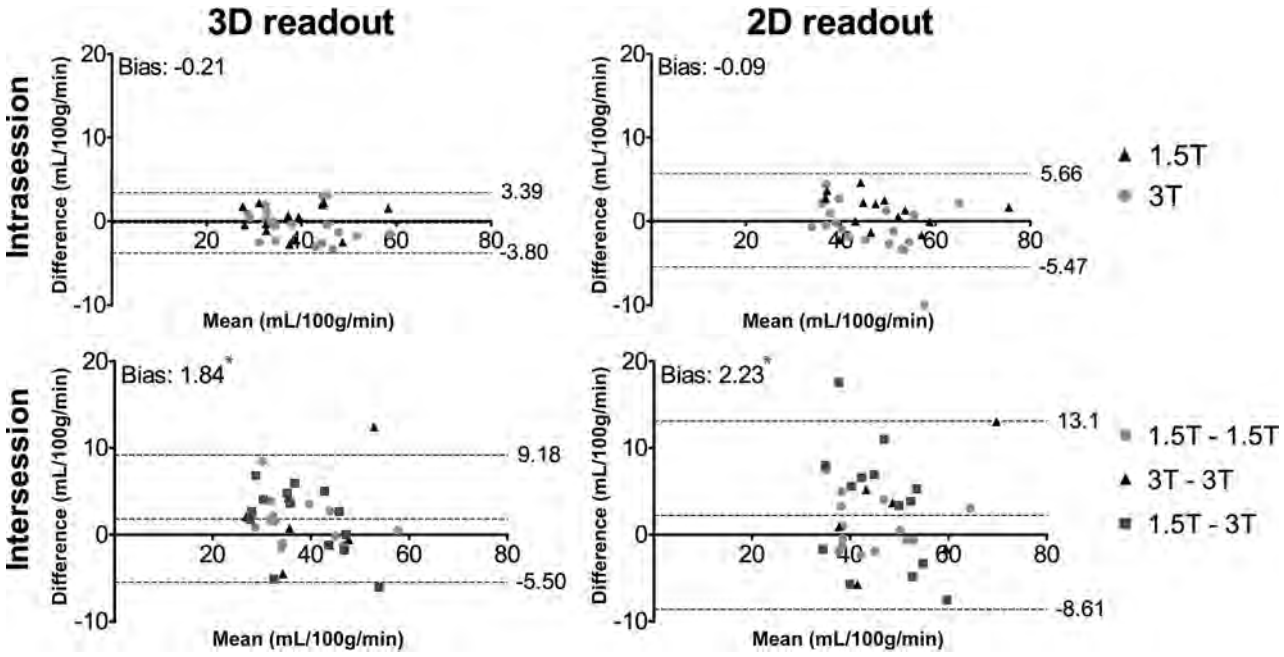

FIG 1. Bland-Altman plots showing agreement on GM CBF between intra- (*upper row*) and intersession (*lower row*) repeated 3D 1800 ms (*left column*) and 2D 1800 ms (*right column*) pCASL scans. The *asterisk* indicates values significantly different from zero ($P < .05$).

Further image processing of the CBF maps was performed off-line in ExploreASL (https://sites.google.com/view/exploreasl), which is detailed in depth elsewhere.[22] Briefly, first, the 3D-T1w images were segmented into GM, WM, and CSF and registered to standard space (Montreal Neurological Institute template space) with a voxel size $1.5 \times 1.5 \times 1.5\,mm^3$ using CAT12 (C. Gaser; Structural Brain Mapping Group, Jena University Hospital).[23] Next, the quantified ASL scans were registered to the 3D-T1w scans by registering the perfusion-weighted maps, the mean label control difference, to the partial GM maps obtained from T1w segmentation using a rigid body registration, with a normalized mutual information criterion. After transforming the ASL images to standard space, the partial GM maps were smoothed to the effective spatial resolution of ASL. The average WB GM CBF was calculated as the average CBF of voxels with >70% partial GM content from the partial GM maps in the ASL resolution. WB CBF was calculated by combining the white matter and GM segmentations and thresholding partial GM + partial WM >70%. PVC was performed using linear regression on a 5 × 5 kernel as described by Asllani et al[17] on GM maps adjusted to the effective spatial resolution to correct for both GM and WM CBF mixing and for differences in effective spatial resolution.[24] In this study, we report GM CBF, without PVC, unless otherwise mentioned.

The spatial CoV was calculated in GM using the CBF maps before PVC:[18]

$$1)\ Spatial\ CoV = (SD_{ROI}/Mean_{ROI}) \times 100\%.$$

Statistical Analysis

To assess the effects of field strength on reproducibility, we divided participants into groups of 1.5T ($n = 14$) and 3T ($n = 20$) for intrasession and 1.5T–1.5T ($n = 6$), 1.5T–3T ($n = 14$), and 3T–3T ($n = 14$) for intersession comparison. For intrasession repeatability, repeated scans of the first scan sessions were used. For intersession reproducibility, the first 3D 1800 ms and 2D 1800 ms scans of both sessions were used.

CBF and spatial CoV data were tested for normality using a Shapiro-Wilk test. Scan types were compared using general linear models; repeated measures ANOVA, with a post hoc Tukey multiple comparison test when comparing normally distributed data, and a Friedman test, with post hoc Dunn multiple comparison test when comparing non-normally distributed data, were included in the analysis.

Repeatability and reproducibility assessment were performed on GM CBF values without PVC. First, the differences in CBF (ΔCBF) and spatial CoV (Δspatial CoV) between intrasession and intersession repeated measurements were calculated for each participant individually. Intrasession differences were calculated as 3D 1800 ms run 1 – 3D 1800 ms run 2; intersession differences were calculated as 3D 1800 ms run 1 session 1 – 3D 1800 ms run 1 session 2. To investigate whether there was a statistically significant correlation between the participants' age and ΔCBF and Δspatial CoV, we performed a Spearman rank correlation test. Next, as a measure for variability at a group level, the within-subject coefficient of variation (wsCV) was calculated as the ratio of the SD of the differences between the repeated measurements over the mean of the repeated measurements:

$$2)\ wsCV = 100\% \times (SD_{\Delta}\ \text{Mean}).$$

The effect of variations in acquisition parameters was evaluated using the pCASL scans of the first session of all volunteers. First, the mean pair-wise difference, or bias, in observed GM CBF between the recommended 3D acquisitions and acquisitions with

Table 1: Bias in GM spatial CoV between intra- and intersession repeated 3D and 2D acquisitions[a]

	GM Spatial CoV	
	3D	2D
Intrasession	–0.001 (–0.044, 0.042)	–0.004 (–0.044, 0.035)
Intersession	–0.004 (–0.085, 0.078)	–0.002 (–0.125, 0.120)

[a] Numbers in parentheses are 95% limits of agreement.

Table 2: Spearman's ρ and corresponding *P* values between age and ΔCBF and between age and Δspatial CoV from 3D and 2D ASL scans

	3D		2D	
	Spearman's ρ	*P* Value	Spearman's ρ	*P* Value
ΔCBF				
Intrasession	–0.18	.31	–0.17	.34
Intersession	0.05	.80	0.05	.78
Δspatial CoV				
Intrasession	0.07	.71	0.04	.82
Intersession	0.15	.39	0.20	.26

Table 3: Intra- and intersession wsCV of GM CBF and GM spatial CoV from 3D 1800 ms and 2D 1800 ms scans

	GM CBF		GM Spatial CoV	
	3D	2D	3D	2D
Intrasession				
1.5T ($n = 14$)	4.4%	4.0%	7.6%	4.5%
3T ($n = 20$)	4.7%	6.7%	5.1%	4.3%
Intersession				
1.5T–1.5T ($n = 6$)	13.5%	11.7%	6.9%	8.4%
1.5T–3T ($n = 14$)	10.0%	14.8%	15.5%	19.1%
3T–3T ($n = 14$)	6.8%	6.6%	11.1%	7.6%

parameter variations was calculated by subtracting the CBF value from the images with deviating settings from the recommended 3D acquisition. To test whether the bias was statistically significantly different from zero, we performed a 1-sample *t* test. To examine whether the variance across the pair-wise differences between the recommended and deviating ASL acquisitions was significantly different compared with the variance across the pair-wise differences between repeated consensus paper acquisitions, we used the Pitman-Morgan test, a test for equal variance taking repeated measures into account. Statistical significance was defined as $P < .05$.

RESULTS

Visual inspection showed a large variation in global mean perfusion values among the participants, shown in the Online Figure. Local values of cortical perfusion ranged from 100 mL/100g/min in some participants to relatively low values of about 25 mL/100g/min in other participants.

Repeatability and Reproducibility

First, the GM CBF agreement among repeated, identical, recommendation ASL acquisitions was assessed (Fig 1). For the intrasession repeated scans, the 3D and 2D scans showed 95% limits of agreement of –3.80, 3.39 mL/100g/min and –5.47, 5.66 ml/100g/min, respectively. The intersession repeated scans showed

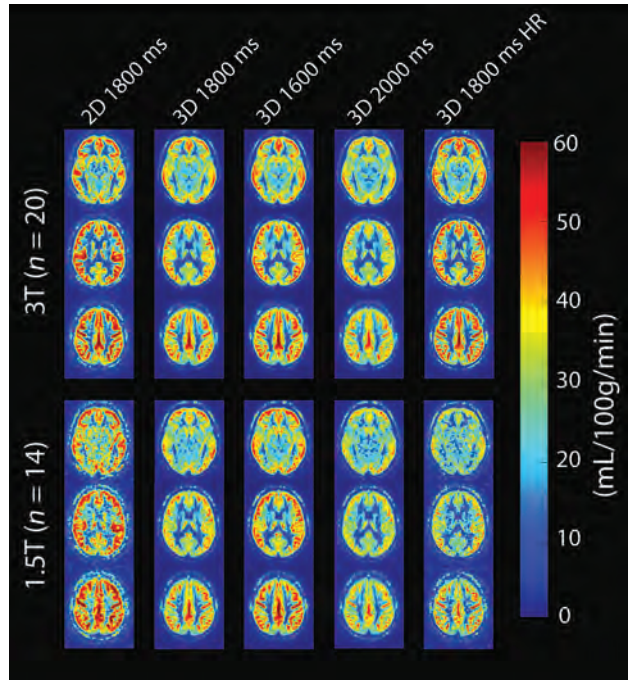

FIG 2. Three axial slices from group-averaged CBF maps of all pCASL acquisitions at both field strengths. Average age of participants scanned at 1.5T and 3T was 62 ± 12 years and 56 ± 20 years, respectively. HR indicates high resolution.

95% limits of agreement of –5.50, 9.18 mL/100g/min and –8.61, 13.1 mL/100g/min for 3D and 2D scans, respectively.

The bias in GM spatial CoV, together with the 95% limits of agreement, between repeated 3D and 2D scans, was also calculated (Table 1). None of the observed biases in the GM spatial CoV were significantly different from zero.

No statistically significant correlation between ΔCBF and age or between Δspatial CoV and age was observed using the Spearman rank correlation test (Table 2).

The wsCV of GM CBF and spatial CoV was calculated for both field strengths and all field strength combinations (Table 3). After PVC, the wsCV of GM CBF was similar (data not shown). Intrasession variations were similar at both field strengths. Intersession CBF variability was lowest when scanning twice at 3T. In contrast, intersession spatial CoV variability was lowest when scanning twice at 1.5T.

Scan Parameter Variations

Averaged ASL scans showed that both 2D 1800 ms and 3D 1800 ms high-resolution scans have similar anatomic detail at 3T but had reduced SNR at 1.5T (Fig 2). The high-resolution acquisition at 1.5T was excluded from further analysis because the image quality of individual scans was insufficient to perform further analysis. The other 3D-GraSE images were of good quality at both field strengths.

CBF data from several acquisitions showed a non-normal distribution and required nonparametric testing (Online Table 3). A trend of decreasing CBF with increasing PLD was observed (Fig 3). This resulted in statistically significant differences between scans with PLDs of 1600 and 2000 ms ($P < .05$).

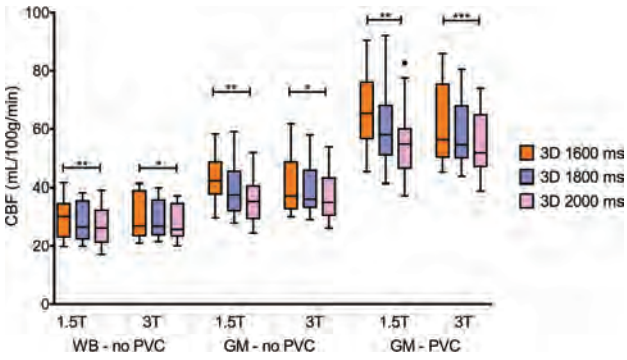

FIG 3. Boxplots showing WB and GM CBF without PVC and GM with PVC per PLD and field strength. One, two, and three *asterisks* indicate *P* values < .05, .01, and .001, respectively.

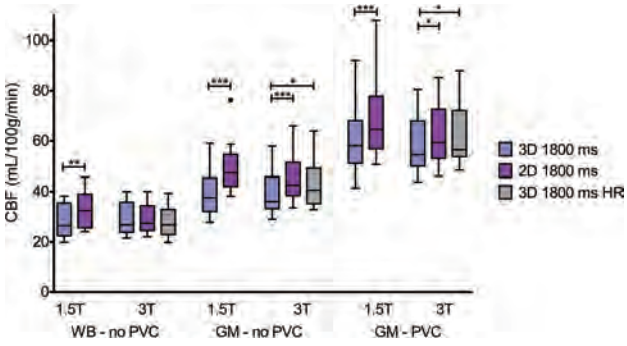

FIG 4. Boxplots showing WB and GM CBF without PVC and GM with PVC, per readout and field strength. One, two, and three *asterisks* indicate *P* values < .05, .01, and .001, respectively. HR indicates high resolution.

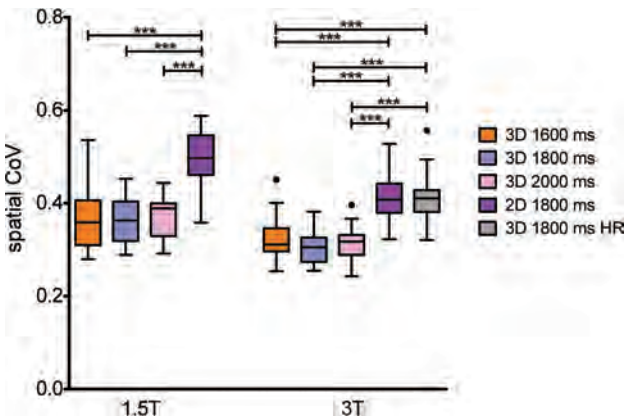

FIG 5. Boxplots showing GM spatial CoV per scan type and field strength. Three *asterisks* indicate *P* values < .001. HR indicates high resolution.

Statistically significant differences in measured CBF were also observed between acquisitions with different readout types (Fig 4). Similar to Fig 3, the differences observed among scans are decreased when comparing WB instead of GM CBF.

At 1.5T, the 2D acquisition resulted in a significantly higher spatial CoV compared with the 3D acquisitions (Fig 5). At 3T, the high-resolution 3D acquisition resulted in significantly higher spatial CoV values compared with the other 3D acquisitions as well.

Acquisition parameter variations resulted in statistically significant pair-wise differences in GM CBF ($P < .05$) (Table 4). Nevertheless, for most combinations, the variance across the observed pair-wise differences was not significantly different compared with the variance across the pair-wise differences between repeated recommendation ASL acquisitions. Moreover, we observed an increase in pair-wise differences among different pCASL acquisitions when scanning at 1.5T compared with 3T. At 3T, the 2D-EPI acquisition showed the best agreement with the 3D 1800 ms high-resolution acquisition.

DISCUSSION

In this study, we have shown that intrasession repeatability and intersession reproducibility of CBF measurements are similar at 3T and 1.5T and do not show a statistically significant correlation with age. Additionally, we observed that variations in image readout (2D versus 3D) do not have a significant effect on the reproducibility of the CBF measurements. These findings are in agreement with previous reproducibility studies reporting intrasession reproducibility of 3.5%–5.5%[14] and intersession reproducibility of 10.8%–11.3%[10] and are comparable in precision with respect to ^{15}O-H_2O PET.[13] Results are also in line with studies on reproducibility using different labeling and readout techniques[10,14,15,25] and the effect of PLD on CBF reproducibility.[26]

Although reproducibility was similar using different pCASL acquisition parameters and different image readouts, the average CBF values did differ. We observed that differences in measured CBF between 2D and 3D readouts were more pronounced in GM compared with WB CBF. This finding could be explained by the difference in effective resolution between 2D and 3D readouts. Reduced effective resolution results in more severe partial volume effects and hence affects GM CBF, due to GM and WM CBF mixing, more than WB CBF, in which mixing has a limited effect on the mean. CBF values were also affected by differences in PLD. We suspect that these differences are due to the single-compartment model that was used for quantification, which does not take into account that the duration that the label decays with the tissue T1 differs among the 1600-, 1800-. and 2000-ms PLD sequences. More advanced multicompartment or model-free approaches could account for the T1-decay in blood as well as in tissue.[27-29] Using an arterial blood T1 recently determined by Li et al,[30] in 2017, we have simulated that a dual compartment model would account for 68% of the observed difference between the shortest and longest PLD scans (data not shown). The remaining difference could be explained by insufficient delivery of labeled blood in our short PLD data. However, this effect would result in higher spatial CoV, which was not observed in our data.

We have shown that the intrasession repeatability and intersession reproducibility of the spatial CoV, just like CBF, do not show a statistically significant relationship with age. However, spatial CoV values were higher at 1.5T compared with 3T. This finding could be due to the shorter blood T1, which leads to less signal in distal compared with proximal areas, increasing the spatial CoV. We investigated this effect by calculating the spatial CoV for each imaging slice individually at both field strengths for a subset of our data. Only at 1.5T was a small upward trend in spatial CoV observed at higher slices (data not shown). This might indicate

Table 4: Pair-wise differences (mean ± SD) between observed GM CBF (mL/100g/min), without PVC, from different pCASL acquisitions

	3D 1800 ms	2D 1800 ms	3D 1600 ms	3D 2000 ms	3D 1800 ms HR
3T					
3D 1800 ms	–0.46 ± 1.88[a]	–6.14 ± 1.45[b]	–2.10 ± 3.20[bc]	2.21 ± 1.85[b]	–3.65 ± 2.00[b]
2D 1800 ms		–0.65 ± 3.13[a]	4.04 ± 2.95[bc]	8.35 ± 2.12[b]	2.49 ± 2.02[b]
1.5T					
3D 1800 ms	0.15 ± 1.77[a]	–11.03 ± 3.21[bc]	–3.78 ± 2.30[b]	2.83 ± 2.06[b]	
2D 1800 ms		1.15 ± 2.04[a]	7.25 ± 4.05[bc]	13.86 ± 3.95[bc]	

Note:—HR indicates high-resolution.

[a] Differences between repeated identical pCASL acquisitions with consensus paper parameter settings.

[b] A bias that is significantly different from zero ($P < .05$).

[c] A significantly different variance across the observed pair-wise differences between acquisitions compared with the variance across the pair-wise differences between repeated consensus paper parameter settings ($P < .05$).

that at 1.5T, distal parts of the brain show a higher spatial CoV due to faster T1 relaxation at 1.5T compared with 3T.

The higher mean spatial CoV values subsequently lead to lower intersession wsCV when scanning twice at 1.5T. Moreover, we did observe an increased spatial CoV in scans with a higher effective resolution, which can be explained by noisier acquisitions and/or higher contrast in these scans. A first investigation of this effect showed that scans with more temporal fluctuations of the ASL signal resulted in higher spatial CoV values (data not shown). Therefore, we conclude that both CBF and spatial CoV are affected by the effective resolution of the ASL acquisition. While the existing partial volume correction methods for GM CBF can deal with this issue,[17,24] a similar method that takes into account the differences in GM distribution changes with differences in effective resolution needs to be proposed and validated to be able to account for the resolution-related issues in spatial CoV calculation.

We observed that scan parameter variations compared with the recommended ASL parameters resulted in significant changes in the observed CBF values. Nevertheless, we consider the observed differences in CBF due to changes in PLD acceptable because the maximum bias between our 3D 1800 ms and 3D 1600 ms acquisitions at 1.5T was <10% of the mean CBF. Moreover, the variance across the pair-wise difference was only once significantly affected for the 3D 1600 ms acquisition at 3T, indicating that these scan parameter variations only introduce an offset in the measured CBF but not in a different distribution around the mean CBF value. Comparing standard 3D and 2D ASL acquisitions resulted in a greater bias. At 3T however, the 3D-GraSE acquisition can be optimized to match the effective resolution of the 2D-EPI acquisition. This process results in less mixing of GM and WM signal, reducing the bias in measured CBF. This effect was already hypothesized by Mutsaerts et al, in 2014, based on previous work comparing 3D and 2D ASL scans.[10,31,32] Overall, the bias between recommended and deviating pCASL acquisitions gets more pronounced at 1.5T compared with 3T. This difference could be explained by the decreased SNR and increased loss of label during the PLD, due to the shorter relaxation time of blood at a lower field strength. Therefore, acquisitions at 1.5T should be compared with great care and only when the readout type is not changed.

This study has some limitations. Our subjects frequently participate in MR imaging examinations and therefore are trained to lie still for a long time. While this allows us to study the reproducibility of the sequence in the strictly technical sense, the reproducibility in clinical practice might be affected by patient movement. Although motion correction and outlier rejection are typically used by ASL processing software, we expect that motion during the acquisition can still reduce SNR and lead to slight blurring due to imperfect interpolation in the motion correction. This might lead to a decrease of reproducibility, possibly affecting the 3D sequences more because each average of a 3D sequence is typically acquired over multiple shots and does not allow simple motion correction as in 2D readouts. We included relatively few young participants, but because the between-subject variability is usually lower in younger participants and our reproducibility in young volunteers was in agreement with that in previous studies, the effect is probably limited. Furthermore, for practical reasons, not every combination of scanning at 3T and 1.5T systems was performed in all volunteers, decreasing the available sample size for some combinations. In the scan parameter settings, some small differences such as shot length and through-plane resolution between 1.5T and 3T sequences remained. Although this might have slightly influenced comparisons between field strenghts, this was necessary to make the sequences comparable while maintaining acceptable image quality.

CONCLUSIONS

With this work, we provide insights that can help ASL acquisition parameter optimization in the setting of clinical practice as well as in clinical trials in which MR imaging systems with different ASL applications are used. Our data show that ASL imaging is well reproducible at 3T and 1.5T and that the differences between repeated measurements show no statistically significant correlation with age. It should be noted that, Scanning at 3T offers more tolerance for scan parameter variations compared with 1.5T and allows more extensive acquisition parameter optimization, resulting in good agreement among ASL acquisitions. We advise that clinical comparisons at 1.5T should be made only on the basis of scans with identical acquisitions settings. With these precautions taken into account, our findings advocate the use of ASL as a cost-effective and safe alternative to contrast agent–based perfusion at both field strengths.

ACKNOWLEDGMENTS

The authors thank Professor M.J.P. van Osch for the useful discussions and proofreading of this work.

Disclosures: Kim van de Ven—*UNRELATED: Employment*: Philips Healthcare.

REFERENCES

1. Detre JA, Leigh JS, Williams DS, et al. **Perfusion imaging.** *Magn Reson Med* 1992;23:37–45 CrossRef Medline
2. Telischak NA, Detre JA, Zaharchuk G. **Arterial spin labeling MRI: clinical applications in the brain.** *J Magn Reson Imaging* 2015;41:1165–80 CrossRef Medline
3. Detre JA, Rao H, Wang DJ, et al. **Applications of arterial spin labeled MRI in the brain.** *J Magn Reson Imaging* 2012;35:1026–37 CrossRef Medline
4. Hendrikse J, Petersen ET, Golay X. **Vascular disorders: insights from arterial spin labeling.** *Neuroimaging Clin N Am* 2012;22:259–69 CrossRef Medline
5. Garcia DM, Duhamel G, Alsop DC. **Efficiency of inversion pulses for background suppressed arterial spin labeling.** *Magn Reson Med* 2005;54:366–72 CrossRef Medline
6. Ye FQ, Frank JA, Weinberger DR, et al. **Noise reduction in 3D perfusion imaging by attenuating the static signal in arterial spin tagging (ASSIST).** *Magn Reson Med* 2000;44:92–100 CrossRef Medline
7. Günther M, Oshio K, Feinberg DA. **Single-shot 3D imaging techniques improve arterial spin labeling perfusion measurements.** *Magn Reson Med* 2005;54:491–98 CrossRef Medline
8. Alsop DC, Detre JA, Golay X, et al. **Recommended implementation of arterial spin-labeled perfusion MRI for clinical applications: a consensus of the ISMRM Perfusion Study group and the European Consortium for ASL in Dementia.** *Magn Reson Med* 2015;73:102–16 CrossRef Medline
9. Keil VC, Smits M, Thust S, et al. **The long road from invention to implementation: a PAN-European neuroradiological survey on quantitative MRI techniques in clinical practice.** In: *Proceedings of the Annual Meeting and Exhibition of the International Society for Magnetic Resonance in Medicine,* Virtual; August 8–14, 2020
10. Mutsaerts HJ, Steketee RM, Heijtel DF, et al. **Inter-vendor reproducibility of pseudo-continuous arterial spin labeling at 3 Tesla.** *PLoS One* 2014;9:e104108 CrossRef Medline
11. Mutsaerts HJ, van Osch MJ, Zelaya FO, et al. **Multi-vendor reliability of arterial spin labeling perfusion MRI using a near-identical sequence: implications for multi-center studies.** *Neuroimage* 2015;113:143–52 CrossRef Medline
12. Zaharchuk G. **Arterial spin labeling for acute stroke: practical considerations.** *Transl Stroke Res* 2012;3:228–35 CrossRef Medline
13. Heijtel DF, Mutsaerts HJ, Bakker E, et al. **Accuracy and precision of pseudo-continuous arterial spin labeling perfusion during baseline and hypercapnia: a head-to-head comparison with 15O H2O positron emission tomography.** *Neuroimage* 2014;92:182–92 CrossRef Medline
14. Chen Y, Wang DJ, Detre JA. **Test-retest reliability of arterial spin labeling with common labeling strategies.** *J Magn Reson Imaging* 2011;33:940–49 CrossRef Medline
15. Gevers S, van Osch MJ, Bokkers RP, et al. **Intra- and multicenter reproducibility of pulsed, continuous and pseudo-continuous arterial spin labeling methods for measuring cerebral perfusion.** *J Cereb Blood Flow Metab* 2011;31:1706–15 CrossRef Medline
16. Biagi L, Abbruzzese A, Bianchi MC, et al. **Age dependence of cerebral perfusion assessed by magnetic resonance continuous arterial spin labeling.** *J Magn Reson Imaging* 2007;25:696–702 CrossRef Medline
17. Asllani I, Borogovac A, Brown TR. **Regression algorithm correcting for partial volume effects in arterial spin labeling MRI.** *Magn Reson Med* 2008;60:1362–71 CrossRef Medline
18. Mutsaerts HJ, Petr J, Václavů L, et al. **The spatial coefficient of variation in arterial spin labeling cerebral blood flow images.** *J Cereb Blood Flow Metab* 2017;37:3184–92 CrossRef Medline
19. Ibaraki M, Nakamura K, Toyoshima H, et al. **Spatial coefficient of variation in pseudo-continuous arterial spin labeling cerebral blood flow images as a hemodynamic measure for cerebrovascular steno-occlusive disease: a comparative 15 O positron emission tomography study.** *J Cereb Blood Flow Metab* 2019;39:173–81 CrossRef Medline
20. Robertson AD, Matta G, Basile VS, et al. **Temporal and spatial variances in arterial spin-labeling are inversely related to large-artery blood velocity.** *AJNR Am J Neuroradiol* 2017;38:1555–61 CrossRef Medline
21. Mutsaerts HJ, Petr J, Bokkers RP, et al. **Spatial coefficient of variation of arterial spin labeling MRI as a cerebrovascular correlate of carotid occlusive disease.** *PLoS One* 2020;15:e0229444 CrossRef Medline
22. Mutsaerts HJ, Petr J, Groot P, et al. **ExploreASL: an image processing pipeline for multi-center ASL perfusion MRI studies.** *Neuroimage* 2020;219:117031 CrossRef Medline
23. Pfefferbaum A, Chanraud S, Pitel AL, et al. **Partial volume segmentation with adaptive maximum a posteriori (MAP) approach.** *Psychiatry Res* 2010;182:266–73 CrossRef Medline
24. Petr J, Mutsaerts HJ, De Vita E, et al. **Effects of systematic partial volume errors on the estimation of gray matter cerebral blood flow with arterial spin labeling MRI.** *MAGMA* 2018;31:725–34 CrossRef Medline
25. Mezue M, Segerdahl AR, Okell TW, et al. **Optimization and reliability of multiple postlabeling delay pseudo-continuous arterial spin labeling during rest and stimulus-induced functional task activation.** *J Cereb Blood Flow Metab* 2014;34:1919–27 CrossRef Medline
26. Wu B, Lou X, Wu X, et al. **Intra- and interscanner reliability and reproducibility of 3D whole-brain pseudo-continuous arterial spin-labeling MR perfusion at 3T.** *J Magn Reson Imaging* 2014;39:402–09 CrossRef Medline
27. Zhou J, Wilson DA, Ulatowski JA, et al. **Two-compartment exchange model for perfusion quantification using arterial spin tagging.** *J Cereb Blood Flow Metab* 2001;21:440–55 CrossRef Medline
28. Petersen ET, Lim T, Golay X. **Model-free arterial spin labeling quantification approach for perfusion MRI.** *Magn Reson Med* 2006;55:219–32 CrossRef Medline
29. Chappell MA, Woolrich MW, Petersen ET, et al. **Comparing model-based and model-free analysis methods for QUASAR arterial spin labeling perfusion quantification.** *Magn Reson Med* 2013;69:1466–75 CrossRef Medline
30. Li W, Liu P, Lu H, et al. **Fast measurement of blood T1 in the human carotid artery at 3T: accuracy, precision, and reproducibility.** *Magn Reson Med* 2017;77:2296–2302 CrossRef Medline
31. Kilroy E, Apostolova L, Liu C, et al. **Reliability of two-dimensional and three-dimensional pseudo-continuous arterial spin labeling perfusion MRI in elderly populations: comparison with 15o-water positron emission tomography.** *J Magn Reson Imaging* 2014;39:931–39 CrossRef Medline
32. Vidorreta M, Wang Z, Rodriguez I, et al. **Comparison of 2D and 3D single-shot ASL perfusion fMRI sequences.** *Neuroimage* 2013;66:662–71 CrossRef Medline

High-Resolution Gadolinium-Enhanced MR Cisternography Using Compressed-Sensing T1 SPACE Technique for Detection of Intracranial CSF Leaks

I.E. Duman, T. Demerath, A. Stadler, S. Elsheikh, E. Raithel, C. Forman, T. Hildenbrand, M. Shah, J. Grauvogel, C. Scheiwe, H. Urbach, and S. Meckel

ABSTRACT

SUMMARY: In patients with CSF rhinorrhea, accurate identification of the CSF leakage site is crucial for surgical planning. We describe the application of a novel gadolinium-enhanced high-resolution 3D compressed-sensing T1 SPACE technique for MR cisternography and compare findings with CT cisternography and intraoperative results. In our pilot experience with 7 patients, precise detection of CSF leaks was feasible using compressed-sensing T1 SPACE, which appeared to be superior to CT cisternography.

ABBREVIATIONS: CS = compressed-sensing; CTC = CT cisternography; MRC = MR cisternography; SPACE = sampling perfection with application-optimized contrasts by using different flip angle evolution

CSF rhinorrhea develops after traumatic or iatrogenic injury to the dura mater, though spontaneous cases have also been reported. Traumatic CSF leaks often close spontaneously and may be treated conservatively. However, if persistent, the CSF leakage site may be a port of entry for bacteria, causing meningitis or other complications, and may need surgical repair. Identification of the precise preoperative leakage site is crucial for surgery and increases success rate while reducing the risk of complications. Although high-resolution CT is commonly the initial noninvasive study of choice, it may not be sufficient to accurately determine the location of a CSF leak.[1,2] Intrathecal gadolinium-enhanced MR cisternography (MRC) has been recently introduced with studies reporting its safety and success in locating cranial CSF fistulas.[1,2]

Recently, a highly accelerated 3D compressed-sensing T1 sampling perfection with application-optimized contrasts by using different flip angle evolution (CS T1 SPACE) sequence (Siemens) has been introduced in MR neuroimaging, mainly as a tool for the assessment of intracranial vessel walls because of its excellent black-blood imaging capabilities.[3] The use of this technique for MRC after intrathecal gadolinium application may be advantageous because it offers a global 3D view of the entire skull base, meninges, and brain with high spatial detail and high SNR and contrast-to-noise ratio. Moreover, fusion images combining 3D CS T1 SPACE with high-resolution CT may add important information on bony landmarks for surgical planning and intraoperative navigation.

This article illustrates our pilot experience using high-resolution CS T1 SPACE MRC for presurgical localization of CSF leaks in patients with CSF rhinorrhea. We compared imaging findings with CT cisternography (CTC) and intraoperative results.

TECHNIQUES

After introduction of a novel CS T1 SPACE MRC technique, we perform combined CTC and MRC in all patients with CSF rhinorrhea confirmed by positive B2-transferrin test result. The indication for cisternography was given by a neurosurgeon or otorhinolaryngologist based on the patient's clinical findings suspicious of a cranial CSF leak. Written informed consent for the intrathecal gadolinium injection as an off-label application and for the MR imaging scan was obtained from all patients.

After intrathecal injection of iodine contrast agent (15 mL of Solutrast 250 M, Bracco Altana Pharma), saline (4 mL) mixed with 0.5 mL of gadoteridol (ProHance, Bracco Diagnostics) is injected into the subarachnoid space. Thereafter, patients are positioned prone in the 30°–40° Trendelenburg position for 10 minutes. CTC images are acquired first in a prone position. During transfer to the CT suite (10–20 min), the patient is kept in bed in a prone position. Later (between 1.5–3 hours after contrast media injection), MRC is obtained in a supine position. Between both examinations, the patient is kept lying in bed in an observation room.

Received May 19, 2020; accepted after revision August 16.

From the Departments of Neuroradiology (I.E.D., T.D., A.S., S.E., H.U., S.M.), Otorhinolaryngology (T.H.), and Neurosurgery (M.S., J.G., C.S.), University of Freburg Medical Center, Faculty of Medicine, University of Freiburg, Freiburg Germany, and Siemens Healthcare GmbH (E.R., C.F.), Erlangen, Germany.

Paper previously presented at Virtual Conference of the German Society of Neuroradiology, October 7–9, 2020; Frankfurt, Germany.

Please address correspondence to Ikram Eda Duman, MD, Department of Neuroradiology, University of Freiburg Medical Center, Faculty of Medicine, University of Freiburg, Breisacherstr. 64, 79106 Freiburg, Germany; e-mail: edda_ikram@hotmail.com

Indicates article with supplemental on-line table.

Indicates article with supplemental on-line photos.

Indicates article with supplemental on-line videos.

http://dx.doi.org/10.3174/ajnr.A6852

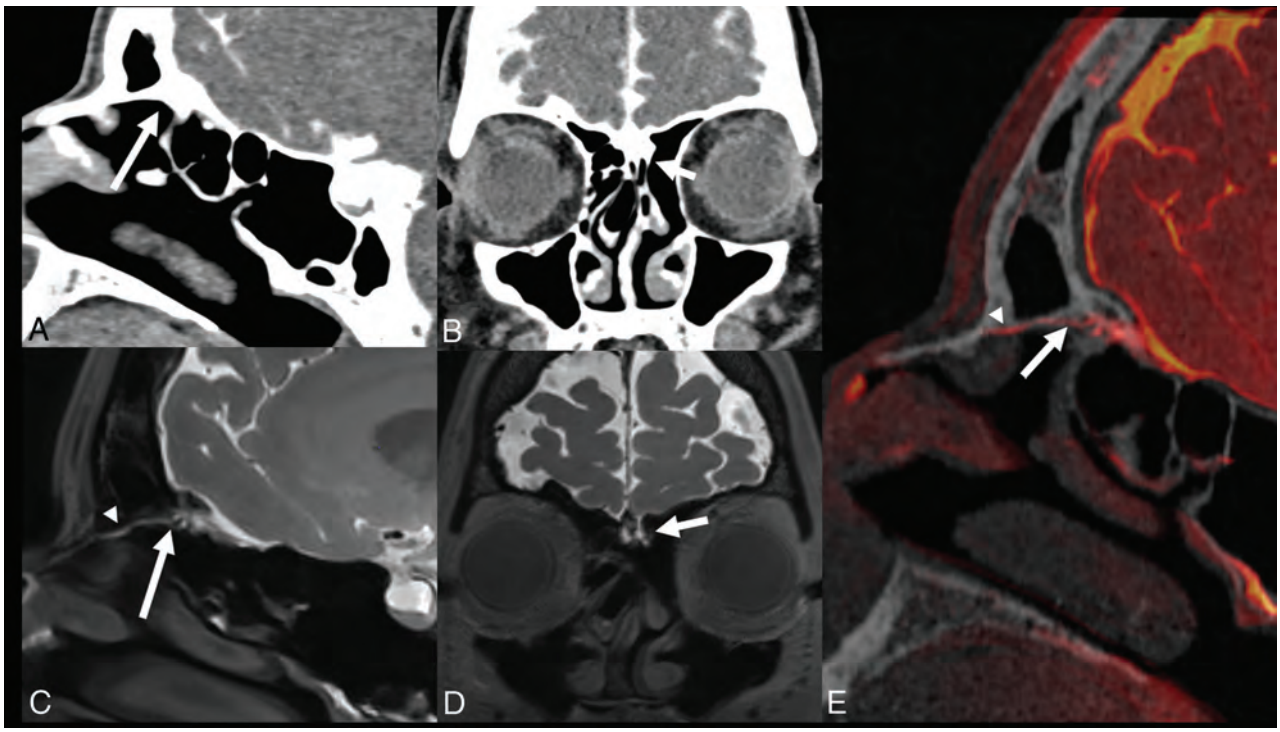

FIG 1. A 55-year-old woman (patient 1) who was readmitted for recurrent spontaneous left-sided CSF rhinorrhea and persistent slight headaches while sitting or standing after previous endoscopic sinus surgery. One year earlier, sealing of cribriform plate with TachoSil (Takeda Pharma) for suspected CSF leak had been performed. CT cisternography (soft tissue window level, W: 350; L: 50) is unremarkable, even in retrospect (*A* and *B arrows*). CS SPACE MR cisternography demonstrates a subtle CSF leak originating from the anterior rim of the left cribriform plate near foramen cecum (*C* and *D, arrows*) with a thin CSF collection extending to the anterior nasal cavity (*arrowheads* in *C and E*). The site correlated with the patient's intraoperative findings. After surgical repair, the patient was free of CSF rhinorrhea.

CTC is performed on a 64-section CT scanner (Somatom CT Definition AS, Siemens): section acquisition, 2 × 0.6 × 64, by means of a z-flying focal spot; gantry rotation, 0.5 seconds; tube voltage, 80 kV; tube current–time product, 236 mAs/pitch; sharp kernel (B60) reconstructed images (field of view, 100 mm; section thickness, 0.6 mm; increment, 0.4 mm). Bone and soft tissue algorithms were applied to enhance bone and contrast media details.

For MRC, a highly accelerated CS T1 SPACE sequence was applied on a 3T whole-body MR scanner (Magnetom Prisma, Siemens) using a 64-channel head and neck coil. The sequence uses a Poisson-disc variable-density acquisition with elliptical *k*-space coverage. Image reconstruction was done by combination of CS with L1 norm-based regularization in the Wavelet domain and parallel imaging (number of iterations, 20; regularization parameter, 0.0013). A whole-head sagittal T1-weighted CS SPACE protocol (TR/TE, 800/5.1 ms; field of view, 210 × 210 mm^2; 256 slices; section thickness, 0.60 mm; matrix, 384 × 384; fat saturation; pixel bandwidth, 450 Hz/px; echo-train length, 0; total scan time, 6:50 min) with a *k*-space undersampling factor of 0.22 was implemented, which yields an approximate 5-fold acceleration compared with full *k*-space sampling. The CS SPACE T1 sequence had an almost isotropic 3D resolution (0.5 × 0.5 × 0.6 mm^3).[3]

Syngo.via software (Siemens) was used to overlay 3D CS T1 SPACE and CTC images to delineate areas of leaks.

Between November 2019 and March 2020, 7 patients (mean age, 53.1 years; 5 females, 2 males) with CSF rhinorrhea underwent 8 combined CTC/MRC studies (On-line Table). All CSF leaks were precisely depicted on CS T1 SPACE images (Fig 1). In 5 CTC studies, leaks were missed (patient 1, Fig 1), falsely located (patient 2, study 1; On-line Fig 1*A–C*), or only suspected (patient 2, study 2; On-line Figs 1*D–F*, patients 3 and 4). All CSF leaks detected on MRC correlated with findings at surgical repair (On-line Videos 1 and 2).

DISCUSSION

In patients with CSF rhinorrhea, precise presurgical localization of CSF leaks is crucial for the success rate of surgery. High-resolution CT and CTC after intrathecal contrast application are both limited in the ability to demonstrate the site of a CSF leak, particularly in patients with multiple osseous defects or small or inactive leaks during imaging.[1,2] Anatomically accurate delineation of even a very small dural dehiscence may also be very difficult to diagnose on CTC images in the absence of a larger bony defect.[1,2]

Standard gadolinium-enhanced MRC is a promising technique that may permit direct, sensitive visualization of the site of CSF leakage.[1,2,4-6] Although intrathecal gadolinium injection is not approved by the US Food and Drug Administration, several studies have reported its safe off-label use with long-term follow-up after 4.2 years.[1,2] Gadolinium-enhanced MRC has certain advantages over CTC. Although gadolinium distributes readily in the subarachnoid space, the high viscosity of the iodinated contrast agent may impair its free distribution and passage into slowly flowing CSF fistulas. Moreover, CTC

requires high radiation dose and may not be able to differentiate CSF leakage from adjacent bone structures. In our series, all patients had confirmation of CSF leakage by surgery. In 5 of 8 CTC studies, the exact site of leakage could not be identified or was only suspected, and in 1 case, the suspected bony defect did not correlate with the site of leakage (patient 4). Related to different patient positioning in MR imaging (supine) and CT (prone), whereas more posterior dependent accumulation of leaked fluid was visible on MRC, CT showed anterior accumulation toward the nasal cavity (patient 4).

The application of 3D CS T1 SPACE for MRC appears particularly attractive because it covers the entire skull base and sinonasal and brain structures. Precise visualization of CSF leaks is enhanced related to its almost isotropic submillimeter 3D resolution, high SNR and contrast-to-noise ratio, and increased contrast between bony or aerated air cell structures, CSF, and soft tissues.[3] The conspicuity of contrast medium leakage may also be enhanced because of saturation of medullary bone fat in the cranial base. Compared with earlier reports of gadolinium-enhanced MRC techniques that used spin-echo T1-weighted imaging at 1.5 T,[4,5] the CS SPACE T1 technique appears advantageous for visualization of small CSF leaks because of 3D capability, increased spatial resolution, and SNR at 3T.

However, delineation of osseous anatomy at the skull base remains indispensable for surgical planning and intraoperative navigation. Thus, MRC–CTC fusion images combine the advantages of both techniques and allowed, in our series, accurate localization of the CSF leaks. Such fusion images may be alternatively created by combining MRC with low-dose bone-window CT images, thereby skipping the necessity for contrast-enhanced CTC.

Shortcomings of this study relate to the small number of retrospective cases, representing our very early clinical experience with the novel MRC method, which has to our knowledge not yet been described before. Technical limitations relate to the relatively long CS data processing times and relative vulnerability of the sequence to motion.

CONCLUSIONS

High-resolution gadolinium-enhanced CS T1 SPACE MRC is a promising method for detection of CSF leaks in patients with CSF rhinorrhea. In our pilot experience, this technique appears superior to standard CTC. Future prospective comparative studies are necessary to define the diagnostic accuracy of this technique.

Disclosures: Samer Elsheikh—*UNRELATED: Grants/Grants Pending:* Bracco Imaging*; *Payment for Lectures Including Service on Speakers Bureaus:* Daiichi Medical. Esther Raithel—*UNRELATED: Employment:* Siemens Healthcare GmbH, Comments: I am an employee. Christoph Forman—*RELATED: Other:* Employee of Siemens Healthcare GmbH, *Comments*: Salary; *UNRELATED: Employment:* Siemens Healthcare GmbH; *Stock/Stock Options:* Siemens Healthineers AG. Horst Urbach—*UNRELATED: Board Membership:* Co-editor *Clin Neuroradiol*; *Payment for Lectures Including Service on Speakers Bureaus:* Bayer, Bracco, Eisai, Stryker, UCB pharma. Stephan Meckel—*UNRELATED: Grants/Grants Pending:* Bracco S.p.A., Italy.* *Money paid to institution.

REFERENCES

1. Reddy M, Baugnon K. **Imaging of cerebrospinal fluid rhinorrhea and otorrhea.** *Radiol Clin North Am* 2017;55:167–87 CrossRef Medline
2. Eljazzar R, Loewenstern J, Dai JB, et al. **Detection of cerebrospinal fluid leaks: is there a radiologic standard of care? A systematic review.** *World Neurosurg* 2019;127:307–15 CrossRef Medline
3. Guggenberger K, Krafft AJ, Ludwig U, et al. **High-resolution compressed-sensing T1 black-blood MRI: a new multipurpose sequence in vascular neuroimaging?** *Clin Neuroradiol* 2019 Dec 18 [Epub ahead of print] CrossRef Medline
4. Aydin K, Terzibasioglu E, Sencer S, et al. **Localization of cerebrospinal fluid leaks by gadolinium-enhanced magnetic resonance cisternography: a 5-year single-center experience.** *Neurosurgery* 2008;62:584–89 CrossRef Medline
5. Selcuk H, Albayram S, Ozer H, et al. **Intrathecal gadolinium-enhanced MR cisternography in the evaluation of CSF leakage.** *AJNR Am J Neuroradiol* 2010;31:71–75 CrossRefMedline
6. Jinkins JR, Rudwan M, Krumina G, et al. **Intrathecal gadolinium-enhanced MR cisternography in the evaluation of clinically suspected cerebrospinal fluid rhinorrhea in humans: early experience.** *Radiology* 2002;222:555–59 CrossRef Medline

Neck Location on the Outer Convexity is a Predictor of Incomplete Occlusion in Treatment with the Pipeline Embolization Device: Clinical and Angiographic Outcomes

T. Sunohara, H. Imamura, M. Goto, R. Fukumitsu, S. Matsumoto, N. Fukui, Y. Oomura, T. Akiyama, T. Fukuda, K. Go, S. Kajiura, M. Shigeyasu, K. Asakura, R. Horii, C. Sakai, and N. Sakai

ABSTRACT

BACKGROUND AND PURPOSE: With the increasing use of the Pipeline Embolization Device for the treatment of aneurysms, predictors of clinical and angiographic outcomes are needed. This study aimed to identify predictors of incomplete occlusion at last angiographic follow-up.

MATERIALS AND METHODS: In our retrospective, single-center cohort study, 105 ICA aneurysms in 89 subjects were treated with Pipeline Embolization Devices. Patients were followed per standardized protocol. Clinical and angiographic outcomes were analyzed. We introduced a new morphologic classification based on the included angle of the parent artery against the neck location: outer convexity type (included angle, $<160°$), inner convexity type (included angle, $>200°$), and lateral wall type ($160° \leq$ included angle $\leq 200°$). This classification reflects the metal coverage rate and flow dynamics.

RESULTS: Imaging data were acquired in 95.3% of aneurysms persistent at 6 months. Complete occlusion was achieved in 70.5%, and incomplete occlusion, in 29.5% at last follow-up. Multivariable regression analysis revealed that 60 years of age or older (OR, 5.70; $P = .001$), aneurysms with the branching artery from the dome (OR, 10.56; $P = .002$), fusiform aneurysms (OR, 10.2; $P = .009$), and outer convexity–type saccular aneurysms (versus inner convexity type: OR, 30.3; $P < .001$; versus lateral wall type: OR, 9.71; $P = .001$) were independently associated with a higher rate of incomplete occlusion at the last follow-up. No permanent neurologic deficits or rupture were observed in the follow-up period.

CONCLUSIONS: The aneurysm neck located on the outer convexity is a new, incomplete occlusion predictor, joining older age, fusiform aneurysms, and aneurysms with the branching artery from the dome. No permanent neurologic deficits or rupture was observed in the follow-up, even with incomplete occlusion.

ABBREVIATIONS: MCR = metal coverage ratio; PED = Pipeline Embolization Device

Flow-diversion stents with the Pipeline Embolization Device (PED; Medtronic) were first reported in 2008.[1] Since then, multiple trials[2-6] and retrospective studies[3,7,8] have reported the safety and efficacy of the PED in the treatment of intracranial aneurysms. Long-term follow-up data showed a 95.2% occlusion rate at 5 years after treatment[3,8] and no evidence of recanalization of previously occluded aneurysms.[3] Angiographic and clinical long-term follow-up data are important because incomplete occlusion leads to retreatment or rerupture in coil embolization.[9]

Several factors such as age, sex, smoking, fusiform-type aneurysms, small aspect ratios, and dome-neck ratios have been reported to be predictors of incomplete or complete occlusion.[10-17] However, there is debate about outcomes when using these factors because of limited analysis of the confounding factors. Moreover, the follow-up imaging rate of incomplete occlusion is sometimes insufficient (around 50% at 6 months).[1] Additionally, the same morphologic indices used in coil embolization were used in previous PED studies, even though the 2 methods are different in their treatment mechanism for aneurysms. The metal coverage ratio (MCR)[18-20] is an important metric of PED treatment.

Although the MCR correlates with the occlusion rate,[19] it is calculated after treatment and additional work-up is needed to acquire it. Therefore, in this study, we introduced a new classification based on the included angle of the parent artery against the neck location for the aneurysm, which can be measured before the PED treatment and complements the MCR: outer convexity type, inner convexity type, and lateral wall type. In addition, we clarified factors, including our new classification, affecting incomplete occlusion and clinical

Received June 10, 2020; accepted after revision August 11.

From the Department of Neurosurgery, Kobe City Medical Center General Hospital, Kobe, Japan.

Please address correspondence to Tadashi Sunohara, MD, PhD, Kobe City Medical Center General Hospital, Department of Neurosurgery, 2-1-1 Minami-cho, Minatojima, Chuo-ku, Kobe, 650-0047, Japan; e-mail: tadashi_sunohara@kcho.jp

Indicates article with supplemental online tables.

http://dx.doi.org/10.3174/ajnr.A6859

outcome in PED treatment, on the basis of data with a high follow-up rate.

MATERIALS AND METHODS

Study Design

A retrospective analysis of consecutive aneurysms treated with PED placement between July 2015 and July 2019 at a single institution was performed. The inclusion criteria consisted of all adult patients with intracranial unruptured aneurysms treated with the PED who had undergone angiographic follow-up. All aneurysm morphologies (ie, saccular, fusiform, and so forth) and intracranial locations were included. Institutional review board approval was obtained at the center before commencement of the study. Informed consent was obtained in the form of an opt-out on the Web site. Those who opted out were excluded from the study (0 patients). We collected the following information: patient demographics, aneurysm and PED characteristics, procedural complications, and angiographic and functional outcomes.

Procedural Details

Patients received aspirin, 100 mg, and clopidogrel, 75 mg daily, for 10–14 days before the intervention. Platelet function testing was routinely performed with the VerifyNow P2Y12 assay and the VerifyNow Aspirin assay (Accumetrics) on the day before the procedure. Clopidogrel nonresponders were identified on the basis of established cutoff values of >220, and aspirin nonresponders, of >550. If a patient was identified as a clopidogrel responder, the clopidogrel was continued. If a patient was identified as a clopidogrel nonresponder, the treatment was switched to prasugrel, 3.5 mg daily, with a 1-time loading dose of 20 mg administered 24 hours before the procedure. If a patient was identified as an aspirin nonresponder, the daily dose of aspirin was increased to 200 mg. Dual-antiplatelet therapy was continued for at least 6 months after the procedure, and single-antiplatelet therapy was continued indefinitely thereafter.

Patients were under general anesthesia, and all patients were anticoagulated with heparin throughout the procedure. The 8F guiding catheter, 5F Navien (Medtronic) distal-access catheter, and a Marksman (Medtronic) microcatheter were used in a coaxial system as a standard combination at the institute.

Angiographic Outcome

Angiographic outcome was assessed with DSA or MRA on the basis of the follow-up protocol. At 6 months after the procedure, all patients and aneurysms were assessed with DSA. If aneurysms were completely occluded at DSA, a follow-up assessment was performed with MRA 6–12 months thereafter. In the case of partial occlusion at DSA, follow-up DSA was performed 3–6 months later. In the case of nearly complete occlusion at DSA, follow-up DSA or MRA was performed 3–6 months later at the discretion of the operator.

Aneurysm occlusion on the follow-up DSA was assessed by trained interventionalists. Follow-up MRA was assessed by a radiologist blinded to the clinical history and a trained interventionalist. Occlusion was categorized as complete occlusion (100%), near-complete occlusion (90%–99%), and partial occlusion (<90%) at DSA or MRA. Both near-complete and partial occlusion were collectively defined as incomplete occlusion.

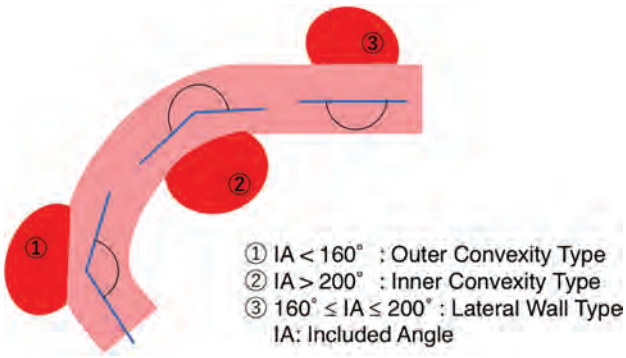

FIGURE. Classification of saccular aneurysms.

Classification of Saccular Aneurysms

Saccular aneurysms were classified into 3 subtypes based on the included angle of the parent artery against the neck location. The included angle is the angle formed by the arc of the internal carotid artery against the aneurysm neck location. The angle was measured by 2 workstations (Xtra Vision R1.3.2, Philips Healthcare, and SYNAPSE VINCENT V5.2, Fujifilm), and the aneurysm was categorized as outer convexity (included angle, <160°;), inner convexity (included angle, >200°), or lateral wall (160° ≤ included angle ≤200°) (Figure).

Clinical Outcome

Functional outcome was assessed with the mRS at each follow-up by the neurosurgeon and interventionalist.

Statistical Analysis

Statistical analysis was performed with JMP software, Version 10 (SAS Institute). In the univariable analysis, variables were compared among groups with the nonparametric test for continuous variables and the χ^2 test for categoric variables to identify predictors of incomplete occlusion and bad neurologic outcome. Statistical significance was defined as $P < .05$. Multivariable logistic regression was performed on candidate predictor variables to identify variables independently associated with incomplete occlusion and clinical outcome at the last angiographic follow-up after controlling for potential confounders.

Baseline and Aneurysm Characteristics

A total of 108 sequential aneurysms treated with PED placement at a single institution were identified. Of these, 105 (97.2%) aneurysms treated by 91 PED procedures in 89 patients (median age, 58 years; female/male ratio, 4.9:1) had angiographic follow-up and were included in this study. All treatments were for unruptured aneurysms. Aneurysms were along the ICA. The locations and measurements are shown in Table 1. Aneurysms including the branching artery from the dome were present in 15.2%. The morphologic types of saccular aneurysms were composed of the outer convexity type in 35.7%, inner convexity type in 29.6%, and lateral wall type in 34.7%. Among patients, 28.6% exhibited symptoms from cranial nerve compression before treatment (Table 1).

Table 1: Baseline characteristics of aneurysms and patient demographics

	Value
Patients ($n = 89$)	
Age (yr)	
Median (range)	58 (20–88)
Sex	
Female	74 (83.1%)
Male	15 (16.9%)
Current smoking	30 (28.6%)
Pretreatment mRS	
0–2	89 (100%)
3–5	0 (0%)
Symptomatic cranial nerve compression	26 (28.6%)
Aneurysms ($n = 105$)	
Measurements (mm)	
Median (range)	
Maximum diameter	10.5 (2–33)
Neck size of saccular aneurysms	6.4 (2–14)
Height of saccular aneurysms	6.0 (0.9−28)
Aneurysm type	
Saccular	98 (93.3%)
Fusiform	7 (6.7%)
Aneurysm location	
ICA petrous	4 (3.8%)
ICA cavernous	31 (29.5%)
ICA paraclinoid	58 (55.2%)
ICA C1 segment	12 (11.4%)
Branching artery from dome	16 (15.2%)
Multiple aneurysms	13 (14.3%)
Morphologic types of saccular aneurysm	
Outer convexity	35 (35.7%)
Inner convexity	29 (29.6%)
Lateral wall	34 (34.7%)
Procedures ($n = 91$)	
No. of Pipelines	
1	90 (98.9%)
2	1 (1.1%)

Table 2: Outcome measures

	Value
Platelet function test	
Yes	89 (100%)
No	0 (0%)
Clopidogrel responder	
Yes	66 (74.2%)
No	23 (25.8%)
Angiographic outcome	
Imaging follow-up	
Median (range) (mo)	27 (9–60)
Data availability	89/92 (96.7%)
Long-term imaging follow-up rate with aneurysm persistent at 6 mo	41/43 (95.3%)
Occlusion rate at 6 mo	
Complete (100%)	62 (59.0%)
Near-complete (90%–99%)	20 (19.0%)
Partial (<90%)	23 (22.0%)
Occlusion rate at last follow-up	
Complete (100%)	74 (70.5%)
Near-complete (90%–99%)	17 (16.2%)
Partial (<90%)	14 (13.3%)
Adjunctive coil	35 (33.3%)
Retreatment	5 (5.5%)
Clinical outcome	
Posttreatment mRS	
0–2	84 (94.4%)
3–5	5 (5.6%)
6 (death)	0 (0%)
mRS at last follow-up	
Improved	16 (18.0%)
No change	73 (82.0%)
Worsened	0 (0%)
Neurologic complications	
Thromboembolic	40 (44.0%)
Symptomatic	6 (6.6%)
Hemorrhagic	3 (3.3%)
Symptomatic	0 (0%)
Symptomatic cranial nerve compression	1 (1.1%)
Long-term outcome	
Rupture of aneurysm at follow-up	0 (0%)
Compression improved at follow-up	10 (37.0%)
Permanent neurologic complication	0 (0%)
Permanent neurologic death	0 (0%)

Treatment Outcome

The median length of the angiographic follow-up was 27 months (range, 9–60 months). All patients (89 patients, 105 aneurysms) had 6-month angiographic follow-up. Table 2 shows the occlusion rate at 6-months after treatment and at the last follow-up. The long-term imaging follow-up rate of patients with incomplete occlusion at 6-month DSA was 95.3% (41/43). The median length of the angiographic follow-up of patients with incomplete occlusion at 6-month DSA was 27.5 months (range, 10–54 months). An adjunctive coil was used in 33.3% of aneurysms, most of which were intradural aneurysms. Retreatment was performed in 5.5% of aneurysms and was exclusively endovascular. The mRS scores just after PED placement were 0–2 in 94.4% of procedures and 3–5 in 5.6% because of ischemic stroke or the worsening of cranial nerve compression. At the last follow-up, the mRS scores were improved in 18.0% of patients. Improvement included pre-existing cranial nerve compression symptoms or postprocedural symptomatic stroke. Symptomatic neurologic complications appeared in 7.7% of procedures. Symptomatic thromboembolic complications were encountered in 6.6% of procedures, and symptomatic hemorrhagic complications, in 0%. In 1 case, a symptom of cranial nerve compression appeared after treatment because of a thrombosing aneurysm. In 37.0%, cranial nerve compression was improved in the follow-up period. The mortality rate was 0%, the postprocedural morbidity rate was 7.7%, and the permanent morbidity rate was 0% (Table 2).

Predictor of Incomplete Occlusion

The following factors were tested as predictors of aneurysm occlusion: age, sex, current smoker/nonsmoker, aneurysm type (saccular or fusiform), complications, maximum dome diameter of the aneurysm, neck diameter, aneurysm height, dome/neck ratio, ASPECTS ratio, adjunctive coil usage, presence of aneurysms with the branching artery from the dome, and the classification of the saccular aneurysm. By means of a univariable analysis, age (older than 60 years, $P = .002$), fusiform aneurysms ($P = .012$), aneurysms with the branching artery from the dome ($P < .001$), and outer convexity type ($P < .001$) were associated with significantly higher rates of incomplete occlusion at the last follow-up (Online Table 1).

Table 3: Multivariable regression analysis of predictors for incomplete occlusion at last follow-up overall[a]

	OR	95% CI	*P* Value
Age (≥60 years)	5.70	1.99–19.5	.001
Branching artery from dome	10.56	2.36–63.2	.002
Fusiform	10.23	1.77–86.3	.009
Type			
OC/IC	30.3	4.96–595	<.001
OC/LW	9.71	2.45–52.0	.001
LW/IC	3.12	0.31–70.4	.34

Note:—OC indicates outer convexity–type saccular aneurysm; IC, inner convexity–type saccular aneurysm; LW, lateral wall–type saccular aneurysm.

[a] $n = 105$; complete occlusion, 74; incomplete occlusion, 31. Significant predictors of incomplete occlusion include age older than 60 years, aneurysms with the branching artery from the dome, fusiform aneurysm, and outer convexity type.

Table 4: Multivariable regression analysis for incomplete occlusion using outer convexity type and aneurysms with a branching artery

Parameter	OR	95% CI	*P* Value
Outer convexity type (+) and branch (+)	162	21.5–3587	<.001
Outer convexity type (+) and branch (–)	16.6	4.54–81.2	<.001
Outer convexity type (–) and branch (+)	9	1–73.2	.05
Outer convexity type (–) and branch (–)	1	–	–

Note:—Branch indicates aneurysm with branching artery from dome; –, not applicable..

The significant predictors of incomplete occlusion at the last follow-up in the univariable analysis were further analyzed with a multivariable logistic regression. Age (older than 60 years; OR, 5.70; 95% CI, 1.99–19.5; $P = .001$), aneurysms with the branching artery from the dome (OR, 10.56; 95% CI, 2.36–63.2; $P = .002$), fusiform aneurysms (OR, 10.23; 95% CI, 1.77–86.3; $P = .009$), and outer convexity–type saccular aneurysms (versus inner convexity type: OR, 30.3; 95% CI, 4.96–595; $P < .001$; versus lateral wall type: OR, 9.71; 95% CI, 2.45–52.0; $P = .001$) were independently associated with a higher rate of incomplete occlusion at the last follow-up (Table 3). The number of each occlusion status per aneurysm type is shown in Online Table 2.

Among the 16 aneurysms with a branching artery from the dome, 10 aneurysms were the outer convexity type. Among the 35 outer convexity–type aneurysms, 10 aneurysms had the branching artery from the dome. Although multivariable logistic regression revealed that outer convexity–type and aneurysms with the branching artery from the dome were independent predictors of incomplete occlusion, there is a possible interaction between these 2 factors; therefore, further analysis was performed (Table 4). On the basis of double-negative aneurysms as a reference, aneurysms of the outer convexity type with the branching artery from the dome (OR, 162; 95% CI, 21.5–3587; $P < .001$) were most susceptible to becoming an incomplete occlusion, followed by outer convexity–type aneurysms without the branching artery from the dome (OR, 16.6; 95% CI, 4.54–81.2; $P < .001$) and non-outer convexity–type aneurysms with the branching artery from the dome (OR, 9.0; 95% CI, 1.0–73.2; $P = .05$).

Predictor of Bad Clinical Outcomes

The posttreatment mRS was 0–2 in 94.4% (84/89) of procedures and 3–5 in 5.6% (5/89). The complications of deteriorated mRS included symptomatic thromboembolic strokes and newly appearing cranial nerve neuropathy due to thrombosing aneurysms. No major thromboembolic strokes occurred, and all patients were improved at 6-month follow-up. The follow-up mRS score was improved in 18% (16/89) and showed no change in 82% (73/89). These improvements included not only symptomatic thromboembolic strokes but also cranial nerve neuropathy caused by compression due to large/giant aneurysms. The mRS at the final follow-up was 0–2 in all patients. The permanent neurologic complication rate was 0%, and the permanent neurologic death was 0%. In the long-term follow-up, no aneurysms were ruptured despite incomplete occlusion (Table 2).

DISCUSSION

In this study, we assessed predictors of incomplete occlusion and clinical outcome on the basis of high-follow-up-rate data. Several factors affecting complete/incomplete occlusion rates were previously reported (Online Table 3).[10-13,15,16,21-26] However, these previous reports disagree about these predictors due to the limited analysis of confounding factors for each candidate predictor and an insufficient follow-up rate for incomplete occlusion cases. Additionally, the same morphologic index based on coil embolization was used in these analyses, even though the PED and coil embolization use different mechanisms to treat aneurysms.[11,17]

In the present study, we included previously reported factors as much as possible to assess the possibility of confounding factors. Additionally, we added the type of saccular aneurysm based on the location of the neck of the aneurysm against the arterial curvature as a morphologic factor. This new classification indirectly reflects the MCR, which is the major index of the occlusion mechanism of PED[18-20] and was reported to correlate with complete occlusion.[18,19]

On the basis of our multivariable regression analysis, in addition to age (older than 60 years; OR, 5.70; $P = .001$), fusiform aneurysms (OR, 10.23; $P = .009$), and aneurysms with the branching artery from the dome (OR, 10.56; $P = .002$), outer convexity–type saccular aneurysms (versus inner convexity type: OR, 30.3; $P < .001$; versus lateral wall type: OR, 9.71; $P = .001$) were independently associated with a higher rate of incomplete occlusion at the last follow-up. Further analysis found an interaction between outer convexity–type aneurysms and aneurysms with the branching artery from the dome and that this interaction (OR, 162; $P < .001$) was most susceptible to becoming an incomplete occlusion, followed by outer convexity–type aneurysms without the branching artery from the dome (OR, 16.6; $P < .001$) and non-outer convexity–type aneurysms with the branching artery from the dome (OR, 9.0; $P = .05$).

Our study is based on a single-center consecutive retrospective cohort. Among patients, 96.7% (89/92) had DSA at 6 months after treatment. The long-term imaging follow-up rate for aneurysms with incomplete occlusion at 6 months was 95.3% (41/43), and the median length of imaging follow-up for patients with

incomplete occlusion at 6-month DSA was 27.5 months (range, 10–54 months). Each factor affecting our findings is discussed below.

Predictors of Aneurysm Occlusion

Type of Neck Location Related to Variation in Occlusion Rates. No previous report has proposed our saccular aneurysm classification with regard to the PED. The advantage of this classification is that it is simple and needs minimal, if any, software or calculations.

According to the mechanisms of aneurysm occlusion by PED previously reported,[18-20,27-29] hemodynamics[30-36] and endothelialization[29,37-41] are key factors and MCR and porosity are key indices for successful PED treatment. Our classification based on the curvature of the parent artery indirectly reflects the MCR and flow dynamics around the neck of the aneurysm and relates to the aneurysmal occlusion. MCR and porosity are the major indices of the occlusion mechanism of the PED and inverses of each other.[18-20,37-39,42] The MCR is the portion of the ostium of the aneurysm covered by the metal of the flow diverter.[20] In general, devices with a higher MCR provide a better scaffold for endothelialization.[39-41]

Two studies[18,19] reported that the local metal coverage of the stent at the aneurysmal neck correlates with the occlusion of the aneurysm; a 35% metal coverage at the neck predicted >95% angiographic aneurysm occlusion with a specificity of 100% and sensitivity of 53.8%. The PED is designed to have an MCR of 30%. However, the MCR will change with the angle of the PED. Wang and Yuan[18] reported the relationship between the MCR and the bending angle of the PED, showing that the MCR could range from 19% to 63%, depending on the angle. Additionally, the MCR would become lower, and the porosity, higher in the outer convexity compared with their values in the inner concavity of the curvature of the parent artery.[20,42-44] On the basis of those previous studies, we estimated that the local MCR around the neck of the aneurysm in the outer convexity type is <30%. We estimated the MCR to be >35% for the inner convexity type and lateral wall type, though the MCR tends to be higher for the inner convexity.[43,44] Therefore, our new classification of saccular aneurysms indirectly reflects the MCR around the aneurysmal neck and has an effect on the occlusion rate.

A neck location with outer convexity is also disadvantageous for PED treatment from the viewpoint of hemodynamics. From a computational fluid dynamics analysis, successful flow diversion depends on the following: 1) the flow resistance force of the flow diverter to decrease the flow velocity magnitude,[30] 2) decreased jet flow into the aneurysm,[31] 3) the aneurysm neck geometry,[31] and 4) the patient-specific inflow threshold[32] and other parameters such as the inflow rate, aneurysmal velocity reduction, and so forth.[33] The flow velocity is faster at the outer convex side of a curved vessel than at the inner concave side, and the flow vector is toward the aneurysm in the outer convexity type.[34,35] Therefore, the flow velocity magnitude and the jet flow into the aneurysm are higher in the outer convexity type than in other types of saccular aneurysms.

According to a computational fluid dynamics analysis of flow diveters,[36] the velocity magnitude of the inflow stream of the aneurysm sac and the inflow volume rate increase as the curvature of the parent artery increases and are higher if the curvature angle is large after the flow-diverter placement.[36] That study provides a theoretic explanation for why the outer convexity type resists complete occlusion compared with inner convexity and lateral wall types.

An overlapped flow-diverter placement was reported to be effective in decreasing the inflow volume rate, to overcome the possibility of incomplete occlusion in the outer convexity type.[36] Technical manipulation is also recommended, such as a dynamic push-pull technique over the aneurysm orifice, which enhances the intended flow diversion, to compensate for the low MCR with the outer convexity type.[45]

Age-Related Variation of Occlusion Rates

Our data also showed that older age was one of the predictor of incomplete occlusion, consistent with a previous report.[10]

The mechanism of occlusion in PED-treated aneurysms, as mentioned above, could account for why older age was a predictor. The migration of endothelial cells slows with age,[46] slowing endothelialization of the PED. Furthermore, atherosclerosis, which is also more common in older patients, could also contribute because the irregular shape of the endoluminal surface of the artery could form a gap between the endoluminal surface of the artery and the PED, resulting in an endoleak to the aneurysm through the nonendothelialized area.[11]

Branch-Related Variations in Occlusion Rates

Aneurysms with the branching artery from the dome being a solid predictor of incomplete occlusion is consistent with several reports.[22-26] The ophthalmic artery, posterior communicating artery, and anterior choroidal artery were all relevant in our series. In cases of aneurysms with the branching artery from the dome, when the branch has blood demand, blood flow through the PED inhibits endothelialization, resulting in remnant flow to the aneurysm and incomplete occlusion. Notably, this factor was independent from and had interaction with the type of neck location.

Fusiform or Saccular Variation in Occlusion Rates

Our data also showed that fusiform aneurysms were a significant predictor of incomplete occlusion compared with saccular aneurysms, consistent with previous studies.[11,16,25] The reason could be the occlusion mechanisms of the PED. In the case of fusiform aneurysms, a wider surface area of the PED is exposed to the aneurysm without support by the vessel wall compared with saccular aneurysms. These areas are more likely to be devoid of endothelialization.[47]

Predictor of Clinical Outcome

We also assessed predictors of the clinical outcome; however, no ruptures of aneurysms were observed in the follow-up periods. These findings indicate that aneurysms treated with the PED are clinically safe and stable, even with aneurysm remnants, as reported previously.[12]

Limitations

The limitations of the study include its retrospective design with all the inherent biases associated with such a study design. Although this study is from a single center and thus warranted a unified treatment procedure, antiplatelet regimen, and follow-up imaging protocol, the retrospective nature of this study and

analysis from a single center introduce sampling bias and possibly limit external validity.

Twelve aneurysms with incomplete occlusion had follow-ups of <2 years. The possibility for these aneurysms to occlude thereafter could affect the results because complete aneurysmal occlusion is expected to occur up to 2 years post-PED deployment.[48]

Finally, because some patients had multiple aneurysms, we performed multiple logistic regression using generalized estimating equations to consider intrapatient correlations.

CONCLUSIONS

In this study, on the basis of high follow-up data, we analyzed the angiographic and clinical outcomes of unruptured ICA aneurysms after PED treatment. Clinically, ICA aneurysms were safe without rupture in the follow-up period, even with aneurysm remnants. Angiographically, in addition to age, fusiform aneurysms, and aneurysms with the branching artery from the dome, the outer convexity–type of saccular aneurysm was a predictor of incomplete occlusion.

ACKNOWLEDGMENTS

We are grateful to Yuuji Naramoto, MD, Rikuo Nishii, MD, and Yasuhiro Yamamoto, MD, at the Department of Neurosurgery, Kobe City Medical Center General Hospital, Kobe, for collecting some of the data. We thank Dr Peter Karagiannis and Sofia Science Writing for critical reading and proofreading of the manuscript. We are grateful to Chisato Miyakoshi, MD, MSc, at the Department of Pediatrics, Kobe City Medical Center General Hospital, Kobe, for the consultation on statistics analysis.

Disclosures: Nobuyuki Sakai—*UNRELATED*: *Grants/Grants Pending*: Medtronic, NeuroVasc, Terumo; Payment for Lectures Including Service on Speakers Bureaus: ASAHI INTEC, Biomedical Solutions, Johnson & Johnson, Medtronic, Stryker, Terumo.

REFERENCES

1. Fiorella D, Woo HH, Albuquerque FC, et al. **Definitive reconstruction of circumferential, fusiform intracranial aneurysms with the Pipeline Embolization Device.** *Neurosurgery* 2008;62:1115–20; discussion 1120–21 CrossRef Medline
2. Becske T, Kallmes DF, Saatci I, et al. **Pipeline for uncoilable or failed aneurysms: results from a multicenter clinical trial.** *Radiology* 2013;267:858–68 CrossRef Medline
3. Becske T, Brinjikji W, Potts MB, et al. **Long-term clinical and angiographic outcomes following Pipeline Embolization Device treatment of complex internal carotid artery aneurysms: five-year results of the Pipeline for Uncoilable or Failed Aneurysms trial.** *Neurosurgery* 2017;80:40–48 CrossRef Medline
4. Kallmes DF, Hanel R, Lopes D, et al. **International retrospective study of the Pipeline Embolization Device: a multicenter aneurysm treatment study.** *AJNR Am J Neuroradiol* 2015;36:108–15 CrossRef Medline
5. Becske T, Potts MB, Shapiro M, et al. **Pipeline for Uncoilable or Failed Aneurysms: 3-year follow-up results.** *J Neurosurg* 2017;127:81–88 CrossRef Medline
6. Nelson PK, Lylyk P, Szikora I, et al. **The Pipeline Embolization Device for the intracranial treatment of aneurysms trial.** *AJNR Am J Neuroradiol* 2011;32:34–40 CrossRef
7. Lylyk P, Miranda C, Ceratto R, et al. **Curative endovascular reconstruction of cerebral aneurysms with the Pipeline Embolization Device: the Buenos Aires experience.** *Neurosurgery* 2009;64:632–42 CrossRef Medline
8. Kallmes DF, Brinjikji W, Cekirge S, et al. **Safety and efficacy of the Pipeline Embolization Device for treatment of intracranial aneurysms: a pooled analysis of 3 large studies.** *J Neurosurg* 2017;127:775–80 CrossRef Medline
9. Munich SA, Cress MC, Rangel-Castilla L, et al. **Neck remnants and the risk of aneurysm rupture after endovascular treatment with coiling or stent-assisted coiling: much ado about nothing?** *Clin Neurosurg* 2019;84:421–47 CrossRef Medline
10. Adeeb N, Moore JM, Wirtz M, et al. **Predictors of incomplete occlusion following Pipeline embolization of intracranial aneurysms: is it less effective in older patients?** *AJNR Am J Neuroradiol* 2017;38:2295–300 CrossRef Medline
11. Shapiro M, Becske T, Nelson PK. **Learning from failure: persistence of aneurysms following Pipeline embolization.** *J Neurosurg* 2017;126:578–85 CrossRef Medline
12. Madaelil TP, Grossberg JA, Howard BM, et al. **Aneurysm remnants after flow diversion: clinical and angiographic outcomes.** *AJNR Am J Neuroradiol* 2019;40:694–98 CrossRef Medline
13. Liang B, Lesley WS, Robinson TM, et al. **Off-label application of Pipeline Embolization Device for intracranial aneurysms.** *Neurointervention* 2019;14:116–24 CrossRef Medline
14. Zhang Y, Liang F, Zhang Y, et al. **Exploring the feasibility of Pipeline Embolization Device compared with stent-assisted coiling to treat non-saccular, unruptured, intradural vertebral artery aneurysms.** *Front Neurol* 2019;10:275 CrossRefMedline
15. O'Kelly CJ, Spears J, Chow M, et al. **Canadian experience with the Pipeline Embolization Device for repair of unruptured intracranial aneurysms.** *AJNR Am J Neuroradiol* 2013;34:381–87 CrossRef Medline
16. Jabbour P, Chalouhi N, Tjoumakaris S, et al. **The Pipeline Embolization Device: learning curve and predictors of complications and aneurysm obliteration.** *Neurosurgery* 2013;73:113–20 CrossRef Medline
17. Li Y, Kim J, Ahmed A. **Effect of aneurysm morphologic parameters on occlusion rates following Pipeline embolization.** *Clin Neurol Neurosurg* 2019;183:105395 CrossRef Medline
18. Wang K, Yuan S. **Actual metal coverage at the neck is critical for flow-diverting stents in treating intracranial aneurysms.** *AJNR Am J Neuroradiol* 2013;34:31–32 CrossRef Medline
19. Wang K, Huang Q, Hong B, et al. **Correlation of aneurysm occlusion with actual metal coverage at neck after implantation of flow-diverting stent in rabbit models.** *Neuroradiology* 2012;54:607–13 CrossRef Medline
20. Jou LD, Chintalapani G, Mawad ME. **Metal coverage ratio of Pipeline Embolization Device for treatment of unruptured aneurysms: reality check.** *Interv Neuroradiol* 2016;22:42–48 CrossRef Medline
21. Brasiliense LBC, Aguilar-Salinas P, Miller DA, et al. **Analysis of predictors and probability of aneurysm occlusion in the internal carotid artery after treatment with Pipeline Embolization Device.** *World Neurosurg* 2017;107:641–48 CrossRef Medline
22. Puffer RC, Lanzino G, Kallmes D, et al. **Patency of the ophthalmic artery after flow diversion treatment of paraclinoid aneurysms.** *J Neurosurg* 2012;116:892–96 CrossRef Medline
23. Raz E, Shapiro M, Becske T, et al. **Anterior choroidal artery patency and clinical follow-up after coverage with the Pipeline Embolization Device.** *AJNR Am J Neuroradiol* 2015;36:937–42 CrossRef Medline
24. Vedantam A, Rao VY, Shaltoni HM, et al. **Incidence and clinical implications of carotid branch occlusion following treatment of internal carotid artery aneurysms with the Pipeline Embolization Device.** *Neurosurgery* 2015;76:173–78 CrossRef Medline
25. Moshayedi H, Omofoye OA, Yap E, et al. **Factors affecting the obliteration rate of intracranial aneurysms treated with a single Pipeline Embolization Device.** *World Neurosurg* 2017;104:2–5 CrossRef Medline

26. Volker M, Anastasios M, Jan B, al. **Treatment of intracranial aneurysms with the Pipeline Embolization Device only: a single center experience.** *Neurointervention* 2018;13;32–40 CrossRef Medline
27. Chua MM, Silveira L, Moore J, et al. **Flow diversion for treatment of intracranial aneurysms: mechanism and implications.** *Ann Neurol* 2019;85:793–800 CrossRef Medline
28. Schneiders JJ, VanBavel E, Majoie CB, et al. **A flow-diverting stent is not a pressure-diverting stent.** *AJNR Am J Neuroradiol* 2013;34:1–4 CrossRef Medline
29. Kadirvel R, Ding YH, Dai D, et al. **Cellular mechanisms of aneurysm occlusion after treatment with a flow diverter.** *Radiology* 2014;270:394–99 CrossRef Medline
30. Zhang Y, Chong W, Qian Y. **Investigation of intracranial aneurysm hemodynamics following flow diverter stent treatment.** *Med Eng Phys* 2013;35:608–15 CrossRef Medline
31. Chong W, Zhang Y, Qian Y, et al. **Computational hemodynamics analysis of intracranial aneurysms treated with flow diverters: correlation with clinical outcomes.** *AJNR Am J Neuroradiol* 2014;35:136–42 CrossRef Medline
32. Berg P, Saalfeld S, Janiga G, et al. **Virtual stenting of intracranial aneurysms: a pilot study for the prediction of treatment success based on hemodynamic simulations.** *Int J Artif Organs* 2018;41:698–705 CrossRef Medline
33. Paliwal N, Damiano RJ, Davies JM, et al. **Association between hemodynamic modifications and clinical outcome of intracranial aneurysms treated using flow diverters.** *Proc SPIE Int Soc Opt Eng* 2017;10135:101352F CrossRef Medline
34. Kalpakli A. **Experimental study of turbulent flows through pipe bends.** *KTH Royal Institute of Technology* 2012;6–29
35. van Wyk S, Wittberg LP, Bulusu KV, et al. **Non-Newtonian perspectives on pulsatile blood-analog flows in a 180° curved artery model.** *Physics of Fluids* 2015;27:71901 CrossRef
36. Xu J, Wu Z, Yu Y, et al. **Combined effects of flow diverting strategies and parent artery curvature on aneurysmal hemodynamics: a CFD study.** *PLoS One* 2015;10:e0138648 CrossRef Medline
37. Marosfoi M, Langan ET, Strittmatter L, et al. **In situ tissue engineering: endothelial growth patterns as a function of flow diverter design.** *J Neurointerv Surg* 2017;9:994–98 CrossRef Medline
38. Sadasivan C, Cesar L, Seong J, et al. **An original flow diversion device for the treatment of intracranial aneurysms: evaluation in the rabbit elastase-induced model.** *Stroke* 2009;40:952–58 CrossRef Medline
39. Panchendrabose K, Muram S, Mitha AP. **Promoting endothelialization of flow-diverting stents: a review.** *J Neurointerv Surg* 2020 June 2. [Epub ahead of print] CrossRef Medline
40. Raymond J, Darsaut TE, Makoyeva A, et al. **Endovascular treatment with flow diverters may fail to occlude experimental bifurcation aneurysms.** *Neuroradiology* 2013;55:1355–63 CrossRef Medline
41. Hong B, Wang K, Huang Q, et al. **Effects of metal coverage rate of flow diversion device on neointimal growth at side branch ostium and stented artery: an animal experiment in rabbit abdominal aorta.** *Neuroradiology* 2012;54:849–55 CrossRef Medline
42. Ma D, Dumont TM, Kosukegawa H, et al. **High-Fidelity Virtual Stenting (HiFiVS) for intracranial aneurysm flow diversion: in vitro and in silico.** *Ann Biomed Eng* 2013;41:2143–56 CrossRef Medline
43. Bing F, Darsaut TE, Salazkin I, et al. **Stents and flow diverters in the treatment of aneurysms: device deformation in vivo may alter porosity and impact efficacy.** *Neuroradiology* 2013;55:85–92 CrossRef Medline
44. Aurboonyawat T, Blanc R, Schmidt P, et al. **An in vitro study of Silk stent morphology.** *Neuroradiology* 2011;53:659–67 CrossRef Medline
45. Ma D, Xiang J, Choi H, et al. **Enhanced aneurysmal flow diversion using a dynamic push-pull technique: an experimental and modeling study.** *AJNR Am J Neuroradiol* 2014;35:1779–85 CrossRef Medline
46. Lähteenvuo J, Rosenzweig A. **Effects of aging on angiogenesis.** *Circ Res* 2012;110:1252–63 CrossRef Medline
47. Szikora I, Turányi E, Marosfoi M. **Evolution of flow-diverter endothelialization and thrombus organization in giant fusiform aneurysms after flow diversion: a histopathologic study.** *AJNR Am J Neuroradiol* 2015;36:1716–20 CrossRef Medline
48. Gupta R, Ogilvy CS, Moore JM, et al. **Proposal of a follow-up imaging strategy following Pipeline flow diversion treatment of intracranial aneurysms.** *J Neurosurg* 2018;131:32–39 CrossRef Medline

Imaging Artifacts of Liquid Embolic Agents on Conventional CT in an Experimental in Vitro Model

N. Schmitt, R.O. Floca, D. Paech, R.A. El Shafie, F. Seker, M. Bendszus, M.A. Möhlenbruch, and D.F. Vollherbst

ABSTRACT

BACKGROUND AND PURPOSE: Endovascular embolization using liquid embolic agents is a safe and effective treatment option for AVMs and dural arteriovenous fistulas. The aim of this study was to assess the degree of artifact inducement by the most frequently used liquid embolic agents in conventional CT in an experimental in vitro model.

MATERIALS AND METHODS: Dimethyl-sulfoxide–compatible tubes were filled with the following liquid embolic agents ($n = 10$, respectively): Onyx 18, all variants of Squid, PHIL 25%, PHIL LV, and *n*-BCA mixed with iodized oil. After inserting the tubes into a CT imaging phantom, we acquired images. Artifacts were graded quantitatively by the use of Hounsfield units in a donut-shaped ROI using a customized software application that was specifically designed for this study and were graded qualitatively using a 5-point scale.

RESULTS: Quantitative and qualitative analyses revealed the most artifacts for Onyx 18 and the least artifacts for *n*-BCA, PHIL 25%, and PHIL LV. Squid caused more artifacts compared with PHIL, both for the low-viscosity and for the extra-low-viscosity versions (eg, quantitative analysis, Squid 18: mean ± SD, 30.3 ± 9.7 HU versus PHIL 25%: mean ± SD, 10.6 ± 0.8 HU; $P < .001$). Differences between the standard and low-density variants of Squid were observed only quantitatively for Squid 12. There were no statistical differences between the different concentrations of Squid and PHIL.

CONCLUSIONS: In this systematic in vitro analysis investigating the most commonly used liquid embolic agents, relevant differences in CT imaging artifacts could be demonstrated. Ethylene-vinyl alcohol–based liquid embolic agents induced more artifacts compared with liquid embolic agents that use iodine as a radiopaque component.

ABBREVIATIONS: EVOH = ethylene-vinyl alcohol; LD = low density; LEA = liquid embolic agent; LV = low viscosity; MITK = Medical Imaging Interaction Toolkit; n-BCA = n-butyl cyanoacrylate

In addition to microneurosurgery and stereotactic radiation therapy, endovascular embolization using liquid embolic agents (LEAs) is an effective treatment mode for the therapy of cerebral AVMs or cranial dural AVFs. Depending on the type and extension of the vascular malformation, the endovascular treatment can be performed either alone or in combination with one of the other methods.[1]

For the treatment of such vascular malformations, several LEAs, each with different properties, are currently available on the market. The most commonly used nonadhesive material is Onyx (Medtronic), a LEA consisting of an ethylene-vinyl alcohol (EVOH) copolymer, dimethyl-sulfoxide, and tantalum powder. Numerous studies have demonstrated the effectiveness and safety of Onyx for the treatment of vascular malformations.[2,3] Another LEA, also based on EVOH and tantalum powder is Squid (Balt Extrusion), which has been commercially available since 2012, with its low-viscosity versions, Squid 18 and Squid 18 low density (LD), and its extra-low-viscosity versions, Squid 12 and Squid 12 LD. For adequate visibility during embolization, radiopacity for these 5 nonadhesive agents is induced by the admixed tantalum powder.[4,5] The difference between Onyx and Squid is that for Squid, the tantalum powder consists of a smaller "micronized" grain size, which is aimed at enhancing the homogeneity in radiopacity and improving the visibility during longer injections times.[5] The aim of the LD variants of Squid is to reduce the

Received June 10, 2020; accepted after revision August 14.

From the Departments of Neuroradiology (N.S., F.S., M.B., M.A.M., D.F.V.) and Radiation Oncology (R.O.F., R.A.E.S.), Heidelberg University Hospital, Heidelberg, Germany; Medical and Biological Informatics (R.O.F.), and Department of Radiology (D.P.), German Cancer Research Center, Heidelberg, Germany; and Heidelberg Institute for Radiation Oncology and National Center for Radiation Research in Oncology (R.O.F.), Heidelberg, Germany.

This work received technical support from Balt and MicroVention.

The authors had full control of the data and its analysis throughout the study. No outside interests have influenced our results.

Please address correspondence to Dominik F. Vollherbst, MD, Department of Neuroradiology, Heidelberg University Hospital, INF 400, 69120 Heidelberg, Germany; e-mail: Dominik.Vollherbst@med.uni-heidelberg.de

http://dx.doi.org/10.3174/ajnr.A6867

FIG 1. Schematic illustration of the donut-shaped ROI created by the MITK with an inner radius of 6 mm and an outer radius of 26 mm. The tube filled with the LEA of interest was placed centrally with a radius equal to the radius of the donut hole. For each tube, the measurement was performed with an ROI in 5 different positions according to the length of the LEA cast.

radiopacity to improve the differentiation of the embolized and nonembolized parts of the malformation without influencing the embolic properties.

A further commercially available LEA, which was introduced recently, is Precipitating Hydrophobic Injectable Liquid (PHIL; MicroVention) with its low-viscosity version PHIL 25% and its extra-low-viscosity version PHIL low viscosity (LV).[6,7] PHIL is a nonadhesive precipitating embolic agent that consists of 2 specific copolymers [poly(lactide-co-glycolide) and polyhydroxyethylmethacrylate] as its active ingredients and triiodophenol (an iodine compound), which is covalently bound to the copolymers, thus enabling the intrinsic radiopacity of PHIL.[8,9]

Before the introduction of these nonadhesive embolic agents, which are all based on the mechanism of precipitation, liquid embolization was predominantly performed with adhesive cyanoacrylates. The active component of cyanoacrylates is n-butyl cyanoacrylate (*n*-BCA), which is available in different chemical compositions and is normally mixed with iodized oil for adequate radiopacity. Even though the use of cyanoacrylates has decreased since the introduction of the above-mentioned nonadhesive LEAs,[10,11] *n*-BCA and its derivates are still used effectively in particular situations, for example, for the treatment of high-flow malformations and for specific techniques such as the pressure cooker technique.[12]

A major drawback of LEAs is imaging artifacts, predominantly in CT.[13,14] Because intracranial vascular malformations are associated with an increased risk of peri- and postprocedural hemorrhage, embolization-related artifacts can represent a crucial obstacle in the detection of intracranial blood during or after embolization in CT.[15] Furthermore, some vascular malformations, especially complex AVMs, cannot be completely occluded by endovascular means, requiring subsequent radiation therapy afterward.[1] The corresponding treatment-planning recordings are usually based on conventional CT imaging.[16] Thus, embolization-related artifacts represent another substantial drawback for adequate and safe treatment planning of further radiation projects.[17-19]

Systematic data for imaging artifacts of LEAs is rare. To our knowledge, to date, only a few reports with low case numbers that investigated the imaging artifacts of the above-mentioned LEAs (Onyx versus PHIL and Onyx versus Squid) are available.[13,14] The differences in CT artifacts between Squid and PHIL, between nonadhesive LEAs and *n*-BCA, and imaging artifacts of the extra-low viscosity LEAs Squid 12 and PHIL LV were not the focus of research until now.

The aim of the present study was the systematic assessment of artifacts of the most commonly used LEAs in conventional CT in an in vitro tube model.

MATERIALS AND METHODS

Sample Preparation

Dimethyl-sulfoxide–compatible tubes, with a length of 30 mm, an outer diameter of 8 mm, and an inner diameter of 4 mm, were used for this study. In a first step, the tubes were flushed with warm saline (38.0°C; NaCl, 0.9%). As is recommended for clinical use, each of the examined LEAs was prepared in accordance with the manufacturer's instructions. Afterward, complete filling of the tubes was performed with Onyx 18, all variants of Squid (Squid 18, Squid 18 LD, Squid 12, and Squid 12 LD), PHIL 25%, PHIL LV, and *n*-BCA mixed with iodized oil (Lipiodol Ultra-Fluid; Guerbet) in a ratio of 1:1. Ten tubes were filled and investigated per LEA. As a control group, tubes ($n = 10$) were filled with saline 0.9%.

Imaging

To ensure a homogeneous distribution of the LEAs within the tubes, we obtained a single-shot x-ray immediately after filling. Directly afterwards, the filled tubes were inserted into a custom-made CT phantom, as previously described by Daubner et al.[20] The average density was similar to that of brain tissue (mean, 33.9 ± .9 HU). The beam path for all CT scans was orthogonal to the LEA-filled tubes, to ensure an optimal spread of artifacts. Conventional CT was performed with standard settings according to clinical practice with a tube voltage of 120 kV and a tube current of 20 mAs on a 64-section multidetector, single-source scanner (Somatom Definition AS; Siemens). A standard imaging protocol was used according to recommendations by the manufacturer and used as in clinical routine. In a next step, all images were reconstructed with a J40s kernel at a section thickness of 4 mm.

Quantitative Analysis of the Imaging Artifacts

Quantitative analysis of the LEA-related artifacts was conducted with the Medical Imaging Interaction Toolkit (MITK, Germany Cancer Research Center, Division of Medical Image Computing, Heidelberg, Germany; https://docs.mitk.org/2018.04/) in the axial plane.[21] Therefore, a customized feature of the MITK software was specifically implemented for this study. This feature allowed us to place a standardized ROI with a donut-shaped configuration adjacent to and surrounding the center of each filled tube. This standardized ROI with a donut-shaped configuration ensured that the LEA-filled tube was excluded from the analysis, thus preventing distortion of the artifacts by the LEA. The outer radius of the donut-shaped ROI was set at 26 mm, while the inner radius was set at 6 mm, whereas the tube itself, with an outer diameter of 8 mm, was positioned at the center of the donut hole (Fig 1). For an adequate placement of the ROI, the width and the level of the window were adjusted manually for each measurement. According to the length of the LEA cast, 5 ROIs were set in different positions with a distance of 4 mm along the tube to ensure that all artifacts were taken into account.

The degree of imaging artifact production was assessed by calculating the SD of the Hounsfield units in the ROI, as described previously.[13,14] Because streak artifacts in conventional CT usually consist of alternating areas of very high- and very low-density, respectively, using the SD as a measurement for the degree of artifact production has the advantage of not being canceled out, as might be the case for the mean of the Hounsfield unit values.[19]

Qualitative Analysis of the Imaging Artifacts

Qualitative analyses of the conventional CT images were performed on a PACS workstation by 2 different readers (reader 1 with 4 years; reader 2 with 9 years of experience in diagnostic imaging, respectively), blinded to the type of LEA and saline. The reconstructed images were all reviewed in slices with a thickness of 4 mm in the axial plane in a standard CT brain window with a width of 80 and a level of 40. The observers were not allowed to adjust the window.

The degree of artifacts was graded on a 5-point scale:[22] 1) severe artifacts, 2) marked artifacts, 3) moderate artifacts, 4) minor artifacts, and 5) no artifacts.

Statistics

GraphPad Prism software (Version 8.4.2; GraphPad Software) was used for statistical analysis. The interreader agreement for the qualitative image analysis was assessed using an unweighted Cohen κ coefficient.[23] The κ values were interpreted as follows: $\leq$0.20, poor agreement; 0.21–0.40, fair agreement; 0.41–0.60, moderate agreement; 0.61–0.80, good agreement; and 0.81–1.00, very good agreement.[24] Data are presented as mean ± SD. To evaluate statistical differences among the study groups, we performed the Kruskal-Wallis test. To test for differences among the individual study groups, we used the Dunn test for multiple comparisons using statistical hypothesis testing as a post hoc test. The Dunn test was performed only for corresponding LEA variants, low-viscosity variants (Onyx 18 versus Squid 18 versus PHIL 25%), extra-low-viscosity variants (Squid 12 versus PHIL LV), and LD variants of Squid (Squid 18 versus Squid 18 LD and Squid 12 versus Squid 12 LD), to reduce the number of statistical tests. *n*-BCA and the control group were compared with Onyx 18 and all Squid and PHIL variants, respectively. The significance level was defined at $P < .05$.

RESULTS

The results of the quantitative image analysis are summarized in Tables 1 and 2, and Fig 2. Representative CT images of the examined LEAs are demonstrated in Fig 3. The results of the qualitative analysis are demonstrated in Fig 4 and Table 3. There was very good agreement for the qualitative grading of artifacts in conventional CT (κ = 0.954; range, 0.902–1.0). The Kruskal-Wallis test showed a statistically significant difference ($P < .001$) in the degree of artifacts among all study groups of the quantitative and qualitative analyses. Regarding the low-viscosity LEAs, Onyx 18 and Squid 18 induced a higher degree of artifacts compared with PHIL 25% for both the quantitative and qualitative analyses (eg, $P < .001$ for Onyx 18 and $P < .001$ for Squid 18 for the quantitative analysis). No difference was observed between Onyx 18 and Squid 18 (eg, $P > .999$ for the qualitative analysis). For the extra-low-viscosity LEAs in both analyses, more severe artifacts were caused by Squid 12 compared with PHIL LV (eg, $P < .001$ for the quantitative analysis). Compared with *n*-BCA, only the standard versions

Table 1: Summary of the quantitative imaging analysis

Liquid Embolic Agent	SD of Donut-Shaped ROI	*P* Value[a]
Onyx 18	56.6 ± 20.1 HU	
Squid 18	30.3 ± 9.7 HU	
Squid 18 LD	18.5 ± 6.8 HU	
Squid 12	33.4 ± 17.3 HU	
Squid 12 LD	19.4 ± 7.7 HU	$P < .001$
PHIL 25%	10.6 ± 0.8 HU	
PHIL LV	10.1 ± 0.9 HU	
n-BCA/iodized oil	11.9 ± 1.0 HU	
Saline	5.1 ± 0.1 HU	

[a]Kruskal-Wallis test; for the *P* values of the post hoc analysis, see Table 2.

Table 2: Summary of the results of the post hoc Dunn test for the quantitative analysis

Liquid Embolic Agent	Onyx 18	Squid 18	Squid 18 LD	Squid 12	Squid 12 LD	PHIL 25%	PHIL LV	*n*-BCA/Iodized Oil
Saline	$P < .001$[a]	$P < .001$[a]	$P < .001$[a]	$P < .001$[a]	$P < .001$[a]	$P = .001$[a]	$P = .034$[a]	$P < .001$[a]
n-BCA/iodized oil	$P < .001$[a]	$P < .001$[a]	$P = .106$	$P < .001$[a]	$P = .468$	$P = .987$	$P = .096$	
PHIL LV	NA	NA	NA	$P < .001$	NA	$P > .999$		
PHIL 25%	$P < .001$[a]	$P < .001$[a]	NA	NA	NA			
Squid 12 LD	NA	NA	$P > .999$	$P = .013$[a]				
Squid 12	NA	$P > .999$	NA					
Squid 18 LD	NA	$P = .057$						
Squid 18	$P = .118$							

Note:—NA indicates no *P* value available because the Dunn test was only performed for corresponding LEA variants.
[a] Statistical significance.

of the EVOH-based LEAs (Onyx 18, Squid 18, and Squid 12) showed more artifacts quantitatively and qualitatively (eg, $P < .001$ for Onyx 18, $P = .004$ for Squid 18, and $P = .003$ for Squid 12 in qualitative statistics). The degree of artifacts was lowest for the saline-filled tubes (control group), reaching statistical significance in all groups except for PHIL 25%, PHIL LV, and *n*-BCA in the qualitative analysis. When we compared the standard and the LD variants of Squid, the degree of artifacts tended to be lower for Squid 18 LD and Squid 12 LD; however, they were only statistically significant for quantitative analysis of Squid 12 ($P = .013$). The versions of PHIL and Squid with different viscosities (eg, PHIL 25% versus PHIL LV and Squid 18 versus Squid 12) did not show significant differences.

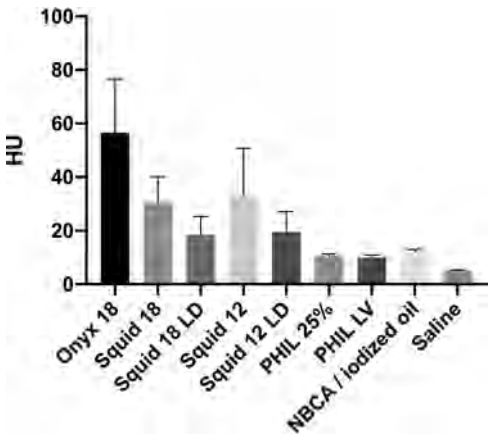

FIG 2. Illustration of the results of the quantitative image analysis. Different degrees of artifacts were observed among all study groups. Post hoc testing showed differences among the different types of LEAs (eg, Squid 18 versus PHIL 25% and Squid 12 versus PHIL LV). *Bars* indicate mean; *whiskers*, SD.

DISCUSSION

Endovascular embolization using LEAs is an established treatment option for AVMs and DAVFs.[1] Currently, various embolic agents are commercially available, each with specific properties.[25,26] One of the main disadvantages of LEAs is the generation of imaging artifacts in peri- and postprocedural CT.[4,13]

In the present study, we demonstrated that the imaging artifacts induced by LEAs vary to a substantial degree. EVOH-based LEAs induce more artifacts compared with a copolymer-based LEA, which uses covalently bound iodine as a radiopaque component, while *n*-BCA and iodized oil induce only minor artifacts on conventional CT.

To date, to the best of our knowledge, only 2 studies have investigated the difference in CT imaging artifacts of nonadhesive liquid embolic agents.[13,14] Vollherbst et al[13] compared the imaging artifacts of Onyx and PHIL in an experimental animal study and reported a higher degree of artifacts for Onyx 18 compared with PHIL 25% on conventional CT. In an experimental in vitro tube model, Pop et al[14] investigated Onyx and Squid regarding their production of CT imaging artifacts. Their results demonstrated fewer imaging artifacts for all variants of Squid compared with Onyx 18 as well as for the LD variants compared with their normal-density counterparts on conventional CT. Furthermore, they observed lower artifacts for Squid 18 than for Squid 12.[14]

Systematic analyses of imaging artifacts on conventional CT between Squid and PHIL, between nonadhesive LEAs and *n*-BCA, as well as artifacts of the extra-low-viscosity LEAs Squid 12 and PHIL LV have not been reported until now.

Regarding the present study, there are 3 major advantages: 1) The customized donut-shaped ROI was used for the image analysis; 2) all LEAs that are commonly used for embolization of cerebral vascular malformations were investigated in parallel; and 3) there was a high case number of the experiments per study group.

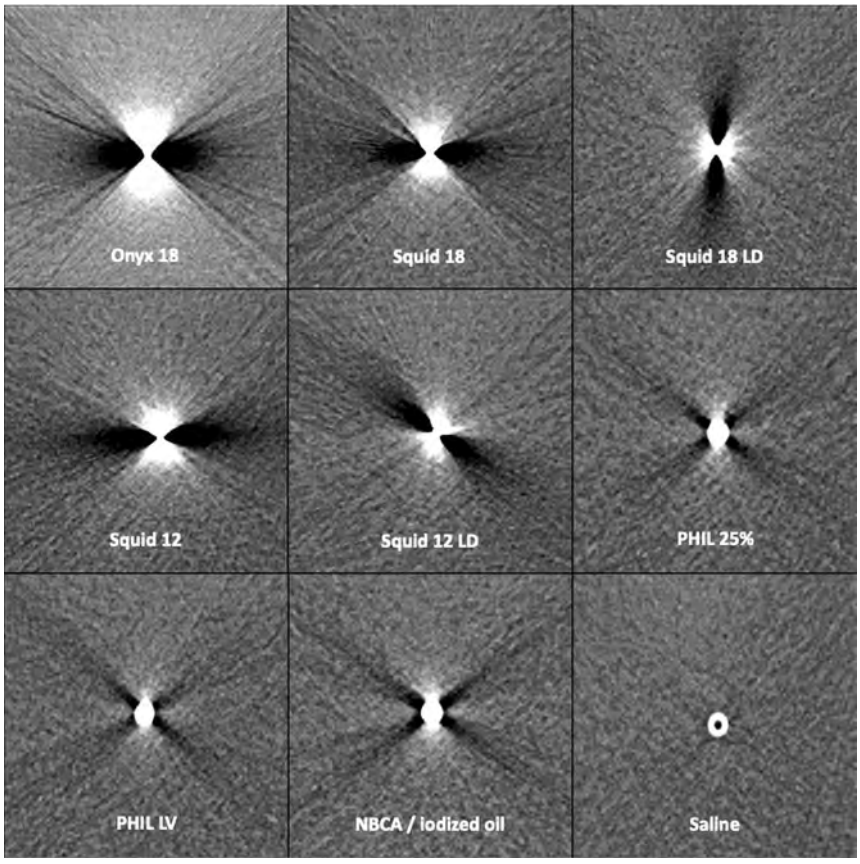

FIG 3. Representative CT images in the axial plane in a standard brain window with a width of 80 and a length of 40. Note the more severe artifacts for the EVOH-based LEAs (Onyx and Squid) and the relatively low degree of artifacts for LEAs that used iodine as a radiopaque component (PHIL and *n*-BCA/iodized oil).

In both aforementioned studies, the analysis was performed by setting a round or rectangular ROI in the direct vicinity of the filled tubes without taking all artifacts into account. Using a customized feature of the MITK software, which was specifically designed for the present study, allowed us to set a standardized donut-shaped ROI adjacent to and surrounding the center of each filled tube. This approach has the major advantage of considering all artifacts around the liquid embolic agent and at the same time not taking the filled tubes into account. Accordingly, this technique of quantitative analysis enabled a more precise evaluation as well as a more adequate comparability of the CT imaging artifacts of the different study groups. To ensure that the artifacts in all CT image slices were taken into account, we placed 5 ROIs according to the length of the cast of each tube for each of the different LEAs.

Furthermore, previous studies compared only the imaging artifacts of Onyx versus PHIL and Onyx versus Squid while performing a relatively low number of experiments per LEA. In the present study, a systematic assessment of 8 commonly used LEAs was performed with 10 experiments per study group. In addition, the imaging artifacts of the different LEAs were compared with saline-filled tubes serving as a control group, while in the 2 above-mentioned previous studies, no control groups were included.

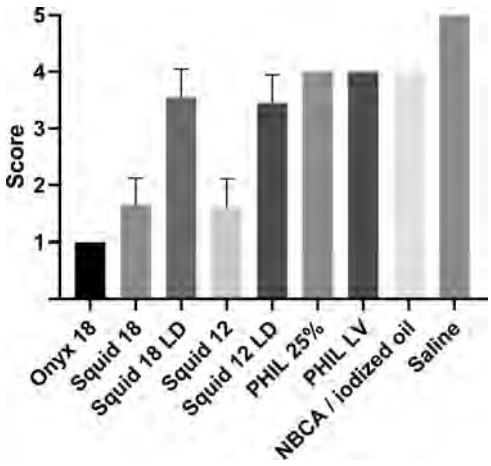

FIG 4. Illustration of the results of the qualitative image analysis using a 5-point scale. Different degrees of artifacts were observed among all study groups using the Dunn test for multiple comparisons with statistical hypothesis testing. *Bars* indicate mean; *whiskers*, SD. Five-point scale: 1) severe artifacts, 2) marked artifacts, 3) moderate artifacts, 4) minor artifacts, and 5) no artifacts.

The low degree of artifact production of PHIL compared with the EVOH-based LEAs Onyx and Squid can be explained by the chemical elements that cause radiopacity. The atomic number of the admixed radiopaque materials seems to have a major impact on the production of imaging artifacts predominantly caused by beam-hardening on conventional CT.[19] The higher atomic number of tantalum (atomic number 73) as part of Onyx and Squid leads to more artifacts compared with iodine (atomic number 53) as part of PHIL.

In the experimental study of Pop et al,[14] Onyx 18 produced more artifacts than Squid 18. In our study, there was also a tendency toward more artifacts for Onyx 18, however, without reaching statistical significance. As initially indicated, the LD variants of Squid mainly aim to improve the x-ray visibility of the embolized and nonembolized portions of vascular malformations during the embolization procedure. Comparing the normal-density variants and the LD variants of Squid, we observed a lower degree of imaging artifacts for the LD variants; however, the level of statistical significance was reached only for Squid 12 in the quantitative analysis ($P = .013$). Because the LD variants contain a 30% lower concentration of tantalum, the findings of our study suggest that this effect might be lower than expected and that the concentration of tantalum has only a moderate impact on artifacts in CT imaging.

The artifacts of cyanoacrylates have not been specifically investigated until now. Because *n*-BCA is not inherently visible, in clinical practice it is mixed with iodized oil for adequate visibility.[27] Accordingly, imaging artifacts of this LEA are caused by the iodized oil component and not by *n*-BCA. Iodized oil, which is composed of iodine combined with ethyl esters of fatty acids of poppyseed oil, affects not only the radiopacity of the mixture but also the embolization properties: the higher the concentration of iodized oil, the less viscous the embolic mixture. In our systematic investigation, *n*-BCA mixed with iodized oil produced less CT artifacts than the EVOH-based LEAs, but there were only statistical differences for Onyx 18 and the standard versions of Squid. In clinical practice, the concentration that was investigated in the present study (1:1) is relatively high and is predominantly used for high-flow shunts or for special techniques, such as the pressure cooker technique. For the effective embolization of larger vascular malformations, a lower viscosity of the LEA and therefore a higher concentration of iodized oil are usually needed.[12] For *n*-BCA/iodized mixtures with higher concentrations of iodized oil, higher levels of artifacts can be expected.

Table 3: Summary of the results of the post hoc Dunn test for the qualitative analysis

Liquid Embolic Agent	Onyx 18	Squid 18	Squid 18 LD	Squid 12	Squid 12 LD	PHIL 25%	PHIL LV	*n*-BCA/Iodized Oil
Saline	$P < .001$[a]	$P < .001$[a]	$P = .022$[a]	$P < .001$[a]	$P = .009$[a]	$P = .665$	$P = .665$	$P = .665$
n-BCA/iodized oil	$P < .001$[a]	$P = .004$[a]	$P > .999$	$P = .003$[a]	$P > .999$	$P > .999$	$P > .999$	
PHIL LV	NA	NA	NA	$P = .003$[a]	NA	$P > .999$		
PHIL 25%	$P < .001$[a]	$P = .004$[a]	NA	NA	NA			
Squid 12 LD	NA	NA	$P > .999$	$P = .311$				
Squid 12	NA	$P > .999$	NA					
Squid 18 LD	NA	$P = .201$						
Squid 18	$P > .999$							

Note:—NA indicates no *P* value available because the Dunn test was performed for only corresponding LEA variants.
[a] Statistical significance.

We acknowledge that this study has some limitations. In general, the transferability of an in vitro model to clinical practice is limited. While the tube model allowed a highly standardized analysis and comparison of artifacts, a more complex 3D model would have better resembled a human vascular malformation. Only 1 tube size and only 1 mixture of *n*-BCA/iodized oil were investigated, but different tube sizes and different concentrations of *n*-BCA/iodized oil may result in different findings. Furthermore, the tubes were not flushed continuously with saline during the injection of the LEAs, and this feature may have an influence on the results.

CONCLUSIONS

In investigating the most commonly used LEAs, marked differences in CT imaging artifacts could be demonstrated. The EVOH-based LEAs Onyx and Squid induced more artifacts compared with PHIL. *n*-BCA mixed with iodized oil induced only minor artifacts in conventional CT.

Disclosures: Niclas Schmitt—*OTHER RELATIONSHIPS*: Regarding our work, there was technical support by Balt and MicroVention. The authors had full control of the data and its analysis throughout the study. No outside interests have influenced our results. Daniel Paech—*UNRELATED*: *Grants/Grants Pending*: German Research Foundation grant*; *Travel/Accommodations/Meeting Expenses Unrelated to Activities Listed*: Siemens, *Comments*: travel support to CEST Workshop, Beijing 2018. Martin Bendszus—*UNRELATED*: *Board Membership*: Data and Safety Monitoring Board for Vascular Dynamics, Boehringer; *Consultancy*: Codman, Braun; *Grants/Grants Pending*: German Research Foundation, European Union, Hopp Foundation, Novartis, Siemens, Stryker, Medtronic, Guerbet*; *Payment for Lectures Including Service on Speakers Bureaus*: Novartis, Teva Pharmaceutical Industries, Codman, Guerbet, Merck, Grifols, Bayer AG, Leverkusen, Germany. Markus A. Möhlenbruch—*UNRELATED*: *Consultancy*: Medtronic, MicroVention, Stryker*; *Grants/Grants Pending*: Balt, MicroVention, Medtronic, Stryker*; *Payment for Lectures Including Service on Speakers Bureaus*: MicroVention, Medtronic, Stryker.* Dominik F. Vollherbst—*UNRELATED*: *Travel/Accommodations/Meeting Expenses Unrelated to Activities Listed*: MicroVention, Stryker, *Comments*: travel support*; *OTHER RELATIONSHIPS*: This study was technically supported by Balt and MicroVention (provision of the embolic agents). *Money paid to institution.

REFERENCES

1. Friedlander RM. **Clinical practice: arteriovenous malformations of the brain.** *N Engl J Med* 2007;356:2704–12 CrossRef Medline
2. van Rooij WJ, Sluzewski M, Beute GN. **Brain AVM embolization with Onyx.** *AJNR Am J Neuroradiol* 2007;28:172–77; discussion 178 Medline
3. Weber W, Kis B, Siekmann R, et al. **Endovascular treatment of intracranial arteriovenous malformations with Onyx: technical aspects.** *AJNR Am J Neuroradiol* 2007;28:371–77 Medline
4. Saatci I, Cekirge HS, Ciceri EF, et al. **CT and MR imaging findings and their implications in the follow-up of patients with intracranial aneurysms treated with endosaccular occlusion with Onyx.** *AJNR Am J Neuroradiol* 2003;24:567–78 Medline
5. Mason JR, Dodge C, Benndorf G. **Quantification of tantalum sedimentation rates in liquid embolic agents.** *Interv Neuroradiol* 2018;24:574–79 CrossRef Medline
6. Varadharajan S, Ramalingaiah AH, Saini J, et al. **Precipitating hydrophobic injectable liquid embolization of intracranial vascular shunts: initial experience and technical note.** *J Neurosurg* 2018;129:1217–22 CrossRef Medline
7. Vollherbst DF, Otto R, Hantz M, et al. **Investigation of a new version of the liquid embolic agent PHIL with extra-low-viscosity in an endovascular embolization model.** *AJNR Am J Neuroradiol* 2018;39:1696–1702 CrossRef Medline
8. Vollherbst DF, Sommer CM, Ulfert C, et al. **Liquid embolic agents for endovascular embolization: evaluation of an established (Onyx) and a novel (PHIL) embolic agent in an in vitro AVM model.** *AJNR Am J Neuroradiol* 2017;38:1377–82 CrossRef Medline
9. Vollherbst DF, Otto R, von Deimling A, et al. **Evaluation of a novel liquid embolic agent (precipitating hydrophobic injectable liquid (PHIL)) in an animal endovascular embolization model.** *J Neurointerv Surg* 2018;10:268–74 CrossRef Medline
10. Elsenousi A, Aletich VA, Alaraj A. **Neurological outcomes and cure rates of embolization of brain arteriovenous malformations with n-butyl cyanoacrylate or Onyx: a meta-analysis.** *J Neurointerv Surg* 2016;8:265–72 CrossRef Medline
11. Gross BA, Albuquerque FC, Moon K, et al. **Evolution of treatment and a detailed analysis of occlusion, recurrence, and clinical outcomes in an endovascular library of 260 dural arteriovenous fistulas.** *J Neurosurg* 2017;126:1884–93 CrossRef Medline
12. Chapot R, Stracke P, Velasco A, et al. **The pressure cooker technique for the treatment of brain AVMs.** *J Neuroradiol* 2014;41:87–91 CrossRef Medline
13. Vollherbst DF, Otto R, Do T, et al. **Imaging artifacts of Onyx and PHIL on conventional CT, cone-beam CT and MRI in an animal model.** *Interv Neuroradiol* 2018;24:693–701 CrossRef Medline
14. Pop R, Mertz L, Ilyes A, et al. **Beam hardening artifacts of liquid embolic agents: comparison between Squid and Onyx.** *J Neurointerv Surg* 2019;11:706–09 CrossRef Medline
15. Lv X, Wu Z, Li Y, et al. **Hemorrhage risk after partial endovascular n-BCA and Onyx embolization for brain arteriovenous malformation.** *Neurol Res* 2012;34:552–56 CrossRef Medline
16. Pereira GC, Traughber M, Muzic RF Jr. **The role of imaging in radiation therapy planning: past, present, and future.** *Biomed Res Int* 2014;2014:231090 CrossRef Medline
17. Shtraus N, Schifter D, Corn BW, et al. **Radiosurgical treatment planning of AVM following embolization with Onyx: possible dosage error in treatment planning can be averted.** *J Neurooncol* 2010;98:271–76 CrossRef Medline
18. Roberts DA, Balter JM, Chaudhary N, et al. **Dosimetric measurements of Onyx embolization material for stereotactic radiosurgery.** *Med Phys* 2012;39:6672–81 CrossRef Medline
19. Giantsoudi D, De Man B, Verburg J, et al. **Metal artifacts in computed tomography for radiation therapy planning: dosimetric effects and impact of metal artifact reduction.** *Phys Med Biol* 2017;62:R49–80 CrossRef Medline
20. Daubner D, Spieth S, Cerhova J, et al. **Measuring ventricular width on cranial computed tomography: feasibility of dose reduction in a custom-made adult phantom.** *Rofo* 2016;188:73–81 CrossRef Medline
21. Nolden M, Zelzer S, Seitel A, et al. **The Medical Imaging Interaction Toolkit: challenges and advances: 10 years of open-source development.** *Int J Comput Assist Radiology Surg* 2013;8:607–20 CrossRef Medline
22. Weiß J, Schabel C, Bongers M, et al. **Impact of iterative metal artifact reduction on diagnostic image quality in patients with dental hardware.** *Acta Radiol* 2017;58:279–85 CrossRef Medline
23. Cohen J. **A coefficient of agreement for nominal scales.** *Educ Psychol Meas* 1960;20:37–46 CrossRef
24. Altman DG. *Practical Statistics for Medical Research*. CRC Press; 1990
25. Gross BA, Du R. **Diagnosis and treatment of vascular malformations of the brain.** *Curr Treat Options Neurol* 2014;16:279 CrossRef Medline
26. Rammos S, Bortolotti C, Lanzino G. **Endovascular management of intracranial dural arteriovenous fistulae.** *Neurosurg Clin N Am* 2014;25:539–49 CrossRef Medline
27. Stoesslein F, Ditscherlein G, Romaniuk PA. **Experimental studies on new liquid embolization mixtures (histoacryl-lipiodol, histoacryl-panthopaque).** *Cardiovasc Intervent Radiol* 1982;5:264–67 CrossRef Medline

Intentional Stent Stenosis to Prevent Hyperperfusion Syndrome after Carotid Artery Stenting for Extremely High-Grade Stenosis

T. Mori, K. Yoshioka, Y. Tanno, and S. Kasakura

ABSTRACT

BACKGROUND AND PURPOSE: Intracranial hemorrhage due to hyperperfusion syndrome is a severe carotid artery stent placement complication of extremely high-grade stenosis, causing hemodynamic insufficiency. To prevent hyperperfusion syndrome, we attempted intentional residual stent stenosis and implemented "gentle" carotid artery stent placement, defined as carotid artery stent placement using a closed-cell stent coupled with slight balloon predilation, without balloon postdilation. Gradual stent expansion was expected. We investigated the incidence of hyperperfusion syndrome and long-term outcomes after gentle carotid artery stent placement.

MATERIALS AND METHODS: We included patients who underwent carotid artery stent placement for extremely high-grade stenosis from January 2015 to March 2019. We defined extremely high-grade stenosis as carotid stenosis with conventional angiographic "slow flow" and a reduced MCA signal intensity on MRA. A reduced MCA signal intensity was defined as MCA with a relative signal intensity of <0.9 in the ipsilateral compared with the contralateral MCA. We evaluated the stent diameter, CBF on SPECT, hyperperfusion syndrome, and intracranial hemorrhage. We defined hyperperfusion syndrome as a triad of ipsilateral headache, seizure, and hemiparesis.

RESULTS: Twenty-eight of the 191 patients met our inclusion criteria. After carotid artery stent placement, their median minimal stent diameter was 2.9 mm, which expanded to 3.9 mm at 4 months. Neither cerebral hyperperfusion syndrome nor intracranial hemorrhage occurred.

CONCLUSIONS: The gentle carotid artery stent placement strategy for intentional residual stent stenosis may prevent hyperperfusion syndrome in high-risk patients. Stents spontaneously dilated in 4 months.

ABBREVIATIONS: AI = asymmetric index; $AVDO_2$ = arteriovenous difference of oxygen; CAS = carotid artery stent placement; HI = hemodynamic insufficiency; ex-HS = extremely high-grade carotid artery stenosis; HPP = hyperperfusion phenomenon; HPS = hyperperfusion syndrome; ICH = intracerebral hemorrhage; MLD = minimal luminal diameter; OEF = oxygen extraction fraction; PSV = peak systolic velocity; rCBF = regional CBF; SI = signal intensity

Hyperperfusion syndrome (HPS) is a critical complication of carotid revascularization.[1-4] HPS occurs after revascularization of extremely high-grade carotid artery stenosis (ex-HS) causing cerebral hemodynamic insufficiency.[1,5] SPECT was used in Japan to assess hemodynamic insufficiency before carotid artery stent placement (CAS) in 127 (82.5%) of 154 institutions;[6] however, the risk of HPS was evaluated routinely by only 102 (15.5%) of 664 anesthesiologists in a US survey about carotid endarterectomy,[7] and SPECT was not included in the survey. Thus, a simple index to identify high-risk patients is required. Classic angiographic "slow flow" in the MCA[4] or reduced MCA signal intensity (SI) on MRA[8] is a feasible index in most facilities. We, therefore, defined an ex-HS with a carotid artery stenosis rate of > 80% or a minimal luminal diameter (MLD) of <1 mm, coupled with angiographic slow flow and reduced SI in the ipsilateral MCA, as hemodynamic insufficiency (HI) criteria.

The prevention of HPS has not been established,[9,10] though staged revascularization is a treatment option.[11,12] Therefore, we attempted to perform intentional residual stent stenosis to prevent marked hyperperfusion after CAS. To retain stent stenosis intentionally, we implemented "gentle" CAS, defined as CAS using a closed-cell stent coupled with slight balloon predilation, without poststenting balloon dilation. Compared with open-cell stents, the closed-cell stents may slowly self-expand and decrease embolic complications by avoiding dislodgement of the plaque

Received June 25, 2020; accepted after revision August 14.

From the Department of Stroke Treatment, Shonan Kamakura General Hospital, Kamakura, Japan.

Paper previously presented, in part, at: International Stroke Conference, February 6–8, 2019; Honolulu, Hawaii (ATP156).

Please address correspondence to Takahisa Mori, MD, PhD, Department of Stroke Treatment, Shonan Kamakura General Hospital, Okamoto 1370-1, Kamakura City, Kanagawa 247-8533, Japan; e-mail: morit-koc@umin.net

Indicates article with supplemental online tables.

Indicates article with supplemental online photos.

http://dx.doi.org/10.3174/ajnr.A6853

while the stent expands, because the radial force in closed-cell stents is weaker than that in open-cell stents.[13] Gradual and gentle self-expansion of the stent was the expected outcome.

We investigated the incidences of hyperperfusion phenomenon (HPP), HPS, and intracranial hemorrhage (ICH) and the long-term clinical and angiographic outcomes after gentle CAS for ex-HS identified by the HI criteria.[8] Furthermore, we evaluated the validity of the HI criteria.

MATERIALS AND METHODS

For this retrospective observational cohort study, we included patients who underwent elective gentle CAS for ex-HS from January 2015 to March 2019 and MRA and DWI before and after CAS. We measured the carotid artery stenosis rate according to the NASCET criteria.[14] We defined elective CAS as scheduled CAS in asymptomatic patients or in those who had experienced their latest ischemic attack ≥30 days prior. We excluded patients under the following circumstances: 1) They underwent CAS within 29 days of the last ischemic attack, 2) had an ipsilateral CAS history, 3) had a contraindication to MR imaging, 4) experienced unsuccessful introduction of a stent, 5) underwent CAS for lesions without ex-HS, or 6) underwent CAS with an open-cell stent for ex-HS.

Evaluation

We evaluated the patients' baseline characteristics; the relative SI of the M1 segment on MRA; carotid lesions with high signal in T1-weighted black-blood MR imaging;[15] the MLD before CAS; the carotid artery stenosis rate (NASCET method) before and after CAS;[14] the minimal stent diameter immediately after and at 4 months after CAS; additional balloon angioplasty for severe stenosis at 4 months; HPP, ICH, and HPS after CAS; number of patients with new ischemic lesions and the number of lesions as observed on DWI after CAS; any symptomatic stroke or myocardial infarction within 30 days after CAS; and any symptomatic stroke within 4 months after CAS. To estimate the HI degree, we accessed the ultrasonographic peak systolic velocity (PSV), SPECT,[16] blood-sampling arteriovenous differences of oxygen ($AVDO_2$), and the oxygen extraction fraction (OEF) before and after CAS.[17,18] Furthermore, we investigated the minimal stent diameter immediately after additional balloon angioplasty in patients who underwent additional balloon angioplasty at 4 months.

Slow Flow in the MCA

Evidence of slow flow in the MCA was defined as external carotid circulation delineation earlier than that of the corresponding internal carotid circulation.[4]

Reduced MCA Signal Intensity

We measured the SI on the bilateral MCA M1 segments on MRA and defined MCA relative SI as follows: (SI on the Affected-Side M1) / (SI on the Contralateral M1).

We defined the reduced MCA SI as an MCA relative SI of < 0.9.

MRA and DWI

We performed MRA and DWI using a 3T MR imaging machine equipped with an 8-channel sensitivity encoding head coil. 3D TOF-MRA was performed using a 3D fast-field echo sequence. The DWI protocol was echo-planar imaging. The parameters are summarized in Online Table 1. The baseline MRA and DWI values were obtained the day before CAS. A second MRA and DWI were performed between 24 and 48 hours after CAS, and only new lesions, with reference to the baseline DWI, were regarded as new ischemic lesions due to CAS.

Gentle CAS for Intentional Residual Stent Stenosis

Patients provided written informed consent to undergo CAS. We performed CAS through transbrachial catheterization with the patient under local anesthesia. A 6F (0.088-inch internal diameter) guiding sheath, 90-cm long, designed for transbrachial access, was positioned in the affected common carotid artery proximal to the stenosis.[19] All patients received 5000 U of heparin intravenously immediately after the 6F guiding sheath was introduced into the brachial artery. A 5F temporary bipolar pacing (J-Tip) catheter was positioned in the right ventricle through the femoral vein to prevent bradycardia or cardiac arrest during CAS. We coaxially introduced a 0.010-inch flexible microguidewire and a microcatheter through the ex-HS. We replaced the flexible microguidewire with a 0.014-inch hard guidewire and replaced the microcatheter coaxially with a filter as the embolic distal protection device. We performed balloon predilation with a semicompliant balloon catheter and subsequently deployed a closed-cell stent over the residual stenosis. We did not perform poststenting balloon dilation of the residual stent stenosis (Online Table 2).

For balloon predilation, we used 3.0- and 4.0-mm-diameter balloon catheters for lesions with and without hyperintensity on T1-weighted black-blood MR imaging, respectively.[15,20] Lesions with hyperintensity on T1 black-blood MR imaging have been reported to be vulnerable,[15,] and we used a 3.0-mm balloon for these lesions to facilitate a gentler procedure. We inflated the balloons at 8 atm of nominal pressure and did not inflate balloons to diameters greater than the nominal.

Conventional Angiographic Investigation after CAS and Repeat Treatment of Significant Stenosis

We expected the stent to self-expand during a few months, as reported previously.[21] Some stents, however, can fail to expand and in-stent restenosis may occur; therefore, we performed conventional angiography at 4 months (within the range of 3–6 months after CAS) to accurately assess the in-stent carotid artery stenosis rate and measure the stent diameter, as reported in previous studies,[22,23] in addition to ultrasonographic investigation. We defined an in-stent stenosis rate of >70% as significant stenosis. When the MLD was significantly stenotic at 4 months, we performed additional balloon angioplasty of the in-stent stenosis with a semicompliant 5.0-mm-diameter balloon and inflated it at 14 atm of the rated burst pressure. The diameter of the balloon was increased to 5.17 mm. We obtained fluoroscopic images of the stent using digital angiography and measured the minimal stent diameter on the lateral-view image immediately after CAS and after 4 months. When additional balloon angioplasty

was performed at 4 months, the minimal stent diameter was measured after the procedure.

$AVDO_2$ and OEF

Before positioning a temporary pacing catheter, we introduced a 4F catheter into the dominant-sided jugular bulb via transfemoral venous access.[17] We measured the arterial oxygen content ($CtaO_2$) and the venous oxygen content ($CtvO_2$) with a blood gas analyzer.[17,18] The $AVDO_2$ was calculated as follows: $AVDO_2 = CtaO_2–CtvO_2$. The OEF was calculated as follows: $OEF = (CtaO2–CtvO_2) / CtaO_2$.

SPECT

We performed SPECT and measured the CBF at 1 week before and 3 or 4 hours after CAS. We measured the CBF with iodine 123 *N*-isopropyl-p-iodoamphetamine (^{123}I-IMP) combined with a graph plot method. A dose of 185 MBq of ^{123}I-IMP was infused rapidly into the right cubital vein. ROIs were automatically set with the CBF analyzing software (NeuroFlexor; Aggero MedTech).

The asymmetric index percentage (AI%) was defined as follows: (CBF in the Affected MCA Territory/CBF in the Contralateral MCA Territory) × 100 (%).

The regional CBF percentage (rCBF%) was defined as follows: (CBF in the Affected MCA Territory/CBF in the Ipsilateral Cerebellum) × 100 (%).

HPP

We assessed the HPP according to 4 SPECT definitions: 1) AI% before and after CAS, <100% and >100%, respectively; [24] 2) AI% before and after CAS, <100% and >120%, respectively;[10] 3) rCBF% after CAS–rCBF% before CAS, >10%;[16] and 4) rCBF% increase, defined as follows: [(rCBF% after CAS–rCBF% before CAS)/rCBF% before CAS] × 100, > 100% (doubling).[4]

HPS

In 1981, HPS was defined as a clinical triad of ipsilateral headache, seizures, and neurologic deficits in the absence of cerebral ischemia after a successful carotid endarterectomy.[3]

Management before and after CAS

Patients began receiving dual-antiplatelet therapy, comprising clopidogrel (75 mg/day) and pletal (Cilostazol) (100 mg/day) administration[25,26] for at least 7 days before CAS, and they continued to receive this therapy for 3–6 months of angiographic investigation. On the day before CAS, the patients received the following sedative drugs via the oral route: 2.5 g of TSUMURA Yokukansan (TJ-54; Kampo, a Japanese herbal medicine), 3 times a day,[27] and 2.0 g of etizolam, twice a day. TJ-54 and etizolam were administered until 7 and 2 days after CAS, respectively. When blood pressure was elevated after CAS, antihypertensive drugs were administered until 7 days after CAS to reduce the systolic and diastolic blood pressures to below 150 and 90 mm Hg, respectively.

Ethics Approval

All procedures performed in the study were in accordance with the ethical standards of the institution at which the study was performed and the 1964 Declaration of Helsinki. The relevant ethics committee approved our retrospective analysis (TGE01011-024). Written informed consent for participation and publication was not required. The study was based on an opt-out model of enrollment, which was permitted by the ethics committee.

Statistical Analysis

Non-normally distributed continuous variables are expressed as medians and interquartile ranges. For nonparametric data, the Wilcoxon signed rank test was used to compare paired variables. A P value $< .05$ was considered statistically significant. We used the JMP software (Version 15.1; SAS Institute) for all statistical analyses.

RESULTS

Twenty-eight (14.7%) of the 191 patients who were scheduled to undergo CAS during the study period met our inclusion criteria (Online Fig 1). Their age (median, interquartile range) was 78 years (72–81 years). Twenty-five patients (89%) were men, 16 (57%) were symptomatic, and vascular risk factors were controlled (Online Table 3). They did not have a contralateral ex-HS or occlusion of the carotid artery.

Nine patients (32.1%) with hyperintensity on T1-weighted black-blood MR imaging underwent balloon predilation with a semicompliant 3.0-mm balloon catheter. The median NASCET% decreased after CAS ($P < .001$). The median MLD values before and after CAS were 0.63 and 2.9 mm, respectively ($P < .001$). Gentle CAS successfully provided intentional residual stent stenosis (Fig 1). The MCA relative SI increased after CAS ($P < .001$), and the PSV decreased after CAS ($P < .001$). The AI% and rCBF% increased after CAS ($P < .001$). The $AVDO_2$ decreased ($P = .02$), and the OEF remained unchanged after CAS (Table). The HI criteria successfully identified patients with HI.

Blood pressure after CAS was controlled (Table). The incidence of HPP was dependent on the definition. HPP occurred in 11 patients according to definition 1, in 1 patient according to definition 2, and in 8 patients according to definition 3 (Figs 1 and 2). HPP did not occur according to definition 4, and CBF was not doubled. The patient with HPP of definition 2 was included in those of definitions 1 and 3. In patients with HPP, the stents were stenotic after CAS. AI% and rCBF% slightly increased after CAS, and $AVDO_2$ and OEF reciprocally decreased (Online Table 4).

Neither HPS nor ICH occurred, and no patient experienced symptomatic cerebral infarction immediately after CAS. Neither stroke nor myocardial infarction occurred within 30 days, though 1 patient died due to heart failure 26 days after CAS.

Twenty-five (92.6%) of 27 surviving patients underwent conventional angiography at 4 months. The stent spontaneously and sufficiently expanded, and the median minimal stent diameter increased from 2.9 to 3.9 mm at 4 months ($P < .001$) (Online Fig 2). Three patients (3/25; 12.0%) had severe in-stent stenosis and underwent additional balloon angioplasty with the 5.0-mm balloon at 14 atm. Their stents were sufficiently dilated from 3.2- to 4.4-mm median minimal stent diameter. No HPS or ICH occurred after additional balloon angioplasty. One of 2 patients who withdrew from angiographic investigation underwent ultrasonography at 4 months, which revealed a PSV of 52.7 cm/s, no

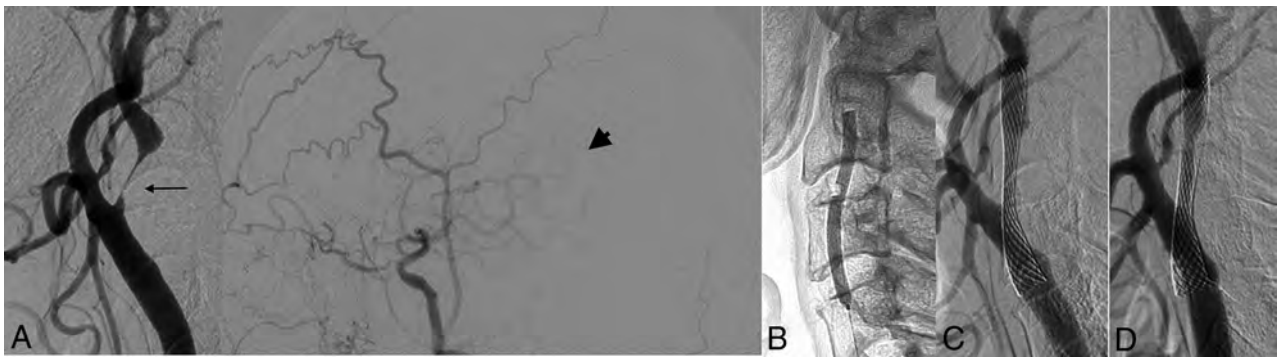

FIG 1. Angiograms before and during gentle CAS and at 4 months. *A*, Angiograms before CAS reveal extremely high-grade stenosis (*arrow*) and a "reduced MCA perfusion territory" in the middle cerebral artery (*arrowhead*). *B*, An inflated balloon with a 3.0-mm diameter. *C*, Angiography after CAS shows a residual stent stenosis. *D*, Angiography at 4 months shows self-expansion of the stent.

Changes in luminal diameters and hemodynamic factors before and after CAS

CAS Procedure Strategy (n = 28)	Gentle CAS: Intentional Residual Stent Stenosis	
	Before	After
NASCET (%) (median) (IQR)	81.8 (77.9–89.1)	39.5 (29.6–51.1)[a]
MLD before and MSD after CAS (median) (IQR) (mm)	0.63 (0.4–0.94)	2.9 (2.6–3.7)[a]
MCA relative SI (median) (IQR)	0.73 (0.57–0.85)	1.01 (0.9–1.06)[a]
PSV (median) (IQR) (cm/s)	316 (198.8–389.9)	91.9 (70.7–144)[a]
AI% (median) (IQR)	96.9 (92.3–100.0)	100.8 (93.6–103.9)[b]
rCBF% (median) (IQR)	88.9 (83.7–94.8)	94.6 (91.4–100.6)[b]
$AVDO_2$ (median) (IQR) (O_2 mL/mL)	6.9 (6.0–7.8)	6.3 (5.1–6.8)[c]
OEF (median) (IQR)	0.41 (0.37–0.46)	0.41 (0.35–0.43)
SBP (median) (IQR) (mm Hg)	153.5 (142.5–167.5)	132.5 (115.8–140.8[a]
DBP (median) (IQR) (mm Hg)	77.5 (70–87.8)	67 (62–71.8)[a]
Average BP (median) (IQR) (mm Hg)	104.9 (94.7–110.9)	88.7 (82.8–90.8)[a]

Note:—IQR indicates interquartile range; DBP, diastolic blood pressure; MSD, minimal stent diameter; SBP, systolic blood pressure.
[a] $P < .0001$ between paired groups.
[b] $P < .01$.
[c] $P < .05$.

stenosis, and no turbulent flow inside the stent. No strokes occurred in the 27 patients within 4 months after CAS.

DISCUSSION

Our results suggested that the HI criteria were effective as a simple, valid tool to identify high-risk patients and that the gentle CAS strategy successfully provided intentional stent stenosis and prevented HPS and ICH in high-risk patients with ex-HS. Stents spontaneously dilated at 4 months, and 12.0% of them achieved sufficient dilation without HPS or ICH after long-term additional balloon angioplasty.

Ex-HS, defined by the HI criteria, identified high-risk patients with HI. High-risk patients can be identified without SPECT or OEF when the HI criteria are used hereafter. The AI% and rCBF% of these patients slightly increased, and the $AVDO_2$ decreased reciprocally after CAS. HPP was dependent on the definition and occurred in 0–11 patients after CAS. In 8 patients with HPP of definition 3, rCBF% slightly increased from 80.2% to 94.9%. This rCBF% increase is similar to that of a previous report in which the average AI% increased from 70.3% to 87.6% in 9 patients after stage 1 angioplasty, before stage 2 stent placement.[12] A previous study reported that inadequate dilation or extensive dissection occurred in 4 of 44 patients after stage 1 angioplasty. The 4 patients underwent regular CAS immediately, and HPP occurred in all of them.[28] Inadequate dilation or extensive dissection, however, was not considered in our patients because they underwent CAS immediately after slight balloon predilation. Residual stent stenosis might contribute to the prevention of a marked increase in CBF and the maintenance of cerebral autoregulation. The stent stenosis resulted in a slight increase in CBF and a reciprocal decrease in $AVDO_2$ and OEF immediately after CAS. Therefore, neither HPS nor ICH occurred after CAS.

Strict control of postoperative blood pressure is defined as the maintenance of blood pressure at least below the preoperative value immediately after surgical procedures;[9] thus, blood pressure in the present study was strictly controlled. Strict control of postoperative blood pressure prevents ICH after carotid endarterectomy (CEA); however, it is unsuccessful in preventing ICH after CAS.[9] Residual stent stenosis successfully prevented ICH after CAS in the present high-risk patients.

Previous studies have been reported on CAS without post-CAS balloon dilation[29] and CAS without any balloon dilation.[30] Primary CAS without any balloon dilation was performed with 2 types of open-cell stents. Transient ischemic attacks occurred in 4.3% of patients within 24 hours; 1 patient died at 11 days due to stent thrombosis.[30] In our series, no transient ischemic attacks

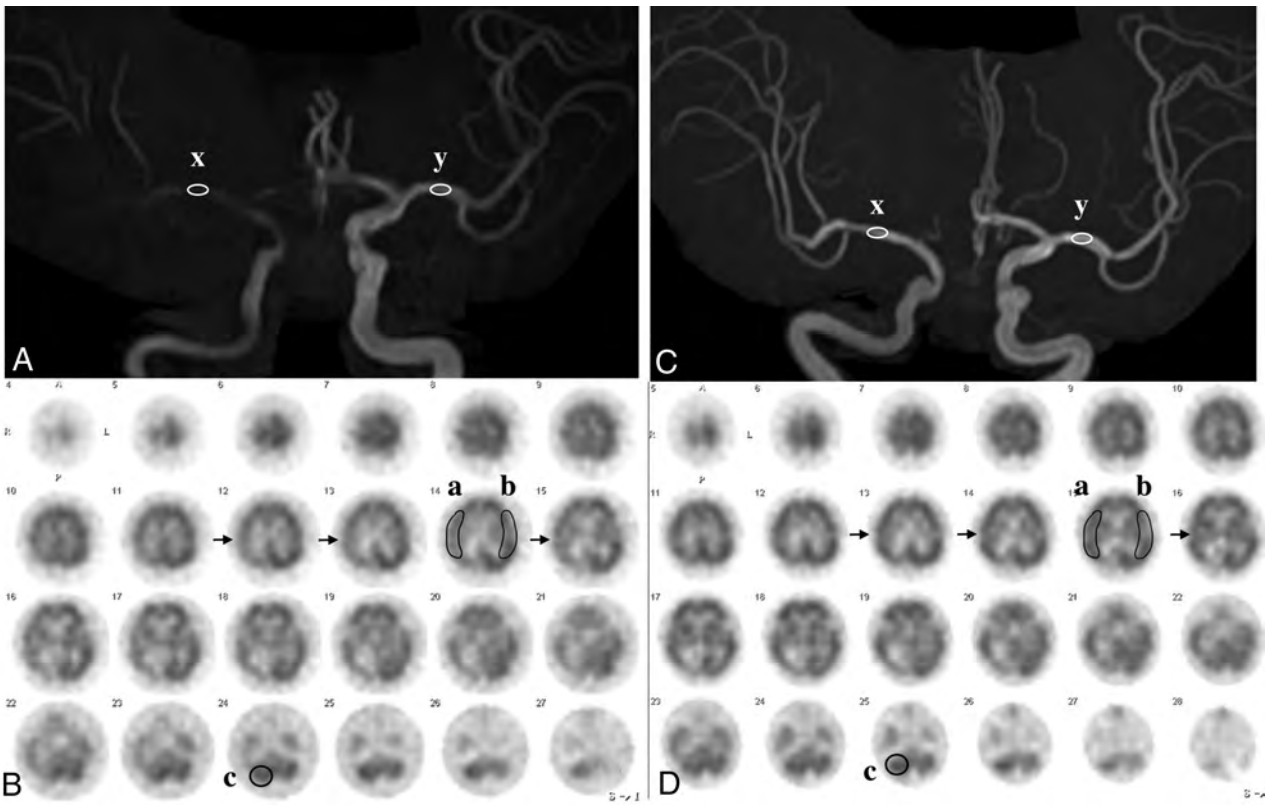

FIG 2. MRA and SPECT in the same case as in Fig 1. *A*, MRA before CAS reveals an MCA rSI value of 0.44: [(x: 784) divided by (y: 1775)]. *B*, SPECT before CAS demonstrates a CBF decrease in the right MCA territory (*arrows*). AI was 80.3%% [(a: 31.94) divided by (b: 39.78)], and rCBF% was 83.9% [(a: 31.94) divided by (c: 38.07)]. *C*, MRA after CAS reveals an MCA rSI of 1.16: [(x: 2967) divided by (y: 2667)]. *D*, SPECT after CAS demonstrates a CBF increase in the right MCA territory (*arrows*). AI% was 92.7% [(a: 37.95) divided by (b: 40.93)] and rCBF% was 99.9% [(a: 37.95) divided by (c: 37.99)]. rSI indicates relative signal intensity.

occurred within 24 hours, and no stent thrombosis occurred within 30 days. These results may be associated with the closed-cell stent and slight balloon predilation in our series. Primary CAS may be a treatment option for ex-HS when a closed-cell stent is selected, though high restenosis (12.8%) and repeat angioplasty (14.8%) rates have been reported.[21,30] In our series, 12.0% of patients underwent long-term staged balloon angiography.

Gentle CAS for intentional residual stent stenosis can be performed in 1 session because its strategy is simpler and more feasible than staged angioplasty, which requires invasive procedures in 2 sessions.[12,28] Staged angioplasty has been attempted in only 27.1% of Japanese institutions.[6] Gentle CAS could become the first-line treatment for high-risk patients with ex-HS when combined with long-term staged angioplasty.

Limitations

Our study had several limitations. A small number of patients were included, and the study was a retrospective and observational cohort study without a control group. Standardization of how to evaluate the MRA relative SI is required. The sensitivity and specificity of the HI criteria have not been assessed. We used the same types of balloon catheters, filter devices, and the same closed-cell stents in all 28 patients. Our results cannot be generalized to other types of balloon catheters, filter devices, or closed-cell stents. Therefore, an appropriate balloon catheter and balloon size for predilation and an appropriate stent must be determined.

A prospective study with a large sample size is required to assess intentional residual stent stenosis of high-risk ex-HS.

CONCLUSIONS

The gentle CAS strategy of intentionally leaving a stent stenosis was feasible and prevented HPS in high-risk patients with ex-HS. Stents spontaneously dilated within 4 months, and 12.0% of patients achieved sufficient dilation without HPS or ICH after long-term staged balloon angioplasty. Intentional residual stent stenosis could become the first-line treatment for high-risk ex-HS.

Disclosures: Takahisa Mori—*UNRELATED*: *Board Membership*: one of the Editorial Board members of the *American Journal of Neuroradiology*; *Royalties*: Medikit, *Comments*: less than US $2500/year.

REFERENCES

1. Mori T, Fukuoka M, Kazita K, et al. **Intraventricular hemorrhage after carotid stenting.** *J Endovasc Surg* 1999;6:337–41 CrossRef Medline
2. Abou-Chebl A, Yadav JS, Reginelli JP, et al. **Intracranial hemorrhage and hyperperfusion syndrome following carotid artery stenting: risk factors, prevention, and treatment.** *J Am Coll Cardiol* 2004;43:1596–601 CrossRef Medline
3. Sundt TM Jr, Sharbrough FW, Piepgras DG, et al. **Correlation of cerebral blood flow and electroencephalographic changes during carotid endarterectomy: with results of surgery and hemodynamics of cerebral ischemia.** *Mayo Clin Proc* 1981;56:533–43 Medline

4. Piepgras DG, Morgan MK, Sundt TM Jr, et al. **Intracerebral hemorrhage after carotid endarterectomy.** *J Neurosurg* 1988;68:532–36 CrossRef Medline
5. Nomura JI, Uwano I, Sasaki M, et al. **Preoperative cerebral oxygen extraction fraction imaging generated from 7T MR quantitative susceptibility mapping predicts development of cerebral hyperperfusion following carotid endarterectomy.** *AJNR Am J Neuroradiol* 2017;38:2327–33 CrossRef Medline
6. Hayakawa M, Matsumaru Y, Sakai N, et al; for the STrategy of Optimal carotid revascularization for high-risk Patients of Cerebral Hyperperfusion Syndrome (STOP CHS) study group. **Periprocedural evaluation and management against cerebral hyperperfusion syndrome after carotid artery stenting in Japan: a nationwide questionnaire survey.** *Journal of Neuroendovascular Therapy* 2017;11:341–50 CrossRef
7. Greene NH, Minhaj MM, Zaky AF, et al. **Perioperative management of carotid endarterectomy: a survey of clinicians' backgrounds and practices.** *J Cardiothorac Vasc Anesth* 2014;28:990–93 CrossRef Medline
8. Kuroda H, Ogasawara K, Hirooka R, et al. **Prediction of cerebral hyperperfusion after carotid endarterectomy using middle cerebral artery signal intensity in preoperative single-slab 3-dimensional time-of-flight magnetic resonance angiography.** *Neurosurgery* 2009;64:1065–71; discussion 1071–72 CrossRef Medline
9. Ogasawara K, Sakai N, Kuroiwa T, et al; Japanese Society for Treatment at Neck in Cerebrovascular Disease Study Group. **Intracranial hemorrhage associated with cerebral hyperperfusion syndrome following carotid endarterectomy and carotid artery stenting: retrospective review of 4494 patients.** *J Neurosurg* 2007;107:1130–36 CrossRef Medline
10. Niimi J, Tasaka K, Nemoto F, et al. **A patient with stenosis of the cervical internal carotid artery in whom hyperperfusion syndrome occurred after staged angioplasty.** *Journal of Neuroendovascular Therapy* 2017;11:634–39 CrossRef
11. Yoshimoto T, Shirasaka T, Yoshidumi T, et al. **Stepwise revascularization for prevention of postoperative hyperperfusion.** *Neurol Med Chir (Tokyo)* 2006;46:283–87; discussion 288–89 CrossRef Medline
12. Yoshimura S, Kitajima H, Enomoto Y, et al. **Staged angioplasty for carotid artery stenosis to prevent postoperative hyperperfusion.** *Neurosurgery* 2009;64:ons122–28; discussion ons128–29 CrossRef Medline
13. Voûte MT, Hendriks JM, van Laanen JH, et al. **Radial force measurements in carotid stents: influence of stent design and length of the lesion.** *J Vasc Interv Radiol* 2011;22:661–66 CrossRef Medline
14. Barnett HJ, Taylor DW, Eliasziw M, et al. **Benefit of carotid endarterectomy in patients with symptomatic moderate or severe stenosis: North American Symptomatic Carotid Endarterectomy Trial Collaborators.** *N Engl J Med* 1998;339:1415–25 CrossRef Medline
15. Kurosaki Y, Yoshida K, Fukumitsu R, et al. **Carotid artery plaque assessment using quantitative expansive remodeling evaluation and MRI plaque signal intensity.** *J Neursurg* 2016;124:736–42 CrossRef Medline
16. Iwata T, Mori T, Tajiri H, et al. **Predictors of hyperperfusion syndrome before and immediately after carotid artery stenting in single-photon emission computed tomography and transcranial color-coded real-time sonography studies.** *Neurosurgery* 2011;68:649–55 CrossRef Medline
17. Iwata T, Mori T, Miyazaki Y, et al. **Global oxygen extraction fraction by blood sampling to anticipate cerebral hyperperfusion phenomenon after carotid artery stenting.** *Neurosurgery* 2014;75:546–51 CrossRef Medline
18. Iwata T, Mori T, Tanno Y, et al. **Measurement of oxygen extraction fraction by blood sampling to estimate severe cerebral hemodynamic failure and anticipate cerebral hyperperfusion syndrome following carotid artery stenting.** *J Neurointerv Surg* 2018;10:1063–66 CrossRef Medline
19. Iwata T, Mori T, Miyazaki Y, et al. **Initial experience of a novel sheath guide for transbrachial carotid artery stenting: technical note.** *J Neurointerv Surg* 2013;5(Suppl 1):i77–80 CrossRef Medline
20. Yoshimura S, Yamada K, Kawasaki M, et al. **High-intensity signal on time-of-flight magnetic resonance angiography indicates carotid plaques at high risk for cerebral embolism during stenting.** *Stroke* 2011;42:3132–37 CrossRef Medline
21. Bussière M, Pelz DM, Kalapos P, et al. **Results using a self-expanding stent alone in the treatment of severe symptomatic carotid bifurcation stenosis.** *J Neurosurg* 2008;109:454–60 CrossRef Medline
22. Kimura T, Yokoi H, Nakagawa Y, et al. **Three-year follow-up after implantation of metallic coronary-artery stents.** *N Engl J Med* 1996;334:561–66 CrossRef Medline
23. Mori T, Kazita K, Chokyu K, et al. **Short-term arteriographic and clinical outcome after cerebral angioplasty and stenting for intracranial vertebrobasilar and carotid atherosclerotic occlusive disease.** *AJNR Am J Neuroradiol* 2000;21:249–54 Medline
24. Kaku Y, Yoshimura S, Kokuzawa J. **Factors predictive of cerebral hyperperfusion after carotid angioplasty and stent placement.** *AJNR Am J Neuroradiol* 2004;25:1403–08 Medline
25. Takigawa T, Matsumaru Y, Hayakawa M, et al. **Cilostazol reduces restenosis after carotid artery stenting.** *J Vasc Surg* 2010;51:51–56 CrossRef Medline
26. Miyazaki Y, Mori T, Iwata T, et al. **Continuous daily use of Cilostazol prevents in-stent restenosis following carotid artery stenting: serial angiographic investigation of 229 lesions.** *J Neurointerv Surg* 2016;8:471–75 CrossRef Medline
27. Nakazaki M, Mori T, Iwata T, et al. **Retrospective analysis of the effectiveness of yokukansan (Japanese herbal medicine (TJ-54) in the treatment of delirium following acute stroke** [in Japanese]. *No Shinkei Geka* 2013;41:765–71 Medline
28. Uchida K, Yoshimura S, Shirakawa M, et al. **Experience of staged angioplasty to avoid hyperperfusion syndrome for carotid artery stenosis.** *Neurol Med Chir (Tokyo)* 2015;55:824–29 CrossRef Medline
29. Ogata A, Sonobe M, Kato N, et al. **Carotid artery stenting without post-stenting balloon dilatation.** *J Neurointerv Surg* 2014;6:517–20 CrossRef Medline
30. Baldi S, Zander T, Rabellino M, et al. **Carotid artery stenting without angioplasty and cerebral protection: a single-center experience with up to 7 years' follow-up.** *AJNR Am J Neuroradiol* 2011;32:759–63 CrossRef Medline

COVID-19 Stroke Apical Lung Examination Study: A Diagnostic and Prognostic Imaging Biomarker in Suspected Acute Stroke

J. Siddiqui, F. Bala, S. Sciacca, A.M. Falzon, M. Benger, S.A. Matloob, F.N.A.C. Miller, R.J. Simister, I. Chatterjee, L.K. Sztriha, I. Davagnanam, and T.C. Booth

ABSTRACT

BACKGROUND AND PURPOSE: Diagnosis of coronavirus disease 2019 (COVID-19) relies on clinical features and reverse-transcriptase polymerase chain reaction testing, but the sensitivity is limited. Carotid CTA is a routine acute stroke investigation and includes the lung apices. We evaluated CTA as a potential COVID-19 diagnostic imaging biomarker.

MATERIALS AND METHODS: This was a multicenter, retrospective study ($n = 225$) including CTAs of patients with suspected acute stroke from 3 hyperacute stroke units (March-April 2020). We evaluated the reliability and accuracy of candidate diagnostic imaging biomarkers. Demographics, clinical features, and risk factors for COVID-19 and stroke were analyzed using univariate and multivariate statistics.

RESULTS: Apical ground-glass opacification was present in 22.2% (50/225) of patients. Ground-glass opacification had high interrater reliability (Fleiss $\kappa = 0.81$; 95% CI, 0.68–0.95) and, compared with reverse-transcriptase polymerase chain reaction, had good diagnostic performance (sensitivity, 75% [95% CI, 56–87]; specificity, 81% [95% CI, 71–88]; OR = 11.65 [95% CI, 4.14–32.78]; $P < .001$) on multivariate analysis. In contrast, all other contemporaneous demographic, clinical, and imaging features available at CTA were not diagnostic for COVID-19. The presence of apical ground-glass opacification was an independent predictor of increased 30-day mortality (18.0% versus 5.7%, $P = .017$; hazard ratio = 3.51; 95% CI, 1.42–8.66; $P = .006$).

CONCLUSIONS: We identified a simple, reliable, and accurate COVID-19 diagnostic and prognostic imaging biomarker obtained from CTA lung apices: the presence or absence of ground-glass opacification. Our findings have important implications in the management of patients presenting with suspected stroke through early identification of COVID-19 and the subsequent limitation of disease transmission.

ABBREVIATIONS: BSTI = British Society of Thoracic Imaging; COVID-19 = coronavirus disease 2019; GGO = ground-glass opacification; IRR = interrater reliability; RT-PCR = reverse-transcriptase polymerase chain reaction; SARS-CoV-2 = Severe Acute Respiratory Syndrome coronavirus 2

The Severe Acute Respiratory Syndrome coronavirus 2 (SARS-CoV-2) was given pandemic status by the World Health Organization in March 2020.[1,2] When symptomatic, coronavirus disease 2019 (COVID-19) typically causes mild, self-limiting respiratory features. However, a severe lower respiratory and multisystem disease may occur, necessitating hospitalization.[3] Approximately 6.0% of patients with COVID-19 die, and 12% require intensive care support.[4-7]

Symptoms alone are insufficient for a diagnosis due to a high prevalence of asymptomatic carriers and a variable presymptomatic incubation period (2–14 days).[8,9] The diagnostic reference standard is the reverse-transcriptase polymerase chain reaction

Received July 1, 2020; accepted after revision August 17.

From the Departments of Neuroradiology (J.S., F.B., T.C.B.), Neurology (M.B., L.K.S.), and Radiology (F.N.A.C.M.), King's College Hospital, National Health Service Foundation Trust, London, UK; Lysholm Department of Neuroradiology (S.S., A.M.F., I.D.) and Department of Neurosurgery (S.A.M.), National Hospital for Neurology and Neurosurgery, University College London Hospitals, National Health Service Foundation Trust, London, UK; Comprehensive Stroke Service (R.J.S., I.C.), University College London Hospitals, National Health Service Foundation Trust, London, UK; Stroke Research Centre (R.J.S.), and Brain Repair and Rehabilitation Unit (I.D.), University College London Queen Square Institute of Neurology, London, UK; and School of Biomedical Engineering and Imaging Sciences (T.C.B.), King's College London, Rayne Institute, St. Thomas' Hospital, London, UK.

J. Siddiqui and F. Bala are joint first authors and have contributed equally to this work.

This work was supported by the Wellcome/Engineering and Physical Sciences Research Council Center for Medical Engineering (WT 203148/Z/16/Z).

Please address correspondence to Thomas C. Booth, PhD, School of Biomedical Engineering and Imaging Sciences, King's College London, Rayne Institute, 4th Floor, Lambeth Wing, St. Thomas' Hospital, London SE1 7EH, UK; e-mail: thomas.booth@kcl.ac.uk; @ThomasCBooth

Indicates open access to non-subscribers at www.ajnr.org
Indicates article with supplemental on-line appendix and table.
Indicates article with supplemental on-line photo.
http://dx.doi.org/10.3174/ajnr.A6832

(RT-PCR) test using nasopharyngeal swabs or bronchial secretions, but it is constrained by a sensitivity of 60%–73%[1-12] and a timescale of hours to yield results, with no point-of-care test widely available. A dedicated chest CT is likely to be more sensitive than RT-PCR for COVID-19, which, according to 1 study of 1014 patients, has a sensitivity of 88% compared with 59%.[11] However, patients with suspected stroke are not always suspected of having COVID-19. Furthermore, in many health care systems, including in the United States and the United Kingdom, the routine use of chest CT for COVID-19 diagnosis is not feasible or recommended in patients suspected of having COVID-19.[13,14]

The classic COVID-19 appearance on chest CT is ground-glass opacification (GGO), with a predilection for the lower lobes and posterior segments.[15-18] While lung apices are included on carotid CTA during acute-stroke investigations, they may be overlooked when vascular causes of stroke are the focus.[19] Abdominal CT has shown lower lobe pulmonary abnormalities consistent with COVID-19 in those with a low clinical suspicion for infection.[20,21] However, there is no evidence determining the prevalence of such findings in the lung apices, nor the relationship between the extent of lung included on CTA and diagnostic accuracy, nor whether COVID-19 diagnostic imaging biomarkers can be obtained from CTA. This is particularly pertinent because COVID-19 appears to be associated with TIAs and strokes.[22-26]

This multicenter, observational study aimed to derive diagnostic imaging biomarkers using CTA to facilitate early identification of patients with COVID-19.

MATERIALS AND METHODS

Study Design

The National Health Research Authority and Research Ethics Committee approved this study. The authors declare no conflicts of interest. There is no overlap in subjects from prior publications.

We identified, retrospectively, adult patients (18 years of age or older) undergoing a CT of the head and CTA for acute stroke investigations at 3 hyperacute stroke units, King's College Hospital, Princess Royal University Hospital, and University College London Hospitals from March 25, 2020, to April 24, 2020 (corresponding to the time and location of the United Kingdom COVID-19 epicenter). We excluded CTAs that were nondiagnostic or performed for nonacute reasons. For reference, a control group of the same number of patients undergoing acute-stroke investigations during the same period in 2019 was also reviewed.

Imaging

The acute-stroke imaging protocol consisted of noncontrast CT of the head followed by a craniocervical arterial phase acquisition after intravenous injection of 50 mL of iohexol, 647 mg/mL (5 mL/s) (Omnipaque 300; GE Healthcare); 1 mL/kg of iohexol, 647 mg/mL (4 mL/s) (Omnipaque 300; GE Healthcare); or 50 mL of iohexol, 755 mg/mL (4 mL/s) (Omnipaque 350; GE Healthcare). The scans were performed on multidetector CT scanners (Optima 660, 64-section; Discovery 750, 128-section [both GE Healthcare]; Aquilion Prime 320 slice (Toshiba); Definition AS, 128-section [Siemens]).

The main scanning parameters were as follows for CT of the head/CTA studies respectively: tube voltage = 140 kV(peak)/100 kVp; automatic tube current modulation = 100–515/5–480 mAs; pitch = 0.55/0.8 mm; matrix = 512 × 512 (both); section thickness = 5/0.625 mm; FOV = 230 × 230 mm (both). All images were then reconstructed with a section thickness of 0.625 mm, with the same increments.

Data Collection

Blinded to radiologic findings, we obtained demographic and clinical data from electronic medical records (Sunrise; Epic Electronic Health Records). Data included respiratory and stroke clinical features on admission, risk factors for stroke and COVID-19 transmission, and clinical outcome. The details of RT-PCR testing were also recorded (Altona Diagnostics, Hologic, and Abbott Laboratories).

All imaging examinations were independently evaluated by fellowship-trained neuroradiologists, (J.S., F.B., S.S., A.M.F., with 7, 6, 6, and 3 years' experience, respectively), blinded to the clinical data and the RT-PCR results. Readers analyzed the images on the PACS using source images, maximum intensity projections, and multiplanar reformatting. The coronal depth of the lung apices imaged was measured for both lungs. CTA studies were reviewed in the axial plane using lung window and vascular window settings (window width/level, 1500/-500 Hounsfield units [HU] and 600/150 HU, respectively).

To find diagnostic imaging biomarkers for COVID-19 that would be easy to apply by radiologists who are not specialized in chest radiology, we evaluated the presence of GGO and any other pulmonary finding within the lung apices on CTA. Cases in which GGO was unequivocally due to dependency, breathing artifacts, or expiratory change were excluded. GGO was also subclassified as focal or diffuse, central or peripheral, and unilateral or bilateral.

We also used categories based on the British Society of Thoracic Imaging (BSTI) COVID-19 Guidance for Reporting Radiology (a nonvalidated guideline implemented at the start of COVID-19; On-line Table 1) (https://www.bsti.org.uk/media/resources/files/BSTI_COVID-19_Radiology_Guidance_version_2_16.03.20.pdf). All readers, along with a thoracic radiologist with 18 years' experience as a reference standard reader, gave a 3-point likelihood score to rate the lesions (COVID-19-typical lesions, indeterminate lesions, and non-COVID-19 lesions).

Statistics

Descriptive statistics were used to summarize data.

We determined the agreement between measures from multiple independent readers using the Fleiss κ coefficient with standard interpretation guidelines.[27,28] We selected features for which there was "substantial" (0.61–0.80) or "almost perfect" agreement (0.81–1.0) for further accuracy evaluation using confusion matrix outcomes.

Comparative statistics were used to analyze differences in 2020 and 2019 baseline data. Normality of distributions was assessed using the Shapiro-Wilk test. For univariate analyses, we used χ^2 tests for categoric variables (or Fisher exact tests when cell frequency was <5) and the Student t test for continuous data (or the Mann-Whitney U test for non-normal distributions). With regard to the number of events in our study, we were limited by the number of confounders we could include in the multivariate logistic regression, so we followed the recommendation that a minimum

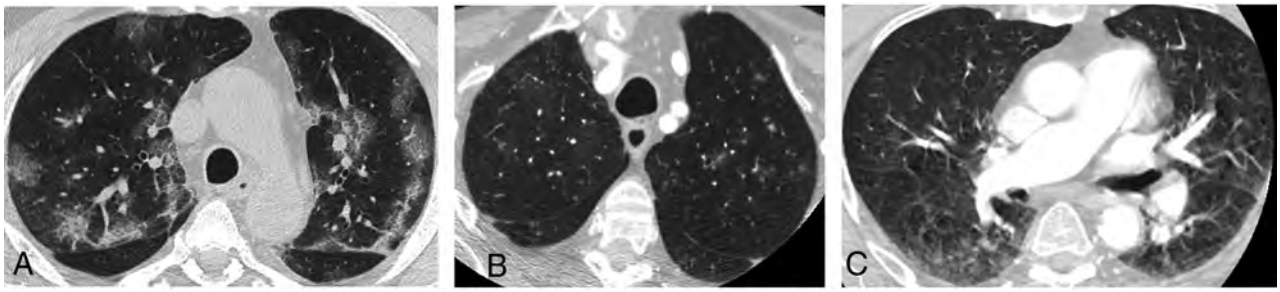

FIG 1. *A*, There are multiple, bilateral, focal, peripheral-predominant areas of ground-glass opacification, commonly seen in patients with COVID-19 pulmonary infection. *B*, There are multiple, focal 5- to 6-mm nodules with surrounding ground-glass change in the left upper lobe. This is an indeterminate COVID-19 appearance and would be more suggestive of atypical or fungal infection. *C*, There is bilateral ground-glass opacification posteriorly, more on the right, consistent with dependent change. This is a characteristic appearance, not associated with COVID-19, and classically disappears in the prone position. There is also a general hazy appearance not seen in *A* and *B*, which does not represent abnormal lung and is artifactual due to movement.

of 10 events per variable be incorporated to maintain model validity.[29,30] $P < .05$ was considered statistically significant.

We also evaluated the relationship between the presence of apical GGO and a craniocaudal measurement of the lung included on the coronal CT scan, by calculating the point biserial correlation coefficient. GGO was tested as a predictor of survival using a multivariate Cox proportional hazards regression model. Statistical analysis was performed using SPSS Statistics (Version 26.0; IBM).

RESULTS

Baseline Characteristics

Two hundred twenty-five patients were identified during the 2020 COVID-19 period (On-line Figure *A*). The patients' baseline characteristics in 2019 and 2020 were described and compared (On-line Table 2). The mean hospital stay of survivors was shorter in 2020 (9.7 versus 4.4 days; $P = .04$). There was no overall difference in clinical and imaging stroke-severity scores, thrombolysis, thrombectomy, or mortality rates.

Imaging Characteristics

We observed apical GGO in 22.2% (50/225) of patients in 2020. In 2020, when using the descriptive COVID-19 CT grading system, 28.0% (14/50) of those with GGO were rated as COVID-19-typical; 24.0% (12/50), indeterminate; and 48.0% (24/50), non-COVID-19; all features were more common than in 2019 ($P < .001$) (Fig 1).

To ensure that these potential diagnostic imaging biomarkers were reliable, we determined the interobserver agreement of these CTA findings in the setting of a neuroradiology department. The interrater reliability (IRR) was almost perfect (Fleiss $\kappa = 0.81$; 95% CI, 0.68–0.95) for rating of the presence or absence of apical GGO (On-line Table 3). By means of a descriptive COVID-19 CT grading system, the IRR among 4 neuroradiologist raters was substantial (Fleiss $\kappa = 0.74$; 95% CI, 0·64–0·84). The IRR was lower but remained substantial when adding a reference standard rating (Fleiss $\kappa = 0.65$; 95% CI, 0.60–0.71). When we reduced the 3-point scale to a 2-point scale (COVID-19-typical/indeterminate versus non-COVID-19/normal), the IRR improved to almost perfect among the neuroradiologists (Fleiss $\kappa = 0.88$; 95% CI, 0.75–1.0), and it also improved when adding a reference standard rating (Fleiss $\kappa = 0.79$; 95% CI, 0.71–0.86). Nonetheless, the IRR was highest among neuroradiologist raters for the well-defined tasks of looking at apical GGO subfeatures: focal versus nonfocal (diffuse/normal), bilateral versus nonbilateral (unilateral/normal), and peripheral versus nonperipheral (central/normal), which gave Fleiss κ scores of 0.90 (95% CI, 0.80–1.00), 0.98 (95% CI, 0.87–1.0), and 0.87 (95% CI, 0.78–0.98) respectively.

RT-PCR Cohort Characteristics

Forty-seven percent (106/225) of patients underwent RT-PCR testing, and 26.4% (28/106) had positive findings (On-line Table 4). A test was performed at or immediately before CTA in 44.3% (47/106) of patients; findings in 23.4% (11/47) were positive, but the result was available at the time of CTA in only 14.9% (7/47). The patients with positive findings on RT-PCR had a higher mortality rate (28.6% [8/28] versus 7.7% [6/78], $P = .009$) and received intravenous thrombolysis more often (32.1% [9/28] versus 12.8% [10/78], $P = .02$). There was no difference in any demographic or clinical characteristics, with the exception of oxygen saturation, which was lower in patients with a positive RT-PCR result ($P = .03$). In contrast, all imaging biomarkers were seen more commonly in patients with a positive RT-PCR result ($P < .001$). We determined the diagnostic accuracy of these imaging biomarkers for SARS-CoV-2 using RT-PCR as the reference standard, having shown their reliability (interrater analyses above).

We measured the sensitivity, specificity, and positive predictive and negative predictive values. The presence of GGO was the most sensitive biomarker, and the descriptive COVID-19 CT grading system using a 2-point scale was the most specific (Table 1). Because the presence of GGO was the most sensitive diagnostic imaging biomarker and the simplest for a clinician to use with high interrater reliability, we incorporated this variable into a multivariate analysis (Table 2), comparing it with other clinical and imaging features immediately available on hospital admission. We included all features in which univariate analysis (On-line Table 4) showed group comparison differences of $P \leq .05$. Only the presence of GGO showed an increased likelihood of a positive RT-PCR result (OR = 11.65; 95% CI, 4.14–32.78; $P < .001$).

In summary, radiologists who were not specialized in chest radiology evaluated the presence or absence of apical GGO. This measurement had a very high IRR (Fleiss $\kappa = 0.81$; 95% CI, 0.68–0.95) and, when compared with the RT-PCR result, had good COVID-19 diagnostic performance with a sensitivity of 75%

Table 1: Diagnostic accuracy of imaging biomarkers on CTA in determining patients tested for SARS-CoV-2 ($n = 106$)

	Sensitivity (95% CI)	Specificity (95% CI)	PPV (95% CI)	NPV (95% CI)
Presence of GGO	75% (56–87)	81% (71–88)	58% (41–74)	90% (79–95)
Focal GGO	46% (29–64)	90% (81–95)	62% (39–81)	82% (72–89)
Bilateral GGO	57% (37–75)	82% (72–89)	53% (35–71)	84% (73–91)
Peripheral GGO	68% (49–82)	88% (79–94)	68% (48–83)	88% (79–94)
COVID-19-typical/in-determinate[a]	64% (46–79)	92% (84–94)	77% (50–92)	88% (74–95)

Note:—PPV indicates positive predictive value; NPV, negative predictive value.
[a] COVID-19-typical alone gave a low sensitivity (36%) and was excluded from further analysis. COVID-19 CT imaging definitions are listed in On-line Table 1.

Table 2: Multivariate analysis using clinical and imaging features to determine the likelihood of SARS-CoV-2 ($n = 106$)[a]

	OR	OR (95% CI)	*P* Value
Infarct	0.47	0.13–1.72	.25
Oxygen saturation	1.00	0.97–1.02	.78
Presence of GGO	11.65	4.14–32.78	<.001[b]

[a] With regard to total number of patients with confirmed SARS-CoV-2 (28/106), only the 3 most discriminant characteristics from the univariate analysis ($P \leq .05$) were included. If all 6 variables $P \leq .10$ or all 10 variables $P \leq .20$ were included in the model, the only significant predictor of positive PCR result was the presence of GGO ($P < .001$), but these findings are at an increased risk of bias in the OR estimation.
[b] *P* value <.05.

(95% CI, 56–87) and a specificity of 81% (95% CI, 71–88) and OR = 11.65 (95% CI, 4.14–32.78; $P < .001$) on multivariate analysis. While the presence of GGO alone is the simplest feature to understand and measure, we determined that GGO subfeatures (peripheral, focal, or bilateral) or a descriptive grading system were more specific but less sensitive. The grading system gave the highest specificity of 92% (95% CI, 84–94).

Apical GGO Cohort Characteristics

We also examined whether apical GGO (On-line Figure *B*), regardless of RT-PCR results, revealed useful information (On-line Table 5). Patients with GGO versus patients without GGO, stroke parameters differed in patients with GGO (50/225) with a higher rate of carotid occlusion on CTA (16.0% versus 3.4%, $P = .004$) and a greater clinical deficit (mean NIHSS score, 6.2 versus 9.4; $P = .02$). In terms of clinical features associated with pneumonia, patients with GGO more often had a cough ($P = .002$), fever ($P = .004$), a higher respiratory rate ($P = .005$), and lower oxygen saturation ($P = .001$). Patients with GGO had a higher mortality rate 18.0% (9/50) versus 5.7% (10/175) ($P = .02$), and survivors stayed longer in the hospital (3.8 versus 6.6 days, $P = .004$). We performed a multivariate analysis (On-line Table 6) incorporating all demographic, clinical, and imaging features immediately available on hospital admission when univariate analysis (On-line Table 5) had shown a group comparison difference of $P < .01$. Carotid occlusion, subjective fever, and lower oxygen saturation showed an increased likelihood of GGO. Carotid occlusion and oxygen saturation were the most predictive features (OR = 6.82; 95% CI, 1.97–23.53; $P = .002$; OR = 0.81; 95% CI, 0.69–0.95; $P = .009$, respectively).

Biomarker group differences were not due to a difference in the craniocaudal extent of the lung included on CTA (Table 1 and On-line Table 5). Furthermore, during the limited range assessed (mean, 8.06 ± 2.5 cm), there was no correlation between this coronal measurement and the presence of GGO (point biserial correlation coefficient = 0.053); thus, we were unable to show an incentive to increase the extent of apical lung included during CTA.

The presence of GGO was an independent predictor of increased 30-day mortality (18.0% versus 5.7%, $P = .02$; hazard ratio = 3.51 [95% CI, 1.42–8.66], $P = .006$; Fig 2 and On-line Tables 5–7).

DISCUSSION

Early identification of patients with COVID-19 is essential for treatment and viral control. Therefore, the search for alternative diagnostic biomarkers for COVID-19 is mandated in the context of asymptomatic and presymptomatic infection and the variable sensitivity of SARS-CoV-2 RT-PCR testing.[8-12] We have assessed candidate biomarkers in those patients who present with suspected acute stroke and undergo immediate CTA. We have shown that an imaging feature, the presence or absence of apical GGO, which is simple to assess, is a reliable and accurate COVID-19 diagnostic biomarker. In contrast, all other contemporaneous demographic, clinical, and imaging features available at the time of CTA were not helpful in the early identification of COVID-19. Furthermore, we have shown that the same biomarker is a prognostic biomarker predictive of 30-day mortality. All our findings have not been reported previously.

RT-PCR testing was performed at or before CTA in 44% (47/106) of patients, and 23% (11/47) of tests had positive findings. SARS-CoV-2 RT-PCR testing has limitations as a reference standard due to the diagnostic performance of the assay and external factors related to sampling performance, location, and timing.[11] Even with many health care systems now adopting routine RT-PCR screening on admission, there may be a relatively long processing time.[11] Indeed, in our cohort, results were available in only 15% (7/47) of cases at the time of CTA, thus emphasizing the utility of any reliable alternative opportunistically-derived diagnostic COVID-19 biomarkers.

Given that the presence of apical GGO was simple to assess and a reliable and accurate diagnostic biomarker for COVID-19, we examined whether patients with apical GGO, regardless of whether a RT-PCR test had been performed, also revealed useful information on admission. GGO was an independent predictor of increased 30-day mortality (18.0% versus 5.7%. $P = .017$; hazard ratio = 3.51; 95% CI, 1.42–8.66; $P = .006$). A contributory mechanism to this COVID-19-related excess mortality might be thromboembolic because increased carotid occlusion was associated with GGO (16.0% versus 3.4%, $P = .004$; OR = 6.82; 95% CI, 1.97–23.53; $P = .002$) and was likely an independent predictor of death. This is concordant with reports that COVID-19 is prothrombotic with a putative increase in patients presenting with TIAs and strokes.[22-26] An

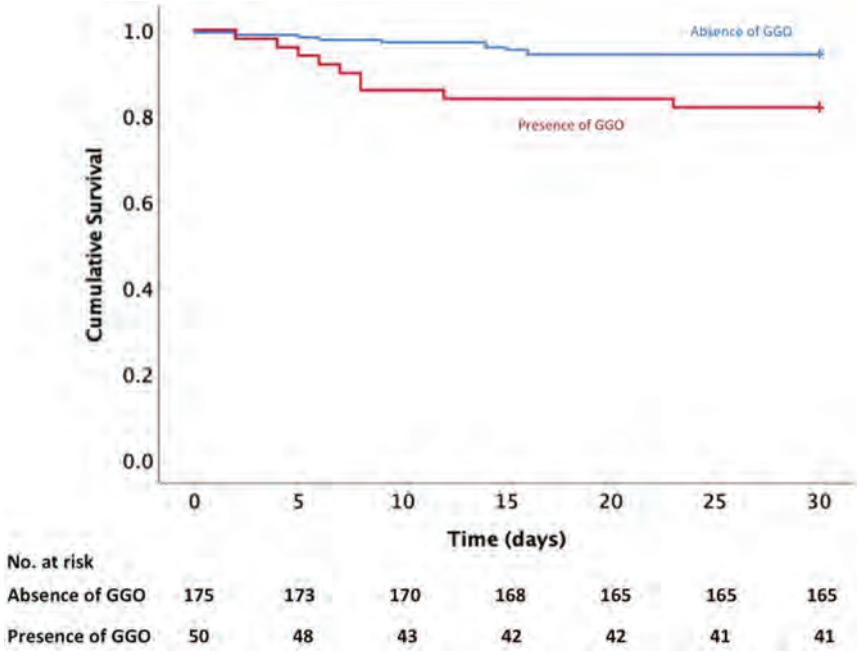

FIG 2. Kaplan-Meier analysis. Association between GGO and mortality was evaluated using Kaplan-Meier survival analysis; 82.0% of patients in the group with GGO were alive at 30 days compared with 94.3% in the group without GGO ($P = .005$).

implication is that GGO may not be an entirely incidental finding in this cohort of patients with suspected acute stroke. We also noted that unlike patients grouped by RT-PCR results, survivors stayed in the hospital longer ($P = .004$), plausibly because of the morbidity associated with pneumonitis (or other causes because this is a multisystem disease).

The study most similar to ours analyzed 118 CTA studies performed as stroke investigations and found that 28% (33/118) had lung findings typical for COVID-19 and 93.9% (31/33) had a positive SARS-CoV-2 RT-PCR infection.[31] Another small retrospective study showed apical lung abnormalities on craniocervical CTA in 10/17 (58/8%) patients with COVID-19 pneumonia whose diagnosis was unknown at the time of CT scanning.[32] Again, these studies emphasize the importance of careful scrutiny of the lung apices. Our study sampled a greater number of patients than both of these, demonstrating the frequency of ground-glass opacification similar to that in the first study; however, it also included statistics on interrater reliability, diagnostic performance of the biomarker, and survival data, which were not included in either of these studies.

A further study analyzed 119 nonchest CT scans, including abdominal ($n = 101$) and cervical spine ($n = 18$) imaging.[21] Fifty-two percent (62/119) of patients were suspected of having COVID-19 and underwent RT-PCR testing before the CT reading; 48% (57/119) were not suspected of having COVID-19. The presence of pneumonia was seen in 64% (76/119), leading to a diagnosis of COVID-19 in 37% (44/119). The prevalence of pneumonia was higher (64%) than the presence of apical GGO in our cohort (22%), plausibly due to a broader definition of COVID-19-typical abnormality and 102/119 patients (84%) undergoing abdominal imaging, including the lung bases. The lung bases likely yield more COVID-19-typical abnormalities than the apices, given the predilection for lower lobe and posterior segment involvement.[15-18] The diagnostic reliability and accuracy metrics including IRR, sensitivity, and specificity were not reported.

The implications of our findings plausibly include earlier selection of the appropriate level of personal protective equipment and attendant staff numbers, triage to appropriate inpatient ward settings, self-isolation, and contact tracing.[33] Guidance on selection of personal protective equipment often changes on the basis of available evidence, and risk stratification is the key to this in a number of health care settings.[34,35] Biomarkers, such as a scan positive for GGO, should heighten awareness of a potential positive case, possibly changing staff personal protective equipment requirements (eg, from a fluid-repellant surgical mask to an FFP2 or N95 mask) and also directing a patient to a side room instead of an open ward, pending RT-PCR results. This patient group may additionally find it difficult to wear a mask, hence increasing the importance of staff protection. Our data therefore have important safety implications for daily clinical practice as well as prognostic information, given the increased mortality in those with COVID-19 shown in our cohort.

Our study has a number of strengths. It is multicenter and is the only study robustly assessing the apices for GGO. Its main limitation is its retrospective nature; however, no prospective studies exist in the literature relating to COVID-19 imaging. The use of the nonvalidated BSTI COVID-19 guidelines in some parts of the study may also be a limitation; however, no validated pulmonary scoring system yet exists for COVID-19 nor does this issue interfere with our conclusions.

CONCLUSIONS

This study demonstrates that the presence of apical GGO on carotid CTA in patients presenting with suspected acute stroke is a simple, reliable, and accurate diagnostic and prognostic COVID-19 biomarker. This can now be tested prospectively for further validation. These findings mandate vigilance in apical assessment by all radiologists and clinicians involved in acute stroke care, particularly relevant given the sensitivity of currently available SARS-CoV-2 RT-PCR testing.

ACKNOWLEDGMENTS

The authors acknowledge the South London Specialist Virology Centre, Viapath, Infections Sciences, in this study.

REFERENCES

1. World Health Organization. **Naming the coronavirus disease (COVID-19) and the virus that causes it**. https://www.who.int/

emergencies/diseases/novel-coronavirus-2019/technical-guidance/naming-the-coronavirus-disease-(covid-2019)-and-the-virus-that-causes-it. Accessed June 20, 2020
2. World Health Organization. **WHO Director-General's opening remarks at the media briefing on COVID-19 - 11 March 2020.** WHO Director-General's opening remarks at the media briefing on COVID-19 - 11 March 2020. Accessed June 20, 2020
3. Huang C, Wang Y, Li X, et al. **Clinical features of patients infected with 2019 novel coronavirus in Wuhan, China**. *Lancet* 2020;395:497–506 CrossRef Medline
4. Grasselli G, Pesenti A, Cecconi M. **Critical care utilization for the COVID-19 outbreak in Lombardy, Italy: early experience and forecast during an emergency response**. *JAMA* 2020 Mar 13. [Epub ahead of print] CrossRef
5. Remuzzi A, Remuzzi G. **COVID-19 and Italy: what next?** *Lancet* 2020;395:1225–28 CrossRef Medline
6. Phua J, Weng L, Ling L, et al; Asian Critical Care Clinical Trials Group. **Intensive care management of coronavirus disease 2019 (COVID-19): challenges and recommendations**. *Lancet Respir Med* 2020;8:506–17 CrossRef Medline
7. Worldometer. **COVID-19 Coronavirus Pandemic**. https://www.worldometers.info/coronavirus/. Accessed 20th June, 2020
8. Day M. **Covid-19: four fifths of cases are asymptomatic, China figures indicate**. *Br Med J* 2020;369:m1375 CrossRef Medline
9. Lauer SA, Grantz KH, Bi Q, et al. **The incubation period of coronavirus disease 2019 (COVID-19) from publicly reported confirmed cases: estimation and application**. *Ann Intern Med* 2020;172:577–82 CrossRef Medline
10. Yang Y, Yang M, Shen C, et al. **Evaluating the accuracy of different respiratory specimens in the laboratory diagnosis and monitoring the viral shedding of 2019-nCoV infections**. *medRXiv*. http://medrxiv.org/lookup/doi/10.1101/2020.02.11.20021493. Accessed June 20, 2020
11. Ai T, Yang Z, Hou H, et al. **Correlation of chest CT and RT-PCR testing in coronavirus disease 2019 (COVID-19) in China: a report of 1014 cases**. *Radiology* 2020;296:E32–40 CrossRef Medline
12. Fang Y, Zhang H, Xie J, et al. **Sensitivity of chest CT for COVID-19: comparison to RT-PCR**. *Radiology* 2020;296:E115–17 CrossRef Medline
13. American College of Radiology. **ACR Recommendations for the Use of Chest Radiography and Computed Tomography (CT) for Suspected COVID-19 Infection**. https://www.acr.org/Advocacy-and-Economics/ACR-Position-Statements/Recommendations-for-Chest-Radiography-and-CT-for-Suspected-COVID19-Infection. Accessed June 20, 2020
14. The Royal College of Radiologists. **The role of CT chest during the COVID-19 crisis**. https://www.rcr.ac.uk/college/coronavirus-covid-19-what-rcr-doing/clinical-information/role-ct-chest-during-covid-19. Accessed June 20, 2020
15. Wong HY, Lam HYS Fong AH, et al. **Frequency and distribution of chest radiographic findings in COVID-19 positive patients**. *Radiology* 2020;296:E72–78 CrossRef Medline
16. Chung M, Bernheim A, Mei X, et al. **CT imaging features of 2019 novel coronavirus (2019-nCoV)**. *Radiology* 2020;295:202–07 CrossRef Medline
17. Bernheim A, Mei X, Huang M, et al. **Chest CT findings in coronavirus disease-19 (COVID-19): relationship to duration of infection**. *Radiology* 2020;295:200463 CrossRef Medline
18. Caruso D, Zerunian M, Polici M, et al. **Chest CT features of COVID-19 in Rome, Italy**. *Radiology* 2020;296:E79–85 CrossRef Medline
19. Kanesa-Thasan R, Cox M, Patel M, et al. **Actionable vascular and other incidental findings on CTA in patients undergoing acute stroke intervention**. *Neuroradiol J* 2018;31:572–77 CrossRef Medline
20. Vu D, Ruggiero M, Choi WS, et al. **Three unsuspected CT diagnoses of COVID-19**. *Emerg Radiol* 2020;27:229–32 CrossRef Medline
21. Hossain R, Lazarus MS, Roudenko A, et al. **CT scans obtained for non-pulmonary indications: associated respiratory findings of COVID-19**. *Radiology* 2020;296:E173–79 CrossRef Medline
22. Klok FA, Kruip MJ, van der Meer NJ, et al. **Incidence of thrombotic complications in critically ill ICU patients with COVID-19**. *Thromb Res* 2020;191:145–47 CrossRef Medline
23. Mao L, Jin H, Wang M, et al. **Neurologic manifestations of hospitalized patients with coronavirus disease 2019 in Wuhan, China**. *JAMA Neurol* 2020;77:683–89 CrossRef Medline
24. Helms J, Tacquard C, Severac F, et al; CRICS TRIGGERSEP Group (Clinical Research in Intensive Care and Sepsis Trial Group for Global Evaluation and Research in Sepsis). **High risk of thrombosis in patients with severe SARS-CoV-2 infection: a multicenter prospective cohort study**. *Intensive Care Med* 2020;46:1089–98 CrossRef Medline
25. Connors JM, Levy JH. **Thromboinflammation and the hypercoagulability of COVID-19**. *J Thromb Haemost* 2020;18:1559–61 CrossRef Medline
26. Oxley TJ, Mocco J, Majidi S, et al. **Large-vessel stroke as a presenting feature of covid-19 in the young**. *N Engl J Med* 2020;382:e60 CrossRef Medline
27. Fleiss JL. **Measuring nominal scale agreement among many raters**. *Psychol Bull* 1971;76:378–82 CrossRef
28. Landis JR, Koch GG. **The measurement of observer agreement for categorical data**. *Biometrics* 1977;33:159–74 Medline
29. Harrell FE Jr, Lee KL, Matchar DB, et al. **Regression models for prognostic prediction: advantages, problems, and suggested solutions**. *Cancer Treat Rep* 1985;69:1071–77 Medline
30. Peduzzi P, Concato J, Kemper E, et al. **A simulation study of the number of events per variable in logistic regression analysis**. *J Clin Epidemiol* 1996;49:1373–79 CrossRef Medline
31. Kihira S, Schefflein J, Chung M, et al. **Incidental COVID-19 related apical lung findings on stroke CTA during the COVID-19 pandemic**. *J Neurointerv Surg* 2020;12:669–72 CrossRef Medline
32. Applewhite BP, Buch K, Yoon BC, et al. **Lung apical findings in coronavirus disease (COVID-19) infection on neck and cervical spine CT**. *Emegr Radiol* 2020 Jul 21. [Epub ahead of print] CrossRef Medline
33. Public Health England. **COVID-19: Guidance for the remobilisation of services within health and care settings: infection prevention and control recommendations**. https://assets.publishing.service.gov.uk/government/uploads/system/uploads/attachment_data/file/886668/COVID-19_Infection_prevention_and_control_guidance_complete.pdf. Accessed June 20, 2020
34. Sayburn A. **Covid-19: PHE upgrades PPE advice for all patient contacts with risk of infection**. *Br Med J* 2020;369:m1391 CrossRef Medline
35. Forrester JD, Nassar AK, Maggio PM, et al. **Precautions for operating team members during the COVID-19 pandemic**. *J Am Coll Surg* 2020;230:1098–1101 CrossRef Medline

Plaque Composition as a Predictor of Plaque Ulceration in Carotid Artery Atherosclerosis: The Plaque At RISK Study

K. Dilba, D.H.K. van Dam-Nolen, A.C. van Dijk, M. Kassem, A.F.W. van der Steen, P.J. Koudstaal, P.J. Nederkoorn, J. Hendrikse, M.E. Kooi, J.J. Wentzel, and A. van der Lugt

ABSTRACT

BACKGROUND AND PURPOSE: Plaque ulceration is a marker of previous plaque rupture. We studied the association between atherosclerotic plaque composition at baseline and plaque ulceration at baseline and follow-up.

MATERIALS AND METHODS: We included symptomatic patients with a carotid stenosis of <70% who underwent MDCTA and MR imaging at baseline ($n = 180$). MDCTA was repeated at 2 years ($n = 73$). We assessed the presence of ulceration using MDCTA. Baseline MR imaging was used to assess the vessel wall volume and the presence and volume of plaque components (intraplaque hemorrhage, lipid-rich necrotic core, and calcifications) and the fibrous cap status. Associations at baseline were evaluated with binary logistic regression and reported with an OR and its 95% CI. Simple statistical testing was performed in the follow-up analysis.

RESULTS: At baseline, the prevalence of plaque ulceration was 27% (49/180). Increased wall volume (OR = 12.1; 95% CI, 3.5–42.0), higher relative lipid-rich necrotic core (OR = 1.7; 95% CI, 1.3–2.2), higher relative intraplaque hemorrhage volume (OR = 1.7; 95% CI, 1.3–2.2), and a thin-or-ruptured fibrous cap (OR = 3.4; 95% CI, 1.7–6.7) were associated with the presence of ulcerations at baseline. In 8% (6/73) of the patients, a new ulcer developed. Plaques with a new ulceration at follow-up had at baseline a larger wall volume (1.04 cm^3 [IQR, 0.97–1.16 cm^3] versus 0.86 cm^3 [IQR, 0.73–1.00 cm^3]; $P = .029$), a larger relative lipid-rich necrotic core volume (23% [IQR, 13–31%] versus 2% [IQR, 0–14%]; $P = .002$), and a larger relative intraplaque hemorrhage volume (14% [IQR, 8–24%] versus 0% [IQR, 0–5%]; $P < .001$).

CONCLUSIONS: Large atherosclerotic plaques and plaques with intraplaque hemorrhage and lipid-rich necrotic cores were associated with plaque ulcerations at baseline and follow-up.

ABBREVIATIONS: AUC = area under the curve; IPH = intraplaque hemorrhage; IQR = interquartile range; LRNC = lipid-rich necrotic core; TRFC = thick versus thin-or-ruptured fibrous cap

Atherosclerosis in the carotid arteries is one of the leading causes of ischemic stroke with arterio-arterial embolism as the main mechanism.[1,2] The degree of lumen stenosis and the symptomatic status of the patient are currently used for risk assessment and treatment decision-making.[3,4] Patients with severe (≥70%) and moderate (50%–69%) carotid artery stenosis benefit from carotid endarterectomy; however, the number needed to treat to prevent recurrent stroke is relatively high.[5] Moreover, almost half of neurologic events occur in patients with a low degree of stenosis.[6,7] This finding has triggered investigations into other markers that may help to identify patients with a high risk of recurrent stroke. Much attention has been paid to markers of atherosclerosis, like plaque composition and plaque ulceration, with the aim of identifying vulnerable plaques.[8] These vulnerable plaques have a high risk of rupture, which results in thrombus formation and embolization of plaque material and/or thrombus migrating into the intracranial circulation, thereby causing vascular occlusion and a subsequent ischemic stroke.[2]

Plaque composition is predictive of future cerebrovascular events.[9-12] Atherosclerotic plaque ulceration, visible as plaque-

Received March 3, 2020; accepted after revision August 9.

From the Departments of Radiology and Nuclear Medicine (K.D., D.H.K.v.D.-N., A.C.v.D., A.v.d.L.), Cardiology (K.D., A.F.W.v.d.S., J.J.W.), and Neurology (A.C.v.D., P.J.K.), Erasmus University Medical Center Rotterdam, Rotterdam, the Netherlands; Department of Radiology and Nuclear Medicine (M.K., M.E.K.), CARIM School for Cardiovascular Diseases, Maastricht University Medical Center+, Maastricht, the Netherlands; Department of Neurology (P.J.N.), University Medical Center Amsterdam, Amsterdam, the Netherlands; and Department of Radiology (J.H.), University Medical Center Utrecht, Utrecht, the Netherlands.

This research was performed within the framework of the Center for Translational Molecular Medicine (www.ctmm.nl), project PARISK (Plaque At RISK; grant 01C-202) and supported by the Dutch Heart Foundation. Kristina Dilba was supported, in part, by Toegepaste en Technische Wetenschappen, project No. 10813.

Please address correspondence to Aad van der Lugt, MD, PhD, Erasmus University Medical Center Rotterdam, Department of Radiology and Nuclear medicine, Room Ne 507, Dr. Molewaterplein 40, 3015 GD, Rotterdam, the Netherlands; e-mail: a.vanderlugt@erasmusmc.nl

Indicates open access to non-subscribers at www.ajnr.org

http://dx.doi.org/10.3174/ajnr.A6868

surface disruption, which is a marker of previous plaque rupture, is also correlated with recurrent symptoms and associated with a higher risk of ischemic stroke.[13,14] However, the relation between vulnerable plaque components and plaque rupture is rarely investigated. Both plaque composition and ulceration can be assessed in vivo with different imaging modalities, but MR imaging is the best technique to assess plaque composition due to its superior soft-tissue contrast,[15] whereas MDCTA exceeds MR imaging in the detection of plaque ulcerations due to its excellent spatial resolution with the possibility of multiplanar reconstruction.[16,17]

Most previous studies investigated the relation between plaque ulcerations and plaque features using a cross-sectional study design. Generally, it was found that intraplaque hemorrhage (IPH), large lipid-rich necrotic core (LRNC), and thinning or ruptured fibrous cap were associated with the presence of ulcerations,[18-21] while the presence of calcifications was inversely related to ulcerations.[19] A prospective study in asymptomatic patients with severe carotid artery stenosis revealed that LRNC volume was a predictor of new surface disruption.[22,23] The aim of the current study was to investigate, in symptomatic patients with mild-to-moderate (30%–69%) carotid artery stenosis, which plaque components at baseline are predictive of plaque rupture at follow-up.

MATERIALS AND METHODS

Study Population

This study is a substudy of the Plaque At RISK (PARISK) study (clinicaltrials.gov NCT01208025); details of the study design have been previously described in the study-design article.[24] The PARISK study is a Dutch prospective, multicenter cohort study aimed at identifying patients with mild-to-moderate carotid artery stenosis with an increased risk of recurrent stroke by noninvasive plaque imaging.

From September 2010 to December 2014, we included 240 patients with recent (<3 months) TIA, amaurosis fugax, or minor stroke due to ischemia in the territory of the carotid artery and 30%–69% ipsilateral carotid artery stenosis who were not scheduled for carotid endarterectomy. The degree of lumen stenosis was determined with Doppler ultrasonography or MDCTA. The upper cutoff value of 69% was based on the North American Symptomatic Endarterectomy Trial (NASCET) criteria.[25] The lower cutoff value was an atherosclerotic plaque with a thickness of at least 2–3 mm, which corresponds to European Carotid Surgery Trial (ECST) stenosis of approximately 30%.[3]

Noninvasive plaque imaging (Doppler ultrasonography, MDCTA, MR imaging) was scheduled in all patients at baseline. The follow-up imaging was scheduled in 118 patients. For the cross-sectional analysis, we selected patients who underwent both MDCTA and MR imaging at baseline. For the prospective analysis, we selected patients who, in addition to baseline MDCTA and MR imaging, underwent MDCTA at follow-up.

The study was approved by the institutional medical ethics committees of all participating centers (Erasmus University Medical Center Rotterdam, Maastricht University Medical Center, University Medical Center Amsterdam, University Medical Center Utrecht). Written informed consent was obtained from each participant before enrollment.

Cardiovascular Risk Factors at Baseline

Body mass index was recorded. Hypertension was defined as a systolic blood pressure of >140 mm Hg or a diastolic blood pressure of >90 mm Hg with at least 15 minutes of continuous noninvasive blood pressure measurement or treatment with antihypertensive medication. Hypercholesterolemia was defined as fasting total cholesterol of >5 mmol/L or the use of cholesterol-lowering medication. Diabetes mellitus was defined as a fasting serum glucose level of >6.9 mmol/L, a 2-hour post-load glucose level of >11.0 mmol/L, or the use of antidiabetic medication. Smoking status was assessed at the time of the TIA or ischemic stroke and divided in 2 categories: current smoker or not a current smoker.

MDCTA Data Acquisition and Analysis

We performed image acquisition using a standardized protocol, as previously described in the study-design article.[24] MDCTA of the carotid artery was performed if no contraindications for MDCTA were present (glomerular filtration rate, <60 mL/min; a documented allergy to MDCTA contrast media). All MDCTA images were transferred to a workstation equipped with dedicated 3D analysis software (syngo.via; Siemens). The multiplanar reformatting application allowed analysis of both carotid arteries in oblique, coronal, and sagittal planes.

The symptomatic artery was analyzed. The degree of lumen stenosis in the carotid bifurcation was measured according to the ECST and NASCET criteria, perpendicular to the central lumen line.[3,6] Plaque surface morphology was evaluated and classified as either ulcerated or nonulcerated. Plaque ulceration was defined as an extension of contrast material of >1 mm into the atherosclerotic plaque, being visible in at least 2 perpendicular planes.[21] In addition, the number of ulcerations per artery was recorded.

Plaque surface morphology was evaluated by 2 trained readers at baseline (B.H. and A.C.v.D.) and follow-up (K.D. and D.H.K.v.D.-N.). The trained readers (B.H., A.C.v.D., K.D., and D.H.K.v.D.-N.) were physicians who were first trained on a training set to identify the presence of ulceration on MDCTA. They had to successfully complete this training set before they assessed the ulcerations on the PARISK dataset.[18] The third observer who was consulted for consensus in case of no agreement was a neuroradiologist with >25 years of experience (A.v.d.L.).

Temporal changes in plaque surface morphology were also evaluated by 2 trained readers (K.D. and D.H.K.v.D.-N.) by visual comparison of baseline and follow-up images in which an ulceration was detected, and a subdivision was made among new ulceration, persistent ulceration, and healed ulceration.

Image software (National Institutes of Health) was used to quantify calcifications in the symptomatic carotid artery within 3 cm proximal and distal to the bifurcation. We used a threshold of 600 HU to differentiate calcifications from contrast material in the lumen; calcification volume was expressed in cubic millimeters.[26]

MR Imaging Data Acquisition and Analysis

All MR imaging examinations were performed on 3T whole-body MR imaging scanners (Achieva, Philips Healthcare, or Discovery MR 750, GE Healthcare) using an 8-channel phased-array coil (Shanghai Chenguang Medical Technologies) or a 4-channel phased-array coil with an angulated setup (PACC-GS30.

Machnet B.V.), respectively. MR imaging of the carotid artery was performed if no contraindications for MR imaging were present (claustrophobia). Imaging protocols included 5 sequences that were comparable among centers (Philips: 3D-TOF fast-field echo, 3D-T1WI inversion recovery Turbo field echo, 2D-T2WI TSE, 2D-T1WI Quadruple inversion recovery TSE pre- and postcontrast; GE Healthcare: 3D fast-spoiled gradient-recalled, 3D-T1WI fast-spoiled gradient-recalled, 2D-T2WI double inversion recovery FSE, 2D-T1WI double inversion recovery FSE pre- and postcontrast). More detailed information of the sequences was previously described in the study-design article.[24]

Six observers who were trained in the same institution to delineate plaque components evaluated the MR images of the symptomatic carotid artery with the VesselMass software (Department of Radiology, Leiden University Medical Center). All observers were extensively trained to manually delineate the vessel wall and plaque components on a test set. Subsequently, they had to demonstrate good interobserver agreement for all parameters (interclass correlation coefficient/κ values $\geq$ 0.6) on a validation set that was delineated by experts with >15 years of experience (M.E.K. and A.v.d.L.) before they could start delineating the MR images of the PARISK study.

The observers manually delineated the contours of the inner and outer vessel wall, LRNC, IPH, and calcifications using VesselMass. Then, the software (VesselMass) automatically generated a report with the areas of the lumen, the vessel wall, and each plaque component in each MR imaging section and the total volumes on all MR imaging slices of each plaque component, the lumen, and the vessel wall. The total volumes are the sum of the total area in each section multiplied by the section thickness, taking into account the section gap. The observers were blinded to clinical data and other imaging tests.

A total of 9 MR imaging slices of 2 mm each covering the entire plaque (4 slices in the common carotid artery proximal to bifurcation and 5 slices in the internal carotid artery distal to bifurcation) were included in analysis. The volumes of the lumen, wall (the total volume of the vessel wall including the plaque in 9 MR imaging slices), and total vessel (calculated as lumen volume + wall volume) were used to calculate relative wall volume to total vessel volume (Wall Volume / Total Vessel Volume × 100%). For each plaque, the presence and volumes of an LRNC, IPH, and calcifications were assessed using multisequence imaging criteria previously validated with histology.[27] When the LRNC also had internal IPH, we reported the internal IPH as IPH. In addition, the IPH volume was always considered as part of the LRNC.[28] The relative volume of plaque components to wall volume was calculated (eg, Percentage IPH = IPH Volume / Wall Volume × 100%). Fibrous cap status was divided in 2 categories: thick versus thin-or-ruptured fibrous cap (TRFC) based on previously published criteria.[29]

Statistical Analysis

Categoric variables are presented as absolute numbers and relative frequencies. Continuous variables are presented as mean ± SD or as median with interquartile range (IQR). First, clinical characteristics and plaque parameters in patients with and without an ulceration at baseline and in patients with and without a new ulceration at 2-year follow-up were compared. Continuous variables were compared using a *t* test or Mann-Whitney *U* test, and categoric data were evaluated using the χ^2 or Fisher exact test.

The association between plaque characteristics and the presence of an ulcer at baseline (cross-sectional analysis) was evaluated using binary logistic regression and reported with ORs and 95% confidence intervals. The relative volumes of LRNC, IPH, and calcifications were natural log-transformed after adding 1% to deal with volumes of zero [eg, ln(% IPH Volume + 1)] due to skewed distribution. Because a larger vessel wall volume increased both the risk of having a plaque ulceration and the presence and size of different plaque components, we adjusted the significant associations between plaque composition and plaque ulceration for wall volume. Additional adjustment was performed for all known risk factors (age, sex, body mass index, hypertension, hypercholesterolemia, diabetes mellitus). A sensitivity analysis was performed to test the importance of time intervals among the following: 1) event to MDCTA baseline, 2) event to MR imaging baseline, and 3) MDCTA baseline to MR imaging baseline on the found associations. Because of the relatively low number of new ulcers, only simple statistical testing was performed using the Mann-Whitney *U* test and Fisher Exact test in the prospective analysis. Plaque parameters were taken as predictors, and the presence of an ulcer, as an outcome variable. A receiver operating characteristic curve and an area under the curve (AUC) were performed to establish the strength of the found associations. $P < .05$ was considered significant (2-sided). All calculations were performed using SPSS, Version 21 (IBM, 2012).

RESULTS

Patient Characteristics

From the 240 included patients in the PARISK study, 193 patients underwent both MDCTA and MR imaging at baseline. Thirteen patients were excluded because of poor MDCTA baseline quality ($n = 2$), poor MR imaging quality ($n = 5$), and inadequate MR imaging scan range ($n = 6$). Thus, for cross-sectional analysis, 180 patients were eligible. From these 180 patients, 118 were scheduled for follow-up imaging, but only 75 (64%) patients underwent MDCTA after 2 years of follow-up. The main reasons that follow-up imaging was not performed were logistic problems ($n = 17$), contraindications to contrast material ($n = 14$), withdrawal of informed consent ($n = 9$), and death ($n = 3$). An additional 2 patients were excluded because of carotid endarterectomy in the symptomatic carotid artery between the baseline and follow-up scan ($n = 1$) and poor MDCTA follow-up quality. Therefore, 73 patients were eligible for prospective analysis. Figure 1 shows a flow diagram of participants included and excluded from the study.

Clinical characteristics of the included patients at baseline are shown in Table 1. The median age of the study population was 68 years (range, 63–73 years); 71% (127/180) of the participants were men.

Baseline Imaging Characteristics

The time interval between the neurologic event and baseline MDCTA was 34 days (IQR, 15–55 days), and the time between the neurologic event and MR imaging, 47 days (IQR, 30–67

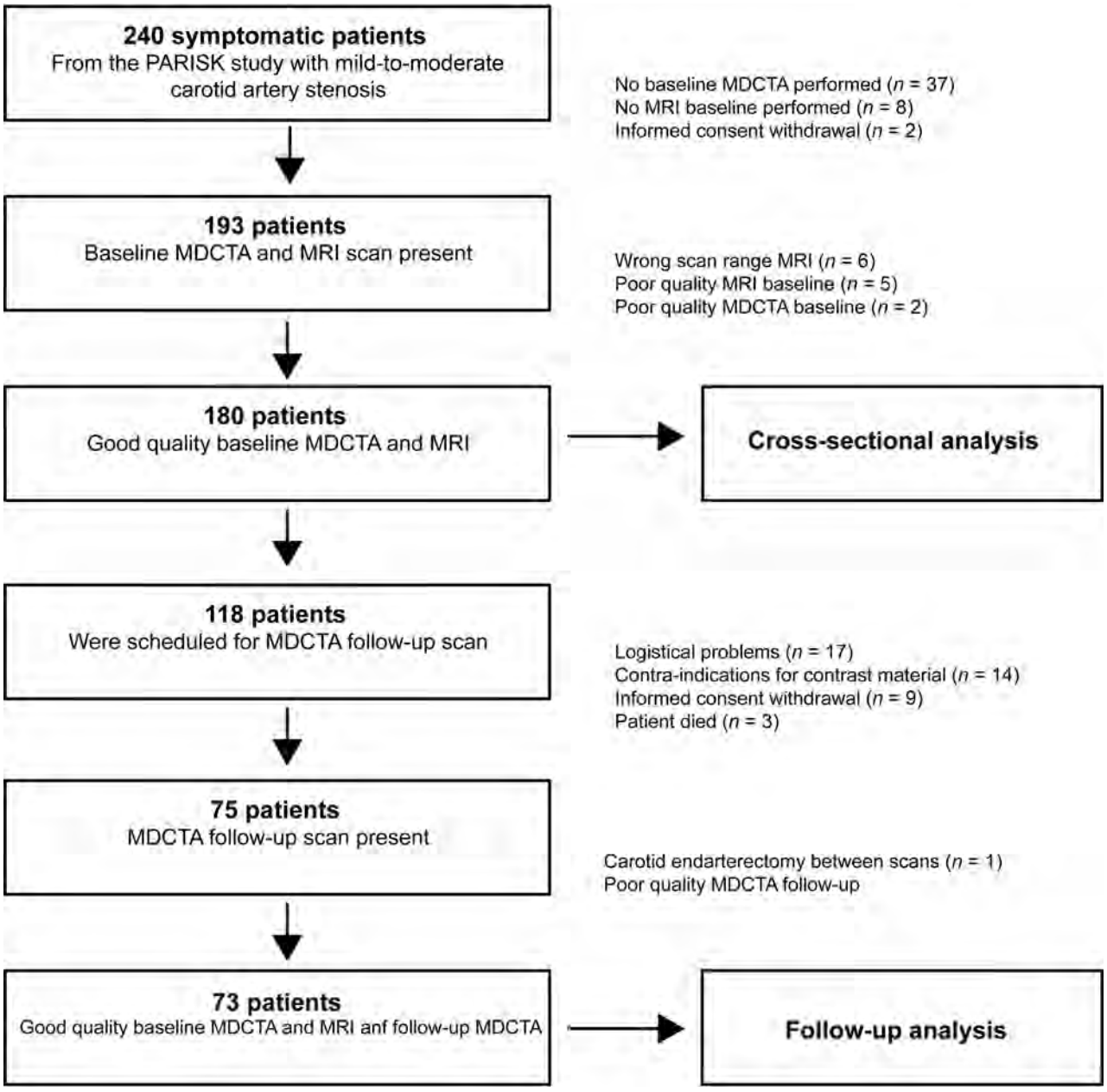

FIG 1. Flow diagram explaining the reasons for exclusion of a number of carotid arteries in the final data analysis.

days). The median time between MDCTA and MR imaging baseline scans was 1 day (IQR, 1–25 days) (Table 1).

LRNC and IPH were present in 116 (64%) and 69 (38%) symptomatic carotid arteries, respectively. Most plaques (162, 90%) contained calcifications at baseline. A TRFC was present in 77 (43%) of the symptomatic carotid arteries.

Baseline Analysis

At baseline, 27% (49/180) of the patients had a plaque ulceration in the symptomatic carotid artery. Imaging characteristics of the carotid arteries with and without plaque ulceration are shown in Table 2. Increased total vessel volume, wall volume, and lumen stenosis were associated with the presence of ulcerations at baseline. LRNC, IPH presence, and TRFC were also associated with ulcerated plaques. Moreover, a higher relative LRNC volume and IPH volume were associated with ulcerations at baseline. Results of binary logistic regression and receiver operating characteristic analysis for significant associations are shown in Table 2.

After we adjusted for wall volume, LRNC and IPH presence (as dichotomous variable) were no longer significantly related to the presence of plaque ulceration (OR = 1.5; 95% CI, 0.6–3.3 and OR = 1.6; 95% CI, 0.8–3.4, respectively), but the TRFC remained significantly associated with plaque ulceration at baseline (OR = 2.4; 95% CI, 1.2–5). After we adjusted for wall volume, relative LRNC volume and IPH volume remained significantly related to the presence of plaque ulceration (OR = 1.5; 95% CI, 1.1–1.9 and OR = 1.5; 95% CI, 1.1–2.0, respectively). Additional adjustment for all known risk factors did not change the found associations for relative LRNC volume and IPH volume (OR = 1.5; 95% CI, 1.1–1.9 and OR = 1.5; 95% CI, 1.1–2.1, respectively). The results

Table 1: The comparison of clinical characteristics and scan intervals between plaques with and without an ulcer at baseline[a]

	All Baseline ($n = 180$)	Ulcer Baseline Absent ($n = 131$)	Ulcer Baseline Present ($n = 49$)	*P* Value
Characteristics				
Age (yr)	68 (63–73)	68 (62–73)	69 (64–73)	.41
Sex (male)	127 (71%)	122 (70%)	5 (83%)	.67
BMI (kg/m^2)	26 (24–29)	25 (24–29)	27 (24–29)	.45
Classification event				0.01
TIA	76 (42%)	64 (49%)	12 (25%)	
Stroke	85 (47%)	54 (41%)	31 (63%)	
Amaurosis fugax	19 (11%)	13 (10%)	6 (12%)	
Hypertension	117 (65%)	85 (65%)	32 (65%)	1.00
Hypercholesterolemia	140 (78%)	101 (77%)	39 (80%)	.84
Diabetes mellitus	42 (23%)	35 (27%)	7 (14%)	.11
Current smoker	43 (24%)	35 (27%)	8 (16%)	.17
Interval event/MDCTA (days)	34 (15–55)	36 (16–53)	35 (13–59)	.85
Interval event/MR imaging (days)	47 (30–67)	46 (30–67)	48 (28–69)	.87
Interval MDCTA/MR imaging (days)	1 (1–25)	1 (1–27)	1 (1–17)	.70

Note:—BMI indicates body mass index.
[a] Data are median (IQR) or No. (%).

Table 2: Characteristics of plaques with and without an ulcer at baseline

	Ulcer Absent ($n = 131$) Median (IQR) or No. (%)	Ulcer Present ($n = 49$) Median (IQR) or No. (%)	Binary Logistic Regression OR (95% CI)	ROC Analysis AUC (95% CI)
NASCET (%)	8 (0–29)	21 (0–37)	1.01 (1.00–1.03)	0.61 (0.52–0.71)
ECST (%)	55 (45–65)	59 (48–70)	1.02 (1.00–1.05)	
Minimal diameter (mm)	4 (3.3–4.9)	3.4 (2.8–4.7)	0.06 (0.00–1.00)	0.40 (0.30–0.50)
Total vessel volume (cm^3)	1.41 (1.16–1.64)	1.60 (1.29–2.12)	4.9 (2.1–11.4)	0.64 (0.54–0.74)
Lumen volume (cm^3)	0.56 (0.45–0.72)	0.58 (0.46–0.80)	2.8 (0.6–12.1)	
Wall volume (cm^3)	0.85 (0.70–0.98)	1.02 (0.77–1.28)	12.1 (3.5–42.0)	0.67 (0.58–0.77)
% Wall volume	59 (53–66)	61 (57–68)	1.01 (0.99–1.04)	
LRNC presence	78 (60%)	38 (78%)	2.4 (1.1–5.0)	0.59 (0.50–0.68)
% LRNC volume	1 (0–10)	15 (1–31)	1.7 (1.3–2.2)	0.70 (0.60–0.79)
IPH presence	42 (32%)	27 (55%)	2.6 (1.3–5.1)	0.61 (0.52–0.71)
% IPH volume	0 (0–3)	5 (0–23)	1.7 (1.3–2.2)	0.67 (0.56–0.76)
Calcifications presence MR imaging	118 (90%)	44 (90%)	0.97 (0.33–2.88)	
% Calcifications volume MR imaging	5 (2–8)	3 (1–7)	0.73 (0.50–1.07)	
Calcification presence MDCTA	117 (89%)	45 (92%)	0.74 (0.23–2.38)	
Calcification absolute volume MDCTA (mm^3)	31.4 (4.3–80.4)	15.8 (2.8–51.9)	0.99 (0.999–1.002)	
Thin-or-ruptured FC	45 (34%)[a,b]	32 (65%)	3.4 (1.7–6.7)	0.65 (0.56–0.74)

Note:—FC indicates fibrous cap.
[a] Four were missing.
[b] Four had bad quality.

did not change after adjustment for time intervals among the following: 1) event to MDCTA baseline, 2) event to MR imaging baseline, and 3) MDCTA baseline to MR imaging baseline.

Follow-Up Analysis

A total of 73 patients were eligible for prospective analysis. The time period between the baseline and follow-up MDCTA scans was 25 ± 2 months. An ulceration at baseline was present in 19 of the 73 symptomatic plaques (26%). Most (81%; 59 of the 73 plaques) of the plaque surfaces remained unchanged: Fifty-one plaques had no ulceration at baseline and follow-up, and 8 plaques had a persistent ulceration at baseline and follow-up. Of the 14 symptomatic plaques that changed during follow-up, 8 ulcers were present at baseline and disappeared after 2 years (Fig 2). In the other 6 plaques (8%), a new ulcer developed at 2-year follow-up: A new ulceration was seen in 2 plaques with an ulceration at baseline; a new ulceration was seen in a plaque with an ulceration at baseline that disappeared at follow-up; and a new ulceration was seen in 3 plaques without an ulceration at baseline. Figure 2 illustrates an example of a new ulcer development.

All 6 plaques that developed a new ulcer contained LRNC, IPH, calcifications, and a TRFC at baseline. The prevalence of IPH and a TRFC at baseline was significantly higher in plaques with a new ulcer at follow-up than in plaques without one (100% versus 31%; $P = .002$ and 100% versus 42%; $P = .009$, respectively) (Table 3). Plaques that developed a new ulceration had a slightly greater wall volume (1.04 cm^3 [IQR, 0.97–1.16 cm^3] versus 0.86 cm^3 [IQR, 0.73–1.00 cm^3]; $P = .029$), a higher relative LRNC volume (23% [IQR, 13–31%] versus 2% [IQR, 0–14%]; $P = .002$), and a higher relative IPH volume (14% [IQR, 8–24%] versus 0% [IQR, 0–5%;

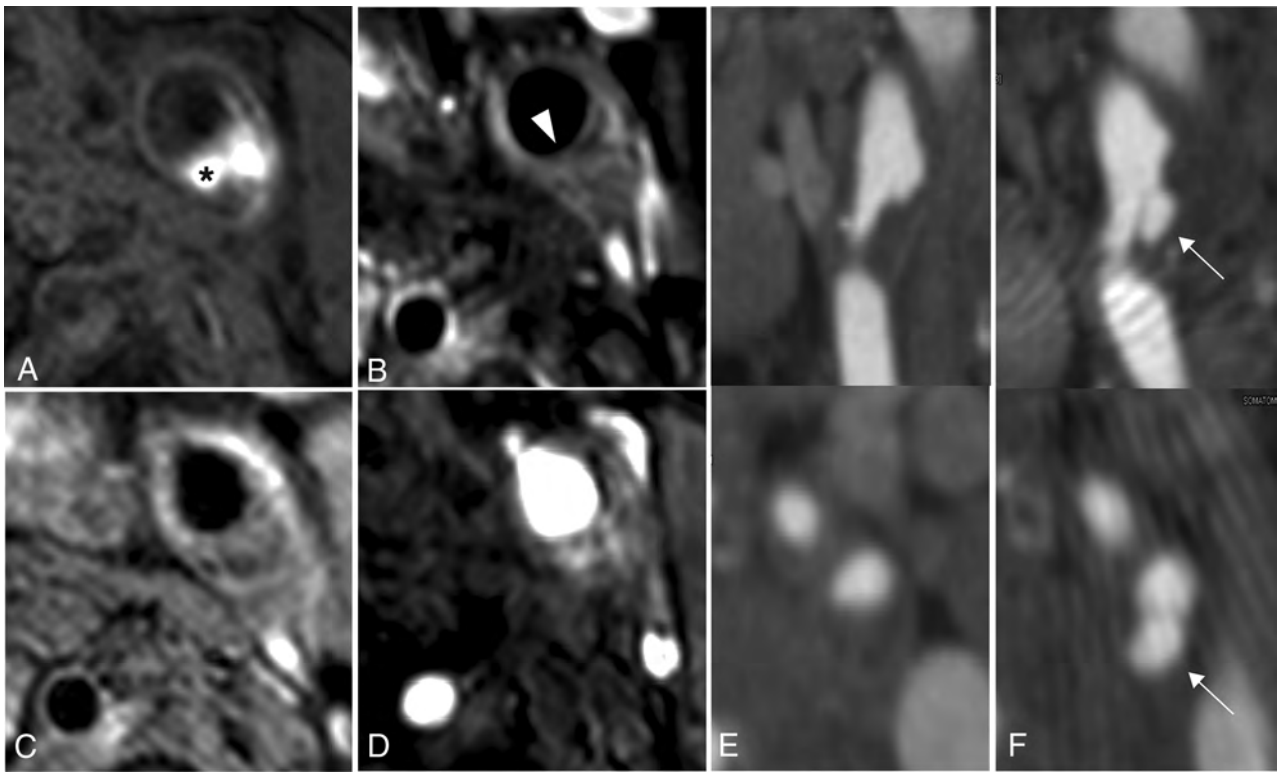

FIG 2. Ulceration development during follow-up and plaque composition at baseline of a 56-year-old female patient. MR imaging of carotid plaque proximal to the ulceration: precontrast T1-weighted turbo field echo sequence (*A*), postcontrast T1-weighted quadruple inversion recovery TSE sequence (*B*), T2-weighted TSE sequence (*C*), time-of-flight sequence (*D*), and MDCTA of irregular plaque at baseline (*E*) and of ulceration at 2-year follow-up (*F*). The *asterisk* marks the intraplaque hemorrhage. The *white arrowhead* points to thin-or-ruptured fibrous cap. *White arrows* point to the ulceration.

Table 3: Characteristics of plaques with and without a new ulceration at 2-year follow-up[a]

	New Ulceration Absent (*n* = 67)	New Ulceration Present (*n* = 6)	*P* Value
NASCET (%)	16 (0–34)	11 (0–34)	.95
ECST (%)	57 (47–68)	62 (53–71)	.45
Minimal diameter (mm)	3.8 (2.8–4.6)	3.4 (2.9–4.8)	.80
Total vessel volume (cm^3)	1.49 (1.2–1.75)	1.61 (1.53–1.87)	.17
Lumen volume (cm^3)	0.54 (0.44–0.77)	0.59 (0.55–0.69)	.43
Wall volume (cm^3)	0.86 (0.73–1.00)	1.04 (0.97–1.16)	.029
% Wall volume	60 (52–67)	64 (59–67)	.37
LRNC presence	41 (61%)	6 (100%)	.08
% LRNC volume	2 (0–14)	23 (13–31)	.002
IPH presence	21 (31%)	6 (100%)	.002
% IPH volume	0 (0–5)	14 (8–24)	<.001
Calcifications presence MR imaging	63 (94%)	6 (100%)	1.00
% Calcifications volume MR imaging	5 (3–8)	6 (2–9)	.79
Calcifications presence MDCTA	60 (90%)	5 (83%)	.52
Calcifications, absolute volume MDCTA (mm^3)	32.0 (7.0–100.3)	1.9 (0.8–91.3)	.15
Thin-or-ruptured FC	28 (42%)	6 (100%)	.009

Note:—FC indicates fibrous cap.
[a] Data are median (IQR) or No. (%).

$P < 0.001$) (Table 3). Receiver operating characteristic analysis showed that the wall volume was a fair classifier (AUC = 0.77 [95% CI, 0.66–0.88]), and the relative LRNC and IPH volumes were both strong classifiers for new ulcer development (AUC = 0.87 [95% CI, 0.77–0.97] and AUC = 0.88 [95% CI, 0.79–0.97], respectively).

DISCUSSION

This cross-sectional, prospective, multicenter study of symptomatic patients with mild-to-moderate carotid artery stenosis showed that the presence and development of atherosclerotic plaque ulcerations are associated with large plaque volume and a high content of LRNC and IPH. This finding confirms that plaque composition is an important risk factor for plaque rupture, even in plaques without significant lumen stenosis. The relation between plaque composition and plaque rupture helps to better understand the pathophysiologic pathway from atherosclerosis to a cerebral ischemic event.

Previous studies have mainly focused on the relation between vulnerable plaque components and ischemic events.[8,10] The current view on the pathophysiology of cerebrovascular ischemic events due to atherosclerosis is

first the development of plaques with a specific composition, which makes the plaque more vulnerable to plaque rupture. Rupture may result in embolization of plaque material to the intracranial circulation, which occludes the vessel and causes symptoms. More important is the formation of thrombus on a plaque rupture, resulting in embolization of thrombus into the intracranial circulation. Ischemic events are more frequently caused by this pathway than by reduced blood flow or blood pressure due to significant luminal stenosis because most events occur in atherosclerotic carotid disease without severe stenosis. Despite knowledge about this cascade leading to events, the relation between plaque composition and atherosclerotic plaque rupture has hardly been investigated in vivo. Understanding the pathophysiology of atherosclerotic plaque rupture can support the development of preventive strategies of medical treatment that affect the vulnerable components of the plaque and thereby the risk of ischemic stroke. It could also be used to optimize patient selection for carotid endarterectomy on the basis of screening for vulnerable plaque composition.

The results of the current cross-sectional analysis are in line with previous cross-sectional studies. The first study linking plaque ulceration to plaque composition was performed by Lovett et al,[21] who analyzed carotid artery specimens obtained during endarterectomy and demonstrated that angiographic ulcerations were associated with IPH and a large LRNC. Since then, several cross-sectional studies reported similar associations between plaque composition based on imaging and plaque ulceration. Both Homburg et al,[19]and Saba et al[20] found, using CT of the plaque, that relative LRNC content was associated with plaque ulceration, whereas calcification proportion was inversely associated with plaque ulceration. A pilot study of the PARISK study demonstrated a relation and colocalization between IPH and disrupted plaque surface.[18] The current study confirmed these findings and also that wall volume is a strong confounder of the relationship between plaque composition and plaque ulceration. After we adjusted for wall volume, IPH and a large LRNC remained significantly associated with ulceration. However, longitudinal studies are needed to prove a real link between plaque composition and plaque ulceration.

Underhill et al[22] found, in a longitudinal study, results similar to ours: a higher percentage wall area, relative LRNC volume, and the presence of LRNC and IPH being predictive of plaque rupture. Nevertheless, our study differs from theirs in some aspects. First, our imaging protocol was different. In contrast to their MR imaging protocol, we used a postcontrast sequence that improves LRNC detection[30] and a heavily T1-weighted TFE sequence, which proved to be optimal for the detection of IPH.[31,32] We were able to evaluate IPH volumes instead of the presence of IPH only. Second, we used different imaging modalities to establish the presence of ulcerations. Underhill et al used MR imaging and defined plaque rupture as plaque ulceration and/or fibrous cap rupture. We defined plaque rupture as the presence of plaque ulceration only using MDCTA. Wu et al[33] demonstrated findings similar to ours by establishing a relationship between carotid artery score, which is mainly a reflection of the extent of LRNC in the plaque, and incident disrupted luminal surface.

Our study has limitations. Because of a relatively small study population that underwent follow-up imaging and a low incidence of ulcerations, multivariable analysis in the longitudinal analysis with adjustment for wall volume could not be performed.

Despite a low ulcer incidence at follow-up, very significant differences were found between plaques with and without a newly developed ulcer. Therefore, we are convinced that meaningful conclusions could be drawn regarding the relation between plaque composition and plaque ulceration risk. Furthermore, it could also be relevant to analyze the atherosclerotic plaque at the asymptomatic contralateral side. However, we did not analyze the asymptomatic artery for 2 reasons. First, the presence of plaque ulcerations at baseline CTA for an asymptomatic artery was low: Only 9% (17/180) of the asymptomatic arteries visualized by MDCTA had an ulcer at baseline. Moreover, none of the asymptomatic arteries developed a new ulcer after 2-year follow-up. Furthermore, the PARISK study focused the imaging examinations on the symptomatic side. Due to this focus, the contralateral artery was not imaged completely with MR imaging because the alignment of the scan range was performed with the symptomatic artery. This situation resulted in a lower number of asymptomatic arteries eligible for analysis.

A strength of our study is that we combined MDCTA and MR imaging to accurately assess plaque composition with MR imaging and plaque ulceration with MDCTA. Moreover, we used a standard MR imaging range for evaluation of plaque geometry volumes and plaque component volumes. A total of 9 slices was used in the final volume calculations, consisting of the same number of slices in the ICA and the common carotid artery. Therefore, the relative volumes are not biased because of different scan ranges, which may include different lengths of the common carotid artery and ICA. In addition, we noticed that all 6 new ulcerations at follow-up developed within this scan range. Finally, our population had a mild-to-moderate stenosis in contrast to previous studies that mainly focused on severe stenotic arteries, in which carotid endarterectomy was proved to be beneficial. Potentially, patients with mild stenosis and a high-risk plaque may also benefit from carotid endarterectomy, and the number needed to treat in patients with moderate stenosis can probably be improved.

CONCLUSIONS

The presence and development of plaque ulcerations are associated with large atherosclerotic plaques and a high content of IPH and a LRNC. Identification of predictors for plaque ulceration may prove clinically valuable for preventing plaque rupture and possible recurrent stroke.

ACKNOWLEDGMENTS

We wish to thank Burhan Hussain for the plaque surface morphology score on MDCTA at baseline.

Disclosures: Kristine Dilba—*RELATED: Support for Travel to Meetings for the Study or Other Purposes*: Toegepaste en Technische Wetenschappen, grant No. 10813 (Stichting Technische Wetenschappen, Dutch Research Council, the Netherlands).* Mohamed Kassem—*RELATED*: *Grant*: The Dutch Research Council, *Comments*:

Hestia Impulse. Paul J. Nederkoorn—*UNRELATED*: *GRANTS*: Dutch Heart Foundation and Netherlands Health Organisation. M. Eline Kooi—*RELATED*: *Grant*: Center for Translational Molecular Medicine PARISK*; *UNRELATED*: *Employment*: Maastricht University Medical Center; *Grants/Grants Pending*: Dutch Research Council, Horizon 2020 Initial Training Networks, Stichting De Weijerhorst*; *Travel/Accommodations/Meeting Expenses Unrelated to Activities Listed*: American Heart Association stroke conference, Society for Magnetic Resonance Angiography meeting, Le Fil Rouge meeting, symposium European Society for Cardiology, *Comments*: I am regularly invited as a speaker, and part of my expenses are reimbursed.* Jolanda J. Wentzel—*RELATED*: *Grant*: Toegepaste en Technische Wetenschappen, *Comments*: grant for the salary of K. Dilba, grant No. STW 10813.* Anouk C. van Dijk—*RELATED*: *Grant*: Center for Translational Molecular Medicine, Dutch Heart Foundation, *Comments*: This research was performed within the framework of the Center for Translational Molecular Medicine (www.ctmm.nl), project PARISK (Plaque At RISK; grant 01C-202) and supported by the Dutch Heart Foundation.* *Money paid to the institution.

REFERENCES

1. Petty GW, Brown RD Jr, Whisnant JP, et al. **Ischemic stroke subtypes: a population-based study of incidence and risk factors.** *Stroke* 1999;30:2513–16 CrossRef Medline
2. Imbesi SG, Kerber CW. **Why do ulcerated atherosclerotic carotid artery plaques embolize? A flow dynamics study.** *AJNR Am J Neuroradiol* 1998;19:761–66 Medline
3. **Randomised trial of endarterectomy for recently symptomatic carotid stenosis: final results of the MRC European Carotid Surgery Trial (ECST).** *Lancet* 1998;351:1379–87 Medline
4. Qureshi AI, Alexandrov AV, Tegeler CH, et al; Society of Vascular and Interventional Neurology. **Guidelines for screening of extracranial carotid artery disease: a statement for healthcare professionals from the multidisciplinary practice guidelines committee of the American Society of Neuroimaging; cosponsored by the Society of Vascular and Interventional Neurology.** *J Neuroimaging* 2007;17:19–47 CrossRef Medline
5. Rothwell PM, Eliasziw M, Gutnikov SA, et al. **Analysis of pooled data from the randomised controlled trials of endarterectomy for symptomatic carotid stenosis.** *Lancet* 2003;361:107–16 CrossRef Medline
6. North American Symptomatic Carotid Endarterectomy Trial Collaborators, et al. **Beneficial effect of carotid endarterectomy in symptomatic patients with high-grade carotid stenosis.** *N Engl J Med* 1991;325:445–53 Medline
7. **Carotid Surgery Trial: interim results for symptomatic patients with severe (70–99%) or with mild (0–29%) carotid stenosis—European Carotid Surgery Trialists' Collaborative Group**. *Lancet* 1991;337:1235–43 Medline
8. Zhao H, Zhao X, Liu X, et al. **Association of carotid atherosclerotic plaque features with acute ischemic stroke: a magnetic resonance imaging study.** *Eur J Radiol* 2013;82:e465-70 CrossRef Medline
9. Takaya N, Yuan C, Chu B, et al. **Association between carotid plaque characteristics and subsequent ischemic cerebrovascular events: a prospective assessment with MRI—initial results.** *Stroke* 2006;37:818–23 CrossRef Medline
10. Altaf N, Daniels L, Morgan PS, et al. **Detection of intraplaque hemorrhage by magnetic resonance imaging in symptomatic patients with mild to moderate carotid stenosis predicts recurrent neurological events.** *J Vasc Surg* 2008;47:337–42 CrossRef Medline
11. Gupta A, Baradaran H, Schweitzer AD, et al. **Carotid plaque MRI and stroke risk: a systematic review and meta-analysis.** *Stroke* 2013;44:3071–77 CrossRef Medline
12. Schindler A, Schinner R, Altaf N, et al. **Prediction of stroke risk by detection of hemorrhage in carotid plaques: meta-analysis of individual patient data.** *JACC Cardiovasc Imaging* 2020;13(2 Pt 1):395–406 CrossRef Medline
13. Brinjikji W, Rabinstein AA, Lanzino G, et al. **Ultrasound characteristics of symptomatic carotid plaques: a systematic review and meta-analysis.** *Cerebrovasc Dis* 2015;40:165–74 CrossRef Medline
14. Eliasziw M, Streifler JY, Fox AJ, et al. **Significance of plaque ulceration in symptomatic patients with high-grade carotid stenosis: North American Symptomatic Carotid Endarterectomy Trial.** *Stroke* 1994;25:304–08 CrossRef Medline
15. Cai JM, Hatsukami TS, Ferguson MS, et al. **Classification of human carotid atherosclerotic lesions with in vivo multicontrast magnetic resonance imaging.** *Circulation* 2002;106:1368–73 CrossRef Medline
16. Rafailidis V, Chryssogonidis I, Tegos T, et al. **Imaging of the ulcerated carotid atherosclerotic plaque: a review of the literature.** *Insights Imaging* 2017;8:213–25 CrossRef Medline
17. Anzidei M, Napoli A, Zaccagna F, et al. **Diagnostic accuracy of colour Doppler ultrasonography, CT angiography and blood-pool-enhanced MR angiography in assessing carotid stenosis: a comparative study with DSA in 170 patients** (in Italian). *Radiol Med* 2012;117:54–71 CrossRef Medline
18. van Dijk AC, Truijman MT, Hussain B, et al. **Intraplaque hemorrhage and the plaque surface in carotid atherosclerosis: the Plaque At RISK Study (PARISK).** *AJNR Am J Neuroradiol* 2015;36:2127–33 CrossRef Medline
19. Homburg PJ, Rozie S, van Gils MJ, et al. **Association between carotid artery plaque ulceration and plaque composition evaluated with multidetector CT angiography.** *Stroke* 2011;42:367–72 CrossRef Medline
20. Saba L, Sanfilippo R, Sannia S, et al. **Association between carotid artery plaque volume, composition, and ulceration: a retrospective assessment with MDCT.** *AJR Am J Roentgenol* 2012;199:151–56 CrossRef Medline
21. Lovett JK, Gallagher PJ, Hands LJ, et al. **Histological correlates of carotid plaque surface morphology on lumen contrast imaging.** *Circulation* 2004;110:2190–97 CrossRef Medline
22. Underhill HR, Yuan C, Yarnykh VL, et al. **Predictors of surface disruption with MR imaging in asymptomatic carotid artery stenosis.** *AJNR Am J Neuroradiol* 2010;31:487–93 CrossRef Medline
23. Xu D, Hippe DS, Underhill HR, et al. **Prediction of high-risk plaque development and plaque progression with the carotid atherosclerosis score.** *JACC Cardiovasc Imaging* 2014;7:366–73 CrossRef Medline
24. Truijman MT, Kooi ME, van Dijk AC, et al. **Plaque At RISK (PARISK): prospective multicenter study to improve diagnosis of high-risk carotid plaques.** *Int J Stroke* 2014;9:747–54 CrossRef Medline
25. **North American Symptomatic Carotid Endarterectomy Trial: methods, patient characteristics, and progress.** *Stroke* 1991;22:711–20 CrossRef Medline
26. de Weert TT, Cakir H, Rozie S, et al. **Intracranial internal carotid artery calcifications: association with vascular risk factors and ischemic cerebrovascular disease.** *AJNR Am J Neuroradiol* 2009;30:177–84 CrossRef Medline
27. Kwee RM, Teule GJ, van Oostenbrugge RJ, et al. **Multimodality imaging of carotid artery plaques: 18F-fluoro-2-deoxyglucose positron emission tomography, computed tomography, and magnetic resonance imaging.** *Stroke* 2009;40:3718–24 CrossRef Medline
28. Cappendijk VC, Heeneman S, Kessels AG, et al. **Comparison of single-sequence T1WI TFE MRI with multisequence MRI for the quantification of lipid-rich necrotic core in atherosclerotic plaque.** *J Magn Reson Imaging* 2008;27:1347–55 CrossRef Medline
29. Kwee RM, van Engelshoven JM, Mess WH, et al. **Reproducibility of fibrous cap status assessment of carotid artery plaques by contrast-enhanced MRI.** *Stroke* 2009;40:3017–21 CrossRef Medline
30. Takaya N, Cai J, Ferguson MS, et al. **Intra- and interreader reproducibility of magnetic resonance imaging for quantifying the lipid-rich necrotic core is improved with gadolinium contrast enhancement.** *J Magn Reson Imaging* 2006;24:203–10 CrossRef Medline
31. Cappendijk VC, Cleutjens KB, Heeneman S, et al. **In vivo detection of hemorrhage in human atherosclerotic plaques with magnetic resonance imaging.** *J Magn Reson Imaging* 2004;20:105–10 CrossRef Medline
32. Bitar R, Moody AR, Leung G, et al. **In vivo 3D high-spatial-resolution MR imaging of intraplaque hemorrhage.** *Radiology* 2008;249:259–67 CrossRef Medline
33. Wu Z, Yang C, Tang D. **In vivo serial MRI-based models and statistical methods to quantify sensitivity and specificity of mechanical predictors for carotid plaque rupture: location and beyond.** *J Biomech Eng* 2011;133:064503 CrossRef Medline

Imaging Parameters of the Ipsilateral Medial Geniculate Body May Predict Prognosis of Patients with Idiopathic Unilateral Sudden Sensorineural Hearing Loss on the Basis of Diffusion Spectrum Imaging

Y. Zhang, Z. Zhang, X. Jia, X. Guan, Y. Lyu, J. Yang, and T. Jiang

ABSTRACT

BACKGROUND AND PURPOSE: Idiopathic sudden sensorineural hearing loss is an acute unexplained onset of hearing loss. We examined the central auditory pathway abnormalities in patients with unilateral idiopathic sudden sensorineural hearing loss using diffusion spectrum imaging and the relationships between hearing recovery and diffusion spectrum imaging parameters.

MATERIALS AND METHODS: Forty-eight patients with unilateral idiopathic sudden sensorineural hearing loss with a duration of ≤2 weeks (range, 8.9 ± 4.3 days) and 20 healthy subjects underwent diffusion spectrum imaging tractography. Hearing levels were evaluated using a pure-tone average at initial presentation and 3-month follow-up. Clinical characteristics and MR imaging findings were assessed.

RESULTS: Compared with healthy control subjects, the generalized fractional anisotropy values of patients decreased significantly in the bilateral posterior limbs of the internal capsule, with no differences between the ipsilateral and contralateral sides. The quantitative anisotropy values decreased in the Brodmann area 41, contralateral medial geniculate body, bilateral lateral lemniscus, anterior limb of internal capsule, middle temporal gyrus, and anterior corona radiata. Furthermore, at 3-month follow-up, 14 patients had <15 dB of hearing gain. Receiver operating characteristic curve analysis demonstrated that generalized fractional anisotropy in the ipsilateral medial geniculate body was related to prognosis (sensitivity = 64.7%; specificity = 85.7%; area under the curve = 0.796, 95% CI, 0.661–0.931; $P < .01$).

CONCLUSIONS: Diffusion spectrum imaging can detect abnormalities of white matter microstructure along the central auditory pathway in patients with unilateral idiopathic sudden sensorineural hearing loss. The generalized fractional anisotropy value of the ipsilateral medial geniculate body may help to predict recovery outcomes.

ABBREVIATIONS: DSI = diffusion spectrum imaging; FA = fractional anisotropy; GFA = generalized fractional anisotropy; ISSHL = idiopathic sudden sensorineural hearing loss; MGB = medial geniculate body; QA = quantitative anisotropy

Hearing plays a crucial role in communication with the outside world. Idiopathic sudden sensorineural hearing loss (ISSHL) is an acute unexplained onset of hearing loss from a cochlear or retrocochlear origin.[1,2] Sudden sensorineural hearing loss affects approximately 5–27 per 100,000 people annually, and the incidence has increased across recent decades.[3,4] Viral infections, cochlear ischemia, autoimmune processes, and metabolic derangement have been proposed as potential etiologies. Treatment options include steroids and other medications, hyperbaric oxygen therapy, and other complementary and alternative treatments. However, selection of treatments may be difficult due to the variety of possible etiologies.[2] Additionally, the hearing prognosis in individual cases is quite uncertain.

High-resolution MR imaging can detect the pathologic changes in the inner ear and the cochlea, providing new insights into the etiology of ISSHL.[5] A number of studies have examined the prognostic value of white matter abnormalities in hearing loss using T2WI or FLAIR sequences with conflicting results.[6,7] White matter microstructural changes along the auditory pathway have not been well-evaluated, but DTI is becoming a method to study the central auditory pathways.[8,9] DTI is sensitive to the highly directional structure

Received March 30, 2020; accepted after revision August 29.

From the Departments of Hyperbaric Oxygen (Y.Z., J.Y.) and Radiology (Z.Z., X.J., Y.L., T.J.), Beijing Chaoyang Hospital, and Department of Radiology (X.G.), Beijing Shijitan Hospital, Capital Medical University, Beijing, China.

Y. Zhang and Z. Zhang are joint first authors.

This study was funded by Beijing Science and Technology Program (Z161100000116067).

Please address correspondence to Jing Yang, MD, Beijing Chaoyang Hospital, 8 Gongren Tiyuchang Nanlu, Chaoyang District, Beijing, CN 100020; e-mail: BJCY1hospitalHBO@126.com

Indicates open access to non-subscribers at www.ajnr.org
Indicates article with supplemental online table.

http://dx.doi.org/10.3174/ajnr.A6874

of white matter, which can reflect the structural or functional changes of white matter. Fractional anisotropy (FA), as a DTI parameter, is considered a marker of fiber tract integrity. On the basis of a recent systematic review, white matter changes can be detected by DTI in patients with sensorineural hearing loss.[10] However, DTI needs larger sample sizes for standardization, and the spatial resolution limits the further use of DTI in the auditory pathway. By contrast, diffusion spectrum imaging (DSI) generalizes DTI by acquiring more directions in *q*-space, either by high-angular-resolution diffusion imaging shells, a cube on a Cartesian grid, or Q-ball imaging.[11] Also compared with DTI, DSI can provide a better estimate of areas of crossing or kissing fibers, demyelination, and axonal remodeling.[12]

The aim of the present study was to investigate the value of DSI in detecting microstructural abnormalities of the central auditory pathway in patients with ISSHL and to assess the correlations between clinical outcomes and DSI parameters.

MATERIALS AND METHODS

Subjects

The study included 48 patients with unilateral ISSHL. The duration was ≤2 weeks with mild-to-profound hearing loss. All subjects were inpatients between January 2018 and October 2019 and were diagnosed by an otolaryngologist. The inclusion criteria were as follows: the presence of an unexplained unilateral sensorineural hearing loss of ≥30 dB in at least 3 contiguous audiometric frequencies that developed within 3 days. The exclusion criteria were as follows: 1) a history of Ménière disease, otitis media, or cholesteatoma; 2) history of cerebral infarction; 3) existing anatomic abnormality of the inner ear and auditory pathway; 4) previous otologic surgery; 5) systemic ototoxic drug therapy; 6) images with motion artifacts or patients who cannot tolerate MR imaging; and 7) failure to obtain a 3-month follow-up. As healthy controls, 20 subjects with normal hearing (10 women, 10 men) without a history of neurologic disorders were recruited. This clinical study was approved by the ethics committee of Beijing Chaoyang Hospital, Capital Medical University (assurance No. 2016−88). Written informed consent was obtained before the examination.

Clinical Characteristics and Audiologic Evaluation

The demographic data and medical history of patients were collected. Pure-tone audiometry was evaluated at initial presentation and at 3-month follow-up. The pure-tone average was calculated as the average at 250, 500, 1000, 2000, 4000, and 8000 Hz. The severity of hearing loss was graded by the pure-tone average as follows: mild (≤40 dB), moderate (41−70 dB), severe (71−90 dB), or profound (≥91 dB) hearing loss. The audiogram shapes were classified into 4 subtypes: low-frequency type, high-frequency type, flat type, and profound type.[13]

Hearing recovery was classified according to the Siegel criteria, as follows:[1] 1) healing: final hearing level of ≤25 dB; 2) partial recovery: hearing gain of ≥15 dB and final hearing level of 25–45 dB; 3) slight recovery: hearing gain of ≥15 dB and final hearing level of ≥45 dB; and 4) no response: hearing gain of <15 dB or a final hearing threshold of >75 dB. Healing, partial, and slight recoveries were considered improvement.

Treatment Process

All patients with ISSHL were treated with the same protocol. Systemic steroid therapy was administered to each patient, involving 1 mg/kg/day (maximum, 60 mg) of oral prednisolone for the first 5−6 days.[13] Hyperbaric oxygen therapy was initiated within 14 days of onset and applied at a pressure of 2.0 atm for 60 minutes once daily. The use of other medicine was in accordance with the guidelines of the Chinese Medical Association of Otorhinolaryngology, Head and Neck Surgery.[13]

Image Acquisition and Processing

MR imaging was performed with a 3T Magnetom Prisma scanner (Siemens) using a 64-channel head coil. For structural MR imaging scans for anatomic reference, high-resolution anatomic MR imaging was performed using T1W1 with a rapid-acquisition gradient-echo. The details of the scan parameters are as follows: TE = 2.27 ms, TR = 2300 ms, flip angle = 8°, layer number = 208, voxel = 1.0 × 1.0 × 1.0 mm, and FOV = 256 × 256 mm. DSI data were collected using a twice-refocused spin-echo EPI sequence and multiple *q*-values (TE = 79 ms, TR = 7200 ms, FOV = 220 × 220 mm, voxel size = 2.2 × 2.2 × 2.2 mm^3, b maximum = 3000 s/mm^2, and 257 directions for a scan time of 15 minutes) as previously described.[14] For DSI data reconstruction, the study used a generalized *q*-sampling imaging reconstruction of the orientation distribution functions (discrete sampling direction = 362, average diffusion distance = 1.2 mm) as previously reported.[11] The space-normalization method was used in the CSF calibration to determine the location of CSF and to unify the diffusion amount relative to CSF as free-water diffusion.

Fiber tracking was conducted using DSIStudio (Johns Hopkins University). ROIs were selected in the auditory neural pathway, including the superior olivary nucleus, inferior colliculus, lateral lemniscus, medial geniculate bodies (MGB), anterior limb of the internal capsule, posterior limb of the internal capsule, Heschl gyrus, superior temporal gyrus, middle temporal and inferior temporal gyri, anterior corona radiata, posterior corona radiata, auditory radiation, and Brodmann areas 41 and 42. Fiber tractography was performed in multifiber orientations (step size in each orientation = 1.0 mm, minimum fiber length = 20 mm, turning-angle threshold = 60°), as reported.[15] The same method was adopted to determine the next moving direction if multiple fiber orientations existed, which involved the fiber orientation nearest to the incoming direction and a turning angle of <60°. The next moving directional estimate of each voxel was weighted by 20% of the previous incoming direction and 80% of the nearest fiber orientation, to smooth the tracks. This process was repeated until the quantified anisotropy (QA) of the fiber orientation was below the preset threshold (range, 0.13−0.17 depending on controls) or no fiber extended in the 60°-angle range. The image was standardized to match and correct the diffusion image in the Montreal Neurological Institute anatomic template.[16] An optical fiber-tracking algorithm based on Streamline Tracking Technique (https://www.mathworks.com/matlabcentral/fileexchange/34008-dti-fiber-tractography-streamline-tracking-technique) was then implemented, and the QA and generalized fractional anisotropy (GFA) parameters of each ROI were obtained by DSIStudio software.

Table 1: Demographic data, medical comorbidities, and audiometric characteristics

Study Characteristics	All Patients ($n = 48$)	Outcome		P Value
		Nonimprovement Group ($n = 14$)	Improvement Group ($n = 34$)	
Sex (%)				
Male	25 (52.1)	7 (28.0)	18 (72.0)	.85
Female	23 (47.9)	7 (30.4)	16 (69.6)	
Hypertension (%)				
Yes	17 (35.4)	5 (29.4)	12 (70.6)	.97
No	31 (64.6)	9 (29.0)	22 (71.0)	
Type 2 diabetes (%)				
Yes	10 (20.8)	2 (20.0)	8 (80.0)	.47
No	38 (79.2)	12 (31.6)	26 (68.4)	
Hyperlipidemia (%)				
Yes	15 (31.2)	4 (26.7)	11 (73.3)	.79
No	33 (68.8)	10 (26.3)	23 (69.7)	
Affected ear (%)				
Left	29 (60.4)	7 (24.1)	22 (75.9)	.34
Right	19 (39.6)	7 (36.8)	12 (63.2)	
Age (mean ± SD) (yr)	52.3 ± 10.8	53.5 ± 11.7	51.88 ± 10.5	.64
Duration (mean ± SD) (day)	8.9 ± 4.3	10.2 ± 5.0	8.4 ± 3.9	.17
PTA (mean ± SD) (dB)	64.3 ± 25.6	59.5 ± 26.1	75.93 ± 20.7	.10
Audiogram shape (%)				
Low-frequency	10 (20.8)	1 (10.0)	9 (90.0)	.45
High-frequency	11 (22.9)	4 (36.4)	7 (63.6)	
Flat	14 (29.2)	4 (28.6)	10 (71.4)	
Profound	13 (27.1)	5 (38.5)	8 (61.5)	
Hearing loss severity based on PTA (%)				
Mild (40 dB)	15 (31.3)	1 (6.7)	14 (93.3)	.12
Moderate (41–60 dB)	6 (12.5)	3 (50.0)	3 (50.0)	
Severe (61–90 dB)	18 (37.5)	7 (38.9)	11 (61.1)	
Profound (≥91 dB)	9 (18.7)	3 (33.3)	6 (66.7)	

Note:—PTA indicates pure-tone average.

Statistical Analysis

All statistical analyses were performed using statistical software (SPSS, Version 26.0; IBM). Quantitative data are described as mean ± SD. Categoric data are presented as frequencies. On the basis of data distribution, the Student t test or Mann-Whitney U test was used to compare means between the 2 groups, the paired-t test or Wilcoxon matched-pairs signed rank test was used to compare DSI parameters between both sides in the same subjects, and a 1-way ANOVA or the Kruskal-Wallis rank sum test was used to compare DSI parameters between both sides of patients with those in the healthy control group. Bonferroni correction for multiple testing was applied with a significance level of $P < .05/N$ (N equals the number of ROIs). The χ^2 test was used to compare categoric data. Receiver operating characteristic curves were plotted; then, the optimum cutoff points of GFA and QA were determined. The area under the curve was used as an estimation of diagnostic accuracy. A value of $P < .05$ was considered statistically significant.

RESULTS

Demographic and Audiometric Data

The demographic data, medical comorbidities, and audiometric characteristics are summarized in Table 1. In total, there were 48 patients with unilateral ISSHL, including 25 (52.1%) men and 23 (47.9%) women, with a mean age of 52.3 ± 10.8 years (range, 23–68 years). The mean duration between the onset of ISSHL and MR imaging was 8.9 ± 4.3 days (range, 1–14 days). The ISSHL was left-sided in 29 (60.4%) cases, while there were 19 (39.6%) right-sided cases. Hypertension (35.4%) was the most common medical comorbidity, followed by hyperlipidemia (31.2%) and type 2 diabetes (20.8%). The mean pure-tone average at onset presentation was 64.3 ± 25.6 dB (range, 30–110 dB), of which severe hearing loss (37.5%) was the most common finding, followed by mild (31.3%), extremely severe (18.7%), and moderate (12.5%) hearing loss. The audiogram shape was a low-frequency type in 20.8% of patients, a high-frequency type in 22.9%, a flat type in 29.2%, and a profound type in 27.1%.

On the basis of the hearing recovery at the end of the 3-month follow-up period, 48 patients were further divided into 2 groups: an improvement group (hearing gain of ≥15 dB, $n = 34$) and nonimprovement group (<15 dB of hearing gain, $n = 14$). However, there were no obvious differences in the above demographic and audiometric characteristics between the groups (Table 1).

Characteristics of DSI Parameter Changes in Unilateral ISSHL

The DSI parameters (GFA, QA) of 20 healthy, age-matched control subjects (range, 27–60 years of age; mean age, 47.9 ± 12.5 years; $P = .089$) are shown in Table 2. There were no obvious differences in DSI parameters between the left and right sides of healthy subjects in any of the 13 ROIs. Therefore, a mean value of the left and right sides for each healthy subject in each of the ROIs was used for comparison with patients with unilateral ISSHL.

Differences in DSI Parameters between Patients with Unilateral ISSHL and Healthy Subjects

The DSI tractography parameters of patients with unilateral ISSHL and healthy subjects, including QA and GFA for each ROI, are shown in Tables 3 and 4.

Compared with the heathy control group, the GFA values of patients with unilateral ISSHL significantly decreased only in the bilateral posterior limb of the internal capsule ($P < .01$, $P < .05$ after Bonferroni correction). In addition, there was no obvious difference between the ipsilateral and contralateral sides.

The QA values significantly decreased in Brodmann area 41, the contralateral MGB, bilateral lateral lemniscus, anterior limb of the internal capsule, middle temporal gyrus, and anterior corona radiata compared with the healthy control subjects ($P < .01$, $P < .05$ after Bonferroni correction). Furthermore, obvious differences between the ipsilateral and contralateral sides were found in none of the above sites.

Differences in QA and GFA between Both Sides of the Same Patient

This study also compared these DSI parameters between both sides of each patient in the different outcome groups (Online Table). In the nonimprovement group, neither GFA nor QA values were different on either side of each patient. By contrast, in the improvement group, the GFA values of the ipsilateral MGB and lateral lemniscus were significantly higher than the contralateral parameters of the same patient ($P < .05$ after Bonferroni correction).

Prognostic Value of DSI Parameters

The prognostic values of QA and GFA in the different ROIs are shown in the Online Table. Compared with the nonimprovement group, the GFA value of the ipsilateral MGB was higher in the improvement group ($P < .05$ after Bonferroni correction). The fiber-tracking image of MGB is shown in Fig 1. According to receiver operating characteristic curves, the GFA of the ipsilateral MGB had a cutoff point of 0.0967 based on the Youden Index, an area under the curve of 0.796 (95% CI, 0.661–0.931; $P = .001$), sensitivity of 64.7%, and specificity of 85.7% (Fig 2).

Table 2: Characteristics of diffusion spectrum imaging parameters in healthy subjects[a]

ROIs	Parameters	Left Side	Right Side	*P* Value
Superior olivary nucleus	QA	0.6725 ± 0.0783	0.6584 ± 0.0910	.55
	GFA	0.0902 ± 0.0062	0.0896 ± 0.0081	.64
Inferior colliculus	QA	0.6531 ± 0.0800	0.6463 ± 0.0827	.76
	GFA	0.0936 ± 0.0052	0.0943 ± 0.0055	.41
Medial geniculate body	QA	0.6324 ± 0.0814	0.6327 ± 0.0923	.98
	GFA	0.0990 ± 0.0083	0.0968 ± 0.0077	.26
Lateral lemniscus	QA	0.6530 ± 0.0815	0.6486 ± 0.0687	.83
	GFA	0.0930 ± 0.0088	0.0925 ± 0.0055	.76
Anterior limb of internal capsule	QA	0.5717 ± 0.0754	0.5871 ± 0.0754	.45
	GFA	0.0853 ± 0.0053	0.0877 ± 0.0044	.08
Posterior limb of internal capsule	QA	0.6947 ± 0.0635	0.6907 ± 0.0551	.81
	GFA	0.1046 ± 0.0035	0.1046 ± 0.0027	.97
Heschl	QA	0.6054 ± 0.0916	0.5792 ± 0.0763	.27
	GFA	0.0882 ± 0.0074	0.0831 ± 0.0141	.18
Superior temporal gyrus	QA	0.5974 ± 0.0762	0.5941 ± 0.0731	.87
	GFA	0.0928 ± 0.0042	0.0912 ± 0.0037	.09
Middle temporal gyrus	QA	0.6020 ± 0.0752	0.6064 ± 0.0720	.83
	GFA	0.0935 ± 0.0033	0.0929 ± 0.0029	.46
Inferior temporal gyrus	QA	0.5594 ± 0.0661	0.5731 ± 0.0686	.47
	GFA	0.0849 ± 0.0079	0.0871 ± 0.0069	.06
Anterior corona radiata	QA	0.5868 ± 0.0717	0.5711 ± 0.0638	.41
	GFA	0.0951 ± 0.0044	0.0937 ± 0.0039	.06
Posterior corona radiata	QA	0.7172 ± 0.0814	0.7081 ± 0.0785	.68
	GFA	0.1135 ± 0.0071	0.1126 ± 0.0077	.36
Auditory radiation	QA	0.6727 ± 0.0783	0.6617 ± 0.0827	.62
	GFA	0.1021 ± 0.0061	0.1010 ± 0.0070	.49
Brodmann area 41	QA	0.6350 ± 0.0790		
	GFA	0.0960 ± 0.0034		
Brodmann area 42	QA	0.5483 ± 0.0793		
	GFA	0.0831 ± 0.0090		

[a] Data are mean ± SD.

DISCUSSION

In humans, the primary acoustic circuit is made up of the auditory nerve, brain stem, thalamus, and auditory cortex. In the cochlea, sound is transduced into a neural signal and then travels via the cochlear nerve to a synapse at the dorsal and ventral cochlear nuclei in the medulla oblongata. Then, the fibers project to the ipsilateral superior olivary nucleus or decussate to the contralateral superior olivary nucleus. Fibers further ascend to the inferior colliculus in the midbrain via the lateral lemniscus and subsequently

Table 3: Differences in GFA between patients with unilateral ISSHL (hearing loss ipsilateral side and contralateral side) and healthy subjects[a]

ROIs	Patients with Unilateral ISSHL		Healthy Controls	*P* Value
	Hearing Loss Ipsilateral Side ($n = 48$)	Hearing Loss Contralateral Side ($n = 48$)	($n = 20$)	
Superior olivary nucleus	0.0898 ± 0.0142	0.0922 ± 0.0163	0.08993 ± 0.0066	.69
Inferior colliculus	0.0951 ± 0.0090	0.0948 ± 0.0067	0.0939 ± 0.0050	.84
Medial geniculate body	0.0963 ± 0.0116	0.0940 ± 0.0098	0.0979 ± 0.0067	.31
Lateral lemniscus	0.0951 ± 0.0084	0.0911 ± 0092	0.0928 ± 0.0061	.07
Anterior limb of internal capsule	0.0816 ± 0.0068	0.0815 ± 0.0071	0.0865 ± 0.0038	.01
Posterior limb of internal capsule	0.0984 ± 0.0073[c]	0.0997 ± 0.0051[b]	0.1046 ± 0.0026	.001
Heschl	0.0829 ± 0.0228	0.0842 ± 0.0140	0.0857 ± 0.0078	.83
Superior temporal gyrus	0.0894 ± 0.0070	0.0892 ± 0.0079	0.0920 ± 0.0034	.28
Middle temporal gyrus	0.0920 ± 0.0057	0.0907 ± 0.0061	0.0932 ± 0.0026	.20
Inferior temporal gyrus	0.0850 ± 0.0084	0.0850 ± 0.0071	0.0859 ± 0.0064	.89
Anterior corona radiata	0.0884 ± 0.0075	0.0881 ± 0.0076	0.0941 ± 0.0039	.005
Posterior corona radiata	0.1084 ± 0.0093	0.1079 ± 0.0091	0.1131 ± 0.0071	.08
Auditory radiation	0.0997 ± 0.0089	0.0992 ± 0.0093	0.1015 ± 0.0057	.61
Brodmann area 41	0.0950 ± 0.0074		0.0960 ± 0.0034	.47
Brodmann area 42	0.0812 ± 0.0085		0.0831 ± 0.0090	.41

[a] Data are mean ± SD.
[b] Compared with the control group, $P < .05$ after Bonferroni correction.
[c] Compared with the control group, $P < .01$ after Bonferroni correction.

Table 4: Differences in QA between patients with unilateral ISSHL (hearing loss ipsilateral side and contralateral side) and healthy subjects[a]

ROIs	Patients with Unilateral ISSHL		Healthy Controls ($n = 20$)	*P* Value
	Hearing Loss Ipsilateral Side ($n = 48$)	Hearing Loss Contralateral Side ($n = 48$)		
Superior olivary nucleus	0.5883 ± 0.1047	0.6058 ± 0.0989	0.6578 ± 0.0852	.04
Inferior colliculus	0.6006 ± 0.0844	0.5949 ± 0.0787	0.6463 ± 0.0860	.06
Medial geniculate body	0.5607 ± 0.0949	0.5395 ± 0.0876[b]	0.6309 ± 0.0883	.001
Lateral lemniscus	0.5986 ± 0.0903[c]	0.5588 ± 0.1002[b]	0.6527 ± 0.0714	.001
Anterior limb of internal capsule	0.4798 ± 0.0778[b]	0.4825 ± 0.0868[b]	0.5799 ± 0.0646	<.001
Posterior limb of internal capsule	0.6264 ± 0.1115	0.6342 ± 0.0974	0.6895 ± 0.0585	.04
Heschl	0.4931 ± 0.1452	0.5029 ± 0.1011	0.5840 ± 0.0799	.01
Superior temporal gyrus	0.5249 ± 0.0812	0.5266 ± 0.0820	0.5918 ± 0.0759	.005
Middle temporal gyrus	0.5421 ± 0.0732[c]	0.5345 ± 0.0730[c]	0.6026 ± 0.0780	.002
Inferior temporal gyrus	0.4969 ± 0.0659	0.4852 ± 0.0914	0.5639 ± 0.0674	.001
Anterior corona radiata	0.5000 ± 0.0691[b]	0.4985 ± 0.0676[b]	0.0580 ± 0.0739	<.001
Posterior corona radiata	0.6537 ± 0.0988	0.6484 ± 0.0916	0.7148 ± 0.0837	.02
Auditory radiation	0.5950 ± 0.0848	0.5948 ± 0.0860	0.6607 ± 0.0819	.008
Brodmann area 41	0.5515 ± 0.1041[c]		0.6303 ± 0.0850	.002
Brodmann area 42	0.4792 ± 0.0756		0.5421 ± 0.0860	.004

[a] Data are mean ± SD.
[b] Compared with the control group, $P < .01$ after Bonferroni correction.
[c] Compared with the control group, $P < .05$ after Bonferroni correction.

project to the MGB in the thalamus. Finally, the acoustic radiation from the MGB transmits the auditory information to the temporal cortex through the internal capsule.[17]

Most studies examining white matter microstructure in sensorineural hearing loss have focused on long-term patients, and the auditory cortex, inferior colliculus, and lateral lemniscus are the most widely studied regions using DTI.[10] Some DTI studies have focused on only the lateral lemniscus and inferior colliculus because the 2 sides are more distinguishable along the auditory pathway.[8] In these regions, the auditory nerve fibers are predominantly oriented vertically, while other regions including the cochlear nuclei, superior olivary body, and MGB contain longitudinal, transverse, and oblique fibers, leading to poor spatial resolution and signal-to-noise ratio.[8,17,18] By contrast, DSI was reported to have the highest sensitivity for detecting crossing fibers compared with DTI and diffusional kurtosis imaging.[19] Therefore, in this study, we chose DSI to detect microstructural abnormalities along the central auditory pathway and to assess the correlations of clinical outcomes with DSI parameters.

An observed decrease in FA is likely attributed to axonal loss and/or demyelination.[18] GFA, as the SD of diffusion directions within a voxel, is the parameter of DSI simulation of FA deriving from DTI.[12] QA is an anisotropy index similar to FA, but it is calculated for each orientation-distribution function peak in each voxel.[20] The decrease of QA and GFA both can reflect the damage to white matter, just like FA.

A major finding of this study was the prognostic value of GFA in the ipsilateral MGB. In addition, the QA value decreased on the contralateral side of the MGB. A relationship between QA reduction of the contralateral MGB and the severity of hearing loss was found in our previous research.[21] The MGB plays a central role in auditory processing. It is the efferent and afferent tracts to the primary auditory cortex, responsible for the complex perception of sounds.[22] Huang et al[23] also reported that FA in the MGB is a valuable predictive biomarker of cochlear implantation outcome. This report confirmed that MGB may have predictive value in the process of hearing rehabilitation.

Given that 70%–80% of the fibers cross to the contralateral side, and only 20%–30%, to the ipsilateral side, how does GFA of the ipsilateral MGB affect prognosis? In the improvement group, GFA of the ipsilateral MGB was significantly higher than that of the contralateral side of the same patient, while there were no differences between the ipsilateral and contralateral sides of each patient in the nonimprovement group. These data suggest that the ipsilateral side of nerve fiber integrity was better in patients with good prognosis. Langers et al[24] found that the stimulation to deaf ears of patients with unilateral hearing loss can cause weak responses in the MGB, and these responses were strongest ipsilateral to the deaf side. In contrast, the response of the MGB to stimulation was dominantly contralateral in the subjects with normal hearing. Thus, speculatively, ipsilateral compensation may have occurred because of the contralateral injury. The better ipsilateral fiber integrity is conducive to the transmission of nerve impulses, which may improve the prognosis. Further studies are required to confirm the mechanism of hearing recovery in patients with unilateral ISSHL. Yang et al[25] also reported that the decreased hearing level of the opposite ear was a poor prognostic factor in elderly patients with unilateral sensorineural hearing loss. This effect of the opposite ear on prognosis may also explain why better fiber integrity of the hearing loss on the ipsilateral side was associated with better prognosis. This finding is because 70%–80% of the fibers of the opposite ear cross over to the hearing loss on the ipsilateral side.

Prognostic factors for ISSHL have been reported in several studies, including age, degree of hearing loss, shape of the audiogram, duration between the onset of hearing loss and treatment, and complications such as hypertension and hyperlipidemia, of which the severity of the initial hearing loss is considered the most important.[26] By contrast, we found no differences in the above indices between patients with different hearing outcomes. Only 6 (12.5%) cases of moderate hearing loss were observed in the present study

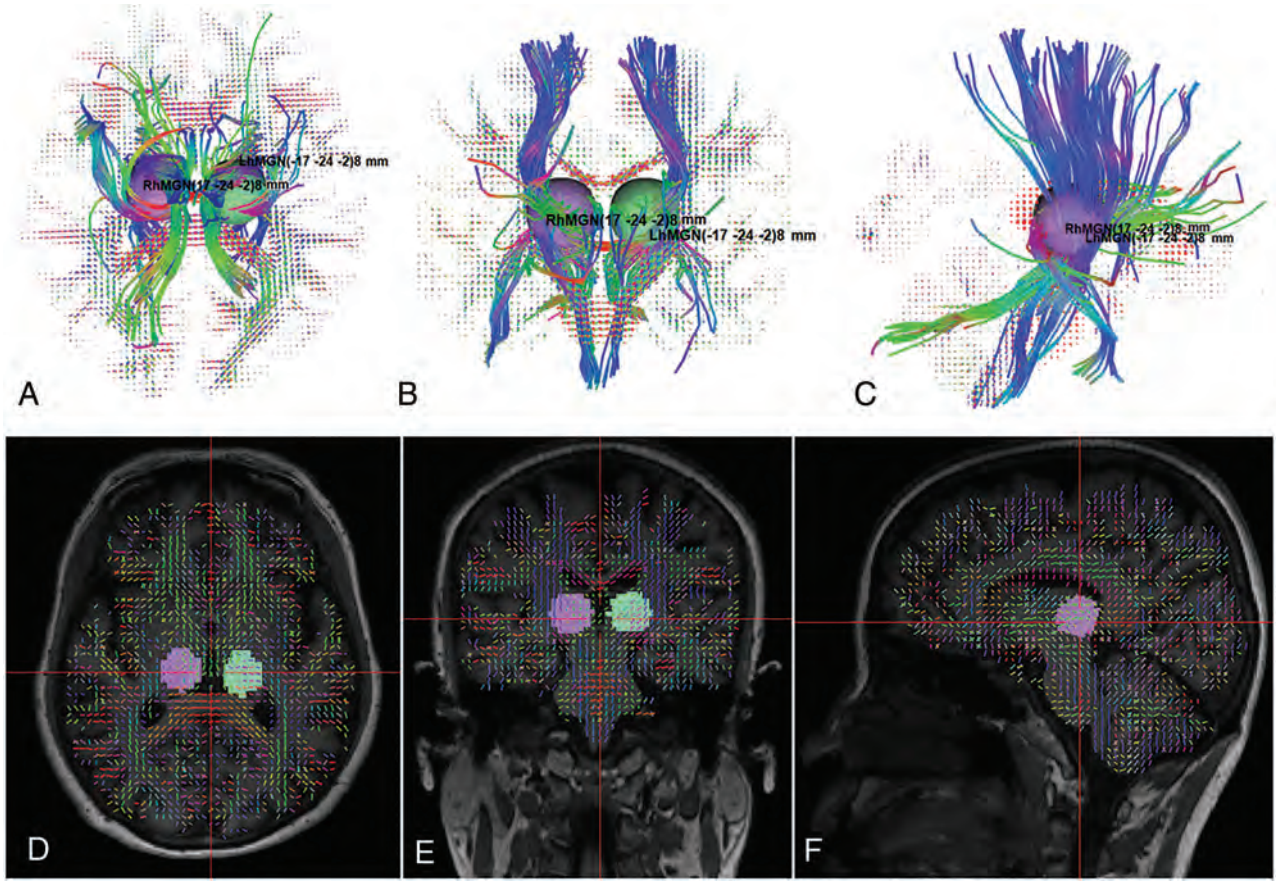

FIG 1. Fiber tractography of the MGB from diffusion spectrum imaging: *A*, Axial. *B*, Coronal. *C*, Sagittal. ROIs on the QA map: *D*, Axial. *E*, Coronal. *F*, Sagittal. RhMGN indicates Right MGB; LhMGN, Left MGB.

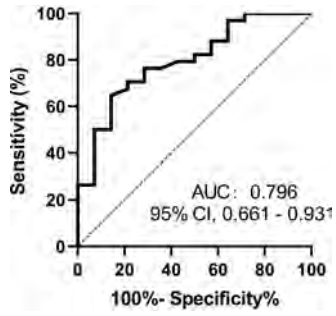

FIG 2. The receiver operating characteristic curves of GFA in the ipsilateral MGB. AUC indicates area under the curve.

(less than the other 3 severities), which may partially explain the absence of effects of hearing loss on prognosis.

This study also showed a decrease of QA value in the lateral lemniscus. However, differing from some previous studies, this study failed to find changes in the inferior colliculus. For example, Wu et al[18] reported significant differences of FA in both the lateral lemniscus and inferior colliculus of patients with sensorineural hearing loss, while Lin et al[17] reported an inverse relationship between the severity of hearing impairment and FA values in those 2 sites. Lee et al[27] found greater differences in the inferior colliculus (the site of convergence for input from multiple lower auditory nuclei) compared with the lateral colliculus, suggesting increased sensitivity of the inferior colliculus to injury. Furthermore, Chang et al[9] thought that the inferior colliculus was the most common region of the central auditory pathway showing a reduced FA. Nevertheless, in that study, FA of the inferior colliculus decreased in all 8 patients with bilateral hearing loss, but in only 1 of 2 patients with unilateral hearing loss. By contrast, in a study focused on patients with hearing loss with chronic tinnitus, Husain et al[28] found no change in FA in those 2 sites. Most interesting, in a DTI study examining the effect of disease duration on the central auditory nerve fibers in patients with ISSHL, there was no change in the DTI index of those 2 sites with a duration of <1 week, while significant changes were found in patients with a duration of >2 years.[8] Thus, we speculated that the duration of hearing loss may impact the structural changes in the auditory pathways because of compensation. Overall, these data suggest that unilateral or bilateral hearing loss and different durations may explain, at least in part, our contrasting findings in the inferior colliculus.

Consistent with our results, Shang et al[29] found a reduction of DTI parameters in the anterior and posterior limbs of the internal capsule, the middle temporal gyrus, and the anterior corona radiata in unilateral deafness. They thought axonal demyelination was the main mechanism of structural change. Lexical/semantic processing requires input from the middle temporal gyrus. In addition to our finding of bilateral white matter damage, Fan et al[30] found a decrease of gray matter in

the contralateral middle temporal gyrus of patients with hearing loss. Husain et al[28] also found decreased FA values in the internal capsule. The internal capsule is important to auditory function because it contains most of the afferent auditory fibers that enter the cortical area. Most auditory fibers are located in the posterior limb of the internal capsule. The anterior limb of the internal capsule is related to cognitive function because it connects the thalamus and prefrontal cortex, conveying cognition fibers.[31] A study of patients with tinnitus also showed that the anterior corona radiation is one of the most changed areas in white matter.[32] These above results indicate that we need to pay more attention to cognitive function and tinnitus in future research of ISSHL.

Finally, this study also found that QA decreased in Brodmann Area 41. Brodmann Area 41 is the primary auditory area. The results suggested that the short-term course of disease may already have affected the structural changes in the auditory area. However, changes in this area have not been reported in previous DTI studies in patients with ISSHL; these changes need further research and verification.

There were several limitations in our study. The patients were enrolled from a single institution, and the data were analyzed retrospectively. Furthermore, all patients received the same treatment strategy. Thus, we were unable to compare the effects of different treatment strategies on fiber integrity.

CONCLUSIONS

Our data suggest that DSI can detect abnormalities of white matter microstructure along the central auditory pathway in patients with unilateral ISSHL, and GFA in the ipsilateral MGB may help to predict recovery outcomes.

ACKNOWLEDGMENTS

The authors thank the staff from the Department of Otolaryngology at Beijing Chaoyang Hospital.

Disclosures: Yi Zhang—*RELATED*: *Grant*: Beijing Municipal Commission of Science and Technology*; *Fees for Participation in Review Activities Such as Data-Monitoring Boards, Statistical Analysis, End-Point Committees, and the Like*: Beijing Municipal Commission of Science and Technology.* Zihao Zhang—*RELATED*: *Grant*: Beijing Municipal Commission of Science and Technology*; *Fees for Participation in Review Activities Such as Data-Monitoring Boards, Statistical Analysis, End-Point Committees, and the Like*: Beijing Municipal Commission of Science and Technology.* Xiaojiao Guan—*RELATED*: *Grant*: Beijing Municipal Commission of Science and Technology*; *Fees for Participation in Review Activities Such as Data-Monitoring Boards, Statistical Analysis, End-Point Committees, and the Like*: Beijing Municipal Commission of Science and Technology.* Yuelei Lyu—*RELATED*: *Grant*: Beijing Chaoyang Hospital*; *Consulting Fee Or Honorarium*: Beijing Chaoyang Hospital*; *Support for Travel to Meetings for the Study or Other Purposes*: Beijing Chaoyang Hospital*; *Fees for Participation in Review Activities Such as Data-Monitoring Boards, Statistical Analysis, End-Point Committees, and the Like*: Beijing Chaoyang Hospital.* Jing Yang—*RELATED*: *Grant*: Beijing Municipal Commission of Science and Technology*; *Fees for Participation in Review Activities Such as Data-Monitoring Boards, Statistical Analysis, End-Point Committees, and the Like*: Beijing Municipal Commission of Science and Technology.* Tao Jiang—*RELATED*: *Grant*: Beijing Municipal Commission of Science and Technology*; *Fees for Participation in Review Activities Such as Data-Monitoring Boards, Statistical Analysis, End-Point Committees, and the Like*: Beijing Municipal Commission of Science and Technology.* Xiuqin Jia—*RELATED*: *Grant*: Beijing Municipal Commission of Science and Technology*; *Fees for Participation in Review Activities Such as Data-Monitoring Boards, Statistical Analysis, End-Point Committees, and the Like*: Beijing Municipal Commission of Science and Technology.* *Money paid to the institution.

REFERENCES

1. Xie Y, Orabi NA, Zwolan TA, et al. **Outcomes of unilateral idiopathic sudden sensorineural hearing loss: two decades of experience.** *Laryngoscope Investig Otolaryngol* 2019;4:693–702 CrossRef Medline
2. Ahmadzai N, Kilty S, Cheng W, et al. **A systematic review and network meta-analysis of existing pharmacologic therapies in patients with idiopathic sudden sensorineural hearing loss.** *PLoS One* 2019;14:e022171 CrossRef Medline
3. Chandrasekhar SS, Tsai Do BS, Schwartz SR, et al. **Clinical practice guideline: sudden hearing loss (update).** *Otolaryngol Head Neck Surg* 2019;161:S1–45 CrossRef Medline
4. Jalali MM, Nasimidoust Azgomi M. **Metabolic syndrome components and sudden sensorineural hearing loss: a case-control study.** *Eur Arch Otorhinolaryngol* 2020;277:1023–29 CrossRef Medline
5. Ciorba A, Bianchini C, Crema L, et al. **White matter lesions and sudden sensorineural hearing loss.** *J Clin Neurosci* 2019;65:6–10 CrossRef Medline
6. Fusconi M, Attanasio G, Capitani F, et al. **Is there a relation between sudden sensorineural hearing loss and white matter lesions.** *Eur Arch Otorhinolaryngol* 2019;276:3043–49 CrossRef Medline
7. Dicuonzo F, Purciariello S, De Marco A, et al. **MR evaluation of encephalic leukoaraiosis in sudden sensorineural hearing loss (SSNHL) patients.** *Neurol Sci* 2019;40:357–62 CrossRef Medline
8. Zhu K, He Y, Hou J, et al. **Diffusion tensor imaging study of central auditory pathway in patients with acquired sensorineural hearing loss.** *J of Audiol and Speech Pathol* 2015;23:143–46 CrossRef
9. Chang Y, Lee SH, Lee YJ, et al. **Auditory neural pathway evaluation on sensorineural hearing loss using diffusion tensor imaging.** *Neuroreport* 2004;15:1699–703 CrossRef Medline
10. Tarabichi O, Kozin ED, Kanumuri VV, et al. **Diffusion tensor imaging of central auditory pathways in patients with sensorineural hearing loss: a systematic review.** *Otolaryngol Head Neck Surg* 2018;158:432–42 CrossRef Medline
11. Yeh FC, Wedeen VJ, Tseng WY. **Generalized q-sampling imaging.** *IEEE Trans Med Imaging* 2010;29:1626–35 CrossRef Medline
12. Hodgson K, Adluru G, Richards LG, et al. **Predicting motor outcomes in stroke patients using diffusion spectrum MRI microstructural measures.** *Front Neurol* 2019;10:72 CrossRef Medline
13. Editorial Board of Chinese Journal of Otorhinolaryngology Head and Neck Surgery; Society of Otorhinolaryngology Head and Neck Surgery, Chinese Medical Association. **Guideline of diagnosis and treatment of sudden deafness (2015)** [in Chinese]. *Zhonghua Er Bi Yan Hou Tou Jing Wai Ke Za Zhi* 2015;50:443–47 Medline
14. Wedeen VJ, Hagmann P, Tseng WY, et al. **Mapping complex tissue architecture with diffusion spectrum magnetic resonance imaging.** *Magn Reson Med* 2005;54:1377–86 CrossRef Medline
15. Fernández-Miranda JC, Wang Y, Pathak S, et al. **Asymmetry, connectivity, and segmentation of the arcuate fascicle in the human brain.** *Brain Struct Funct* 2015;220:1665–80 CrossRef Medline
16. Fernandez-Miranda JC, Pathak S, Engh J, et al. **High-definition fiber tractography of the human brain: neuroanatomical validation and neurosurgical applications.** *Neurosurgery* 2012;71:430–53 CrossRef Medline
17. Lin Y, Wang J, Wu C, et al. **Diffusion tensor imaging of the auditory pathway in sensorineural hearing loss: changes in radial diffusivity and diffusion anisotropy.** *J Magn Reson Imaging* 2008;28:598–603 CrossRef Medline
18. Wu CM, Ng SH, Liu TC. **Diffusion tensor imaging of the subcortical auditory tract in subjects with long-term unilateral sensorineural hearing loss.** *Audiol Neurootol* 2009;14:248–53 CrossRef Medline
19. Glenn GR, Kuo LW, Chao YP, et al. **Mapping the orientation of white matter fiber bundles: a comparative study of diffusion tensor imaging, diffusional kurtosis imaging, and diffusion spectrum imaging.** *AJNR Am J Neuroradiol* 2016;37:1216–22 CrossRef Medline
20. Yeh FC, Verstynen TD, Wang Y, et al. **Deterministic diffusion fiber tracking improved by quantitative anisotropy.** *PLoS One* 2013;8:e80713 CrossRef Medline

21. Zhang Z, Jia X, Guan X, et al. **White matter abnormalities of auditory neural pathway in sudden sensorineural hearing loss using diffusion spectrum imaging: different findings from tinnitus.** *Front Neurosci* 2020;14:200 CrossRef Medline
22. Bartlett EL. **The organization and physiology of the auditory thalamus and its role in processing acoustic features important for speech perception.** *Brain Lang* 2013;126:29–48 CrossRef Medline
23. Huang L, Zheng W, Wu C, et al. **Diffusion tensor imaging of the auditory neural pathway for clinical outcome of cochlear implantation in pediatric congenital sensorineural hearing loss patients.** *PLoS One* 2015;10:e0140643 CrossRef Medline
24. Langers DR, van Dijk P, Backes WH. **Lateralization, connectivity and plasticity in the human central auditory system.** *Neuroimage* 2005;28:490–99 CrossRef Medline
25. Huafeng Y, Hongqin W, Wenna Z, Yuan L, Peng X. **Clinical characteristics and prognosis of elderly patients with idiopathic sudden sensorineural hearing loss.** *Acta Otolaryngol* 2019;139:866–69 CrossRef Medline
26. Lee HY, Kim DK, Park YH, et al. **Prognostic factors for profound sudden idiopathic sensorineural hearing loss: a multicenter retrospective study.** *Eur Arch Otorhinolaryngol* 2017;274:143–49 CrossRef Medline
27. Lee SH, Chang Y, Lee JE, et al. **The values of diffusion tensor imaging and functional MRI in evaluating profound sensorineural hearing loss.** *Cochlear Implants Int* 2004;5(Suppl 1):149–52 CrossRef Medline
28. Husain FT, Medina RE, Davis CW, et al. **Neuroanatomical changes due to hearing loss and chronic tinnitus: a combined VBM and DTI study.** *Brain Res* 2011;1369:74–88 CrossRef Medline
29. Shang Y, Hinkley LB, Cai C, et al. **Functional and structural brain plasticity in adult onset single-sided deafness.** *Front Hum Neurosci* 2018;12:474 CrossRef Medline
30. Fan W, Zhang W, Li J, et al. **Altered contralateral auditory cortical morphology in unilateral sudden sensorineural hearing loss.** *Otol Neurotol* 2015;36:1622–27 CrossRef Medline
31. Yin B, Li DD, Huang H, et al. **Longitudinal changes in diffusion tensor imaging following mild traumatic brain injury and correlation with outcome.** *Front Neural Circuits* 2019;13:28 CrossRef Medline
32. Yoo HB, De Ridder D, Vanneste S. **White matter changes in tinnitus: is it all age and hearing loss.** *Brain Connect* 2016;6:84–93 CrossRef Medline

The Many Faces of Persistent Stapedial Artery: CT Findings and Embryologic Explanations

Z.J. LoVerde, D.P. Shlapak, J.C. Benson, M.L. Carlson, and J.I. Lane

ABSTRACT

SUMMARY: Persistent stapedial artery is a vascular anomaly with both clinical and surgical implications. Because of its scarcity, however, it remains underrecognized on imaging. Presented here is a series of 10 cases, demonstrating characteristic CT findings associated with this vascular anomaly and its most common pathognomonic imaging signs. The variable morphologic configurations and their corresponding embryologic underpinnings are described. Clinical and surgical implications of this rare anomaly are discussed.

ABBREVIATION: PSA = persistent stapedial artery; MMA = middle meningeal artery; CCA = common carotid artery; CTC = caroticotympanic canaliculus; ITC = inferior tympanic canaliculus; CHL = conductive hearing loss; ECA = external carotid artery; ICA = internal carotid artery; CTA = caroticotympanic artery; ITA = inferior tympanic artery; FNC = facial nerve canal

Persistent stapedial artery (PSA) is a rare vascular anomaly, with an estimated prevalence of 0.02%–0.5%.[1,2] Although its existence has been well documented dating back to Hyrtl in 1836,[3] its characteristics on advanced imaging are sparse. Classic studies have focused mainly on surgical encounters,[4-6] histologic dissection,[2,7-10] tomography,[11] or angiography.[12-14] More recent elucidations on CT[13-17] are limited by small sample size, few multiplanar reconstructions, and relatively cursory discussions of its morphologic variability. Several cases have been described using MR angiography.[18,19] The purpose of this case series is to provide a clear, image-rich resource on CT appearance of a PSA and a focused embryologic framework to facilitate understanding its variable configurations.

METHODS

A systematic search of a single-center registry of radiologic reports was performed to identify high-resolution temporal bone CT examinations between January 1, 2005, and March 10, 2020, using the term "persistent stapedial artery." Eleven patients were reviewed by a single attending neuroradiologist with more than 20 years of experience and a Certificate of Added Qualification in neuroradiology. All examinations were performed on multidetector scanners from a single vendor (Siemens) ranging from 64- to 192-section platforms. Standard reconstructions in axial, coronal, and Pöschl planes were reviewed on a PACS workstation (Visage Imaging) in conjunction with multiplanar reformations. Of these cases, 2 were excluded because they demonstrated an absent foramen spinosum but no additional findings of a PSA, with presumed ophthalmic origin of the middle meningeal artery (MMA). Hence, 9 patients were included in the final cohort. Characteristic imaging findings and representative images were described.

RESULTS

Radiologic Findings

Of the 9 included patients (10 affected ears), 6 PSAs were left-sided and 4 right-sided, including 1 bilateral. All had an absent ipsilateral foramen spinosum and a visible vessel traversing the cochlear promontory. Seven had an associated enlarged caroticotympanic canaliculus (CTC); the other 3 had an enlarged inferior tympanic canaliculus (ITC). Six had an associated duplicated fallopian canal. An observable vessel within the obturator foramen of the stapes was noted in 8 cases; in the remaining 2, 1 vessel traversed anterior to a dysplastic stapedial crus, and the other was obscured by granulation tissue (confirmed at surgery).

Clinical Data

Three patients had underlying congenital anomalies, including ipsilateral congenital cholesteatoma, ipsilateral congenital aerodigestive venolymphatic malformation, and chromosome 3q duplication or trisomy. Four patients had conductive hearing loss (CHL) documented by audiogram, with air-bone gaps ranging from 20–60 dB, 1 of which was alternatively attributable to congenital cholesteatoma. The single patient with bilateral PSAs (right PSA confirmed at surgery) had bilateral CHL, right greater than left, and remote left

Received April 25, 2020; accepted after revision August 11.

From the Departments of Radiology (Z.J.L., D.P.S., J.C.B., J.I.L.) and Otolaryngology–Head and Neck Surgery (M.L.C.), Mayo Clinic, Rochester, Minnesota.

INSTITUTIONAL REVIEW BOARD APPROVAL: 20-002533.

Please address correspondence to Darya P. Shlapak, MD, MBA, Department of Radiology, Mayo Clinic, 200 1st St. SW, Rochester, MN 55905; e-mail: shlapak.darya@mayo.edu
http://dx.doi.org/10.3174/ajnr.A6851

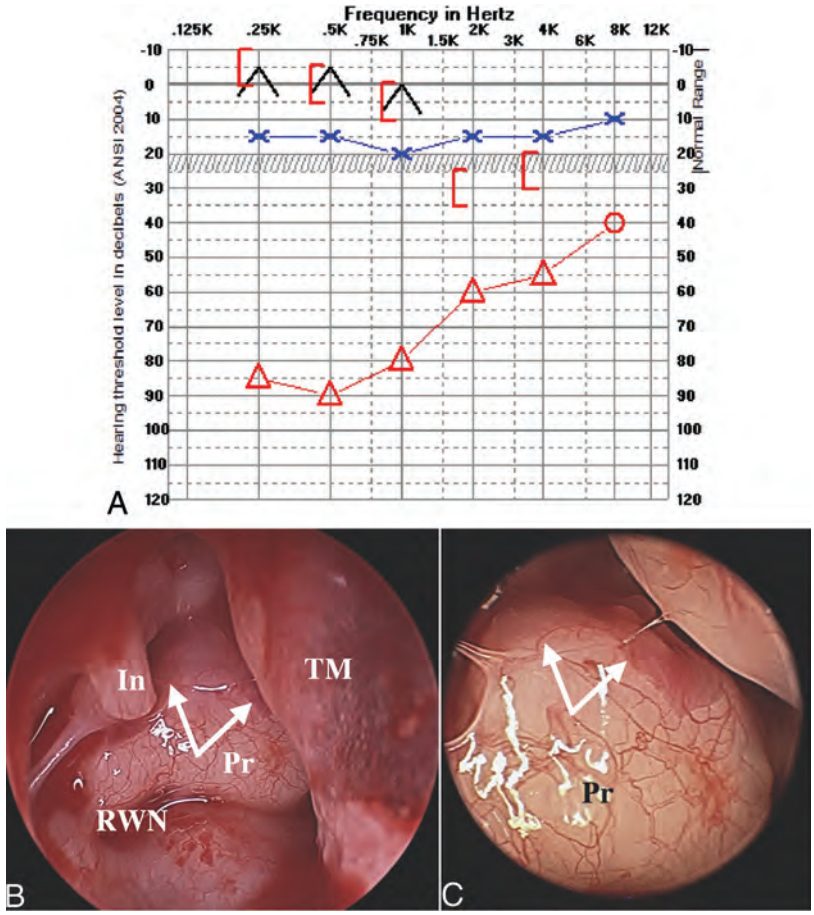

FIG 1. *A*, Preoperative audiogram demonstrates a right-sided near-maximal CHL and normal hearing thresholds in the left ear. *B* and *C*, Right middle ear intraoperative endoscopy demonstrates right PSA (*white arrows*) coursing over the surface of the cochlear promontory. Notably, the inferior half of the artery was encased within promontory bone; however, the superior aspect was dehiscent and easily visible during surgery. In this patient, the artery and facial nerve were pulsatile. In = incus; Pr = promontory of cochlea; RWN = round window niche; TM = tympanic membrane.

middle ear surgery. One patient with CHL reported concomitant pulsatile tinnitus. Four PSAs were considered purely incidental without attributable symptoms. Two patients had normal audiograms, 1 had a coincidental sensorineural deficit, and 2 did not have audiograms performed. Three PSA cases were confirmed by exploratory middle ear surgery. Of these, 1 PSA was intentionally divided followed by ossicular chain reconstruction in a patient with history of congenital cholesteatoma. Postoperatively, this patient experienced significant improvement in CHL and normal facial nerve function. The other 2 surgeries were aborted after encounter of the PSA, 1 because of bleeding, ultimately controlled, and the other because of concern for potential facial nerve injury with artery division, given prominent pulsations within the facial nerve substance. Fig 1 demonstrates a preoperative audiogram (*A*) and intraoperative endoscopic photographs (*B* and *C*) for 1 of the patients. The main imaging and clinical findings are summarized in the Table.

DISCUSSION

Embryologic Origins

Understanding the embryology and typical regression pattern of the stapedial artery helps to explain its intratemporal course. Much of our fundamental

Patient characteristics and prevalence of associated persistent stapedial artery findings

Case	Side	Associated Anomalies	CHL	Duplicated FNC	Fr Spn	Coch Prom Vessel	Large CTC	Large ITC	Stapes Obturator Artery	Surgical Confirmation
1	L	None	+	+	–	+	+	–	+	–
2	L	Ipsilateral congenital cholesteatoma and dysplastic anterior stapedial crus	+	–	–	+	+	–	+	+
3	L	None	N/A	+	–	+	–	+	+	–
4	L	None	–	–	–	+	–	+	+	–
5	R	Ipsilateral congenital aerodigestive venolymphatic malformation and dysplastic stapes	+	–	–	+	+	–	–[c]	+
6	R	Chromosome 3q duplication or trisomy	N/A	+	–	+	+	–	+	–
7	R	None	–	+	–	+	–	+	+	–
8	L	None	–	–	–	+	+	–	+	–
9[a]	R	None	+	+	–	+	+	–	–[d]	+
10[a]	L	None	+[b]	+	–	+	+	–	+	–

[a] #9 and #10: bilateral PSA; same patient.
[b] #10 remote middle ear surgery, not otherwise specified.
[c] #5 PSA anterior to the dysplastic crus.
[d] #9 granulation tissue obscured artery.

Note:—Findings are marked as either present (+) or absent (–) in each patient. Coch Prom indicates cochlear promontory; FNC = facial nerve canal; Fr Spn = foramen spinosum; N/A = not applicable.

understanding results from embryologic investigations performed by Congdon,[20] later clarified by Padget[21] and summarized by Altmann[22] and Steffen[23] in the early and mid-20th century.

Within the 6 embryonic pharyngeal arches, paired arterial arches course from the aortic sac to the ipsilateral of the paired descending dorsal aortas. The first and second arches give rise to the ventral pharyngeal artery, later to become the external carotid artery (ECA); the third arch artery becomes the proximal ICA; and the ventral third–fourth arch junction becomes the common carotid artery (Fig 2). The hyoid artery is the dorsal remnant of the second aortic arch and constitutes the stem of stapedial artery, around which the stapedial ring will form, giving rise to the characteristic obturator foramen of the stapes.[10,24] Immediately beyond the stapes, the stapedial artery ramifies into an upper division, which has a dorsal branch to become the MMA, ventral branch to supply the orbit, and a lower (maxillomandibular) division with infraorbital and mandibular branches.

Later, an anastomotic branch develops between the maxillomandibular division of the stapedial artery and plexiform branches of the distal ventral pharyngeal artery, connecting the ICA and ECA systems. This anastomosis will become the internal maxillary artery and results in an annexation of stapedial territorial supply by the ECA, allowing for normal involution of the stapedial and hyoid arteries (Fig 3*A*).

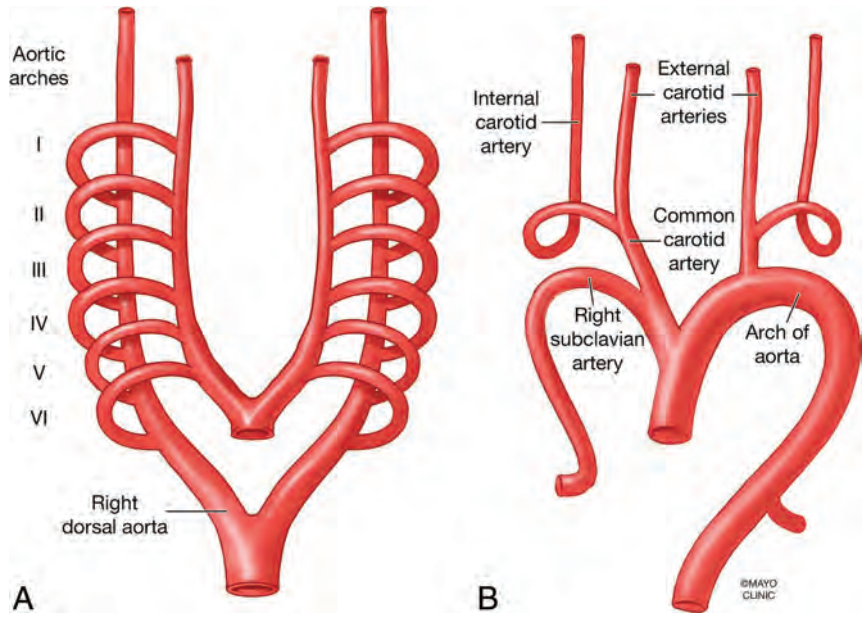

FIG 2. Primitive aortic arches embryology. *A*, Paired 6 aortic arches course from the aortic sac to the ipsilateral descending dorsal aorta (right dorsal aorta is annotated). *B*, First and 2nd arches give rise to the ventral pharyngeal artery, later to become ECA; the 3rd arch becomes proximal ICA; and the ventral 3rd–4th arch junction becomes the common carotid artery. Used with permission of Mayo Foundation for Medical Education and Research, all rights reserved.

Anatomic Variants

The anatomic variations are best categorized proximally by their arterial origins and distally by their transmitting osseous foramina. In the most straightforward proximal arrangement, the PSA is supplied by an enlarged caroticotympanic artery (CTA), a remnant of the embryonic hyoid artery stem arising from the petrous ICA by way of the

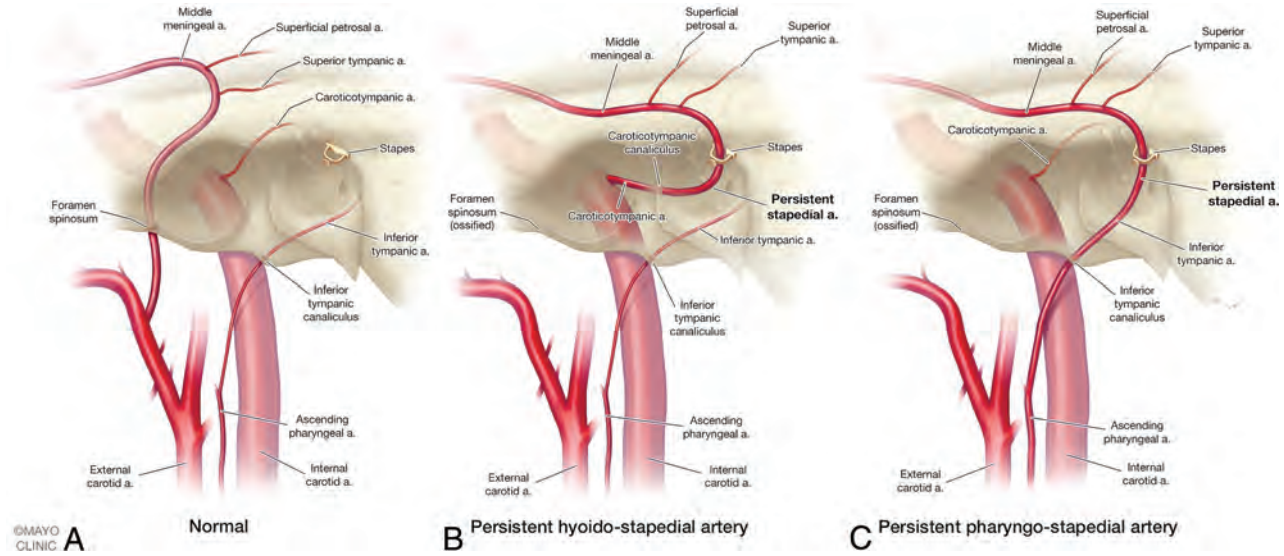

FIG 3. Normal carotid vascular anatomy (*A*) and anatomic variants of persistent stapedial artery (PSA, *B* and *C*). *B*, PSA is supplied by an enlarged caroticotympanic artery, a remnant of the embryonic hyoid artery stem arising from the petrous ICA via caroticotympanic canaliculus; this anatomic variant is referred to as persistent hyoidostapedial artery. *C*, PSA is supplied by an enlarged inferior tympanic artery, a branch of the ascending pharyngeal artery, which travels through the inferior tympanic canaliculus into the middle ear, anastomosing with the embryonic hyoid artery; this anatomic variant is referred to as persistent pharyngostapedial artery. Used with permission of Mayo Foundation for Medical Education and Research, all rights reserved.

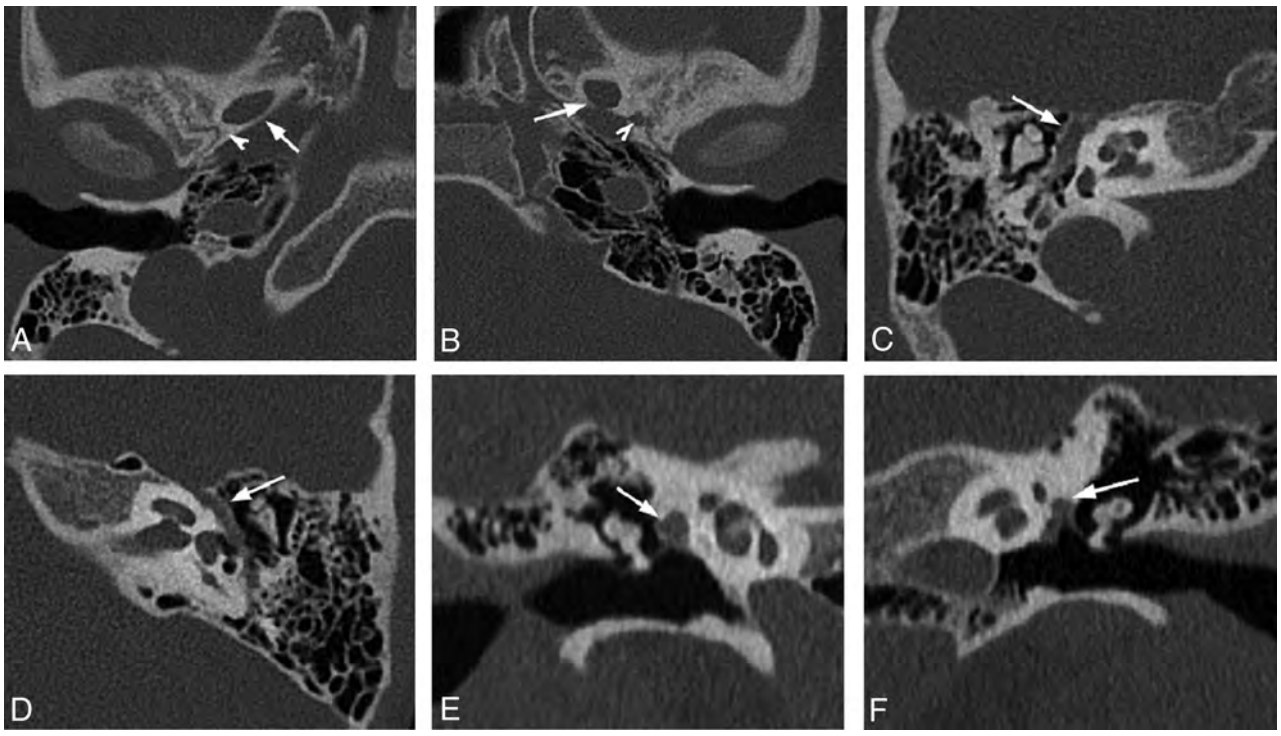

FIG 4. Nonspecific findings of PSA. Axial oblique CT reconstructions of right (*A*) and left (*B*) temporal bones in the same patient with the right PSA demonstrate normal foramen spinosum on the left and absent on the right at its expected location (*arrowheads*); note the normal foramen ovale on both sides (*arrows*). Axial (*C*) and coronal (*E*) oblique reconstructions of nonduplicated, enlarged tympanic segment of the right facial nerve canal (FNC). Nonduplicated FNC is enlarged to accommodate facial nerve and PSA (*arrows*). Compare with normal nonenlarged left FNC in similar planes, *D* and *F* (*arrows*).

CTC, referred to as a persistent hyoidostapedial artery (Fig 3*B*). The foramen spinosum is typically absent but may rarely persist if the PSA retains distribution to the maxillary artery through the MMA ("complete" hyoidostapedial artery).[25] In normal development, the CTA typically completely involutes[26,27] or anastomoses with the anterior tympanic and stylomastoid arteries.

Alternatively, the PSA may be supplied by an enlarged inferior tympanic artery (ITA), a branch of the ascending pharyngeal artery. The ITA travels through the ITC (Jacobson canal) into the middle ear, anastomosing, normally only transiently, with the embryonic hyoid artery. Because the ITA derives from the embryonic ventral pharyngeal artery, this has been referred to as a persistent pharyngostapedial artery (Fig 3*C*).[18,28]

An "aberrant" ICA results from involution or agenesis of the orthotopic distal cervical ICA. The detoured ICA represents an enlargement of both the ITA and CTA, with a resultant flow reversal in the CTA to supply the horizontal petrous ICA. When present in conjunction with a PSA, this has been termed an aberrant carotid stapedial artery.[28] An exceedingly rare variation but present in the current series (case 4) involves enlargement of both the CTA and ITA supplying the PSA with preserved orthotopic cervical ICA, referred to as a pharyngohyostapedial artery.[14,29]

Distal variation is at the fallopian canal level, which may be duplicated or enlarged. In duplication, PSA enters the tympanic segment of the fallopian canal through an inferior dehiscence and then exits laterally into a separate bony canal just posterior to the cochleariform process. This discrepancy may be the result of embryonic exploitation of alternate vascular pathways involving 2 divisions of the petrous branch of the MMA, namely, the superior tympanic artery and superficial petrosal artery. The superior tympanic artery enters the temporal bone through the superior tympanic canaliculus near the facial hiatus, following the lesser petrosal nerve, and the superficial petrosal artery travels within the fallopian canal with the facial nerve.[10,12,30] Depending on which of these 2 is involved, either a duplicated (superior tympanic) or an enlarged (superficial petrosal) facial canal may be seen.[15] In both settings, PSA subsequently traverses the floor of the middle cranial fossa, dividing laterally to become the MMA and to anastomose medially with orbital vessels.[23,31]

Except for the "complete" hyoidostapedial artery variant, nearly all types of PSA typically have an absent ipsilateral foramen spinosum as did all cases in our series. In normal development, foramen spinosum forms around the maxillomandibular division of the stapedial artery near its anastomosis with the ventral pharyngeal artery. The absence or transience of this anastomosis in the setting of a PSA prevents foramen formation. Nevertheless, the absence of foramen spinosum is not specific to a PSA because it can also be associated with other variant origins of the MMA.[32]

IMAGING SIGNS

Classic PSA imaging features include absent foramen spinosum (Fig 4*A*, -*B*) and enlargement of the anterior portion of the tympanic segment of the facial nerve canal (Fig 4*C*–*F*), neither of which is specific. Herein, we describe the most common CT findings that provide direct evidence of a PSA, allowing radiologists to more confidently identify this rare anomaly.

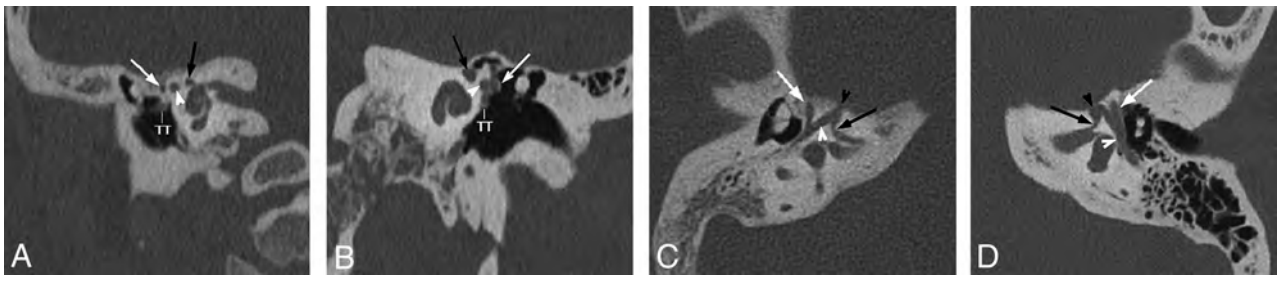

FIG 5. Right ear (*A*) and left ear (*B*) coronal CT images from 2 patients demonstrate an additional lumen lateral to the tympanic facial canal ("3-eyed snail") representing the bifurcation of the PSA as it traverses the floor of the middle cranial fossa to give rise the middle meningeal artery (*white arrows*). Labyrinthine (*black arrows*) and tympanic (*white arrowheads*) segments of the facial nerve represent usually seen "2 eyes of the snail." Right ear (*C*) and left ear (*D*) axial CT images in the same patients demonstrate duplication of the anterior segment of the tympanic facial nerve canal (*white arrows*). The labyrinthine segment (*black arrows*), tympanic segment (*white arrowheads*), and PSA canal intersect to form an "N" on the left (*D*) and a reverse "N" on the right (*C*). Geniculate ganglion is seen anteromedially (*black arrowheads*). TT = tensor tympani.

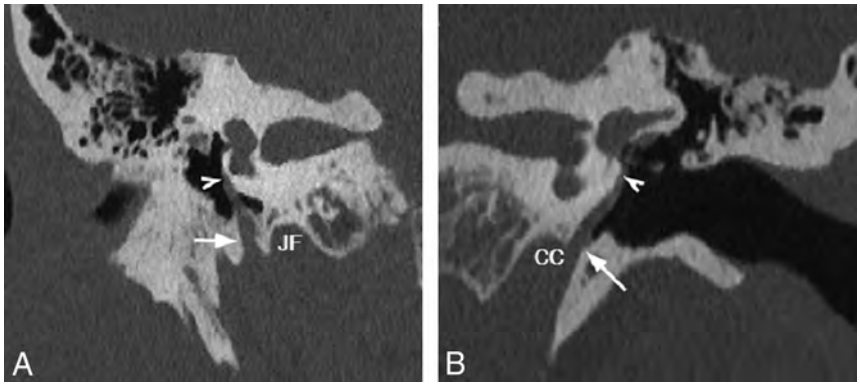

FIG 6. Coronal oblique CT reconstructions demonstrate PSA coursing over the lateral surface of the cochlear promontory (string sign). Right PSA (*A*) arises from the inferior tympanic canaliculus (*arrow*), and left PSA (*B*) takes its origin from the carotid canal via caroticotympanic canaliculus (*arrow*), both traversing cephalad over the cochlear promontory (*arrowheads*). CC = carotid canal; JF = jugular foramen.

Imaging Signs: "Three-Eyed Snail" Sign

As previously discussed, an osseous canal sometimes separates the facial nerve and the stapedial artery. This results in a characteristic appearance on coronal imaging planes, predictably altering the common anatomic radiologic landmark known as the "snail eyes." The usual "2 eyes" correspond to the labyrinthine and tympanic segments of the facial nerve in cross-section; the snail shell is implied by the cochlear spiral. In cases of PSA with a duplicated facial nerve canal, a rounded soft tissue mass lateral to the tympanic segment of the facial nerve is seen in the coronal plane, giving the impression of a "third eye" (Fig 5*A*, -*B*). This sign was observed in 6 of 10 PSA cases (60%) in our series.

Imaging Signs: "N" Sign

As an axial corollary to the "3-eyed snail" sign, PSA can have a characteristic appearance at the level of the geniculate ganglion. Here, the distal tympanic segment of the PSA appears as a tubular soft tissue attenuation coursing lateral to tympanic segment of the facial canal. This attenuation adds an additional limb to the classic upside down "V" shape of the facial nerve canal at the level of the geniculate ganglion, transforming the "V" into an "N" if on the left and reverse "N" if on the right side (Fig 5*C*, -*D*). Expectedly, this sign was also observed in 6 of 10 PSA cases (60%) in our series.

Imaging Signs: "String" Sign

In both sagittal and coronal planes, the vertically oriented proximal PSA can be observed as a thin linear soft tissue attenuation coursing over the cochlear promontory after emerging from its bony channel (either the inferior tympanic or caroticotympanic canaliculi), referred to as the "string sign" (Fig 6). The trajectory of the "string" varies by subtype, with the pharyngostapedial artery (from the ITA) coursing along the posterior surface just anterior to the round window niche and the hyoidostapedial artery (from the CTA) taking a more anterior course (Fig 7). This sign was observed in all 10 PSA cases (100%) in our series.

Imaging Signs: "Ringer" Sign

The PSA may be observed in cross-section as a discrete dot within the obturator foramen, typically marginating the inner aspect of the stapedial anterior crus. In this view, it is reminiscent of a horseshoe encircling a stake, a configuration known as a "ringer" in the parlance of the popular lawn game (Fig 8). In 8 of 10 PSA cases (80%) in our series, this imaging finding could be readily identified.

CLINICAL IMPLICATIONS

Although most patients with a PSA are asymptomatic, a variety of symptoms have been reported, most commonly CHL and pulsatile tinnitus. These 2 symptoms were corroborated by the current series. CHL may result from ossicular dampening caused by the traversing PSA or a concomitant malformation of the stapes suprastructure, such as the one in the current series with an absent anterior stapedial crus. None of the patients in the current series had clinical findings suggestive of a footplate fixation. The cause of pulsatile tinnitus is best explained by sound transmission through the cochlear promontory to the cochlea and potentially

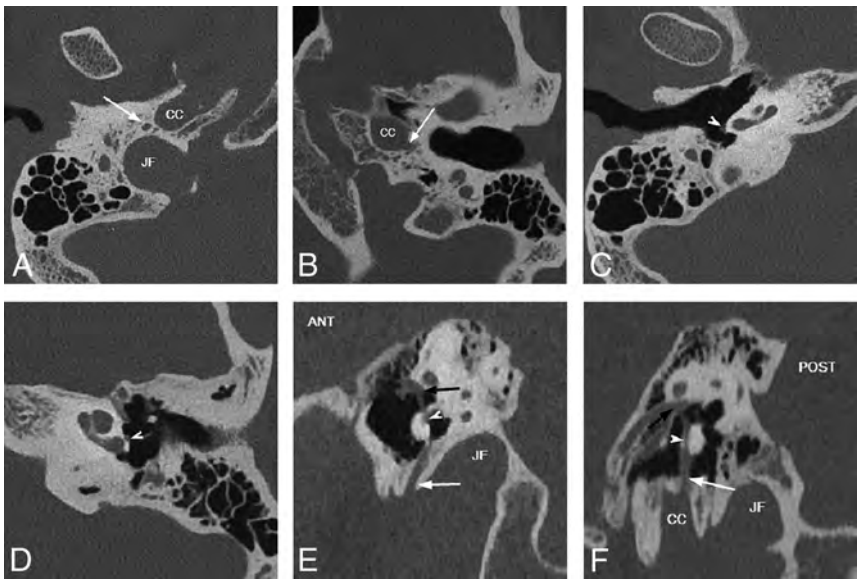

FIG 7. Variable origin of the PSA. Axial (*A–D*) and sagittal oblique (*E* and *F*) CT reconstructions. In *A, C,* and *E,* PSA arises from the ITC posterolateral to the carotid canal (CC) and anterior to the jugular foramen (JF), (*white arrows*). In *B, D,* and *F,* PSA arises directly from CC via CTC (*white arrows*). Note the posterior position of the PSA on the cochlear promontory with ITC origin versus the anterior position with CTC origin (*white arrowheads*), best seen on sagittal reconstructions, *E* and *F*, PSA traverses oval window niche to enter tympanic segment of the facial nerve canal (*black arrows*). ANT = anterior; POST = posterior.

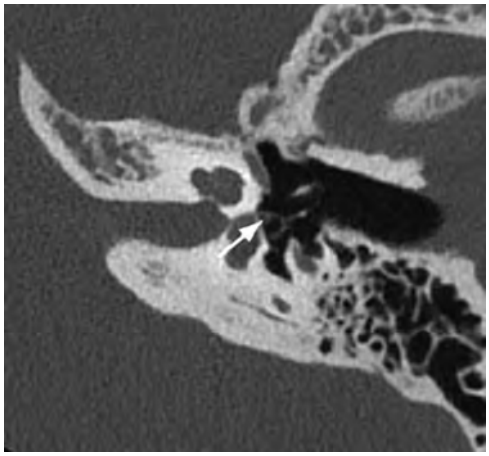

FIG 8. PSA courses through the obturator foramen of the stapes. Oblique axial CT reconstruction demonstrates cross-section of the artery along the inner margin of the anterior crus of the stapes (*arrow*) resembling a horseshoe on a stake (ringer sign).

by pulsations transmission via the stapes, where the PSA may abut stapedial crura. The symptom of pulsatile tinnitus may be more pronounced in patients with concomitant CHL.

The presence of a PSA historically has been a cause for perioperative concern, primarily because of bleeding risk and cerebral ischemia.[33,34] The primary risk of PSA transection is facial nerve palsy resulting from nerve injury or ischemia. In the current series, 1 PSA was successfully transected, in line with recent studies demonstrating surgical feasibility without significant complications in most patients with PSA. However, as is clear from the other 2 surgically aborted cases in our series, PSA can potentially pose a concern for a surgeon. Current strategies for symptomatic PSAs include transection of the vessel, particularly for pulsatile tinnitus, and/or ossicular chain reconstruction for CHL.[1,35,36]

PSA has been reported in association with numerous congenital anomalies and conditions, including trisomies 13, 15, and 21, Paget disease, otosclerosis, thalidomide deformities, anencephaly, congenital immunodeficiency, and neurofibromatosis.[10,15] The current series also documents associated congenital anomalies in 3 of 9 patients, including ipsilateral congenital cholesteatoma, ipsilateral congenital aerodigestive venolymphatic malformation, and chromosome 3q duplication or trisomy.

To date, this is the largest published series of CT findings in PSA. This imaging review highlights several pathognomonic CT signs and morphologic variations, which can give radiologists confidence identifying this vessel. Additionally, given significant association with congenital anomalies, the presence of a PSA on CT should prompt further investigation for potential concurrent imaging abnormalities. Although most of the described signs proving direct evidence of PSA are largely only appreciable on high-resolution temporal bone CT on workstations with reformat capabilities, absence of the foramen spinosum on routine head CTs may give a clue to a variant arterial anatomy, and further investigation could be suggested in an appropriate clinical setting. Additionally, because virtually all routine head CTs nowadays are acquired helically, source images at 0.625 or 0.75 mm might permit resolution high enough to visualize PSA above the absent foramen spinosum.

CONCLUSIONS

PSA is probably best understood as a spectrum of anomalous embryonic vessels that may persist postnatally in various forms. When encountered on CT, systematic evaluation of its proximal and distal course may help clarify its embryonic origin. As discussed, PSA may be both a structural cause for the patient's symptoms and an important factor for surgical planning and is therefore a variant worthy of consideration and comment when identified.

REFERENCES

1. Govaerts PJ, Marquet TF, Cremers WRJ, et al. **Persistent stapedial artery: does it prevent successful surgery?** *Ann Otol Rhinol Laryngol* 1993;102:724–28 CrossRef Medline
2. Moreano EH, Paparella MM, Zelterman D, et al. **Prevalence of facial canal dehiscence and of persistent stapedial artery in the human middle ear: a report of 1000 temporal bones.** *Laryngoscope* 1994;104:309–20 CrossRef Medline

3. Hyrtl J. **Neue beobachtungen aus dem gebiete der menschlichen und vergleichenden anatomie.** *Med Jahrb d Oesterreich Staates* 1836;10:457–66
4. House HP, Patterson ME. **Persistent stapedial artery: report of two cases.** *Trans Am Acad Ophthalmol Otolaryngol* 1964;68:644–46 Medline
5. Mahajan AC, Chaudhary N, Mishra M. **Persistent stapedial artery: an otomicroscopic finding.** *Int J Anat Var* 2018;11:2013–14
6. Pahor AL, Hussain SS. **Persistent stapedial artery.** *J Laryngol Otol* 1992;106:254–57 CrossRef Medline
7. Diamond MK. **Homologies of the stapedial artery in humans, with a reconstruction of the primitive stapedial artery configuration of euprimates.** *Am J Phys Anthropol* 1991;84:433–62 CrossRef Medline
8. Diamond MK. **Unusual example of a persistent stapedial artery in a human.** *Anat Rec* 1987;218:345–54 CrossRef Medline
9. Kelemen G. **Arteria stapedia, in bilateral persistence.** *AMA Arch Otolaryngol* 1958;67:668–77 CrossRef Medline
10. Marion M, Hinojosa R, Khan AA. **Persistence of the stapedial artery: a histopathologic study.** *Otolaryngol Head Neck Surg* 1985;93:298–312 CrossRef Medline
11. Guinto J, Garrabrant EC, Radcliffe WB. **Radiology of the persistent stapedial artery.** *Radiology* 1972;105:365–69 CrossRef Medline
12. Baltsavias G, Kumar R, Valavanis A. **The pharyngo-tympano-stapedial variant of the middle meningeal artery. A case report.** *Interv Neuroradiol* 2012;18:255–58 CrossRef Medline
13. Silbergleit R, Quint DJ, Mehta BA, et al. **The persistent stapedial artery.** *AJNR Am J Neuroradiol* 2000;21:572–77 Medline
14. Lefournier V, Vasdev A, Bessou P, et al. **A persistent pharyngohyostapedial artery: embryologic implications.** *AJNR Am J Neuroradiol* 1999;20:271–74 Medline
15. Thiers FA, Sakai O, Poe DS, Curtin HD. **Persistent stapedial artery: CT findings.** *AJNR Am J Neuroradiol* 2000;21:1551–54 Medline
16. Dimmick SJ, Faulder KC. **Normal variants of the cerebral circulation at multidetector CT angiography.** *Radiographics* 2009;29:1027–43 CrossRef Medline
17. Nica MI, Cosnard G. **Persistent stapedial artery: a congenital anomaly to know.** *JBR-BTR* 2013;96:22–24 CrossRef Medline
18. Jehl J, Jeunet L, Berraiah M, et al. **Bilateral persistent pharyngo-stapedial arteries revealed during evaluation of a carotid-cavernous fistula. 3 Tesla MR angiographic aspects.** *Interv Neuroradiol* 2006;12:327–34 CrossRef Medline
19. Hatipoglu HG, Cetin MA, Yuksel E, et al. **A case of a coexisting aberrant internal carotid artery and persistent stapedial artery: the role of MR angiography in the diagnosis.** *Ear Nose Throat J* 2011;90: E17–20 CrossRef Medline
20. Congdon E. **Transformation of the aortic-arch system during the development of the human embryo.** *Contrib Embryol* 1922;14
21. Padget D. **The development of the cranial arteries in the human embryo.** *Contrib Embryol* 1948;32:205–61
22. Altmann F. **Anomalies of the internal carotid artery and its branches; their embryological and comparative anatomical significance. Report of a new case of persistent stapedial artery in man.** *Laryngoscope* 1947;57:313–39 Medline
23. Steffen TN. **Vascular anomalies of the middle ear.** *Laryngoscope* 1968;78:171–97 CrossRef Medline
24. Strickland EM, Hanson JR, Anson BJ. **Branchial sources of auditory ossicles in man. I. Literature.** *Arch Otolaryngol* 1962;76:100–22 CrossRef Medline
25. Rodesch G, Choi I, Lasjaunias P. **Complete persistence of the hyoido-stapedial artery in man.** *Surg Radiology Anat* 1991;13:63–65 CrossRef Medline
26. Andreo JC, Caldas Navarro JA, Toledo Filho JL, et al. **Caroticotympanic artery: anatomically a normal branch or a variation of the internal carotid artery?** *Cells Tissues Organs (Print)* 2000;166:319–22 CrossRef Medline
27. Quisling RG, Rhoton AL. **Intrapetrous carotid artery branches: radioanatomic analysis.** *Radiology* 1979;131:133–36 CrossRef Medline
28. Hitier M, Zhang M, Labrousse M, et al. **Persistent stapedial arteries in human: from phylogeny to surgical consequences.** *Surg Radiology Anat* 2013;35:883–91 CrossRef Medline
29. Moret J, Delvert JC, Bretonneau CH, et al. **Vascularization of the ear: normal-variations-glomus tumors.** *J Neuroradiol* 1982;9:209–60 Medline
30. Nager GT, Nager M. **The arteries of the human middle ear, with particular regard to the blood supply of the auditory ossicles.** *Ann Otol Rhinol Laryngol* 1953;62:923–49 CrossRef Medline
31. Alexander G. **Ein fall von persistenz der arteria stapedia beim menschen.** *Monatsschr Ohrenheilkd Laryngorhinol* 1899;33:273–76
32. Royle G, Motson R. **An anomalous origin of the middle meningeal artery.** *J Neurol Neurosurg Psychiatry* 1973;36:874–76 CrossRef Medline
33. Wardrop P, Kerr AI, Moussa SA. **Persistent stapedial artery preventing successful cochlear implantation: a case report.** *Ann Otol Rhinol Laryngol Suppl* 1995;166:443–45 Medline
34. Hogg ID, Stephens CB, Arnold GE. **Theoretical anomalies of the stapedial artery.** *Ann Otol Rhinol Laryngol* 1972;81:860–70 CrossRef Medline
35. Goderie TPM, Alkhateeb WHF, Smit CF, et al. **Surgical management of a persistent stapedial artery: a review.** *Otol Neurotol* 2017;38:788–91 CrossRef Medline
36. Breheret R, Bizon A, Tanguy JY, et al. **Persistent stapedial artery with otosclerosis.** *Ann Otolaryngol Chir Cervicofac* 2009;126:259–63 CrossRef Medline

Characteristic Cochlear Hypoplasia in Patients with Walker-Warburg Syndrome: A Radiologic Study of the Inner Ear in α-Dystroglycan–Related Muscular Disorders

G. Talenti, C. Robson, M.S. Severino, C.A. Alves, D. Chitayat, H. Dahmoush, L. Smith, F. Muntoni, S.I. Blaser, and F. D'Arco

ABSTRACT

BACKGROUND AND PURPOSE: Walker-Warburg syndrome, muscle-eye-brain disease, and Fukuyama congenital muscular dystrophy are α-dystroglycan–related muscular disorders associated with brain malformations and eye abnormalities in which no structural inner ear abnormality has been described radiologically. We collected patients from 6 tertiary pediatric hospitals and reported the radiologic features and frequency of inner ear dysplasias.

MATERIALS AND METHODS: Patients previously diagnosed clinicoradiologically with Walker-Warburg syndrome, muscle-eye-brain disease, or Fukuyama congenital muscular dystrophy were included. We recorded the pathogenic variant, when available. Brain MR imaging and/or CT findings were reviewed in consensus, and inner ear anomalies were classified according to previous description in the literature. We then correlated the clinicoradiologic phenotype with the inner ear phenotype.

RESULTS: Thirteen patients fulfilled the criteria for the Walker-Warburg syndrome phenotype, 8 for muscle-eye-brain disease, and 3 for Fukuyama congenital muscular dystrophy. A dysplastic cochlea was demonstrated in 17/24. The most frequent finding was a pronounced cochlear hypoplasia type 4 with a very small anteriorly offset turn beyond the normal-appearing basal turn (12/13 patients with Walker-Warburg syndrome and 1/11 with muscle-eye-brain disease or Fukuyama congenital muscular dystophy). Two of 8 patients with muscle-eye-brain disease, 1/3 with Fukuyama congenital muscular dystrophy, and 1/13 with Walker-Warburg syndrome showed a less severe cochlear hypoplasia type 4. The remaining patients without Walker-Warburg syndrome were healthy. The vestibule and lateral semicircular canals of all patients were normal. Cranial nerve VIII was present in all patients with diagnostic MR imaging.

CONCLUSIONS: Most patients with the severe α-dystroglycanopathy Walker-Warburg syndrome phenotype have a highly characteristic cochlear hypoplasia type 4. Patients with the milder variants, muscle-eye-brain disease and Fukuyama congenital muscular dystrophy, more frequently have a normal cochlea or milder forms of hypoplasia.

ABBREVIATIONS: CH = cochlear hypoplasia; CH4 AOUT = cochlear hypoplasia type 4 with anterior offset of the upper turn; FCMD = Fukuyama congenital muscular dystrophy; MEB = muscle-eye-brain disease; SNHL = sensorineural hearing loss; WWS = Walker-Warburg syndrome

The α-dystroglycanopathies constitute a heterogeneous group of autosomal recessive disorders associated with muscular dystrophy due to a functional defect in the glycosylation of α-dystroglycan, a cellular membrane adhesion complex that forms a bridge between the cytoskeleton and components of the extracellular matrix such as laminin.[1] Most dystroglycanopathies involve a number of genes that code for glycosyltransferases, affecting the complex glycosylation of α-dystroglycan and therefore limiting its ability to bind the extracellular-matrix ligands

Received June 6, 2020; accepted after revision August 16.

From the Department of Diagnostics and Pathology (G.T.), Neuroradiology Unit, Verona University Hospital, Verona, Italy; Division of Neuroradiology (C.R.), Department of Radiology, Boston Children's Hospital and Harvard Medical School, Boston, Massachusetts; Neuroradiology Unit (M.S.S.), Istituti di Ricovero e Cura a Carattere Scientifico, Istituto Giannina Gaslini, Genova, Italy; Department of Radiology and Division of Neuroradiology (C.A.A.), Children's Hospital of Philadelphia, Philadelphia, Pennsylvania; The Prenatal Diagnosis and Medical Genetics Program (D.C.), Department of Obstetrics and Gynecology, Mount Sinai Hospital University of Toronto, Toronto, Ontario, Canada; Department of Radiology (H.D.), Lucile Packard Children's Hospital, Stanford University School of Medicine, Stanford, California; Dental and Maxillofacial Surgery Department (L.S.), Great Ormond Street Hospital, London, UK; Dubowitz Neuromuscular Centre (F.M.), UCL Great Ormond Street Institute of Child Health and Great Ormond Street Hospital, London, UK; Division of Neuroradiology (S.I.B.), Department of Diagnostic Imaging, The Hospital for Sick Children, Toronto, Ontario, Canada; and Neuroradiology Unit (F.D.), Department of Radiology, Great Ormond Street Hospital for Children, National Health Service Trust, London, UK.

This work was supported by the National Institute for Health Research, Great Ormond Street Hospital Biomedical Research Centre.

Please address correspondence to Felice D'Arco, MD, Neuroradiology Unit, Department of Radiology, Great Ormond St Hospital for Children NHS Trust, Gr. Ormond Street, WC1N3JH – London, United Kingdom;
e-mail: felice.d'arco@gosh.nhs.uk

http://dx.doi.org/10.3174/ajnr.A6858

(secondary dystroglycanopathies).[2] Rare mutations in dystroglycan itself are also recognized (primary dystroglycanopathies).

Mutations in at least 18 genes have been found to be involved in the glycosylation of α-dystroglycan,[1,3] and the list is growing. However, a precise genotype-phenotype correlation is not possible, and the disease spectrum includes multiple phenotypes with overlapping clinical features and severity. This is because the effect of the mutation on the protein is more important than the gene per se because of the different degrees of α-dystroglycan hypoglycosylation.[3,4]

Among these phenotypes, at the most severe end of the spectrum, Walker-Warburg syndrome (WWS), muscle-eye-brain disease (MEB), and Fukuyama congenital muscular dystrophy (FCMD) demonstrate brain malformations and ocular abnormalities, in addition to muscular dystrophy. Not surprisingly, the presence of malformations of cortical development of variable severity is associated with epilepsy and motor and language deficits.[5] The characteristic malformations of cortical development in these patients, a cobblestone lissencephaly/polymicrogyria-like cortex, result from variable-sized gaps in the pial basement membrane and overmigration of neuronal cells, related to the role of α-dystroglycan in the developing brain functioning as a link between radial glial cells and the pial basement membrane.[3]

Genetic mutations are an increasingly recognized cause of congenital hereditary sensorineural hearing loss (SNHL) and can be associated with various types of inner ear dysplasias.[6,7] Syndromic associations have also been described, with multiple additional abnormalities involving other organ systems and, in some cases, recognition of a specific type of inner ear dysplasia that can guide genetic testing.[8,9]

There are only a few anecdotal reports of hearing loss in muscular dystrophy, including α-dystroglycanopathies, but no structural abnormality has been described in a series of patients, to our knowledge.[1,10-13]

We hereby report the radiologic characteristics, frequency, and correlation with the clinicoradiologic phenotype of inner ear dysplasias encountered in a population of patients with α-dystroglycanopathy collected from 6 tertiary pediatric hospitals.

MATERIALS AND METHODS

Cases were identified using the electronic patient record system of each institution, searching for WWS, MEB, and FCMD diagnoses and adding relevant keyword searches (eg, "a-dystroglycanopathy," "congenital muscular dystrophy," "cobblestone cortex," and "cerebellar cysts"). Appropriate governance permissions from each site were obtained.

Only patients previously diagnosed clinicoradiologically as having WWS, MEB, or FCMD were included. According to previous literature,[3,4,10,11] a WWS phenotype was defined with observation of very early neurologic symptom onset (prenatally or at birth) and extreme brain abnormalities: complete agyria or severe lissencephaly/cobblestone, marked hydrocephalus, severe cerebellar hypoplasia/dysplasia, and complete or partial absence of the corpus callosum. In addition, a severely hypoplastic and "kinked" brain stem was determined as a characteristic feature of WWS and considered an inclusion criterion in this category.[10] Eye abnormalities include congenital cataracts, microphthalmia, and buphthalmos.

MEB and FCMD phenotypes were defined when brain abnormalities were less severe than those seen with WWS: pachygyria/polymicrogyria-like/cobblestone cortex with preferential frontoparietal involvement, cerebellar hypo/dysplasia, and less severe brain stem anomalies, including a posterior "bowing" (a posterior concavity less severe than that observed in kinked brain stem).[3,10] Despite a recognized radiologic overlap between MEB and FCMD,[4] clinically, cardiac and respiratory problems with less severe epilepsy were more typical of FCMD, while more severe ocular abnormalities and the absence of cardiac/respiratory features were more in keeping with MEB.[3,10,11]

When pathogenic genetic mutations were available, they were recorded; however, given the weak genotype/phenotype correlation in these disorders, we correlated the clinicoradiologic phenotype with the inner ear phenotype.

The authors retrospectively reviewed, by consensus, the brain MR imaging and/or CT findings (anonymized). MRIs were acquired on different scanners (both 1.5T and 3T) and with different protocols. An axial T2 brain sequence (section thickness, 2–3 mm) or a high-resolution 3D steady-state sequence of the internal auditory meatus was used to assess the inner ears. The axial T2 was considered diagnostic when cochleae were visualized in at least 2 slices (basal turns in the most caudal one and middle/apical turns in the cranial one).

Available CT scans were acquired with a standard brain protocol and subsequent bone algorithm reconstructions (1-mm section thickness).

Inner ear anomalies were reviewed and classified according to previous literature.[6,9] More specifically, cochlear hypoplasia (CH) was defined as a cochlea with a small external size and a less than normal number of 2½–2¾ turns. The definition of each CH subtype was previously described in histologic and radiologic studies:[6,12] 1) CH-1: tiny budlike cochlea without an internal structure; 2) CH-2: a small cochlea with a modiolus or interscalar septa, which are present but defective; 3) CH-3: the internal and external architecture (modiolus, interscalar septa) is similar to that of a normal cochlea, but the overall size is smaller with fewer or shorter turns; and 4) CH-4: a small cochlea with a normal basal turn but hypoplastic middle and apical turns.

In addition, an anterior offset of the cochlear middle turn was recorded when there was "anteromedial angulation and displacement of the middle and apical turns of the cochlea away from the basal turn," similar to the cochlea malformation described in branchio-oto-renal syndrome.[13]

Patients who did not fulfill the clinicoradiologic criteria for WWS, MEB, or FCMD or with images suboptimal for cochlear assessment were excluded.

RESULTS

After initial research, we excluded 3 patients: 2 with MEB with suboptimal images and an aborted 20-week fetus with severe cortical malformation and kinking of the brain stem but without clinical criteria or genetic mutations available at the time of the report and no postnatal MR imaging performed.

Twenty-four patients with congenital muscular dystrophy due to secondary dystroglycanopathies were found. Fourteen (14/24) were males (age range, 1 day to 21 years). Thirteen of 24 showed a

Demographic, genetic and radiological characteristics of the patients

	Sex	Age at Imaging	Clinicoradiologic Phenotype	Genetic Mutation	Cochlear Phenotype	Imaging Where Cochlea Was Assessed
Patient 1	M	5 mo	WWS	*POMT1*	CH4 AOUT	MR imaging brain, CT brain
Patient 2	M	3 mo	WWS	*POMT1*	CH4 AOUT	MR imaging brain, CT brain
Patient 3	F	15 days	WWS	*POMT2*	CH4 AOUT	MR imaging brain, CT brain
Patient 4	F	1 day	WWS	*POMT1*	CH4 AOUT	MR imaging brain (axial T2)
Patient 5	M	1 day	WWS	*FKRP*	CH4 AOUT	MR imaging brain, CT brain
Patient 6	M	4 yr	WWS	Not available	CH 4 (less severe phenotype)	MR imaging brain (axial T2)
Patient 7	F	2 mo	WWS	Not available	CH4 AOUT	MR imaging brain (axial T2)
Patient 8	M	9 days	WWS	Not available	CH4 AOUT	MR imaging brain (axial T2)
Patient 9	F	4 mo	WWS	*B3GNT1*	CH4 AOUT	MR imaging brain, CT brain
Patient 10	F	18 mo	WWS	*FKTN*	CH4 AOUT	MR imaging brain, CT brain
Patient 11	F	7 mo	WWS	*POMT1*	CH4 AOUT	MR imaging brain, CT brain, 3D T2 IAMs
Patient 12	M	3 mo	WWS	Not available	CH4 AOUT	MR imaging brain (axial T2)
Patient 13	F	2 mo	WWS	Not available	CH4 AOUT	MR imaging brain (axial T2)
Patient 14	M	2.5 yr	MEB	*POMGnT1*	CH 4 (less severe phenotype)	MR imaging brain (axial T2)
Patient 15	F	7 yr	MEB	*POMGNT1*	Normal	MR imaging brain, CT brain
Patient 16	M	3 mo	MEB	*POMGnT1*	Normal	MR imaging brain, CT brain
Patient 17	M	2 days	MEB	*POMGnT1*	Normal	MR imaging brain (axial T2)
Patient 18	M	21 yr	MEB	*POMGnT1*	Normal	MR imaging brain (axial T2)
Patient 19	M	1 yr	MEB	*POMT2*	CH4 AOUT	MR imaging brain (axial T2), 3D-T2 IAMs
Patient 20	M	11 mo	MEB	*POMGNT2*	CH 4 (less severe phenotype)	MR imaging brain (axial T2)
Patient 21	M	9 mo	MEB	Not available	Normal	MR imaging brain (axial T2)
Patient 22	M	6 mo	Fukuyama	*FKRP*	Normal	MR imaging brain (axial T2)
Patient 23	F	2 days	Fukuyama	*FKRP*	CH 4 (less severe phenotype)	MR imaging brain, CT brain
Patient 24	F	14 mo	Fukuyama	Not available	Normal	MR imaging brain (axial T2)

Note:—IAMs indicates internal auditory meatus.

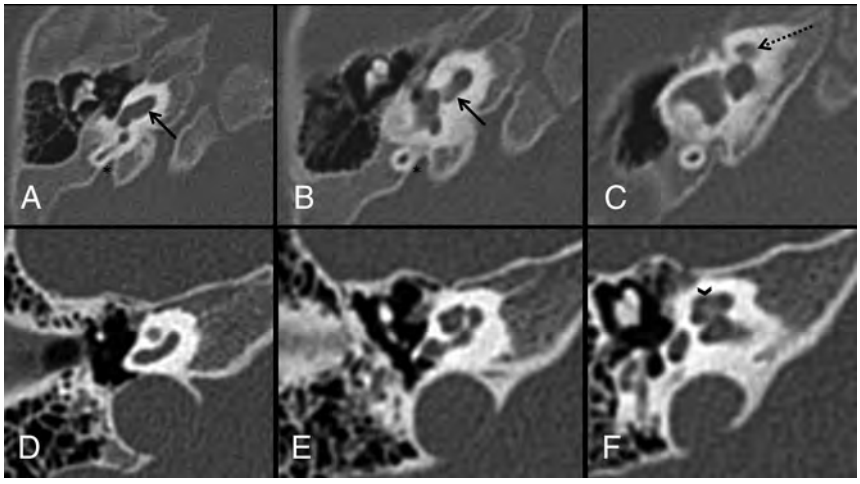

FIG 1. Axial CT with thin bone reformats in patient 1. The WWS phenotype and *POMT1* variant (*A*, *B*, and *C*) show a characteristic CH4 AOUT with a normal basal turn (*arrows* in *A* and *B*) and a very hypoplastic and anteromedially displaced upper part of the cochlea (*dashed arrow* in *C*). The abnormality was symmetric on both sides. Note the normal appearance of the semicircular canals and vestibule. The vestibular aqueducts (*asterisk* in *A* and *B*), despite looking slightly enlarged on subjective analysis, were within normal limits when measured. A normal cochlea for comparison (*D*, *E*, and *F*) shows well-developed middle and apical turns (*arrowhead* in *F*).

WWS phenotype; 8/24, an MEB phenotype; and 3/24, an FCMD phenotype. Genetic confirmation was available in 17/24 cases: 5 *POMGNT1*, 4 *POMT1*, 2 *POMT2*, 3 FKRP, 1 FKTN, 1 *B3GNT1*, and 1 *POMGNT2*.

Dysplastic cochlear morphology was found in 17/24; in all cases, the abnormality was bilateral and symmetric. Cochlear morphology appeared normal in 7/24 (Table).

The most frequent finding was characteristic cochlear hypoplasia with a normal basal turn and extremely hypoplastic upper turns that appeared offset anteriorly with respect to the basal turn. Given the normal basal turn, this was classified as a CH type 4 (Figs 1 and 2).

This morphology was found in 13/24 patients. Most interestingly, the pronounced CH4 with an anterior offset of the upper turn (CH4 AOUT) was present in 12/13 of patients with WWS but only 1/11 of the remaining phenotypes, a patient with MEB. The remaining patient with WWS also had a small cochlea with a normal basal turn (CH4)[6,12] but with better developed upper turns, similar to the other less severe CH4 found in some of the patients with MEB and FCMD (Fig 3). Among the MEB phenotypes, 5/8 patients had normal cochleae, 1/8 had CH4 AOUT, and 2/8 showed a less severe form of CH4. Patients with

FCMD had normal cochleae in 2/3 cases, while 1 subject had a less severe form of CH4. In all patients, we found that the vestibules and semicircular canals were normal (Fig 2). The vestibulocochlear nerves were bilaterally present in all cases (on axial T2 images).

No audiometric correlation was available because hearing function is not routinely evaluated in these patients.

DISCUSSION

Mutations in 18 currently known genes can cause defective glycosylation of α-dystroglycan and, consequently, a subset of congenital muscular dystrophies called secondary dystroglycanopathies. These diseases vary in severity from mild adult-onset limb-girdle muscular dystrophy to more severe phenotypes with early-onset and eye and brain involvement.[3] Brain malformations have been extensively described in patients at the severe end of the clinical spectrum and were used as one of the diagnostic criteria, even before the genetic profile was recognized.[14]

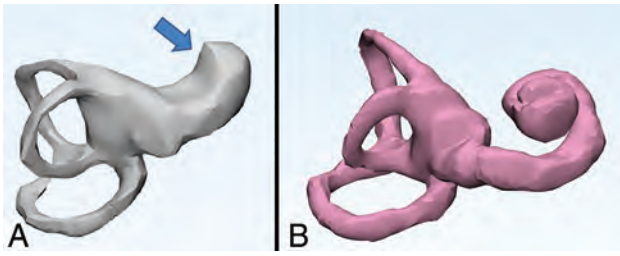

FIG 2. 3D volume-rendering of the CH4 AOUT in patient 2 with a WWS phenotype and *POMT1* variant (*A*) in comparison with a healthy control (*B*). Note the marked cochlear hypoplasia in *A* (*arrow*) in comparison with normal 2½ cochlear turns in *B*. The vestibule and lateral semicircular canals are normal in both patients.

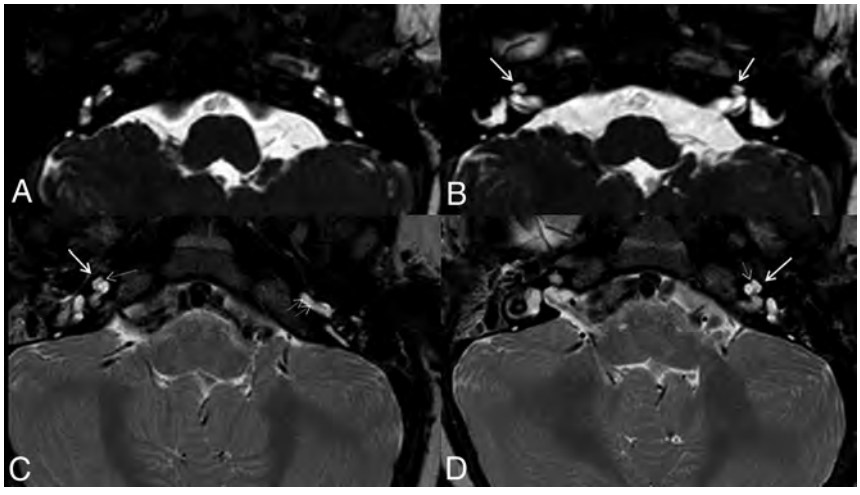

FIG 3. A variable cochlear appearance in MEB phenotypes. High-resolution steady-state (CISS) images in patient 19 (*A* and *B*) show a pronounced hypoplastic cochlea, similar to the cases of WWS with a small "budlike" protuberance that is anteriorly offset (*arrows* in *B*). Axial T2 (section thickness, 3 mm) in patient 20 shows a hypoplastic cochlea with a more developed middle turn (*arrows* in *C* and *D*) and visualization of medial interscalar septum (*thin dotted arrow*). Note the thin linear hypointensity within the fluid signal of the basal turn, in keeping with a preserved lamina spiralis well-seen in both patients (*double arrow* in *C*).

An important concept, useful in the interpretation of our data, is that in secondary dystroglycanopathies, a precise genotype/phenotype correlation is not possible because the mutations in the same gene can cause a variety of different phenotypes and these diseases should be considered as a clinicoradiologic spectrum. This is mainly due to the effect of individual mutations on the glycosylation of α-dystroglycan, with WWS representing the extremely severe variant.[3,4] A relatively milder form of congenital muscular dystrophy with structural brain involvement is represented by MEB/FCMD, usually associated with founder mutations in *POMGNT1* and *FKTN,* but less frequently associated with most of the other genes.[4,11]

Thus, we decided to correlate the clinicoradiologic phenotype (rather than genotype) with inner ear appearances, and in doing so, we found that 100% of patients with WWS showed striking cochlear abnormalities (12/13 had a characteristic CH4 AOUT), while only 4/11 with MEB/FCMD had cochlear abnormalities and only 1 had CH4 AOUT. Therefore, the cochlea seems to predict the brain to some extent.

Very few reports of children with congenital muscular dystrophies and SNHL have been previously published.[15] Carss et al[1] published a case series of 8 patients with α-dystroglycanopathy due to *GMPPB* variants: among them, a patient with an MED/FCMD phenotype and "pontine and cerebellar hypoplasia" had SNHL. Later on, a patient with a *FKRP* variant was reported to have unusually severe eye abnormalities and SNHL.[16] Bilateral SNHL has been recently reported in 12 subjects with the *B3GALNT2* variant, severe brain malformations (mostly cobblestone/polymicrogyria spectrum and pontocerebellar hypoplasia/dysplasia), and epilepsy, but no morphologic description of the inner ear anomalies was available.[17] Furthermore, microstructural changes in the cochlea have been described in a laminin-deficient *dy* mouse model of congenital muscular dystrophy, implying that laminin is critical in the cochlear function and development.[18] The role of the laminin is further supported by the presence of antibodies against laminin in various forms of hearing loss.[19] Finally, SNHL has been noted in a patient with limb-girdle muscular dystrophy[20] and in 2 siblings with arthrogryposis multiplex congenita and cobblestone lissencephaly.[21]

Hence, hearing loss may be a largely under-recognized feature of the severe α-dystroglycanopathies with central nervous system involvement, noting that the genetic link is not as yet well-established.

It is interesting that all the inner ear dysplasias in this series exclusively involved the cochlear portion of the labyrinth. No other abnormality was found in the inner ear (normal vestibule and semicircular canals).

A number of gene families are of critical importance in the embryogenesis of the otic capsule–derived structures (eg, *FOX*, *DIX*, *FGF*, *PAX*, and *SOX*), and correlations have been found between some pathogenic genes and characteristic inner ear malformations.[9,22,23] Moreover, some of these genes are significantly involved in the embryogenesis of other systems, producing quite notable syndromic associations.[8]

According to the "compartment boundary model" of inner ear development, particular genes are involved in the development of the ventral portion of the otic capsule (ie, cochlear morphogenesis), while others are involved in the development of the vestibule or semicircular canals.

Although much is still unknown about the "symphony of inner ear development control genes" (as described by Chatterjee et al[24]), we know that for instance, *Shh* maintains *Pax2* in the medial and ventral wall of the forming otic vesicle determining the cochlear fate, while *wnt* and *Dlx5/Dlx6* are involved in the development of the vestibule and semicircular canals.

In fact, *Pax2* knockout mice demonstrate an absent cochlea, while other genes can account for the loss of ≥1 semicircular canal.[22] It is then possible that in dystroglycanopathies, the functions of ≥1 gene determining exclusively the cochlear fate, rather than the development of the otic capsule as a whole, are impaired.

There is other evidence that may be relevant in explaining the specific cochlear phenotype in our patients: 1) The sensory precursor cells are under the control of many cyclin-dependent kinase inhibitors, including p27, which is more active when the cochlea starts to develop the middle and apical turns and after the development of the basal turn (exactly when the cochlear development is arrested in case of CH4);[25] and 2) the GG domain (a widely distributed protein motif) is present in *POMGnT1* (mutated in MEB) but also in cases of nonsyndromic hearing loss.[1,17,26]

Finally, insights can come from the embryology; according to Sennaroglu,[7] CH-4 is likely a genetically determined hypoplasia in which the arrest in the membranous labyrinth development happens between the 10th and 20th week before the middle and apical turns reach normal size but the basal turn has already fully developed. Therefore, it is possible that the CH4 morphology in patients with WWS is due to a genetically determined arrested development between the 10th and 20th week, associated with the malfunction of genes that are specifically involved in the development of the cochlea. Cochlear hypoplasia type 4 can also be found in other genetically determined syndromes[8] and does not constitute a pathognomonic feature of dystroglycanopathies. However, in the appropriate clinicoradiologic context, such a marked hypoplastic phenotype seems to be fairly specific for the WWS phenotype.

The main limitation of this study is its retrospective nature and the fact that all except 2 MR imaging studies consisted of routine brain sequences rather than detailed sequences for the inner ear. Nevertheless, on CT and 2- to 3-mm axial T2-weighted images of the brain, the cochlea can be adequately assessed by experienced pediatric neuroradiologists in consensus. If possible, adding a high-resolution 3D steady-state sequence to the MR imaging protocol would be ideal to depict the abnormality. Also, when available, we found that thin bone reformats of a CT of the head obtained for hydrocephalus are enough to characterize the cochlear abnormalities in those patients.

Another potential bias lies in the clinical diagnosis of these syndromes, which, in itself, is often challenging and commonly presents with overlapping features. To avoid misinterpretation of the correct diagnosis, a clinical and radiologic analysis was required to confirm that each subject fulfilled the criteria for each syndrome.

CONCLUSIONS

This is the first radiologic description of inner ear dysplasias in a relatively large series of patients with α-dystroglycanopathies characterized by distinct pronounced hypoplasia of the middle cochlear turns, which appears anteriorly offset from the basal turn, with an absent/deficient apical turn in most WWS phenotypes and with less frequent and less marked dysplasia (but again limited to the cochlea) in the MEB and FCMD phenotypes. This evidence lays the foundation for further studies investigating the genetic link between ear development and α-dystroglycanopathies, which may help in understanding the factors specifically responsible for cochlear development.

ACKNOWLEDGMENTS

We would like to thank Mr Juling Ong, consultant craniofacial and pediatric plastic surgeon at Great Ormond Street Hospital, for supervising the 3D reformatting and 3D printing of the cochlear abnormalities.

Disclosures: Mariasavina Severino—*UNRELATED*: *Employment*: Neuroradiology Consultant at Istituti di Ricovero e Cura a Carattere Scientifico, Istituto Giannina Gaslini. Francesco Muntoni—*UNRELATED*: *Consultancy*: Sarepta Therapeutics, Biogen, AveXis, Pfizer, Roche, *Comments*: SABs; *Grants/Grants Pending*: Sarepta Therapeutics, Biogen, *Comments*: investigator-initiated studies; *Payment for Lectures Including Service on Speakers Bureaus*: Sarepta Therapeutics, Biogen, AveXis, Roche, *Comments*: meetings and symposia. Susan I. Blaser—*UNRELATED*: *Royalties*: Elsevier.

REFERENCES

1. Carss KJ, Stevens E, Foley AR, et al; UK10K Consortium. **Mutations in GDP-mannose pyrophosphorylase B cause congenital and limb-girdle muscular dystrophies associated with hypoglycosylation of α-dystroglycan.** *Am J Hum Genet* 2013;93:29–41 CrossRef Medline
2. Brancaccio A. **A molecular overview of the primary dystroglycanopathies.** *J Cell Mol Med* 2019;23:3058–62 CrossRef Medline
3. Brun BN, Mockler SR, Laubscher KM, et al. **Comparison of brain MRI findings with language and motor function in the dystroglycanopathies.** *Neurology* 2017;88:623–29 CrossRef Medline
4. Godfrey C, Clement E, Mein R, et al. **Refining genotype phenotype correlations in muscular dystrophies with defective glycosylation of dystroglycan.** *Brain* 2007;130:2725–35 CrossRef Medline
5. Martin PT. **The dystroglycanopathies: the new disorders of O-linked glycosylation.** *Semin Pediatr Neurol* 2005;12:152–58 CrossRef Medline
6. Talenti G, Manara R, Brotto D, et al. **High-resolution 3 T magnetic resonance findings in cochlear hypoplasias and incomplete partition anomalies: a pictorial essay.** *Br J Radiol* 2018;91:20180120 CrossRef Medline

7. Sennaroglu L. **Histopathology of inner ear malformations: do we have enough evidence to explain pathophysiology?.** *Cochlear Implants Int* 2016;17:3–20 CrossRef Medline
8. D'Arco F, Youssef A, Ioannidou E, et al. **Temporal bone and intracranial abnormalities in syndromic causes of hearing loss: an updated guide.** *Eur J Radiol* 2020;123:108803 CrossRef Medline
9. D'Arco F, Sanverdi E, O'Brien WT, et al. **The link between inner ear malformations and the rest of the body: what we know so far about genetic, imaging and histology.** *Neuroradiology* 2020;62:539–44 CrossRef Medline
10. Barkovich AJ. **Neuroimaging manifestations and classification of congenital muscular dystrophies.** *AJNR Am J Neuroradiol* 1998;198: 1389–96 Medline
11. Kang PB, Morrison L, Iannaccone ST, et al; Guideline Development Subcommittee of the American Academy of Neurology and the Practice Issues Review Panel of the American Association of Neuromuscular & Electrodiagnostic Medicine. **Evidence-based guideline summary: evaluation, diagnosis, and management of congenital muscular dystrophy: Report of the Guideline Development Subcommittee of the American Academy of Neurology and the Practice Issues Review Panel of the American Association of Neuromuscular & Electrodiagnostic Medicine.** *Neurology* 2015;85:1432–78 CrossRef Medline
12. Sennaroğlu L, Bajin MD, Pamuk E, et al. **Cochlear hypoplasia type four with anteriorly displaced facial nerve canal.** *Otol Neurotol* 2016;37:e407–09 CrossRef Medline
13. Hsu A, Desai N, Paldino MJ. **The unwound cochlea: a specific imaging marker of branchio-oto-renal syndrome.** *AJNR Am J Neuroradiol* 2018;39:2345–49 CrossRef Medline
14. Dobyns WB, Pagon RA, Armstrong D, et al. **Diagnostic criteria for Walker-Warburg syndrome.** *Am J Med Genet* 1989;32:195–210 CrossRef Medline
15. Bigoni S, Mauro A, Ferlini A, et al. **Cochlear malformation and sensorineural hearing loss in the Silver-Russell Syndrome.** *Minerva Pediatr* 2018;70:380–81 CrossRef
16. Kava M, Chitayat D, Blaser S, et al. **Eye and brain abnormalities in congenital muscular dystrophies caused by fukutin-related protein gene (FKRP) mutations.** *Pediatr Neurol* 2013;49:374–78 CrossRef Medline
17. Al Dhaibani MA, El-Hattab AW, Ismayl O, et al. **B3GALNT2-related dystroglycanopathy: expansion of the phenotype with novel mutation associated with muscle-eye-brain disease, Walker-Warburg Syndrome, epileptic encephalopathy-West syndrome, and sensorineural hearing loss.** *Neuropediatrics* 2018;49:289–95 CrossRef Medline
18. Pillers DA, Kempton JB, Duncan NM, et al. **Hearing loss in the laminin-deficient dy mouse model of congenital muscular dystrophy.** *Mol Genet Metab* 2002;76:217–24 CrossRef Medline
19. Klein R, Timpl R, Zanetti FR, et al. *Ann Otol Rhinol Laryngol* 1989;98:537–42 CrossRef Medline
20. Oexle K, Herrmann R, Dodé C, et al. **Neurosensory hearing loss in secondary adhalinopathy.** *Neuropediatrics* 1996;27:32–36 CrossRef Medline
21. Seidahmed MZ, Sunada Y, Ozo CO, et al. **Lethal congenital muscular dystrophy in two sibs with arthrogryposis multiplex: new entity or variant of cobblestone lissencephaly syndrome?** *Neuropediatrics* 1996;27:305–10 CrossRef Medline
22. Som PM, Curtin HD, Liu K, et al. **Current embryology of the temporal bone, Part I: the inner ear.** *Neurographics* 2016;6:250–65 CrossRef
23. Siddiqui A, D'Amico A, Colafati GS, et al. **Hypothalamic malformations in patients with X-linked deafness and incomplete partition type 3.** *Neuroradiology* 2019;61:949–52 CrossRef Medline
24. Chatterjee S, Kraus P, Lufkin T. **A symphony of inner ear developmental control genes.** *BMC Genet* 2010;11:68 CrossRef Medline
25. Kelly MC, Chen P. **Development of form and function in the mammalian cochlea.** *Curr Opin Neurobiol* 2009;19:395–401 CrossRef Medline
26. Guo J, Cheng H, Zhao S, et al. **GG: a domain involved in phage LTF apparatus and implicated in human MEB and non-syndromic hearing loss diseases.** *FEBS Lett* 2006;580:581–84 CrossRef Medline

Arterial Spin-Labeling Perfusion for PHACE Syndrome

M.D. Mamlouk, A. Vossough, L. Caschera, M. Maheshwari, and C.P. Hess

ABSTRACT

BACKGROUND AND PURPOSE: Arterial stroke is a rare-but-reported complication in patients with posterior fossa brain malformations, hemangiomas, arterial anomalies, coarctation of the aorta and cardiac defects, and eye abnormalities (PHACE) syndrome. Currently, stroke risk is inferred by the severity of arterial anomalies identified on MRA, though no evidenced-based data exist. The purpose of our study was to determine whether arterial spin-labeling MR imaging perfusion can detect alterations in CBF in patients with PHACE syndrome.

MATERIALS AND METHODS: Records were reviewed from 3 institutions for all patients with PHACE syndrome who underwent arterial spin-labeling from 2000 to 2019. CBF was qualitatively investigated with arterial spin-labeling to determine whether there was decreased or normal perfusion. Arterial anomalies were characterized on MRA imaging, and parenchymal brain findings were evaluated on conventional MR imaging sequences.

RESULTS: Forty-one patients with PHACE syndrome had arterial spin-labeling imaging. There were 30 females and 11 males (age range, 7 days to 15 years). Of the 41 patients, 10 (24%) had decreased CBF signal corresponding to a major arterial territory. Ten of 10 patients had decreased CBF signal in the anterior circulation, 2/10 had decreased anterior and posterior circulation CBF signal, 2/10 had decreased bilateral anterior circulation CBF signal, and 1/10 had globally decreased CBF signal. Forty of 41 (97.5%) patients had at least 1 arteriopathy, and in those with decreased CBF signal, the arteriopathy corresponded to the CBF signal alteration in 10/10 patients.

CONCLUSIONS: Arterial spin-labeling can potentially characterize hemodynamic changes in patients with PHACE syndrome.

ABBREVIATIONS: ASL = arterial spin-labeling; PHACE = posterior fossa brain malformations, hemangiomas, arterial anomalies, coarctation of the aorta and cardiac defects, and eye abnormalities

Arterial ischemic stroke is a rare-but-devastating complication in a minority of patients with posterior fossa brain malformations, hemangiomas, arterial anomalies, coarctation of the aorta and cardiac defects, and eye abnormalities (PHACE) syndrome. Stroke has been reported in multiple patients with PHACE syndrome,[1-6] but the etiology of stroke is poorly understood.[1] Possible mechanisms for stroke with PHACE include the following: 1) artery-to-artery embolisms, 2) ischemia from reduced blood flow, or 3) cardioembolism. These etiologies are predicated on arteriopathies in the brain, neck, and aortic arch, which are the most common extracutaneous finding in patients with PHACE syndrome.[7] In 1 study, arteriopathies were observed in 91% of 33 patients[8] and ranged from an anomalous course to marked stenosis with a Moyamoya pattern.[3] Currently, stroke risk is only inferred by the severity of these arteriopathies identified on MRA imaging.[9] Despite knowledge of the types of arteriopathies in PHACE,[3] it is unclear why certain patients with arteriopathies experience a stroke and others do not, even if there are severe anomalies in both subsets. To date, no evidence-based data exist on stroke risk in PHACE syndrome.

Received May 28, 2020; accepted after revision August 19.

From the Department of Radiology (M.D.M.), The Permanente Medical Group, Kaiser Permanente Medical Center, Santa Clara, Santa Clara, California; Department of Radiology and Biomedical Imaging (M.D.M., C.P.H.), University of California, San Francisco, San Francisco, California; Department of Radiology (A.V., L.C.), Children's Hospital of Philadelphia, Perelman School of Medicine, University of Pennsylvania, Philadelphia, Pennsylvania; Department of Radiology (L.C.), La Fondazione Institute for Research, Hospitalization and Health Care Ca' Granda Ospedale Maggiore di Milano Policlinico, Milan, Italy; and Department of Radiology (M.M.), Medical College of Wisconsin, Children's Hospital of Wisconsin, Milwaukee, Wisconsin.

Paper previously presented as an abstract at: International Society and Study of Vascular Anomalies Workshop, May 14–15, 2020; Virtual.

Please address correspondence to Mark D. Mamlouk, MD, Department of Radiology, The Permanente Medical Group, Kaiser Permanente Medical Center, Santa Clara, 700 Lawrence Expy, Santa Clara, CA 95051; e-mail: mark.d.mamlouk@kp.org, mark.mamlouk@ucsf.edu; @MarkMamloukMD

Indicates open access to non-subscribers at www.ajnr.org
Indicates article with supplemental online table.
http://dx.doi.org/10.3174/ajnr.A6871

Arterial spin-labeling (ASL) is a noncontrast MR imaging perfusion sequence that has been studied in patients with stroke and vasculopathies, particularly with the Moyamoya pattern and has proved useful in analyzing CBF.[10,11] In the setting of PHACE syndrome, the concept of ASL imaging has been introduced[12,13] as well as for other cutaneous vascular anomalies.[12-14] The purpose of our study was to determine whether ASL perfusion can detect alterations in CBF in patients with PHACE syndrome.

MATERIALS AND METHODS

Study Population

This study was approved by the institutional review boards at each of the 3 hospitals (University of California, San Francisco; University of Pennsylvania; Medical College of Wisconsin), which waived the requirement for informed consent. Electronic medical records were reviewed from the 3 institutions for all patients with PHACE syndrome who underwent MR imaging with ASL from 2000 to 2019. All patients were discussed in the vascular anomalies clinic or in subspecialized pediatric dermatology clinics for cutaneous vascular anomalies at the respective institutions, where the diagnosis of PHACE syndrome was rendered using the latest PHACE syndrome consensus guidelines.[9] Many patients were treated with propranolol for hemangioma, though this information was not fully available on each patient and these data were not collected in this study.

ASL Technique

Details of the ASL imaging technique varied depending on the institution, MR imaging vendor, and type of ASL acquisition scheme. ASL performed on 3T MR imaging systems (GE Healthcare) included pseudocontinous labeling with a background-suppressed 3D spiral acquisition with the following parameters: TR/TE = 4409/10.6 ms; labeling period = 1500 ms; postlabel delay = 1500 ms; FOV = 20 cm; matrix = 128 × 128. ASL performed on 1.5 or 3T (Siemens) MRI systems included 2D or 3D pulsed labeling with the following parameters: TR/TE = 2500/14 ms; labeling period = 700 ms; postlabel delay = 1800–1990 ms; FOV = 20 cm; matrix = 64 × 64. The postlabel delay on each MR imaging system was specified using the vendor's prefixed setting, and the parameter was not adjusted for age.

Imaging Review

Five neuroradiologists with 1, 7, 13, 16, and 16 years of postresidency experience in neuroimaging and arterial spin-labeling techniques and participation in a vascular anomalies clinic reviewed the MR images. CBF maps derived from ASL were qualitatively evaluated to determine whether there was decreased or normal perfusion within a major arterial territory. At least 1 neuroradiologist reviewed the images at each institution. In certain instances, 2 neuroradiologists assessed the imaging, and the evaluation was made by consensus. Arterial anomalies were characterized on the available noncontrast or contrast-enhanced MRA. The MRA images were evaluated in the same setting as the ASL images, and the neuroradiologists were not blinded to each set of images. The types of arteriopathies evaluated included the following: dysgenesis, narrowing, nonvisualization, persistent embryonic carotid-vertebrobasilar arterial connections, and abnormalities in the arterial course and/or origin.[3] The descriptor "dysgenesis" was used to describe bizarre looping, elongation, kinking, and aneurysmal enlargement.[3] Parenchymal brain findings were assessed on DWI and T2/FLAIR, including the presence of acute or chronic infarct and any other developmental anomalies. The location of hemangiomas was also noted. If the hemangioma had involuted by the time of scanning, the location was recorded from the physical examination findings or previous assessments in the electronic chart.

RESULTS

Patient Characteristics and ASL Findings

Forty-one patients with PHACE syndrome had MR imaging examinations with ASL imaging (Online Table). There were 30 females (73%) and 11 males (27%). The ages ranged from 7 days to 15 years (median, 1 year; interquartile range, 3 months to 6.5 years). Of the 41 patients, 10 (24%) had decreased CBF signal corresponding to a major arterial territory. Ten of 10 patients had decreased CBF signal in the anterior circulation, 2/10 had decreased anterior and posterior circulation CBF signal, 2/10 had decreased bilateral anterior circulation CBF signal, and 1/10 had globally decreased CBF signal. Forty of 41 (97.5%) patients had at least 1 arteriopathy, and in those with decreased CBF signal, the arteriopathy corresponded to the CBF signal alteration in 10/10 patients. The 10 patients with decreased ASL signal had arteriopathies that demonstrated nonvisualization or narrowing of the major vessels supplying that vascular territory. Representative cases are seen in Figs 1–3.

Conventional MR Imaging Findings

None of the patients in this cohort had MR imaging evidence of acute or chronic infarct. Twenty-two of 41 (54%) patients had posterior fossa abnormalities, such as cerebellar dysgenesis or Dandy-Walker malformation. Sixteen of 41 (39%) patients had trigeminal cistern enlargement, which has been described in PHACE syndrome and is possibly related to aberrant migration of the cephalic neural crest in a metameric distribution.[15] Fourteen of 41 (34%) patients had hemangiomas identified on imaging, while the remaining hemangiomas had involuted by the time of scanning. The hemangiomas were ipsilateral to the arteriopathy in 16 of the 17 patients

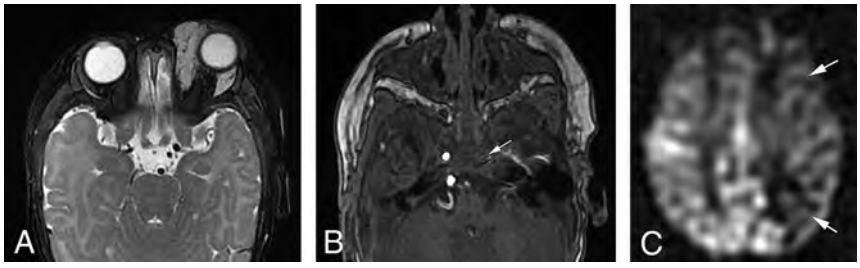

FIG 1. Decreased CBF in PHACE syndrome. *A*, Axial T2-weighted fat-suppressed image shows a left periorbital hemangioma. *B*, Axial time-of-flight MRA shows absence of the left cavernous ICA (*arrow*), which was reconstituted on the relatively more superior images (not shown). *C*, Axial ASL imaging shows decreased CBF signal in the left ICA territory (*arrows*).

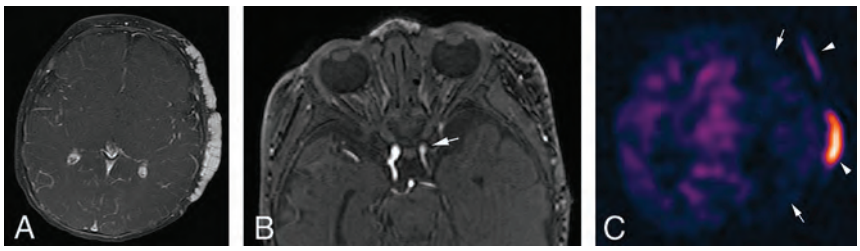

FIG 2. Decreased CBF in PHACE syndrome. *A*, Axial T1-weighted contrast-enhanced fat-suppressed image shows hemangiomas in the left frontoparietal scalp. *B*, Axial time-of-flight MRA shows a hypoplastic left cavernous ICA (*arrow*). *C*, Axial ASL imaging shows decreased CBF signal in the left ICA territory (*arrows*). The scalp hemangiomas show hyperintense signal (*arrowheads*) due to their arterial vascularity.

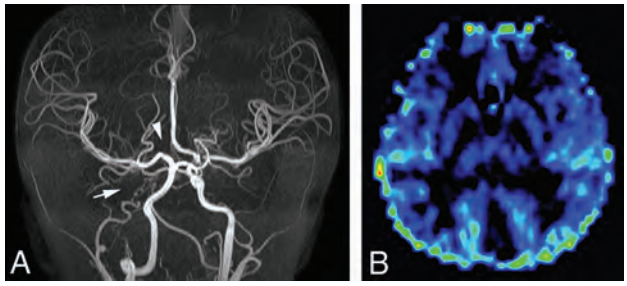

FIG 3. Normal CBF signal in PHACE syndrome. *A*, Time-of-flight MRA reconstruction shows absence of the right cervical and intracranial ICA (*arrow*). The right A1 anterior cerebral artery segment is also absent (*arrowhead*). *B*, Axial ASL imaging shows symmetric CBF bilaterally. This case shows that despite a severe arteriopathy, ASL provides additional value by showing normal CBF signal.

(94%) with unilateral arteriopathy, which is in keeping with findings in another publication.[3] The physical examination findings of these remaining hemangiomas are described in the Online Table.

DISCUSSION

To our knowledge, this multicenter study of 41 patients represents the largest cohort to date of patients with PHACE syndrome scanned with ASL perfusion imaging. While nearly every patient (40/41) had an arteriopathy, only approximately one-quarter of patients (10/41) had decreased CBF signal in at least 1 major arterial territory. All patients with decreased CBF signal had involvement of the anterior circulation. None of the patients had acute or chronic infarction.

These findings suggest that ASL may serve a role in the imaging evaluation of patients with PHACE syndrome. The addition of ASL to the MR imaging/MRA protocol for PHACE can provide a potential physiologic assessment of stroke risk in future studies, as has been demonstrated in other intracranial arteriopathies.[10,11] Relying solely on the structural arterial anomalies may overestimate the risk of stroke because the CBF may still be normal, given the collateral supply (Fig 3). This physiologic metric can potentially aid with risk stratification.

The risk of stroke in PHACE syndrome is not based solely on the complex arteriopathies but is likely multifactorial. Stroke risk may be potentially related to beta blocker use. Propranolol is the widely accepted first-line pharmacologic treatment agent for complicated infantile hemangiomas.[16,17] Beta blockers could decrease cardiac output, reduce cerebral perfusion, and result in watershed infarcts, especially if there is a corresponding arteriopathy such as an absent vessel or severe stenosis.[18] Increasing research related to propranolol therapy in PHACE syndrome has shown that the drug is well-tolerated with respect to stroke risk. A recent multicenter retrospective study of 76 patients treated with propranolol for infantile hemangioma in PHACE syndrome showed no serious adverse effect or stroke.[18] Despite these reassuring data, stroke is still possible. One case report described an infant receiving propranolol at 11 months of age and developing a large right MCA infarct on MR imaging at 18 months of age. It is unclear whether the patient was still receiving propranolol at the time of the infarct, but the propranolol could have been a risk factor.[5] ASL could be used as a helpful adjunct before propranolol therapy to help inform and potentially mitigate stroke risk.

In our practice, we have started to use the combination of ASL and MRA to provide a more complete picture of cerebrovascular hemodynamics in this group of patients before propranolol therapy. If there is a high risk of stroke based on CBF data and arterial anatomy, then propranolol is administered at the lowest possible dose and titrated judiciously in a monitored setting. Obviously, further research is needed to show the utility and efficacy of this practice. Hypoglycemia is another potential side effect of propranolol therapy for children with infantile hemangiomas. The mechanism is not fully understood but is possibly related to inhibition of β-adrenergic-mediated glycogenolysis, gluconeogenesis, and lipolysis, which impairs glucose homeostasis.[19]

The pathogenesis of arteriopathies in PHACE syndrome is poorly understood. In addition, the genetics of PHACE syndrome has not been well-elucidated but is hypothesized to be secondary to low-level postzygotic variants.[20] Despite a candidate potential locus identified on 7q33 in 2 individuals,[21] more recent research suggests that the affected gene in PHACE syndrome has not been discovered because the variant allele frequency of the mosaic mutations is extremely low.[20] Further analysis with next-generation sequencing may provide causative mutations in PHACE syndrome.

ASL can provide additional assessment in PHACE beyond analysis of CBF. Hemangiomas are vascular tumors and show markedly hyperintense signal on ASL (Fig 2*C*).[12-14] While hemangiomas are usually well seen on postcontrast T1 imaging, particularly with the use of fat suppression, ASL could increase lesion conspicuity for improved hemangioma detection, especially if fat suppression is not used or in locations that could be overlooked such as the internal auditory canals.[22] Another advantage of ASL is its noncontrast technique. While we generally administer contrast to all patients with PHACE being scanned, ASL could also be performed to evaluate deep hemangiomas if contrast cannot be given or if refused by the patient or family. A sample MR imaging/MRA PHACE syndrome protocol is listed in the Table.

Sample MR imaging protocol for suspected PHACE syndrome[a]

Sequence	Feature Evaluated
Coronal and axial T2 fat-suppressed head and neck	Facial hemangioma, extent of lesion, possible hemangioma in airway
Axial DWI brain	Acute ischemia
Sagittal T1 or spoiled gradient-echo head and neck	Midline intracranial structures including pituitary gland, myelination
Axial ASL head and neck	Cerebral blood flow, hemangioma
Axial time-of-flight MRA head and neck	Arterial abnormalities
Coronal contrast-enhanced dynamic MRA/MRV neck, if needed	Arterial abnormalities, including evaluation of the aortic arch
Axial contrast-enhanced T1 fat-suppressed head and neck	Enhancement pattern
Coronal contrast-enhanced T1 fat-suppressed internal auditory canals	Hemangioma in the internal auditory canals

[a] Modified from Mamlouk et al[13] with permission from Elsevier.

The utility and appearance of ASL imaging in cerebrovascular arteriopathies such as those seen in PHACE syndrome are dependent on a few factors that can potentially be a limitation if not properly recognized. Depending on the postlabel imaging time and severity of cerebrovascular stenosis, and hence arterial transit time, the appearance of ASL maps may be different. Typically, in single-delay ASL evaluations, the postlabel delay time is chosen so that by the time the brain is imaged, most of the label has ideally moved from the large arteries into the brain parenchyma, allowing more accurate parenchymal evaluation of CBF. In cases of arterial narrowing, slow flow, or flow through proximal collaterals, the label may still be mostly within the larger arteries and not yet transited into the parenchyma. There is also an additional confounder. The ASL label signal is T1-based and, therefore, has a very short time before inevitable longitudinal relaxation rapidly decreases the label brightness, which eventually loses signal very quickly and returns to normal. Therefore, in cases of more severe transit time delays, the low signal on ASL CBF maps may be due to the paucity of the remaining label in the assessed parenchyma rather than a true proportional decrease in CBF. In these cases of severe transit time delays, the parenchymal CBF map may be more transit time–weighted than being truly CBF-weighted.

This underestimation of parenchymal CBF should be recognized in these physiologic states. This phenomenon can lead to errors and bias in the quantitative measurement of CBF in patients with PHACE syndrome with severe stenoses. Multidelay ASL, which is less commonly used and not commercially available from all MR imaging vendors, can partially mitigate this problem, though in severe arterial transit delay, this problem of underestimated CBF remains a potential problem. Velocity-selective ASL has been shown to be less sensitive to arterial transit delay inaccuracies of CBF measurement and may also be useful.[23]

Our study has limitations, including its retrospective nature. Different ASL techniques were used across our various institutions. Although these may be perceived as a limitation, use of different ASL techniques may potentially be a strength as well because it demonstrates the utility of the technique across a range of imaging schemes. On the other hand, differing parameters such as the labeling period and postlabel delay time could result in different CBF appearances in the same patient. In addition, these labeling periods and postlabel delays were not changed when scanning neonates versus children, the former having faster heart rates, possibly requiring a different postlabel delay.[24] Another limitation is that because CBF changes were evaluated qualitatively, there was a subjective component in the assessment. However, the neuroradiologists in this study were experienced in the use and limitations of ASL for cerebrovascular disease evaluation. Finally, the lack of propranolol data in our study is another limitation of the assessment on whether the decreased CBF signal in some of our patients was due to PHACE syndrome or propranolol or both. Further research is needed in this specific patient cohort.

CONCLUSIONS

This study of 41 patients with PHACE syndrome shows the potential role of ASL imaging in demonstrating the hemodynamic changes in this patient group. In this cohort, only one-quarter of the studied patients had decreased CBF corresponding to a major arterial distribution, and none of the patients had acute or chronic ischemia. In all patients with decreased CBF, the arteriopathies demonstrated nonvisualization or narrowing of the major vessels supplying that vascular territory. Further studies are needed to validate these results.

Disclosures: Christopher P. Hess—*UNRELATED*: *Consultancy*: Focused Ultrasound Foundation, *Comments*: personal fees, Data and Safety Monitoring Board member; *Expert Testimony*: various legal firms, *Comments*: personal fees, medical expert witness; *Payment for Lectures Including Service on Speakers Bureaus:* EUROKONGRESS GmbH, *Comments*: professional conference travel; *Travel/Accommodations/Meeting Expenses Unrelated to Activities Listed*: Siemens, *Comments*: research travel; *Other:* GE Healthcare, *Comments*: personal fees, consultant.

REFERENCES

1. Siegel DH, Tefft KA, Kelly T, et al. **Stroke in children with posterior fossa brain malformations, hemangiomas, arterial anomalies, coarctation of the aorta and cardiac defects, and eye abnormalities (PHACE) syndrome: a systematic review of the literature.** *Stroke* 2012;43:1672–74 CrossRef Medline
2. Drolet BA, Dohil M, Golomb MR, et al. **Early stroke and cerebral vasculopathy in children with facial hemangiomas and PHACE association.** *Pediatrics* 2006;117:959–64 CrossRef Medline
3. Hess CP, Fullerton HJ, Metry DW, et al. **Cervical and intracranial arterial anomalies in 70 patients with PHACE syndrome.** *AJNR Am J Neuroradiol* 2010;31:1980–86 CrossRef Medline
4. Heyer GL, Millar WS, Ghatan S, et al. **The neurologic aspects of PHACE: case report and review of the literature.** *Pediatr Neurol* 2006;35:419–24 CrossRef Medline
5. Jack AS, Chow MM, Fiorillo L, et al. **Bilateral pial synangiosis in a child with PHACE syndrome.** *J Neurosurg Pediatr* 2016;17:70–75 CrossRef Medline
6. Jernigan S, Storey A, Hammer C, et al. **Moyamoya syndrome and PHACE syndrome: clinical and radiographic characterization of the intracranial arteriopathy and response to surgical revascularization.** *J Neurosurg Pediatr* 2019;23:493–97 CrossRef Medline

7. Metry DW, Garzon MC, Drolet BA, et al. **PHACE syndrome: current knowledge, future directions.** *Pediatr Dermatol* 2009;26:381–98 CrossRef Medline
8. Haggstrom AN, Garzon MC, Baselga E, et al. **Risk for PHACE syndrome in infants with large facial hemangiomas.** *Pediatrics* 2010;126: e418–26 CrossRef Medline
9. Garzon MC, Epstein LG, Heyer GL, et al. **PHACE syndrome: consensus-derived diagnosis and care recommendations.** *J Pediatr* 2016;178:24–33.e22 CrossRef Medline
10. Haller S, Zaharchuk G, Thomas DL, et al. **Arterial spin labeling perfusion of the brain: emerging clinical applications.** *Radiology* 2016;281:337–56 CrossRef Medline
11. Lee S, Yun TJ, Yoo RE, et al. **Monitoring cerebral perfusion changes after revascularization in patients with Moyamoya disease by using arterial spin-labeling MR imaging.** *Radiology* 2018;288:565–72 CrossRef Medline
12. Mamlouk MD, Hess CP. **Arterial spin-labeled perfusion for vascular anomalies in the pediatric head and neck.** *Clin Imaging* 2016;40:1040–46 CrossRef Medline
13. Mamlouk MD, Nicholson AD, Cooke DL, et al. **Tips and tricks to optimize MRI protocols for cutaneous vascular anomalies.** *Clin Imaging* 2017;45:71–80 CrossRef Medline
14. Boulouis G, Dangouloff-Ros V, Boccara O, et al. **Arterial spin-labeling to discriminate pediatric cervicofacial soft-tissue vascular anomalies.** *AJNR Am J Neuroradiol* 2017;38:633–38 CrossRef Medline
15. Wright JN, Wycoco V. **Asymmetric Meckel cave enlargement: a potential marker of PHACES syndrome.** *AJNR Am J Neuroradiol* 2017;38:1223–27 CrossRef Medline
16. Krowchuk DP, Frieden IJ, Mancini AJ, et al; Subcommittee on The Management of Infantile Hemangiomas. **Clinical practice guideline for the management of infantile hemangiomas.** *Pediatrics* 2019;143: e20183475 CrossRef Medline
17. Léaute-Labrèze C, Boccara O, Degrugillier-Chopinet C, et al. **Safety of oral propranolol for the treatment of infantile hemangioma: a systematic review.** *Pediatrics* 2016;138:e20160353 CrossRef Medline
18. Olsen GM, Hansen LM, Stefanko NS, et al. **Evaluating the safety of oral propranolol therapy in patients with PHACE syndrome.** *JAMA Dermatol* 2020;156:186–90 CrossRef Medline
19. Holland KE, Frieden IJ, Frommelt PC, et al. **Hypoglycemia in children taking propranolol for the treatment of infantile hemangioma.** *Arch Dermatol* 2010;146:775–78 CrossRef Medline
20. Siegel DH. **PHACE syndrome: infantile hemangiomas associated with multiple congenital anomalies—clues to the cause.** *Am J Med Genet C Semin Med Genet* 2018;178:407–13 CrossRef Medline
21. Mitchell S, Siegel DH, Shieh JT, et al. **Candidate locus analysis for PHACE syndrome.** *Am J Med Genet A* 2012;158a:1363–67 CrossRef Medline
22. Mamlouk MD, Zimmerman B, Mathes EF, et al. **Hearing loss in PHACE syndrome: clinical and radiologic findings.** *Childs Nerv Syst* 2018;34:1717–24 CrossRef Medline
23. Bolar DS, Gagoski B, Orbach DB, et al. **Comparison of CBF measured with combined velocity-selective arterial spin-labeling and pulsed arterial spin-labeling to blood flow patterns assessed by conventional angiography in pediatric Moyamoya.** *AJNR Am J Neuroradioly* 2019;40:1842–49 CrossRef Medline
24. Alsop DC, Detre JA, Golay X, et al. **Recommended implementation of arterial spin-labeled perfusion MRI for clinical applications: a consensus of the ISMRM perfusion study group and the European consortium for ASL in dementia.** *Magn Reson Med* 2015;73:102–16 CrossRef Medline

Pilot Study of Hyperpolarized ^{13}C Metabolic Imaging in Pediatric Patients with Diffuse Intrinsic Pontine Glioma and Other CNS Cancers

A.W. Autry, I. Park, C. Kline, H.-Y. Chen, J.W. Gordon, S. Raber, C. Hoffman, Y. Kim, K. Okamoto, D.B. Vigneron, J.M. Lupo, M. Prados, Y. Li, D. Xu, and S. Mueller

ABSTRACT

BACKGROUND AND PURPOSE: Pediatric CNS tumors commonly present challenges for radiographic interpretation on conventional MR imaging. This study sought to investigate the safety and tolerability of hyperpolarized carbon-13 (HP-^{13}C) metabolic imaging in pediatric patients with brain tumors.

MATERIALS AND METHODS: Pediatric patients 3 to 18 years of age who were previously diagnosed with a brain tumor and could undergo MR imaging without sedation were eligible to enroll in this safety study of HP [1-^{13}C]pyruvate. Participants received a one-time injection of HP [1-^{13}C]pyruvate and were imaged using dynamic HP-^{13}C MR imaging. We assessed 2 dose levels: 0.34 mL/kg and the highest tolerated adult dose of 0.43 mL/kg. Participants were monitored throughout imaging and for 60 minutes postinjection, including pre- and postinjection electrocardiograms and vital sign measurements.

RESULTS: Between February 2017 and July 2019, ten participants (9 males; median age, 14 years; range, 10–17 years) were enrolled, of whom 6 completed injection of HP [1-^{13}C]pyruvate and dynamic HP-^{13}C MR imaging. Four participants failed to undergo HP-^{13}C MR imaging due to technical failures related to generating HP [1-^{13}C]pyruvate or MR imaging operability. HP [1-^{13}C]pyruvate was well-tolerated in all participants who completed the study, with no dose-limiting toxicities or adverse events observed at either 0.34 ($n = 3$) or 0.43 ($n = 3$) mL/kg. HP [1-^{13}C]pyruvate demonstrated characteristic conversion to [1-^{13}C]lactate and [^{13}C]bicarbonate in the brain. Due to poor accrual, the study was closed after only 3 participants were enrolled at the highest dose level.

CONCLUSIONS: Dynamic HP-^{13}C MR imaging was safely performed in 6 pediatric patients with CNS tumors and demonstrated HP [1-^{13}C]pyruvate brain metabolism.

ABBREVIATIONS: aSNR = apparent total SNR; EPSI = echo-planar spectroscopic imaging; DIPG = diffuse intrinsic pontine glioma; HP-^{13}C = hyperpolarized carbon-13

Pediatric brain tumors are the most commonly encountered solid tumors in childhood and now contribute to most cancer-related deaths in children.[1] Among these tumors, diffuse intrinsic pontine glioma (DIPG) poses the gravest threat, with the median overall survival in children being only 9 months from diagnosis, despite exhaustive research efforts.[2] In managing pediatric brain tumors, a key issue facing the neuro-oncology community is the lack of imaging biomarkers that can support definitive and rapid assessment of response or resistance to treatment. While treatment response has traditionally been evaluated through MR imaging, there remain considerable challenges to radiographic interpretations of disease status. These potential shortcomings are exacerbated in the setting of novel therapies, such as immunotherapy, where there are no current standards to determine treatment effect versus disease progression based on imaging alone.

Because of the challenges in monitoring pediatric brain tumors using standard MR imaging, hyperpolarized carbon-13 (HP-^{13}C) MR imaging presents a promising molecular methodology that

Received June 10, 2020; accepted after revision August 19.

From the Department of Radiology and Biomedical Imaging (A.W.A., H.-Y.C., J.W.G., Y.K., K.O., D.B.V., J.M.L., Y.L., D.X.); Division of Hematology/Oncology (C.K., S.R., C.H., M.P., S.M.), Department of Pediatrics; Departments of Neurology (C.K., S.M.), Bioengineering and Therapeutic Sciences (D.B.V.), and Neurological Surgery (D.B.V., M.P., S.M.); and UCSF/UC Berkeley Joint Graduate Group in Bioengineering (D.B.V., J.M.L., D.X.), University of California, San Francisco, San Francisco, California; and Department of Radiology (I.P.), Chonnam National University College of Medicine and Hospital, Gwangju, Korea.

A.W. Autry, I. Park, and C. Kline contributed equally to this work.

This study was supported by the Kure It-UCSF Grant for Underfunded Cancer Research (S.M.), as well as National Institutes of Health T32 Training Fellowship T32 CA151022 (A.W.A.) and P41 EB0341598 grants.

Please address correspondence to Duan Xu, MD, Department of Radiology and Biomedical Imaging, University of California, San Francisco, 1700 4th St, Room 303B, San Francisco, California 94158; e-mail: Duan.Xu@ucsf.edu

Indicates open access to non-subscribers at www.ajnr.org
Indicates article with supplemental online tables.
http://dx.doi.org/10.3174/ajnr.A6937

can potentially extend current imaging capabilities. HP-^{13}C MR imaging has enabled the noninvasive investigation of in vivo brain metabolism using molecular probes whose signal is transiently enhanced via dynamic nuclear polarization.[3] In studies of the adult brain,[4-8] intravenously injected HP [1-^{13}C]pyruvate was shown to safely transport across the BBB and undergo enzymatic conversion to downstream metabolites [1-^{13}C]lactate and [^{13}C]bicarbonate, which serve as respective markers of glycolysis[9] and oxidative phosphorylation.[10] Given the metabolic alterations associated with cancer,[11,12] several of these imaging studies were designed to demonstrate the feasibility of HP-^{13}C MR imaging in patients with gliomas[4,5] and also characterize serial imaging.[8] Kinetic modeling of serial data has most importantly shown evidence of aberrant metabolism in patients with progressive glioblastoma.[8] Additionally, earlier studies in patients with prostate cancer have indicated potential clinical relevance, based on the elevated ratio of [1-^{13}C]lactate to [1-^{13}C]pyruvate in biopsy-proved disease.[13]

Despite advances in the molecular characterization of pediatric brain tumors, development of imaging biomarkers has remained elusive.[2] Recent preclinical work evaluating [1-^{13}C]pyruvate metabolism in human-derived orthotopic DIPG xenografts revealed that elevated levels of [1-^{13}C]lactate could distinguish tumor from healthy brain stem tissue.[14] These data, derived from a disease model recapitulating human histopathology, provided evidence that HP-^{13}C imaging may offer relevant metabolic biomarkers of central nervous system tumors.[15] Because DIPG lesions typically demonstrate only T2/FLAIR hyperintensity with little or no contrast enhancement in the weakly perfused environment of the brain stem,[16] these results are promising for a variety of pediatric brain tumors with similarly challenging radiographic presentations. In the setting of recurrent disease, in which standard MR imaging may not have distinct characteristics to confirm active disease versus treatment effect, such biomarkers could provide considerable value. They are also particularly relevant in the context of monitoring the efficacy of targeted treatment, as indicated by recent investigations of treatment response to histone deacetylase inhibitors in preclinical models of glioblastoma.[17]

The potential to identify tumor metabolism and biomarkers of treatment response combined with the preclinical and clinical support for HP [1-^{13}C]pyruvate provided the basis for investigating the use of HP [1-^{13}C]pyruvate in PNOC011, a "pilot study of safety and toxicity of acquiring HP-^{13}C imaging in children with brain tumors" within the Pacific Pediatric Neuro-Oncology Consortium. The objectives of PNOC011 were to assess the safety and feasibility of HP-^{13}C imaging in pediatric patients with brain tumors as a first step toward developing HP methodologies in this population. Herein, we describe our experience in PNOC011 using HP [1-^{13}C]pyruvate in a dose-escalation study evaluating pediatric patients with a variety of brain tumors.

MATERIALS AND METHODS

Study Design

PNOC011 was an open-label, limited Phase I trial using a standard 3 + 3 design to assess the safety of the investigational imaging agent HP [1-^{13}C]pyruvate across 2 dose levels in pediatric patients with brain tumors. Dose level 1 was 80% of the highest tolerated dose for adults (0.34 mL/kg). Dose level 2 was 100% of the highest tolerated dose for adults (0.43 mL/kg). The intent of the study was to enroll a minimum of 3 participants per dose level and a total of 6 participants at the highest tolerated dose level.

Participant Population

The single-center trial was conducted at the University of California, San Francisco, and designed to assess the safety and feasibility of HP [1-^{13}C]pyruvate given intravenously for dynamic HP-^{13}C MR imaging. Participants were recruited from the pediatric neuro-oncology clinic at the University of California, San Francisco, according to enrollment guidelines stipulating that subjects be 3–18 years of age and previously diagnosed with a brain tumor. Key inclusion criteria were a Karnofsky Performance Status Scale or Lansky Play-Performance Scale score of $\geq$70; no severe, uncontrolled medical illness; not pregnant or breastfeeding; use of effective contraception; and ability to provide informed consent. Key exclusion criteria included an inability to follow study procedures and a history or evidence of cardiac dysfunction. Any participant who was undergoing active anticancer therapy or on another investigational trial at the time of enrollment on PNOC011 was discussed with and approved by the study chair (S.M.). All participants and families provided informed consent or assent, as applicable, before initiation of protocol interventions.

This study was approved by the University of California, San Francisco institutional review board and the FDA under Investigational New Drug No. 131057 (S.M.). The trial was registered on clinicaltrials.gov under NCT02947373.

Study Assessments

Before enrollment, participants underwent a complete neurologic examination, assessment of a performance score, evaluation of complete blood counts, liver function tests, and evaluation of electrolyte levels, as well as a baseline electrocardiogram. During and for 60 minutes after completion of the injection and imaging acquisition, the participant underwent continuous heart rate monitoring. Oxygen saturation and blood pressure were assessed every 15 minutes for a total of 60 minutes after completion of injection. An electrocardiogram was also repeated 60 minutes after the injection. Participants were contacted by the study team at 24 and 48 hours after completion of the injection to assess any toxicities related to HP [1-^{13}C]pyruvate.

During the injection and imaging acquisition, a minimum of 2 pediatric advanced life-support–certified providers were present to monitor any acute events related to study procedures (C.K., C.H., S.R., S.M.).

Study End Points

The primary end point of the study was safety based on the National Cancer Institute Common Terminology Criteria for Adverse Events, Version 4.0. Adverse events and serious adverse events were reported from the time of enrollment to 48 hours post-injection. Dose-limiting toxicities were defined as any HP [1-^{13}C]pyruvate–related grade 2 or higher toxicity (excluding asymptomatic laboratory evaluations). Adverse events and serious adverse events were reviewed weekly by the study chair (S.M.) and the Pacific Pediatric Neuro-Oncology Consortium leadership (S.M., M.P.) per the Pacific Pediatric Neuro-Oncology Consortium

standardized operating procedures for safety review of clinical trials. The University of California, San Francisco Data Monitoring and Safety Committee monitored the trial.

The secondary end point was image quality, which was assessed qualitatively on the basis of descriptive characteristics only.

^{13}C Hardware and Calibration

All experiments were performed on a clinical 3T whole-body scanner (MR 750; GE Healthcare) equipped with 32-channel multi-nuclear imaging capability. Either an 8-channel bilateral paddle coil or a 32-channel head array coil with ^{13}C hardware configuration was used for optimal ^{13}C signal reception.[18] Transmit radiofrequency power was calibrated on a head-shaped phantom containing unenriched ethylene glycol (anhydrous, 99.8% $HOCH_2CH_2OH$; Sigma Aldrich).

Sample Polarization and Quality Control

Dynamic nuclear polarization of [1-^{13}C]pyruvate was performed using a 5T Spinlab polarizer (GE Healthcare) designed for clinical research applications.[4] To maintain an International Organization for Standardization 5 environment, pharmacists used an isolator (Getinge Group; Getinge 4-Glove Isolator Laminar Airflow, No. 2989; Getinge, France) and a clean bench laminar flow hood for the preparation of human [1-^{13}C]pyruvate doses. Pharmacy kits filled with a mixture of 1.432-g [1-^{13}C] pyruvic acid (Millipore Sigma) and a 28-mg electron paramagnetic agent (AH111501; GE Healthcare) were loaded into the Spinlab and polarized for at least 2.5 hours with 140-GHz microwave radiation at 5 T and 0.8 K. Following polarization, the pyruvate and trityl radical solution was rapidly dissolved in sterile water and passed through a filter under pressure to achieve a residual trityl concentration of <3 μM. This solution was then collected in a receiver vessel, neutralized, and diluted with a sodium hydroxide tris (hydroxymethyl) aminomethane/ethylenediaminetetraacetic acid buffer solution. An integrated quality control system rapidly measured the resulting pH, temperature, residual electron paramagnetic agent concentration, volume, pyruvate concentration, and polarization level. The solution passed through a terminal sterilization filter (Saint-Gobain PureFlo® D65R disc filter, 0.2 μm; Zenpure) before being collected in a Medrad syringe (Bayer HealthCare).

The quality control criteria for pharmacist release of the sample were the following: 1) polarization, ≥15%; 2) pyruvate concentration, 220–280 mM; 3) electron paramagnetic agent concentration, ≤3.0 μM; 4) pH, 5.0–9.0; 5) temperature, 25–37 °C; 6) volume, >38 mL; and 7) bubble point test on the sterilizing filter passed at 50 psi. The injected volume of HP[1-^{13}C] pyruvate was based on a dosage of 0.34 mL/kg (dose level 1, $n = 3$) or 0.43 mL/kg (dose level 2, $n = 3$). The dose was delivered at a rate of 1–3 mL/s, less than the 5 mL/s used for adults, followed by a 20-mL sterile saline flush at the same rate.

Imaging Protocol

Before imaging, a peripheral intravenous catheter was placed for administration of HP [1-^{13}C]pyruvate. T2-weighted fast spin-echo images (TR/TE = 4000/60 ms, FOV = 26 cm, 192 × 256 matrix, 5-mm section thickness, and number of excitations = 2) acquired with the ^{1}H body coil served as an anatomic reference for prescribing ^{13}C sequences. A 1-mL standard containing 8 mol/L of ^{13}C-urea was embedded in both 8- and 32-channel phased array receiver coils to provide an in vivo frequency reference for [1-^{13}C]pyruvate: $f_{pyruvate} = f_{urea} + 270$ Hz. On pharmacist approval of sample safety, participants were injected with HP [1-^{13}C]pyruvate and imaged beginning 0–5 seconds after the saline flush by either dynamic ^{13}C EPI or echo-planar spectroscopic imaging (EPSI).

The EPI sequence (TR/TE = 62.5 ms/21.7 ms, FOV = 24 × 24 cm^2, 8 slices, 20 time points, 3-second temporal resolution, 60-second acquisition time) was acquired with 3.38–4.50 cm^3 spatial resolution and offered whole-brain coverage (Online Table 1).[19] By means of spectral-spatial radiofrequency pulses, individual [1-^{13}C]pyruvate, [1-^{13}C]lactate, and [^{13}C]bicarbonate resonances were sequentially excited over interleaved acquisitions with flip angles $\alpha_{pyruvate}/\alpha_{lactate}/\alpha_{bicarbonate} = 20^{\circ}/30^{\circ}/30^{\circ}$. In the case of EPSI (TR/TE = 130/6.1 ms, 24 time points, 3-second temporal resolution, 72-second acquisition time), single-section spectroscopic imaging data were acquired with a spatial resolution of 8 cm^3 and flip angles of 10° for all metabolites (Online Table 1).[20]

Two participants were repositioned after study protocol injection and HP-^{13}C imaging for a short ^{1}H-MR imaging examination without gadolinium contrast using a 32-channel ^{1}H coil (Nova Medical, Wilmington, Massachusetts). This examination included 3D T1-weighted inversion recovery echo-spoiled gradient-echo images (TR/TE/TI = 6652/2448/450 ms, resolution = 1.5 × 1 × 1 mm^3, FOV = 25.6 cm, matrix = 256 × 256), and 3D T2-weighted FLAIR images (TR/TE/TI = 6250/138/1702 ms, resolution = 1.5 × 1 × 1 mm^3, FOV = 25.6 cm, matrix = 256 × 256). This imaging was performed to obtain quality proton images to overlay the carbon data.

Postprocessing of ^{13}C Data

Dynamic EPI and EPSI ^{13}C data were processed according to previously described methods[21] and postprocessed to enhance the signal.[22] These data were then summed across time to display the total metabolite signal. The apparent total signal-to-noise ratio (aSNR) in the brain was computed by dividing the temporally summed metabolite signal, peak height values in the case of EPSI, by the SD of the noise outside the head.

RESULTS

A total of 10 pediatric participants (9 males; median age, 14 years; range, 10–17 years) were enrolled (Table 1 and Online Table 2). Two additional participants consented to participate in the study but did not enroll (one due to disease progression and not returning to University of California, San Francisco for follow-up and the other due to changing his mind about participation). Due to technical issues related to generating HP [1-^{13}C]pyruvate ($n = 3$) or MR imaging scanner operability ($n = 1$), 4 participants consented and enrolled, but did not undergo HP-^{13}C MR imaging or injection of HP [1-^{13}C]pyruvate. Details of the remaining 6 participants who underwent HP-^{13}C MR imaging with injection of HP [1-^{13}C]pyruvate can be found in Online Table 2 (5 males; median age, 14 years; range, 10–17 years). Diagnoses included DIPG ($n = 3$), pineoblastoma ($n = 1$), medulloblastoma ($n = 1$), and adamantinomatous craniopharyngioma ($n = 1$). Of these 6 participants, 3 were on active therapy at the time of HP-^{13}C imaging. Following injection of HP

[1-^{13}C]pyruvate, there were no adverse events in any participant at dose levels 1 or 2 based on assessments by supervising personnel and electrocardiogram and vital sign monitoring.

Table 2 provides the quality control measurements recorded for each dissolution of HP [1-^{13}C]pyruvate before injection, including the delivered dosage volume (16–36 mL) and concentration (230–242 mM), with the time to injection ranging from 53 to 75 seconds.

Dynamic HP-^{13}C imaging was successfully performed on participants using both the imaging- and spectroscopy-based acquisition schemes. Individual scan parameters are reported along with aSNR values from normal brain in Online Table 1. On the basis of the maximum aSNR that was calculated in the brain for each examination after applying signal-enhancement postprocessing techniques,[22] HP [1-^{13}C]pyruvate (aSNR, $7.85 \times 10^2 - 3.52 \times 10^5$), [1-^{13}C]lactate (aSNR, $1.75 \times 10^2 - 7.20 \times 10^4$), and [^{13}C]bicarbonate (aSNR, $64 - 1.52 \times 10^4$) were detectable across all participants (Online Table 1). Incidentally, each of the EPSI datasets was acquired with the paddle receiver coils, which allowed relatively high aSNR based on their proximity to the head.

Figure 1 shows HP-^{13}C EPI data from a 9-year-old male participant (P-01) with DIPG, which have been overlaid on FLAIR images that demonstrated a hyper- and hypointense T2 lesion, indicated by the yellow arrows. Temporally summed signal from ^{13}C-labeled metabolites provided evidence that HP [1-^{13}C]pyruvate was transported across the BBB and subsequently underwent conversion to both [1-^{13}C]lactate and [^{13}C]bicarbonate. On the basis of visual inspection, the [1-^{13}C]lactate signal in this anatomic lesion displayed a slight elevation relative to the normal-appearing contralateral brain stem (Fig 1, middle row). The same region is highlighted by the signal ratio map of [1-^{13}C]lactate to [1-^{13}C]pyruvate, which is free from the receive profile of ^{13}C hardware sensitivity (Fig 1, bottom row). At the time of study imaging, the patient was about 3 months from completion of radiation and undergoing therapy with convection-enhanced delivery with MTX110 (liquid panobinostat) coinfused with gadoteridol. Most interesting, on visual review of contrast-enhanced MR imaging of tumor regions previously treated with convection-enhanced delivery, the area of elevated lactate had not been reached with prior treatments.

Figure 2 displays HP-^{13}C EPSI spectra from a 12-year-old male participant (P-02) with DIPG who was undergoing therapy with trametinib and everolimus. These HP-^{13}C spectra are shown in relation to a FLAIR image demonstrating a T2-hyperintense lesion. Temporally summed ^{13}C spectra from a single section depict individual resonances of [1-^{13}C]pyruvate, [1-^{13}C]lactate, and [^{13}C]bicarbonate (aliased from 160.8 ppm) throughout the inferior brain section (Fig 2*A*). Spectra from voxels corresponding with normal-appearing tissue (Fig 2*B*) and the lesion (Fig 2*C*) are annotated for metabolite reference. Due to the relatively large voxel size (8 cm^3), some of the signal from Fig 2*B* is external to the brain, particularly in the case of [1-^{13}C]alanine.

Table 1: Participant demographics

Demographics	
Consented ($n = 12$)	
Age (median) (range) (yr)	14 (8–17)
Males (No.) (%)	10 (83)
Treatment (No. of patients)	
Completed protocol therapy	6
Eligible, withdrawn[a]	6
Completed ^{13}C injection ($n = 6$)	
Age (median) (range) (yr)	14 (10–17)
Males (No.) (%)	5 (83)
Diagnosis (anatomic location) (No.) (%)	
Diffuse intrinsic pontine glioma (pons)	3 (50)
Craniopharyngioma (suprasellar)	1 (17)
Medulloblastoma (posterior fossa)	1 (17)
Pineoblastoma (pineal gland)	1 (17)
Dose level (No. of patients)	
Dose level 1	3
Dose level 2	3
Safety (No. of events)	
Dose level toxicity	0
Adverse events	0

[a] Withdrawn due to the following: technical issue with MR imaging scanner ($n = 1$) or generating HP [1-^{13}C]pyruvate ($n = 3$); change in participant choice to participate ($n = 1$); or disease progression before participation and participant did not return to University of California, San Francisco for follow-up treatment ($n = 1$).

DISCUSSION

Pediatric central nervous system tumors have historically presented challenges to radiographic interpretation of disease status on standard MR imaging, thereby prompting the exploration of alternative imaging strategies. Furthermore, current standard imaging frequently fails to adequately identify response or early treatment failure, particularly in the setting of developmental therapeutics, such as immunotherapy. PNOC011 demonstrated the tolerability of dynamic HP-^{13}C metabolic imaging in pediatric participants with DIPG and other central nervous system tumors, while characterizing population-specific features of HP data. Injections of HP [1-^{13}C]pyruvate were well-tolerated by all 6 participants without any reports of related adverse events. Based on the tolerance of HP [1-^{13}C]pyruvate and the ability to detect conversion to downstream metabolites in real time, there is evidence that HP-^{13}C techniques may inform about metabolism relevant to investigating pediatric DIPG and other brain malignancies.

Table 2: Quality control for HP-^{13}C injections

Participant ID	EPA Conc. (μM)	[1-^{13}C] Pyruvate Conc. (mM)	Volume Injected (mL)	Polarization (%)	Temp. (°C)	pH	Time to Injection (sec)
P-01	1.6	230	23.0	44.0	34.6	7.7	56
P-02	0.6	232	21.8	42.5	31.9	7.6	75
P-03	0.5	235	16.0	38.8	31.0	7.7	66
P-04	0.3	230	36.0	38.1	30.7	7.7	53
P-05	0.5	231	20.8	43.9	32.1	7.6	55
P-06	1.4	242	22.2	33.6	30.9	7.5	70

Note:—EPA indicates electron paramagnetic agent; Conc., concentration; Temp, temperature.

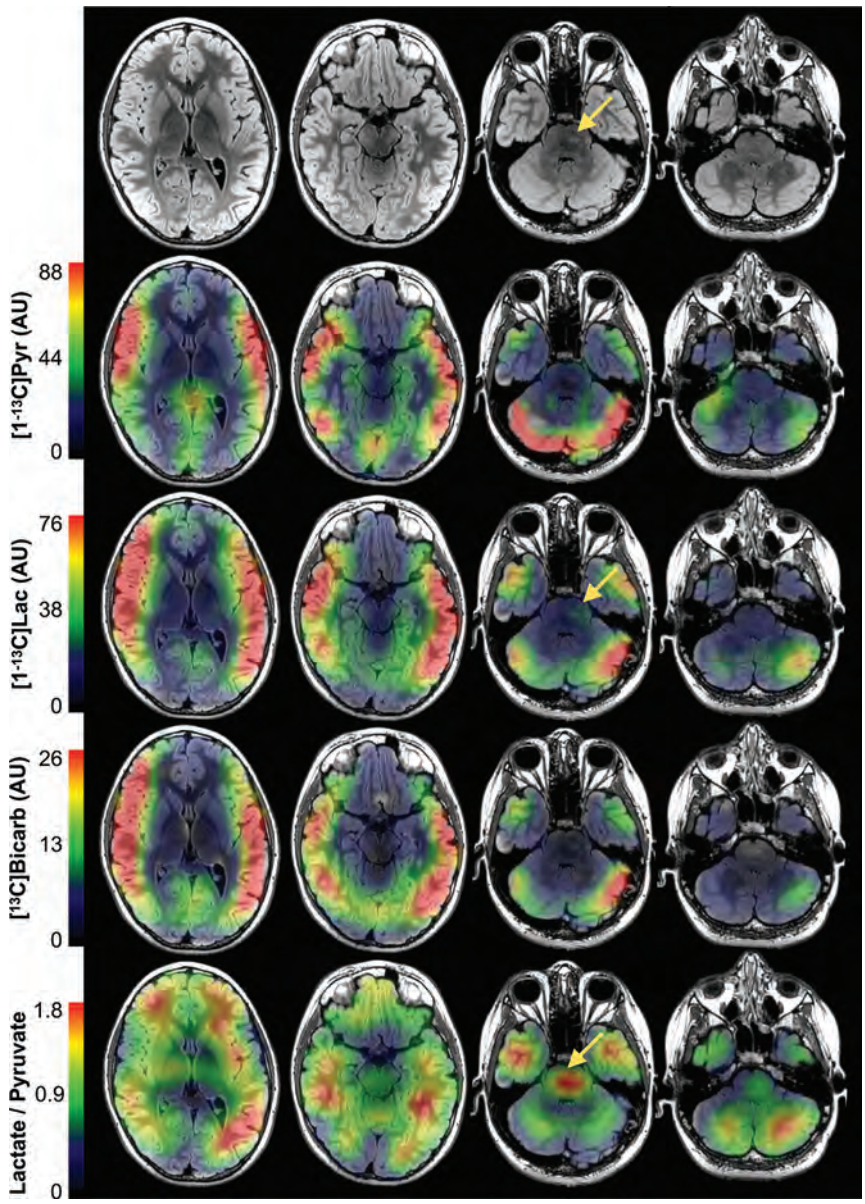

FIG 1. HP-^{13}C imaging of DIPG. HP-^{13}C EPI of a 9-year-old male participant (P-01) with DIPG following injection of HP [1-^{13}C]pyruvate. Maps of the temporally summed signal from HP [1-^{13}C]pyruvate and downstream metabolites [1-^{13}C]lactate and [^{13}C]bicarbonate are overlaid on ^{1}H FLAIR images, along with the ratio of [1-^{13}C]lactate to [1-^{13}C]pyruvate, which removes the shading of ^{13}C hardware sensitivity. Within the hyper- and hypointense T2 lesion indicated by the *yellow arrows*, there is a subtle increase in [1-^{13}C]lactate signal relative to the normal-appearing contralateral brain stem. The ratio of [1-^{13}C]lactate to [1-^{13}C]pyruvate also demonstrates a local maximum in this anatomic lesion (*yellow arrow*). Pyr indicates pyruvate; Lac, lactate; Bicarb, bicarbonate; AU, arbitrary units.

Demonstrating the preliminary safety profile of HP-^{13}C imaging in pediatric patients with a variety of CNS tumors represents a considerable advance with regard to translating this methodology to children. Within this population, the safety evaluation of HP [1-^{13}C]pyruvate is of fundamental importance, and the experience thus far from the current study has matched the tolerability shown in adult brain studies.[4–8] In addition to the record of safety, this study was able to provide evidence that HP-^{13}C imaging can capture metabolically relevant data. As reported in adults,[4–8] HP [1-^{13}C]pyruvate displayed transport across the BBB and subsequent conversion to [1-^{13}C]lactate and [^{13}C]bicarbonate over experimental time scales of approximately 60–72 seconds. Given the quality of these data, as measured by aSNR, HP-^{13}C imaging appears to hold promise for investigating aberrant metabolism in pediatric brain tumors.

Several features of pediatric HP-^{13}C imaging that were characterized in this study will inform the design of future clinical trials. Notably, children demonstrated more rapid delivery of HP [1-^{13}C]pyruvate to the brain following injection compared with adults,[4] which is supported by the literature on their circulatory systems[23] and may also reflect higher monocarboxylate transporter activity.[24] This result has implications for HP-^{13}C acquisitions because the kinetic modeling of [1-^{13}C]pyruvate metabolism requires that the inflow of [1-^{13}C]pyruvate be adequately sampled by imaging to quantify dynamic conversion. Thus, acquisitions should commence immediately following the completion of the injection. With respect to imaging of DIPG, the brain stem presented unique challenges because of its deep location in the head, which limited the detectability of ^{13}C signal by the receiver hardware. Freedom in positioning the paddle ^{13}C receivers helped reduce this issue by maximizing the proximity to the anatomic lesion;[18] however, other pediatric indications may benefit from custom-designed detector arrays that better conform to the surface of the head. While the spatial resolution was relatively low in this study (3.38–8 cm^3), variable resolution acquisition strategies[25] and maintaining a short time to injection through quality control practices should greatly improve this issue.

One key limitation of this study was that only 3 participants were injected at the highest dose level. The initial study intent was to enroll 6 participants at the highest tolerated dose to most accurately assess toxicity of this novel imaging technology in children and as per standard 3 + 3 statistical design. The failure to sufficiently enroll patients was largely due to the following: 1) limitations in enrolling pediatric patients who did not require anesthesia for brain imaging, 2) technical challenges that led to the failure of MR imaging or HP-^{13}C injection (4 of 10 patients), and 3) coordinating MR research imaging with other standard-of-care imaging in an effort to limit the impact and stress on pediatric patients. Unfortunately, anesthesia has been shown to alter HP acquisitions

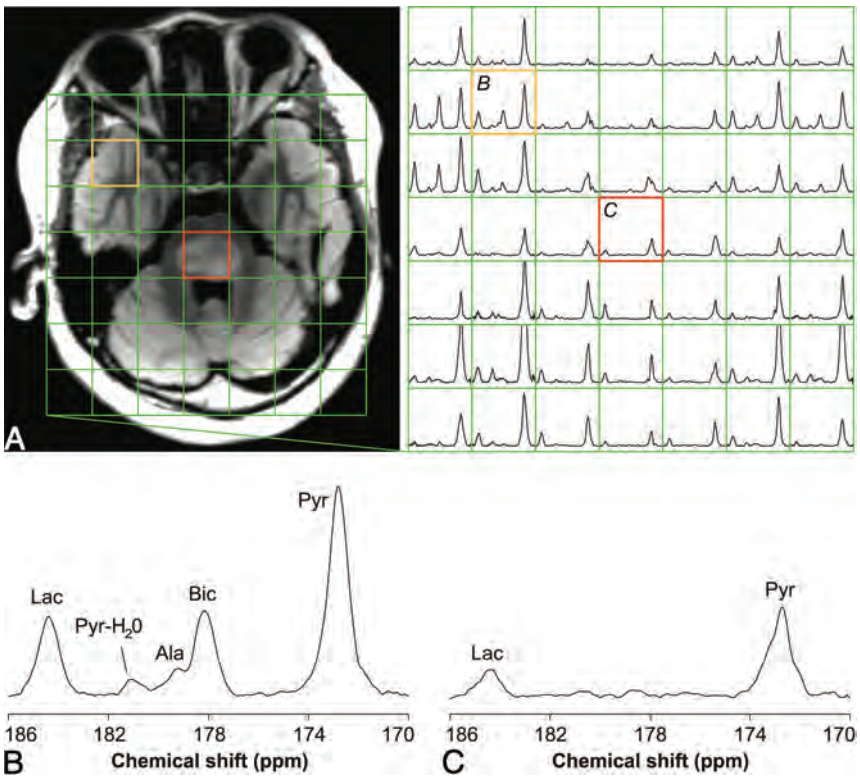

FIG 2. HP-^{13}C spectroscopy of DIPG. HP-^{13}C EPSI of a 12-year-old male participant (P-02) with DIPG following injection of HP [1-^{13}C]pyruvate. Temporally summed ^{13}C spectra are shown together with their spatial correspondence to a ^{1}H FLAIR image from the center of the 2-cm-thick ^{13}C volume (*A*). Spectra from normal-appearing tissue (*B*) and the lesion (*C*) illustrate individual HP metabolite resonances. The [^{13}C]bicarbonate resonance is aliased from 160.8 ppm. Pyr indicates [1-^{13}C]pyruvate; Pyr-H_2O, [1-^{13}C]pyruvate-hydrate; Lac, [1-^{13}C]lactate; Bic, [^{13}C]bicarbonate; Ala, [1-^{13}C]alanine exclusively from outside the brain.

in preclinical models, so this may be a confound for applying this technique in the youngest populations.[26] However, from a technical standpoint, injection-related failures can be overcome with evolving quality control procedures that preemptively address common issues.

Our group did identify particular challenges in the pediatric setting with regard to participation in nontherapeutic research studies because patients and families are already required to complete a large number of clinically relevant imaging and hospital visits. Such considerations in the pediatric setting must be taken into account for future imaging-based trials. One mechanism to potentially overcome these challenges would be to incorporate research imaging alongside interventional research studies. Another consideration for our trial is that we used weight-based volumes of metabolic contrast agent to facilitate consistent dosing across each dose level. While these volumes may display variability based on [1-^{13}C]pyruvate mass, our study design remains aligned with what has been done in prior investigations of adults.[4-8]

Because effective therapeutic options for many pediatric brain tumors are limited, radiation therapy and experimental treatments, such as immunotherapy, frequently become standard-of-care options. As molecular characterization for pediatric brain tumors evolves and more individually tailored therapies become available in the future, pediatric neuro-oncology will need to advance reliable imaging markers for evaluating response and resistance to treatment. From the results obtained in PNOC011, HP-^{13}C imaging may assist in developing imaging markers that reflect underlying brain metabolism and offer such insight.

CONCLUSIONS

The safety and tolerability of dynamic HP-^{13}C MR imaging with intravenously injected HP [1-^{13}C]pyruvate in 6 pediatric patients with CNS tumors are very promising. Future studies with larger populations and options to incorporate HP-^{13}C MR imaging alongside interventional studies will more comprehensively inform on the utility of HP-^{13}C imaging for identifying imaging biomarkers.

ACKNOWLEDGMENTS

We thank all the children and their families for their participation. We also thank the entire Pacific Pediatric Neuro-Oncology Consortium operation team for their support of the development and conduct of the study.

Disclosures: Adam W. Autry—*RELATED*: *Grant*: National Institutes of Health, Kure It-UCSF Grant for Unfunded Cancer Research, *Comments*: National Institutes of Health grant P41 EB0341598, Kure it-UCSF Grant for Unfunded Cancer Research*; *Other*: National Institutes of Health/National Cancer Institute, *Comments*: T32 Training Fellowship T32 CA151022. Cassie Kline—*UNRELATED*: *Grants/Grants Pending*: Cannonball Kids cancer foundation, Frank A. Campini Foundation, National Institutes of Health KL2 Scholars Program. Hsin-Yu Chen—*RELATED*: *Grant*: National Institutes of Health, Kure It-UCSF Grant for Unfunded Cancer Research, *Comments*: This study was supported by the Kure It-UCSF Grant for Underfunded Cancer Research (S.M.) and the National Institutes of Health P41 EB0341598 grant.* Yaewon Kim—*RELATED*: *Grant*: National Institutes of Health, Kure It-UCSF Grant for Unfunded Cancer Research, *Comments*: National Institutes of Health P41 EB0341598, Kure It-UCSF Grant for Underfunded Cancer Research.* Janine M. Lupo—*UNRELATED*: *Grants/Grants Pending*: GE Healthcare, *Comments*: research funding.* Michael Prados—*RELATED*: *Grant*: Kure It-UCSF Grant for Unfunded Cancer Research and University of California, San Francisco Comprehensive Cancer Center, *Comments*: nonprofit philanthropic group (Kure It-UCSF Grant for Unfunded Cancer Research), University of California, San Francisco Cancer Center: supplement grant (parent grant from the National Cancer Institute).* Sabine Mueller—*RELATED*: *Grant*: Kure It-UCSF Grant for Unfunded Cancer Research, *Comments*: research grant to support the clinical trial. The foundation had no impact on the design or analysis.* Duan Xu—*RELATED*: *Grant*: National Institutes of Health P41 EB0341598.* *Money paid to the institution.

REFERENCES

1. Ostrom QT, Gino C, Gittlem H, et al. **CBTRUS statistical report: primary brain and other central nervous system tumors diagnosed in the United States in 2012–2016.** *Neuro Oncol* 2019;21:v1–100 CrossRef Medline
2. Cohen KJ, Heideman RL, Zhou T, et al. **Temozolomide in the treatment of children with newly diagnosed diffuse intrinsic pontine**

gliomas: a report from the Children's Oncology Group. *Neuro Oncol* 2011;13:410–16 CrossRef Medline
3. Ardenkjaer-Larsen JH, Fridlund B, Gram A, et al. **Increase in signal-to-noise ratio of >10,000 times in liquid-state NMR**. *Proc Natl Acady of Sci U S A* 2003;100:10158–63 CrossRef Medline
4. Park I, Larson PEZ, Gordon JW, et al. **Development of methods and feasibility of using hyperpolarized carbon-13 imaging data for evaluating brain metabolism in patient studies.** *Magn Reson Med* 2018;80:864–73 CrossRef Medline
5. Miloushev VZ, Granlund KL, Boltyanskiy R, et al. **Metabolic imaging of the human brain with hyperpolarized ^{13}C pyruvate demonstrates ^{13}C lactate production in brain tumor patients.** *Cancer Res* 2018;78:3755–60 CrossRef Medline
6. Grist JT, McLean MA, Riemer F, et al. **Quantifying normal human brain metabolism using hyperpolarized [1-13C]pyruvate and magnetic resonance imaging.** *Neuroimage* 2019;189:171–79 CrossRef Medline
7. Lee CY, Soliman H, Geraghty BJ, et al. **Lactate topography of the human brain using hyperpolarized ^{13}C-MRI.** *Neuroimage* 2020;204:116202 CrossRef Medline
8. Autry AW, Gordon JW, Chen HY, et al. **Characterization of serial hyperpolarized ^{13}C metabolic imaging in patients with glioma.** *Neuroimage Clin* 2020;27:102323 CrossRef Medline
9. Lunt YL, Vander Heiden MG. **Aerobic glycolysis: meeting the metabolic requirements of cell proliferation.** *Annu Rev Cell Dev Biol* 2011;27:441–64 CrossRef Medline
10. Saraste M. **Oxidative phosphorylation at the fin de siècle.** *Science* 1999;283:1488–93 CrossRef Medline
11. Warburg O. **On respiratory impairment in cancer cells.** *Science* 1956;124:269–70 Medline
12. Ward PS, Thompson CB. **Metabolic reprogramming: a cancer hallmark even Warburg did not anticipate.** *Cancer Cell* 2012;21:297–308 CrossRef Medline
13. Nelson SJ, Kurhanewicz J, Vigneron DB, et al. **Metabolic imaging of patients with prostate cancer using hyperpolarized [1-^{13}C]pyruvate.** *Sci Transl Med* 2013;5:198ra108 CrossRef Medline
14. Autry AW, Hashimuza R, James CD, et al. **Measuring tumor metabolism in pediatric diffuse intrinsic pontine glioma using hyperpolarized carbon-13 MR metabolic imaging.** *Contrast Media Mol Imaging* 2018;2018:3215658 CrossRef Medline
15. Park I, Autry A, Chen Y, et al. **Hyperpolarized carbon-13 metabolic imaging of pediatric patients with brain tumors: initial experience.** *In: Proceedings of the Joint Meeting of the International Society for Magnetic Resonance in Medicine and the European Society for Magnetic Resonance in Medicine and Biology*, Paris, France. June 16–18, 2018
16. Warren KE. **Diffuse intrinsic pontine glioma: poised for progress.** *Front Oncol* 2012;2:205 CrossRef Medline
17. Radoul M, Najac C, Viswanath P, et al. **HDAC inhibition in glioblastoma monitored by hyperpolarized 13C MRSI.** *NMR Biomed* 2019;32:e4044 CrossRef Medline
18. Autry AW, Gordon JW, Carvajal L, et al. **Comparison between 8- and 32-channel phased-array receive coils for in vivo hyperpolarized ^{13}C imaging of the human brain.** *Magn Reson Med* 2019;82:833–41 CrossRef Medline
19. Gordon JW, Chen HY, Autry AW, et al. **Translation of carbon-13 EPI for hyperpolarized MR molecular imaging of prostate and brain cancer patients.** *Magn Reson Med* 2019;81:2702–09 CrossRef Medline
20. Larson PE, Bok R, Kerr AB, et al. **Investigation of tumor hyperpolarized [1-^{13}C]-pyruvate dynamics using time-resolved multiband RF excitation echo-planar MRSI.** *Magn Reson Med* 2010;63:582–91 CrossRef Medline
21. Crane JC, Gordon JW, Chen HY, et al. **Hyperpolarized 13C MRI data acquisition and analysis in prostate and brain at University of California, San Francisco.** *NMR in Biomedicine* 2020 Mar 19. [Epub ahead of print] CrossRef Medline
22. Chen HY, Autry AW, Brender JR, et al. **Tensor image enhancement and optimal multichannel receiver combination analyses for human hyperpolarized ^{13}C MRSI.** *Mag Reson Med* 2020 June 5. [Epub ahead of print] CrossRef Medline
23. Wu C, Honarmand AR, Schnell S, et al. **Age-related changes of normal cerebral and cardiac blood flow in children and adults aged 7 months to 61 years.** *J Am Heart Assoc* 2016;5:e002657 CrossRef Medline
24. Miranda-Goncalves V, Honavar M, Pinheiro C, et al. **Monocarboxylate transporters (MCTs) in gliomas: expression and exploitation as therapeutic targets.** *Neuro Oncol* 2013;15:172–88 CrossRef Medline
25. Gordon JW, Autry AW, Tang S, et al. **A variable resolution approach for improved acquisition of hyperpolarized ^{13}C metabolic MRI.** *Magn Reson Med* 2020;84:2943–52 CrossRef Medline
26. Josan S, Hurd R, Billingsley K, et al. **Effects of isoflurane anesthesia on hyperpolarized ^{13}C metabolic measurements in rat brain.** *Magn Reson Med* 2013;70:1117–24 CrossRef Medline

Idiopathic Neonatal Subpial Hemorrhage with Underlying Cerebral Infarct: Imaging Features and Clinical Outcome

Z. Assis, A. Kirton, A. Pauranik, M. Sherriff, and X.-C. Wei

ABSTRACT

BACKGROUND AND PURPOSE: Neonatal subpial hemorrhage with underlying cerebral infarct is a previously described but poorly understood clinicoradiographic syndrome. We sought to further characterize the cranial ultrasound and MR imaging characteristics and associated outcomes of this condition across the full range of gestational ages, including extreme and very preterm neonates.

MATERIALS AND METHODS: This was a single tertiary pediatric center retrospective case series. Brain MR imaging and cranial ultrasound of neonates with subpial hemorrhage with underlying cerebral infarct were identified from a population-based radiology registry (2006–2020). Original images were reviewed by 2 neuroradiologists blinded to history and outcome. Clinical presentation, course, and outcome at >12 months were abstracted from medical records. The diagnostic utility of cranial ultrasound was compared with that of MR imaging.

RESULTS: Sixteen patients were included (median gestational age, 36.5 weeks; range, 27–41 weeks; 31% premature). MR images were obtained acutely at the time of presentation between days 0 and 9 of life. On T2WI and DWI, a consistent presence of a hypointense subpial bleed and an underlying hyperintense cerebral cortex were recognized, which created a distinct MR imaging pattern resembling the yin-yang symbol. Findings of all the MRAs and MRVs were normal. Cranial ultrasound detected 6 of 7 MR imaging lesions with sonographic features correlating well with MR imaging. The 3 extreme or very preterm neonates did not survive. The remainder survived with relatively mild neurologic deficits.

CONCLUSIONS: Subpial hemorrhage with underlying infarction is a recognizable condition with unique MR imaging and sonographic features. Improved recognition may advance understanding of risk factors and outcomes.

ABBREVIATION: GRE = gradient recalled-echo

Most children with perinatal stroke experience life-long neurologic disabilities.[1,2] Among the many subtypes of perinatal stroke, there is increasing awareness of neonatal subpial hemorrhage with underlying cerebral infarction diagnosed in the neonatal period.[3] This entity was first described by Huang and Robertson.[4] In their report of 7 term neonates who had spontaneous superficial parenchymal and leptomeningeal hemorrhage on CT and MR imaging, 4 had short-term clinical follow-up and were neurologically normal. Recently, Cain et al[5] reported 17 neonates who had subpial hemorrhage with underlying intraparenchymal cytotoxic edema on MR imaging shortly after birth. All of these term or late-preterm neonates survived except for one who succumbed to complications of congenital heart disease.

With such rare descriptions, the incidence, pathogenesis, possible risk factors, and outcomes of this clinicoradiographic syndrome are unknown. The condition has also been inconsistently named, contributing to under-recognition and hindering studies of pathogenesis, management, and outcome. To our knowledge, occurrence in early preterm neonates has not been reported. Moreover, the sonographic features and diagnostic value of cranial ultrasound have not been described despite this technique often being the first-line in critically ill and preterm neonates.

In this study, we report the MR imaging and cranial ultrasound features of 16 neonates, including preterm infants, with imaging features suggestive of subpial hemorrhage with underlying brain parenchymal hemorrhagic infarction.

Received June 26, 2020; accepted after revision August 19.

From the Departments of Radiology (Z.A., A.K., A.P., X.-C.W.), Clinical Neurosciences and Pediatrics (A.K.), University of Calgary, Calgary, Alberta, Canada; and Department of Diagnostic Imaging (Z.A., A.P., M.S., X.-C.W.), Alberta Children's Hospital, Calgary, Alberta, Canada.

This study was previously presented, in part, at: Annual Meeting of the American Society of Pediatric Neuroradiology, January 18–20, 2019; New Orleans, Louisiana.

Please address correspondence to Xing-Chang Wei, MB, MSc, FRCPC, Diagnostic Imaging, Alberta Children's Hospital, 28 Oki Dr NW, Calgary, AB T3B 6A8, Canada; e-mail: weix@ucalgary.ca

http://dx.doi.org/10.3174/ajnr.A6872

Table 1: Patient demographics, clinical presentation, and outcomes

Clinical Parameter	Subgroups	Value
Maternal age	Mean age in years	33.5 (27–39)
Gestational age at birth (weeks)	Term (≥37)	11/16
	Moderate-to-late preterm (32–37)	2/16
	Very preterm (28–32)	2/16
	Extremely preterm (≤ 28)	1/16
Sex	Male	5/16
	Female	11/16
Mode of delivery	Vaginal	13/16
	Cesarean delivery	3/16
Birth weight	<2.5 kg	5/16
	>2.5 kg	11/16
	Mean	2.2 kg
Birth assistance in vaginal delivery	No assistance	10/13
	Vacuum assistance	3/13
Clinical presentation	Apnea	10/16
	Seizure	9/16
	Encephalopathy	3/16
APGAR score at 1 min		6.3 (range, 1–9)
APGAR score at 5 min		8.4 (range, 4–9)
Age at onset of symptoms		2.1 days (range, 1–6 days of life)
Age at most recent follow-up		18.8 months (range, 1–90 months)
Abnormal coagulation/hematology profile	Maternal	0/16
	Neonatal	1/16 (elevated hematocrit)
Outcome	Death	3/16 (1 extremely preterm, 2 very preterm)
	With neurologic deficits	2/16
	No neurologic deficits	11/16

MATERIALS AND METHODS

Population

The participants were retrospectively identified by a pediatric neuroradiologist through a neuroimaging teaching case data base stored on the institutional (Alberta Children's Hospital, Calgary) computer system. The terms "hemorrhage" and "neonate" were searched in the data base. Clinical images of the returned subjects were retrospectively reviewed on the clinical PACS, from which subjects who had subpial hemorrhage were included in this study. Information of patient demographics, clinical course, and laboratory investigation was collected from the electronic medical chart. The study was approved by the institutional research ethics board.

Image Acquisition

MR images of the brain were obtained for clinical reasons on different clinical scanners in 3 different hospitals (Alberta Children's Hospital, Foothills Medical Centre and South Health Campus, all located in Calgary city) in the city from April 2006 to April 2020. Scanners were 1.5T or 3T in field strength. The MR imaging and specific scanning parameters varied, but the same essential anatomic sequences used in the current study were always performed, including sagittal and axial T1WI, axial and coronal FSE T2WI, axial DWI (and coronal in some cases), and axial gradient recalled-echo (GRE) T2*-weighted imaging. Coronal DWI was performed in all initial scans and in most of the follow-up scans. SWI was performed in some cases instead of GRE T2*WI. TOF-MRA and non-contrast MRV, including 2D-TOF-MRV and 3D phase-contrast MRV, were performed in most cases (see RESULTS).

Cranial ultrasound studies were performed on a variety of machines in multiple centers during the same timeframe. Standard oblique sagittal and oblique coronal still images and cine loops were obtained through the anterior fontanelle in all cases.

Image Analysis

Analysis was performed by 2 pediatric neuroradiologists (Z.A., X.-C.W.), who were blinded to clinical presentation and outcome. Clinical images were retrospectively reviewed on the clinical PACS. The presence, location, size, and signal intensity of subpial hemorrhage and the underlying brain parenchyma were recorded on a standardized data-capture form. All available MRA and MRV images were reviewed. For those participants with multiple MR imaging and sonographic scans, the initial scans were analyzed to assess the diagnostic performance of MR imaging and ultrasound. Follow-up MR images were analyzed to assess the natural course of the disease. In addition, the MRA images from later scans were reviewed to exclude vascular malformations that may not have been detected in earlier scans. Cranial ultrasound findings were compared with brain MR imaging findings.

RESULTS

Population

Sixteen patients were included in the study. Patient demographics are summarized in Table 1. Most ($n = 11$) were born at term gestation (≥37 weeks), 2 were moderate-to-late preterm (32–37 weeks), 2 were very preterm (28–32 weeks), and 1 was extremely preterm (≤28 weeks). Of note, almost 70% of the infants were born by vaginal delivery.

Clinical Presentation, Investigations, and Outcome

Clinical presentation and outcome are also summarized in Table 1. Perinatal histories were generally unremarkable. No maternal

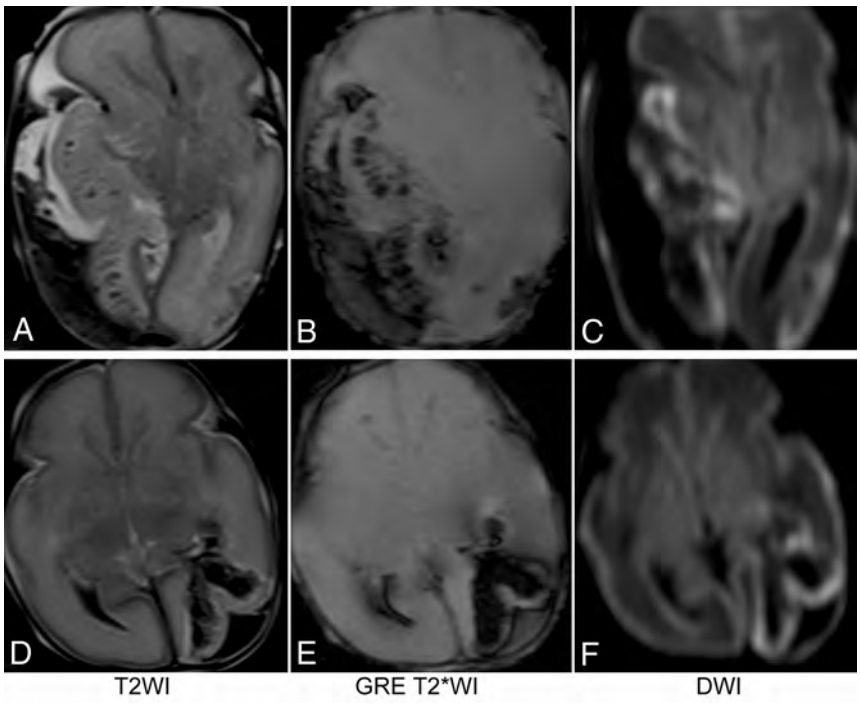

FIG 1. MR imaging of 2 preterm neonates who did not survive to discharge from the neonatal unit. The first patient (*A–C*) was born at 27 weeks 3 days' gestation and had a large subpial hemorrhage and a large underlying hemorrhagic infarct. The second patient (*D–F*) was born at 28 weeks 1 day of gestation. She had a relatively small subpial hemorrhage and underlying hemorrhagic infarct but had engorged deep medullary veins in the bilateral cerebral hemispheres that may have had small thrombosis (not shown).

history of smoking or substance abuse was found. Three patients had a history of controlled gestational hypertension. APGAR scores were available for 12 of the 16 neonates (9 term, 3 preterm) and were usually normal. Of note, 3 of the 16 patients had a clinical presentation of encephalopathy, all of whom were preterm. None of them were diagnosed with other neurologic conditions such as hypoxic-ischemic encephalopathy. Symptoms were seen as early as 4 hours after birth to 6 days of life.

Eight patients were investigated with electroencephalography, of which 7 showed abnormalities in the form of focal epileptiform discharges and 1 was unremarkable. Six of the 7 electroencephalograpies with abnormal findings were lateralized to the side of the subpial hemorrhage. In 2 of these 6 patients, the seizure origin on electroencephalography was consistent with the location of hemorrhage and infarction, while in the other 4 patients, the seizure origin could not be further localized. Coagulation profiles, including complete blood count, partial thromboplastin time, and international normalized ratio, were completed in all patients and were unremarkable. One patient had prenatal maternal group B streptococcal culture, for which antibiotic treatment was given, but the child was negative with no sepsis or meningitis. All neonates had at least a partial septic work-up, all of which were negative for sepsis (systemic infection).

All patients received standardized neurocritical care. Seizures were managed acutely with antiseizure medications, including levetiracetam, phenobarbital, and phenytoin. One preterm patient underwent a decompression craniectomy on day 4 of life to relieve the mass effect associated with a large hemorrhage (Fig 1*A–C*).

All 3 patients born extremely preterm or very preterm did not survive to discharge. One had a prenatal diagnosis of trisomy 21, severe oligohydramnios, and microcephaly on prenatal ultrasound and succumbed to severe renal failure. The other 2 patients did not have major diseases other than the intracranial abnormalities.

The other 13 patients survived and appeared to have good outcomes at a median of 18.8 months (range, 1–90 months). Among them, 11 patients had no residual seizures, neurologic deficits, or developmental issues on follow-up. One had recurrent seizures, which were controlled by low-dose levetiracetam. Another term neonate had occasional periodic breathing, which was managed with home oxygen. One patient had hemianopia on clinical examination at 2 months.

MR Imaging at Presentation

The results of the initial MR imaging and cranial ultrasound scans are summarized in Table 2. Seven patients had ultrasound as the first neuroimaging examination followed by MR imaging, and 8 had MR imaging only. One patient had cranial ultrasound only. The image quality of all scans was deemed satisfactory.

All lesions were unilateral and neocortical. Most (69%) lesions were located in the temporal lobes, followed by the frontal (19%), parietal (6%), and occipital (6%) lobes. No lesion was located in the posterior fossa. Two (2/16) patients had small contralateral subdural bleeds. On MR imaging, 8/15 patients showed mass effect in the form of a midline shift and/or uncal herniation. Of the 8 cases, 3 patients had only midline shift, and the remaining 5 had a combination of midline shift with uncal herniation. Some degree of regional mass effect with effacement of adjacent sulci was seen in all cases. No tonsillar herniation was observed.

On the initial MR imaging, irrespective of the location and size of the lesion, 2 key components were consistently seen on all MR images. The first was a focal subpial collection of fluid extending into the adjacent cerebral sulci associated with widening of the cerebral sulci and flattening of the underlying parenchyma. The subpial collection consistently demonstrated mild-to-moderately hyperintense T1 signal, markedly hypointense T2 signal, and increased diffusivity on DWI and ADC maps, consistent with acute or subacute bleed (Fig 2).

The second component of the lesion was signal change in adjacent brain parenchyma. This included the cortex as well as subcortical and deeper white matter immediately underneath the

Table 2: MR imaging and cranial ultrasound data and findings at presentation

	No.	Percentage
Imaging data		
MR imaging and US	7	
MR imaging only	8	
US only	1	
Age at imaging (range) (day)		
MR imaging	3.2 (1–9)	
US	2.7 (1–7)	
MR imaging field strength (1.5T:3T)		12:3
MR imaging sequences		
Core sequences[a]	15/15	
GRE T2*WI	11/15	
SWI	4/15	
MRV performed		
On initial MRI	10/15	
On repeat MRI within 4 days	3/15	
MRA performed		
On initial MRI	9/15	
On repeat MRI within 6 weeks	3/15	
Lesion laterality (right:left)	10:6	62%:38%
Lesion location		
Temporal	11/16	69%
Frontal	3/16	19%
Parietal	1/16	6%
Occipital	1/16	6%
Parenchymal diffusion restriction	15/15	100%
Parenchymal hemorrhage	11/15	50%
Intraventricular hemorrhage	3/15	18%
Midline shift	8/15	50%
Yin-yang sign on MRI	15/15	100%
Yin-yang sign on US	6/6	100%

Note:—US indicates ultrasound.

[a] The core MR images include sagittal and axial T1WI, axial and coronal FSE T2WI, and axial and coronal DWI.

subpial hemorrhage. On 4 of 15 MR imaging scans, no intra-axial hemorrhage was present in the parenchyma. In these cases, both the cortex and white matter lesions consistently demonstrated uniformly hypointense T1 signal, hyperintense T2 signal, restricted diffusion, and isointense signal on GRE T2*WI or SWI (Fig 2*A–D*). On 6 of 15 MR imaging scans, a small amount of hemorrhage was present in the subcortical and deep white matter components of the lesion. In these cases, the involved cortex consistently demonstrated hypointense T1 signal, hyperintense T2 signal, restricted diffusion, and isointense signal on GRE T2*WI, while the underlying white matter showed heterogeneous signal on T1WI and T2WI and was predominantly hypointense on DWI and GRE T2*WI (Fig 2*E–H*). On the remaining 5 MR images, a larger amount of hemorrhage was present in the subcortical and deep white matter. In these cases, the involved cortex consistently demonstrated hypointense T1 signal, hyperintense T2 signal, and restricted diffusion and large blooming artifacts on GRE T2*WI. The underlying white matter demonstrated heterogeneous signal on T1WI and T2WI and was predominantly hypointense on DWI and GRE T2*WI (Fig 2*A–D*). The signal characteristics of each group are summarized in Table 3.

On T2WI and DWI, the consistent presence of a dark, hypointense, subpial bleed and an underlying bright, hyperintense cerebral cortex created a distinct MR imaging pattern, resembling the yin-yang symbol in Chinese philosophy (Fig 3).

Two of the 3 patients who did not survive had MR imaging at days 1 and 2 of life, respectively. One of them was born at 27 weeks' gestation and had a large subpial hemorrhage and a large underlying hemorrhagic infarct (Fig 1*A–C*). The other patient was born at 28 weeks' gestation. She had a relatively small subpial hemorrhage and an underlying hemorrhagic infarct but also demonstrated engorged deep medullary veins bilaterally, suggestive of deep cerebral sinovenous thrombosis, though this could not be confirmed on imaging (Fig 1*D–F*). Both showed small amounts of intraventricular hemorrhage without evidence of germinal matrix hemorrhage.

Among the 15 patients who had MR images, 13 had MR venography completed either on their initial MR images or on a repeat scan within 4 days (Table 2). None of the MR venograms demonstrated thrombosis in the dural venous sinuses or the cerebral veins. Twelve patients had MR angiograms on either their initial MR images or the repeat scans within 6 weeks, all of which had normal findings.

Cranial Ultrasound

Seven patients had cranial ultrasound before brain MR imaging. The time interval between the ultrasound and MR imaging was an average of 13 hours (range, 5–24 hours). Cranial ultrasound detected the subpial hemorrhage with underlying infarct in 6 of 7 patients. The patient with false-negative ultrasound findings had the smallest lesion in this cohort, about half the size of the lesion of the first patient in Fig 2*A–D*. On the 6 sonographic scans positive for idiopathic subpial hemorrhage with underlying cerebral infarct, the subpial hemorrhage and the underlying parenchymal abnormality could be separated in all cases. Lesion size and shape correlated well with MR imaging on subjective review, though a quantitative analysis was not performed. The subpial hemorrhage was hypoechoic in 4 patients, mildly hyperechoic in 1 patient, and moderately hyperechoic in another. While the infarcted cerebral cortex and the underlying white matter with hemorrhagic infarct can be readily differentiated from each other on MR imaging, the 2 components could not be separated on ultrasound. Nonetheless, the combination of hypoechoic or mildly hyperechoic subpial collection of bleeds and the underlying markedly echogenic brain parenchyma gives a distinct sonographic pattern similar to the MR imaging yin-yang sign (Fig 4).

One of the patients had 2 cranial ultrasound scans as the only neuroimaging studies before succumbing to disease. He was born at 30 weeks' gestation. The ultrasound findings in this patient were similar to those of the other 7.

Among the 8 patients who underwent cranial ultrasound, only 3 had follow-up cranial ultrasound scans. One of the 3 had 14 repeat scans, one had 2, and the other had 1. Three of the follow-up scans were obtained 1–4 days after the initial scan, which showed no obvious change in size, shape, or echogenicity of the subpial hemorrhage or the underlying brain parenchymal lesion. Three of the follow-up scans were obtained 8–11 days after the initial scan, which showed a mildly decreased size of the subpial hemorrhage and the underlying brain parenchymal lesion, while the subpial

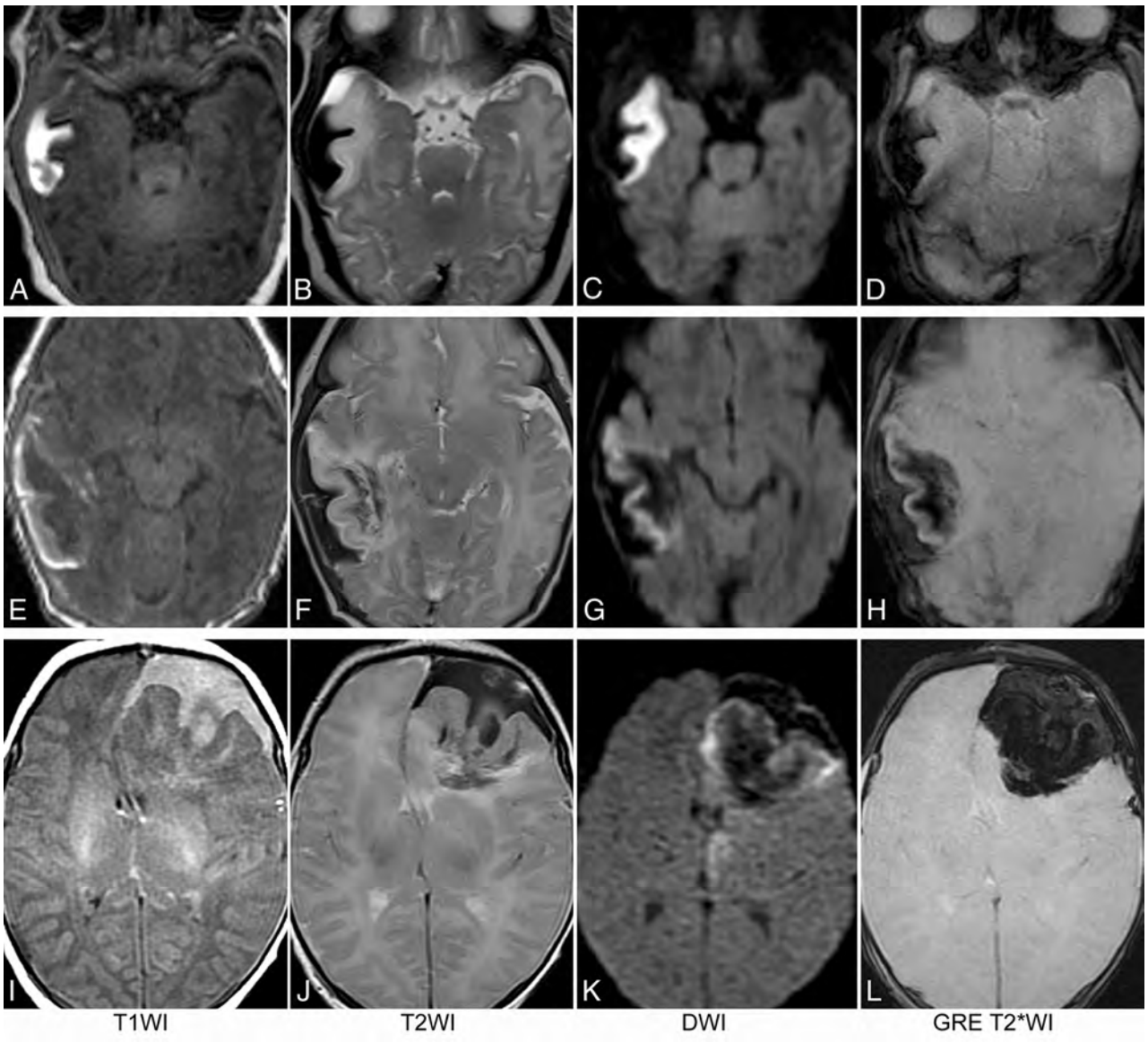

FIG 2. MR images of 3 term neonates. The subpial hemorrhage consistently shows hyperintense T1 signal, hypointense T2 signal, no restricted diffusion, and hypointense signal on GRE T2*WI. In the first patient (*A–D*), the underlying cerebral cortex and white matter have no hemorrhage. In the second patient (*E–H*), a mild fan-shaped hemorrhage is seen in the underlying white matter, resulting in a hypointense signal on T2WI, DWI, and T2*WI, while the cerebral cortex remains hyperintense on T2WI, DWI, and T2*WI. In the third patient (*I–L*), more severe hemorrhage is seen in the underlying white matter, leading to an obscured cerebral cortex on T2*WI and a partially obscured cortex on DWI.

Table 3: Appearance of subpial hemorrhage and underlying brain parenchyma on initial MR imaging and US

Subpial Bleed, Parenchymal Lesion	MRI				US
	T1WI	T2WI	DWI	T2*WI	
	↑	↓	↓	↓	↓ or ↑
Cortical infarct with no WM hemorrhage (4/15)					
Cortex	↓	↑	↑	↔	↑
WM	↓	↑	↑	↔	
Cortical infarct with small WM hemorrhage (6/15)					
Cortex	↓	↑	↑	↔	↑
WM	Mixed	Mixed	↓	↓	
Cortical infarct with large WM hemorrhage (5/15)					
Cortex	↓	↑	↑	↓	↑
WM	Mixed	Mixed	↓	↓	

Note:—↔ indicates isointense or isoechoic; ↑, hyperintense or hyperechoic; ↓, hypointense or hypoechoic; US, ultrasound.

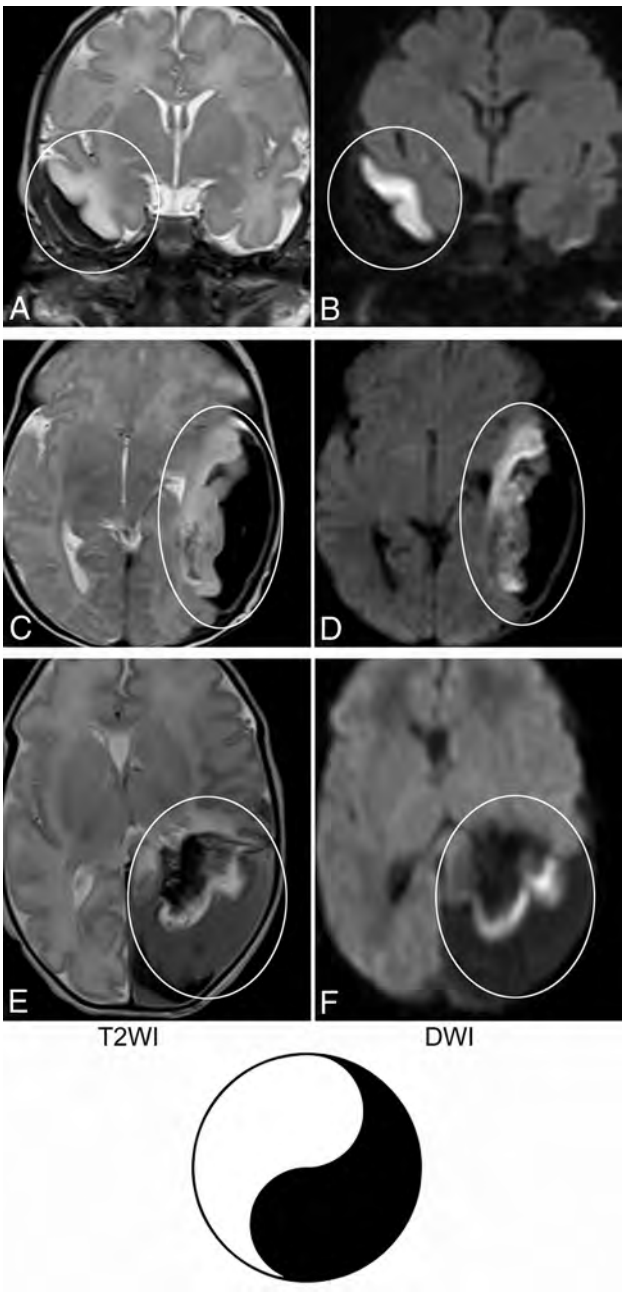

FIG 3. Yin-yang sign. T2WI and DWI of 3 term neonates with subpial hemorrhage are shown. In the brain parenchyma underlying the subpial bleed, no hemorrhage is seen in the first patient (*A* and *B*); mild hemorrhage, in the second patient (*C* and *D*); and severe hemorrhage, in the third patient (*E* and *F*). Irrespective of the presence or degree of intraparenchymal hemorrhage, the combination of a dark subpial fluid collection and a bright underlying cerebral cortex forms a consistent, distinct image pattern (*circled* areas in *A*–*F*), resembling the yin-yang symbol in Chinese philosophy.

hemorrhage changed from being hypoechoic to mildly echogenic and the underlying brain parenchymal lesions changed from being markedly echogenic to mildly echogenic.

Follow-Up MR Imaging

Twelve of the 15 patients had follow-up MR imaging, among whom 7 patients had 1 follow-up scan, 8 had 2, and 1 had 3. The MR imaging appearances of the subpial hemorrhage and underlying brain parenchyma on follow-up scans are summarized in Table 4. Of note, none of the follow-up MR images showed an interval increase in the size of the subpial hemorrhage or the underlying brain abnormality compared with the initial scans.

DISCUSSION

In 2004, Huang and Robertson[4] first reported 7 term neonates with idiopathic superficial parenchymal and leptomeningeal (ie, subpial or subarachnoid) hemorrhage on MR imaging and CT. Not until 16 years later did Cain et al[5] report MR images of another cohort of 17 term and late-preterm neonates with subpial hemorrhage and cytotoxic edema in the underlying brain parenchyma. Our study expands the description of this unique syndrome, reporting 16 neonates with subpial hemorrhage and underlying cerebral infarction. The contributions of this study are multifold.

First, our cohort of patients included 3 either extremely preterm (≤ 28 weeks' gestation) or very preterm (28–32 weeks' gestation) neonates, all of whom did not survive to discharge. In the case series of Huang and Robertson[4] and that of Cain et al,[5] the patients were either term or late-preterm, and all survived with relatively minor neurologic deficits. Our sample size is small, preterm neonates are already at high risk of mortality, and the direct cause of death may not be attributable to the intracranial abnormalities. Therefore, we cannot draw any conclusions regarding possible associations between this radiographic syndrome and outcome. However, we hope these descriptions will improve recognition of this disorder by neonatologists and neurologists and alert them that extremely preterm or very preterm neonates with this condition may not have the same relatively good outcome as late-preterm or term neonates.

Second, we studied the sonographic features of idiopathic subpial hemorrhage with underlying cerebral infarction. In previous studies, only CT and MR images were analyzed and reported. However, because cranial ultrasound is often the first imaging technique in evaluating neonates with neurologic concerns due to its easy accessibility and ability to be performed at the bedside, it is valuable to understand the utility of ultrasound in diagnosing this disease. In this study, we compared ultrasound images of 7 neonates with their MR images obtained 5–24 hours later. We found that ultrasound was able to detect the lesions in 6 of the 7 patients, with the only false-negative ultrasound occurring in the patient with the smallest lesion. We also found that once the lesion was detected, ultrasound was able to separate and delineate the extra-axial pial hemorrhage and the underlying parenchymal abnormality, with their sizes and shapes correlating well with the MR imaging (Fig 4). To our knowledge, this is the first report on the value of cranial ultrasound in the diagnosis of this disease.

Third, we further analyzed the MR imaging features of the subpial hemorrhage and underlying infarct. We found that the underlying infarcted brain parenchyma often has concurrent hemorrhage, observed in 11 of 15 scans, which is similar to the reported 76% incidence of concurrent hemorrhage by Cain et al[5] (Fig 2). In addition, we recognized the consistent combination of

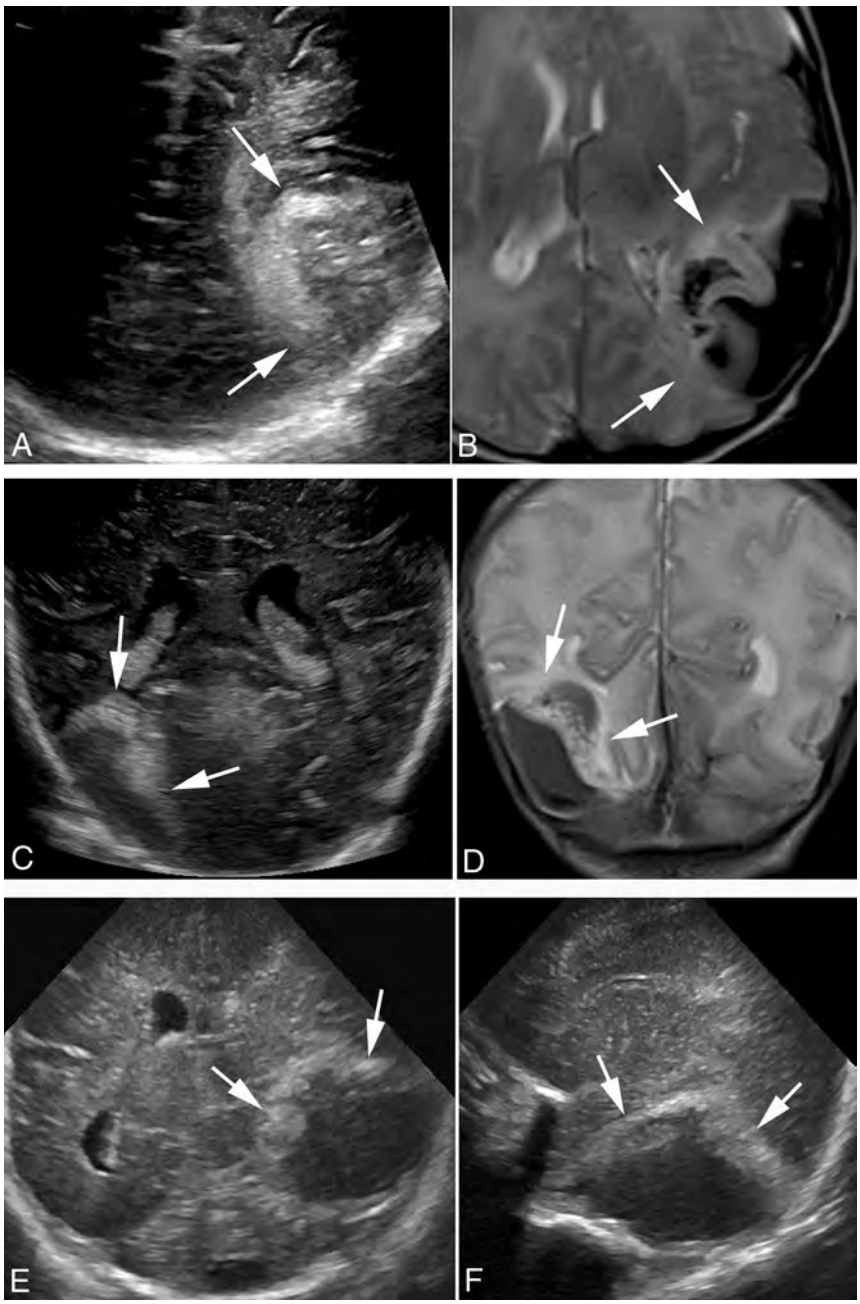

FIG 4. Ultrasound images of subpial hemorrhage with underlying cerebral infarct compared with MR images. The ultrasound images (*A* and *C*) were obtained <24 hours before the MR images (*B* and *D*) of a late-preterm neonate (*A* and *B*) and a term neonate (*C* and *D*). Ultrasound is able to detect both the subpial hemorrhage and underlying cerebral infarct in both patients (*arrows*). The subpial collection of bleeds is mildly echogenic in the first patient (*A* and *B*) and hypoechoic in the second patient (*C* and *D*), even though they are all hypointense on T2-weighed MR images. Ultrasound is unable to differentiate the infarcted cerebral cortex from the underlying white matter with hemorrhagic infarct. The ultrasound images in the lower panel are from a very preterm neonate who did not have brain MR imaging performed before succumbing to disease.

a bright, hyperintense appearance of the cerebral cortex with the dark, hypointense overlying subpial hemorrhage on T2WI and DWI, which creates a distinct imaging pattern that resembles the yin-yang symbol in Chinese philosophy (Fig 3). Similarly, on ultrasound, a consistent combination of a dark or grayish subpial collection of subpial bleeds with the underlying bright, echogenic brain parenchyma was seen in all 6 cases, which also gives a distinct imaging pattern that resembles the yin-yang sign (Fig 4). Such a distinctive and memorable imaging biomarker may facilitate recognition by radiologists and clinicians.

Furthermore, we studied the natural course of the disease on serial MR images. On the follow-up MR images, neither the subpial hemorrhage nor the underlying infarct progressed with time. This observation may be useful clinically in guiding imaging follow-up of these patients.

Unfortunately, even though the imaging pattern of the subpial hemorrhage with underlying infarct described here and in previous reports[4,5] is characteristic, the pathophysiology remains unknown. Subpial hemorrhages have been described using various terminologies in the literature, including leptomeningeal hemorrhage, superficial lobar hemorrhage, pial hemorrhage, extra-axial bleed with underlying infarct, and so forth.[4,6,7] Many hypotheses have been proposed for the pathogenesis of this disease. Huang and Robertson[4] suggested that local trauma with contusion or venous compression or occlusion may be the cause of the spontaneous superficial parenchymal and leptomeningeal hemorrhage in their cohort of term neonates. In our series, almost 70% of the infants were born by vaginal delivery. However, emerging evidence, including large case-controlled studies of neonatal hemorrhagic stroke, is confirming a lack of association with birth trauma.[8] The study by Cain et al[5] also concluded that a relationship with birth trauma was unlikely and that the imaging findings were instead suggestive of a nonarterial, deep venous pattern of hemorrhagic ischemia. Slaughter et al[9] reported 7 term neonates with superficial temporal lobe hemorrhagic infarcts who presented immediately after birth to 14 days. Review of their MR images showed that at least 5 of their 7 cases had the yin-yang sign on T2WI. They attributed the findings to possible thrombosis of the vein of Labbe or other superficial temporal veins. However, they could not demonstrate a direct sign of venous thrombosis confidently on MRV. Neonatal cerebral sinovenous thrombosis is a well-described entity with similar imaging features; the inability of MRV to demonstrate venous thrombosis when the

Table 4: Appearances of subpial hemorrhage and underlying brain parenchyma on follow-up MR imaging

Time Interval between Initial and Follow-Up MR Imaging	No. of Scans	Follow-Up MR (Appearances Compared with Initial MRI)	
		Subpial Hemorrhage	Underlying Cerebral Infarct
1–6 days	8	Similar size and shape	Similar size and shape
7–13 weeks	4	Evolved into fluid collection with less mass effect	Decreased size
13–28 weeks	6	Evolved into fluid collection with no mass effect	Decreased size

disease is limited to ≥1 small cortical vein is well-known.[10,11] While our retrospective, uncontrolled series cannot define the exact mechanisms, we would favor a similar mechanism as the most likely pathophysiology.

It also remains unclear whether it could be a cerebral venous infarct that causes secondary subpial hemorrhage; or instead, could a subpial hemorrhage cause venous compression and subsequent venous infarction of the underlying brain? The pia mater is a single-cell layered membrane closely adherent to the brain surface, only separated by a potential subpial space. The subpial space contains blood vessels and varying amounts of collagen. Arteries coursing through this space are always surrounded by the pia mater as they enter the parenchyma. However, the veins coursing through the subpial space may or may not be invested by the pia mater.[12] Hence, it could be speculated that cortical veins, unlike cortical arteries, which have little-or-no leptomeningeal investment around them, can bleed directly into the subpial space. A certain amount of blood collection in the subpial space may potentially compress the underlying brain parenchyma, causing venous congestion, medullary vein thrombosis, and subsequent venous infarct. The presence of linear fan-shaped prominent deep medullary veins in some of our patients may represent deep medullary venous thrombosis, which would not be detectable on a MR venogram. On the other hand, while a strong network of trabeculae exists along veins and arteries in the subarachnoid space, this trabecular network is lacking around veins in the subpial space. This feature lends a potential mechanism for decompression of hemorrhage in superficial infarcts into the subpial space.[13]

Apnea and respiratory distress were the most presenting symptoms in our cohorts of patients (Table 1). These are not likely attributable to the direct effects of the hemorrhage itself (ie, compression). The proportion presenting with such clinical signs would seem comparable with other populations of neonates with acute, acquired focal brain injury. Whether this is due to seizures or other common respiratory reasons for neonates to be admitted to the neonatal intensive care units cannot be determined.

Our study is limited by its small sample size and its retrospective nature. The information on follow-up is limited and only available until a median of 18 months of age. A more thorough follow-up such as a Bayley scale assessment could not be realized in the current study design. As with all perinatal brain injury studies, true outcomes usually can only be determined with more comprehensive measures performed >5 years from birth. We hope further descriptions of the unique imaging findings will improve recognition and future studies to better understand pathophysiology and outcomes.

CONCLUSIONS

Subpial hemorrhage with underlying cerebral infarct is a condition that has a unique MR imaging and sonographic pattern that resembles the yin-yang symbol in Chinese philosophy. Ultrasound is able to detect all the subpial hemorrhages and underlying cerebral infarcts seen on MR imaging except for those that are relatively small. While this condition can occur in term and late-preterm neonates as previously reported, it can also occur in neonates born at extremely preterm or very preterm gestation. While the former group of patients has relatively mild neurologic sequelae, the latter group may have grave clinical outcomes. The pathophysiology of this condition is still not fully understood. We hope the further characterization of the imaging findings in our study will, to some degree, facilitate a better recognition in clinical practice and further research in the future.

ACKNOWLEDGMENTS

The authors would like to thank Amalia Floer for her administrative assistance.

Disclosures: Zarina Assis—*UNRELATED*: *Employment*: Radiologist at Alberta Children's Hospital, Calgary, Alberta, Canada. Adam Kirton—*UNRELATED*: *Expert Testimony*: occasional medical expert.

REFERENCES

1. Dunbar M, Kirton A. **Perinatal stroke: mechanisms, management, and outcomes of early cerebrovascular brain injury.** *Lancet Child Adolesc Health* 2018;2:666–76 CrossRef Medline
2. Dunbar M, Kirton A. **Perinatal stroke.** *Semin Pediatr Neurol* 2019;32:100767 CrossRef Medline
3. Lee S, Mirsky DM, Beslow LA, et al; International Paediatric Stroke Study Neuroimaging Consortium and the Paediatric Stroke Neuroimaging Consortium. **Pathways for neuroimaging of neonatal stroke.** *Pediatr Neurol* 2017;69:37–48 CrossRef Medline
4. Huang AH, Robertson RL. **Spontaneous superficial parenchymal and leptomeningeal hemorrhage in term neonates.** *AJNR Am J Neuroradiol* 2004;25:469–75 Medline
5. Cain DW, Dingman AL, Armstrong J, et al. **Subpial hemorrhage of the neonate.** *Stroke* 2020;51:315–18 CrossRef Medline
6. Bergman I, Bauer RE, Barmada MA, et al. **Intracerebral hemorrhage in the full-term neonatal infant.** *Pediatrics* 1985;75:488–96 Medline

7. Hanigan WC, Powell FC, Palagallo G, et al. **Lobar hemorrhages in full-term neonates.** *Childs Nerv Syst* 1995;11:276–80 CrossRef Medline
8. Cole L, Dewey D, Letourneau N, et al. **Clinical characteristics, risk factors, and outcomes associated with neonatal hemorrhagic stroke: a population-based case-control study.** *JAMA Pediatr* 2017;171:230–38 CrossRef Medline
9. Slaughter L, Egelhoff J, Balmakund T. **Neurologic outcome in neonatal temporal lobe hemorrhagic venous infarcts.** *J Child Neurol* 2009;24:1236–42 CrossRef Medline
10. deVeber G, Andrew M, Adams C, et al; Canadian Pediatric Ischemic Stroke Study Group. **Cerebral sinovenous thrombosis in children.** *N Engl J Med* 2001;345:417–23 CrossRef Medline
11. Jordan LC, Rafay MF, Smith SE, et al; International Pediatric Stroke Study Group. **Antithrombotic treatment in neonatal cerebral sinovenous thrombosis: results of the International Pediatric Stroke Study.** *J Pediatr* 2010;156:704–10 CrossRef Medline
12. Weller RO, Sharp MM, Christodoulides M, et al. **The meninges as barriers and facilitators for the movement of fluid, cells and pathogens related to the rodent and human CNS.** *Acta Neuropathol* 2018;135:363–85 CrossRef Medline
13. Gunda D, Cornwell BO, Dahmoush HM, et al. **Pediatric central nervous system imaging of nonaccidental trauma: beyond subdural hematomas.** *Radiographics* 2019;39:213–28 CrossRef Medline

Tractography of the Cerebellar Peduncles in Second- and Third-Trimester Fetuses

F. Machado-Rivas, O. Afacan, S. Khan, B. Marami, C.K. Rollins, C. Ortinau, C. Velasco-Annis, S.K. Warfield, A. Gholipour, and C. Jaimes

ABSTRACT

BACKGROUND AND PURPOSE: Little is known about microstructural development of cerebellar white matter in vivo. This study aimed to investigate developmental changes of the cerebellar peduncles in second- and third-trimester healthy fetuses using motion-corrected DTI and tractography.

MATERIALS AND METHODS: 3T data of 81 healthy fetuses were reviewed. Structural imaging consisted of multiplanar T2-single-shot sequences; DTI consisted of a series of 12-direction diffusion. A robust motion-tracked section-to-volume registration algorithm reconstructed images. ROI-based deterministic tractography was performed using anatomic landmarks described in postnatal tractography. Asymmetry was evaluated qualitatively with a perceived difference of >25% between sides. Linear regression evaluated gestational age as a predictor of tract volume, ADC, and fractional anisotropy.

RESULTS: Twenty-four cases were excluded due to low-quality reconstructions. Fifty-eight fetuses with a median gestational age of 30.6 weeks (interquartile range, 7 weeks) were analyzed. The superior cerebellar peduncle was identified in 39 subjects (69%), and it was symmetric in 15 (38%). The middle cerebellar peduncle was identified in all subjects and appeared symmetric; in 13 subjects (22%), two distinct subcomponents were identified. The inferior cerebellar peduncle was not found in any subject. There was a significant increase in volume for the superior cerebellar peduncle and middle cerebellar peduncle (both, $P < .05$), an increase in fractional anisotropy (both, $P < .001$), and a decrease in ADC (both, $P < .001$) with gestational age. The middle cerebellar peduncle had higher volume ($P < .001$) and fractional anisotropy ($P = .002$) and lower ADC ($P < .001$) than the superior cerebellar peduncle after controlling for gestational age.

CONCLUSIONS: A robust motion-tracked section-to-volume registration algorithm enabled deterministic tractography of the superior cerebellar peduncle and middle cerebellar peduncle in vivo and allowed characterization of developmental changes.

ABBREVIATIONS: FA = fractional anisotropy; GA = gestational age; ICP = inferior cerebellar peduncle; MCP = middle cerebellar peduncle; MCP_{cog} = cognitive pathway of middle cerebellar peduncle; MCP_{mot} = motor pathway of middle cerebellar peduncle; MT-SVR = motion-tracked slice-to-volume registration; SCP = superior cerebellar peduncle

In the second half of pregnancy, the cerebellum is growing rapidly and is extremely vulnerable.[1] Despite the increasingly recognized association of antenatal and perinatal cerebellar injury with adverse motor and neurologic outcomes later in life,[2-5] little is known about normal cerebellar developmental in the later part of gestation, in particular with regard to changes in microstructure. In fact, most existing fetal MR imaging data addresses primarily changes in cerebellar volume with gestational age (GA) or changes in volume and

Received May 11, 2020; accepted after revision August 24.

Computational Radiology Laboratory (F.M.-R., O.A., S.K., B.M., C.V.-A., S.K.W., A.G., C.J.), Department of Radiology, Department of Neurology (C.K.R.), and Fetal-Neonatal Neuroimaging and Developmental Science Center (C.J.), Boston Children's Hospital, Boston, Massachusetts; Harvard Medical School (F.M.-R., O.A., S.K., B.M., C.K.R., S.K.W., A.G., C.J.), Boston, Massachusetts; and Department of Pediatrics (C.O.), Washington University School of Medicine in St. Louis, St. Louis, Missouri.

The content is solely the responsibility of the authors and does not necessarily represent the official views of the National Institutes of Health, the Fetal Health Foundation or the McKnight Foundation.

Research reported in this study was supported, in part, by the American Academy of Neurology, grant/award No. ???????; a Clinical Research Training Fellowship; the Fetal Health Foundation; the McKnight Foundation; the National Alliance for Research on Schizophrenia and Depression, grant/award No. ???????; Young Investigator; National Heart, Lung, and Blood Institute, grant/award No. K23HL141602; Scholar Award from the Pediatric Heart Network; National Institute of Neurological Disorders and Stroke, grant/award No. K23NS101120; National Institutes of Health, grant/award Nos. R01EB013248, R01EB018988, R01NS106030; and a Schlaeger Fellowship for Neuroscience Research.

Please address correspondence to Camilo Jaimes, MD, Harvard Medical School, Boston, MA 02115; e-mail: camilo.jaimescobos@childrens.harvard.edu

Indicates open access to non-subscribers at www.ajnr.org

Indicates article with supplemental on-line tables.

Indicates article with supplemental on-line photo.

http://dx.doi.org/10.3174/ajnr.A6869

their association with specific diseases such as congenital heart disease.[6-8]

In vivo evaluation of cerebellar microstructure using fetal MR imaging has been limited by the technical challenges related to imaging the gravid abdomen, particularly patient motion. However, data from ex vivo MR imaging studies are promising. For instance, Takahashi et al[9,10] performed high-resolution ex vivo DTI of fetal specimens and demonstrated the feasibility of using tractography to outline the cerebellar peduncles prenatally. Even though tractography of the cerebellar peduncles has been sporadically reported in vivo in technical articles or general review articles on fetal DTI,[11] the GA-related microstructural changes that occur in the cerebellar peduncles in the second half of pregnancy remain largely unexplored.

Recent advances in hardware and software have improved fetal MR imaging substantially. The use of 3T magnets, which have been shown to be safe, results in improvement of the SNR and spatial resolution, which is advantageous to image the small structures of the fetal brain.[12,13] In addition, postprocessing algorithms that enable reconstruction of motion-corrected fetal DTI data are increasingly available and have been used by several groups to characterize the development of the supratentorial white matter tracts in vivo.[14-16] We hypothesize that fetal DTI performed at 3T and processed with a robust section-to-volume motion-correction and registration[14] algorithm will enable tractography of the cerebellar peduncles in fetuses in the second and third trimesters of pregnancy. We aimed to characterize fetal cerebellar tract microstructure and to investigate tract-specific developmental changes.

MATERIALS AND METHODS

Subjects

This was an institutional review board–approved and Health Insurance Portability and Accountability Act–compliant study. We performed a retrospective analysis of MR imaging data that were previously collected for a prospective study of normal fetal brain development in healthy pregnant volunteers and for a study on developmental abnormalities of the brain in fetuses with congenital heart disease.[15,17] Inclusion criteria for those studies were the following: 1) normal pregnancy on routine prenatal care, 1) maternal age 18–45 years, gestational age (GA) of at least 18 weeks, and 3) availability of fetal DTI data. Exclusion criteria were the following: 1) maternal contraindication to MR imaging, 2) known congenital infection in the fetus, 3) abnormalities in the fetus (known from prior clinical care, or detected during the research fetal MR imaging), 4) chromosomal abnormalities, and 5) multiple-gestation pregnancy. Only control subjects enrolled in the congenital heart disease study were eligible for our analysis. Pregnant volunteers were recruited through our institution's intranet and through pamphlets for participation in a research scan at various clinics. The informed consent process (which included a written informed consent form) was completed for each patient.

Image Acquisition

Fetal MRIs were acquired on a 3T MR imaging scanner (Skyra or Prisma; Siemens) using an 18-channel body-array coil, without maternal breath-holding or sedation. Structural brain images were acquired with multiple T2-weighted HASTE scans in the orthogonal plane with the following sequence parameters: TR = 1400–2000 ms, TE = 100–120 ms, 0.9- to 1.1-mm in-plane resolution, 2-mm thickness with no interslice space, acquisition matrix size = 256 × 204, 256 × 256, or 320 × 320 with a 2- or 4-section interleaved acquisition. Diffusion data were acquired with 2–8 scans in orthogonal planes with respect to the fetal head. The diffusion acquisitions included 1 or 2 $b = 0$ s/mm^2 images and 12 diffusion-sensitized images at $b = 500$ s/mm^2 with TR = 3000–4000 ms, TE = 60 ms, in-plane resolution = 2 mm, and section thickness = 2–4 mm.

Image Processing

Structural data were processed with an automated motion-robust fetal MR imaging volume-reconstruction algorithm that created a 3D isotropic intensity-normalized T2WI volume of the fetal brain from multiple HASTE scans.[18] Diffusion data were processed using a validated section-to-volume registration algorithm with a motion-trajectory-estimation framework, referred to as motion-tracked section-to-volume registration (MT-SVR).[14,19] Briefly, the MT-SVR does the following: 1) estimates the relative motion of the fetal brain for every diffusion-sensitized section using a state-space model and registering the section into a reference space, which is the reconstructed T2WI volume; 2) excludes data corrupted by intraslice motion; and 3) estimates the diffusion tensor at every voxel of the reference space using the motion-compensated data. For most subjects, 3–4 acquisitions in the coronal and axial planes were used to reconstruct DTI data. To perform tractography, we used the Diffusion Toolkit (Version 0.6.4.1; TrackVis; http://www.trackvis.org/dtk/). We used an angle threshold of 35° to stop tract propagation and an automatic fractional anisotropy (FA) mask threshold as determined by the Diffusion Toolkit.[20] A deterministic tractography with fiber assignment by continuous tracking approach with user-defined ROIs was used.

Image Segmentation and Analysis

We reviewed data from 82 fetuses. The DTI sequences were performed in all subjects, independent of whether the fetus was active or whether other artifacts, such as ghosting or susceptibility, degraded the acquisitions. Before image segmentation for our study, we performed a visual quality-assessment inspection of the MT-SVR-processed data by reconstructing whole-brain tracts. If there were gross distortions on whole-brain tracts, the reconstruction was excluded from the analysis and designated as "low-quality" reconstruction.

The cerebellar peduncles were segmented by placing ROIs in anatomically relevant landmarks using a combination of T2WI reconstructed images and scalar diffusion maps (FA, ADC, and trace diffusion). A trained research fellow (F.M.-R.) placed ROIs that were subsequently reviewed by a pediatric neuroradiologist with experience in fetal imaging (C.J.). The selection of ROIs was based on the anatomic landmarks of previously published studies on cerebellar peduncle tractography by Catani et al[21] and used by Re et al.[22] Specifically, for the superior cerebellar peduncles (SCPs), the ROIs were placed in the cerebellar hemispheres and in the midbrain. The ROI in the cerebellar hemispheres was placed in a single coronal section, just posterior to the fastigial point, covering the entire area of the cerebellum. The ROI for the

midbrain was placed in the coronal plane, anterior to the insertion of the SCP and the cerebral aqueduct, encompassing the upper half of the midbrain. For the MCP, the ROIs were placed in the cerebellar hemispheres (same as above) and the pons. The ROI for the pons was placed in a single coronal section through the midpons, covering its entire SI dimension from the pontomesencephalic sulcus to the pontomedullary sulcus. For the inferior cerebellar peduncle (ICP), ROIs were placed in the cerebellar hemispheres and the medulla. The ROI for the medulla was placed in a single axial section at the level of the outlet of the fourth ventricle. All ROIs were drawn using TrackVis (Trackvis 0.6.1) (Online Figure).

To evaluate the outcome of the tractography, a pediatric neuroradiologist visually inspected the tracts. If tracts conforming to the expected course of the SCP, middle cerebellar peduncle (MCP), or IPC were demonstrated, the reconstruction was considered successful. For tracts that were successfully demonstrated, we described the appearance as either symmetric or asymmetric between the right and left sides; a perceived difference of >25% in length or the number of tracts between sides was considered asymmetric. Given the exploratory nature of this study, we did not perform quantitative analysis of lateral asymmetry because it could relate to technical parametera rather than biologic differences. For each peduncle, we recorded the tract volume, ADC, and FA. Using the temporal motion-tracking feature of the MT-SVR algorithm, we also recorded absolute motion data (millimeters) during the diffusion acquisitions.[14] We performed a subanalysis of the individual components of the MCP that have been described in prior postnatal tractography studies.[22] The subcomponents include those associated with cognitive (cognitive pathway of the MCP [MCP_{cog}]) and motor and sensory (motor pathway of the MCP [MCP_{mot}]) functions. The MCP_{cog} was defined by the inferior and lateral tracts that extend from the rostral pons to the cerebellar hemispheres. The MCP_{mot} was defined as the superior and medial tracts that extend from the caudal pons to the cerebellar hemispheres.[22,23]

Statistical Analysis

Descriptive statistics summarized the demographic information and other categoric variables. The association between "low-quality data" and fetal position (breech or cephalic) was evaluated with a Fisher exact test. Similarly, differences in the frequency of rightward and leftward asymmetries as determined by qualitative inspection were evaluated using a Fisher exact test. Success in anatomic tract delineation, after excluding low-quality data, and its association with GA and motion were evaluated using Wilcoxon rank sum tests. A multiple linear regression analysis was used to evaluate tract-specific changes. We estimated the rate of change per week by evaluating GA as a predictor of volume, FA, and ADC for each anatomic tract (SCP, MCP, and ICP). Then, we performed an ANCOVA to compare the rate of change between tracts. STATA/SE, Version 15.1 (StataCorp) software was used to perform all analyses.

RESULTS

Sample Characteristics

Of 82 fetuses evaluated, 76 were in a cephalic position and 6 were in a breech position. A total of 24 fetuses could not be analyzed due to low-quality reconstruction/failure (see Online Table 1 for a list of failed cases and related artifacts). There was no association between tractography DTI reconstruction failure and fetal position ($P = .570$). Of the 58 subjects in which tractography of DTI reconstruction was of acceptable quality, 38 were male, 19 were female, with the sex of 1 fetus unknown. The median GA was 30 weeks 4 days (interquartile range, 7 weeks). The youngest subject was 21 weeks 2 days, and the oldest subject was 37 weeks.

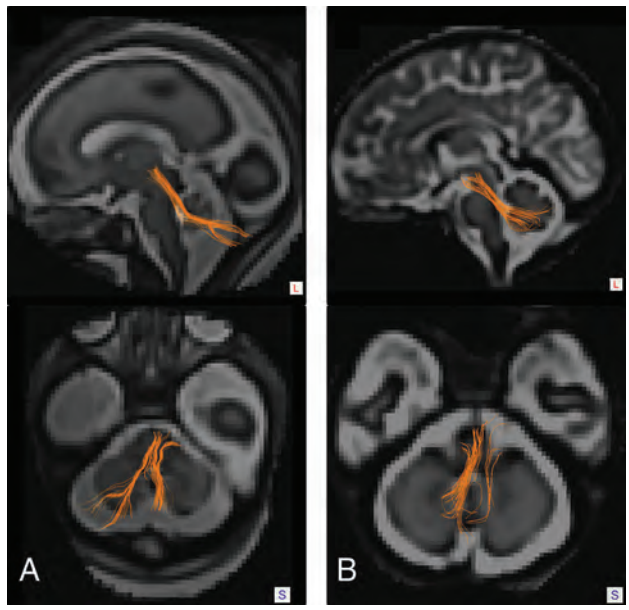

FIG 1. Tractography of the cerebellar peduncles in fetuses of varying gestational ages. Sagittal and axial tractography images overlaid on super-resolution T2 reconstructions show successful and symmetric delineation of the SCP in a 26-week 5-day-old male fetus (*A*). Sagittal and axial tractography images in a 36-week 2-day-old male fetus show successful tractography with asymmetry in the SCP reconstructions (*B*).

Anatomic Analysis of Tracts

We identified the SCP (Fig 1) in 39 of 58 subjects (69%), of which 15 had symmetric tract representation. Of the 24 subjects with asymmetric SCPs, 13 (54.2%) had a rightward asymmetry and 11 (45.8%) had a leftward asymmetry ($P = .683$). There was no significant difference in GA ($P = .4420$) or absolute motion ($P = .567$) between subjects with successful SCP tractography and those without successful delineation of the tract. Similarly, there were no significant differences in the GA ($P = .520$) or absolute motion ($P = .601$) between subjects with symmetric and asymmetric tract representation. A summary of GA and absolute motion metrics is available in Online Table 2.

The MCP was identified in all 58 subjects, and the reconstruction was symmetric in all (Fig 2). Distinct MCP_{cog} and MCP_{mot} were identified in 13 subjects (22%) (Fig 3). In subjects without a clear distinction of subcomponents, the MCP coursed inferiorly and laterally, extending from the rostral pons to the cerebellar hemispheres. There was no significant difference in GA ($P = .520$) or absolute motion ($P = .457$) between subjects with visualization of the 2 subcomponents versus those in which the subcomponents were not clearly distinct.

The ICP was not identified in any of the subjects analyzed.

Age-Related Changes

There was a significant increase in tract volume with GA for the SCP (0.020 mL/week) and MCP (0.159 mL/week) (all, $P < .05$) (Fig 4*A*). There was a significant difference ($P < .001$) between linear regression models for the SCP and the MCP, with the MCP having, on average, greater volume than the SCP after controlling for GA. FA increased with GA for both the SCP (0.00685/week) and the MCP (0.00815/week) (all, $P < .001$). The FA was significantly higher ($P = .002$) for the MCP linear regression model compared SCP after controlling for GA (Fig 4*B*). The ADC decreased with the GA for the SCP (−0.0000259 mm^2/s/week) and for the MCP (−0.0000253 mm^2/s/week) (all, $P < .001$). The ADC was significantly lower ($P < .001$) in the SCP linear regression model relative to the MCP after controlling for GA (Fig 4*C*).

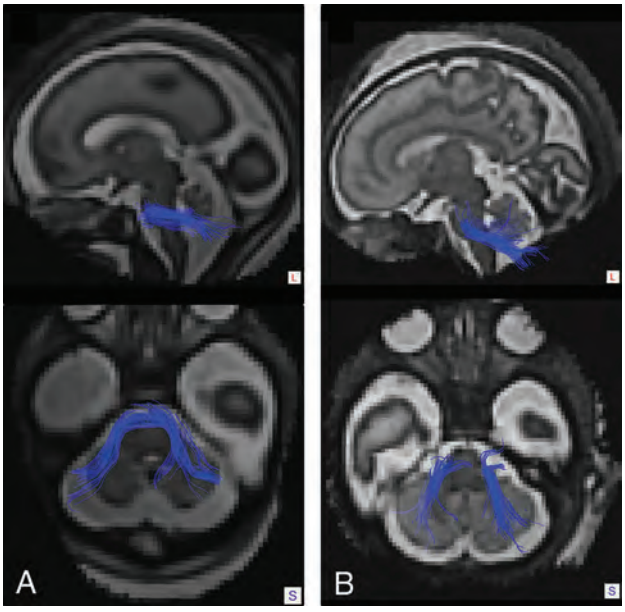

FIG 2. Tractography of the MVPs in fetuses of varying gestational ages. Sagittal and axial tractography images overlaid on super-resolution T2 reconstructions show successful and symmetric delineation of the MCP in a 26-week 5-dayold male fetus (*A*) and in a 33-week 6-day-old male fetus (*B*). Note symmetric representation of both tracts in the reconstructions.

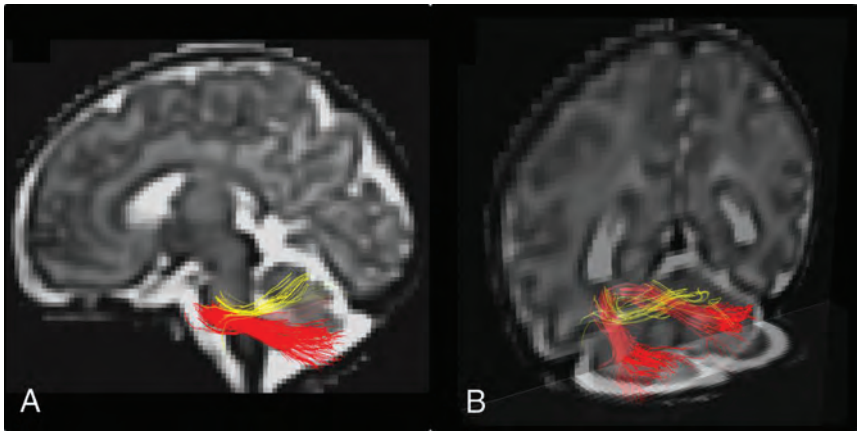

FIG 3. Tractography of the subcomponents of the MCP in a 36-week 2-day old male fetus. Sagittal (*A*) and posterior coronal oblique (*B*) tractography images overlaid on super-resolution T2 reconstructions show a clear distinction between the MCP_{cog} (red) and the MCP_{mot} (yellow). The MCP_{cog} is larger and extends from the rostral pons to the lateral and inferior cerebellar hemispheres describing an oblique course. The MCP_{mot} arises more caudally in the pons and extends toward the superior cerebellum, describing a more horizontal course.

DISCUSSION

The motion artifacts of fetal MR imaging and the small size of the cerebellum have, until now, precluded the evaluation of fetal cerebellar microstructure with DTI. Using a recently introduced MT-SVR algorithm, we successfully performed DTI-based tractography of the SCP and MCP in 58 healthy second- and third-trimester fetuses and explored tract-specific developmental changes. By analyzing exclusively fetuses from normal pregnancies (with further confirmation on structural images at the time of the research scan), we minimized the risk of inadvertently introducing a bias into our analysis, which can occur when analyzing data from subjects referred for evaluation of suspected abnormalities. Our tractography analyses confirm a prenatal onset for differences in ADC, FA, and volume between the SCP and MCP and indicate that these differences arise as early as the second trimester. The MT-SVR reconstructions also enabled identification of distinct white matter bundles of the MCP in some subjects. The possibility of investigating tract-specific macro- and microstructural changes in the fetal cerebellar peduncles could improve our understanding of early functional specialization of the cerebellum, its selective vulnerability in the second half of pregnancy, and the complex neurologic sequelae associated with early cerebellar injury and developmental abnormalities.[2-4,24,25]

Prior studies using ex vivo high-angular-resolution diffusion imaging of fixed specimens showed the feasibility of performing tractography of the SCP, MCP, and ICP as early as the 17th week of postconceptional age.[9,10] The small size of the peduncles, the intricate posterior fossa anatomy, and artifacts related to fetal motion probably hindered these analyses on prior fetal tractography studies.[26] Dovjak et al[27] had illustrated the cerebellar peduncles using DTI and tractography in a few individual fetuses, but a systematic analysis of developmental changes in these tracts has not been performed. The MT-SVR algorithm mitigates the motion artifacts by correcting the relative position of every diffusion section acquired, removing data affected by intraslice motion, and reconstructing the DTI with high spatial resolution, thereby addressing some of the major challenges mentioned above. The failure to identify the ICP likely reflects the small size and complexity of this tract, rather than limitations of the postprocessing algorithm, because prior reports on postnatal cerebellar tractography were unable to identify the ICP in infants younger than 2 months of age.[22]

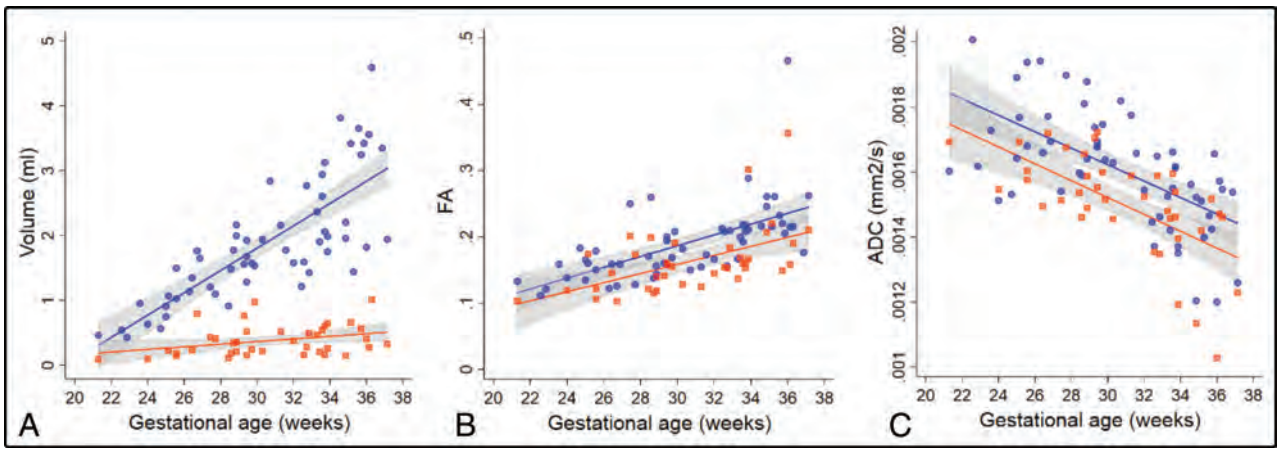

FIG 4. Changes in volume (*A*), FA (*B*), and ADC (*C*) for gestational age. Linear fit models are shown for the MCP (blue) and the SCP (orange), with their respective 95% confidence intervals (gray). Individual tract values for MCP (*circles*) and SCP (squares) are displayed.

The SCP followed its expected oblique course from the cerebellar hemispheres to the midbrain. In slightly more than half of the subjects, the tract appeared asymmetric, which we attribute to premature termination of the tractography driven by technical limitations. Artifacts in the fetal MR imaging, such as ghosting and low SNR from dielectric effects, are not homogeneously distributed across the image and are not mitigated by the MT-SVR algorithm, a feature that could result in some of the observed asymmetries. Considerations of spatial resolution and residual motion appear to be unrelated to these observations or play only a minor role because we did not find differences in GA or motion between subjects with symmetric and asymmetric reconstructions.

The anatomic details of the MCP tractography also correlated well with postnatal imaging and known neuroanatomy.[22,28] The MCP was seen in all subjects and always showed a symmetric reconstruction. The robustness of the reconstruction of this tract is at least, in part, the result of its larger size. The robust reconstruction of the MCP permitted identification of the MCP_{cog} and MCP_{mot} in approximately one-quarter of the fetuses. These distinct white matter bundles have been described in prior tractography studies postnatally and are thought to represent the cerebral and spinal components of the MCP (brachium pontis).[23]

We found significant age-related changes in ADC, FA, and volume in the SCP and MCP, which represent microstructural maturation and somatic growth. The rate of growth of the MCP outpaced that of the SCP; this trend is known to exist in early infancy, but our results confirm the prenatal onset of this divergence and suggest that it arises as early as the second trimester.[22] Re et al[22] reported that the MCP_{cog} is the largest component of the MCP and that it grows faster than the MCP_{mot}, though we did not perform volumetric analysis of these tracts due to the small sample size; subjective review of the tract morphology coincides with this description, with the MCP_{cog} appearing larger than the MCP_{mot} (Fig 3). Furthermore, in cases in which the individual tracts were not distinctly identified, the dominant configuration of the MCP appeared to follow that of the MCP_{cog} fibers.

For both tracts, the ADC decreased with age and the FA increased with age, a finding that is frequently observed with progressing GA and postnatal age. Although there are significant differences in the absolute ADC and FA values between the 2 tracts, both exhibited fairly similar rates of change. Diffusion changes in the fetal white matter are the result of a complex series of cellular and compositional changes and are not solely explained by myelination. Back et al[29] and Zanin et al[30] characterized the series of events that occur with fetal white matter maturation using histology and imaging, respectively, including axonal organization, myelination gliosis, and ultimately myelin deposition. Some of these processes, such as myelination gliosis, are hypothesized to have a larger effect on ADC than on FA, whereas others, such as myelin deposition and axonal reorganization, are believed to influence both.[29,30]

A good example of the potential utility of tractography to enhance diagnosis is posterior fossa malformations such as Joubert syndrome.[31] While the morphologic findings of Joubert syndrome are readily apparent on postnatal imaging (small cerebellar vermis, thickened SCP with a horizontal configuration [molar tooth]), some of these may be difficult to identify in young fetuses, motion degraded scans, or oblique acquisitions. The lack of decussation of the SCP, a characteristic feature of Joubert syndrome, results in a unique parallel configuration on postnatal tractography that could help the radiologist identify the disorder with greater certainty in fetal MR imaging.[32,33] Tractography of the cerebellar peduncles and other posterior fossa tracts could also help in the identification of a variety of axonal guidance disorders (eg, tubulinopathies, pontine tegmental cap dysplasia), which are known to harbor aberrations in white matter connections.[34,35] Tractography could also improve our understanding of the emerging abnormalities in the fetal cerebellum in disorders such as congenital heart disease and intrauterine growth restriction, which are known to impact cerebellar development.[6,36] Even though the existing literature focuses on volumetric analysis of these structures, the distinct physiology of SCP and MCP could provide insights into the specific networks that have been affected, such is the case of long-term follow-up of white matter injury of prematurity, in which

abnormalities in the SCP correlate with motor outcomes and abnormalities in the MCP correlate with a lower intelligence quotient at 7 years of age.[37]

The current study has several limitations. First, we performed a qualitative analysis of only lateral asymmetry of the tracts analyzed. Given that there are still some limitations to the technique, including premature termination of fiber tracking, the complex trajectories of these tracts (decussate in the midline) and the inability to reliably evaluate crossing fibers with the diffusion tensor model, we consider that a potential quantitative analysis of lateral asymmetries was prone to type I and II errors, particularly given the absence of any difference on the qualitative analysis. Second, although we can infer some of the biologic mechanisms that underlie the change in diffusivity based on prior studies of histopathology, we do not have direct histologic correlation of these findings. Third, although the technique appears promising in studying normal cerebellar development and injury prenatally, additional studies testing specific clinical hypothesis are needed. Our diffusion MR imaging protocol involved repeat acquisitions with 12 gradient directions. In the presence of fetal motion that perturbed gradient directions, this scheme resembled a high-angular-resolution diffusion imaging protocol with jittered q-space samples on the sphere (with 1 b-value). Nonetheless, the relatively low spatial resolution of the fetal diffusion scans (compared with the small size of the fetal cerebellar structures) and residual motion artifacts reduced our ability to visualize and assess decussation of the SCP on color FA or tensor images in this study.

CONCLUSIONS

Fetal DTI processed with a robust MT-SVR algorithm enabled deterministic tractography of the SCP and MCP in vivo. The reconstructions also permitted detailed characterization of tract-specific developmental changes in volume, ADC, and FA that set the trends for growth and maturation of these pathways in early postnatal life.

Disclosures: Fedel Machado-Rivas—*RELATED*: *Grant*: Research reported in this study was supported, in part, by the National Institute of Biomedical Imaging and Bioengineering and the National Institute of Neurological Disorders and Stroke of the National Institutes of Health Award Nos. R01EB018988, R01NS106030, and R01EB013248; a Technological Innovations in Neuroscience Award from the McKnight Foundation; a Schlaeger Fellowship for Neuroscience Research; and the Fetal Health Foundation. The content is solely the responsibility of the authors and does not necessarily represent the official views of the Fetal Health Foundation or the McKnight Foundation.* Bahram Marami—*RELATED*: *Grant*: Research reported in this study was supported, in part, by the National Institute of Biomedical Imaging and Bioengineering and the National Institute of Neurological Disorders and Stroke of the National Institutes of Health under Award Nos. R01EB018988, R01NS106030, and R01EB013248; a Technological Innovations in Neuroscience Award from the McKnight Foundation; a Schlaeger Fellowship for Neuroscience Research; and the Fetal Health Foundation. The content is solely the responsibility of the authors and does not necessarily represent the official views of the National Institutes of Health, Fetal Health Foundation, or the McKnight Foundation.* Caitlin Rollins—*RELATED*: *Grant*: National Institutes of Health/National Institute of Neurological Disorders and Stroke*; *UNRELATED*: *Expert Testimony*: McCann Law, *Comments*: expert opinion writing; *Grants/Grants Pending*: National Institutes of Health, Children's Heart Foundation. Cynthia Ortinau—*RELATED*: *Grant*: National Institutes of Health, *Comments*: National Institutes of Health/National Heart, Lung, and Blood Institute award No. K23HL141602.* Simon Warfield—*RELATED*: *Grant*: National Institutes of Health.* Ali Gholipour—*RELATED*: *Grant*: National Institutes of Health, *Comments*: The imaging and image processing in this article was partly supported by grants from the National Institutes of Health*; *UNRELATED*: *Employment*: Boston Children's Hospital and Worcester Polytechnic Institute, *Comments*: paid through employment as research and teaching faculty; *Grants/Grants Pending*: National Institutes of Health.* *Money paid to the institution.

REFERENCES

1. Volpe JJ. **Cerebellum of the premature infant: rapidly developing, vulnerable, clinically important.** *J Child Neurol* 2009;24:1085–104 CrossRef Medline
2. Tarui T, Limperopoulos C, Sullivan NR, et al. **Long-term developmental outcome of children with a fetal diagnosis of isolated inferior vermian hypoplasia.** *Arch Dis Child Fetal Neonatal Ed* 2014;99: F54–58 CrossRef Medline
3. Limperopoulos C, Bassan H, Gauvreau K, et al. **Does cerebellar injury in premature infants contribute to the high prevalence of long-term cognitive, learning, and behavioral disability in survivors?** *Pediatrics* 2007;120:584–93 CrossRef Medline
4. Matthews LG, Inder TE, Pascoe L, et al. **Longitudinal preterm cerebellar volume: perinatal and neurodevelopmental outcome associations.** *Cerebellum* 2018;17:610–27 CrossRef Medline
5. Shah DK, Anderson PJ, Carlin JB, et al. **Reduction in cerebellar volumes in preterm infants: relationship to white matter injury and neurodevelopment at two years of age.** *Pediatr Res* 2006;60:97–102 CrossRef Medline
6. Olshaker H, Ber R, Hoffman D, et al. **Volumetric brain MRI study in fetuses with congenital heart disease.** *AJNR Am J Neuroradiol* 2018;39:1164–69 CrossRef Medline
7. Bouyssi-Kobar M, Du Plessis AJ, McCarter R, et al. **Third trimester brain growth in preterm infants compared with in utero healthy fetuses.** *Pediatrics* 2016;138:e20161640 CrossRef Medline
8. Hooker JD, Khan MA, Farkas AB, et al. **Third-trimester in utero fetal brain diffusion tensor imaging fiber tractography: a prospective longitudinal characterization of normal white matter tract development.** *Pediatr Radiol* 2020;50:973–83 CrossRef Medline
9. Takahashi E, Song JW, Folkerth RD, et al. **Detection of postmortem human cerebellar cortex and white matter pathways using high angular resolution diffusion tractography: a feasibility study.** *Neuroimage* 2013;68:105–11 CrossRef Medline
10. Takahashi E, Hayashi E, Schmahmann JD, et al. **Development of cerebellar connectivity in human fetal brains revealed by high angular resolution diffusion tractography.** *Neuroimage* 2014;96:326–33 CrossRef Medline
11. Kasprian G, Del Río M, Prayer D. **Fetal diffusion imaging: pearls and solutions.** *Top Magn Reson Imaging* 2010;21:387–94 CrossRef Medline
12. Chartier AL, Bouvier MJ, McPherson DR, et al. **The safety of maternal and fetal MRI at 3T.** *AJR Am Roentgenol* 2019;213:1170–73 CrossRef Medline
13. Jaimes C, Delgado J, Cunnane MB, et al. **Does 3-T fetal MRI induce adverse acoustic effects in the neonate? A preliminary study comparing postnatal auditory test performance of fetuses scanned at 1.5 and 3 T.** *Pediatr Radiol* 2019;49:37–45 CrossRef Medline
14. Marami B, Mohseni Salehi SS, Afacan O, et al. **Temporal slice registration and robust diffusion-tensor reconstruction for improved fetal brain structural connectivity analysis.** *Neuroimage* 2017;156:475–88 CrossRef Medline
15. Khan S, Vasung L, Marami B, et al. **Fetal brain growth portrayed by a spatiotemporal diffusion tensor MRI atlas computed from in utero images.** *Neuroimage* 2019;185:593–608 CrossRef Medline
16. Jaimes C, Machado-Rivas F, Afacan O, et al. **In vivo characterization of emerging white matter microstructure in the fetal brain in the third trimester.** *Hum Brain Mapp* 2020;41:3177–85 CrossRef Medline
17. Jaimes C, Rofeberg V, Stopp C, et al. **Association of isolated congenital heart disease with fetal brain maturation.** *AJNR Am J Neuroradiol* 2020;41:1525–31 CrossRef Medline
18. Kainz B, Steinberger M, Wein W, et al. **Fast volume reconstruction from motion corrupted stacks of 2D slices.** *IEEE Trans Med Imaging* 2015;34:1901–13 CrossRef Medline
19. Marami B, Scherrer B, Afacan O, et al. **Motion-robust diffusion-weighted brain MRI reconstruction through slice-level registration-based motion tracking.** *IEEE Trans Med Imaging* 2016;35:2258–69 CrossRef Medline
20. Wang R, Benner T, Sorensen AG, et al. **Diffusion Toolkit: A Software Package for Diffusion Imaging Data Processing and Tractography.**

http://trackvis.org/faq/2007_ISMRM_diffusion_toolkit.pdf. Accessed ???????
21. Catani M, Thiebaut de Schotten M. **A diffusion tensor imaging tractography atlas for virtual in vivo dissections.** *Cortex* 2008;44:1105–32 CrossRef Medline
22. Re TJ, Levman J, Lim AR, et al. **High-angular resolution diffusion imaging tractography of cerebellar pathways from newborns to young adults.** *Brain Behav* 2017;7:e00589 CrossRef Medline
23. Voogd J, Ruigrok TJ. Cerebellum and precerebellar nuclei. In: ??????, *The Human Nervous System*. Elsevier; 2012:471–74
24. Semmel ES, Dotson VM, Burns TG, et al. **Posterior cerebellar volume and executive function in young adults with congenital heart disease.** *J Int Neuropsychol Soc* 2018;24:939–48 CrossRef Medline
25. Srivastava S, Prohl AK, Scherrer B, et al; TACERN Study Group. **Cerebellar volume as an imaging marker of development in infants with tuberous sclerosis complex.** *Neurology* 2018;90:e1493–50 CrossRef Medline
26. Kasprian G, Brugger PC, Schöpf V, et al. **Assessing prenatal white matter connectivity in commissural agenesis.** *Brain* 2013;136:168–79 CrossRef Medline
27. Dovjak GO, Brugger PC, Gruber GM, et al. **OC03.02: 3D fetal MRI visualisation of cerebellar white matter tracts.** *Ultrasound Obstet Gynecol* 2019;54:6–6 CrossRef
28. Bruckert L, Shpanskaya K, McKenna ES, et al. **Age-dependent white matter characteristics of the cerebellar peduncles from infancy through adolescence.** *Cerebellum* 2019;18:372–87 CrossRef Medline
29. Back SA, Luo NL, Borenstein NS, et al. **Arrested oligodendrocyte lineage progression during human cerebral white matter development: dissociation between the timing of progenitor differentiation and myelinogenesis.** *J Neuropathol Exp Neurol* 2002;61:197–211 CrossRef Medline
30. Zanin E, Ranjeva JP, Confort-Gouny S, et al. **White matter maturation of normal human fetal brain: an in vivo diffusion tensor tractography study.** *Brain Behav* 2011;1:95–108 CrossRef Medline
31. Poretti A, Boltshauser E, Loenneker T, et al. **Diffusion tensor imaging in Joubert syndrome.** *AJNR Am J Neuroradiol* 2007;28:1929–33 CrossRef Medline
32. Hsu CC, Kwan GN, Bhuta S. **High-resolution diffusion tensor imaging and tractography in Joubert syndrome: beyond molar tooth sign.** *Pediatr Neurol* 2015;53:47–52 CrossRef Medline
33. Widjaja E, Blaser S, Raybaud C. **Diffusion tensor imaging of midline posterior fossa malformations.** *Pediatr Radiol* 2006;36:510–57 CrossRef Medline
34. Jissendi-Tchofo P, Doherty D, McGillivray G, et al. **Pontine tegmental cap dysplasia: MR imaging and diffusion tensor imaging features of impaired axonal navigation.** *AJNR Am J Neuroradiol* 2009;30:113–19 CrossRef Medline
35. Grant PE, Im K, Ahtam B, et al. **Altered white matter organization in the TUBB3 E410K syndrome.** *Cereb Cortex* 2019;29:3561–76 CrossRef Medline
36. Polat A, Barlow S, Ber R, et al. **Volumetric MRI study of the intrauterine growth restriction fetal brain.** *Eur Radiol* 2017;27:2110–18 CrossRef Medline
37. Shany E, Inder TE, Goshen S, et al. **Diffusion tensor tractography of the cerebellar peduncles in prematurely born 7-year-old children.** *Cerebellum* 2017;16:314–25 CrossRef Medline

Cervical Spinal Cord Compression and Sleep-Disordered Breathing in Syndromic Craniosynostosis

B.K. den Ottelander, R. de Goederen, C.A. de Planque, S.J. Baart, M.L.C. van Veelen, L.J.A. Corel, K.F.M. Joosten, I.M.J. Mathijssen, and M.H.G. Dremmen

ABSTRACT

BACKGROUND AND PURPOSE: Cerebellar tonsillar herniation arises frequently in syndromic craniosynostosis and causes central and obstructive apneas in other diseases through spinal cord compression. The purposes of this study were the following: 1) to determine the prevalence of cervical spinal cord compression in syndromic craniosynostosis, and 2) to evaluate its connection with sleep-disordered breathing.

MATERIALS AND METHODS: This was a cross-sectional study including patients with syndromic craniosynostosis who underwent MR imaging and polysomnography. Measures encompassed the compression ratio at the level of the odontoid process and foramen magnum and the cervicomedullary angle. MR imaging studies of controls were included. Linear mixed models were developed to compare patients with syndromic craniosynostosis with controls and to evaluate the association between obstructive and central sleep apneas and MR imaging parameters.

RESULTS: One hundred twenty-two MR imaging scans and polysomnographies in 89 patients were paired; 131 MR imaging scans in controls were included. The mean age at polysomnography was 5.7 years (range, 0.02–18.9 years). The compression ratio at the level of the odontoid process was comparable with that in controls; the compression ratio at the level of the foramen magnum was significantly higher in patients with Crouzon syndrome (+27.1, $P < .001$). The cervicomedullary angle was significantly smaller in Apert, Crouzon, and Saethre-Chotzen syndromes (−4.4°, $P = .01$; −10.2°, $P < .001$; −5.2°, $P = .049$). The compression ratios at the level of the odontoid process and the foramen magnum, the cervicomedullary angle, and age were not associated with obstructive apneas ($P > .05$). Only age was associated with central apneas ($P = .02$).

CONCLUSIONS: The prevalence of cervical spinal cord compression in syndromic craniosynostosis is low and is not correlated to sleep disturbances. However, considering the high prevalence of obstructive sleep apnea in syndromic craniosynostosis and the low prevalence of compression and central sleep apnea in our study, we would, nevertheless, recommend a polysomnography in case of compression on MR imaging studies.

ABBREVIATIONS: cAHI = central apnea-hypopnea index; CMA = cervicomedullary angle; CR-1 = compression ratio at the level of the odontoid process; CR-2 = compression ratio at the level of the foramen magnum; oAHI = obstructive apnea-hypopnea index; OSA = obstructive sleep apnea; PSG = polysomnography

Syndromic craniosynostosis, such as Apert, Crouzon, Muenke, and Saethre-Chotzen syndromes, includes premature fusion of calvarial sutures in the presence of a genetic mutation and other anomalies.[1] Additional anomalies differ per syndrome and include but are not limited to midface hypoplasia, exorbitism, hearing loss, visual disturbances such as strabismus and amblyopia, and behavioral problems.[2-5] Patients with syndromic craniosynostosis are at risk of developing intracranial hypertension, which is associated with the presence of craniocerebral disproportion, venous hypertension, obstructive sleep apnea (OSA), and CSF outflow obstruction leading to hydrocephalus.[6-9]

Sleep disturbances are a well-known issue in patients with syndromic craniosynostosis. OSA is the most common sleep disorder

Received May 29, 2020; accepted after revision August 19.

From the Dutch Craniofacial Center (B.K.d.O., R.D.G., C.A.d.P., I.M.J.M.), Department of Plastic and Reconstructive Surgery and Hand Surgery; Department of Neurosurgery (M.L.C.v.V.); Pediatric Intensive Care Unit (L.J.A.C., K.F.M.J.); and Department of Radiology (M.H.G.D.), Erasmus MC Sophia Children's Hospital, University Medical Center Rotterdam, Rotterdam, the Netherlands; and Department of Biostatistics (S.J.B.), Erasmus MC, University Medical Center Rotterdam, Rotterdam, the Netherlands.

Please address correspondence to Bianca K. den Ottelander, MD, Dutch Craniofacial Center, Sophia Children's Hospital, Erasmus University Medical Center Wytemaweg 80, 2015 CN, Rotterdam, the Netherlands; e-mail: b.denottelander@erasmusmc.nl

Indicates article with supplemental on-line photo.

http://dx.doi.org/10.3174/ajnr.A6881

and arises mainly in Apert and Crouzon syndromes because of severe distortion of the midface anatomy. As a consequence, the prevalence of OSA varies among the syndromes and ranges between 10% and 70%.[8,10] Central sleep apnea is less common, arises in approximately 4% of the patients, and seems to improve with age.[11] OSA is an important risk factor for the development of intracranial hemorrhage in syndromic craniosynostosis and potentially leads to developmental issues and cardiovascular and metabolic morbidity in children in general.[12-16] Likewise, sleep-disordered breathing is associated with a lower quality of life.[15]

Cerebellar tonsillar herniation is frequently diagnosed in syndromic craniosynostosis and is known to cause central and obstructive apneas in other diseases through spinal cord compression.[17-22] Previous research showed that Chiari I malformations are not associated with central sleep apneas in syndromic craniosynostosis.[23] However, compression of the cervical spinal cord itself was not evaluated. Patients with syndromic craniosynostosis might be at risk for compression of the spinal cord itself at several levels. First, compression at the level of the foramen magnum may exist before patients develop a Chiari I malformation, because the cerebellar tonsils are present in the foramen magnum even when patients have a tonsillar descent of <5 mm.[24] Second, the configuration of the craniocervical junction is altered in syndromic craniosynostosis, and an altered position of the dens with respect to the foramen magnum may cause ventral brain stem compression.[25]

The purposes of this study were the following: 1) to determine the prevalence of cervical spinal cord compression in syndromic craniosynostosis, and 2) to evaluate its connection with sleep-disordered breathing. On the basis of previous research, we hypothesized that there is no association between cervical spinal cord compression and sleep-disordered breathing in syndromic craniosynostosis.

MATERIALS AND METHODS

We included all patients who were born between 1990 and 2017 with syndromic craniosynostosis (Apert, Crouzon, Muenke, and Saethre-Chotzen syndromes) and treated at the Dutch Craniofacial Center, Rotterdam, the Netherlands. Children born after 2005 were prospectively included. Patients who did not undergo polysomnography (PSG) and MR imaging examinations were excluded. Institutional review board approval was obtained (MEC-2005–273, 2016–312); informed consent was waived by the institutional review board because these examinations are a part of standard care. MR imaging examinations and sleep studies were paired on the basis of the time interval between the MR imaging scan and the sleep study: Within the first year of life, the maximum time interval was 3 months, whereas a 1-year time interval was the maximum in children 1 year of age or older. MR imaging examinations of healthy controls were included to compare spinal cord parameters in craniosynostosis and controls.

Neuroimaging

All MR imaging studies were acquired with a 1.5 T scanner (Signa Excite HD; GE Healthcare) and were a part of standard care. The imaging protocol included a 3D T2-weighted MR image with isometric voxels (imaging parameters: section thickness, 1.6 mm; no section gap; FOV, 20 cm; matrix size, 224 × 224; TE, 90 ms; and TR, 2500 ms); and a 3D echo-spoiled gradient-echo T1-weighted MR image (imaging parameters: section thickness, 2 mm; no section gap; FOV, 22.4 cm; matrix size, 224 × 224; TE, 3.1 ms; and TR, 9.9 ms). A 3D reformatting platform (AquariusNET; TeraRecon) was used to align scans in all planes and to perform the measurements. Three measurements were performed to evaluate the presence and extent of spinal cord compression:

1. The compression ratio at the level of the odontoid process (CR-1) was measured on the axial planes on the 3D T2-weighted sequence (Figure). CR-1 is associated with symptomatic myelopathy in conditions other than syndromic craniosynostosis when it is <0.40.[26] The formula used was the following:

$$\frac{\text{Anterior– Posterior Diameter of the Spinal Cord (mm)}}{\text{Latero– Lateral Diameter of the Spinal Cord (mm)}}.$$

   To establish consistency in all measurements, we aligned the axial plane perpendicular to the spinal cord in the sagittal plane.
2. The compression ratio at the level of the foramen magnum (CR-2) was calculated as follows:

$$\frac{\text{Area Spinal Cord (mm)}}{\text{Foramen Magnum Area (mm}^2\text{)} - \text{Area Cerebellar Tonsils (if present in mm}^2\text{)}} \times 100.$$

   See the Figure for an example. The CR-2 was measured on the 3D T1-weighted sequences. CR-2 was used as a derivative of the "crowdedness" at the level of the foramen magnum.
3. The cervicomedullary angle (CMA, in degrees) was measured at the midsagittal planes on the 3D T2-weighted sequence and was defined as the angle between the line parallel to the ventral surface of the medulla and the line parallel to the ventral surface of the upper cervical cord (Figure). The CMA can be used to quantify the amount of basilar invagination and has been correlated to clinical evidence of brain stem compression/myelopathy when the angle is <135°.[27,28]

Controls

To compare CR-1, CR-2, and the CMA in syndromic craniosynostosis versus the healthy population, we included controls in the study. The control group consisted of subjects who were scanned for clinical reasons (eg, cholesteatoma, Epileptic insult, trauma, headaches) but had no intracranial pathology on the MR image or during follow-up.

Interrater Reliability

All measurements were performed by the first author (B.K.d.O.); additional measurements by the third author (C.A.d.P.) were used to calculate the interrater reliability. Both observers had >1 year of experience in measuring skull base parameters in children with syndromic craniosynostosis and were supervised by M.H.G.D., who is an experienced pediatric neuroradiologist. To assess the interrater reliability, the intraclass correlation coefficient was calculated for the above-stated measurements.

Sleep Studies

All patients underwent routine clinical or ambulant sleep studies. Scoring of the PSGs was performed according to the 2012 update of the American Association of Sleep Medicine manual for the scoring of sleep and associated events.[29] For the evaluation of obstructive events, we calculated the obstructive apnea-hypopnea index (oAHI): the number of obstructive and mixed apneas and obstructive hypopneas with desaturation/arousal, divided by the total sleep time. The oAHI includes a measure to quantify OSA and is usually classified as mild (oAHI, ≥1–5), moderate (oAHI, ≥5–10) or severe (oAHI, ≥10). Central breathing difficulties were evaluated by calculation of the central apnea-hypopnea index (cAHI): the number of central and mixed apneas and hypopneas with desaturation, divided by the total sleep time. Findings of the cAHI are abnormal if they are >5.[29]

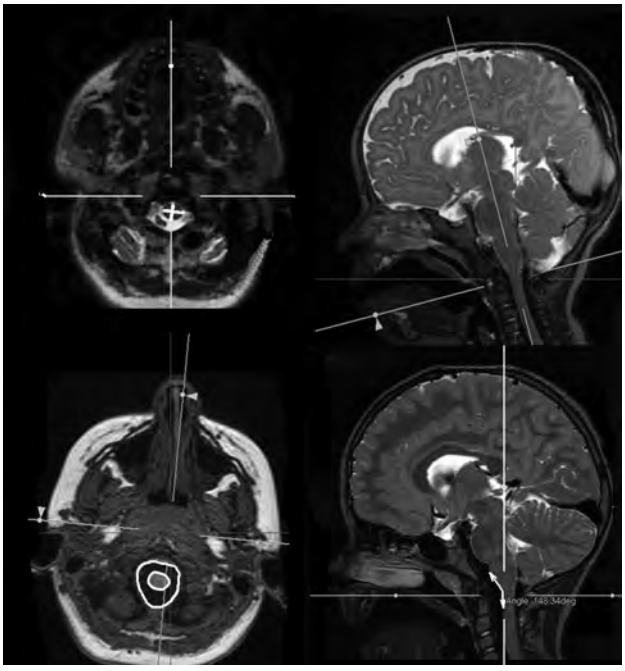

FIGURE. Axial and sagittal T2-weigthed MR imageing at the level of the odontoid process (*above*). *Left*: CR-1 measurement (anterior-posterior diameter/Latero-lateral diameter) *Right*: Perpendicular alignment for CR-1 measurement. Axial T1-weigthed MR image at the level of the foramen magnum and sagittal T2-weighted image in the midline (*below*). *Left*: CR-2 measurement (spinal cord area [yellow]/foramen magnum area × 100). *Right*: Cervicomedullary angle.

Table 1: Characteristics of patients with syndromic craniosynostosis and controls

	Syndromic Craniosynostosis (n = 122)	Controls (n = 131)
Syndrome (No. of cases)		
Apert	34	NA
Crouzon	65	NA
Muenke	12	NA
Saethre-Chotzen	11	NA
Mean age (yr)	5.70 (range, 0.24–18.92)	9.90 (range, 0.01–18.20)
Mean CR-1	0.63 (range, 0.32–1.03)	0.64 (range, 0.43–0.87)
Mean CR-2	0.41 (range, 0.12–1.00)	0.28 (range, 0.08–0.80)
Mean CMA	149.92 (range, 122.06–167.78)	157.07 (range, 136.04–174.21)

Note:—NA indicates not applicable.

Statistical Analysis

The analysis was performed in R statistical software (Version 3.6.1; package nlme, Version 3.1; package ggplot2, Version 3.2.1; http://www.r-project.org). Linear mixed models were developed to correct for repeated measures, age, sex, and syndrome (ie, Apert, Crouzon, Muenke. and Saethre-Chotzen syndromes). The necessity of interaction terms was tested through the omnibus method and subsequently was not entered in all models. Normality was assured by evaluation of the QQ-plots.

We developed 3 separate models comparing patients with syndromic craniosynostosis with controls. CR-1, CR-2, and CMA were the outcome variables in these models; age, sex and syndrome were entered as predictors.

In the fourth model, oAHI was the outcome variable. The CR-1, CR-2, CMA, and age were entered as the predictors. Only patients with craniosynostosis were included in this analysis. Because OSA in syndromic craniosynostosis is caused by a multilevel obstruction,[30] we corrected for upper airway obstruction. The presence of upper airway obstruction was evaluated by reviewing endoscopy results and the physical examination by the plastic surgeons and Ear, Nose and Throat doctors.

In the fifth and last model, the outcome variable was cAHI, whereas the CR-1, CR-2, CMA, and age were the predictors. Again, only the patients with craniosynostosis were included in this model.

RESULTS

One hundred ninety-five MR images and PSGs were identified. After we applied the maximum time interval, 122 MR images and sleep studies in 89 patients were paired, of whom 44 patients were included in earlier studies on sleep disturbances in syndromic craniosynostosis.[8,11,23] Additionally, 131 controls were included. See Table 1 for the patient and control characteristics and Table 2 for the comparison of the parameters in syndromic craniosynostosis versus controls. The Online Figure depicts the distribution of the spinal cord parameters for each syndrome.

Abnormal cervical spinal cord parameters were observed in 8 patients (ie, 9% of the patients). The CR-1 was abnormal in 1 patient who also had an abnormal CMA. The CMA was deviant in 8 patients and significantly differed from that in controls in Apert, Crouzon, and Saethre-Chotzen syndromes. The mean CR-2 was 0.41 (range, 0.12–1.00) and was significantly higher in patients with Crouzon syndrome compared with controls.

All measurements derived from the 122 paired MR images and sleep studies were entered in the analysis. The mean age at the PSG was 5.7 years (range, 0.02–18.9 years). The mean oAHI was 3.2 (range, 0.0–74.6); obstructive sleep apnea (an oAHI of >1) was diagnosed in 41 (34%) patients. The mean cAHI was 1.3 (range, 0.0–13.2); a cAHI of >5.0 was diagnosed in 5 patients. Two of them also had severe OSA, 2 of them

Table 2: β coefficients and *P* values of the comparisons between patients with syndromic craniosynostosis and controls

	CR-1	CR-2	CMA
Apert	–0.02, $P = .39$	1.9, $P = .64$	–4.4, $P = .01$[a]
Crouzon	0.02, $P = .24$	27.6, $P < .001$[a]	–10.2, $P < .001$[a]
Muenke	–0.01, $P = .77$	11.1, $P = .07$	–4.1, $P = .11$
Saethre-Chotzen	0.05, $P = .13$	0.6, $P = .92$	–5.2, $P = .049$[a]

[a] Statistically significant difference.

were younger than 1 year of age, and 1 was both younger than 1 year of age and had severe OSA.

Interrater Reliability

The intraclass correlation coefficient was 0.77 for CR-1 and 0.96 for CR-2 and the cervicomedullary angle.

Association between Cervical Spinal Cord Morphology and Sleep Studies

The CR-1, CR-2, CMA, and age were not associated with the oAHI ($P = .12$, $P = .18$, $P = .11$, and $P = .62$, respectively).

Age was inversely associated with cAHI ($P = .02$), whereas CR-1, CR-2, and the CMA were not associated with the cAHI ($P = .47$, $P = .75$, and $P = .44$ respectively).

The patient with a CR-1 of <0.40 did not have OSA or central sleep apnea. Seven of the patients with an abnormal CMA had Crouzon syndrome, and 1 had Apert syndrome: One of these patients had moderate OSA, 2 had mild OSA, and the other 5 patients did not have OSA. The cAHI was <5 in all of these patients.

DISCUSSION

This study shows that the prevalence of cervical spinal cord compression in syndromic craniosynostosis is low (9%). Moreover, cervical spinal cord compression parameters are correlated to sleep disturbances.

The spinal cord morphology at the level of the dens (CR-1) was comparable with that of controls, a finding indicating that the altered position of the dens with respect to the foramen magnum does not cause cervical spinal cord compression at this level. In contrast, crowding at the level of the foramen magnum as measured with the CR-2 was found in patients with Crouzon syndrome. The higher prevalence of tonsillar herniation in this group compared with the normative population and the other craniosynostosis syndromes explains this finding (den Ottelander et al, unpublished data).[31-33] The CMA was significantly smaller in Apert, Crouzon, and Saethre-Chotzen syndromes, explained by the skull base deformation that is known to exist in these syndromes.[34-36]

Age correlated significantly with the cAHI; this finding is to be expected because central apneas are physiologic in neonates and young infants and the finding is in line with previous research.[8,23,29] In contrast, none of the measurements were associated with the oAHI and cAHI, a finding for which there are several explanations. First, cervical spinal cord compression might be absent in patients with syndromic craniosynostosis because CR-1 was comparable with that in the normative population and was only abnormal in 1 patient. Moreover, CR-2 and CMA might be significantly different compared with controls, but to a limited severity, not causing symptomatic myelopathy. Previous research affirms this theory regarding the correlation between hindbrain herniation and the CR-2, because hindbrain herniation did not correlate with sleep-disordered breathing in that study.[23] Additionally, symptomatic myelopathy is described in patients with a CMA <135°,[30] which we found in only 8 patients in our study population, and these patients did not show abnormalities on PSGs. A second explanation for not finding an association between cervical spinal cord parameters and sleep study results might be that previous studies correlated the CR-1 and CMA to symptomatic myelopathy, not describing sleep-disordered breathing.[26,28] Consequently, it is possible that these parameters do correlate with symptomatic myelopathy, but not with sleep-disordered breathing.

The intraclass correlation coefficient was 0.77 for CR-1 and 0.96 for CR-2 and the cervicomedullary angle. The difference in interrater reliability can be explained by the extra step necessary to perform the CR-1 measurement because the images for this measurement were aligned perpendicular to the spinal cord in the sagittal plane.

An important limitation of the statistical analysis on the association between sleep disturbances and cervical spinal cord parameters includes the low prevalence of cervical spinal cord compression, which limits the power to reject these associations. However, only 2 of the 9 the patients who did show compression on MR images had moderate/severe OSA, and none had central sleep apnea; this finding strengthens the hypothesis that there is no association. Second, the prevalence of central sleep apnea was low; thus, a correlation would be even harder to find with the current data. However, in the few patients with central sleep apnea, its presence could be linked to age and OSA, also affirming the hypothesis that there is no correlation.

Our study results confirm the low prevalence of central sleep apnea in syndromic craniosynostosis and the absence of an association between cerebellar tonsillar herniation and sleep disturbances.[11,23] Additionally, we show that the prevalence of cervical spinal cord compression is low. In patients with syndromic craniosynostosis, polysomnographies are a part of the standard of care because of the high prevalence of obstructive sleep apnea. Considering this and the low prevalence of cervical spinal cord compression and central sleep apneas in our study cohort, we would still recommend performing an additional polysomnography in case of evidence of cervical spinal cord compression on MR imaging studies.

CONCLUSIONS

The prevalence of cervical spinal cord compression in syndromic craniosynostosis is low, and cervical spinal cord compression parameters are not correlated with sleep disturbances. However, considering the high prevalence of obstructive sleep apnea in syndromic craniosynostosis and the low prevalence of deviant cervical spinal cord parameters and central sleep apnea in our cohort, we would still recommend performing an additional

polysomnography in case of signs of cervical spinal cord compression on MR imaging studies.

REFERENCES

1. Johnson D, Wilkie AOM. **Craniosynostosis.** *Eur J Hum Genet* 2011;19:369–76 CrossRef Medline
2. Fearon JA. **Evidence-based medicine: craniosynostosis.** *Plast Reconstr Surg* 2014;133:1261–75 CrossRef Medline
3. Reardon W. **Craniosynostosis: diagnosis, evaluation and management.** *J Med Genet* 2000;37:727–27 CrossRef Medline
4. Maliepaard M, Mathijssen IM, Oosterlaan J, et al. **Intellectual, behavioral, and emotional functioning in children with syndromic craniosynostosis.** *Pediatrics* 2014;133:e1608–15 CrossRef Medline
5. Agochukwu NB, Solomon BD, Muenke M. **Hearing loss in syndromic craniosynostoses: introduction and consideration of mechanisms.** *Am J Audiol* 2014;23:135–41 CrossRef Medline
6. Spruijt B, Joosten KF, Driessen C, et al. **Algorithm for the management of intracranial hypertension in children with syndromic craniosynostosis.** *Plast Reconstr Surg* 2015;136:331–40 CrossRef Medline
7. Collmann H, Sorensen N, Krauss J. **Hydrocephalus in craniosynostosis: a review.** *Childs Nerv Syst* 2005;21:902–12 CrossRef Medline
8. Driessen C, Joosten KF, Bannink N, et al. **How does obstructive sleep apnoea evolve in syndromic craniosynostosis? A prospective cohort study.** *Arch Dis Child* 2013;98:538–43 CrossRef Medline
9. Hayward R. **Venous hypertension and craniosynostosis.** *Childs Nerv Syst* 2005;21:880–88 CrossRef Medline
10. den Ottelander BK, de Goederen R, van Veelen MC, et al. **Muenke syndrome: long-term outcome of a syndrome-specific treatment protocol.** *J Neurosurg Pediatr* 2019 Jul 19. [Epub ahead of print] CrossRef Medline
11. Driessen C, Mathijssen IM, De Groot MR, et al. **Does central sleep apnea occur in children with syndromic craniosynostosis?** *Respir Physiol Neurobiol* 2012;181:321–25 CrossRef Medline
12. Freezer NJ, Bucens IK, Robertson CF. **Obstructive sleep apnoea presenting as failure to thrive in infancy.** *J Paediatr Child Health* 1995;31:172–75 CrossRef Medline
13. O'Brien LM, Mervis CB, Holbrook CR, et al. **Neurobehavioral correlates of sleep-disordered breathing in children.** *J Sleep Res* 2004;13:165–72 CrossRef Medline
14. Marcus CL, Greene MG, Carroll JL. **Blood pressure in children with obstructive sleep apnea.** *Am J Respir Crit Care Med* 1998;157:1098–1103 CrossRef Medline
15. Crabtree VM, Varni JW, Gozal D. **Health-related quality of life and depressive symptoms in children with suspected sleep-disordered breathing.** *Sleep* 2004;27:1131–38 CrossRef Medline
16. Franco RA Jr, Rosenfeld RM, Rao M. **First place–resident clinical science award 1999: quality of life for children with obstructive sleep apnea.** *Otolaryngol Head Neck Surg* 2000;123:9–16 CrossRef Medline
17. Petersen MC, Wolraich M, Sherbondy A, et al. **Abnormalities in control of ventilation in newborn infants with myelomeningocele.** *J Pediatr* 1995;126:1011–15 CrossRef Medline
18. Amin R, Sayal P, Sayal A, et al. **The association between sleep-disordered breathing and magnetic resonance imaging findings in a pediatric cohort with Chiari 1 malformation.** *Can Respir J* 2015;22:31–36 CrossRef Medline
19. Dhamija R, Wetjen NM, Slocumb NL, et al. **The role of nocturnal polysomnography in assessing children with Chiari type I malformation.** *Clin Neurol Neurosurg* 2013;115:1837–41 CrossRef Medline
20. Ferre Maso A, Poca MA, de la Calzada MD, et al. **Sleep disturbance: a forgotten syndrome in patients with Chiari I malformation.** *Neurologia* 2014;29:294–304 CrossRef Medline
21. Khatwa U, Ramgopal S, Mylavarapu A, et al. **MRI findings and sleep apnea in children with Chiari I malformation.** *Pediatr Neurol* 2013;48:299–307 CrossRef Medline
22. Leu RM. **Sleep-related breathing disorders and the Chiari 1 malformation.** *Chest* 2015;148:1346–52 CrossRef Medline
23. Driessen C, Joosten KF, Florisson JM, et al. **Sleep apnoea in syndromic craniosynostosis occurs independent of hindbrain herniation.** *Childs Nerv Syst* 2013;29:289–96 CrossRef Medline
24. Tubbs RS. **Definitions and Anatomic Considerations in Chiari I Malformation and Associated Syringomyelia.** *Neurosurg Clin N Am* 2015;26:487–93 CrossRef Medline
25. Ridder T, Anderson RC, Hankinson TC. **Ventral decompression in Chiari malformation, basilar invagination, and related disorders.** *Neurosurg Clin N Am* 2015;26:571–78 CrossRef Medline
26. Kadanka Z Jr, Adamova B, Kerkovsky M, et al. **Predictors of symptomatic myelopathy in degenerative cervical spinal cord compression.** *Brain Behav* 2017;7:e00797 CrossRef Medline
27. Wang S, Wang C, Passias PG, et al. **Interobserver and intraobserver reliability of the cervicomedullary angle in a normal adult population.** *Eur Spine J* 2009;18:1349–54 CrossRef Medline
28. Bundschuh C, Modic MT, Kearney F, et al. **Rheumatoid arthritis of the cervical spine: surface-coil MR imaging.** *AJR Am J Roentgenol* 1988;151:181–87 CrossRef Medline
29. Berry RB, Budhiraja R, Gottlieb DJ, et al; American Academy of Sleep Medicine. **Rules for scoring respiratory events in sleep: update of the 2007 AASM Manual for the Scoring of Sleep and Associated Events: deliberations of the Sleep Apnea Definitions Task Force of the American Academy of Sleep Medicine.** *J Clin Sleep Med* 2012;8:597–619 CrossRef Medline
30. Doerga PN, Spruijt B, Mathijssen IM, et al. **Upper airway endoscopy to optimize obstructive sleep apnea treatment in Apert and Crouzon syndromes.** *J Craniomaxillofac Surg* 2016;44:191–96 CrossRef Medline
31. Cinalli G, Spennato P, Sainte-Rose C, et al. **Chiari malformation in craniosynostosis.** *Childs Nerv Syst* 2005;21:889–901 CrossRef Medline
32. Smith BW, Strahle J, Bapuraj JR, et al. **Distribution of cerebellar tonsil position: implications for understanding Chiari malformation.** *J Neurosurg* 2013;119:812–19 CrossRef Medline
33. Rijken BF, Lequin MH, van der Lijn F, et al. **The role of the posterior fossa in developing Chiari I malformation in children with craniosynostosis syndromes.** *J Craniomaxillofac Surg* 2015;43:813–19 CrossRef Medline
34. McGrath J, Gerety PA, Derderian CA, et al. **Differential closure of the spheno-occipital synchondrosis in syndromic craniosynostosis.** *Plast Reconstr Surg* 2012;130:681e–89 CrossRef Medline
35. Paliga JT, Goldstein JA, Vossough A, et al. **Premature closure of the spheno-occipital synchondrosis in Pfeiffer syndrome: a link to midface hypoplasia.** *J Craniofac Surg* 2014;25:202–05 CrossRef Medline
36. Rijken BF, Lequin MH, Van Veelen ML, et al. **The formation of the foramen magnum and its role in developing ventriculomegaly and Chiari I malformation in children with craniosynostosis syndromes.** *J Craniomaxillofac Surg* 2015;43:1042–48 CrossRef Medline

National Trends in Lumbar Puncture from 2010 to 2018: A Shift Reversal from the Emergency Department to the Hospital Setting for Radiologists and Advanced Practice Providers

L.M. Trunz, A.V. Gandhi, A.D. Karambelkar, S.M. Lange, V.M. Rao, and A.E. Flanders

ABSTRACT

BACKGROUND AND PURPOSE: Prior research has shown substantial shifts in procedure shares between specialty groups providing lumbar punctures. Our aim was to analyze national trends in lumbar punctures among the Medicare population from 2010 to 2018.

MATERIALS AND METHODS: Medicare Part B Physician/Supplier Procedure Summary Master Files from 2010 to 2018 were analyzed for all Current Procedural Terminology, Version 4 codes related to lumbar punctures (62270 and 62272). Lumbar puncture procedure volume and utilization rates were assessed and stratified by place of service and specialty background of the providers.

RESULTS: From 2010 to 2018, the overall number of lumbar puncture procedures essentially has not changed (92,579 versus 92,533). Radiologists hold the largest and an increasing procedure share of diagnostic and overall lumbar punctures (overall share, 45.7% in 2010 [$n = 42,296$] versus 52.3% in 2018 [$n = 48,414$]). Advanced practice providers have increased their procedure share (3.7% in 2010 [$n = 3388$] versus 8.4% in 2018 [$n = 7785$], + 129.8% procedure volume). Emergency medicine physicians and neurologists have a decreasing procedure share (21.8% versus 15.3% and 12.5% versus 8.8%, respectively). The inpatient hospital setting remains the largest place of service for lumbar punctures, recording a 5.3% increase in procedure share. The emergency department lumbar puncture volume has declined, with a 7.4% decrease in the overall procedure share. Similarly, the hospital outpatient department procedure volume has increased (+4%), while the private office volume has decreased (–1.7%).

CONCLUSIONS: During the past decade, lumbar puncture procedures among the Medicare population have remained stable, with a shift in procedure volume from the emergency department and private offices to the hospital setting, which has mainly affected radiologists and advanced practice providers.

ABBREVIATIONS: APP = advanced practice provider; ED = emergency department; LP = lumbar puncture

During the past decades, lumbar punctures (LPs) have been progressively performed with image guidance, and associated with this trend were an increased responsibility and involvement of radiologists.[1] For image guidance, fluoroscopy and CT perform equally well with low effective radiation dosages.[2] Additionally, sonographic guidance can improve LP success rates, especially in a well-selected patient population.[3]

LPs are an essential part of the diagnostic work-up in various neurologic diseases and are divided into diagnostic and therapeutic. Primary indications for diagnostic LPs are suspected CNS infection and measurement of the CSF opening pressure; indications also include subarachnoid hemorrhage, CNS autoimmune disease, neoplastic meningeal disease, and dementia. Therapeutic LPs can be used to either lower the intracranial pressure, for example in the setting of cryptococcal meningitis or idiopathic intracranial hypertension; to administer medications intrathecally (eg, chemotherapy); or as a "shunt trial" in the context of normal pressure hydrocephalus.[4]

Compared with bedside/non-image-guided LPs, image guidance offers several advantages, and multiple factors may contribute to an increasing demand for service. Prior studies have demonstrated fewer traumatic LPs when using fluoroscopic guidance,[5] which improves diagnostic work-up and patient comfort. The increasing prevalence of obesity in the general population[6] resulted in further use of image guidance.[7] Other factors favoring the use of image guidance are in the postoperative setting with hardware and/or osseous fusion or with extensive degenerative changes or scoliosis present.[7] This shift led to radiologists becoming the dominant overall provider of LP procedures between

Received July 6, 2020; accepted after revision August 11.

From the Department of Radiology, Thomas Jefferson University, Philadelphia, Pennsylvania.

Paper previously presented at: Annual Meeting of the American Society of Neuroradiology, May 30 to June 4, 2020; Virtual.

Please address correspondence to Lukas M. Trunz, MD, Thomas Jefferson University, Department of Radiology, Main Building, 132 S 10th St, Suite 780-A, Philadelphia, PA; e-mail: lukas.trunz@jefferson.edu

http://dx.doi.org/10.3174/ajnr.A6870

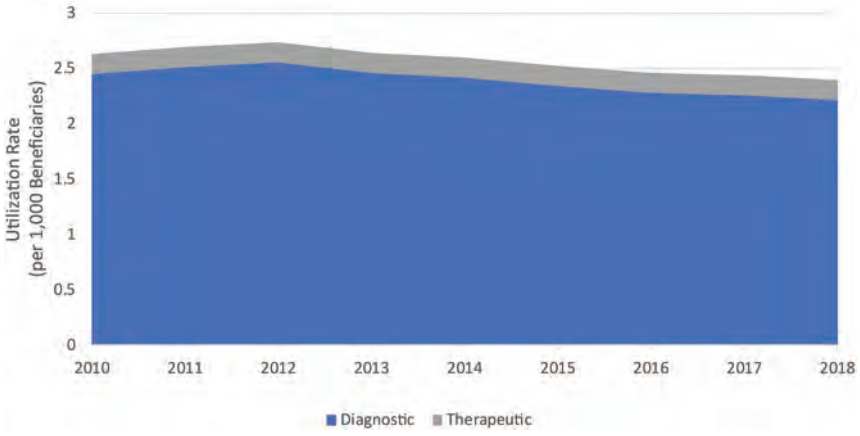

FIG 1. Lumbar puncture utilization rate (diagnostic and therapeutic LPs combined) per 1000 Medicare Fee-for-Service enrollees. After a peak in 2012, the procedure rate successively declined during the remaining decade, corresponding to a 9% decrease of the overall procedure rate from 2010 to 2018.

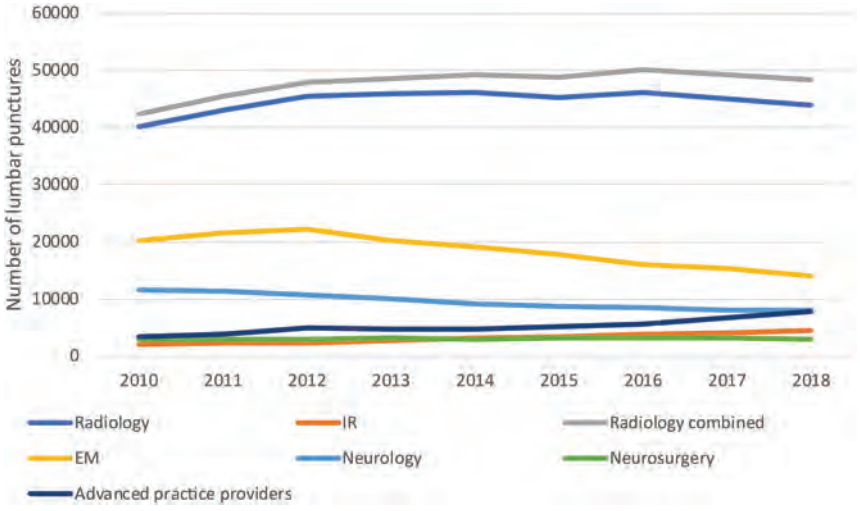

FIG 2. Overall lumbar puncture procedure shares in the United States from 2010 to 2018, by provider specialty. IR indicates interventional radiology; EM, emergency medicine.

1991 and 2011.[1] The purpose of this study was to determine whether radiologists have continued to be the dominant provider of LP procedures stratified by place of service.

MATERIALS AND METHODS

Data were obtained from the Centers for Medicare & Medicaid Services Physician/Supplier Procedure Summary Master Files from 2010 to 2018. These files contain summary tables for all beneficiaries of the nationwide Medicare Part B Fee-for-Service Compliance program (38.7 million in 2018). Data are available for each code in the *Current Procedural Terminology, Fourth Edition* (CTP-4) and include information such as procedure volume, provider specialty, location of services, and payments approved. Provider specialties were determined from the Physician Specialty Classification Codes used by Medicare. Locations at which examinations were performed were determined using Medicare Place-of-Service Codes.

For this study, we determined the number of lumbar punctures performed in hospital outpatient, inpatient, emergency department (ED), and office settings by analyzing the CPT-4 codes contained in the billing claims filed by physicians. We reviewed all CPT-4 codes that represented lumbar punctures (62270 and 62272). For each category, we determined the total number of procedure claims from 2010 to 2018. We also calculated the utilization rate per 1000 Medicare Fee-for-Service beneficiaries for each year. Data analysis was performed using Excel 2015 (Microsoft). These aggregated public use files contain no patient or physician identifiers and are, therefore, exempt from review by an institutional review board.

RESULTS

The overall number of LP procedures essentially has not changed between 2010 and 2018 (92,579 in 2010 and 92,533 in 2018). A minimal decrease in diagnostic LPs (86,347 versus 85,665) and a slight increase in therapeutic LPs (6232 versus 6868) were noted.

For diagnostic LPs, the procedure rate per 1000 Medicare Fee-for-Service enrollees increased from 2.45 in 2010 to a peak of 2.56 in 2012, then gradually declined to 2.21 in 2018 (−13% versus peak). For therapeutic LPs, the procedure rate per 1000 Medicare Fee-for-Service enrollees varied minimally during the decade, from 0.177 in 2010 to a peak of 0.187 in 2016, before it gradually declined back to 0.177 in 2018. For diagnostic and therapeutic LPs combined, the procedure rate per 1000 Medicare Fee-for-Service enrollees increased from 2.63 in 2010 to a peak of 2.73 in 2012, before it steadily declined to 2.39 in 2018. This change corresponds to a 9% decrease in the overall procedure rate during the past decade (Fig 1).

Figure 2 shows the LP share by provider specialty. Overall, radiologists performed 42,296 LP procedures in 2010 versus 48,414 in 2018, representing a 45.7% versus 52.3% procedure share, respectively. These numbers combine diagnostic and interventional radiologists. If evaluated separately, there is a striking increase in the number of cases performed by interventional radiologists: 2167 LPs in 2010 compared with 4459 LPs in 2018 (+105.8% procedure volume). This represents an increase in the overall procedure share from 5.1% to 9.2% within the radiology subgroup and from 2.4% to 4.8% in the overall procedure share. Likewise, advanced practice providers (APPs) (mainly representing nurse practitioners and physician assistants) experienced an

Distribution of diagnostic and therapeutic lumbar puncture procedures performed in 2010 and 2018, by specialty[a]

Year, Type of Procedure	Radiology	Interventional Radiology	Emergency	Neurology	Neurosurgery	Anesthesia	Advanced Practice Providers	Others
2010								
Total ($n = 92,579$)	40,129 (43.3)	2167 (2.4)	20,170 (21.8)	11,607 (12.5)	2960 (3.2)	3416 (3.7)	3388 (3.7)	8742 (9.4)
Diagnostic ($n = 86,347$)	38,675 (44.8)	2060 (2.4)	20,124 (23.3)	10,814 (12.5)	798 (0.9)	2415 (2.8)	3289 (3.8)	8172 (9.5)
Therapeutic ($n = 6232$)	1454 (23.3)	107 (1.7)	46 (0.7)	793 (12.7)	2162 (34.7)	1001 (16.1)	99 (1.6)	570 (9.2)
2018								
Total ($n = 92,533$)	43,955 (47.5)	4459 (4.8)	14,153 (15.3)	8126 (8.8)	2909 (3.2)	2228 (2.4)	7785 (8.4)	8918 (9.6)
Diagnostic ($n = 85,665$)	42,376 (49.5)	4187 (4.9)	14,063 (16.4)	7426 (8.7)	603 (0.7)	1362 (1.6)	7380 (8.6)	8268 (9.6)
Therapeutic ($n = 6868$)	1579 (23.0)	272 (3.9)	90 (1.3)	700 (10.2)	2306 (33.6)	866 (12.6)	405 (5.9)	650 (9.5)

[a] Data are number (%) of procedures.

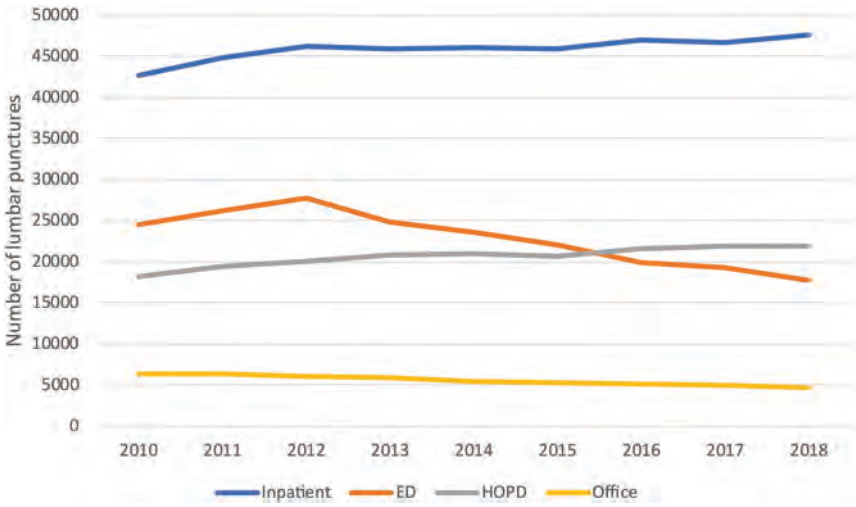

FIG 3. Lumbar puncture procedures in the United States from 2010 to 2018, by place of service performed. HOPD indicates hospital outpatient department.

increase in the overall procedure share from 3.7% in 2010 to 8.4% in 2018 (3388 LPs in 2010 versus 7785 LPs in 2018; +129.8% procedure volume). Besides radiologists, the 2 other major physician groups performing LPs include emergency medicine physicians and neurologists. Emergency medicine physicians and neurologists had a decrease in total numbers and procedure share during the past decade (21.8% versus 15.3%, and 12.5% versus 8.8%, respectively). Besides, a substantial number of total LPs were performed by various known and unknown providers, summarized as "others." Known specialties in this category include internal, pulmonary, and critical care medicine, which performed 4701 LPs in 2018 combined, correlating with a 5.1% procedure share.

Neurosurgery continued to be the leading provider for therapeutic LPs throughout the decade (2306 LPs in 2018, procedure share of 33.6%), followed by radiologists (1851 LPs in 2018, procedure share of 26.9%). The Table demonstrates the distribution of diagnostic and therapeutic LP procedures performed by specialty for 2010 and 2018.

By far, most of the LP procedures were performed in the inpatient hospital setting (42,685 in 2010 versus 47,533 in 2018), with a 5.3% increase in procedure share during the decade (Fig 3). The LP procedure volume in the ED has drastically decreased, recording a 7.4% decrease in the overall procedure share (24,519 in 2010 versus 17,701 in 2018; –27.8% procedure volume). Last, in hospital outpatient departments, the procedure volume has progressively increased (18,200 in 2010 versus 21,889 in 2018), while the private office volume has steadily decreased (6287 in 2010 versus 4672 in 2018).

Figure 4 illustrates the overall procedure share changes by specialty. From 2010 to 2018, the market share for radiologists/interventional radiologists and APPs has increased for diagnostic LPs, while it has declined the most for emergency medicine physicians and neurologists. For therapeutic LPs, neurosurgery keeps the largest market share (33.6% in 2018, a −1.1% decrease), followed by radiology (26.9% in 2018, a +1.9% increase); however, within the radiology subgroup, interventional radiologists have increased their procedure share for therapeutic LPs (3.9% in 2018, a 2.2% increase), while for noninterventional radiologists, the procedure share remained relatively stable (23.0% in 2018, a 0.3% decrease).

DISCUSSION

Kroll et al[1] demonstrated that between 1991 and 2011, LP procedures on Medicare beneficiaries have increased, with radiology becoming the dominant overall provider. While this previous study depicted a roughly 4-fold increase of the LP procedure share for radiologists during 2 decades, the present study shows smaller differences but a continuation of this trend and changes in procedure shares among physician and nonphysician groups.

Although being already the dominant overall provider at the beginning of the previous decade, interventional and noninterventional radiologists combined had the largest procedure share increase during the past 9 years of all groups. This contrasts with many other areas of image-guided procedures in which "turf wars" continue to emerge among different specialties, often to the disadvantage of radiologists.[8] Various minimally invasive procedures, originally developed and performed by radiologists, such as coronary angiography, neurointerventional procedures, or noncardiac peripheral vascular interventions, are now mainly performed by other specialists, including cardiologists, neurosurgeons, and vascular surgeons.[9-11]

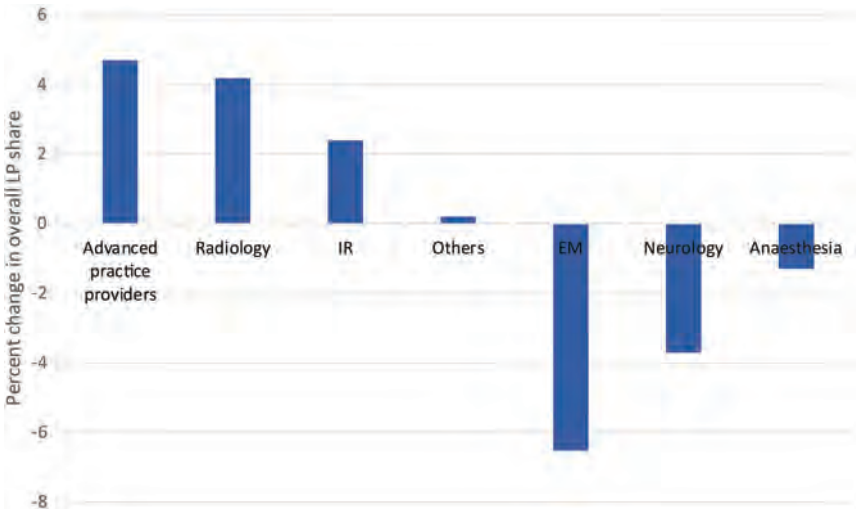

FIG 4. Overall lumbar puncture procedure share changes from 2010 to 2018 by provider specialty. IR indicates interventional radiology; EM, emergency medicine.

Even though there is a provider specialty shift toward radiologists, the underlying reasons leading to this development are likely not solely attributable to the advantages of image guidance or the growing of radiologists' expertise. LPs are time-consuming procedures with relatively low reimbursement rates. In 2018, the national average Medicare physician payment for a diagnostic LP performed was $64.30, and for a therapeutic LP, it was $69.55. In contrast, the Medicare payment for reporting a brain MR imaging with and without contrast was $128.60, and for a lumbar spine MR imaging without contrast, it was $96.58. Additionally, to be able to perform image-guided LPs, other resources such as a fluoroscopy/CT system and a radiology technologist are required. A similar development has been shown with paracentesis and thoracentesis procedures, for which radiologists became the main provider during the past decades,[12] in part due to unfavorable economics that are comparable with that of LP procedures. Simultaneously, the demand for productivity and workload has increased for radiologists and clinicians alike,[13-16] contributing to the relatively low-paid/time-consuming procedures, which could further aggravate stress in daily clinical practice, being, instead, referred to other services.

Nevertheless, this trend also offers distinct opportunities for radiologists. While there is no doubt that radiology services are indispensable to the care of patients, concerns about a prestige problem have been raised in the past by various leaders in the field,[17] and there is broad agreement that it is crucial for the future of radiology to have more direct patient contact. This concept can contain different aspects of patient-centered care and, depending on the subspecialty, may include minimally invasive procedures, outpatient care, or better communication with the patient.[18,19] Furthermore, by reinforcing their role in patient care, radiologists can improve their reputation and strengthen relationships with referring providers.[20]

Another emerging trend demonstrated in this study is the marked increase in procedure shares among APPs. APPs recorded the largest rise in procedure shares among all groups when radiologists and interventional radiologists are considered separately. Likewise, the overall procedure shares of APPs in 2018 are only minimally lower compared with those of neurologists, a previously dominant specialty for LPs. This practice is concurrent with developments described for other procedures such as paracentesis, thoracentesis, fine-needle aspirations and biopsies, and reported nationwide performances of nonvascular invasive procedures by APPs of between approximately 1% and 11%.[21] Reasons for this change are multifactorial, with the progressing physician shortage certainly playing a major role.[22] This trend is likely going to continue, especially with the growing acceptance and comparable procedure outcomes between trained APPs and physicians.[21,23,24]

After a peak in 2012, there has been a steady decline in the performance of LP procedures in EDs. During the previous decades, overcrowding in EDs has become a well-known reality,[25,26] and an increasing number of ED visits has likely further aggravated this situation.[27] Therefore, the development observed in our study might be a reflection of increased demand for throughput in EDs. This change represents a reversal of earlier decade trends, which showed a marked increase of LP procedures in EDs.[1] A decrease in the length of a hospital stay for many diseases/conditions may contribute to an accelerated transfer from the ED to the inpatient setting and the observed increase of inpatient LPs. Outpatient LPs are predominantly performed in the hospital outpatient department setting, which demonstrated steady growth, a development that led to more LPs being performed in the hospital outpatient department setting from 2016 onward than in the ED. Finally, a decreasing number of LPs were performed in private offices during the past decade; however, this represents a continuation of earlier decade trends.[1]

Limitations of this study include, besides its retrospective nature, that Physician/Supplier Procedure Summary Master Files only pertain to the Medicare Part B Fee-for-Service population and our study results are not generalizable because patients with coverage from other federal programs, private health insurance, or those uninsured are not included. Nevertheless, the Physician/Supplier Procedure Summary Master Files are frequently used for this type of study because they are the largest and most reliable data source. Also, due to the increasing share of LPs performed by APPs, the overall percentages for major specialties could be affected if a different number of APPs work under the aegis of supervising specialty groups. However, although LPs performed by APPs are increasing, it is questionable whether they cause significant differences among specialties yet, and they should not account for the observed trends in this study. Further investigations are needed to determine a potential relation between LP procedure shares and the number of APPs working under different specialties.

CONCLUSIONS

The LP procedure volume remained stable during the past decade, with a shift in procedure volume from the ED and private offices to the hospital setting. Radiologists continue to be the dominant provider with a further increase in procedure shares for both noninterventional and interventional radiologists. Besides radiologists, APPs experienced a large increase in procedure volume, which reflects nationwide trends for other nonvascular invasive procedures performed by APPs.

REFERENCES

1. Kroll H, Duszak R Jr, Nsiah E, et al. **Trends in lumbar puncture over 2 decades: A dramatic shift to radiology.** *AJR Am J Roentgenol* 2015;204:15–19 CrossRef Medline
2. Brook AD, Burns J, Dauer E, et al. **Comparison of CT and fluoroscopic guidance for lumbar puncture in an obese population with prior failed unguided attempt.** *J Neurointerv Surg* 2014;6:324–28 CrossRef Medline
3. Soni NJ, Franco-Sadud R, Schnobrich D, et al. **Ultrasound guidance for lumbar puncture.** *Neurol Clin Pract* 2016;6:358–68 CrossRef Medline
4. Costerus JM, Brouwer MC, van de Beek D. **Technological advances and changing indications for lumbar puncture in neurological disorders.** *Lancet Neurol* 2018;17:268–78 CrossRef Medline
5. Eskey CJ, Ogilvy CS. **Fluoroscopy-guided lumbar puncture: decreased frequency of traumatic tap and implications for the assessment of CT-negative acute subarachnoid hemorrhage.** *AJNR Am J Neuroradiol* 2001;22:571–76 Medline
6. Hales CM, Fryar CD, Carroll MD, et al. **Trends in obesity and severe obesity prevalence in US youth and adults by sex and age, 2007-2008 to 2015-2016.** *JAMA* 2018;319:1723–25 CrossRef Medline
7. Hudgins PA, Fountain AJ, Chapman PR, et al. **Difficult lumbar puncture: pitfalls and tips from the trenches.** *AJNR Am J Neuroradiol* 2017;38:1276–83 CrossRef Medline
8. Bello J. **Turf issues in radiology and its subspecialties.** *Neuroimaging Clin N Am* 2012;22:411–19 CrossRef Medline
9. Baum RA, Baum S. **Interventional radiology: a half century of innovation.** *Radiology* 2014;273:S75–91 CrossRef Medline
10. Veith FJ. **A look at the future of vascular surgery.** *J Vasc Surg* 2016;64:885–90 CrossRef Medline
11. Choke E, Sayers R. **Viewpoint: adaptation of vascular surgery in the interventional era.** *Heart* 2015;101:342–45 CrossRef Medline
12. Duszak R Jr, Chatterjee AR, Schneider DA. **National fluid shifts: fifteen-year trends in paracentesis and thoracentesis procedures.** *J Am Coll Radiol* 2010;7:859–64 CrossRef Medline
13. Chetlen AL, Chan TL, Ballard DH, et al. **Addressing burnout in radiologists.** *Acad Radiol* 2019;26:526–33 CrossRef Medline
14. Fiscella K, Epstein RM. **So much to do, so little time: care for the socially disadvantaged and the 15-minute visit.** *Arch Intern Med* 2008;168:1843–52 CrossRef Medline
15. Watson AG, McCoy JV, Mathew J, et al. **Impact of physician workload on burnout in the emergency department.** *Psychol Health Med* 2019;24:414–28 CrossRef Medline
16. Nassar AK, Waheed A, Tuma F. **Academic clinicians' workload challenges and burnout analysis.** *Cureus* 2019;11:e6108 CrossRef Medline
17. Levin DC, Rao VM. **Radiology's image problem: ponder the words of some thought leaders in the field.** *J Am Coll Radiol* 2008;5:616–18 CrossRef Medline
18. European Society of Radiology 2009. **The future role of radiology in healthcare.** *Insights Imaging* 2010;1:2–11 CrossRef Medline
19. Siskin G. **Outpatient care of the interventional radiology patient.** *Semin Intervent Radiol* 2006;23:337–45 CrossRef Medline
20. Boland GW. **Visibility of radiologists: Helping to secure your future.** *AJR Am J Roentgenol* 2009;192:1373–74 CrossRef Medline
21. Duszak R Jr, Walls DG, Wang JM, et al. **Expanding roles of nurse practitioners and physician assistants as providers of nonvascular invasive radiology procedures.** *J Am Coll Radiol* 2015;12:284–89 CrossRef Medline
22. Kirch DG, Petelle K. **Addressing the physician shortage: the peril of ignoring demography.** *JAMA* 2017;317:1947–48 CrossRef Medline
23. Murphy FB, Walls G, Tridandapani S, et al. **Comparison of image-guided nonfocal hepatic biopsies performed by physicians and nurse midlevel providers.** *J Am Coll Radiol* 2014;11:1059–63 CrossRef Medline
24. Gilani N, Patel N, Gerkin RD, et al. **The safety and feasibility of large volume paracentesis performed by an experienced nurse practitioner.** *Ann Hepatol* 2009;8:359–63 CrossRef Medline
25. Dickinson G. **Emergency department overcrowding.** *CMAJ* 1989;140:270–71 Medline
26. Trzeciak S, Rivers EP. **Emergency department overcrowding in the United States: an emerging threat to patient safety and public health.** *Emerg Med J* 2003;20:402–05 CrossRef Medline
27. Lane BH, Mallow PJ, Hooker MB, et al. **Trends in United States emergency department visits and associated charges from 2010 to 2016.** *Am J Emerg Med* 2020;38:1576–81 CrossRef Medline

Celebrating 35 Years of the AJNR

January 1986 edition

Magnetic Resonance Demonstration of Normal CSF Flow

John L. Sherman[1, 2]
Charles M. Citrin[1, 3]

The magnetic resonance (MR) imaging appearance and incidence of flowing cerebrospinal fluid (CSF) in the brain were investigated. The MR scans of 46 randomly selected patients with normal examinations were retrospectively reviewed. All patients were studied using both T2-weighted and T1-weighted spin-echo pulse sequences. Thirty-one patients (67%) had decreased intensity in the aqueduct of Sylvius on the T2-weighted images when compared with the intensity of CSF in the lateral ventricles. This was termed the *CSF flow-void sign*. The feature was present in the caudal fourth ventricle in 15 patients (32%) and in the third ventricle in two patients (4%) on T2-weighted scans. It was seen in only 13% of patients on T1-weighted scans. It is believed the CSF flow-void sign represents pulsatile CSF flow. Its recognition is important because it explains the inhomogeneity in the appearance of the CSF, which could be confused with pathologic processes. It may be valuable in the routine evaluation of MR examinations if it does reflect CSF circulatory dynamics.

Magnetic resonance imaging (MRI) has demonstrated the ability to generate striking anatomic images of the brain that were previously seen only by the neurosurgeon or pathologist. Several previous reports have also detailed the appearance of flowing blood on magnetic resonance (MR) images. Rapidly flowing or turbulent blood has been described as having decreased signal [1–3]. We have observed a similar appearance caused by flowing cerebrospinal fluid (CSF) in the aqueduct of Sylvius, the fourth ventricle, and occasionally in the posterior third ventricle and the foramina of Monro. To our knowledge, this is the first report of the use of MRI to study CSF flow.

Materials and Methods

The MR images of 46 subjects with normal ventricles were randomly chosen from our files and subjected to retrospective analysis. The patients were 23–65 years old (average, 40 years). There were 25 men and 21 women. Thirty-two of the patients were referred for MRI of the brain while 14 were referred for cervical MRI.

MR examinations were made via a single-echo eight or 16 multislice technique on a 0.5 T superconductive magnet (Vista-MR, Picker International, Highland Heights, OH). All studies were done using both T2-weighted and T1-weighted pulse sequences. T2-weighted sequences were done with an echo time (TE) of 80 or 100 msec and a repetition time (TR) of 1500–4500 msec. T1-weighted sequences used a TE of 30 or 40 msec with a TR of 500–850 msec. The CSF appears hyperintense relative to brain on T2-weighted sequences and hypointense relative to brain on T1-weighted sequences. All patients were scanned in at least two planes. Contiguous sections were obtained at 5 mm intervals in all patients.

The CSF spaces were examined by the authors for the presence of areas of decreased intensity relative to the CSF in the lateral ventricles, which we term the *CSF flow-void sign*. The sign was specifically noted as present or absent in the aqueduct of Sylvius, the fourth ventricle, and the third ventricle. If the sign was present in the fourth ventricle, its location was described. Both T2-weighted images and T1-weighted images were evaluated. Observations were made on transverse, coronal, and sagittal projections.

Received July 3, 1985; accepted after revision August 26, 1985.

[1] Magnetic Imaging of Washington, 5550 Friendship Blvd., Chevy Chase, MD 20815. Address reprint requests to J. L. Sherman.

[2] Department of Radiology, Uniformed Services University of the Health Sciences, Bethesda, MD 20814.

[3] Department of Radiology, George Washington University School of Medicine, Washington, DC 20037

AJNR 7:3–6, January/February 1986
0195–6108/86/0701–0003

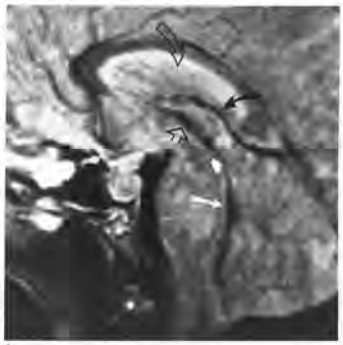

1

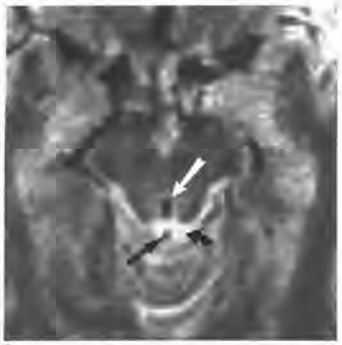

2

Periventricular Hyperintensity as Seen by Magnetic Resonance: Prevalence and Significance

Robert D. Zimmerman[1]
Cynthia A. Fleming
Benjamin C. P. Lee
Leslie A. Saint-Louis
Michael D. F. Deck

Periventricular hyperintensity was identified using long repetition and echo times in spin-echo magnetic resonance imaging of patients with white-matter disease (e.g., multiple sclerosis) caused by local demyelination and in hydrocephalic patients caused by transependymal migration of spinal fluid. A review of 365 consecutives studies revealed that some degree of periventricular hyperintensity is present in most patients (93.5%) regardless of diagnosis. Mild periventricular hyperintensity was seen in patients with no other evidence of intracranial pathology. Periventricular hyperintensity is a normal finding that should not be considered indicative of either demyelinating disease or hydrocephalus. More extensive and severe periventricular hyperintensity is associated with intracerebral pathology, but the finding often is nonspecific. For example, mild periventricular edema from hydrocephalus is impossible to differentiate from the increased periventricular hyperintensity seen in patients with multiple white-matter lesions. Thus, the pattern of periventricular hyperintensity has proven to be of limited value in the clinical assessment of hydrocephalic patients.

One of the earliest and most impressive clinical applications of magnetic resonance imaging (MRI) has been in the evaluation of patients with multiple sclerosis [1–8] and other white-matter diseases [5] including subcortical atherosclerotic encephalopathy [5, 9], radiation necrosis [7], and systemic lupus erythematosus [10]. In these diseases focal and/or diffuse areas of supratentorial white-matter hyperintensity are commonly imaged adjacent to the ventricular lining. In patients with obstructive hydrocephalus MRI scans have demonstrated a smooth, hyperintense halo surrounding the ventricles believed to be indicative of edema from transependymal resorption of cerebrospinal fluid [2, 6, 7, 11]. Because focal and/or diffuse periventricular hyperintensity (PVH) seemed to be present in many patients with a variety of pathologic processes, and even in patients with otherwise normal examinations, a retrospective evaluation of the incidence and possible significance of PVH was undertaken.

Materials and Methods

We retrospectively evaluated MRI studies performed between October 1983 and April 1984 on a 0.5 T superconducting MR imager manufactured by the Technicare Corp. To be included in the study a transversely oriented spin-echo (SE) image with a repetition time (TR) of 1500 msec and echo time (TE) of 90 msec ("T2-weighted") of adequate quality had to be available for review. With this technique intraventricular spinal fluid was approximately isointense to white matter. All scans were obtained with a single-echo multislice technique. Clinical data were correlated with MR findings. A total of 365 cases were evaluated. The patients were 6–84 years of age (mean age, 42). Of the 365 cases, 17 were ≤ 10 years old, 27 were 11–20, 61 were 21–30, 72 were 31–40, 60 were 41–50, 65 were 51–60, 39 were 61–70, and 25 were ≥ 71. The gender distribution was roughly equal.

Five PVH patterns of increasing extent and intensity were delineated: (0) no PVH (fig. 1); (1) discontinuous PVH—rounded hyperintense foci seen at the angles of the frontal horns

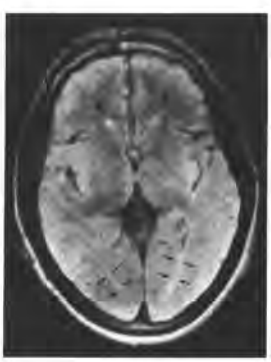

A

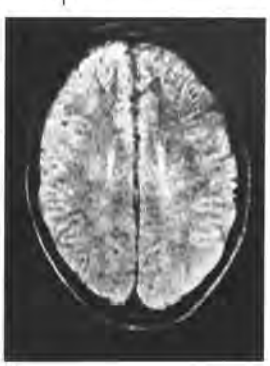

B